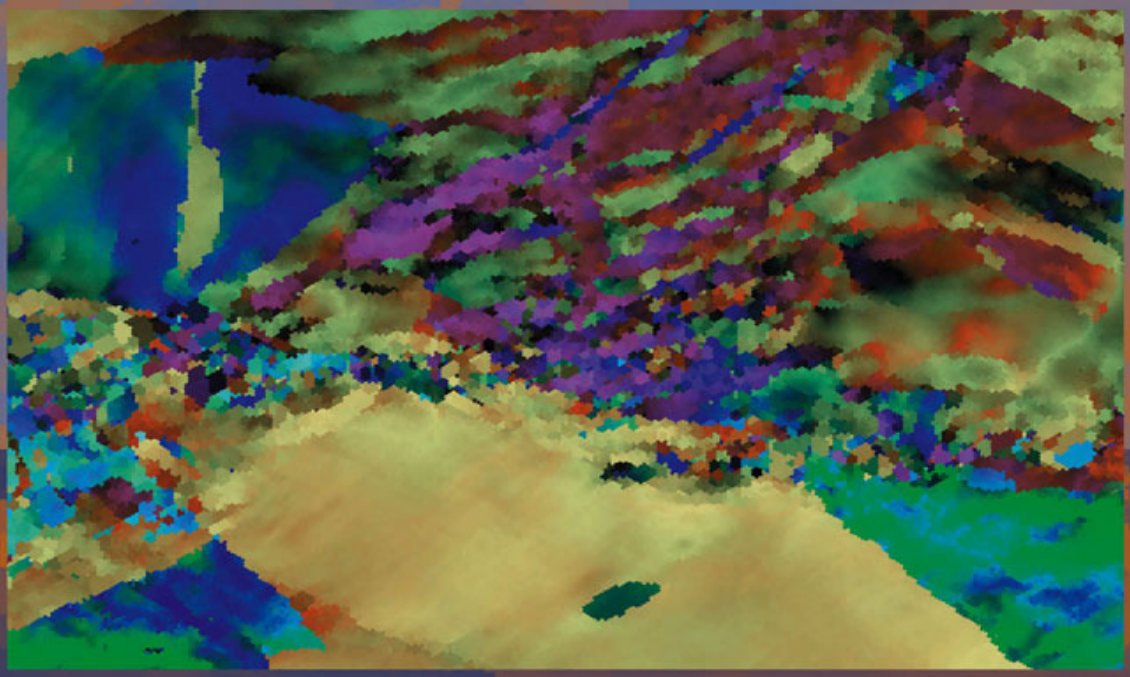
Adam J. Schwartz • Mukul Kumar • Brent L. Adams
David P. Field *Editors*

Electron Backscatter Diffraction in Materials Science



Second Edition

Springer

Electron Backscatter Diffraction in Materials Science

Second Edition

Adam J. Schwartz · Mukul Kumar ·
Brent L. Adams · David P. Field
Editors

Electron Backscatter Diffraction in Materials Science

Second Edition

Springer

Editors
Adam J. Schwartz
Lawrence Livermore National Laboratory
Physical and Life Sciences Directorate
7000 East Avenue
Livermore CA 94550
USA
schwartz6@llnl.gov

Mukul Kumar
Lawrence Livermore National Laboratory
Physical and Life Sciences Directorate
7000 East Avenue
Livermore CA 94550
USA
kumar3@llnl.gov

Brent L. Adams
Department of Mechanical Engineering
Brigham Young University
Provo UT 84602
455B Crabtree Technology Building
USA
b_l_adams@byu.edu

David P. Field
School of Mechanical and Materials
Engineering
Washington State University
Pullman WA 99164-2920
Dana 239E
USA
dfield@wsu.edu

First hard cover printing 2000, Kluwer Academic / Plenum Publishers

ISBN 978-0-387-88135-5
e-ISBN 978-0-387-88136-2
DOI 10.1007/978-0-387-88136-2

Library of Congress Control Number: 2009920955

© Springer Science+Business Media, LLC 2009
All rights reserved. This work may not be translated or copied in whole or in part without the written permission of the publisher (Springer Science+Business Media, LLC, 233 Spring Street, New York, NY 10013, USA), except for brief excerpts in connection with reviews or scholarly analysis. Use in connection with any form of information storage and retrieval, electronic adaptation, computer software, or by similar or dissimilar methodology now known or hereafter developed is forbidden.
The use in this publication of trade names, trademarks, service marks, and similar terms, even if they are not identified as such, is not to be taken as an expression of opinion as to whether or not they are subject to proprietary rights.

Printed on acid-free paper

springer.com

Contents

1 Present State of Electron Backscatter Diffraction and Prospective Developments **1**
Robert A. Schwarzer, David P. Field, Brent L. Adams, Mukul Kumar, and Adam J. Schwartz
1.1 Introduction 1
1.2 Generation and Interpretation of Electron Backscatter Diffraction Patterns 2
1.3 Experimental Set-Up of an EBSD System 3
1.4 The Components of an Automated EBSD System 4
1.4.1 The Pattern Acquisition Device 4
1.4.2 Mechanical Stage and Digital Beam Scanning 5
1.5 Spatial Resolution 7
1.6 SEM Specifications for Good EBSD Performance 9
1.7 The Radon or Hough Transformation for Band Localization . . . 11
1.8 Indexing 12
1.9 Fast EBSD 13
1.10 Ion Blocking Patterns 15
1.11 Conclusions 19

2 Dynamical Simulation of Electron Backscatter Diffraction Patterns **21**
Aimo Winkelmann
2.1 Introduction 21
2.2 Model of Electron Backscatter Diffraction 21
2.3 Dynamical Electron Diffraction in EBSD 22
2.3.1 Dynamical Electron Diffraction in EBSD 22
2.3.2 Dynamical Electron Diffraction in EBSD 23
2.3.3 Dynamical Electron Diffraction in EBSD 24
2.4 Applications 25
2.4.1 A Real-Space View of EBSD 25
2.4.2 Full Scale Simulation of EBSD Patterns 27
2.4.3 The Influence of the Energy Spectrum of the Backscattered Electrons 28
2.4.4 Dynamical Effects of Anisotropic Backscattering 30
2.5 Summary 32

3 Representations of Texture 35
Jeremy K. Mason and Christopher A. Schuh
3.1 Introduction 35
3.2 Rotations and Orientations 36
3.2.1 Defining a Rotation 36
3.2.2 Defining an Orientation 37
3.3 Pole Figures 38
3.4 Discrete Orientations 40
3.4.1 Axis-Angle Parameters 41
3.4.2 Rodrigues Vectors 42
3.4.3 Quaternions 42
3.4.4 Euler Angles 45
3.5 Orientation Distribution Functions 46
3.5.1 Circular Harmonics 46
3.5.2 Spherical Harmonics 47
3.5.3 Hyperspherical Harmonics 48
3.5.4 Generalized Spherical Harmonics 49
3.5.5 Symmetrized Harmonics 49
3.6 Conclusion 50

4 Energy Filtering in EBSD 53
Alwyn Eades, Andrew Deal, Abhishek Bhattacharyya, and Tejpal Hooghan
4.1 Introduction 53
4.2 Background 53
4.3 Energy Filters 54
4.4 Operating the Filter 56
4.5 Early Results 57
4.6 Patterns at Different Energies 60
4.7 Localization of the Signal 61
4.8 Future Energy Filters in EBSD 62
4.9 Summary and Conclusions 62

5 Spherical Kikuchi Maps and Other Rarities 65
Austin P. Day
5.1 Introduction 65
5.2 Electron Backscatter Patterns 65
5.3 Spherical Kikuchi Maps 65
5.4 EBSP Detectors 65
5.5 EBSP Imaging and Uniformity 68
5.6 EBSP Simulation 68
5.7 Spherical Kikuchi Maps from EBSPs 68
5.8 Kikuchi Band Profiles 72
5.9 Spherical Kikuchi Map Inversion 74
5.10 Uses for Spherical Kikuchi Maps 75
5.11 Colour Orientation Contrast Images 76
5.12 STEM in the SEM 76
5.13 Unusual Features in EBSPs 77

6 Application of Electron Backscatter Diffraction to Phase Identification 81
Bassem El-Dasher and Andrew Deal
6.1 Introduction 81
6.2 Considerations for Phase ID with EBSD 82
6.3 Case Studies 84
6.3.1 Simultaneous EBSD/EDS Phase Discrimination 85
6.3.2 Distinguishing γ and γ' in Ni Superalloys 86
6.3.3 Volume Fraction Determination in a Multiphase Alloy . . 89

7 Phase Identification Through Symmetry Determination in EBSD Patterns 97
David J. Dingley and S.I. Wright
7.1 Introduction 97
7.2 Basis of the Phase Identification Method 97
7.3 Determination of the Crystal Unit Cell 98
7.4 Discovering the Lattice Symmetry 100
7.5 Re-Indexing the Pattern According to the Discovered Crystal Class 101
7.6 Examples 102
7.6.1 Case 1, A Cubic Crystal 102
7.6.2 Case 2, A Hexagonal Crystal 104
7.6.3 Case 3, A Trigonal Crystal 104
7.7 Discussion 106

8 Three-Dimensional Orientation Microscopy by Serial Sectioning and EBSD-Based Orientation Mapping in a FIB-SEM 109
Stefan Zaefferer and Stuart I. Wright
8.1 Introduction 109
8.2 The Geometrical Set-Up for 3D Characterisation in a FIB-SEM . 110
8.3 Automatic 3D Orientation Microscopy 113
8.4 Software for 3D Data Analysis 113
8.5 Application Examples 114
8.5.1 The 3D Microstructure and Crystallography of Pearlite Colonies 114
8.5.2 Microstructure of “Nanocrystalline” NiCo Deposits . . . 115
8.6 Discussion 119
8.6.1 Accuracy and Application Limits 119
8.6.2 Materials Issues 120
8.7 Conclusions 120

9 Collection, Processing, and Analysis of Three-Dimensional EBSD Data Sets . . . 123
Michael A. Groeber, David J. Rowenhorst, and Michael D. Uchic
9.1 Introduction . . . 123
9.2 Data Collection . . . 123
9.3 Processing Strategies . . . 124
9.3.1 Registration and Alignment of Sections . . . 124
9.3.2 Segmentation of Grains . . . 126
9.3.3 Clean-Up Routines . . . 127
9.4 Analysis Capabilities . . . 129
9.4.1 Morphological Descriptors . . . 129
9.4.2 Crystallographic Descriptors . . . 133
9.5 Summary . . . 135

10 3D Reconstruction of Digital Microstructures . . . 139
Stephen D. Sintay, Michael A. Groeber, and Anthony D. Rollett
10.1 Motivation . . . 139
10.2 Background . . . 139
10.2.1 2D–3D Inference . . . 139
10.2.2 3D Polycrystal Microstructure Generation . . . 140
10.3 Data Collection and Analysis . . . 140
10.3.1 Data Sources . . . 140
10.3.2 Identifying Features . . . 141
10.3.3 Statistical Description of Features . . . 141
10.4 Methods for 3D Structure Inference . . . 141
10.4.1 Monte Carlo-Based Histogram Fitting . . . 143
10.4.2 Observation-Based Domain Constraint . . . 145
10.5 Generation of 3D Structure . . . 147
10.5.1 Packing of Ellipsoids . . . 147
10.5.2 Relaxation of Boundaries . . . 149
10.6 Quality Analysis . . . 149
10.6.1 Size Distribution Comparison . . . 149
10.6.2 Shape Distribution Comparison . . . 149
10.6.3 Neighborhood Comparison . . . 151
10.6.4 Boundary Structure Comparison . . . 151
10.7 Thoughts on Current Conditions and Future Work . . . 151

11 Direct 3D Simulation of Plastic Flow from EBSD Data . . . 155
Nathan R. Barton, Joel V. Bernier, Ricardo A. Lebensohn, and Anthony D. Rollett
11.1 Introduction . . . 155
11.2 Material and Microstructural Model . . . 156
11.2.1 Three-Dimensional Microstructure Generation . . . 157
11.2.2 Micromechanical Model . . . 158
11.2.3 Finite Element Model . . . 159
11.3 Simulation Results . . . 159
11.4 Directions for Further Computational Development . . . 162
11.5 Conclusions . . . 165

12 First-Order Microstructure Sensitive Design Based on Volume Fractions and Elementary Bounds 169
Surya R. Kalidindi, David T. Fullwood, and Brent L. Adams
12.1 Introduction 169
12.2 Quantification of Microstructure 170
12.3 Microstructure Sensitive Design Framework 170
12.4 Property Closures 172

13 Second-Order Microstructure Sensitive Design Using 2-Point Spatial Correlations 177
David T. Fullwood, Surya R. Kalidindi, and Brent L. Adams
13.1 Introduction 177
13.2 Definition and Properties of the 2-Point Correlation Functions . . 178
13.2.1 Boundary Conditions 179
13.2.2 Properties of the 2-Point Functions 179
13.2.3 Visualization of the 2-Point Functions 179
13.2.4 Metrics from 2-Point Correlations 180
13.2.5 Collecting 2-Point Correlations from Material Samples . 180
13.3 Structure Property Relations 181
13.3.1 Localization Tensors 182
13.3.2 Effective Tensors 184
13.4 Microstructure Design 186

14 Combinatorial Materials Science and EBSD: A High Throughput Experimentation Tool 189
Krishna Rajan
14.1 Introduction 189
14.2 Introduction to Combinatorial Methods 189
14.2.1 High Throughput EBSD Screening 190
14.2.2 Informatics and Data 194
14.3 Summary 196

15 Grain Boundary Networks 201
Bryan W. Reed and Christopher A. Schuh
15.1 Introduction 201
15.2 Measurement and Classification of Local Network Elements . . . 202
15.2.1 General Definitions for Single Boundaries 202
15.2.2 Structures with More than One Boundary 203
15.3 Geometry of the Network Structure 204
15.3.1 Percolation Measures of the Grain Boundary Network . . 205
15.3.2 Crystallographic Constraints 206
15.4 Microstructure-Property Connections 208
15.4.1 Composite Averaging vs. Percolation Theory 209
15.4.2 Crystallographic Correlations 211
15.5 Conclusions and Future Outlook 212

16 Measurement of the Five-Parameter Grain Boundary Distribution from Planar Sections 215
Gregory S. Rohrer and Valerie Randle
16.1 Introduction: Grain Boundary Planes and Properties 215
16.2 Serial Sectioning 216
16.3 Single-Surface Trace Analysis 217
16.4 Five-Parameter Stereological Analysis 218
16.4.1 Parameterization and Discretization of the Space of Grain Boundary Types 218
16.4.2 Measurement of the Grain Boundary Characterization Distribution 219
16.4.3 Performance of the Stereological Analysis 221
16.4.4 Comparison GBCDs Measured Stereologically and by Serial Sectioning in the Dual Beam FIB 223
16.5 Examples of Five-Parameter Analyses 224

17 Strain Mapping Using Electron Backscatter Diffraction 231
Angus J. Wilkinson, David J. Dingley, and Graham Meaden
17.1 Introduction 231
17.1.1 The Need for Local Strain Assessment 231
17.1.2 Competing Strain Mapping Techniques 231
17.1.3 Review of Applications of EBSD to Analysis of Elastic Strains 232
17.2 Cross-Correlation-Based Analysis of EBSD Patterns 234
17.2.1 Geometry: Linking Pattern Shifts to Strain 234
17.2.2 Pattern Shift Measurement 235
17.2.3 Sensitivity Analysis 237
17.2.4 Illustrative Applications 239
17.3 Concluding Remarks 247

18 Mapping and Assessing Plastic Deformation Using EBSD 251
Luke N. Brewer, David P. Field, and Colin C. Merriman
18.1 Plastic Deformation Effects on the EBSD Pattern and Orientation Map 251
18.2 Pattern Rotation Approaches 253
18.2.1 Mapping Orientations and Misorientations 253
18.2.2 Average Misorientation Approaches 255
18.2.3 Measurement and Calculation of GND Densities 258

19 Analysis of Deformation Structures in FCC Materials Using EBSD and TEM Techniques 263
Oleg V. Mishin, Andrew Godfrey, and Dorte Juul Jensen
19.1 Introduction 263
19.2 Orientation Noise in EBSD Data 265
19.2.1 A Quantitative Description of Orientation Noise 265
19.2.2 Postprocessing Orientation Filtering Operations 266
19.3 Quantitative TEM–EBSD Comparison 268
19.4 Heterogeneity in Microstructural Refinement 271

19.4.1 Analysis of Local Heterogeneity 271
19.4.2 Potential for Analysis of Large-Scale Heterogeneities . . 272
19.5 Summary and Conclusions 273

20 Application of EBSD Methods to Severe Plastic Deformation (SPD) and Related Processing Methods 277
Terry R. McNelley, Alexandre P. Zhilyaev, Srinivasan Swaminathan, Jianqing Su, and E. Sarath Menon
20.1 Introduction 277
20.2 Microstructures During the Initial ECAP Pass 278
20.3 Microstructures Developed by Machining 282
20.4 Grain Refinement During FSP 284
20.5 Conclusions 288

21 Applications of EBSD to Microstructural Control in Friction Stir Welding/Processing 291
Sergey Mironov, Yutaka S. Sato, and Hiroyuki Kokawa
21.1 Introduction 291
21.2 Brief Explanations of FSW/P Terminology 292
21.3 Microstructural Evolution 292
21.4 Material Flow 296
21.5 Structure-Properties Relationship 298
21.6 Summary and Future Outlook 299

22 Characterization of Shear Localization and Shock Damage with EBSD 301
John F. Bingert, Veronica Livescu, and Ellen K. Cerreta
22.1 Introduction 301
22.2 Shear Localization 302
22.2.1 Constrained Shear in Pure Fe—Shear Zone Geometry . . 302
22.2.2 Constrained Shear in Pure Fe—Texture Development . . 306
22.2.3 Effect of Morphology on Grain Instability in Cu 307
22.3 Shock Loading Damage in Tantalum 309
22.3.1 Effect of Shock Duration on Incipient Spall Structure . . 310
22.3.2 Effect of Pressure on Incipient Spall Structure 313
22.4 Conclusions 313

23 Texture Separation for α/β Titanium Alloys 317
Ayman A. Salem
23.1 Introduction 317
23.2 Microstructure of α/β Titanium Alloys 317
23.3 Texture of Ti-6Al-4V 318
23.3.1 Separation of Primary and Secondary Alpha Texture . . . 319
23.3.2 EBSD + BSE Imaging Technique 319
23.3.3 EBSD or XRD + Heat Treatment Technique 320
23.4 Texture Separation Using EBSD + EDS Technique 320
23.4.1 Texture Separation Using EBSD + EDS Technique 320
23.4.2 Microstructure Observations 321
23.4.3 Chemical Composition Maps (EDS) 321
23.5 Industrial Application: Controlling Texture During Hot-Rolling of Ti-6Al-4V 322

23.5.1 Microstructure Evolution . . . 323
23.5.2 Overall Texture Evolution . . . 323
23.5.3 Primary-Alpha (α_p) Textures . . . 324
23.5.4 Secondary-Alpha (α_s) Texture . . . 325
23.6 Industrial Application: Controlling Texture During Hot-Rolling of Ti-6Al-4V . . . 326

24 A Review of In Situ EBSD Studies . . . 329
Stuart I. Wright and Matthew M. Nowell
24.1 Introduction . . . 329
24.2 In Situ Postmortem Experiments . . . 330
24.3 Deformation Stage Experiments . . . 331
24.4 Heating Stage Experiments . . . 332
24.4.1 Phase Transformation . . . 332
24.4.2 Recrystallization and Grain Growth . . . 333
24.5 Combined Heating and Tensile Stage Experiments . . . 335
24.6 Conclusions . . . 335

25 Electron Backscatter Diffraction in Low Vacuum Conditions . . . 339
Bassem S. El-Dasher and Sharon G. Torres
25.1 Introduction . . . 339
25.2 Considerations for Low Vacuum EBSD . . . 340
25.3 Example Applications . . . 341
25.3.1 Microstructural Analysis of AlN-TiB_2 Ceramic Composite . . . 341
25.3.2 Characterization of $CaHPO_4 \cdot 2H_2O$ Single Crystals . . . 342

26 EBSD in the Earth Sciences: Applications, Common Practice, and Challenges . . . 345
David J. Prior, Elisabetta Mariani, and John Wheeler
26.1 Development of EBSD in Earth Sciences . . . 345
26.2 Current Practice, Capabilities, and Limitations . . . 346
26.2.1 Range of Materials and Preparation . . . 346
26.2.2 Speed of Data Collection . . . 347
26.2.3 Spatial Resolution . . . 347
26.2.4 Misindexing . . . 348
26.2.5 Polyphase Samples . . . 350
26.3 Application of EBSD in Earth Sciences . . . 351
26.3.1 Rock Deformation and Solid Earth Geophysics . . . 352
26.3.2 Metamorphic Processes . . . 355
26.3.3 Meteorites . . . 356
26.3.4 Other Areas . . . 356
26.4 Conclusions . . . 357

27 Orientation Imaging Microscopy in Research on High Temperature Oxidation 361
Bae-Kyun Kim and Jerzy A. Szpunar
27.1 Introduction 361
27.2 High Temperature Oxidation 362
27.3 Experimental Procedure 363
27.3.1 Oxidation of Samples and Oxide Formation 363
27.3.2 Sample Preparation and Geometry in OIM 364
27.3.3 Microstructure and Texture Measurement 365
27.3.4 Oxidation of Low Carbon Steel 365
27.4 Results and Discussion 368
27.4.1 Grain Growth in Iron Oxide 368
27.4.2 Effect of the Oxidation Process on Microstructure 371
27.4.3 Oxidation of Pure Iron 373
27.5 Cracks and Defects 384
27.6 Conclusion 390

Index 395

Contributors

Brent L. Adams Department of Mechanical Engineering, Brigham Young University, 455B CTB, Provo, UT 84602-4201, USA, b_l_adams@byu.edu

Nathan R. Barton Lawrence Livermore National Laboratory, L-129, 7000 East Avenue, Livermore, CA 94550, USA, barton22@llnl.gov

Joel V. Bernier Lawrence Livermore National Laboratory, L-129, 7000 East Avenue, Livermore, CA 94550, USA, bernier2@llnl.gov

Abhishek Bhattacharyya 1 Becton Drive, Franklin Lakes, NJ 07417 USA, abhatt72@yahoo.com

John F. Bingert Materials Science and Technology Division, Los Alamos National Laboratory, MST-8, MS G755, Los Alamos, NM 87545, USA, bingert@lanl.gov

Luke N. Brewer Sandia National Laboratories, New Mexico, PO Box 5800 MS 1411, Albuquerque, NM 87123-1411, USA, lnbrewe@sandia.gov

Ellen K. Cerreta Los Alamos National Laboratory, MST-8, MS G755, Los Alamos, NM 87545, USA, ecerreta@lanl.gov

Austin P. Day Aunt Daisy Scientific Ltd., Durlow, Dixton Road, Monmount, Gwent NP25 3PP; KE Developments, The Mount, Toft, Cambridge CB23 2RL, United Kingdom, auntdaisy@btinternet.com

Andrew Deal GE Global Research, One Research Circle, Niskayuna, NY 12309, USA, deal@research.ge.com

David J. Dingley H. H. Wills Physics Laboratory, Bristol University, Tyndall Avenue, Bristol BS8 1TL, United Kingdom, djdingley@hotmail.com

Alwyn Eades Department of Materials Science and Engineering, Lehigh University, 5 East Packer Avenue, Bethlehem, PA 18015-3195, USA, jae5@lehigh.edu

Bassem S. El-Dasher Lawrence Livermore National Laboratory, L-367, 7000 East Avenue, Livermore, CA 94550, USA, eldasher2@llnl.gov

David P. Field School of Mechanical and Materials Engineering, Washington State University, Dana 239E, Pullman, WA 99164-2920, USA, dfield@wsu.edu

David T. Fullwood Department of Mechanical Engineering, Brigham Young University, 435 CTB, Provo, UT 84602-4201, USA, dfullwood@byu.edu

Andy Godfrey Laboratory of Advanced Materials, Department of Materials Science and Engineering, Tsinghua University, Beijing 100084, China, awgodfrey@mail.tsinghua.edu.cn

Michael A. Groeber Wright Patterson Air Force Base, 2210 Tenth St. Building 655 Room 110, WPAFB, OH 45433, USA, michael.groeber.ctr@wpafb.af.mil

Tejpal Hooghan Texas Instruments Incorporated, 13536 North Central Expressway, Dallas, TX 75243, USA, thooghan@ti.com

Dorte Juul Jensen Risø National Laboratory for Sustainable Energy, Materials Research Department, Center for Fundamental Research: Metal Structures in Four Dimensions, Technical University of Denmark, Building 228, P.O. Box 49, DK-4000 Roskilde, Denmark, dorte.juul.jensen@risoe.dk, www.risoe.dk

Surya R. Kalidindi Department of Materials Science and Engineering, Drexel University, LeBow 346, 3141 Chestnut Street, Philadelphia, PA 19104, USA, skalidin@coe.drexel.edu

Bae-Kyun Kim Department of Mining and Materials Engineering, McGill University, Montreal, QC Canada; Corporate R&D Institute, Samsung Electro-Mechanics, Suwon, Kyungki-Do, Korea 443-743, baekyun.kim@yahoo.ca, baekyun.kim@samsung.com

Hiroyuki Kokawa Department of Materials Processing, Graduate School of Engineering, Tohoku University, 6-6-02 Aramaki-aza-Aoba, Aoba-ku Sendai 980-8579, Japan, kokawa@material.tohoku.ac.jp

Mukul Kumar Lawrence Livermore National Laboratory, L-356, 7000 East Avenue, Livermore, CA 94550, USA, kumar3@llnl.gov

Ricardo Lebensohn Los Alamos National Laboratory, MST-8, MS G755, Los Alamos, NM 87545, USA, lebenso@lanl.gov

Veronica Livescu Los Alamos National Laboratory, MST-8, MS G755, Los Alamos, NM 87545, USA, vlivescu@lanl.gov

Elisabetta Mariani Department of Earth and Ocean Sciences, University of Liverpool, Liverpool L69 3GP, United Kingdom, mariani@liverpool.ac.uk

Jeremy K. Mason Department of Materials Science and Engineering, Massachusetts Institute of Technology, Cambridge, MA 02139, USA, jkmason@mit.edu

Terry R. McNelley Department of Mechanical and Astronautical Engineering, Naval Postgraduate School, 700 Dyer Road, Monterey, CA 93943-5146, USA, tmcnelley@nps.edu

Graham Meaden BLG Productions Ltd., 3 Sydenham Road, Briston BS6 5SH, United Kingdom, grahammeaden@blueyonder.co.uk

E.S. Menon Department of Mechanical and Astronautical Engineering, Naval Postgraduate School, 700 Dyer Road, Monterey, CA 93943-5146, USA, skmeno1@nps.edu

Colin C. Merriman School of Mechanical and Materials Engineering, Washington State University, PO Box 642920, Pullman, WA 99164-2920, USA, merrimac@wsu.edu

Sergey Mironov Department of Materials Processing, Graduate School of Engineering, Tohoku University, 6-6-02 Aramaki-aza-Aoba, Aoba-ku Sendai 980-8579, Japan, smironov@material.tohoku.ac.jp

Oleg V. Mishin Risø National Laboratory for Sustainable Energy, Materials Research Department, Center for Fundamental Research: Metal Structures in Four Dimensions, Technical University of Denmark, DK-4000 Roskilde, Denmark, oleg.mishin@risoe.dk

Matthew M. Nowell EDAX-TSL, 392 East 12300 South, Suite H, Draper, UT 84020, USA, Matt.Nowell@ametek.com

David J. Prior Department of Earth and Ocean Sciences, University of Liverpool, Liverpool L69 3GP, United Kingdom, davep@liv.ac.uk

Krishna Rajan Department of Materials Science and Engineering, Iowa State University, 2220 Hoover, Ames, IA 50011-2300, USA, krajan@iastate.edu

Valerie Randle School of Engineering, Materials Research Centre, Swansea University, Singleton Park, Swansea SA2 8PP, United Kingdom v.randle@swansea.ac.uk

Bryan W. Reed Lawrence Livermore National Laboratory, L-356, 7000 East Avenue, Livermore, CA 94550, USA, reed12@llnl.gov

Gregory S. Rohrer Department of Materials Science and Engineering, Carnegie Mellon University, 5000 Forbes Avenue, Weh 3325, Pittsburgh, PA 15213, USA, gr20@andrew.cmu.edu

Anthony D. Rollett Department of Materials Science and Engineering, Carnegie Mellon University, 5000 Forbes Avenue, Reh 148, Pittsburgh, PA 15213, USA, rollett@andrew.cmu.edu

David J. Rowenhorst The United States Naval Research Laboratory, Code 6355, Washington, DC 20375, USA, david.rowenhorst@nrl.navy.mil

Ayman A. Salem Wright Patterson Air Force Base, 2210 Tenth St. Building 655 Room 053, WPAFB, OH 45433, USA, ayman.salem@wpafb.af.mil

Yutaka S. Sato Department of Materials Processing, Graduate School of Engineering, Tohoku University, 6-6-02 Aramaki-aza-Aoba, Aoba-ku Sendai 980-8579, Japan, ytksato@material.tohoku.ac.jp

Christopher A. Schuh Department of Materials Science and Engineering, Massachusetts Institute of Technology, Cambridge, MA 02139, USA, schuh@mit.edu

Adam J. Schwartz Lawrence Livermore National Laboratory, L-352, 7000 East Avenue, Livermore, CA 94550, USA, schwartz6@llnl.gov

Robert A. Schwarzer Institute of Physics, Clausthal University of Technology, D-38678 Clausthal-Zellerfeld, Germany, post@robert-schwarzer.de

Stephen D. Sintay Department of Materials Science and Engineering, Carnegie Mellon University, 5000 Forbes Ave. Roberts Hall Room 148, Pittsburgh, PA 15213, USA, ssintay@andrew.cmu.edu

J.-Q Su Naval Postgraduate School, 700 Dyer Road, Monterey, CA 93943-5146, USA, jsu@nps.edu

S. Swaminathan General Electric Co, Bangalore, India, srinivasan.swaminathan@ge.com

Jerzy A. Szpunar Department of Mining and Materials Engineering, McGill University, 3610 University St., Montreal, QC, Canada H3A 2B2, jerzy.szpunar@mcgill.ca

Sharon G. Torres Lawrence Livermore National Laboratory, L-344, 7000 East Avenue, Livermore, CA 94550, USA, torres4@llnl.gov

Michael D. Uchic Wright Patterson Air Force Base, 2210 Tenth St. Building 655 Room 076, WPAFB, OH 45433, USA, michael.uchic@wpafb.af.mil

John Wheeler Department of Earth and Ocean Sciences, University of Liverpool, Liverpool L69 3GP, United Kingdom, johnwh@liverpool.ac.uk

Angus J. Wilkinson Department of Materials, University of Oxford, Parks Road, Oxford OX1 3PH, United Kingdom, angus.wilkinson@materials.ox.ac.uk

Aimo Winkelmann Max-Planck-Institut für Mikrostrukturphysik, Weinberg 2, D-06120 Halle, Germany, winkelm@mpi-halle.mpg.de

Stuart I. Wright EDAX-TSL, 392 East 12300 South, Suite H, Draper, UT 84020, USA, Stuart.Wright@ametek.com

Stefan Zaefferer Max-Planck-Institute for Iron Research, Max-Planck-Straße 1, D-40237 Düsseldorf, Germany, s.zaefferer@mpie.de

Alexander Zhilyaev Institute for Metals Superplasticity Problems, Ufa, 450001 Russia and Centro Nacional de Investigaciones Metalurgicas, Madrid 28040, Spain, zhilyaev@cenim.csic.es, AlexZ@anrb.ru

Abbreviations

1D	1-dimensional
2D	2-dimensional
3D	3-dimensional
AD	analog-to-digital
ADC	arbitrary defined cell
ADR	adaptive mesh refinement
AMIS	average intragrain misorientation
ARB	accumulative roll bonding
AS	advancing side
B/T	basal/transverse
BCC	body centered cubic
BEKD	backscatter electron Kikuchi diffraction
BEKP	backscatter electron Kikuchi pattern
BF	bright field
BKD	backscatter Kikuchi diffraction
BKP	backscatter Kikuchi pattern
BSE	backscatter electron
CA	Cellular Automata
CA	compression axis
CBED	convergent beam electron diffraction
CCD	charge coupled device
CD	crystal deformation
CD	crystal direction
CDF	cumulative distribution function
CFD	chip flow direction
CI	confidence index
CIND	crystallographic interface normal distribution
CIP	computer integrated polarization
COCI	color orientation contrast image
CPO	crystallographic preferred orientations
CSL	coincident site lattice
DA	digital-to-analog
DF	dark field

EBSD	electron backscatter diffraction
EBSP	electron backscatter pattern
ECAE	equal channel angular extrusion
ECAP	equal channel angular pressing
ECP	electron channeling patterns
ED	extrusion direction
EDM	electric discharge machining
EDS	energy dispersive spectroscopy
EDX	energy dispersive x-ray spectroscopy
EM	edge milling
EPMA	electron probe microanalyzer
ESEM	environmental SEM
ESR	equivalent sphere radius
FCC	face-centered cubic
FE	field emission
FE	finite element
FEGSEM	field emission gun SEM
FEM	finite element method
FESEM	field emission SEM
FFT	fast Fourier transform
FIB	focused ion beam
FSP	friction stir processing
FSW	friction stir welding
FSW/P	friction stir welding/processing
FZ	fundamental zone
GAM	grain average misorientation
GB	grain boundary
GD	growth direction
GEM	generalized effective medium
GHAB	general high angle boundary
GND	geometrically necessary dislocations
GOS	grain orientation spread
GSH	generalized spherical harmonics
HAB	high angle boundary
HAGB	high angle grain boundary
HCP	hexagonal close packed
HMR	high misorientation region
HOLZ	higher order Laue zones
HPT	high-pressure torsion
IBP	ion blocking pattern
ICDD	International Centre of Diffraction Data
ICSD	inorganic crystal structure database
ID	identification
IMD	integrated angular misorientation density

IMD	intragranular misorientation deviation
IND	interface normal distribution
IPF	inverse pole figure
IQ	image quality
ITO	indium tin oxide
KAM	kernal average misorientation
kV	kilovolts
LAB	low angle boundary
LAGB	low angle grain boundary
LC	low carbon
LD	long duration
LEED	low-energy electron diffraction
LMR	low misorientation region
LPO	lattice preferred orientation
LSEM	large-strain extrusion machining
LV-EBSD	low-vacuum EBSD
MC	Monte Carlo
MCD	modified crystal deformation
MIMS	mesoscale interface mapping system
MODF	misorientation distribution function
MRD	multiples of random distribution
MSD	microstructure sensitive design
MSMV	maximum subgrid – minimum variance
ND	normal direction
OCF	orientation correlation function
ODF	orientation distribution function
OFHC	oxygen free high conductivity
OIM	orientation imaging microscopy
PC	principal component
PC	personal computer
PCA	principal component analysis
PDF	powder diffraction file
PDF	pair distribution function
PF	pole figure
PQ	pattern quality
PSN	particle-stimulated nucleation
RD	rolling direction
RFN	rake face normal
RHEED	reflection high-energy electron diffraction
RMS	root mean square
RS	retreating side
RVE	representative volume element
SACP	selected area channeling pattern
SAECP	selected area electron channeling patterns

SD	shear direction
SD	short duration
SE	secondary electron
SEM	scanning electron microscope
SIT	silicon intensified target
SKM	spherical Kikuchi map
SM	surface milling
SOS	scalar orientation spread
SPD	severe plastic deformation
SPN	shear plane normal
SSD	statistically stored dislocations
STEM	scanning transmission electron microscope
SZ	stir zone
SZ	shear zone
T	transverse
TCP	tetrahedrally close packed
TD	transverse direction
TEM	transmission electron microscope
TMAZ	thermomechanically affected zone
TMP	thermomechanical processing
TRD	twin related domain
UHV	ultra high vacuum
WD	welding direction
WDS	wavelength dispersive spectroscopy
XRD	x-ray diffraction
YAG	yttrium aluminum garnet

Chapter 1

Present State of Electron Backscatter Diffraction and Prospective Developments

Robert A. Schwarzer, David P. Field, Brent L. Adams, Mukul Kumar, and Adam J. Schwartz

1.1 Introduction

Electron backscatter diffraction (EBSD), when employed as an additional characterization technique to a scanning electron microscope (SEM), enables individual grain orientations, local texture, point-to-point orientation correlations, and phase identification and distributions to be determined routinely on the surfaces of bulk polycrystals. The application has experienced rapid acceptance in metallurgical, materials, and geophysical laboratories within the past decade (Schwartz et al. 2000) due to the wide availability of SEMs, the ease of sample preparation from the bulk, the high speed of data acquisition, and the access to complementary information about the microstructure on a submicron scale. From the same specimen area, surface structure and morphology of the microstructure are characterized in great detail by the relief and orientation contrast in secondary and backscatter electron images, element distributions are accessed by energy dispersive spectroscopy (EDS), wavelength dispersive spectroscopy (WDS), or cathodoluminescence analysis, and the orientations of single grains and phases can now be determined, as a complement, by EBSD.

The first observation of a diffraction pattern in backscattering mode was reported in 1928 by Nishikawa and Kikuchi in the same volume where transmission electron microscopy (TEM) Kikuchi patterns were discussed (Nishikawa and Kikuchi 1928). The researchers placed a recording film to capture the pattern in transmission, and then placed a film in front of the specimen so as to obtain an image from backscattered electrons. This technique was discussed in detail by Alam, Blackman, and Pashley in 1954 (Alam et al. 1954) and later investigated by Venables and co-workers (Venables and Harland 1973; Venables and Bin-Jaya 1977). The early literature dubbed the technique high-angle Kikuchi diffraction and it has been referred to by several additional acronyms in the past two decades. Those that are most notable, other than EBSD, include the more accurate nomenclature of backscatter Kikuchi diffraction (BKD) or backscatter electron Kikuchi diffraction (BEKD). (*Note: Acronyms of EBSP, BKP and BEKP are also common in literature and these refer specifically to the image formed by the diffraction technique—i.e., electron backscatter diffraction* ***pattern***.) The terms "electron backscatter diffraction" and "backscatter Kikuchi diffraction" are often used interchangeably in the literature.

Fully automated EBSD has developed into a mature alternative to X-ray pole figure measurements in quantitative texture analysis without such constraints as ghost problems, defocusing effects, or inconsistent data as a consequence of specimen tilts through large angles. Moreover, automated EBSD has opened new horizons in quantitative texture analysis because of its outstanding high spatial resolution, its access to orientation correlations and orientation stereology, its high speed, and its ability to represent the texture and grain boundary character distribution visually and quantitatively via an orientation map. Because SEMs and commercial EBSD systems are readily available, electron backscatter diffraction is no longer an academic technique

R.A. Schwarzer (✉)
Institute of Physics, Clausthal University of Technology,
D-38678 Clausthal-Zellerfeld, Germany
e-mail: post@robert-schwarzer.de

A.J. Schwartz et al. (eds.), *Electron Backscatter Diffraction in Materials Science*,
DOI 10.1007/978-0-387-88136-2_1, © Springer Science+Business Media, LLC 2009

reserved to only a few select research laboratories, but rather is well on the way to becoming a tool for process development and quality control. Additionally, the technique enables three-dimensional (3D) volumetric reconstruction of the microstructure from consecutive surface sections that are created by mechanical serial section, as described in Chapter 16 by Rohrer and Randle, or focused ion beam (FIB) milling, as discussed in the chapters by Zaefferer and Wright; Groeber, Rowenhort, and Uchic; and Sintay, Groeber, and Rollett. For the purpose of 3D reconstruction and analysis, however, the speed and ease of handling the EBSD system, as well as the capability to re-examine the results at any time, are decisive requirements.

Automated EBSD at present is limited to materials in which grain sizes larger than several tens of nanometers in diameter and several square millimeters in area can be characterized. Surface strains must not be excessive, and the specimens must be compatible with the general requirements of electron microscopy. In particular, the specimens should be conductive and should not decompose in vacuum or under the electron beam. The surface should be reasonably flat and free from foreign layers.

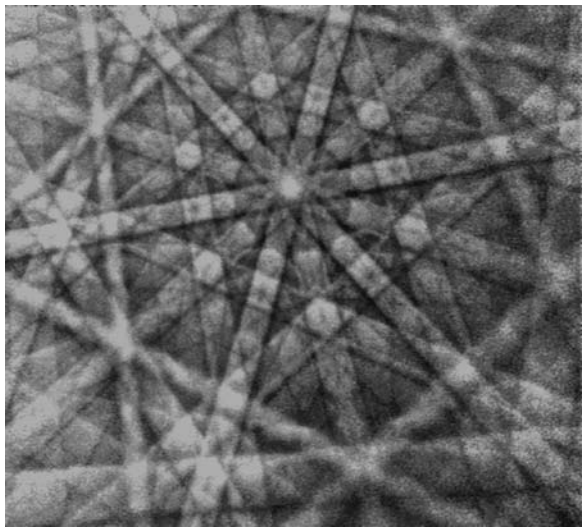


Fig. 1.1 Backscatter Kikuchi pattern from cadmium at 20 keV, acquired with an analog video camera

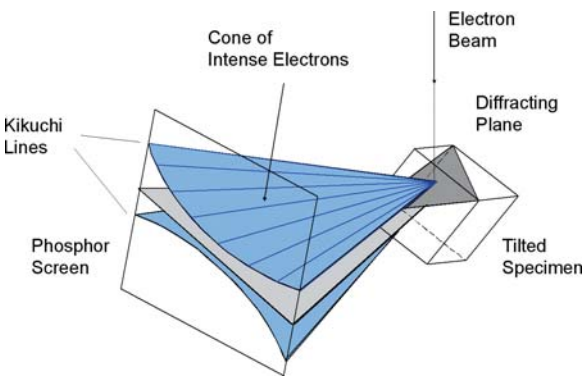


Fig. 1.2 Schematic of the diffracting cones with respect to the reflecting plane, the specimen, and the phosphor screen

1.2 Generation and Interpretation of Electron Backscatter Diffraction Patterns

EBSD patterns are generated on a phosphor screen by backscatter diffraction of a *stationary beam* of high-energy electrons from a volume of crystal material approximately 20 nm deep in the specimen, times the projected area of the incident beam. The characteristic feature of a backscatter Kikuchi pattern is the regular arrangement of parallel bright bands on a steep continuous background (Fig. 1.1), rather than a regular array of diffraction spots as is generated in the TEM in selected area diffraction from a single crystallite. The intersections of Kikuchi bands form prominent and distinct zone axes.

The geometry of a Kikuchi pattern can be interpreted as a gnomonic projection of the crystal lattice on the flat phosphor screen. The point of impingement of the primary beam on the specimen surface is the center of projection. The lattice planes can be imagined to be stretched out to intersect the screen in the center of the lines of their related Kikuchi bands. Figure 1.2 contains a schematic showing the incident beam on the specimen with a given unit cell orientation and a specified diffracting plane giving rise to backscattered "Kikuchi" diffraction. The two diffracting cones are the edges of the Kikuchi band, and the plane through the center of these cones is the geometric projection of the diffracting plane onto the phosphor screen.

When more than one such Kikuchi band is considered, the angles between the projected plane normal orientations correspond to the interplanar angles, and the angular width of a Kikuchi band $\{hkl\}$ is twice

the Bragg angle ϑ_{hkl}. Thus, the width of the bands is related to the interplanar spacing, d_{hkl}, according to Bragg's law:

$$2 \cdot d_{hkl} \cdot \sin \vartheta_{hkl} = n \cdot \lambda \qquad (1.1)$$

where n is the order of reflection and λ is the wavelength of the incident electron beam, which is dependent on the accelerating voltage of the SEM. The extinction rules for the expected reflections (i.e., Kikuchi bands) of the specific crystal structure are determined by the structure factor of the crystal. In addition, higher order reflections may appear as a set of straight lines parallel to the band edges. A decrease in accelerating voltage, U, causes an increase in electron wavelength and hence an increase in the width of the band, which is, to a first approximation, $\vartheta_{hkl} \sim 1/U^{1/2}$. An appreciable increase in band width and a deviation from the usual straight-line approximation to the shape of real conical sections is observed at low accelerating voltages, in particular for high-order Kikuchi lines.

This simple geometric model and the kinematical approximation do not explain the exact intensity distribution in a Kikuchi pattern. To fully quantify the intensity distribution, the dynamical theory of electron diffraction must be employed (Reimer 1985). The mechanisms that lead to the formation of the characteristic diffraction contrast features in EBSD patterns, including Kikuchi bands as well as the prominent circular Kikuchi envelopes around zone axes—by appearances like higher order Laue zone (HOLZ) lines from thin foils in convergent beam electron diffraction (CBED)—have been described with the application of dynamic diffraction. Excellent agreement has been obtained between experimental patterns and simulations in extended many-beam dynamical calculations using the Bloch wave approach (Winkelmann et al. 2007; Winkelmann 2008), as is discussed in Chapter 2 by Winkelmann.

1.3 Experimental Set-Up of an EBSD System

Instrumentation for generating and capturing electron channeling patterns (ECP) from selected small specimen regions is still available with some commercial SEMs, but the spatial resolution rarely exceeds 50 μm, as a consequence of the large spherical aberration of the probe-forming lens and the *pivoting beam*. As a result of the relatively poor resolution and the knowledge that many materials of interest have grain sizes smaller than 50 μm, the EBSD technique has largely taken the place of ECPs in materials and earth sciences investigations. In EBSD, a *stationary beam* is directed onto the grain of interest to form a Kikuchi pattern. The spot size, and hence the interaction volume of the primary beam with the crystal contributing to the pattern, can be made more than two orders of magnitude smaller than with ECP. Spatial resolution, as well as depth resolution in EBSD, depends on specimen tilt, density of the specimen, and accelerating voltage. The lowest practical beam voltage is about 3 keV, if a phosphor screen without an aluminum top layer is used.

For quantitative texture analysis, a statistically significant number of individual grain orientations are required. The interactive, or manual, collection of such a database by the operator is both inconvenient and time consuming. Fully automated methods have been developed for acquisition and indexing of Kikuchi patterns within the SEM (Adams et al. 1993) and within the TEM (Zaefferer and Schwarzer 1994; Schwarzer and Sukkau 1998). A number of commercial systems are currently available, which can be added to new or existing SEMs. Automated EBSD systems generally require little operator input; after the initial set-up of the system, the only input required is the step size. The EBSD software controls the SEM and rasters the beam across the specimen on a user-specified pre-defined grid, pausing at each point only long enough to acquire the backscatter diffraction pattern, index the orientation, and record the x, y coordinates and the orientation vectors. As discussed in detail below, scanning can be performed either by translating the specimen in the x and y directions with respect to the stationary primary beam with a high-precision computer-controlled specimen stage (Adams et al. 1993); or by stepping the primary beam under digital computer-control across the stationary specimen surface in a similar way as in conventional scanning electron microscopy (Kunze et al. 1994). The positions at which diffraction patterns are measured may constitute some clusters of individual points, a dotted line, or a raster field on the specimen surface. For digital beam scanning, a fast and high-resolution (>12 Bit) digital-to-analog (DA) converter is recommended. A fine raster grid allows for very precise positioning of the measured spots on the inclined

specimen surface, so as to correct for distortions of the grid due to the steep tilt of the specimen surface and the image rotation during dynamical focusing of the probe-forming lens.

1.4 The Components of an Automated EBSD System

An automated EBSD system consists of three main parts: the SEM, the pattern acquisition device (or camera), and the software. To achieve the best possible performance, these parts must be considered simultaneously when designing and setting up a system. In general, it is not recommended that you construct your own system from scratch. Significant effort is necessary to ensure the coupled system works synchronously and to develop the complex software for controlling the SEM functions, the pattern acquisition, and the data interpretation.

The following intrinsic difficulties of EBSD must be addressed:

- steep specimen tilt, approximately 70° relative to the incident beam (see Fig. 1.3);
- low contrast and intensity, and high background noise in the backscatter Kikuchi patterns;
- disposition to pattern degradation by contamination and deformation layers;
- decomposition and charging of low-conducting materials under the beam;
- requirements of high speed, high spatial resolution, and high accuracy of measurement.

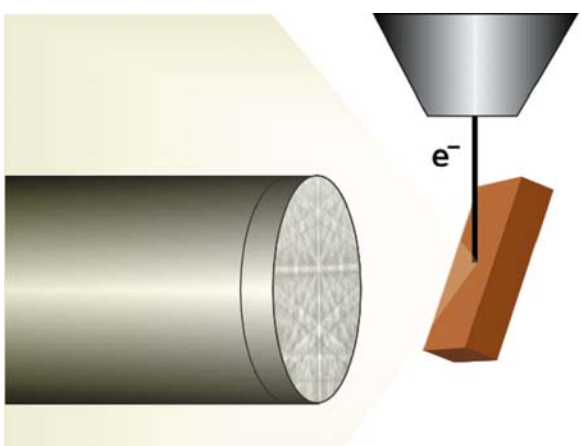


Fig. 1.3 Schematic of the typical EBSD geometry, showing the pole piece of the SEM, the electron beam, the tilted specimen, and the phosphor screen

1.4.1 The Pattern Acquisition Device

The backscatter Kikuchi pattern is commonly projected onto a transparent phosphor screen (approximately 5 cm in diameter), which is about 2 cm away from the specimen. The screen preferably stands parallel with the primary beam and the tilt axis of the stage, but can be rotated about 20 degrees from that plane in any direction. The pattern is either viewed with a high-sensitivity camera through a window from outside the specimen chamber, or the phosphor screen is placed on a fiber optic bundle, which is directly coupled to the camera sensor. The phosphor screen is generally matched to the spectral response of the sensor for optimum performance. Common phosphors employed for EBSD applications include P20 and P43. P20 has a short decay time at high current densities, which occurs in photon counting tubes, but exhibits a long decay at low current densities. This latter property is a good match for direct view low light systems. It is yellow/green emitting at 540 nm and has a decay time of about 1–10 ms with an efficiency (lumens/watt) of 30. P43 phosphor is preferred for most applications with TV camera output, because of its efficiency and linearity. It is also fast enough for most high framerate applications. It is green emitting (548 nm) with a 1.2 ms decay time and an efficiency of 50. A thin, reflective, aluminum coating is often deposited onto the phosphor screen. This coating enhances the brightness of the phosphor by reflecting light back toward the camera. It also acts as somewhat of a passive energy filter in that it absorbs low energy electrons before they arrive at the phosphor screen. The most important function of the coating is to ground the phosphor screen, as an electrically floating phosphor will charge and degrade the performance of the SEM and will interfere with orientation mapping by automated EBSD. (Alternatively, an indium tin oxide (ITO) layer, or some other conductive and transparent coating, can be deposited on the substrate window.)

In most EBSD systems, the acquisition device is mounted on a retractable stage. This enables a precise

translation of screen and camera at a fixed spacing from each other along the optic axis of the camera system so that the diffraction pattern projected onto the screen is kept in focus. A travel of several centimeters is required to provide adequate space for bulky specimens when grain orientations need to be measured to the edge of the material. The accurate displacement of the acquisition device can also be used for calibrating the EBSD system with the "pattern magnification method" or "moving screen method" (Day 1993; Hjelen et al. 1993). When retracting the screen from the specimen, the pattern "zooms" out from the pattern center, which can thus be located quite easily. This feature is used to provide an accurate calibration of the system. The pattern center and the specimen-to-screen distance can be accurately calibrated by measuring the locations of several corresponding zone axes on the non-displaced and the displaced patterns. No initial estimates of the calibration parameters and no knowledge of the crystallography of the sample are required. The displacement should be more or less double the initial specimen-to-screen distance for the reference measurement. However, pattern intensity falls off with the square of the specimen-to-screen distance. Furthermore, the precise movement of the device must be done in situ under vacuum. In order to guarantee a clean vacuum, a bellows system is recommended over the method of greased O-rings.

There are several types of camera systems that have been used for EBSD image detection. Historically, Peltier-cooled and intensified charge coupled device (CCD) cameras and silicon intensified target (SIT) cameras were used for automated work, and the more expensive slow scan CCD cameras were applied for high quality imaging and phase identification. Currently, CCD cameras are used for both rapid scan rate imaging and for high quality EBSD image collection. CCD cameras can produce binned images on the order of $\sim 100 \times 100$ pixels at the rate of near 1000 frames per second with sufficient intensity for reliable indexing. The practical indexing limit is currently in the range of 600–800 images per second, but that number is likely to continue to increase with more powerful computers and optimized image-handling algorithms. To obtain high quality EBSD patterns for phase identification or publication purposes, there is typically no on-chip binning performed and the full image is collected using time averaging techniques to obtain sufficient light intensity and contrast.

Some emphasis has to be placed on the light optics. A high-quality macro lens with a small *f*-stop (large aperture, "fast lens") is a good choice in the case of a short distance between the phosphor screen and the camera sensor chip. The sensitivity of the acquisition system can be almost doubled, at the expense of high cost and practical inconvenience, by coupling the CCD sensor with a (tapered) fiber optic bundle to the phosphor screen. The highest efficiency is expected from on-chip deposition of the phosphor or from direct exposure of the sensor chip to the pattern-forming electrons. Such a sensor chip will presumably be placed inside the specimen chamber, either on a small retractable rod or directly on the specimen stage.

The digital image is the only source of information for pattern recognition. Software can correct for poor image quality or distortions only to some extent. Hence the camera has to be chosen with care, making a trade-off between sensitivity, noise, number of pixels, image quality, and cost. Almost all current EBSD systems have moved to video or digital cameras with solid-state sensors, either to intensified or to integrating CCD cameras. These cameras are economical, and the sensor geometry is fixed without producing undue distortions nor "blooming" or burn-in of bright spots (Schwarzer 1989), as has been the case with former vacuum tube sensors. It is worth mentioning that Peltier-cooling of the sensor chip or the photocathode of the image intensifier, in order to reduce noise, is ineffective at short exposures of less than a second.

1.4.2 Mechanical Stage and Digital Beam Scanning

Two computer-controlled sampling modes are used for automated EBSD: stage-scan mode, in which the specimen is translated mechanically under the focused stationary primary beam (Adams et al. 1993); and digital beam scan mode, in which the focused primary beam is moved across the stationary specimen surface (Kunze et al. 1994). The combination of both modes enables large area scans with high accuracy and speed whereby small, slightly overlapping fields are sampled by digital beam scan and stitched together after coarse mechanical steps of the stage from one field to the next.

Advantages of the mechanical stage scan include: the accommodation of large measured fields, only limited in size by the range of travel of the specimen stage; step size calibration does not depend on SEM magnification; there are no geometric distortions resulting from the tilted specimen surface or beam deflection; and from one measured point to the next, diffraction geometry is identical, i.e., pattern center position, specimen-to-screen distance, background intensity, and focus settings remain constant. Hence, much less elaborate EBSD software is sufficient. A high-performance stage, however, is necessary to keep the specimen surface exactly in the plane of translation. Step sizes less than 0.5 μm in x and y must be possible. Such a computer-controlled, high precision x–y stage is a relatively slow and expensive alternative relative to the digital beam scan. In addition, the mechanical stage has a higher uncertainty of the measurement position due to play or lag in the system.

Digital beam scanning, on the other hand, enables an extremely high speed as well as precision in beam positioning. It is cost-effective and not susceptible to breakage. However, the diffraction geometry and pattern center change at each point on the specimen as a result of the varying beam tilt as the beam is stepped across and down the specimen (Fig. 1.4). Therefore, the system has to be calibrated dynamically from spot to spot ("*autocalibration*" [Schwarzer 1997]). Otherwise, errors in calculated grain orientations may easily exceed several degrees; or indexing of the pattern may fail in particular at low magnifications and with increasing distance of the measured location from the point on which the system had been calibrated initially. Because of the importance of proper calibration, dynamic calibration of the pattern center has been performed on commercial systems since the development of beam scanning in 1994. A simple test for accuracy of calibration can be made by measuring across a large field on a single crystal and checking the uniformity of orientation data. This is also how most systems are calibrated initially. The necessity of a precise calibration of the pattern center as well as the diffraction length (specimen-to-screen distance) has been verified in a computer simulation for transmission Kikuchi patterns by Morawiec (1999).

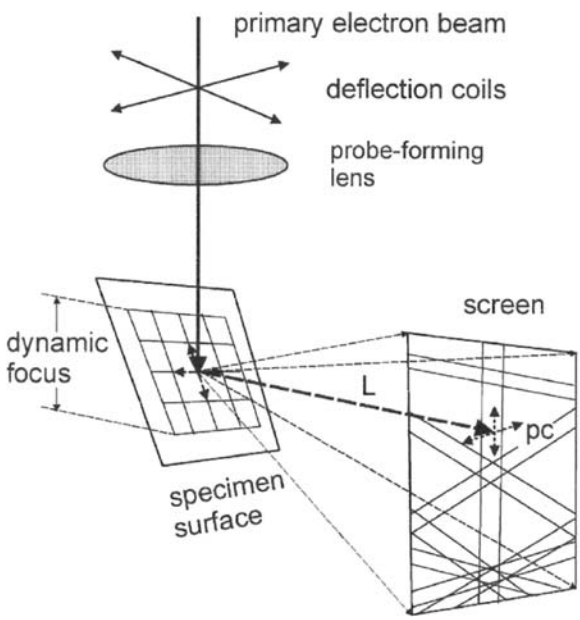


Fig. 1.4 Raster grid on a tilted specimen surface with digital beam scan

The EBSD software must address two additional difficulties with the digital beam scan. As a consequence of the steep forward scattering of electrons, the specimen surface has to be steeply inclined, typically at about 20° to the primary beam (i.e., typically 70° from horizontal) in backscatter diffraction in order to generate a Kikuchi pattern of sufficient intensity. When scanning down the specimen line after line, the primary beam spot runs out of focus—increasing in diameter—so that spatial resolution decreases severely. This holds true for low as well as high magnifications because the requirements of high resolution scale with useful magnification. SEM hardware capabilities for dynamic focusing of most SEMs, however, do not accommodate the steep specimen tilts as required for EBSD, nor do they accommodate specimen tilts about an axis at an oblique angle to the axis of the specimen stage. This latter limitation would demand a free port for the camera on that side of the specimen chamber which is pointing at a right angle to the stage axis.

Defocusing has a detrimental effect on spatial resolution and reliability of indexing, in particular with fine-grain materials; so that dynamic focusing is indispensable not only at low but also at medium magnifications. Pattern quality is a very sensitive indicator of incorrect focus settings due to the diffuseness of Kikuchi patterns. The superposition of two or more diffraction patterns has two adverse effects on indexing. First, the small grains contribute less diffracted intensity to the signal. Their faint patterns are

overlooked at best, at the expense of the larger grains, which are covered by the majority of the primary beam spot. Second, spurious bands from faint patterns may be picked up and enter the set of bands for indexing. Pattern interpretation may then fail because of the inconsistency of reflections; or even worse, a false orientation may be the result. The effect of spurious reflections on the reliability of indexing has been clearly demonstrated in a simulation for transmission Kikuchi patterns (Morawiec 1999). The beam aperture is significantly smaller in SEM with a field emission (FE) gun, so that the depth of focus is substantially increased and the demand for dynamic focusing on steeply tilted surfaces is alleviated to the same extent.

The steep specimen tilt of about 70° from horizontal causes a further complication of EBSD: the beam spot on the specimen is elongated and hence spatial resolution is reduced in vertical direction by about 3 times. Orientation maps, as well as conventional SEM images, when taken at the same specimen tilt, are foreshortened to the same extent. Therefore, allowance must be made for this kind of image distortion in quantitative stereology, either by using different length scales for x and y or by stretching out the foreshortened image.

The signal to noise ratio in EBSD patterns is quite poor. The backscatter Kikuchi pattern is superimposed on a background, which is almost 25 times higher in intensity than the useful signal and depends on the grain orientation, i.e., the actual diffraction pattern. Moreover, the intensity distribution of the background changes during digital beam scans with the position of the beam spot on the specimen surface, as well as with local specimen density (phase) and surface relief. A further fluctuation may be caused by variations of the probe current due to instabilities of the emission current of the gun, drift in the alignment of the column, specimen charging, or build-up of carbon contamination. The quality of diffraction patterns is improved significantly by "flat fielding." In this case, the raw pattern is normalized to a flat field image that contains the background and image artifacts (e.g., scratches on the screen, blind or bright dots on the camera chip), but no features of the Kikuchi pattern. There are several ways to obtain such a flat field image: The beam can be scanned across an area large enough to contain many grains of different orientations. The Kikuchi patterns of these grains are integrated so that they level out to form an even background. The primary beam can also be defocused in spot mode to the extreme so that the Kikuchi patterns fade away. Finally, the background can be reconstructed from the actual diffraction pattern by dedicated software filtering (Field 1997; Schwarzer and Sukkau 1998). In fast EBSD mode (see below) with off-line indexing a sequence of patterns, a flat image can be constructed a posteriori by summing up and averaging several patterns out of the sequence that had been acquired at different positions of the beam spot on the sample. Each of these techniques have specific advantages and limitations. Defocused spot mode, for instance, adequately reduces the shadows due to surface relief. Background reconstruction by filtering is particularly useful in case of a coarse grain microstructure or a strong texture.

Consequently, advanced EBSD software has not only to control the digital beam scan or the mechanical stage scan, but in addition has to control the modes of SEM operation (switching between imaging and spot mode) and pattern acquisition (Schwarzer 1997). Switching the SEM between imaging and spot mode is necessary for automated experimental flat fielding. The final lens currents (respectively, the working distances and magnification) have to be read for autocalibration and dynamic focusing. The final lens current must be set by the computer as a function of x–y beam position for software-controlled dynamic focusing. The accelerating voltage is read as a measure of electron wavelength when the band widths are optionally used for indexing.

1.5 Spatial Resolution

A high spatial resolution in orientation measurement is required for the study of fine grain and heavily deformed materials, of recrystallization and grain growth, of grain boundary characterization, and of nanomaterials. But why does the spatial resolution in EBSD fall more than one order of magnitude behind spatial resolution in conventional SEM imaging, and still further behind when compared to the spatial resolution of a TEM? The inherent resolution of EBSD is governed not by the diameter of the beam spot at the point of impact on the surface, but primarily by the excitation volume—that is, the fraction of the interaction volume of the primary electrons within the

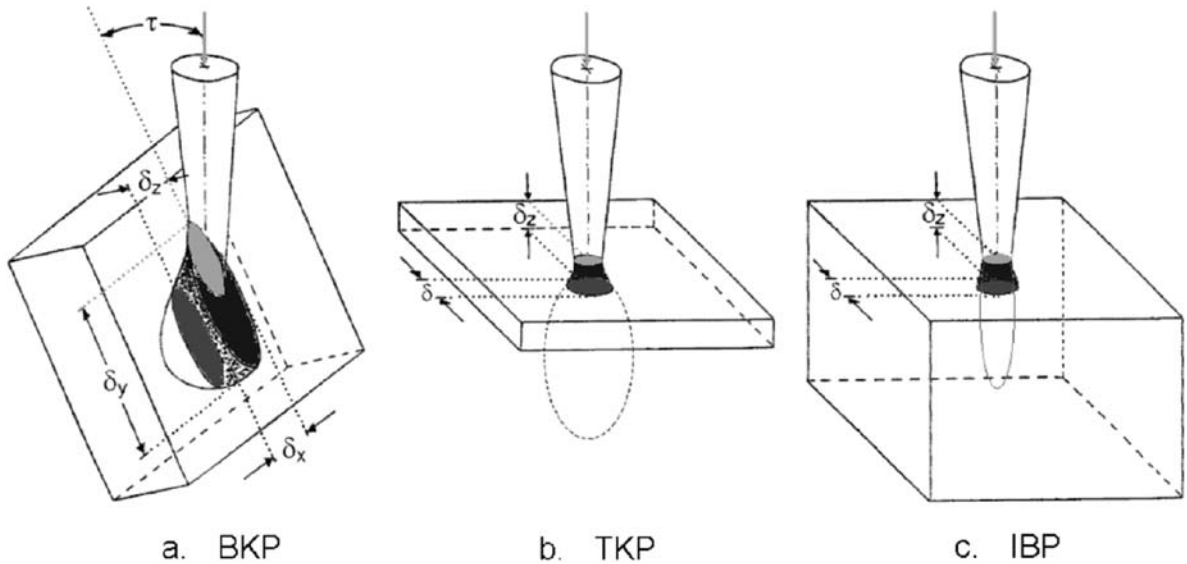


Fig. 1.5 Interaction volume, excitation volume and spatial resolutions, δ, with (**a**) backscatter Kikuchi patterns from a bulk specimen in the SEM, (**b**) transmission Kikuchi patterns from a thin foil in the TEM, and (**c**) ion blocking patterns from a bulk specimen in the scanning ion microscope (schematical representations)

sample from which the pattern forming electrons are backdiffracted and leave the crystal without further scattering. The shading in Fig. 1.5 indicates this volume fraction. This demonstrates why, for orientation microscopy in a SEM, it is not wise to reduce the spot size below the diameter of the excitation volume. The adverse effects would be a reduced beam current, hence less intense patterns, and possibly a strong increase in contamination rate by polymerization of hydrocarbons under the beam.

As a consequence of the steep sample tilt, the elongated projection of the beam spot, and the forward scattering, the spatial resolution in EBSD along the beam direction on the sample surface, δ_v, is about three times worse than δ_x. The information depth, δ_z, is limited by the mean free depth of penetration of the backscattered electrons in the sampled material at the actual beam voltage. The excitation volume increases for light materials and high beam voltages. The TEM, on the other hand, is operated at a significantly higher accelerating voltage than the SEM. However, the spatial resolution, δ, in microbeam TEM diffraction is still approximately the diameter of the beam size, because the sample is thinned to the range of the mean free path of the energetic electrons, so that only a small interaction volume can develop (Fig. 1.5b). In this case, the information depth, d_z, equals the foil thickness.

Spatial resolution in EBSD can be improved to some extent by lowering the beam voltage from typically 20 kV down to a few kV. However, beam brightness and the sensitivity of the phosphor screen, and hence the pattern intensity, are likewise reduced. While the resolution within a grain is of low significance, it becomes quite critical when the beam approaches a grain boundary. An intelligent pattern indexing software program can then improve resolution by taking account of the intensity levels of superimposed patterns, rejecting less likely orientation solutions, and comparing orientations in neighboring pixels.

Spatial resolution with copper is better than 0.05 μm at 20 kV using a tungsten filament, and currently less than about 0.02 μm with a field emission (FE) gun, as a result of the higher beam current in the small probe. This is roughly the same resolution as that predicted by Venables and Harland in 1973. Backscatter diffraction patterns have been found to disappear when a thin foreign surface layer about twice the thickness of the Rutherford elastic mean free path is present at a given

beam energy; i.e., a depth resolution of about 100 nm is assumed for Al, 20 nm for Ni and 10 nm for Au at 40 kV accelerating voltage and 20° angle of incidence to the surface (Michael and Goehner 1994). Theoretical and experimental values of mean free path relate to amorphous materials, but can be significantly larger and orientation dependent in crystals, as a consequence of the channeling effect. Therefore, real information depths in EBSD are expected to be larger than these estimates.

High spatial resolution requires an intense primary beam spot as well as a small interaction volume of the primary electrons beneath the specimen surface. The latter can be reached only by lowering the accelerating voltage significantly from about 20 kV, as is usual in present systems with a thermionic cathode, to less than about 5 kV. A high beam current in a small spot at low accelerating voltages is the domain of the field emission SEM. The drawbacks of low accelerating voltages are the susceptibility of the beam to magnetic stray fields (hence a small working distance is mandatory, which, however, may conflict with the design of current pattern acquisition systems), the low efficiency of present phosphor screens, and the high susceptibility of pattern quality to preparation artifacts or foreign surface layers.

Because spatial resolution depends on the size of the beam spot rather than on the actual magnification of the SEM, a high spatial resolution can be obtained by correct focus settings, irrespective of low magnification. Hence, a large specimen area may be studied by coupling both a mechanical stage and digital beam scan. The accessible specimen area is limited only by the largest field of view of the SEM at the lowest magnification and largest working distance. By slightly oversampling, i.e., by choosing a density of the scanning grid high enough to characterize each grain only a few times on the average, the global texture of a large area can be measured conveniently by orientation microscopy. The advantages over conventional X-ray pole figure measurement are numerous. The selected specimen area is scanned uniformly, and the scanned area can be adjusted to irregular shapes. Inhomogeneities in microstructure and texture remain visible in the orientation maps. Consistent data are obtained, whereas data from X-ray pole-figure measurement may be more or less biased due to large variations of specimen tilt, variations of information depth, and variations of the pole-figure window. The angular instrument resolution is usually higher (about 0.5° with EBSD, whereas X-ray pole figures are measured with typically 3° to 5° angular step width). The X-ray count rate has to be checked for linearity. The ODF calculation from individual grain orientations does not suffer from ghost artifacts. Because almost the same maximum area can be measured with EBSD with digital beam scan and in X-ray pole figure measurements with an oscillation stage, grain statistics are similar and depend on the ratio of average grain size to measured area. Automated EBSD competes well in speed with X-ray diffraction, but is a more universal instrument because of the additional capabilities of the SEM.

1.6 SEM Specifications for Good EBSD Performance

A high beam current is required in spots from 0.02 μm (or slightly less) to 0.5 μm in diameter (to match the material-specific resolution limits of EBSD) at a medium working distance (to accommodate the attachment of the EBSD system and additional detectors), and at accelerating voltages between about 10 kV to 30 kV. A further essential requirement is long-term stability over several hours of the beam current as well as of the mechanics of the specimen stage. Field emission guns have a brightness of about 3 orders of magnitude higher than thermionic emitters, but the crossover—as the effective source of electrons—is less than 10 nm in diameter, as compared to 10 μm for a LaB_6 emitter. FE guns are superior to any thermionic gun in producing high beam current in small probes of 0.02 μm and less, whereas single-crystal LaB_6 emitters are superior when the beam spot exceeds about 0.5 μm. SEMs with a field emission source enable high currents of several tens of nA in beam spots of a few nm diameter, whereas current in small beam spots drops dramatically when produced with a thermionic emitter gun. Therefore, FE SEMs are the first choice for high-speed and high-resolution orientation microscopy. A detector with low sensitivity can be offset by a high beam current only to some extent. It is worth keeping in mind that contamination rate increases rapidly with current density. Therefore, it is wise to focus the beam only down into a useful spot diameter according

to the actual grain size and the physical resolution limit of backscatter Kikuchi diffraction that is in the range of some tens of nm, depending on the material and accelerating voltage. Furthermore, a low beam current is generally desirable for the production of patterns to reduce sample damage and charging of low-conductive materials.

Another invaluable advantage of FE guns is their much smaller beam aperture and hence their larger depth of focus. In the range of spot sizes that are of interest for EBSD, performance depends greatly on the design of the lens system. FE-SEMs are usually optimized for high resolution at low accelerating voltages and short working distances. Cold FE guns in particular suffer from significant current fluctuations and need a regular reconditioning (flashing) after duty periods of about one hour. They are therefore not so well suited for automated EBSD. Schottky FE guns, on the other hand, can reach an adequate long-term stability of the beam current. The main drawback of a FE SEM, however, is the higher costs. Beam currents of thermionic guns with a conventional tungsten hairpin filament are about 4 times lower than currents with a LaB_6 cathode. Tungsten filaments are still standard with medium performance SEM since they are fairly economical, need only a moderately high vacuum in the gun chamber, and are known for their excellent beam current stability. In addition, the lifetime of a tungsten filament may easily exceed 150 hours. When changed on a regular basis and operated with some care, the lifetime is a minor source for interruption of long-term scans. In conclusion, a single-crystal LaB_6 gun is a good economic compromise at present, but the trend goes definitively to Schottky FE guns.

A great challenge of automated EBSD is the study of low-conductive surfaces such as minerals, oxides (as discussed in Chapter 27 by Kim and Szpunar), geological samples (as discussed in Chapter 26 by Prior, Mariani, and Wheeler), hard coatings, integrated circuits with dielectric layers, specimens with non-metallic inclusions, or embedded samples. There are several experimental techniques available which intend either to reduce the resistance of the specimen, to reduce the probe current density, to increase the secondary electron emission coefficient, or to compensate for surface charging (Schwarzer 1994). Charging problems are alleviated to some extent by the steep inclination of the specimen surface to the beam. A conductive coating with carbon—not to say gold or other heavy metals—as in conventional SEM surface imaging, however, is prohibitive, since any foreign layer degrades pattern quality as a consequence of the low information depth in backscatter Kikuchi diffraction. A low-vacuum in the SEM specimen chamber is a convenient means by which to suppress specimen charging as described in Chapter 25 by El-Dasher and Torres. If available, a "variable pressure" SEM working at a chamber pressure in the 1 mbar (100 Pa) range and a beam voltage of about 20 kV or higher is a good choice when insulating materials are in the scope of investigation.

Excessive scattering of the pattern-forming electrons on their path to the phosphor screen is an adverse side effect of low vacuum that results in a diffuse pattern. Hence, the shortest possible specimen-to-screen distance and a high accelerating voltage are mandatory to reduce this unwanted scattering of the pattern-forming electrons when working at a low vacuum in the specimen chamber. With decreasing specimen-to-screen distance, a larger angular section of the Kikuchi pattern is captured. The same translation of the beam spot on the sample with digital beam scan results in the same travel of the pattern center on the screen (cf. Fig. 1.4), but angular deviation of the reference direction increases with decreasing specimen-to-screen distance. Hence, dynamic pattern center calibration becomes indispensable for correct orientation measurement the closer the screen is placed to the specimen.

An essential requirement is a *clean vacuum* in the specimen chamber in order to exclude excessive formation of carbon contamination. A turbomolecular pump backed by a dry roughing pump is therefore recommended, while greased vacuum sealings should be avoided. The specimen stage should accommodate large specimens and a eucentric tilt from 0° to about 75° from the horizontal plane. The *x*–*y* translation should be made in the surface plane of the specimen. A free port of at least 5 cm wide is required at normal direction to the tilt axis of the stage about 1 cm beneath the eucentric point, for mounting the camera and the phosphor screen. Finally, a fast SEM computer interface is mandatory for high speed digital beam scans, flat imaging, and dynamic focusing. Unfortunately, most high-performance SEMs today are not optimized for automated EBSD. Therefore, a trade-off has to be made between the performance of the system, the intended applications, and the available hardware.

1.7 The Radon or Hough Transformation for Band Localization

The geometry of a Kikuchi pattern is unique for a particular crystal structure and crystal lattice orientation. The spacing between a pair of lines, i.e., the band width, corresponds to the Bragg angle, and the center line of the band corresponds to the (imaginary) section line of the set of diffracting lattice planes with the screen. Interplanar angles are obtained from the positions of center lines in the pattern. Hence, it is sufficient for indexing to know the *positions and widths* of some bands in the pattern, because the intersection of bands correspond to zone axes or poles. The grain orientation can then be determined with high precision without having to measure band *intensities* in addition, whilst precise orientation determination from spot patterns in the TEM requires the measurement of spot positions as well as their intensities ("intensity center method"). It is worth mentioning here that the angular distance between crystallographic poles does not depend on the acceleration voltage.

Unlike the computer, the human eye can easily perceive lines, curves, and other regular motifs in diffuse or noisy images. Therefore, the user of an EBSD system can interactively extract band positions from a Kikuchi pattern without complications. The extension to a fully automated EBSD system, however, is not so straightforward. The first step for reliable indexing is to detect bands, and then to select the most suitable ones without the operator's interaction. Even though it seems quite simple to automatically attribute individual points or segments of a line from a general array of points to a specific straight line, this challenging task is still difficult to solve with pattern recognition methods. The problem is further aggravated with backscatter Kikuchi patterns, because diffuse broad bands with non-uniform intensity distributions, rather than sharp straight lines, must be identified on a high background. Therefore, the usual line filtering, gradient, or contour tracing methods are not well suited. The Radon transform (Radon 1917; Deans 1983) or Hough transform (which is a special case of the more general Radon transform) (Hough 1962) is often superior, if the image is noisy and if the motifs to be recognized are fragmentary; but can be described in a parametric form, such as straight lines, circles, or conics. A detailed introduction to the theory and implementations of the Radon transformation has been given by Peter Toft (1996).

The polar equation of a straight line is:

$$r = x \cdot \cos\theta + y \cdot \sin\theta \tag{1.2}$$

r is the distance of the line from the origin, and θ the angle between the x axis and the normal from the origin to the line. Let $f(x, y)$ be a 2-dimensional function (for our purposes a gray-tone image). The mathematical definition of the Radon transformation of $f(x, y)$ for projections along straight lines is then given as:

$$R(\rho, \theta) = \int_{-\infty}^{\infty} \int_{-\infty}^{\infty} f(x, y) \cdot \delta(\rho - x \cdot \cos\theta - y \cdot \sin\theta)\, dx\, dy \tag{1.3}$$

The Radon transform $R(\rho,\theta)$ is a 2-dimensional integral transformation with the kernel $\delta(\rho - x\cdot\cos\theta - y\cdot\sin\theta)$. Here, we consider only a discrete Radon transform, which means the image (i.e., the pattern) is made up by a discrete array (x_r, y_s) of image points (so-called pixels), and the Radon space consists of an array of discrete cells on a Cartesian grid (ρ, θ). The integrals in Eq. (1.3) are replaced by sums. When stepping through the Radon space from one cell (ρ_i, θ_i) to the next, the intensity values of all points (x_i, y_i) on the corresponding Kikuchi line, i, in the pattern are extracted, accumulated, and then stored in this cell (cf. Fig. 1.6). A stripe of uniform intensity is so transformed to a butterfly-shaped peak in Radon space. Lines embedded in the stripe are mapped to cells of constant high intensity, whereas lines intersecting the stripe are mapped to cells of reduced intensity, according to their section length. If the line or the stripe is fragmented, the accumulated peak intensity is reduced according to the

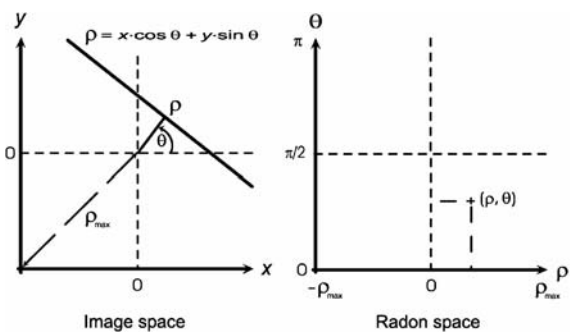


Fig. 1.6 The Radon transformation of a straight line

missing sections, but all co-linear image points are still taken into account correctly. Allowance is made for the decrease in line length with increasing distance from the center of the image frame, as well as for image artifacts, by normalizing the Radon transformation on a Radon transformation of a flat image of the same size.

The task of locating (fragmentary) lines or bands in the diffraction pattern is thus reduced to the simpler task of locating isolated peaks in Radon space. An iteration step can considerably enhance accuracy and save computation time. In a first step, the number of image points in the initial diffraction pattern is reduced by a binning operation before carrying out the transformation. The separation into a high and a low intensity Radon space, R^+ and R^-, reduces interference between dark and bright features in the Kikuchi diffraction patterns, and enables the convenient discrimination of related dark and bright Kikuchi lines (Schwarzer and Sukkau 1998). This separation is recommended in particular for solving transmission Kikuchi patterns and crisp backscatter Kikuchi patterns. The peaks in R^+ space and the cusps in R^- space are then used as "path finders" for one more Radon transformation, but now along stripes in the initial diffraction pattern enclosing the roughly located bands.

The concept of the Hough transform (Hough 1962; Duda and Hart 1972) is similar to the Radon transform. Whereas the Radon transform first accumulates the pixel intensities along a line in the image and then attributes this value to a single cell in Radon space, the Hough transform maps each individual pixel (x_r, y_s) separately from the image onto a sinusoidal curve of constant intensity in Hough space that represents all possible lines through this pixel. Spurious single pixels of high intensity in the image lead to single high-intensity sinusoidal curves. The sinusoidal curves are then overlaid. For co-linear pixels in the image, their sinusoidal curves intersect in a common Hough cell (ρ_1, θ_1) and give rise to a spot whose intensity equals the accumulated intensities along the line in the image. The detection of a line in the image is thus again reduced to the much easier task of detecting a single spot in Hough space. In the case of a Kikuchi band, a "butterfly peak" is finally formed (Krieger Lassen 1994), as is obtained with the Radon transform. So far the results of the Radon and the "modified" Hough transformation of an EBSD pattern are quite similar.

Backmapping can help to concentrate the intensities in Hough space into the most likely peak of the lines of every detected band (Krieger Lassen 1998). A pixel in the image belongs to one line only, unless it is in the rare case the intersection point of lines on crossing Kikuchi bands, and hence should not be mapped into a sinusoid curve, but into a single cell (ρ_1, θ_1) on this curve only. Ideally, this is the intersection point (respectively cell) of all (virtual) sinusoid curves that belong to pixels on the same line in the image. So it is natural to assume that, after overlaying all sinusoid curves of a line, this cell attains highest intensity. A second Hough transformation is therefore calculated, but now the pixels (x_i, y_i) in the image are mapped one after the other by accumulating their intensities only onto these cells (ρ_1, θ_1), rather than onto sinusoid curves. The result is a cleaner, more sparse Hough transformation of the pattern. This time-consuming procedure, however, is unnecessary with the Radon transform, since the line intensities are directly projected into the Radon peak of the band whereby the motif can be processed, e.g., by interrogating the lengths of continuous line sections or the intensity profile along the lines.

In present EBSD systems, the automated extraction of band positions from digitized Kikuchi patterns has replaced interactive measurement of band positions by the operator except for system calibration or in case of superimposed patterns.

1.8 Indexing

The bands thus located are sorted according to their intensities and widths. Indexing is based on the comparison of measured interplanar angles (which correspond to the angles between the Kikuchi bands) and interplanar spacings (which are represented by the band widths) with theoretical values in a look-up table calculated in advance for the actual crystal structure. Typically, the positions of the 5 to 10 smallest and most intense bands are passed to the indexing routine. Consideration of the first 3 to 4 families of {hkl} planes is usually sufficient for solving a backscatter Kikuchi pattern uniquely in the case of high crystal symmetry such as cubic and hcp, whereas increasingly more bands and {hkl} families must be checked and selected in case of pseudosymmetries and lower crystal symmetry. The large angular range of backscatter Kikuchi patterns favors correct indexing. Reference directions

in the specimen space (e.g., specimen normal direction and transverse direction in the specimen surface) are finally indexed, and the crystallographic orientation of the grain is described either in (hkl)[uvw] notation, by three Euler angles, (φ_1, Φ, φ_2), or by the rotation matrix, **g**, which transforms the specimen coordinate system under consideration into the crystal-fixed coordinate system. A simulated Kikuchi pattern to this solution is finally displayed on the monitor for comparison with the actual diffraction pattern. Detailed algorithms for indexing electron backscatter diffraction patterns have been published by many authors, including a complete description in the first edition of *Electron Backscatter Diffraction in Materials Science* (Schwartz et al. 2000).

The maximum number of indexed bands versus the number of bands that have been considered for indexing a pattern can be used as a measure of probability that a correct solution has been found. There are various ways of defining a statistical "confidence index," "confidence level," or "likelihood" (cf. Field 1997). The quantity is most useful in phase discrimination.

The less perfect the diffracting crystal volume, the more diffuse the corresponding Kikuchi pattern. The blur indicates a high density of point defects or dislocations, lattice strain, thermal lattice vibrations due to the Debye-Waller factor, micro-fragmentation of the lattice, or the superposition of diffraction patterns from several grains sampled at a time by the primary beam spot. A diffuse pattern may also result from a foreign surface layer, such as carbon, of excessive thickness (which may have been deposited intentionally in order to avoid specimen charging), a contamination layer due to poor vacuum conditions, a deformation layer from inadequate sample preparation, or a defocused electron beam or EBSD detector. The blur can be expressed as a quantity, named "pattern quality," PQ, (or Image Quality, IQ) by measuring the sharpness of some band edges (profile analysis) or the height of peaks in Hough space, or by performing a Fast Fourier Transform (FFT) (Schwarzer and Sukkau 2003) of either the original diffraction pattern or the Radon transformation. Pattern quality maps of coarse grain materials clearly display grain boundaries and surface scratches, and often show features which look like a dislocation network. Pattern quality can be used to discriminate between deformed and recovered or recrystallized grains in a microstructure.

1.9 Fast EBSD

A high speed of measurement is not only a value by itself in that the sample throughput of the SEM is improved, but is also indispensable for dynamic experiments (e.g., in situ tensile and bending tests or hot stage experiments as described by Wright and Nowell in Chapter 24 of this volume). For this purpose, a set of individual spot positions, such as in the vicinity of triple points, rather than a regular raster field on the specimen can be selected for consecutive measurements. A short time of measurement will also alleviate some difficulties with long-term stability of the SEM.

Mesh refinement (Schwarzer 1999), also called adaptive orientation imaging microscopy (Yang et al. 1999), is an effective means to increase speed. In a first step, an overview of the microstructure is obtained by scanning on a coarse raster grid with a step size slightly smaller than the diameter of the smallest grains. If intragranular structure is of no concern, it is in principle sufficient to measure the orientation of each grain only once. Therefore, a refined mesh is overlaid of half the step size in the second, and of quarter step size in a third loop; but only patterns on those intermediate grid positions will be acquired and evaluated where orientations between neighboring nodal points on the preceding grid differ by more than a preset value. Hence, measurements on the refined meshes in the following passes are concentrated along grain boundaries. Those grid points which could be skipped from measurement are assigned the average orientations of their neighbors. The limitations of this approach are set by small twins that might easily be overlooked in their matrix grains, and by a wide distribution of grain size when mesh refinement becomes inefficient, since the starting mesh grid has to be rather fine in order to observe the smallest grains.

Geometrical features of interest such as grain boundaries or triple points may also be extracted from SE or BSE images of the microstructure by automated pattern recognition methods and then used to choose the locations for orientation measurement. The prerequisite of this technique, called the Mesoscale Interface Mapping System (MIMS; Wu et al. 1999) is a sufficient and unique contrast of the features. Because grains cannot be discriminated with certainty by orientation contrast in a single (BSE) image, a series of orientation contrast images must be acquired either

simultaneously with several BSE detectors placed at different angular positions to the specimen, or in sequence with a single BSE detector by varying the specimen tilt to change orientation contrast from one image to the next. If grain boundaries or phases can be recognized by their relief after a slight etch, the relief contrast in a SE or BSE image can additionally be used to locate these features in the microstructure.

Until 2000, the speed of on-line orientation microscopy with an analog camera as the detector was limited by the video frame rate to less than about 30 orientations per second. There was little motivation to further increase the speed of the indexing software. However, after the introduction of digital cameras, the situation has changed. At present, the acquisition speed exceeds 750 patterns per second on suitable samples (Hjelen 2007). Technical details of "*Fast EBSD*" can be found in Schwarzer (2008a). The essential points of this approach are first, the high-speed acquisition and storing of backscatter Kikuchi patterns as a sequence of raw, unprocessed bitmap images; and second, the repeatable off-line evaluation of the original pattern sequence.

The high sensitivity of the detector is of key importance for high speed. An enormous advance in image sensor performance has been achieved recently mainly due to the demands of small consumer cameras. Although CMOS sensors are superior in speed, CCD sensors still have a higher quantum efficiency and are more sensitive. Recent electron-multiplying CCD (EMCCD) sensors promise some advantages at very low light levels. A proximity focus image intensifier between the phosphor screen and the camera can be used to increase overall sensitivity of the detector.

Pixel binning on the sensor chip is a well-proven means to increase sensitivity and speed. (Each individual photo-sensor on the chip array as well as each image point is called a pixel.) The pre-amplifier on the sensor chip is usually optimized for high dynamics and low noise at full pixel resolution and medium to high illumination levels. This is adequate for most situations in machine vision applications. At faint illumination, however, as is the case in backscatter Kikuchi diffraction in the SEM, the working point of the pre-amplifier drops to the flat foot of the current-voltage characteristic curve; hence the signal from one single photo-sensor is submerged by noise. If n abutting pixels are bundled together on the chip during the read-out procedure, the current to the pre-amplifier is increased n-fold so as to be raised above the noise floor. Furthermore, the number of pixels per image to be transferred to the computer is also reduced by $1/n$, thus speed is likewise increased. Pixel binning ranges from 2 by 2 up to 8 by 8. In principle, a dedicated sensor chip with a coarse array of pixels and correspondingly increased pre-amplification would be superior. The filling factor and capacity per pixel would be higher, with the advantage of higher sensitivity and dynamic range. However, the commercial demand for this type of sensor is too small, whereas consumer and machine vision cameras boast of ever increasing pixel numbers.

The camera interface is an integral component of an EBSD system and warrants discussion. Frame grabbers, as common with conventional analog cameras and with machine vision systems in industry using a CameraLink interface, are gradually being replaced by standardized computer interfaces such as USB-2, Firewire, and Ethernet. CameraLink has been the interface of choice for professional machine vision applications until lately. It is a fast and rugged solution, which complies with several cameras at the same time. The disadvantages are high costs, clumsy cables, a dedicated frame grabber, and proprietary software.

The main advantages of GigE Vision cameras are low cost, a high bandwidth that enables a very fast transfer of the images from the camera to the computer, and thin and inexpensive cables. A cable length of up to 100 m allows the computer to be installed remotely from the SEM and the data to be transferred through an intranet. The digital signal is, in contrast to analog cameras, little affected by interference with electromagnetic stray fields. A highly welcome feature is the standardization of controlling the main camera functions and data transfer with an easy-to-program protocol. Cameras conforming to the GigE Vision standard protocol GenICam (Generic Interface for Cameras) can simply be exchanged without having to modify the driver or software. This is a particular advantage for EBSD systems, because camera performance makes rapid progress from year to year, indeed faster than personal computers. Hence, with a GigE Vision camera as the backbone of an EBSD detector, a hardware upgrade can conveniently be done from time to time.

At the time of writing this book, the speed of pattern solving with high accuracy approaches 600 to 800 patterns per second. According to web sites as of September 2008, commercial manufacturers of EBSD systems

quote indexing rates of 400, at least 400 orientations, and 750 acquired patterns per second on suitable samples. This boost in speed is partially due to improved performance of the computer hardware. The speed of numerical calculations scales with typically 2/3 of the increase in CPU clock rate. Further progress can be made with fast 16-bit DA converters for digital beam control, graphic boards with co-processors, and hard disks. The next generation of solid state hard disks will remove any practical speed limit in storing Kikuchi patterns. The high and uneven background in backscatter Kikuchi patterns can be continually corrected in the camera by subtracting a flat background image pixel by pixel.

A major step ahead has been achieved by improving the software. The speed at which a band can be localized in the pattern scales linearly with the number of pixels in the pattern and the number of (ρ, θ) points in the discrete Radon transformation. The calculation and evaluation of a Radon transformation of 100 by 100 points takes on the average about 10 times longer than indexing the detected bands. Thus, the speed can be quadrupled by simply coarsening the backscatter diffraction patterns and, in conformity, reducing the size of the transformation to one fourth. An unwanted side effect, however, is the much-reduced angular resolution. Depending on pattern quality, a single band can be located in a pattern of 100 by 100 pixels at a typical deviation of $\Delta\alpha = 1.5$–2°, whereas after coarsening to one fourth of this size the angular uncertainty will be twice as large or worse. Hence, the error limits in the indexing routine have to be widened in order to account for this inaccurate band localization. Nevertheless, and as a consequence of this inaccuracy, fewer detected bands are indexed unambiguously. Sometimes this leads to wrong orientations being found, and the fraction of points indexed with high confidence may decrease significantly. It is worth mentioning that the grain orientation is calculated as a best fit from the locations of the n consistently indexed bands. Therefore, its mean error is by $1/n$ less than the mean band deviation. Coarsening the patterns and Radon transformations and, at the same time, allowing a lower reliability of orientation data are appropriate means of increasing speed if only for obtaining a first impression of the texture and of the quality of sample preparation.

The process of separate acquisition and storing of pattern sequences as raw, unprocessed bitmap images is significantly faster than simultaneous acquisition and online pattern solving. In addition, offline pattern solution has many advantages over online orientation microscopy, in particular, because pattern interpretation can be repeated at any time by using the original backscatter Kikuchi sequences (Søfferud et al. 2008).

- Dwell time per pattern is constant, whereas time for indexing depends on the actual grain orientation and phase.
- No artifacts are induced, which frequently occurs in online indexing when synchronization between the acquisition and interpretation of patterns is lacking.
- The extremely high speed of acquisition is limited only by the sensitivity of the camera and the speed of storing the patterns on the hard disk.
- A high acquisition speed is favorable for fast in situ dynamic experiments.
- A high acquisition speed is economical because the usage time of the SEM is short.
- Cold field emitters with typically low stability are accommodated.
- No compromise is made between speed of acquisition and reliability of indexing.
- Pattern indexing and interpretation can be repeated at any time by using the original diffraction patterns.
- The setting parameters of the indexing program can be optimized conveniently after acquisition.
- Reliability of indexing and the presence of a priori unknown phases can be checked.
- Off-line indexing is based on the same philosophy as EDS spectral imaging, where complete X-ray spectra are acquired from 2D arrays of points and evaluated offline.

Because of these advantages, Fast EBSD with offline solving of the acquired pattern sequences will become the standard technique. As an alternative option, the acquisition, storage, and interpretation of the patterns can be performed online as well, but at the disadvantage of reduced speed and reliability.

1.10 Ion Blocking Patterns

Diffraction patterns can be produced not only by electrons or X-rays, but also by ions of several tens of keV kinetic energy when impinging on a crystalline

surface. They have been recorded on special photographic plates, which cover a large solid angle and are called ion blocking patterns (IBP; Tulinov 1965). As a consequence of the much shorter deBroglie wavelength and the specific interaction of ions with solid crystals, IBP have, at first glance, an appearance substantially different from the electron backscatter diffraction pattern. Instead of broad Kikuchi bands, the IBPs show narrow straight black bands, almost lines, with a much higher contrast on a flat background (cf. Figs. 1.1 and 1.7). However, the geometry of IBP and EBSP is quite similar. Thus, the crystal structure and crystal orientation of the diffracting volume can be determined from the intensity distribution and positions of the bands in an IBP (Barrett 1979) in quite a similar way as in an EBSD pattern.

Intense focused ion beams are produced with liquid metal ion sources or with gas field ionization sources (Tondare 2005). An outstanding high source brightness of more than 10^9 A/cm^2 sr He$^+$ ions has been achieved by using a <111> oriented sharp field emitter tip of tungsten so that beam currents up to 100 pA at an energy spread of less than 1 eV and a beam voltage of typically 20–30 kV are practical (Morgan et al. 2006). In addition, because both the chromatic and the diffraction aberrations of the probe forming lens are less affected in this set-up, it is expected that it will be possible to focus the beam from the field ionization source into a probe size down to the subnanometer range. Thanks to the small excitation volume (cf. Fig. 1.5c), a similar high spatial resolution seems possible in ion imaging microscopy and backscatter ion diffraction, which is significantly better than in the SEM.

Ion-induced secondary electrons as well as backscattered ions are used for imaging the specimen surface in the scanning ion microscope. An excellent orientation contrast is obtained from polycrystalline surfaces (Wendt and Nolze 2007; Fig. 1.8). This is a clear indication of the strong blocking effect. When the ion beam impinges on the specimen, it is fanned out over large angles because of the onset of inelastic scattering. Further propagation of the ions in the crystal depends on their direction of movement with respect to the lattice. Ions that propagate at angles wider than certain classical critical angles of incidence to densely packed lattice planes or rows of atoms are blocked and backscattered. Up to certain critical angles with respect to the lattice, the ions are channeled deeper in the crystal and experience less probability of being backscattered. Hence, a low signal of backscattered ions as well as of secondary electrons is detected at these angles. This classical ballistic model of channeling, based on the assumption

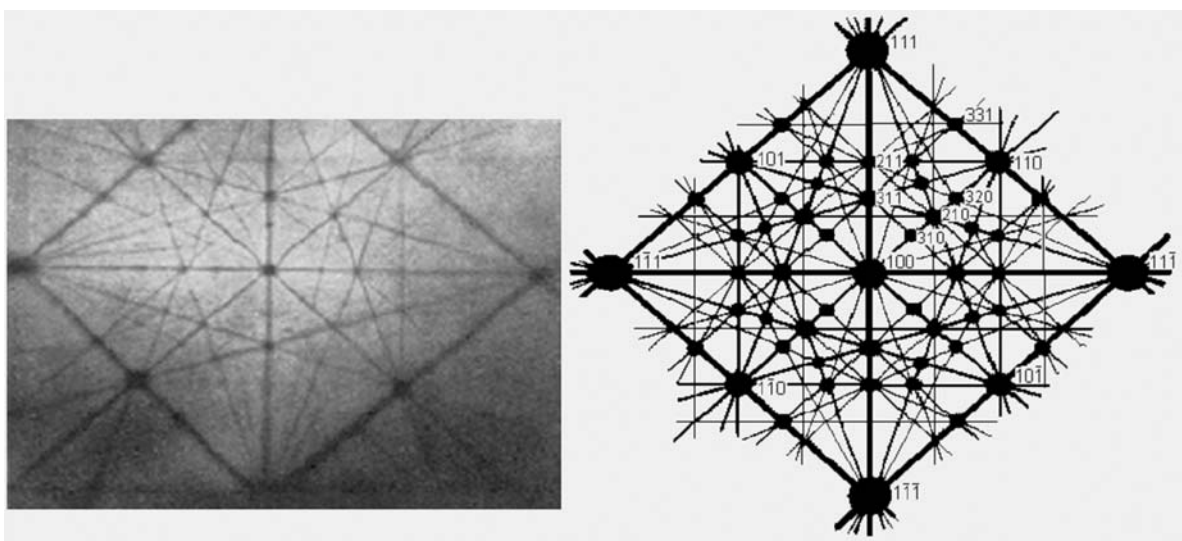


Fig. 1.7 (**left**) Ion blocking pattern from a (100) face when a 200 keV proton beam impinges on a tungsten single crystal, and (**right**) the simulated pattern (after Tulinov 1965, Figs. 10 and 11). The photographic plate was positioned substantially parallel to the specimen surface

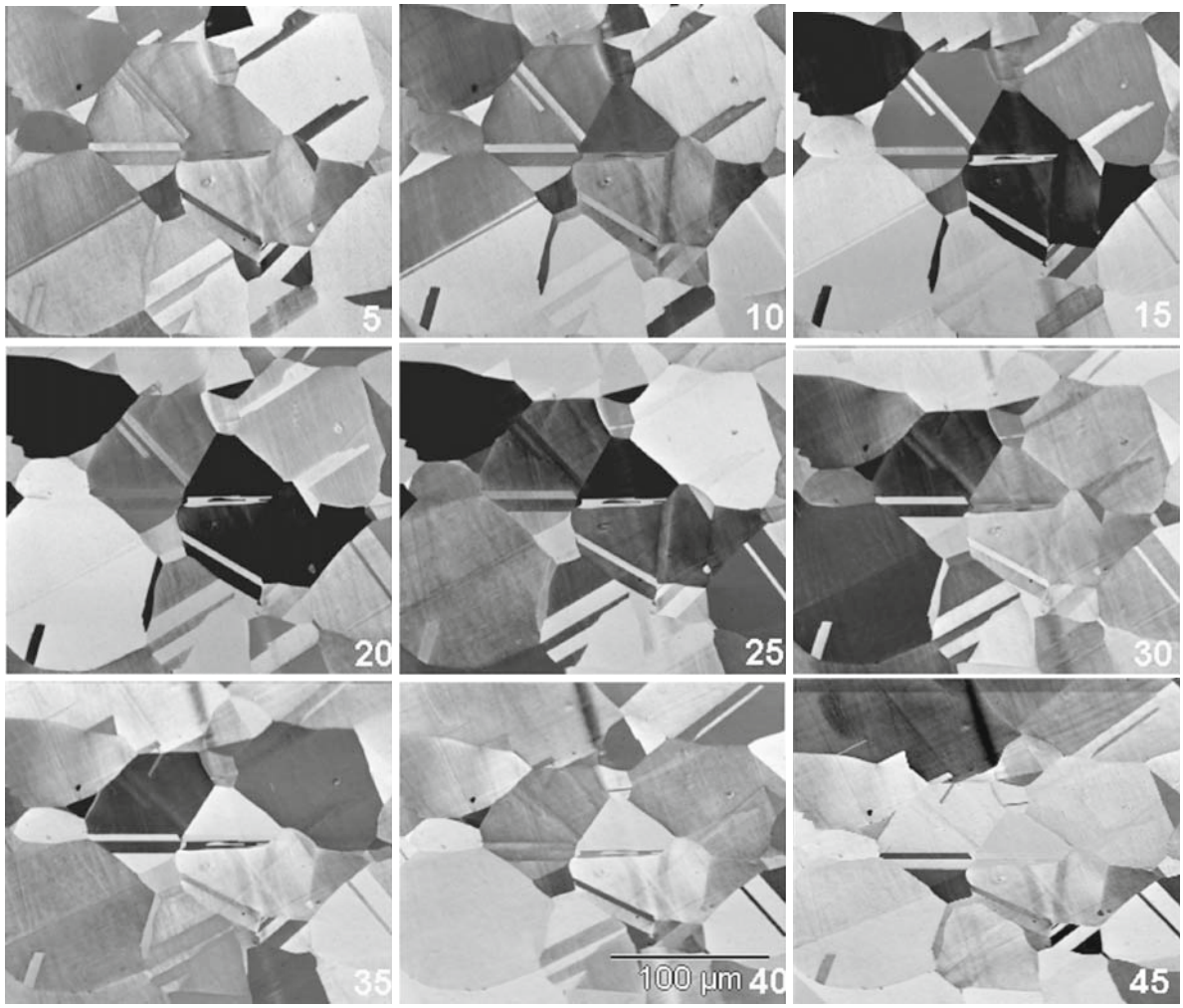


Fig. 1.8 Orientation contrast as a function of specimen tilt in the scanning ion microscope. A polycrystalline copper specimen has been imaged with ion-induced electrons in a scanning ion microscope with a Ga+ liquid metal ion source at 30 keV. The specimen has been tilted about the x-axis of the stage in steps of 5°

of Rutherford scattering, describes the positions of bands in the IBP quite well. The quantum mechanical treatment of ion diffraction must consider a multiple beam approach (Chadderton 1968). The results correspond to those of the classical treatment, in particular that the band width of IBP is within the mass invariant limit of the critical angle, whereas the width of a Kikuchi band in electron diffraction is given by twice the Bragg angle.

For recording the 2D intensity distribution of the backscattered ions, i.e., the ion blocking pattern, an imaging ion detector is required. Ion-sensitive photographic plates are an impractical recording medium for orientation microscopy. Phosphor screens are a proven means for recording electron diffraction patterns, but they are damaged by ion bombardment, so that their sensitivity will drop after exposure to ion blocking patterns. For long-term operation, an open microchannel plate can serve as an ion-to-electron image converter. The converted IBP is projected on a phosphor screen and recorded with a (fiber-optically coupled) CCD camera.

A similar technique as for backscatter Kikuchi diffraction can be used for the acquisition and indexing of IBP. Allowance has to be made in the software for the different background intensities, pattern contrasts,

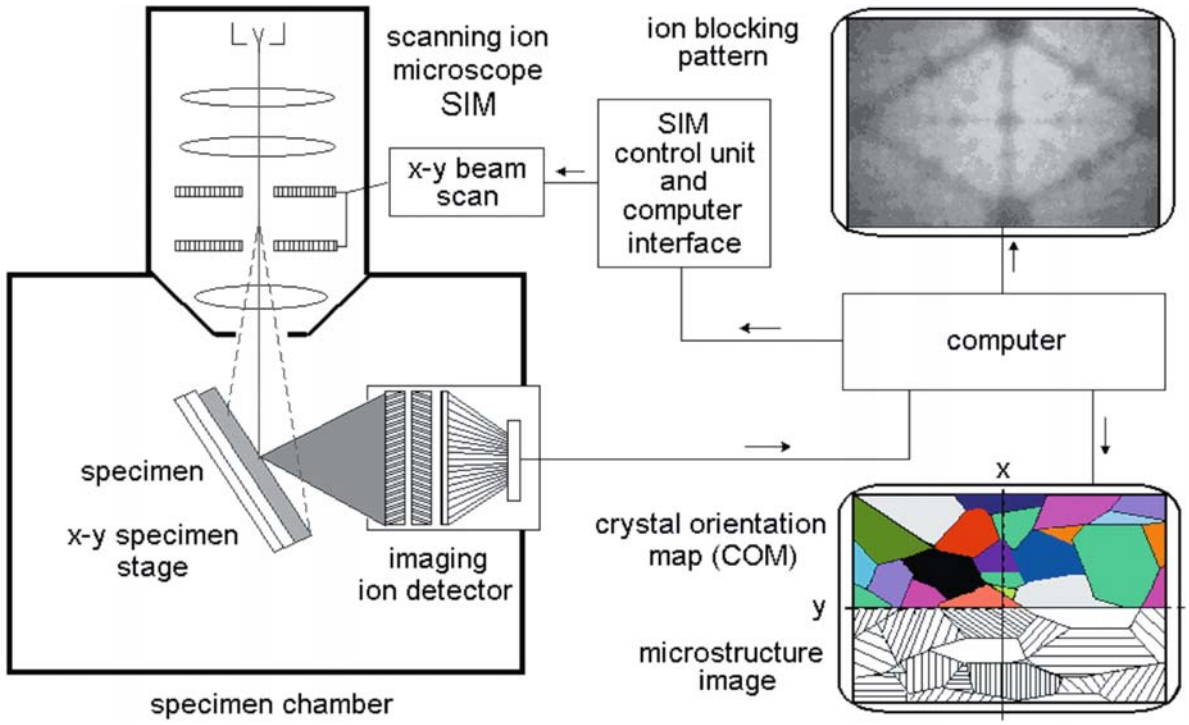


Fig. 1.9 Experimental set-up for orientation microscopy with a computer-controlled scanning ion microscope using ion blocking patterns for grain orientation measurement

and profiles of the Kikuchi bands versus the blocking bands. A schematic set-up of orientation microscopy with IBP and a focused ion beam is shown in Fig. 1.9 (Schwarzer 2007, 2008b).

This method promises the following advantages over EBSD in the SEM:

- It can be technically realized as an accessory to a scanning ion microscope.
- The sample is tilted at moderate angles of about 45° to the primary beam direction to accommodate the wide-angle pick-up of IBP. As a result, the image distortion and spatial resolution in beam direction are markedly reduced as compared to EBSD, where the specimen is steeply tilted to typically 70°.
- Sample preparation is less difficult since deformation layers or foreign surface layers can be removed at a controlled rate in situ by using a primary beam of heavy ions until clear blocking patterns have developed.
- 3D reconstruction of the volumetric microstructure from planar 2D slices is facilitated by controlled ion milling. A smooth surface that shows little damage is produced at a shallow incidence of the beam. For orientation microscopy, the specimen may remain stationary in this position or simply be tilted to a steeper angle to the beam if a higher spatial resolution is required in ion blocking diffraction. In a combined SEM-FIB system, on the contrary, the specimen has to be realigned for grazing incidence FIB surface polishing, requiring subsequent delicate tilt-rotation movement of the specimen to return to the EBSD beam position.
- Specimen charging is less harmful than in the SEM because secondary electrons are released from walls of the specimen chamber by the impact of scattered ions and neutrals. They reduce positive surface charging.

Orientation microscopy in a helium ion microscope (Morgan et al. 2006; Scipioni et al. 2007) affords particular advantages:

- A gas field ionization source can be operated with a variety of ionization gases, for example, hydrogen, oxygen, nitrogen, and noble gases; whereas a liquid

metal ion source is limited to one species of ions (e.g., Ga^+ or In^+) only.
- When using a primary beam of light ions, as for instance protons or He^+, virtually no specimen sputtering is introduced during orientation measurement or during imaging. The contamination rate is low.
- The excitation volume is not significantly larger than the minimum spot size. Spatial and in-depth resolution of orientation microscopy with IBP is expected to approach the subnanometer range.
- By alternating between beams of heavy and light ions, a sequential in-depth investigation is performed, whereby the specimen is maintained stationary (3D orientation microscopy).
- Specimens that adversely react to Ga^+ ions, such as aluminum-based alloys, can be investigated.

1.11 Conclusions

EBSD has become the standard technique for orientation microscopy and texture analysis on bulk polycrystals at a grain-specific level. Reasons include the easy operation of commercial EBSD systems, the wide availability of SEM instruments, and high-speed data acquisition. Normal and inverse pole figures, the complete orientation distribution function (ODF), as well as misorientation distribution and orientation correlation functions (ODE, MODF, OCF), can be constructed from the database of individual grain orientations of selected sample areas of any shape. Morphological parameters such as grain size and grain shape distributions, as well as crystal lattice-related quantities such as crystal perfection and the fraction of recrystallized grains, grain boundaries, misorientations, and the lattice type, can be deduced from a set of individual grain orientations.

The study of fine grained and heavily deformed materials, of nanomaterials, of recrystallization, grain growth, and grain boundary characterization often demands a substantially higher spatial resolution than is achieved with EBSD in the SEM. The combination of scanning ion microscopy and ion blocking diffraction promises a high spatial and depth resolution down to the subnanometer range in imaging and diffraction mode.

Acknowledgments The ion blocking pattern in Fig. 1.7 is a reprint from Tulinov (1965). Permission for reproduction is gratefully acknowledged to Prof. Dr. A.F. Tulinov, Lomonosov Moscow State University, and Uspekhi Fizicheskikh Nauk, Moscow. RS would like to thank Prof. Dr. U. Wendt, University of Magdeburg, Germany, for kindly providing the orientation contrast micrograph in Fig. 1.8. The work of MK and AJS was performed under the auspices of the U.S. Department of Energy at Lawrence Livermore National Laboratory under Contract DE-AC52-07NA27344.

References

Adams BL, Wright SI, Kunze K (1993) Orientation imaging: The emergence of a new microscopy. Met Trans 24A: 819–831

Alam MN, Blackman M, Pashley DW (1954) High-angle Kikuchi patterns. Proc Roy Soc London A221:224–242

Barrett CS (1979) Ion beam scattering applied to crystallography. Naturwissenschaften 57:287–295

Chadderton LT (1968) A correspondence principle for the channelling of fast charged particles. Phil Mag 8(18): 1017–1031

Day A (1993) Developments in the EBSP technique and their application to grain imaging. Ph. D. dissertation, University of Bristol, Bristol, England

Deans SR (1983) The Radon transform and some of its applications. Wiley, New York

Duda RO, Hart PE (1972) Use of the Hough transformation to detect lines and curves in pictures. Comm ACM 15:11–15

Field D (1997) Recent advances in the application of orientation imaging. Ultramicroscopy 67:1–9

Jarle Hjelen AS, N-7079 Flatåsen, Trondheim, Norway (2007) NORDIF ultra-fast EBSD detectors—the UF series. http://www.nordif.com

Hjelen J, Ørsund E, Hoel E, Runde P, Furu T, Nes E (1993) EBSP, progress in technique and applications. Textures Microstruct 20:29–40

Hough PVC (1962) Methods and means for recognizing complex patterns. US patent 3069654

Krieger Lassen NC (1994) Automated determination of crystal orientations from electron backscattering patterns. Ph. D. thesis, Danmarks Tekniske Universitet, DK-2800 Lyngby

Krieger Lassen N (1998) Automatic high-precision measurements of the location and width of Kikuchi bands in electron backscatter diffraction pattern. J Microsc 190:375–391

Kunze K, Zaefferer S, Schwarzer R (1994) Orientierungsmapping mit dem Raster-Elektronenmikroskop. Beitr Elektronenmikroskop Direktabb Oberfl 27:169–176

Michael JR, Goehner RP (1994) Advances in backscattered-electron Kikuchi patterns for crystallographic phase identification. In: Bailey GW, Garratt-Reed AJ (eds), Proceedings of the 52nd annual meeting of the microscopy society of America, San Francisco Press, pp 596–597

Morawiec A (1999) Reliability of automatic orientation determination from Kikuchi patterns. In: Szpunar JA (ed), Proceedings of the 12th international conference on textures of materials. NRC Research Press, Ottawa 1:62–67

Morgan J, Notte J, Hill R, Ward B (2006) An introduction to the helium ion microscope. Microsc Today 14(4):24–31

Nishikawa S, Kikuchi S (1928) The diffraction of cathode rays by calcite. Proc Imperial Acad (Japan) 4:475–477

Radon J (1917) Über die Bestimmung von Funktionen durch ihre Integralwerte längs gewisser Mannigfaltigkeiten. Ber Verh Sächs Akad Wiss Leipzig Math-Naturw Klasse 69:262–267

Reimer L (1985) Scanning electron microscopy. Springer Verlag, Berlin

Schwartz AJ, Kumar M, Adams BL (2000) Electron backscatter diffraction in materials science. Kluwer Academic/Plenum Publishers, New York

Schwarzer R (1989) Die Aufnahme von Reflexions-Kikuchi-Diagrammen im REM mit einer peltiergekühlten, integrie renden CCD-Videokamera. Beitr Elektronenmikr Direktabb Oberfl 22:279–282

Schwarzer RA (1994) Preparation of high-resistance or sensitive samples for grain orientation measurement with electron microscopes. Mater Sci Forum 157–162:201–206

Schwarzer RA (1997) Automated crystal lattice orientation mapping using a computer-controlled SEM. Micron 28: 249–265

Schwarzer RA, Sukkau J (1998) Automated crystal orientation mapping (ACOM) with a computer-controlled TEM by interpreting transmission Kikuchi patterns. Mater Sci Forum 273–275:215–222

Schwarzer RA (1999) Advancements of ACOM and applications to orientation stereology. In: Szpunar JA (ed) Proceedings of the 12th international conference on textures of materials. NRC Research Press, Ottawa 1:52–61

Schwarzer RA, Sukkau J (2003) Automated evaluation of Kikuchi patterns by means of Radon and fast Fourier transformation, and verification by an artificial neural network. Adv Eng Mater 5:601–606

Schwarzer R (2007) Vorrichtung zur Kristallorientierungsmessung mittels Ionen-Blocking-Pattern und einer fokussierten Ionensonde. Patent pending

Schwarzer RA (2008a) A fast ACOM/EBSD system. Arch Metall Mater 53:1–6

Schwarzer RA (2008b) Spatial resolution in ACOM—What will come after EBSD. Microsc Today 16(1):34–37

Scipioni L, Stern L, Notte J (2007) Applications of the helium ion microscope. Microsc Today 15(6):12–15

Søfferud M, Hjelen J, Karlsen M, Breivik T, Krieger Lassen NC, Schwarzer R (2008) Development of an ultra-fast EBSD detector system. In: Luysberg M, Tillmann K, Weirich T (eds) Proceedings of the 14th European microscopy congress, EMC2008, Vol. 1: Instrumentation and methods. Springer-Verlag, Berlin, pp 623–624

Toft P (1996) The Radon transform—Theory and implementation. Ph. D. thesis, Danmarks Tekniske Universitet, DK-2800 Lyngby. Free download from: http://petertoft.dk/PhD/

Tondare VN (2005) Quest for high brightness, monochromatic noble gas ion sources. J Vac Sci Technol A 23:1498–1508

Tulinov AF (1965) On an effect accompanying nuclear reactions in single crystals and its use in various physical investigations. Sov Phys-Doklady 10:463–465 (English translation of the original article of A.F. Tulinov in Doklady Akademii Nauk SSSR 162:546–548)

Venables JA, Harland CJ (1973) Electron back-scattering patterns—A new technique for obtaining crystallographic information in the scanning electron microscope. Phil Mag 27:1193–1200

Venables JA, Bin-Jaya R (1977) Accurate microcrystallography using electron back-scattering patterns. Phil Mag 35: 1317–1328

Wendt U, Nolze G (2007) FIB milling and channeling. GIT Imaging Microsc 9(3):34–36

Winkelmann A, Trager-Cowan C, Sweeney F, Day A, Parbrook P (2007) Many-beam dynamical simulation of electron backscatter diffraction patterns. Ultramicroscopy 107: 414–421

Winkelmann A (2008) Dynamical simulation of electron backscatter diffraction patterns. Chapter 2, this volume

Wu CT, Adams BL, Bauer CL, Casasent D, Morawiec A, Ozdemir S, Talukder A (1999) Mapping the mesoscale interface structure in polycrystalline materials. Microsc Microanal 5(Suppl 2):260–261

Yang W, Adams BL, De Graef M (1999) Adaptive orientation imaging microscopy. In: Szpunar JA (ed) Proceedings of the 12th international conference on textures of materials. NRC Research Press, Ottawa 1:192–197

Zaefferer S, Schwarzer RA (1994) Automated measurement of single grain orientations in the TEM. Z Metallkd 85: 585–591

Chapter 2

Dynamical Simulation of Electron Backscatter Diffraction Patterns

Aimo Winkelmann

2.1 Introduction

To extract the maximum amount of information from experimental electron backscatter diffraction (EBSD) patterns, it is necessary to realistically model the physical processes that lead to the formation of the characteristic diffraction features in the form of Kikuchi bands and lines. Whereas the purely geometrical relations in the observed networks of bands and lines can be explained by mapping out Bragg's law for the relevant reflecting lattice planes, the dynamical theory of electron diffraction is needed to explain the observed *intensities*. This theory takes into account the fact that electrons interact strongly with matter, which leads to multiple elastic and inelastic scattering of the electron waves in a crystal.

To simulate a realistic EBSD pattern, we will need to model the very general situation of an incident electron beam which hits a sample and which subsequently undergoes elastic and inelastic interactions to result in the intensity pattern on the observation screen. The incident primary beam contains electron waves within a relatively narrow range of energies and directions (defined by the properties of the electron gun), whereas the backscattered electrons have a broad spectrum of energies (due to inelastic scattering) and are distributed over all possible directions (due to momentum changes by inelastic as well as elastic scattering). Because the exact solution of the combined elastic and inelastic scattering problem is one of the most difficult problems in electron diffraction theory, we will use a simplified model, which is expected to capture the most important aspects of the problem.

A. Winkelmann (✉)
Max-Planck-Institut für Mikrostrukturphysik, Halle (Saale), Germany
e-mail: winkelm@mpi-halle.mpg.de

2.2 Model of Electron Backscatter Diffraction

For a general description of the intertwined elastic and inelastic redistribution of electrons from the states of the incident beam to the outgoing states, the quantum mechanical density matrix formalism can be used (Dudarev et al. 1993). It enables one to describe in a consistent way the coherent elastic scattering that is at the heart of the diffraction process, together with the loss of energy and the increasing randomization of quantum mechanical phase relationships between the involved states by inelastic scattering. If the relevant states and scattering processes are identified, it is in principle possible to calculate the evolution of the population in those states observed on the phosphor screen in an EBSD experiment.

The density matrix formalism allows the most general description, but a full ab initio treatment of EBSD intensities is very complicated. To make the dynamical simulations useable in practical situations, we will apply a simplified model, which captures the most important aspects of the problem using some reasonable approximations. Our main approximation will be that the inelastic scattering, which produces the sources for the subsequently diffracted electrons, can be handled independently of the diffraction process in the outgoing path (Fig. 2.1). This means that no

A.J. Schwartz et al. (eds.), *Electron Backscatter Diffraction in Materials Science*,
DOI 10.1007/978-0-387-88136-2_2, © Springer Science+Business Media, LLC 2009

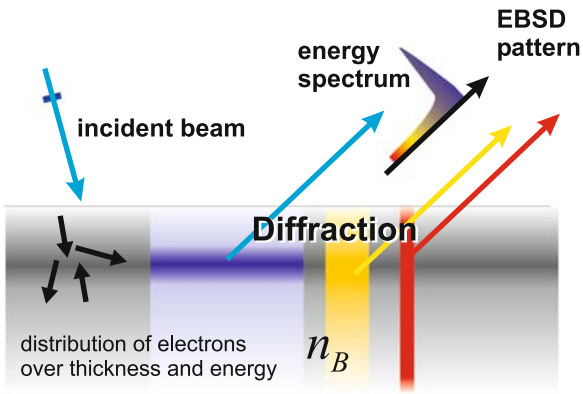


Fig. 2.1 Schematic model for the simulation of EBSD patterns: The multiple elastic and inelastic scattering of primary electrons leads to an incoherent distribution n_B of electrons over energy and thickness. The diffraction is assumed to take place independently for each energy and from each backscattering depth according to the weight function n_B

coherence between the incident electrons and the electrons forming the EBSD pattern is left. We will assume that we know the distribution $n_B(\theta, \phi, \theta_{in}, \phi_{in}, E, t)$ of inelastically scattered electrons at energy E, in a depth t inside the sample that are scattered into the direction (θ,ϕ) if the primary beam is incident from the direction (θ_{in}, ϕ_{in}). In this way, n_B is assumed to represent the accumulated effects of elastic and inelastic scattering from the incident beam; but it also needs to include those electrons which are lost from the diffracted wave field by inelastic scattering in the outgoing path. A practical way to approximately determine $n_B(E, t)$, for instance, is by Monte Carlo simulations. We will see in the following that the observed EBSD intensity distributions can be explained without very detailed assumptions about the function n_B, because in an EBSD experiment, we are actually less interested in the absolute intensities which are inelastically scattered, but rather in the small-scale variations that are introduced by dynamical diffraction on a relatively smooth background of inelastically scattered electrons. In the following, we will assume that $n_B(E, t)$ is given and we will illustrate what consequences different depth distributions will have on the dynamical diffraction intensities.

Under the assumptions of our model, we can symbolically write down the observed intensity I_B as an integral over all inelastically scattered electrons which are diffracted in the outgoing pathway with initial distribution function n_B from the primary energy E_p down to zero kinetic energy, and which come from the sample surface up to a maximum thickness $t_{\max}$:

$$I_B \propto \int_0^{E_p} dE \int_0^{t_{\max}} dt\, D\left[n_B(\theta, \phi, \theta_{in}, \phi_{in}, E, t)\right]. \quad (2.1)$$

The diffraction process of the electrons at energy E is symbolized by an operator D.

2.3 Dynamical Electron Diffraction in EBSD

According to our model, we describe the observed EBSD patterns as a superposition of diffraction patterns from electrons having a fixed energy E. The contributions from different energies are added according to the weight function n_B. In the following, we will introduce the theoretical framework necessary to describe the dynamical diffraction process.

2.3.1 Using the Reciprocity Principle

The reciprocity principle (Fig. 2.2) is based on time reversal symmetry and states that it makes no difference whether we calculate the intensity at point **D** which is due to the elastic scattering of waves emitted from point **P**, or whether we calculate the intensity at point **P** which is due to the scattering of waves emitted from point **D** (Pogany and Turner 1968).

The tremendous advantage of using the time-reversed path in Fig. 2.2b comes from the fact that in Fig. 2.2a we are detecting the intensity at a distance that is basically infinite compared to the separations of the scattering atoms. In this limit, a plane wave is detected at **D**. Turning this around, it means that we can start a *single* plane wave along the direction defined by the point **D** and then we calculate how this single plane wave is scattered by the atoms of the sample. For perfect crystals, the Bloch wave theory is a convenient method to solve this problem. It turns out that by this approach we not only obtain the wave function at a single point **P**, but instead, in a single run we get the wave function in the whole crystal. In this way, we

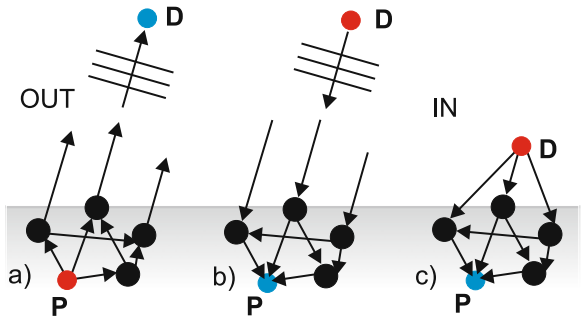


Fig. 2.2 Application of the reciprocity principle for EBSD calculations: (**a**) EBSD patterns are formed by elastic scattering of electrons which are emitted into *all* directions from a point source at **P**. These electrons are detected at point **D** on the phosphor screen, which is practically infinitely far away. In this limit, a plane wave is detected. (**b**) The problem (**a**) is equivalent to starting a plane wave in a *single* direction from **D** and detecting the intensity arriving at point **P**. (**c**) The big advantage of calculating the time-reversed problem in (**b**) stems from the fact that we need only one initial plane wave. This advantage would be lost if **D** is near the crystal surface and we would have to consider waves emitted into all directions whether we start the calculation from **D** or from **P**

are able to analytically integrate the effects of different emitters from various depths and positions in the unit cell.

The reciprocity principle can be used to connect the dominant outgoing diffraction process in EBSD to other types of methods that are governed by the diffraction of ingoing electrons. This includes electron-channelling patterns, where the total number of backscattered electrons is monitored as a function of the incidence angle of an electron beam. Important conclusions for EBSD can be drawn from previous studies of electron channelling patterns by the dynamical theory (Marthinsen and Høier 1986, 1988; Rossouw et al. 1994; Dudarev et al. 1995). Another close connection can be seen between EBSD and methods of transmission electron microscopy (TEM). To describe TEM, the diffraction and corresponding modulation in intensity of transmitted plane waves needs to be calculated. Obviously, this is related to the problem illustrated in Fig. 2.2b, with the principal difference that in TEM, the relevant thickness is the thickness of the sample; whereas in EBSD, the plane wave needs to be evaluated at the thickness of the emitter at point **P**.

There exists a number of computational approaches to describe the diffraction of transmitted electrons. These approaches include most prominently the multislice and the Bloch wave approaches. One can in principle use these existing approaches for TEM simulations to also simulate EBSD patterns (disregarding numerical limitations). We just have to appropriately account for the property of the diffracted wave field that is observed in EBSD: the *probability density inside the crystal* at the atomic positions **P**.

2.3.2 Bloch Wave Formalism

In our simulations, we will apply the Bloch wave approach. This theory solves the diffraction problem for electrons in a perfect crystal lattice by exploiting the fact that the wave function must have a very specific form in a three-dimensionally periodic potential. The use of this method is described in several accessible reviews (Humphreys 1979; Spence and Zuo 1992). In the following we will summarize the most important aspects.

The wave function inside the crystal is described as a superposition of Bloch waves with wave vectors $\mathbf{k}^{(j)}$

$$\Psi(\mathbf{r}) = \sum_j c_j \exp(2\pi i \mathbf{k}^{(j)} \cdot \mathbf{r}) \sum_g C_g^{(j)} \exp(2\pi i \mathbf{g} \cdot \mathbf{r}). \tag{2.2}$$

The aim of this approach is to get the expansion coefficients c_j and $C_g^{(j)}$, as well as the $\mathbf{k}^{(j)}$. After this is accomplished, the wave function Ψ is known and, in the next step, the coupling of the inelastic scattering processes to the diffractionally modulated probability amplitude Ψ is taken into account.

The wave function Ψ is a solution of the Schrödinger equation for an incident plane wave $\exp(2\pi i \mathbf{K_0} \cdot \mathbf{r})$, corresponding to an energy of $h^2 K_0^2/2m$:

$$\frac{-h^2}{8\pi^2 m} \Delta\Psi(\mathbf{r}) - |e| V(\mathbf{r}) \Psi(\mathbf{r}) = \frac{h^2 K_0^2}{2m} \Psi(\mathbf{r}). \tag{2.3}$$

To proceed with the determination of Ψ, one uses the translational invariance of the crystal to write the potential as a Fourier series:

$$U(\mathbf{r}) = U^c(\mathbf{r}) + iU'(\mathbf{r}) = \sum_{\mathbf{g}} U_{\mathbf{g}} \exp(i 2\pi \mathbf{g} \cdot \mathbf{r}). \tag{2.4}$$

U is a scaled potential which is measured in Å^{-2} and which is formed from complex electron structure factors $U_{\mathbf{g}}^{c} = 2m|e|V_{\mathbf{g}}/h^2$, with $V_{\mathbf{g}}$ being a Fourier coefficient of the crystal potential in volts and the relativistic electron mass m. The loss of electrons from the diffracted coherent population due to inelastic effects is taken into account by corresponding Fourier coefficients $U'_{\mathbf{g}}$ of an imaginary part of the crystal potential.

Substitution of these expressions for the wave function and the potential into the Schrödinger equation leads to the standard dispersion relation:

$$[\mathbf{K}^2 - (\mathbf{k}^{(j)} + \mathbf{g})^2]C_{\mathbf{g}}^{(j)} + \sum_h U_{\mathbf{g}-\mathbf{h}} C_{\mathbf{h}}^{(j)} = 0. \quad (2.5)$$

$\mathbf{K}$ is the incident electron wave vector inside the crystal, $K_0^2 = K^2 - U_0^c$, with the mean inner potential U_0^c and the electron wave vector in vacuum $\mathbf{K}_0$.

Then $\mathbf{k}^{(j)}$ is written as:

$$\mathbf{k}^{(j)} = \mathbf{K} + \lambda^{(j)}\mathbf{n}, \quad (2.6)$$

where $\mathbf{n}$ is a unit vector normal to the surface. One can then transform (2.5) into an eigenvalue problem, which gives the eigenvalues $\lambda^{(j)}$ and eigenvectors with elements $C_{\mathbf{g}}^{(j)}$ (Spence and Zuo 1992). This includes the effects due to the tilt of the outgoing direction with respect to the surface (Allen and Rossouw 1989) and is also valid for reciprocal space vectors $\mathbf{g}$ in higher order Laue zones (HOLZ). The boundary conditions at the surface determine the coefficients c_j in (2.2). These quantities are given by the elements of the first column of the inverse of the matrix whose elements are $C_{\mathbf{g}}^{(j)}$. After this, the wave function (2.2) is known.

The Fourier coefficients of the real and the imaginary part of the crystal potential can be calculated from the contributions of the atoms that constitute the unit cell. These contributions can be obtained from published parameterizations for the real and imaginary part of the potential (Weickenmeier and Kohl 1991).

The eigenvalue method described above scales as N^3 with the number N of the included reflecting planes. This quickly leads to impractically long computation times if a large number of reflections has to be included. This can be overcome by the use of the Bethe perturbation scheme, which allows the inclusion of the effects of weak reflections U_h by the transformation into an effective potential of the strong beams U_g^{eff} without increasing the matrix dimensions:

$$U_{\mathbf{g}}^{eff} = U_{\mathbf{g}} - \sum_h \frac{U_{\mathbf{h}} U_{\mathbf{g}-\mathbf{h}}}{2K S_h}, \quad (2.7)$$

where $2KS_h$ is defined by $2KS_h = K^2 - (\mathbf{K} + \mathbf{h})^2$, containing the excitation error S_h. For the use of the Bethe perturbation, beam selection and convergence criteria have been developed in the context of convergent beam electron diffraction (Zuo and Weickenmeier 1995). Strong and weak beams are selected according to their structure factor and the excitation error, describing how strong the influence of a certain reflecting plane is at the considered point in the diffraction pattern.

2.3.3 Inclusion of the Backscattering Process

Using the Bloch wave approach, we can determine the diffraction-induced changes in the probability of an electron to leave the crystal from an arbitrary position $\mathbf{r}$ inside the crystal. The backscattered electrons start predominantly from the positions of the atoms. In a first approximation, this simply means that we need to calculate the probability density $\Psi\Psi^*$ at the atomic positions $\mathbf{P}$. This is straightforward by using Equation (2.2) (Allen and Rossouw 1989). For arbitrary inelastic processes, the interaction of diffracted electrons with the crystal can be modelled by generalized potentials (Allen and Rossouw 1990). In the case of backscattering, these potentials have the form of delta functions (point sources), which are broadened by the thermal vibrations. The dynamically backscattered intensity integrated from depth t_1 to t_2 is then given by (Rossouw et al. 1994):

$$I_{DYN} \propto \sum_{n,ij} Z_n^2 B^{ij}(t_1, t_2) \sum_{\mathbf{g},\mathbf{h}} C_{\mathbf{g}}^{(i)} C_{\mathbf{h}}^{(j)*} \times \exp(-B_n s^2) \exp[2\pi i(\mathbf{g} - \mathbf{h}) \cdot \mathbf{r}_n], \quad (2.8)$$

with atoms at $\mathbf{r}_n$, Debye-Waller factors $\exp(-B_n s^2)$, and a depth integrated interference term $B^{ij}(t_1, t_2)$ of

the Bloch waves i and j:

$$B^{ij}(t_1, t_2) = c_i c_j^* \frac{\exp[2\pi i(\lambda^i - \lambda^{j^*})t_2] - \exp[2\pi i(\lambda^i - \lambda^{j^*})t_1]}{2\pi i(\lambda^i - \lambda^{j^*})}. \quad (2.9)$$

Because the wave functions are known to be of the form in Equation (2.2), the thickness integration for an inelastic source extending from t_1 to t_2 can be carried out analytically.

Using the method described above, the backscattering pattern can be calculated point by point, each describing a well-defined wave vector direction $\mathbf{K}_0$. The application of the Bethe perturbation scheme allows the inclusion of a large number of reflecting planes, so that the large viewing angles in EBSD can be handled (Winkelmann et al. 2007).

2.4 Applications

In this section we will apply the developed computational approach to a number of important basic problems of the EBSD technique.

2.4.1 A Real-Space View of EBSD

To illustrate the basic mechanism behind a typical intensity distribution in Kikuchi bands, we calculated a hypothetical nine-beam EBSD pattern of the $\{110\}$ and $\{200\}$ families of lattice planes from bcc iron, which is shown in the top middle part of Fig. 2.3. It is one of the very useful properties of the Bloch wave approach that we can selectively switch off all other lines in the diffraction pattern because of the one-to-one correspondence between the Fourier coefficients (reciprocal lattice vectors) considered in the many-beam problem and the observed Kikuchi lines. For the simplified EBSD pattern shown in Fig. 2.3, we can now calculate the probability density in the crystal that corresponds to some typical points in the Kikuchi bands. Because the considered lattice planes are perpendicular to the surface, we can show the probability density averaged along the [001] surface normal direction as a two-dimensional plot over 3×3 unit cells in the other panels of Fig. 2.3. The crystal surface is viewed from the direction of the surface normal, the centered atoms of the bcc cells are drawn smaller.

In the right part of Fig. 2.3, we see the probability density corresponding to the middle (d, blue dashed) and to the border (c, red dashed) of a $\{200\}$ Kikuchi band. It is clearly seen that in the middle of the Kikuchi band, the probability density is concentrated at the atomic positions; while at the border of the band, the probability density is focused between the atomic planes. The same process happens for the $\{110\}$ Kikuchi band in the left part of Fig. 2.3, a and b. One sees how nicely the diffracted probability density has to conform to the symmetry implied by the respective lattice planes. This becomes particularly important near the zone axis in the center (e) of the EBSD pattern, where the full interaction of all crossing lattice planes has to be considered. Correspondingly, the probability density is confined to the channel along the [001] atomic columns (lower middle panel of Fig. 2.3; the remaining intensity between the atoms is due to the limited number of 9 beams in the calculation).

From the probability density of diffraction we can draw conclusions regarding the observed intensity in a typical EBSD pattern. There will be high intensity in the pattern in directions where the diffraction probability density overlaps strongly with those places where the inelastic electrons are created. These places coincide with the atomic positions in the case of thermal diffuse (phonon) scattering. In summary, this means that we should see high intensity in the middle of the Kikuchi bands (probability density is focused mainly on the atomic planes), and low intensity at the border (probability density is mainly between the atomic planes).

This explanation suffices for the majority of EBSD patterns taken in standard setups with incidence angles in the order of 70 degrees. However, under special experimental circumstances, a contrast reversal of the observed Kikuchi bands can take place, and the above explanation has to be extended. In early investigations of Kikuchi patterns, it has been observed that the contrast within a band is reversed for electrons leaving the sample with low take-off angles when the *incidence* angle of the electron beam is decreased so that it impinges more steeply on the surface (Alam et al. 1954). In such a situation, the backscattered electrons come from a larger depth below the sample surface (Reimer 1998). Similar contrast reversals of Kikuchi

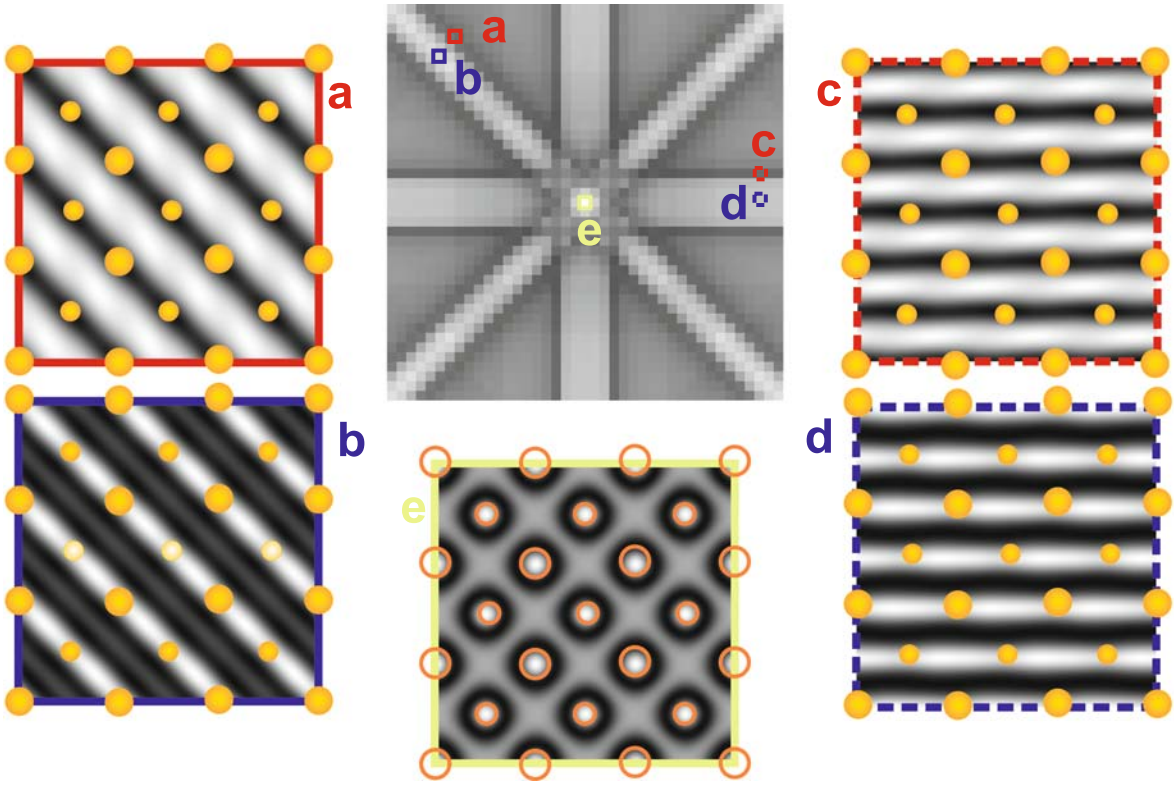


Fig. 2.3 Nine-beam EBSD pattern (*top middle*) of a bcc structure and diffraction probability distributions at selected directions, which are marked by *solid* and *dashed colored squares* in the diffraction pattern. The centered atoms in the bcc structure are drawn smaller

bands have also been observed in transmission electron microscopy, and theoretical models for the thickness dependent contrast reversal of Kikuchi bands in transmission electron diffraction were given (Hall 1970; Chukhovskii et al. 1973).

In the dynamical theory, the contrast reversal with thickness appears due to the much stronger absorption of those Bloch waves which travel along the atomic positions, compared to the Bloch waves which travel between the atomic planes. This has an important consequence if we increase the depth from which the electron waves start the backscatter diffraction process.

This is illustrated in Fig. 2.4 by a simple model calculation, similar to the real-space view of Fig. 2.3. This calculation was carried out for a source which is near the surface (upper part) and another source which is deeper inside the crystal (lower part). In the middle we see the calculated Kikuchi band intensity. On the left of Fig. 2.4, we see the type II wave field which is excited predominantly at the edges of a Kikuchi band. On the right side of Fig. 2.4, we see the type I wave excited in the middle part of a Kikuchi band. We emphasize that the elastic diffraction effect of the excitation of two different types of Bloch waves is *not* a function of thickness. What changes is the number of electrons in both types of fields: in the upper part, both fields are excited almost equally, and the increased overlap of the type I field on the right with the backscattering atoms leads to a high intensity in the middle of the band. In the situation in the lower part of the figure, although the type I wave field geometrically still overlaps better with the atomic positions, this wave field is of very low intensity because it is absorbed strongly. Effectively, the smaller residual overlap of the type II field with the backscattering

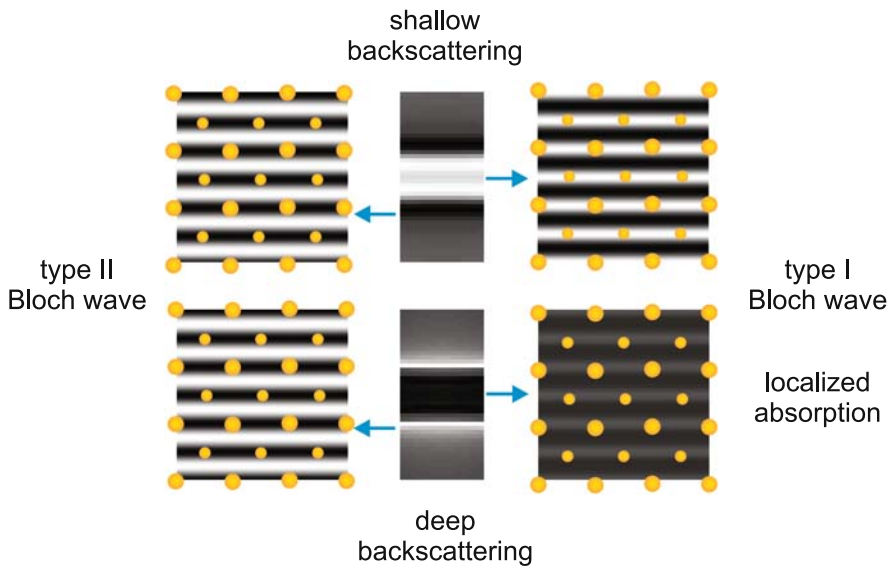


Fig. 2.4 Principle of contrast reversal with increasing thickness. The type I Bloch wave is localized at the atomic planes and is also more strongly absorbed. Beyond a certain thickness, the type I wave is almost completely absorbed. Because the type I wave dominates in the middle of the band, there will be a minimum of intensity for a deep source

atoms on the right still leads to a higher signal on the edges of the Kikuchi band from the deeper source. Correspondingly, we observe a Kikuchi band with inverted contrast.

2.4.2 Full Scale Simulation of EBSD Patterns

We now demonstrate that by inclusion of all relevant lattice planes in a dynamical calculation, we can simulate a complete EBSD pattern with very good agreement to experimentally measured patterns.

As a first example, we choose molybdenum, with a bcc structure and a lattice constant of 3.147 Å. The Debye-Waller factor B was assumed to be 0.25 Å^2 (Peng et al. 1996), and all reflections which appear within 50 degrees from the [001] zone axis to have a minimum lattice spacing of $d_{hkl} > 0.35$Å and a minimum structure amplitude $U_{hkl} > 0.005$Å^{-2}. This leads to a set of about 1200 beams, which need to be taken into account. On average, about 150 beams were treated exactly in the many-beam problem, the rest were taken into account by the Bethe perturbation. We assumed that backscattered electrons were excited from a thickness up to 150 nm. The final simulated picture has been smoothed according to an angular resolution of about 1 mrad. The contrast has been changed very slightly to correspond to the measured pattern. The calculation was carried out for 640 × 480 data points and took 3.5 days on a single CPU of a Pentium D 3.4 GHz processor.

In Fig. 2.5, we show the comparison with an experimental pattern taken at 25 keV incident beam energy. Apart from the increased noise in the outer parts of the experimental pattern, it can be seen that the simulation and the experiment match almost perfectly. Also, the typical ring structures appear in the dynamical calculation. The mechanism that leads to the formation of the rings can be interpreted as a transmission resonance and has been extensively discussed for the case of an incident plane wave, which at the resonance angle θ_r strongly couples to states bound in the atomic column along the respective zone axis (Dudarev and Peng 1993b, a). By reciprocity, we can see that this effect works analogously for the coupling between Bloch waves moving in the potential of an atomic column and outgoing plane waves, which form the ring intensity near the angle θ_r.

The specific reciprocal lattice vectors that label the Fourier coefficients of the crystal potential involved in the transfer of intensity between the atomic column

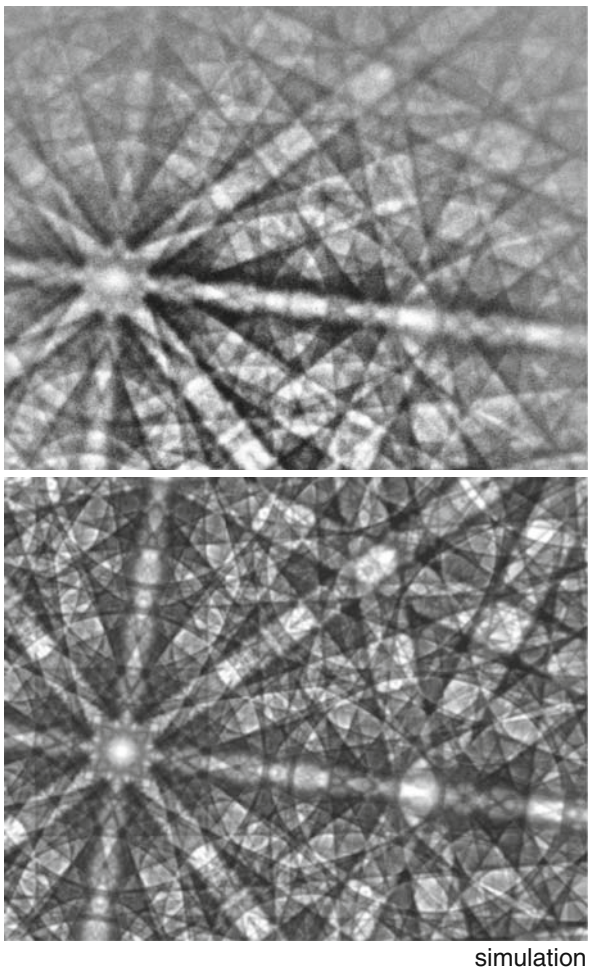


Fig. 2.5 Full scale many-beam dynamical simulation of an EBSD pattern from molybdenum and comparison with an experimental pattern. In the calculation, a total of 1200 reflections were considered; on average 150 reflections were treated exactly, the others were included by perturbation. A lattice constant of c = 3.147 Å was used (experimental pattern courtesy of E. Langer)

and the ring have non-zero components along the respective zone axis. This is why the rings in EBSD patterns have been termed "HOLZ rings" for short (Higher Order Laue Zone). Measuring the diameter of the HOLZ rings allows the estimation of lattice constants, which has been shown to be useful for phase identification using EBSD patterns (Michael and Eades 2000). Due to the inherently many-beam nature of the HOLZ ring effect, it is expected that corresponding dynamical simulations can be additionally applied to extract high precision lattice parameters from measured rings.

2.4.3 The Influence of the Energy Spectrum of the Backscattered Electrons

In view of the good agreement of the simulation shown in Fig. 2.5 with the experiment, it is necessary to analyze the influence of the energy spectrum of the backscattered electrons on the diffraction pattern. We saw that the simulation done at the energy level of the incident electrons with inclusion of a limited angular resolution does in fact match quite nicely to the experiment. Obviously, electrons in a relatively limited energy range below the incident beam energy are decisive for most of the observed diffraction features. Since the width of a Kikuchi band is a function of the energy of the diffracted electrons, an increasingly broader energy spectrum will tend to wash out the diffraction features. A limit on the energy spread which is compatible with an EBSD pattern can be estimated by comparison of the finest structures in the experimental pattern with dynamical simulations that are integrated for a range of energies. We will investigate such a scenario for the case of GaN thin films, which show very detailed patterns.

The simulations have been carried out for a limited field of view of about 25 degrees centered around the $[0\bar{2}1]$ zone axis. We took into account 431 reflectors with a lattice spacing of $d_{hkl} > 0.3$Å and a structure amplitude $U_{hkl} > 0.005$Å^{-2}. The Debye-Waller factor B was assumed at 0.25 Å^2. The calculations were done for 300 × 300 pixels in 50 eV steps, starting from the incident beam energy of 20 kV down to 15 kV.

The experimental pattern is shown in Fig. 2.6e. We see simulated patterns for the energies of 20 kV, 19.5 kV, and 18.5 kV in parts a, b, and c, respectively. By comparing these simulations with the experiment, one immediately recognizes that the central dark spot in the center of the $[0\bar{2}1]$ zone axis is becoming smaller with energy, and at 18.5 kV is already smaller than observed in experiment. A further reduction of the relevant energy range is supported by the feature which is indicated by the arrows. This feature is located near the HOLZ ring around the $[0\bar{2}1]$ zone axis, and it is

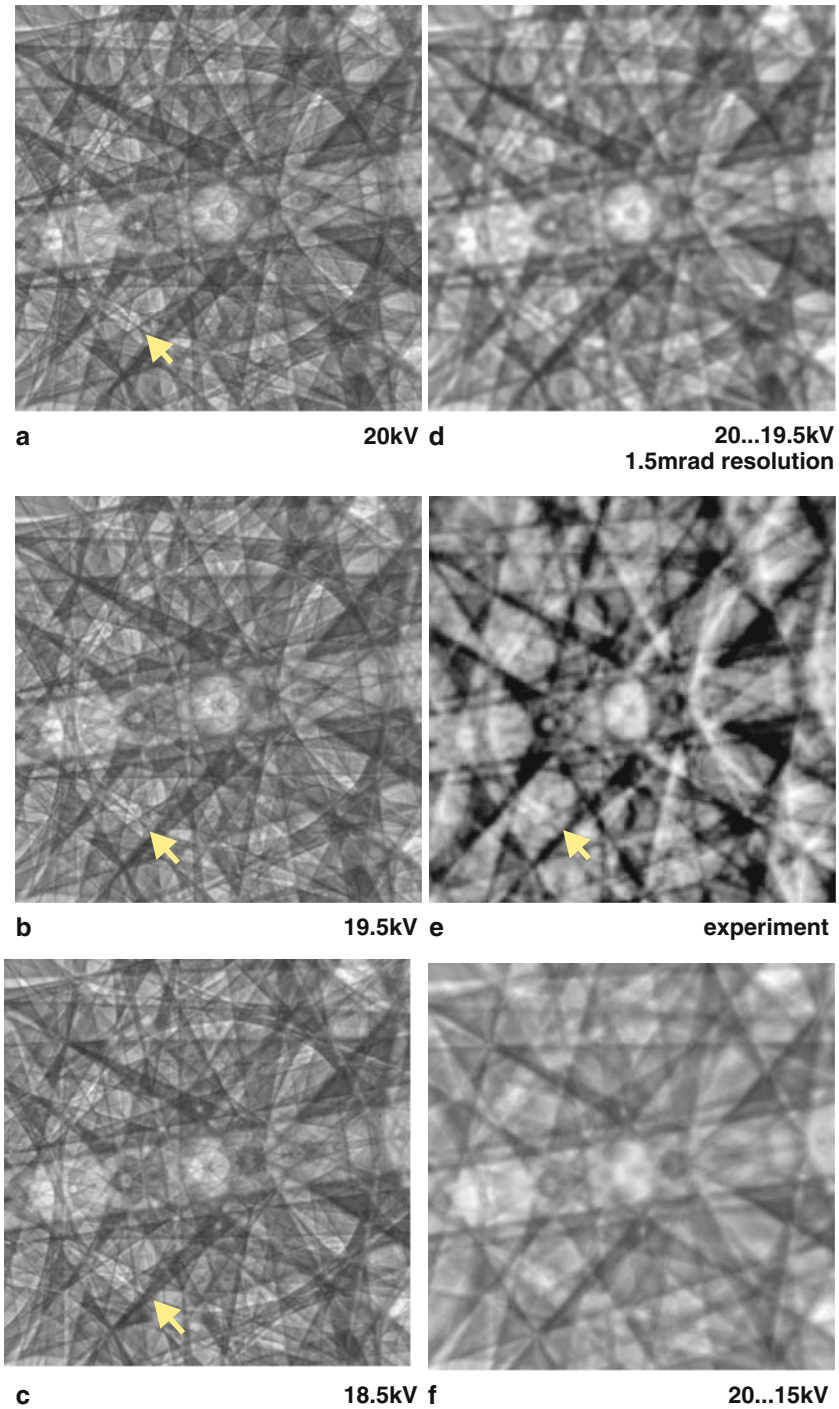


Fig. 2.6 Estimation of the influence of an energy spread in EBSD from GaN: (**a**, **b**, **c**) calculations at the specified energies (without any image processing). Note the delicately changing fine structure in the zone axis in the center of the ring, as well as the change in the feature at which the arrows are pointing. (**d**) average of 11 diffraction patterns in 50 eV steps, from 20 kV to 19.5 kV, with angular averaging according to 1.5 mrad resolution. (**e**) experimental pattern from GaN with incident beam voltage of 20 kV (courtesy of A. P. Day). (**f**) average of 100 diffraction patterns from 20 kV to 15 kV

very sensitive to the electron energy. In the experiment, we notice a gap in the intensity distribution of this feature. In the simulation, we see this gap opening at about 19.5 kV, whereas it is clearly closed at 18.5 kV. In this way, observation of the fine structure in the pattern has given us a clear indication that electrons in the range of 20 kV to 19.5 kV dominate in producing the observed features. In order to see how the averaging of such an energy spread compares to the experiment, we summed 11 patterns in 50 eV steps from 20 kV to 19.5 kV, and we applied an additional angular averaging according to a 1.5 mrad angular resolution. This additional angular broadening takes into account the limited pixel size of the CCD camera plus a possible additional angular smearing of the intensity due to lattice defects and surface contamination. The averaged simulated pattern compares very well with the experimental observations. Taking into account that we have not used any information about the experimental energy spectrum (we assumed $n_B = 1$ for 19.5 . . .20 kV), the possibility of obtaining good agreement with the experiment in a calculation for a single or a very limited number of energies would greatly reduce the required computation times. Our observation compares nicely to experimental observations using energy-filtered EBSD from Si samples. It was found that low loss electrons with energies not less than about 3% of the primary beam are predominant in producing the observed contrast (Deal et al. 2008).

We have seen that the comparison of experimental and simulated energy dependent fine structure in EBSD patterns allows important conclusions regarding the energy spectrum. In many cases, however, EBSD patterns do not show such relatively sharp features as in Fig. 2.6e. This is not necessarily due to a broad energy spectrum, but can also be caused, e.g., by lattice imperfections. From very general considerations, we can expect higher density materials to show a broader energy spectrum due to the increased multiple inelastic scattering (Reimer 1998). This then should correlate with a reduced fine structure in these materials. As an extreme case, we illustrate in Fig. 2.6f that even an energy spread of 5 kV, from 15 kV to 20 kV (100 patterns in 50 eV steps), still leads to pronounced Kikuchi bands with an overall character that might resemble experimental patterns from some materials with not as much fine structure as GaN or Si. It seems that a rather broad energy spectrum is compatible with EBSD patterns that do not show higher order fine structure. In turn this would mean that energy filtering would produce significantly more detail if the loss of fine structure were caused by energy broadening alone (whereas energy filtering would not help if the fine structure is lost due to lattice imperfections). More systematic insight is expected in the future if realistic Monte Carlo simulations of inelastic scattering are coupled with the many-beam dynamical simulations.

2.4.4 Dynamical Effects of Anisotropic Backscattering

In this section we will show which qualitative changes appear in the EBSD patterns if we take into account that the incident electrons are backscattered with different intensity in different directions. The scattering at high kinetic energies is strongly enhanced in the forward direction. Due to the usual geometry of EBSD experiments using relatively shallow incidence angles, a significant anisotropy of the initial distribution of the inelastically scattered electrons with respect to the detected directions is created. This directly influences the overall intensity distribution of the observed EBSD pattern neglecting any diffraction effects: the patterns show higher intensity towards the forward scattering direction and significantly decrease in intensity towards larger backscattering angles. However, within the small angular range of the Kikuchi band cross sections that we are interested in, this will be a relatively smoothly varying background, which can be removed by flat-fielding techniques used for enhancing the diffraction contrast in experimental patterns.

The anisotropy of each distinctive backscattering event (emitting an anisotropic coherent wave) also enters into the dynamical diffraction problem. This results in selective enhancement or suppression of the intensity of Kikuchi lines as a function of their orientation with respect to the incoming beam direction. The mechanism of these excess and deficiency lines has been discussed for the case of transmission electron microscopy Kikuchi patterns (Kainuma 1955).

The excess lines usually appear at scattering angles, which are farther away from the incident beam direction than the deficiency lines. If the backscattered electrons with wave vectors near the incident beam direction have a higher intensity than the wave vectors

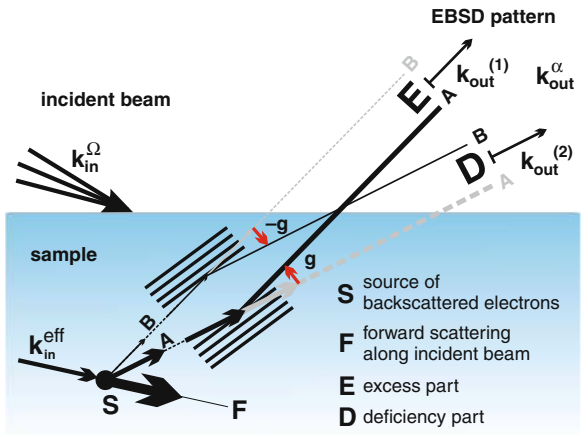


Fig. 2.7 Mechanism of the formation of excess and deficiency lines in EBSD patterns

for larger scattering angles, the intensity is then asymmetrically removed by diffraction from the position of the deficiency line and transferred to the excess line.

In Fig. 2.7, we show the basic ingredients that are necessary to qualitatively understand the excess-deficiency effect in electron backscatter diffraction.

The sources **S** of backscattered electrons are localized at atomic positions inside the crystal. The creation of the backscattered electron waves is not isotropic, and a single electron is scattered into the directions **A** and **B** with different probabilities. What is important for the effect is only that a difference exists between the numbers of electrons that are initially excited into the different directions **A** and **B**. Subsequently, these electrons are dynamically diffracted by the surrounding crystal lattice. In Fig. 2.7, we show the case that beams along **A** will be scattered by lattice plane **g**, whereas beams along **B** will be scattered by **–g**, corresponding to a pair of Kikuchi lines, with a band of increased intensity between them. The intensities along $\mathbf{k}_{out}^{(1)}$ and $\mathbf{k}_{out}^{(2)}$ in the EBSD pattern can be thought to be formed by electrons that are moving into these directions without scattering, plus electrons that are dynamically scattered from other initial directions into these final directions. Assuming equally strong scattering by **g** and **–g**, the dynamical diffraction problem is perfectly symmetric. Correspondingly, the dynamically diffracted intensities in the directions $\mathbf{k}_{out}^{(1)}$ and $\mathbf{k}_{out}^{(2)}$ would not show an excess-deficiency asymmetry if we had the same number of **A** and **B** electrons. Now we consider the case in which **A** is initially stronger than **B**. When there are more **A** electrons than there are **B** electrons, a higher number of electrons is necessarily scattered by **g** away from the initial direction of the **A** electrons into the direction $\mathbf{k}_{out}^{(1)}$, than the number of **B** electrons scattered by **–g** from $\mathbf{k}_{out}^{(1)}$ back to the initial **A** direction $\mathbf{k}_{out}^{(2)}$. By this mechanism more intensity ends up in direction $\mathbf{k}_{out}^{(1)}$ than in direction $\mathbf{k}_{out}^{(2)}$, and the excess **E** and deficiency **D** features are formed.

We have demonstrated a simple and transparent way to incorporate the relevant effects of anisotropic backscattering into Equation (2.8) (Winkelmann 2008). It was assumed that the beams **g** are excited with different strengths according to a function χ that depends on **g** and the incident and detected beam directions:

$$f_n(\mathbf{q}+\mathbf{g}) \propto Z_n \cdot \chi_{\mathbf{g}}(\mathbf{k}_{in}, \mathbf{k}_{out}^{\alpha}). \tag{2.10}$$

For simplicity, we assumed that the relative strength of excitation shows a Gaussian distribution as a function of wave-vector transfer **q** from some effective incident beam direction $\mathbf{k}_{in}^{eff}$:

$$\chi_{\mathbf{g}} = 1 + a \cdot \exp\left(\frac{-(\mathbf{k}_{out}^{\alpha} - \mathbf{k}_{in}^{eff} + \mathbf{g})^2}{b^2}\right). \tag{2.11}$$

In this equation, $\mathbf{q} = \mathbf{k}_{out}^{\alpha} - \mathbf{k}_{in}^{eff}$. The phenomenological parameters *a, b,* and $\mathbf{k}_{in}^{eff}$ have to be chosen for best agreement with the experiment. The factor $\chi_{\mathbf{g}}$ describes the deviation from isotropic scattering, which is obtained by setting all $\chi_{\mathbf{g}} = 1$. With this, a refined version of Equation (2.8) results:

$$I_{DYN}^{ED}(\mathbf{k}_{in}^{eff}, \mathbf{k}_{out}^{eff}) \propto A \sum\nolimits_{n,ij} Z_n^2 B^{ij}(t) \times \sum_{\mathbf{g},\mathbf{h}} \chi_{\mathbf{g}} \chi_{\mathbf{h}} C_{\mathbf{g}}^{(i)} C_{\mathbf{h}}^{(j)*} \exp(-B_n s^2) \exp[2\pi i(\mathbf{g}-\mathbf{h})\cdot\mathbf{r}_n] \tag{2.12}$$

This very simplified model shows the basic properties necessary for the appearance of excess-deficiency features in a transparent way, without increasing the computational load beyond practical limits and without relying on the exact microscopic details. A comparison of the isotropic and anisotropic models with an experimental pattern from CaF_2 is shown in Fig. 2.8. The simulation has been carried out at 19.5 kV using a lattice constant of 5.471 Å, including 673 reflections with a lattice spacing of $d_{hkl} > 0.3$Å and a structure amplitude $U_{hkl} > 0.005$Å^{-2}. The Debye-Waller factor

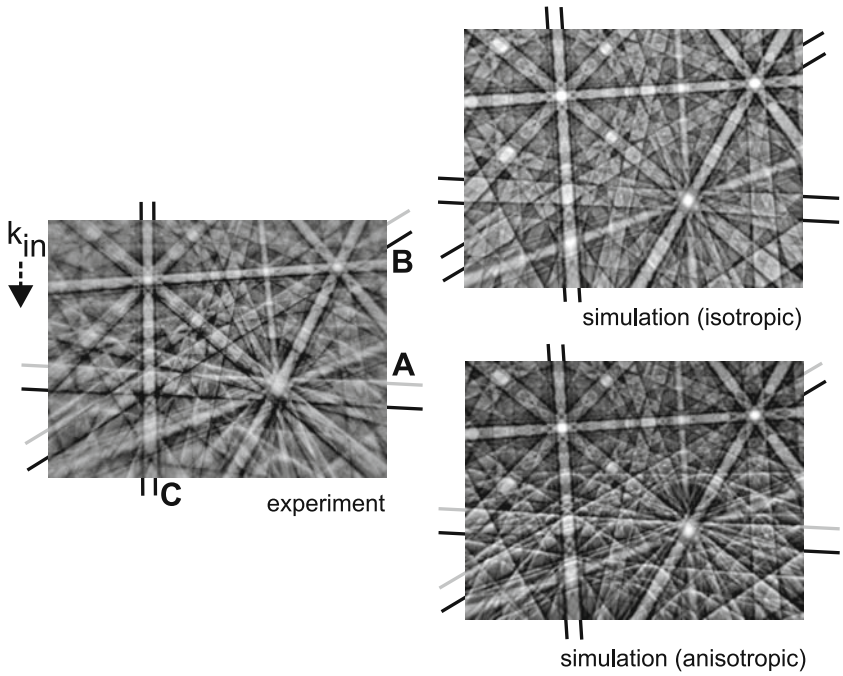


Fig. 2.8 Excess-deficiency effect in EBSD from CaF_2 at 20 kV. *Left:* experimental pattern. *Right:* simulation for an isotropically emitting source (*top*) and for an anisotropic source (*bottom*). The *gray* and *black* lines indicate the relative difference between excess and deficient intensity. The excess-deficiency effect is semi-quantitatively reproduced by the anisotropic model (experimental pattern courtesy of G. Nolze)

B was assumed to be 0.4Å^2. We assumed an angular broadening of 1.5 mrad. For the excess-deficiency model, we used $a = 5000$ and $b = 4.9\text{Å}^{-1}$. The anisotropic model reproduces very well the qualitative changes that are caused by the excess-deficiency effect. The effect resembles an illumination from the top, which corresponds to the incident beam direction. Our model also reproduces the observation that not all lines are affected equally by the excess-deficiency effect: line pair C in Fig. 2.8, which runs almost parallel to the incident beam direction, is not affected much because the inelastic scattering in our model is rotationally symmetric around the effective incident beam direction. This leads to nearly equal intensity scattered by the corresponding **g** and –**g** reflections of the line pair C.

2.5 Summary

We have seen how the Bloch wave approach can be used for a dynamical many-beam description of EBSD patterns. Very good agreement between experiment and simulation is reached in a number of cases. In the future, such dynamical simulations might become a useful tool to push the EBSD technique to new limits in the characterization of materials.

Acknowledgements I would like to thank Carol Trager-Cowan (University of Strathclyde, Glasgow) for starting my involvement with EBSD. Austin P. Day and Gert Nolze are acknowledged for supplying experimental patterns and for inspiring discussions on various aspects of electron backscatter diffraction. Part of this work was supported by the Royal Society of Edinburgh.

References

Alam MN, Blackman M, Pashley DW (1954) High-angle Kikuchi patterns. Proc R Soc Lond A 221(1145):224–242, URL http://www.jstor.org/stable/100898

Allen LJ, Rossouw CJ (1989) Effects of thermal diffuse scattering and surface tilt on diffraction and channeling of fast electrons in CdTe. Phys Rev B 39(12):8313–8321, DOI 10.1103/PhysRevB. 39.8313

Allen LJ, Rossouw CJ (1990) Absorptive potentials due to ionization and thermal diffuse scattering by fast electrons in crystals. Phys Rev B 42(18):11,644–11,654, DOI 10.1103/PhysRevB.42. 11644

Chukhovskii FN, Alexanjan LA, Pinsker ZG (1973) Dynamical treatment of Kikuchi patterns. Acta Cryst A 29:38, DOI 10.1107/S0567739473000094

Deal A, Hooghan T, Eades A (2008) Energy-filtered electron backscatter diffraction. Ultramicroscopy 108:116–125, DOI 10.1016/j.ultramic.2007.03.010

Dudarev SL, Peng LM (1993a) Effects of bulk resonance diffraction on inelastic scattering of high energy electrons by crystals. Proc R Soc Lond A 440:117–133, DOI 10.1098/rspa.1993.0007

Dudarev SL, Peng LM (1993b) Theory of bulk resonance diffraction in THEED. Proc R Soc Lond A 440:95–115, DOI 10.1098/rspa.1993.0006

Dudarev SL, Peng LM, Whelan MJ (1993) Correlations in space and time and dynamical diffraction of high-energy electrons by crystals. Phys Rev B 48:13,408, DOI 10.1103/PhysRevB.48. 13408

Dudarev SL, Rez P, Whelan MJ (1995) Theory of electron backscattering from crystals. Phys Rev B 51:3397, DOI 10.1103/PhysRevB.51.3397

Hall CR (1970) On the thickness dependence of Kikuchi band contrast. Phil Mag 175:63–72, DOI 10.1080/1478643 7008228151

Humphreys CJ (1979) The scattering of fast electrons by crystals. Rep Prog Phys 42(11):1825–1887, DOI 10.1088/0034–4885/42/11/002

Kainuma Y (1955) The theory of Kikuchi patterns. Acta Cryst 8:247, DOI 10.1107/ S0365110X55000832

Marthinsen K, Høier R (1986) Many-beam effects and phase information in electron channeling patterns. Acta Cryst A 42:484–492, DOI 10.1107/S0108767386098835

Marthinsen K, Høier R (1988) Determination of crystal symmetry from electron channeling patterns. Acta Cryst A 44: 693–700, DOI 10.1107/S0108767388003538

Michael JR, Eades JA (2000) Use of reciprocal lattice layer spacing in electron backscatter diffraction pattern analysis. Ultramicroscopy 81:67–81, DOI 10.1016/S0304–3991(99)00119–9

Peng LM, Ren G, Dudarev SL, Whelan MJ (1996) Debye-Waller factors and absorptive scattering factors of elemental crystals. Acta Crystallographica Section A 52(3):456–470, DOI 10.1107/S010876739600089X

Pogany AP, Turner PS (1968) Reciprocity in electron diffraction and microscopy. Acta Cryst A 24:103–109, DOI 10.1107/S0567739468000136

Reimer L (1998) Scanning electron microscopy—physics of image formation and microanalysis. Springer Verlag, Berlin

Rossouw CJ, Miller PR, Josefsson TW, Allen LJ (1994) Zone axis backscattered electron contrast for fast electrons. Phil Mag A 70(6):985–998, DOI 10.1080/01418619408242944

Spence JCH, Zuo JM (1992) Electron microdiffraction. Plenum Press, New York

Weickenmeier A, Kohl H (1991) Computation of absorptive factors for high energy electron diffraction. Acta Cryst A 47:590–597, DOI 10.1107/S0108767391004804

Winkelmann A (2008) Dynamical effects of anisotropic inelastic scattering in electron backscatter diffraction. Ultramicroscopy 108:1546–1550, DOI 10.1016/j.ultramic. 2008.05.002

Winkelmann A, Trager-Cowan C, Sweeney F, Day AP, Parbrook P (2007) Many-beam dynamical simulation of electron backscatter diffraction patterns. Ultramicroscopy 107: 414–421, DOI 10.1016/j.ultramic.2006.10.006

Zuo J, Weickenmeier A (1995) On the beam selection and convergence in the Bloch-wave method. Ultramicroscopy 57(4):375–383, DOI 10.1016/0304 3991(94)00190-X

Chapter 3

Representations of Texture

Jeremy K. Mason and Christopher A. Schuh

3.1 Introduction

The field of materials science and engineering is fundamentally concerned with manipulating the microstructure of materials in order to control their properties. Electron backscatter diffraction (EBSD) dramatically enhances our abilities in this regard, by providing extensive crystallographic orientation information of a given two-dimensional section of a microstructure. As this technique has been developed and combined with chemical analysis and serial sectioning methods, it has become possible to access complete three-dimensional chemistry, phase, and crystal orientation information; in short, the microstructural state of a polycrystal may now be completely quantified.

While these techniques allow an unprecedented opportunity for examining the microstructure-property relationships of materials, in many cases the controlling physics depends on only a relatively small subset of the available information. For example, a variety of the effective tensor properties of materials (e.g., elasticity and transport coefficients) as well as inherently anisotropic, nonlinear properties at the single crystal level (e.g., plasticity and cracking) are governed primarily by the crystallographic texture of, or the distribution of crystal orientations within, a polycrystal. When properties of this type are of interest, it may be reasonable to simplify the analysis of a material by neglecting the spatial information of the microstructure and examining only the orientations of the crystalline grains.

Figure 3.1 illustrates schematically the process of abstraction that is useful when studying texture and the effects of texture on material properties. Figure 3.1(a) shows a complete microstructure, reconstructed from a progression of EBSD maps obtained through serial sectioning, where each grain is colored differently according to its orientation. The central purpose of texture representation is to preferentially examine the orientation of the crystallites without concern for their spatial characteristics, e.g., their arrangement, size, and morphology; to this end, Fig. 3.1(b) shows a schematic representation of the distribution of discrete orientations sampled from a polycrystal. Numerous alternatives exist for the representation of texture information, and these will be covered at length later in this chapter. However, all of these alternatives, including that used in Fig. 3.1(b), significantly distill the dataset represented by Fig. 3.1(a). Even more selective presentation of texture information is not only sometimes feasible, but may be necessary; in certain situations, only a portion of the orientation information is relevant or readily accessible. For example, many properties depend predominantly on the orientation of a single crystallographic axis, as with the *c* axis in transversely isotropic crystals. The representation of these crystallographic axes, or poles, is illustrated in Fig. 3.1(c).

The paradigm of data reduction and distillation exemplified in Fig. 3.1 is not only powerful, but necessary. The acquisition of increasing amounts of data, in and of itself, does not provide the insights that advance the field. These insights depend entirely upon the depth

C.A. Schuh (✉)
Department of Materials Science and Engineering,
Massachusetts Institute of Technology, Cambridge, MA, USA
e-mail: schuh@mit.edu

A.J. Schwartz et al. (eds.), *Electron Backscatter Diffraction in Materials Science*,
DOI 10.1007/978-0-387-88136-2_3, © Springer Science+Business Media, LLC 2009

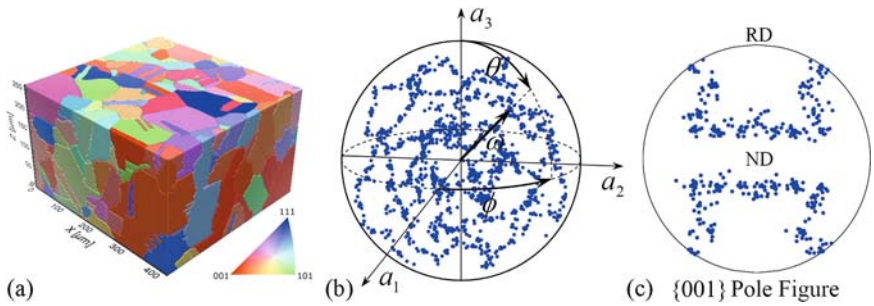


Fig. 3.1 The progressive abstraction of microstructural information. (**a**) Three-dimensional reconstruction of the microstructure of a commercial austenitic stainless steel, containing information on grain size, morphology, and orientation; reproduced from Fig. 5 of Lewis et al. (2008), with permission of Springer Science and Business Media. (**b**) Axis-angle representation of the texture of a crystalline material, completely characterizing the crystallographic orientations present. (**c**) Stereographic projection indicating the orientation of {001} crystallographic planes of a material with a copper texture

of our understanding, and therefore on the skillful and judicious refinement of the data to a form that is both transparent and useful. Unfortunately, as with many unintuitive subjects, the essential content may be unintentionally obscured, or even discarded, during the process of simplification; in the case of crystallographic texture, it is altogether too easy to abandon the most critical information in the interest of depicting the data in a familiar form.

We explore the abstractions of Fig. 3.1 in this chapter, both in a general sense and with specific emphasis on forms common in the materials science community. Since this chapter is intended as an overview of a complex and well-developed field, the reader is referred to various works in the literature for more complete mathematical treatments as the need arises, e.g., Morawiec (2004) and Bunge (1993).

3.2 Rotations and Orientations

EBSD measures the discrete crystallographic orientations of volume elements arranged in a regular manner on the surface of a material. The analysis of material texture therefore begins with an examination of the available methods to parameterize discrete crystallite orientations and present the accumulated orientation information in a clear and concise format. Of course, this requires the definition of an orientation, which in turn requires the definition of a rotation.

3.2.1 Defining a Rotation

While often not appreciated, a certain amount of precision is necessary in the definition of a rotation to be able to relate the rotation to the orientation of a particular object. For example, we may be provided with a rotation matrix, but unless the quantity on which the matrix acts and a method for applying the matrix are specified, the resulting orientation remains unknown. One difficulty is that two conventions for defining a rotation appear in the literature, known as the active and passive conventions.

An active rotation is defined as a transformation of space relative to a stationary coordinate system. A rotation B then brings the vector $\mathbf{u}$ to the vector $\mathbf{u}'$, which is found by left multiplying the column vector of the coordinates of $\mathbf{u}$ by a suitable matrix $\boldsymbol{B}$:

$$\mathbf{u}' = \boldsymbol{B}\mathbf{u}. \tag{3.1}$$

A second rotation of space A with respect to the same, stationary coordinate system similarly brings the vector $\mathbf{u}'$ to the vector $\mathbf{u}''$, found by left multiplying the coordinates of the vector $\mathbf{u}'$ with a suitable matrix $\boldsymbol{A}$:

$$\mathbf{u}'' = \boldsymbol{A}\mathbf{u}' = \boldsymbol{A}\boldsymbol{B}\mathbf{u}. \tag{3.2}$$

By the associativity of matrix multiplication, the combined effect of these rotations on the vector $\mathbf{u}$ may instead be expressed as a left multiplication of $\mathbf{u}$ by

the single matrix $\boldsymbol{AB}$; that is, the combined effect AB of two rotations, B and A, is still a rotation.

A rotation in the passive convention behaves rather differently, by leaving the space fixed and rotating the coordinate system by which points are identified. For an observer attached to the rotating coordinate system, space appears to rotate in the reverse sense to that of the active convention. For example, perform the same rotation B as above, but on the coordinate system rather than on the space. Then the coordinates of the stationary vector $\mathbf{v}$, relative to the rotated coordinate system, become:

$$\mathbf{v}' = \boldsymbol{B}^{-1}\mathbf{v}\,, \tag{3.3}$$

the matrix $\boldsymbol{B}^{-1}$ performing the inverse operation of $\boldsymbol{B}$. This result is generalized to the following relationship: the matrix transforming the coordinates of a vector during a passive rotation is the inverse of the matrix transforming the coordinates of a vector during the corresponding active rotation. The rotation AB that transforms coordinates by the matrix $\boldsymbol{AB}$ in the active convention, then, transforms coordinates by the matrix $(\boldsymbol{AB})^{-1} = \boldsymbol{B}^{-1}\,\boldsymbol{A}^{-1}$ when interpreted in the passive convention; not only the sense of the individual rotations is reversed, but the *order of application* is reversed as well.

The difference between these conventions is demonstrated in Fig. 3.2. The active convention is used in Fig. 3.2(a), where a vector initially on the x axis is aligned with the z axis by a rotation of $\pi/2$ about the z axis and a rotation of $\pi/2$ about the x axis. The equivalent operation to that in (a) is performed in the passive convention in Fig. 3.2(b) by applying the individual rotations to the coordinate system in the same sense, but reversed in order; the coordinate system is rotated by $\pi/2$ about the x axis, then by $\pi/2$ about the resulting z' axis. This operation is equivalent to that in (a) in the sense that the space in Fig. 3.2(a) and the coordinate system in Fig. 3.2(b) experience the same effective rotation by $2\pi/3$ about the $[1\bar{1}1]$ direction. Figure 3.2(c) demonstrates that from the viewpoint of an observer attached to the coordinate system, the apparent rotation in Fig. 3.2(b) is exactly the inverse, namely, a rotation by $-2\pi/3$ about the $[1\bar{1}1]$ direction.

While equivalent in the sense that one may be transformed into the other, the interpretation of matrices expressed in these conventions is clearly different. The convention used must therefore be clearly specified for a discussion of rotations to be meaningful. We use the active convention in the majority of this chapter, for the reason that we find it simpler to interpret a rotation performed relative to a stationary frame of reference than a rotation performed with respect to a frame of reference that changes with every operation.

3.2.2 Defining an Orientation

An orientation is simply the physical result of a sequence of rotations. Rotations must be performed with respect to a coordinate system, usually defined as that system with coordinate axes aligned along the edges (often assumed to be orthogonal) of the sample being examined. The orientation of a crystal is identified with an active rotation that brings a reference

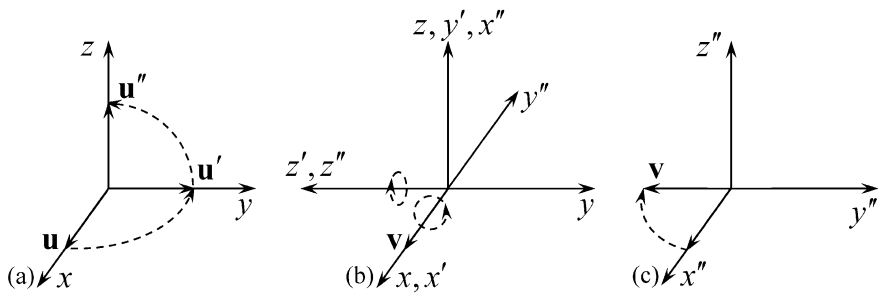


Fig. 3.2 Comparison of rotations performed in the active and passive conventions. (**a**) Rotations in the active convention. A vector $\mathbf{u}$ is rotated by $\pi/2$ about the z axis to $\mathbf{u}'$, then by $\pi/2$ about the x axis to $\mathbf{u}''$. (**b**) Rotations in the passive convention. The coordinate system is rotated by $\pi/2$ about the x axis, then by $\pi/2$ about the z' axis. (**c**) Effect of the passive rotations in (**b**) on $\mathbf{v}$ from the viewpoint of an observer attached to the coordinate system. The vector $\mathbf{v}$ appears to be rotated by $-\pi/2$ about the x axis, then by $-\pi/2$ about the z' axis

crystal aligned with the coordinate system into coincidence with the crystal embedded in the material. The matrix corresponding to this rotation is designated by $\boldsymbol{O}$, though there could be many equivalent such rotations. For example, the configuration resulting from an active rotation of a crystal by $\pi/2$ about the z axis is equivalent to that resulting from a rotation by $5\pi/2$ about the same axis. Some of this redundancy is eliminated by considering only rotations by angles between 0 and π, but there is additional ambiguity that depends on the symmetries of the system.

A reference crystal with cubic symmetry could be initially aligned with the coordinate system in any of twenty-four physically indistinguishable ways. Indicating the symmetry operations of the crystallographic point group by $\boldsymbol{C}_j$, all of the matrices $\boldsymbol{OC}_j$ describe equivalent orientations of the crystal. Furthermore, the sample often exhibits statistical symmetry in the distribution of crystal orientations as a result of processing history. When this symmetry is present, any of the symmetry operations $\boldsymbol{S}_i$ can be applied to the sample without changing the observable characteristics, thereby expanding the set of rotations resulting in physically indistinguishable orientations to $\boldsymbol{S}_i\boldsymbol{OC}_j$. A reasonable discussion of texture requires that an orientation be uniquely identified with just one of these rotations; usually, selecting the rotation with the minimum rotation angle about an axis lying in the standard stereographic triangle is sufficient. A discussion of more subtle cases, where this criterion does not uniquely identify the rotation, is given by, e.g., Grimmer (1980).

3.3 Pole Figures

One of the conventional methods for representing a texture is by means of pole figures. These originated as a natural result of diffraction experiments, and reveal the orientations of particular crystallographic planes rather than of individual crystals. Despite the development of more sophisticated methods of texture representation, the use of pole figures persists for a number of reasons; these include the familiarity of the materials science community with this method of presentation, the relative simplicity of physically interpreting the information displayed in this format, and the existence of many situations in which the orientation of a particular crystallographic plane controls some property of interest.

The orientation of a particular crystallographic plane is completely specified by a single line, passing through the origin and oriented in the direction normal to the plane. This line intersects a unit sphere centered on the origin in two diametrically opposed points. Since the line passes through the origin, either one of these two points uniquely identifies the line. The orientation of a single crystallographic plane is then completely specified by the point of intersection of the normal vector to the plane with the positive hemisphere of the unit sphere; this point is referred to as the pole. (Incidentally, for cubic crystals the pole is identical to the crystallographic axis with the same indices.) An example of a pole, p, corresponding to a given plane orientation is shown in Fig. 3.3.

When the poles of a particular crystallographic plane are considered, and the hemisphere is projected into two dimensions, a *pole figure* is obtained. The most common projection for this purpose is the stereographic projection, which preserves angles but not area; the angle between two lines drawn on the hemisphere is the same as the angle between their projections on the plane, though this comes at the price of changing the apparent density of the poles in the projection. Occasionally, an equal-area projection is useful instead of the stereographic; this projection preserves the apparent density of the poles, but distorts the angles between projected lines. While we use the stereographic projection, several discussions of the benefits

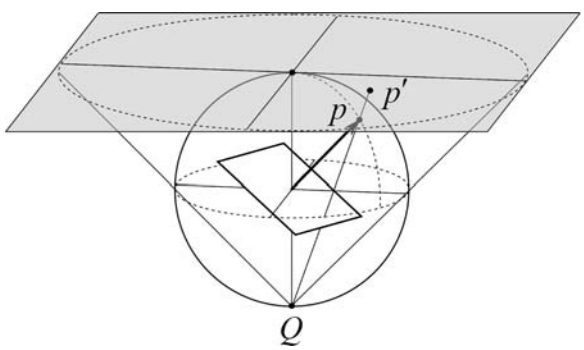


Fig. 3.3 Indication of a crystallographic plane's orientation by a point on the surface of a sphere, projected onto a plane by stereographic projection. The stereographic projection of a point p may be performed by placing a light source at Q and observing the shadow cast by the point p onto the plane at p'

of one projection or the other exist in the literature, e.g., Neumann (1992), Wenk and Kocks (1987).

The stereographic projection of the point p in Fig. 3.3 is given by the point of intersection of the unique line passing through Q and p with the plane of projection at $z = 1$. Mathematically, this projection is given by:

$$x' = \frac{2x}{1+z}, \quad y' = \frac{2y}{1+z}, \tag{3.4}$$

where x, y, and z are the coordinates of the point p, and x' and y' are the coordinates of the point p'. Since they depend on the choice of the point Q and the plane of projection, other formulas for the stereographic projection may differ.

As the method delineated above permits a single pole to be represented as a point in the plane of projection, a distribution of poles can be represented as a collection of points in this plane. A complete description of the discrete poles in a polycrystalline sample is provided by depicting one point per crystal, or one point per volume element. Schematic {111} pole figures for a number of commonly observed textures appear in Fig. 3.4, including the cube, copper, and brass textures. These projections are conventionally depicted in the plane parallel to that of a sheet sample, and the "normal direction" to this plane is labeled "ND." The transverse direction of highest symmetry is usually called the "rolling direction" and is labeled "RD," although this notation is used for nonrolled materials as well.

Since the geometry of the sample indicates a suitable set of axes for this projection, any sample symmetry is generally visible in the resulting pole figures; for example, samples with orthorhombic symmetry were used to generate the pole figures of Fig. 3.4, meaning that a statistically identical pole figure could be reproduced from any one of the four quadrants. Although this symmetry is occasionally exploited and only a portion of the pole figure provided, it is quite common to find the entire pole figure in the literature.

The same is not true for so-called *inverse pole figures*. Whereas a pole figure shows sample directions aligned with a particular crystallographic pole, an inverse pole figure does the opposite, indicating the crystallographic poles aligned with a specified sample direction. This is often of interest for samples in which the processing history strongly identifies a single direction, e.g., the axis of a fiber or wire, or the growth direction of a thin film. The procedure for constructing an inverse pole figure is quite similar to that of a pole figure, with one exception; instead of projecting a crystallographic pole onto a plane determined by the sample geometry, the vector pointing along a given sample direction is projected onto planes determined by the local crystallographic orientation. That is, the projection procedure illustrated in Fig. 3.3 is performed for each crystal or volume element, with the frame of reference always given by the local crystallographic frame. An inverse pole figure is obtained by plotting the results of all of these projections together.

Figure 3.5 shows the normal-direction inverse pole figures for samples with the three textures shown in Fig. 3.4, namely, the cube, copper, and brass textures. Since the frame of reference for an inverse pole figure is always defined by the local crystal orientation, the symmetry of the crystals is reflected in the inverse pole figures. As indicated by the fine lines in Fig. 3.5(a, c, e), the cubic crystal symmetry of the samples with these textures divides the projections into twenty-four stereographic triangles, each containing identical orientation information. The crystal symmetry is exact, rather than statistical, as is the case for sample symmetry, allowing the entire inverse pole figure to be

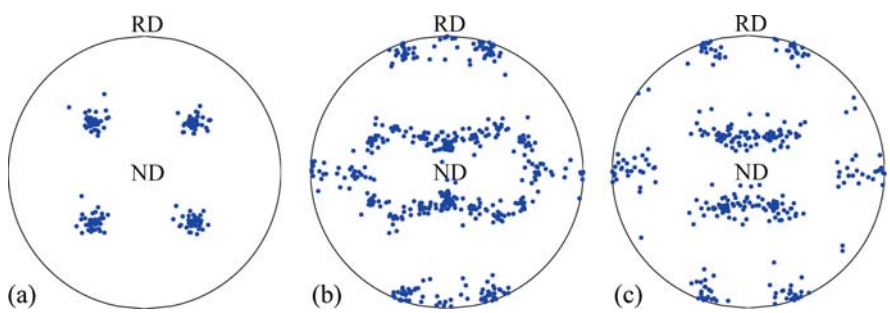


Fig. 3.4 {111} pole figures for (**a**) a cube texture, (**b**) a copper texture, and (**c**) a brass texture. "ND" and "RD" correspond to the "normal direction" and the "rolling direction," respectively, of a sample deformed by rolling

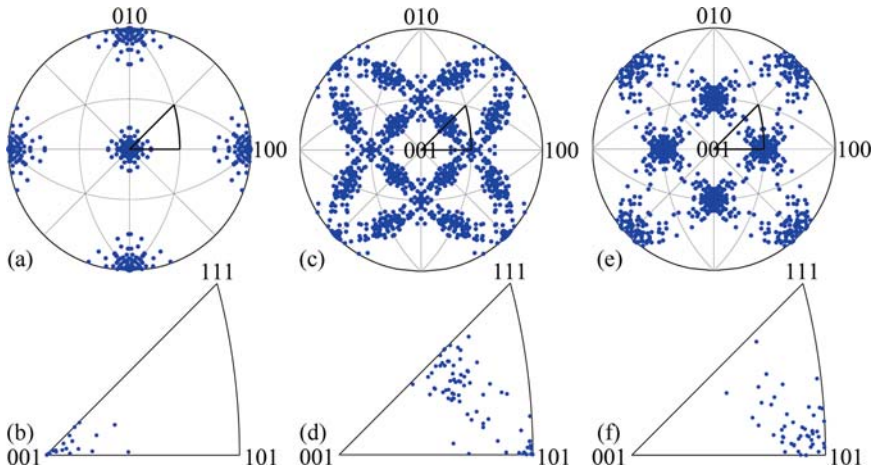


Fig. 3.5 Normal-direction inverse pole figures for the three textures in Fig. 3.4. The inverse pole figure at the *top* of a given column is divided into twenty-four stereographic *triangles*, with the standard stereographic triangle outlined. This *triangle* appears alone at the *bottom* of the column. Miller indices in the figure refer to directions in the local crystallographic frame. (**a**) A cube texture, and (**b**) the standard stereographic triangle of the cube texture. (**c**) A copper texture, and (**d**) the standard stereographic triangle of the copper texture. (**e**) A brass texture, and (**f**) the standard stereographic triangle of the brass texture

recovered exactly from any one of the stereographic triangles. Hence, the twenty-four-fold redundancy strongly encourages presentation by a single stereographic triangle. The standard stereographic triangle of the cubic system is that containing the crystallographic directions $\{hkl\}$ for which $l \geq h \geq k \geq 0$, which we have outlined using bold lines in Fig. 3.5. The usual presentation of an inverse pole figure provides only this standard stereographic triangle, as shown in Fig. 3.5(b, d, f).

It is important to remember that pole figures and inverse pole figures do not explicitly indicate the orientations of crystals in a polycrystalline sample, only the orientations of selected crystalline planes or directions. As suggested by Fig. 3.1, these constructions represent only a fraction of the orientation information that is accessible via EBSD. Occasionally, multiple pole figures, each of a different crystallographic axis, may be presented as a means of illustrating texture; however, there is no explicit means to identify the points on two pole figures originating from a single crystal. There do exist highly developed methods for determining the *most probable* crystal orientation distribution consistent with the pole figures of multiple crystallographic planes (Bunge 1993), but in general pole figures unnecessarily discard a great deal of the available orientation information. Therefore, methods of texture representation that accurately reflect the orientations of crystals, rather than of their planes, are frequently more useful than representation by pole figures.

3.4 Discrete Orientations

Any real, orthogonal, three-by-three matrix of determinant one corresponds to a proper rotation of space in the active convention. The group of rotation matrices with these properties is often considered to be the canonical parameterization of rotations, partly due to the simplicity of applying a rotation matrix to either a vector or to another rotation matrix via the matrix product. As a result, rotation matrices are quite convenient for the algebraic manipulation of discrete orientations; on the other hand, the visualization of a collection of orientations via rotation matrices is rather difficult.

A unique description of an orientation in three dimensions requires only three independent parameters (Wigner 1959). If these can be identified, they can be taken as coordinates of a three-dimensional group space in which individual orientations appear as points. In the case of rotation matrices, each matrix contains nine components. While the direct use of these nine components to form a nine-dimensional group space is unreasonable, there is no obvious way to use only three of the matrix components to represent

an orientation (though there is some motivation for using six [Hopf 1940; Stuelpnagel 1964]). A related difficulty lies in interpreting the physical effect of a rotation matrix; at least to the current authors, this is not transparent except in the simplest cases. The regrettable result is that the use of this convenient and familiar parameterization of rotations is sharply restricted to the algebraic manipulation of discrete orientations, rather than to their visualization.

Partly for this reason, the materials science community employs a number of other parameterizations side by side with rotation matrices, each with their own particular advantages and weaknesses. The analysis of texture information requires familiarity with the most common parameterizations in order to be able to select the most appropriate one for the application at hand. We provide a brief overview of these parameterizations in this section, with particular emphasis on their relative strengths.

3.4.1 Axis-Angle Parameters

A theorem ascribed to Euler states that every displacement of a sphere with a fixed center is equivalent to some rotation of that sphere about an axis by an angle (Euler 1776). Although this description of a rotation requires four parameters, three for the coordinates of the unit vector **n** pointing along the axis of rotation and one for the angle ω, it has the advantage that the physical effect of a rotation described by an axis and angle is easily visualized (see Fig. 3.6[a]). These four parameters may be reduced to three without loss of information by observing that the constraint on the length of **n** allows only two of its three coordinates to be chosen independently. For instance, **n** may be expressed in terms of the spherical coordinates θ and ϕ, at the expense of introducing an asymmetry into the parameters which is inherent to the spherical coordinate system. As pointed out by Frank (1988), a more symmetric method for combining these four parameters into three is to multiply **n** by a simple monotonically increasing function $f(\omega)$:

$$\mathbf{s} = \mathbf{n} f(\omega). \tag{3.5}$$

Varying the function $f(\omega)$ converts the quantity **s** into various *neo-Eulerian mappings*. The close relationship between the axis and angle of a rotation and the corresponding point in the group space of one of these neo-Eulerian mappings is illustrated in Fig. 3.6.

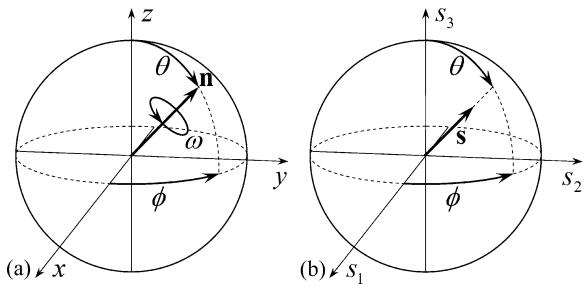


Fig. 3.6 Relationship of the vector **n** and angle ω to the parameters of a neo-Eulerian mapping. (**a**) The result of any series of rotations is equivalent to some rotation performed about an axis parallel to **n** by an angle ω. The vector **n** can be written in terms of the spherical angles θ and ϕ. (**b**) The corresponding point in the group space of a neo-Eulerian mapping with parameters $\mathbf{s} = \mathbf{n} f(\omega)$. The result is nearly as straightforward to interpret as the description using **n** and ω directly

The simplest function of this type is the rotation angle itself. The vector **a** then points in the same direction as the axis of rotation and scales linearly in length with the rotation angle:

$$\mathbf{a} = \mathbf{n}\omega. \tag{3.6}$$

We refer to the components of **a**, and not the four parameters of the separate axis and angle of rotation, as the axis-angle parameters because their behaviour is more reasonable for small rotations and because they appear more often in the literature. Since **n** may point in any direction and ω is constrained to the values $0 \leq \omega \leq \pi$, the group space of these parameters is a solid ball of radius π. Each point on the interior of this ball corresponds to a unique rotation, and diametrically opposed points on the surface correspond to the same two-fold rotation. While the redundant points can be removed by excluding certain portions of the surface (Altmann 1986), the topological properties of the space allow small variations in a physical orientation to correspond to discontinuous changes in the axis-angle parameters as a point jumps from one part of the group space to another. This behaviour is rather inconvenient from the standpoint of numerical calculations.

A more serious drawback of the axis-angle parameterization is the complexity of the multiplication law, or the formula required to calculate the single

rotation equivalent to two rotations performed in succession. This difficulty may be addressed by more deliberate selection of the function multiplying **n**, which provides neo-Eulerian parameterizations with simpler combination laws and certain other useful properties. As a result, the simplicity of the axis-angle parameterization is useful when introducing certain ideas concerning the rotation group, but this parameterization is rarely used for the representation of texture due to the existence of more attractive alternatives.

3.4.2 Rodrigues Vectors

The Rodrigues vector parameterization is a neo-Eulerian mapping introduced into the discussion of texture by Frank (1988). The three parameters of a Rodrigues vector are constructed by multiplying **n** by the tangent of half of ω:

$$\mathbf{r} = \mathbf{n}\tan(\omega/2). \tag{3.7}$$

As with all of the neo-Eulerian parameterizations, this vector points in the same direction as the axis of rotation and increases monotonically in length with the rotation angle ω for angles $0 \leq \omega \leq \pi$. Hence, the interpretation of a Rodrigues vector, as with the axis-angle parameters, is nearly as simple as that of the axis and angle of a rotation directly. One disadvantage of this parameterization, though, is that the magnitude of a Rodrigues vector diverges as the rotation angle approaches π, meaning that a binary rotation cannot be represented with a Rodrigues vector. Furthermore, the unbounded group space brings into question the feasibility of visualizing a texture as a collection of points distributed throughout an infinite volume.

Nevertheless, certain properties of Rodrigues vectors make this parameterization quite favorable for the presentation of texture information. These may be derived from the multiplication law for rotations expressed as Rodrigues vectors; the result of a rotation $\mathbf{r}_B$ followed by a rotation $\mathbf{r}_A$ is determined by (Morawiec and Field 1996):

$$\mathbf{r}_A\mathbf{r}_B = \frac{\mathbf{r}_A + \mathbf{r}_B + \mathbf{r}_A \times \mathbf{r}_B}{1 - \mathbf{r}_A \cdot \mathbf{r}_B}, \tag{3.8}$$

which is a slight rearrangement of the form appearing in the literature. Apart from its relative simplicity, the particular advantage of this multiplication law is that it may be used to show that the trajectory for a continuing rotation about a single axis is a straight line in the Rodrigues space, regardless of the orientation of the reference frame; similarly, any change of the reference frame transforms a line into another line, and a plane into another plane (Frank 1988). The benefit of these properties becomes apparent when considering the effect of symmetry on the group space.

The presence of sample or crystal symmetry partitions the group space into distinct regions known as fundamental zones, defined by the requirement that they contain a unique point for every physically distinguishable orientation of a crystal. That is, a given fundamental zone contains only one of the points corresponding to the set of symmetrically equivalent rotations $\boldsymbol{S}_i\boldsymbol{O}\boldsymbol{C}_j$. The presence of symmetry thereby reduces the matter of visualizing the group space to that of a single fundamental zone, since all of the texture information is contained in each fundamental zone. While for most parameterizations the surfaces of these fundamental zones are curved, it follows from Equation (3.8) that the boundaries of the fundamental zones in Rodrigues space are always planar (Frank 1988). The specific forms of these fundamental zones have been derived for a variety of crystal and sample symmetries, and are generally finite and bounded by planar surfaces (Heinz and Neumann 1991; Morawiec and Field 1996). For materials with sufficiently high crystal symmetry, this has encouraged the presentation of texture information in two dimensions by equidistant planar sections of the fundamental zone. This presentation is used in Fig. 3.7 for a collection of orientations from a copper textured material with cubic crystal symmetry. Figure 3.7(a) displays the orientations in the cubic fundamental zone, and Fig. 3.7(b) gives the conventional sections of this space in two dimensions.

3.4.3 Quaternions

Although quaternions often receive less notice than other parameterizations, their attractive mathematical properties have proven indispensable for a number of subjects with particular relevance to the analysis of information accessible via EBSD. For example, Grimmer used quaternions extensively to develop the theory

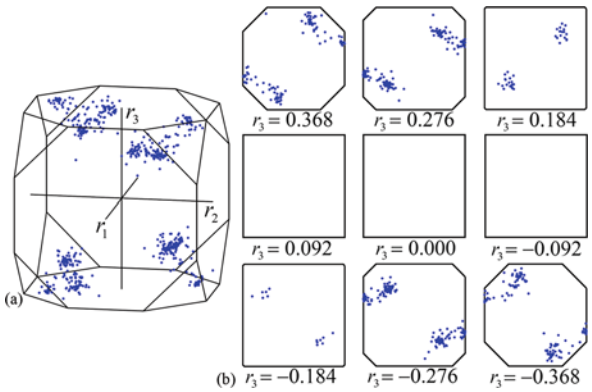


Fig. 3.7 A collection of discrete orientations from a copper textured material with cubic crystal symmetry, depicted in the fundamental zone of Rodrigues space. (**a**) The cubic fundamental zone containing the origin is a truncated cube with six octagonal faces and eight triangular faces. (**b**) The distribution is conventionally plotted in equidistant sections perpendicular to the r_3 axis

of coincident cite lattices (Grimmer 1973, 1974), and they appear in the extension of coincident site lattice theory to triple junctions as performed by Gertsman (2001a, b). Others have used them to determine the mean orientation of a grain as calculated from multiple EBSD measurements (Glez and Driver 2001; Humbert et al. 1996).

A quaternion q is often interpreted as a vector in four-dimensional space. For the study of rotations, the quaternions of interest satisfy the normalization constraint $q_0^2 + q_1^2 + q_2^2 + q_3^2 = 1$, which is assumed in the following. A quaternion is then related to the quantities $\mathbf{n}$ and ω of a rotation by:

$$q = (q_0, \mathbf{q}) = [\cos(\omega/2), \mathbf{n}\sin(\omega/2)], \tag{3.9}$$

where q_0 and $\mathbf{q}$ are conventionally referred to as the scalar and vector parts of the quaternion, respectively. While the description of a three-dimensional rotation requires three parameters and a quaternion contains four, we observe that a rotation is completely specified by just the vector part $\mathbf{q}$, which may be interpreted as a neo-Eulerian mapping. Although the scalar part q_0 appears redundant, the properties of this four-component parameterization strongly encourage the use of the parameter q_0 as well, at the price of a little redundancy.

As normalized vectors in four-dimensional space, quaternions inhabit the region defined as the set of points at a distance of one from the origin, i.e., the unit sphere in four dimensions (or S^3, for those familiar with this notation). Exactly as for a sphere in three dimensions, there is no closed path on the unit sphere in four dimensions that contains a discontinuous change in the values of the quaternion components; the discontinuous change in the values of the axis-angle and Rodrigues vector parameters for rotations in the vicinity of $\omega = \pi$ is simply not present. By including all of the quaternions on this hypersphere, though, every physical orientation is represented twice. Equation (3.9) indicates that given a quaternion $+q$, increasing ω by 2π results in the antipodal quaternion $-q$ with the signs of all the components reversed. Although these quaternions correspond to distinct rotations, they clearly result in the same physical orientation (meaning that one may consider the space inhabited by orientations as RP^3). This may be interpreted as resulting from the trivial symmetry of three-dimensional space, that is, a rotation by 2π about any axis results in an indistinguishable orientation. As in Rodrigues space, the presence of symmetry partitions the quaternion group space into distinct fundamental zones. Actually, Heinz and Neumann derived the boundaries of these regions in Rodrigues space from the properties of the quaternion group space (Heinz and Neumann 1991). The symmetry through a rotation by 2π identifies the fundamental zones as one half of the unit sphere, and we select the half with positive values of q_0 for the representation of textures. Hence, the parameterization of a single orientation by two quaternions is not a particularly serious obstacle.

The advantage of writing the quaternion in Equation (3.9) in terms of half-angle trigonometric functions (and thereby introducing the redundancy in $+q$ and $-q$) rather than full-angle functions is that this form permits the multiplication law to be written in an exceptionally simple form; a rotation expressed by the quaternion q_B followed by q_A results in the quaternion given by (Altmann 1986):

$$\begin{aligned}&[q_{A0}, \mathbf{q}_A][q_{B0}, \mathbf{q}_B]\\ &\quad = [q_{A0}q_{B0} - \mathbf{q}_A{\cdot}\mathbf{q}_B, q_{A0}\mathbf{q}_B + q_{B0}\mathbf{q}_A + \mathbf{q}_A \times \mathbf{q}_B],\end{aligned} \tag{3.10}$$

where quaternions operate to the right. The simplicity of this multiplication law lies in the fact that the components of the resulting quaternion are all linear functions of the components of q_B and q_A. Although this is

a feature of other parameterizations as well (e.g., rotation matrices), the quaternion parameterization is the parameterization of smallest dimension with this property (Stuelpnagel 1964). With respect to numerical calculations, this type of multiplication law tends to be efficient and robust, and there is some indication that quaternions may even be preferable to rotation matrices for this purpose (Funda et al. 1990).

There remains the matter of visualizing a collection of points embedded in a four-dimensional space, i.e., of the necessity of projecting from four dimensions to three, and from three dimensions to two. While there are many projections of the quaternion group space with $q_0 \geq 0$ into three dimensions, we mention only the orthographic and gnomic projections (stereographic and equal-volume projections into three dimensions should generally be considered as well, though the formulas for these are slightly more complex [Frank 1988; Neumann 1992]). The first, the orthographic projection, follows from the observation that the vector part $\mathbf{q}$ of a quaternion q resembles a neo-Eulerian mapping, for which all orientations may be plotted in the analog of the representative spherical volume in Fig. 3.6(b). This method is attractive because there is little additional computation involved, and knowledge of the vector part allows the final component of the quaternion to be quickly reconstructed by applying the normalization constraint. An example of this representation for the crystal orientations in a copper textured material with cubic crystal symmetry is shown in Fig. 3.8 (a).

Meanwhile, the gnomic projection converts a quaternion to the corresponding Rodrigues vector. The projection is performed simply by dividing the vector part of a quaternion by the scalar part, or $\mathbf{r} = \mathbf{q}/q_0$. This suggests that orientation measurements may be analyzed as quaternions and easily projected to the Rodrigues space as a final step for the purpose of visualization.

The parameterizations resulting from the projections suggested above are clearly neo-Eulerian, meaning that a vector within the three-dimensional group space points along the axis of rotation and scales monotonically with the rotation angle. In particular, the value of the rotation angle is constant within a given spherical shell centered on the origin of any neo-Eulerian parameterization. This suggests that the axis and angle of rotations represented by points in any neo-Eulerian group space will be easily identified when the space is sectioned into concentric spherical shells at constant intervals of rotation angle. We use this presentation in Fig. 3.8(b) by sectioning the orthographic projection of Fig. 3.8(a) into concentric spherical shells. Since the symmetry of this texture renders the upper and lower hemispheres identical, we use the stereographic projection (given in Equation 3.4) to project only the upper hemispheres into two dimensions. When this symmetry is not present, the upper and lower hemispheres may be plotted side by side. Points within a given stereographic projection in Fig. 3.8(b) correspond to a particular interval of rotation angle, and their location within the projection indicates the orientation of the rotation axis.

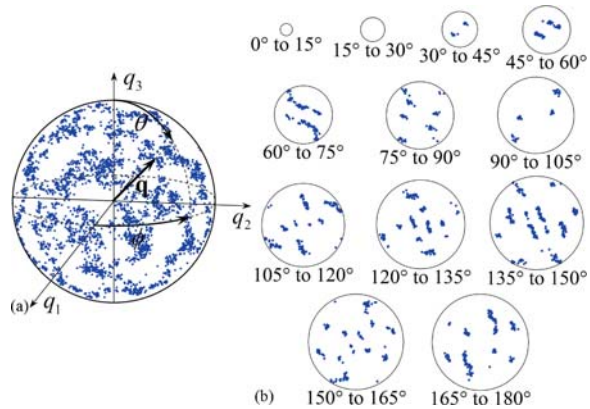


Fig. 3.8 A collection of discrete orientations from a copper textured material with cubic crystal symmetry, depicted in (**a**) the three dimensions inhabited by the vector part $\mathbf{q}$ of a quaternion q, and (**b**) in two dimensions as a collection of stereographic projections of concentric spherical shells of the space in (**a**). This presentation is naturally suited to the spherical shape of the space, and has the advantage that the rotation angle is constant within a given spherical shell, promoting an intuitive interpretation of points displayed in this format

The quaternion parameterization offers some notable advantages, at the price of requiring four parameters instead of three. For example, the quaternion group space includes points for all distinct orientations, and does not contain discontinuities in the parameter values along any trajectory through the space; these cannot simultaneously be properties of any three-dimensional parameterization (Stuelpnagel 1964). Furthermore, the bilinearity of the multiplication law markedly simplifies many functions of orientation when expressed in the quaternion coordinates. The primary obstacle to the use of quaternions is the perceived difficulty in visualizing the group

space, though as shown in Fig. 3.8, this is not actually as difficult as might be expected. While several other reasons strongly supporting the use of quaternions in the field of texture analysis exist, these will be become apparent only in the section on continuous orientation distribution functions.

3.4.4 Euler Angles

Of the options enumerated in this chapter, the Euler angle parameterization is the one most conventionally used for the analysis and presentation of texture information. Instead of deriving from an axis and angle of rotation, this parameterization describes the relative orientation of two coordinate systems with three passive rotations (we follow the passive convention with the Euler angles in order to conform to the majority of the literature on the subject). These rotations are performed about the z, x', and z'' axes, with rotation angles given by the three Euler angles φ_1, Φ, and φ_2, respectively (Bunge 1993). Applying these rotations in the determined sense and order brings one of the coordinate systems into coincidence with the other, as indicated in Fig. 3.9. Meanwhile, plotting the Euler angles on orthogonal axes forms a group space that is 2π-periodic along all three axes. Since, in this

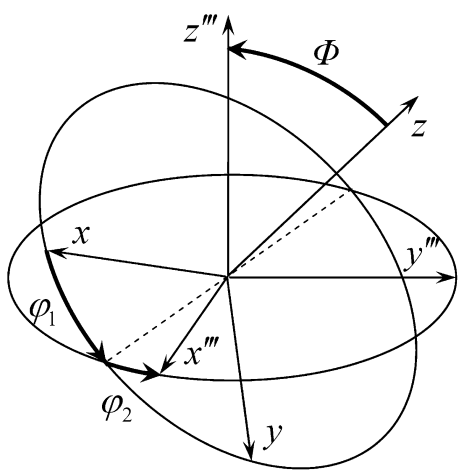


Fig. 3.9 Definition of the orientation of a coordinate system, following the conventional interpretation of the Euler angles. The orientation is determined as the result of three consecutive rotations, performed about the z, x', and z'' axes by the angles φ_1, Φ, and φ_2, respectively

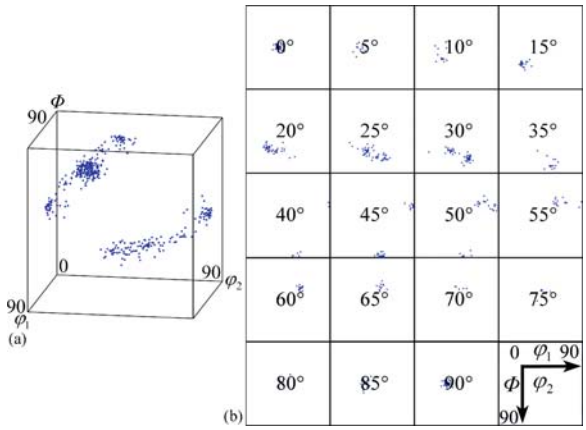


Fig. 3.10 A collection of discrete orientations from a copper textured material with cubic crystal symmetry, depicted in Euler angle space. (**a**) The conventional volume used for cubic crystal symmetry and orthorhombic sample symmetry is bounded by planar surfaces, but contains three fundamental zones. (**b**) The distribution is conventionally plotted in equidistant sections perpendicular to the φ_2 axis

space, a cube of edge length 2π contains two points for every orientation, the Euler angles are generally restricted to the values $0 \leq \varphi_1 < 2\pi$, $0 \leq \Phi \leq \pi$, and $0 \leq \varphi_2 < 2\pi$ to remove the redundant points. Cubic crystal symmetry and orthorhombic sample symmetry reduce the fundamental zone still further, though the resulting surface in Euler angle space is invariably curved. For this reason, the region defined by $0 \leq \varphi_1 \leq \pi/2$, $0 \leq \Phi \leq \pi/2$, and $0 \leq \varphi_1 \leq \pi/2$ is often selected instead for these symmetries, despite the fact that this region contains three points for every orientation (Wenk and Kocks 1987). The benefit of this choice is that the planar surfaces permit a natural presentation in two dimensions by a series of parallel sections, conventionally selected perpendicular to the φ_2 axis. This is the method used in Fig. 3.10 for a collection of orientations from a copper textured material with cubic crystal symmetry, where Fig. 3.10(a) displays the orientations in the Euler angle group space, and Fig. 3.10(b) presents the corresponding conventional two-dimensional sections.

One conspicuous feature of this definition is its asymmetry (Frank 1988). While the neo-Eulerian parameterizations do not single out any particular direction in space, the Euler angles more naturally describe rotations about the x and z axes than about the y axis. This asymmetry has a number of repercussions, among which is the presence of a singularity

in the definition of certain rotations, and therefore a singularity in the group space (Siemens et al. 2007; Stuelpnagel 1964). This occurs for rotations about the z axis, for which $\Phi = 0$. When this Euler angle vanishes, all φ_1 and φ_2 for which $\varphi_1 + \varphi_2$ is constant result in the same orientation. Particularly concerning is that this non-uniqueness applies to the identity operation (the non-rotation) as well; the rotation group is a Lie group, and this requires any proper parameterization of the rotation group to be reasonably behaved in the region around the identity (Gilmore 1974). The singularity often appears in functions of orientations parameterized by the Euler angles as well; for example, the multiplication law for Euler angles (Varshalovish et al. 2008) and the kinematic equations (Stuelpnagel 1964) each contain a singularity when $\Phi = 0$.

More pragmatically, interpreting an orientation parameterized by Euler angles is not as simple as for the neo-Eulerian parameterizations. One of the reasons for this difficulty is that instead of a single rotation, as with the alternatives outlined in the previous sections, the Euler angles require one to envision the result of three consecutive rotations. Furthermore, the effect of any of these rotations is not specified by a single Euler angle, but depends on the preceding rotations because of the use of the passive convention. The situation is mollified slightly by recognizing that the first two Euler angles can be interpreted as a variety of spherical coordinates for the z'' axis with respect to the initial coordinate system. The x'' axis may then be established by following the construction given by, e.g., Wenk and Kocks (1987). Despite this interpretation, though, the current authors find the neo-Eulerian parameterizations far simpler.

3.5 Orientation Distribution Functions

Traditionally, diffraction techniques lacked the spatial resolution to measure the orientations of individual crystals; instead, a diffraction pattern provided probabilistic information about the orientations of many grains within the diffracting region. This information could be used to construct an *orientation distribution function*, indicating the probability of finding a volume element within the material with a particular crystalline orientation. Often, a continuous probability distribution of this type is actually more useful for the analysis of texture information than discrete orientation measurements. More specifically, given a set of continuous functions with a few particular properties, any collection of discrete orientation measurements may be accurately approximated as a linear combination of these functions. The coefficients in this expansion then give an efficient and compact expression of a texture. Indeed, this relatively simple principle is the foundation for the whole of classical texture analysis (Bunge 1993), and continues to motivate recent developments as well, including, e.g., microstructure sensitive design, as discussed in Chapters 12 and 13 of this book.

3.5.1 Circular Harmonics

The expansion of an arbitrary, square-integrable function $f(\phi)$ defined on the unit circle as an infinite linear combination of sines and cosines, i.e., as a Fourier series, is well known. We write the normalized, real circular harmonics as:

$$X^{mc} = \frac{1}{\sqrt{\pi}} \cos(m\phi)$$
$$X^{ms} = \frac{1}{\sqrt{\pi}} \sin(m\phi), \tag{3.11}$$

with integer index $1 \leq m$; for $m = 0$, X^{0s} vanishes and $X^{0c} = 1/\sqrt{2\pi}$. This notation allows the expansion of $f(\phi)$ to be written in the form:

$$f(\phi) = f^{0c}\, X^{0c} + \sum_{m=1}^{\infty} (f^{mc}\, X^{mc} + f^{ms}\, X^{ms}), \tag{3.12}$$

where the coefficients are determined by the inner product of the function $f(\phi)$ with the corresponding basis function, or:

$$f^{mc} = \int_0^{2\pi} f(\phi) X^{mc} d\phi$$
$$f^{ms} = \int_0^{2\pi} f(\phi) X^{ms} d\phi. \tag{3.13}$$

Our purpose in reproducing these formulas is not to instruct in the principles of their use, but rather to provide a sense of continuity with harmonics of a more

direct interest to the representation of texture, namely, the harmonics on the unit sphere and unit hypersphere.

3.5.2 Spherical Harmonics

Whereas a point on a unit circle is specified by a single angle ϕ, a point on a unit sphere is specified by two, the polar $0 \leq \theta \leq \pi$ and azimuthal $0 \leq \phi < 2\pi$ angles. Now, since the transition from two dimensions to three involves the addition of the z axis, and a sphere may be considered as a progression of circles centered on and perpendicular to the z axis, one expects the spherical harmonics to be constructed from circular harmonics modulated by a function of z. This is exactly the case, as is clear from the real spherical harmonics:

$$Y_l^{mc} = (-1)^m \sqrt{\frac{(2l+1)(l-m)!}{2(l+m)!}} P_l^m(\cos\theta) X^{mc}$$
$$Y_l^{ms} = (-1)^m \sqrt{\frac{(2l+1)(l-m)!}{2(l+m)!}} P_l^m(\cos\theta) X^{ms}, \tag{3.14}$$

with integer indices $0 \leq l$ and $1 \leq m \leq l$; when $m = 0$, Y_l^{0s} vanishes and Y_l^{0c} is divided by $\sqrt{2}$ to preserve the normalization. These functions contain the circular harmonics from Equation (3.11), an associated Legendre function P_l^m of $z = \cos\theta$ (defined in Bateman and Erdélyi [1953]; Gradshtein et al. [2000]), and a normalizing expression. With the spherical harmonics in hand, any square-integrable function $f(\theta, \phi)$ on the surface of a sphere may be written as a linear combination in the form:

$$f(\theta,\phi) = \sum_{l=0}^{\infty} \left[f_l^{0c} Y_l^{0c} + \sum_{m=l}^{l} (f_l^{mc} Y_l^{mc} + f_l^{ms} Y_l^{ms}) \right], \tag{3.15}$$

where the coefficients are determined by the inner product of the function $f(\theta, \phi)$ with the corresponding basis function, or:

$$f_l^{mc} = \int_0^{2\pi} \int_0^{\pi} f(\theta,\phi) Y_l^{mc} \sin\theta d\,\theta d\,\phi$$
$$f_l^{ms} = \int_0^{2\pi} \int_0^{\pi} f(\theta,\phi) Y_l^{ms} \sin\theta d\,\theta d\,\phi. \tag{3.16}$$

While Equation (3.15) is an exact expansion for $f(\theta, \phi)$, the calculation of an infinite number of coefficients is not particularly practical. Instead, the expansion is always performed with a finite number of terms by limiting the index l to values less than or equal to $l_{\max}$; this smoothes the resulting approximation, although limiting the number of terms occasionally introduces spurious peaks or valleys as well.

The smoothing performed by limiting the number of terms makes this expansion a convenient method for finding an approximation to a collection of points on the surface of a sphere, as, for instance, the discrete poles for a given crystallographic plane. When normalized, the resulting function is interpreted as the probability density function of observing a pole in a particular area of the sphere's surface. We follow this procedure to calculate the probability density functions for the three {111} pole figures of Fig. 3.4, and plot the results in stereographic projection in Fig. 3.11.

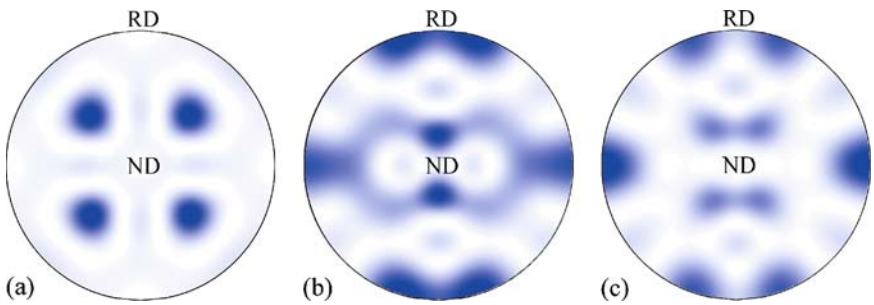


Fig. 3.11 {111} pole figures of the continuous pole distributions for (**a**) a cube texture, (**b**) a copper texture, and (**c**) a brass texture, corresponding to the respective discrete pole figures in Fig. 3.4. The distribution functions are determined by Equation (3.15), with $l_{\max} = 15$. Regions of finite probability density appear in some areas that are empty in the corresponding discrete pole figures because of the use of a limited number of terms, while regions of negative probability density were removed by applying a positivity constraint

3.5.3 Hyperspherical Harmonics

The transition from the sphere to the hypersphere is analogous to that from the circle to the sphere; a point on the unit hypersphere is specified by three angles, namely, the hyperspherical angle $0 \leq \alpha \leq \pi$ where $\alpha = \omega/2$, along with the spherical angles $0 \leq \theta \leq \pi$ and $0 \leq \phi < 2\pi$. The equations relating these angles to the four coordinates w, x, y, and z of four-dimensional space (refer to, e.g., Domokos [1967]; Hicks and Winternitz [1971]) indicate that a unit hypersphere may be considered as a progression of spheres along the w axis. Exactly as with the spherical harmonics, one expects the hyperspherical harmonics to be constructed from spherical harmonics in hyperplanes perpendicular to the w axis, modulated by a function of w. This is visible in the formulas for the real hyperspherical harmonics (Mason and Schuh 2008):

$$Z_{nl}^{mc} = (-1)^l 2^l l! \sqrt{\frac{2}{\pi} \frac{(n+1)(n-l)!}{(n+l+1)!}} \times (\sin\alpha)^l C_{n-l}^{l+1}(\cos\alpha) Y_l^{mc}(\theta, \phi)$$

$$Z_{nl}^{ms} = (-1)^l 2^l l! \sqrt{\frac{2}{\pi} \frac{(n+1)(n-l)!}{(n+l+1)!}} \times (\sin\alpha)^l C_{n-l}^{l+1}(\cos\alpha) Y_l^{ms}(\theta, \phi), \tag{3.17}$$

with integer indices $0 \leq n$, $0 \leq l \leq n$, and $1 \leq m \leq l$; when $m = 0$, Z_{nl}^{0s} vanishes and Z_{nl}^{0c} is divided by $\sqrt{2}$ to preserve the normalization. The formulas for the hyperspherical harmonics contain the spherical harmonics of Equation (3.14), a Gegenbauer polynomial C_{n-1}^{l+1} of $w = \cos\alpha$ (defined in Bateman and Erdélyi [1953]; Gradshtein et al. [2000]), and a normalizing expression. The expansion of any square-integrable function on the unit hypersphere is given in terms of these harmonics by:

$$f(\alpha, \theta, \phi) = \sum_{n=0}^{\infty} \sum_{l=0}^{n} \left[f_{nl}^{0c} Z_{nl}^{0c} + \sum_{m=1}^{l} (f_{nl}^{mc} Z_{nl}^{mc} + f_{nl}^{m} Z_{nl}^{ms}) \right]. \tag{3.18}$$

Provided that the function is real, the coefficients of this expansion are real as well, and are given by the inner products:

$$f_{nl}^{mc} = \int_0^{2\pi} \int_0^{\pi} \int_0^{\pi} f(\alpha, \theta, \phi) Z_{nl}^{mc} \sin^2\alpha d\alpha \sin\theta d\theta d\phi$$

$$f_{nl}^{ms} = \int_0^{2\pi} \int_0^{\pi} \int_0^{\pi} f(\alpha, \theta, \phi) Z_{nl}^{ms} \sin^2\alpha d\alpha \sin\theta d\theta d\phi. \tag{3.19}$$

Since the quaternion group space is precisely the surface of the unit hypersphere, this expansion allows us to find a smooth and analytic function for the probability density of a distribution of crystal orientations written as quaternions, i.e., a texture. As for the spherical harmonics, the number of terms in the expansion is reduced to a finite number by limiting the index n to values less than or equal to $n_{\max}$; this introduces the same type of smoothing and oscillations as does the limitation in l for the expansion of functions on the surface of a sphere.

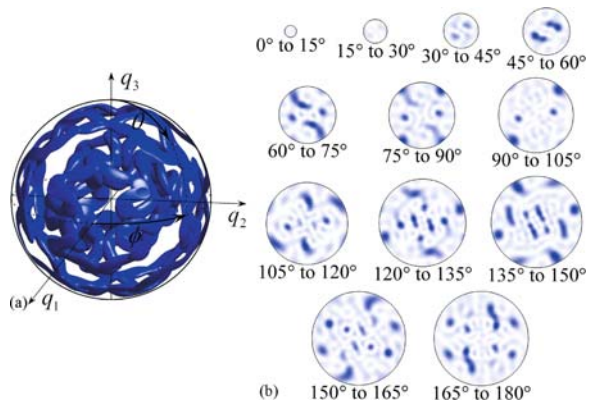


Fig. 3.12 Continuous quaternion distribution for the crystal orientations in a copper textured material, corresponding to the collection of discrete quaternions in Fig. 3.8. The distribution function is determined by Equation (3.18), with $n_{\max} = 24$. (**a**) A single contour of the distribution function in the space of the vector part $\mathbf{q}$ of a quaternion q. (**b**) The distribution function, shown in two dimensions as stereographic projections of concentric spherical shells of the space in (**a**). Regions of finite probability density appear in some areas that are empty in Fig. 3.8(b) because of the use of a limited number of terms, while regions of negative probability density were removed by applying a positivity constraint

As an examination of the degree to which Equation (3.18) is able to reproduce the details of a discrete orientation distribution, we apply the expansion to the collection of discrete quaternions in Fig. 3.8. The result is given in Fig. 3.12, and indicates that despite the inevitable inaccuracies introduced by limiting the number of terms, the probability density function reflects the distribution of the orientation measurements quite accurately. Though this form of analytic expression for a texture has only recently been presented (Mason and Schuh 2008), the guiding principle follows naturally from the well-known expansions of functions on the circle and the sphere using the circular harmonics and spherical harmonics, respectively.

3.5.4 Generalized Spherical Harmonics

One reason that textures have not historically been treated as quaternion distributions is that Bunge, often thought of as the founder of modern texture analysis, instead considered textures as probability density functions in Euler angle space (Bunge 1993). Since the definition of the Euler angles precludes their interpretation as angular coordinates on the surface of a familiar geometrical shape, the basis functions for the Euler angles are generally considered to reside in the space formed by placing the three Euler angles on orthogonal coordinate axes, as in Fig. 3.10(a). These functions, known as the generalized spherical harmonics, resemble the product of two complex spherical harmonics with a shared index l and polar angle Φ, and are given by (Bunge 1993):

$$T_l^{mn} = e^{im\varphi_2} P_l^{mn}(\cos\Phi) e^{in\varphi_1}, \tag{3.20}$$

with integer indices $0 \leq l$, $-l \leq m \leq l$, and $-l \leq n \leq l$. The function P_l^{mn} is occasionally referred to as a generalized associated Legendre function (a definition and derivation are provided in, e.g., Vilenkin [1968]). One practical difference with the hyperspherical harmonics of Equation (3.17) is that the generalized spherical harmonics are complex instead of real, meaning that the expansion of a function as a linear combination of the generalized spherical harmonics generally requires complex coefficients.

A square-integrable function $f(\varphi_1, \Phi, \varphi_2)$ defined within the Euler angle space is expanded as (Bunge 1993):

$$f(\varphi_1, \Phi, \varphi_2) = \sum_{l=0}^{\infty} \sum_{m=-l}^{l} \sum_{n=-l}^{l} D_l^{mn} T_l^{mn}, \tag{3.21}$$

with complex coefficients D_l^{mn}. The coefficients of this expansion are found by taking the inner product of the function with the appropriate generalized spherical harmonic (Bunge 1993):

$$D_l^{mn} = (2l+1) \int_0^{2\pi} \int_0^{2\pi} \int_0^{\pi} f(\varphi_1, \Phi, \varphi_2) \times T_l^{*mn} \frac{\sin\Phi}{8\pi^2} d\Phi d\varphi_1 \varphi_2, \tag{3.22}$$

where the factor of $(2l+1)$ arises from the fact that the inner product of a generalized spherical harmonic with itself is not one, and $*$ indicates the complex conjugate. The labor required to calculate these coefficients is reduced to practical limits by including in the expansion only terms with l less than or equal to some $l_{\max}$, at the expense of some accuracy.

The normalized, strictly positive function $f(\varphi_1, \Phi, \varphi_2)$ may always be interpreted as the probability density of an orientation occurring in the region of φ_1, Φ, and φ_2 in Euler angle space. This expansion was applied to the discrete orientations given as points in the Euler angle space in Fig. 3.10, and the result is shown in Fig. 3.13. The single contour of the distribution function in Fig. 3.13(a) makes clear the interpretation of the copper texture as a "tube" through the Euler angle space, while the two-dimensional format used in Fig. 3.13(b) is the traditional means of reporting a texture graphically in the literature.

3.5.5 Symmetrized Harmonics

While the four expansions outlined in this section apply to any square-integrable function defined on the appropriate space, the function of interest is usually not arbitrary. An orientation distribution function must reflect the crystal and sample symmetries of the material being considered. The knowledge that this function is subject to certain symmetries is quite valuable,

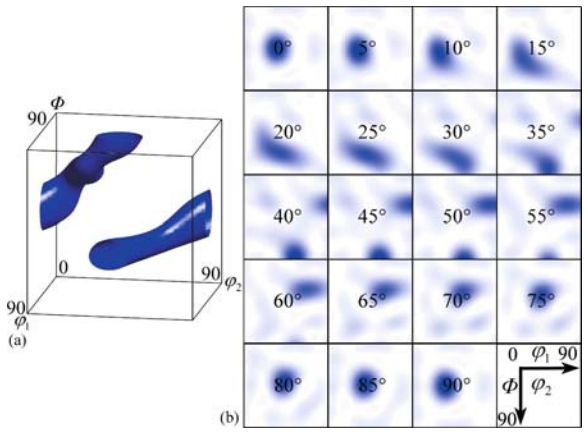


Fig. 3.13 Continuous Euler angle distribution for the crystal orientations in a copper textured material, corresponding to the collection of discrete orientations in Fig. 3.10. The distribution function is determined by Equation (3.21), with $l_{\max} = 12$. (**a**) A single contour of the distribution function in the conventional volume used for cubic crystal symmetry and orthorhombic sample symmetry. (**b**) The distribution function, sectioned perpendicular to the φ_2 axis. Regions of finite probability density appear in some areas that are empty in Fig. 3.10(b) because of the use of a limited number of terms, while regions of negative probability density were removed by applying a positivity constraint

since it allows one to use significantly fewer terms in the expansion than for the general case. The essential idea is that it is only necessary to use the *symmetrized harmonics*, or those linear combinations of harmonics that reflect the symmetries of the system. Any linear combination of the symmetrized harmonics must reflect these same symmetries, and furthermore, any square-integrable function with these symmetries may be decomposed into a linear combination of the symmetrized harmonics. Since the number of symmetrized harmonics is usually just a fraction of the number of general harmonics (and decreases further as the symmetry increases), the reduction in the number of coefficients to calculate is often considerable.

As an example, consider the rotation of a circle about an axis perpendicular to the plane of the circle and passing through its center. If this is a k-fold axis, then the symmetrized circular harmonics are those of Equation (3.11), with m equal to an integer multiple of k. Requiring a function on the circle to conform to this symmetry causes the coefficients of its expansion to vanish for all except these values of m, meaning that the number of coefficients to be calculated is reduced by a factor of k.

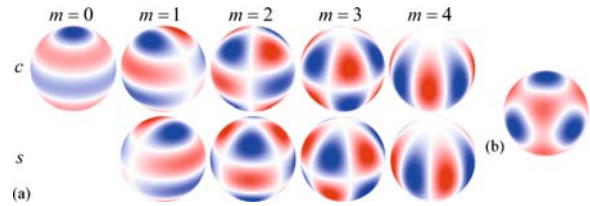


Fig. 3.14 An example of the reduction in the number of harmonics contributing to the expansion of a function on the surface of a sphere when cubic point group symmetry is present; *blue* and *red* correspond to positive and negative values respectively. (**a**) The nine spherical harmonics defined by Equation (3.14) for $l = 4$. The value of the index m is given above the columns, with the harmonic Y_l^{mc} on the *top* and Y_l^{ms} on the *bottom* of a given column. (**b**) Only one linear combination of the single harmonics in (**a**) satisfies the requirements of cubic point group symmetry, reducing the number of coefficients to be calculated for $l = 4$ by eight

The situation is more complicated for the spherical harmonics, since the increase in dimension allows a particular point group symmetry to include multiple rotations performed about different axes. While the theory underlying the procedure is more involved (refer to, e.g., Altmann and Cracknell [1965]; Mueller and Priestley [1966]), the reduction in the number of coefficients to calculate is considerable, as the example given in Fig. 3.14 indicates. Of all the linear combinations of the nine spherical harmonics for $l = 4$ (Fig. 3.14[a]), only one combination satisfies the symmetry of the cubic point group (Fig. 3.14[b]). Furthermore, the ability to derive the symmetrized spherical harmonics is not necessary to reap this benefit, since tables are available that list the symmetrized spherical harmonics (Altmann and Herzig 1994).

Of course, the symmetrization of the generalized spherical harmonics and the hyperspherical harmonics is of particular interest, because of the utility of these functions in the expression of texture. Those interested in the subject should refer to Bunge (1993) for the symmetrization of the generalized spherical harmonics, and to Mason and Schuh (2008) for the description of the symmetrization of the hyperspherical harmonics.

3.6 Conclusion

The various representations outlined in this chapter should be considered as methods for the communication of textures, presumably of materials with

advantageous properties or resulting from particular processing procedures, as observed through EBSD. That is, the representation of texture is fundamentally a means to an end, though one that gives results in accordance with the skill and respect with which it is used. An appropriate selection of the available information, given in a representation that clearly emphasizes the qualities of interest, always reflects the researcher's efforts to disseminate his or her results for the benefit of the research community. While this chapter is nothing more than an outline of a rather extensive field, we hope that the reader has gained some appreciation for the representations of textures that are available, and the fundamental role that they play in the understanding of information acquired through EBSD.

References

Altmann SL (1986) Rotations, quaternions, and double groups. Clarendon Press, Oxford

Altmann SL, Cracknell AP (1965) Lattice harmoncs i. Cubic groups. Rev Mod Phys 37:19–32

Altmann SL, Herzig P (1994) Point-group theory tables. Clarendon Press, New York

Bateman H, Erdélyi A (1953) Higher transcendental functions. McGraw-Hill, New York

Bunge HJ (1993) Texture analysis in materials science: mathematical methods. Cuvillier Verlag, Gottingen

Domokos G (1967) Four-dimensional symmetry. Phys Rev 159:1387–1403

Euler L (1776) Formulae generales pro translatione quacunque corporum rigidorum. Novi Comm Acad Sci Imp Petrop 20:189–207

Frank FC (1988) Orientation mapping. Metall Trans A 19: 403–408

Funda J, Taylor RH, Paul RP (1990) On homogeneous transforms, quaternions, and computational-efficiency. IEEE T Robotic Autom 6: 382–388

Gertsman VY (2001a) Geometrical theory of triple junctions of csl boundaries. Acta Crystallogr A 57:369–377

Gertsman VY (2001b) Coincidence site lattice theory of multicrystalline ensembles. Acta Crystallogr A 57:649–655

Gilmore R (1974) Lie groups, Lie algebras, and some of their applications. Wiley, New York

Glez JC, Driver J (2001) Orientation distribution analysis in deformed grains. J Appl Crystallogr 34:280–288

Gradshtein IS, Ryzhik IM, Jeffrey A (2000) Table of integrals, series, and products. Academic Press, San Diego

Grimmer H (1973) Coincidence rotations for cubic lattices. Scripta Metall Mater 7:1295–1300

Grimmer H (1974) Disorientations and coincidence rotations for cubic lattices. Acta Crystallogr A 30:685–688

Grimmer H (1980) A unique description of the relative orientation of neighboring grains. Acta Crystallogr A 36:382–389

Heinz A, Neumann P (1991) Representation of orientation and disorientation data for cubic, hexagonal, tetragonal and orthorhombic crystals. Acta Crystallogr A 47:780–789

Hicks HR, Winternitz P (1971) Relativistic two-variable expansions for three-body decay amplitudes. Phys Rev D 4: 2339–2351

Hopf H (1940) Systeme symmetrischer bilinearformen und euklidische modelle der projektiven räume. Vierteljschr Naturforsch Ges Zürich 85:165–177

Humbert M, Gey N, Muller J, Esling C (1996) Determination of a mean orientation from a cloud of orientations. Application to electron back-scattering pattern measurements. J Appl Crystallogr 29:662–666

Lewis AC, Jordan KA, Geltmacher AB (2008) Determination of critical microstructural features in an austenitic stainless steel using image-based finite element modeling. Metall Mater Trans A 39A:1109–1117

Mason JK, Schuh CA (2008) Hyperspherical harmonics for the representation of crystallographic texture. Acta Mater, DOI: 10.1016/j.actamat.2008.08.031

Morawiec A (2004) Orientations and rotations: computations in crystallographic textures. Springer, Berlin

Morawiec A, Field DP (1996) Rodrigues parameterization for orientation and misorientation distributions. Philos Mag A 73:1113–1130

Mueller FM, Priestley MG (1966) Inversion of cubic de hass-van alphen data, with an application to palladium. Phys Rev 148, 638–643

Neumann P (1992) The role of geodesic and stereographic projections for the visualization of directions, rotations, and textures. Phys Status Solid A 131:555–567

Siemens M, Hancock J, Siminovitch D (2007) Beyond Euler angles: Exploiting the angle-axis parametrization in a multipole expansion of the rotation operator. Solid State Nucl Mag 31:35–54

Stuelpnagel J (1964) On the parameterization of the three-dimensional rotation group. SIAM Rev 6:422–430

Varshalovish DA, Moskalev AN, Khersonskii VK (2008) Quantum theory of angular momentum. World Scientific, Singapore

Vilenkin NJ (1968) Special functions and the theory of group representations. American Mathematical Society, Providence

Wenk HR, Kocks UF (1987) The representation of orientation distributions. Metall Trans A 18:1083–1092

Wigner EP (1959) Group theory and its application to the quantum mechanics of atomic spectra. Academic Press, New York

Chapter 4

Energy Filtering in EBSD

Alwyn Eades, Andrew Deal, Abhishek Bhattacharyya, and Tejpal Hooghan

4.1 Introduction

Most recent advances in EBSD have centered on increasing automated indexing speed through the prudent use of modern computing capabilities and advances in camera technology. Post-processing routines are also becoming more encompassing and robust. However, few significant gains have been made towards obtaining a better understanding of the underlying physics of the phenomenon. The community's handle on the physics stems largely from lessons learned in transmission electron microscopy (TEM) and from electron channeling pattern (ECP) experiments that, while very insightful, do not complete the picture of EBSD. A better understanding of EBSD physics may lead to significant advances in the technology. Accordingly, in this chapter we discuss our efforts to investigate the formation of EBSD patterns using an energy filter. Others have attempted to filter patterns but we are aware of only one previous publication on the subject (Mancuso et al. 1994). There is a whole field of work on understanding the formation of backscatter diffraction patterns and the measurement of energy-filtered patterns at much lower energies (typically up to 2 keV) than is usual for EBSD. This research is related to surface science and Auger spectroscopy. This work is reviewed in Pronin and Gomoyunova (1998) and will not be discussed further here.

A. Eades (✉)
Department of Materials Science and Engineering, Lehigh University, Bethlehem, PA,USA
e-mail: jae5@lehigh.edu

We describe experiments with an energy filter to obtain patterns made with only those electrons with energies above a selected cut-off. The following results have been obtained: The Kikuchi contrast is stronger in filtered patterns. The highest contrast is in patterns formed with electrons having an energy somewhat below the beam energy. Backscattered electrons of all energies are Bragg reflected and hence contribute to the Kikuchi contrast of the patterns. However, not all electrons contribute equally. Electrons very close to the beam energy give less sharp Kikuchi contrast and electrons far below the beam energy contribute Kikuchi contrast with a higher diffuse background (i.e., with a lower contrast). Filtering the pattern reduces both the depth and the lateral extent of the region contributing to the pattern, and hence opens up the possibility of obtaining maps from materials with a smaller grain size.

4.2 Background

In a scanning electron microscope, the electrons which leave the sample (secondary electrons and backscattered electrons) have a range of energies from the energy of the incident beam down to zero. In EBSD we are not concerned with the lowest energy electrons (the secondary electrons) because they do not contribute to the patterns. The fluorescent screen that is used to acquire the EBSD pattern is usually coated with a thin layer of metal to avoid charging effects in the phosphors, which are insulators. The secondary electrons do not penetrate through this metal layer, and even if they did, the energy they would have would not produce significant luminescence. Thus, only

A.J. Schwartz et al. (eds.), *Electron Backscatter Diffraction in Materials Science*,
DOI 10.1007/978-0-387-88136-2_4, © Springer Science+Business Media, LLC 2009

backscattered electrons are considered. The energy distribution of backscattered electrons depends on several factors (Goldstein et al. 2003): sample tilt, composition, and the energy of the incident beam. The energy distribution from several elements under some typical EBSD conditions (70 degree tilt and a 15 keV beam) is shown in Fig. 4.1.

Although some microscopists have expressed doubts, the general character of this distribution of energies of the backscattered electrons is widely accepted, based both on the results of Monte Carlo simulations and on the results of experiments. What has been less clear is how the electrons across this broad range of energies contribute to the Kikuchi bands, which are the important feature of EBSD patterns. Some authors have suggested that the electrons which contribute most strongly to the Kikuchi contrast are the electrons at the energy of the incident beam (Wells 1999). Others (including the lead author of this paper before the work described here was started) have felt that electrons of all energies would contribute equally to the contrast, so that the final pattern would be a superposition of patterns of all the different energies.

Clearly, for the understanding of EBSD patterns to be improved it is desirable to have information regarding the way in which electrons of different energies contribute to the patterns. This requires energy filtering. This chapter discusses energy filtering and the results of studies using an energy filter. For example, it will be shown that neither of the suggestions described in the previous paragraph turns out to be correct.

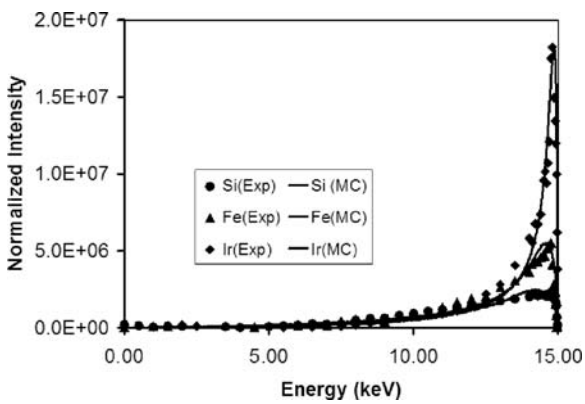


Fig. 4.1 Graph of the number of electrons leaving the sample versus their energy. The beam energy is 15 keV and the sample is tilted to 70 degrees. The graph shows both experimental results (*solid symbols*) and the results of Monte Carlo simulations (*continuous lines*). Since the experimental results were not measured in absolute values, a normalization factor has been introduced to match the overall level of the simulations and experiments. (Neither the experiments nor the simulations include secondary electrons)

4.3 Energy Filters

In a typical EBSD system the screen subtends a very large angle at the sample. Since the distance from the sample to the screen is often smaller than the screen diameter, the angle subtended is generally much greater than 50 degrees. In terms of electron optics, this is enormous. Even with aberration correctors, cylindrically symmetric electron lenses can handle only a few degrees at most. Therefore, the designs of energy filters that will serve in the transmission electron microscope are of no use for filtering EBSD patterns. We are aware of only one reasonably simple method for filtering patterns with such a wide angular range, while keeping the spatial distribution of the electrons: the use of a retarding grid. The idea is that a fine conducting mesh is deployed across the space traversed by the electrons. This mesh is held at a fixed potential. Electrons with an energy corresponding to a value above the mesh potential are transmitted while electrons with lower energies are turned back. This works well with one caveat: for the energy cut-off to be sharp, the electrons must approach the grid *at normal incidence*. If the electrons are incident on the grid at a variety of angles, electrons are rejected at different energies depending on their angle. Moreover, the electrons that go through the grid will be deflected from their original trajectories by an amount that depends on the angle of incidence on the grid. Hence a filter design that does not use normal incidence would give rise to EBSD patterns that are distorted or destroyed.

There are other methods of retaining angular fidelity while performing energy filtering. These methods have generally been applied to analysis in surface science, in photoelectron spectroscopy, for example (Daimon and Matsui 2006; Broekman et al. 2005). The implementation of these spherical and toroidal filters for application to EBSD would require their modification to higher energies and would imply building a special purpose instrument. A recent publication describes such an instrument and its first results (Went et al.

in press). We cannot envisage a device based on these instruments being fitted as an addition to an existing scanning electron microscope.

The principle of making a filter with a normal-incidence grid has been employed for several decades to perform LEED—low-energy electron diffraction (for example: van Hove et al. 1986). In the LEED configuration, the problem of achieving normal incidence is handled by making the grid spherical with the center at the electron source. Figure 4.2 shows a schematic LEED configuration. As shown, there are three grids, not one. The first grid is at ground potential so that the electron trajectories are not affected by the potentials present. The second grid is the filter grid; its potential is set so as to reject electrons of lower energy. The third grid accelerates the electrons to a high potential so that when they strike the fluorescent screen they have sufficient energy to produce a good signal. In LEED this final acceleration is important because the electrons from the sample are of a low energy (on the order of 100 eV). For technical reasons, not relevant here, practical systems often use four grids rather than three.

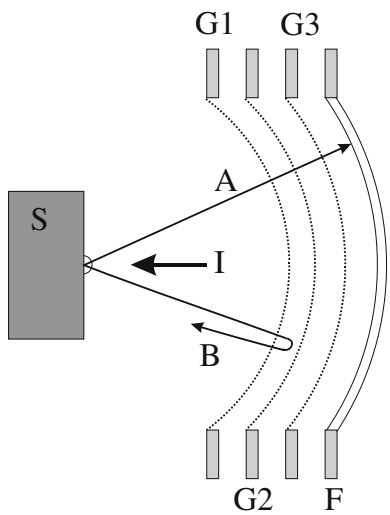


Fig. 4.2 Schematic diagram of a LEED system. The incident electron beam (I) is provided by an electron gun (not shown) and is at normal incidence to the sample (S). The first grid (G1) is at the same potential as the sample so that the trajectories are radial. The second grid (G2) is set at the filter potential. Electrons with energies above the potential of G2 (A) are transmitted, but electrons with energies below this potential (B) are rejected. Electrons that get through the retarding grid are accelerated by the third grid (G3) to hit the fluorescent screen (F). Because of the spherical geometry, the transmitted electrons travel in straight lines

For present purposes, commercial LEED systems have the inconvenience that they have the center of the pattern blocked by the need to provide an electron gun to put the incident beam at normal incidence to the sample. The end result is that such systems are typically mounted on 6-inch or 8-inch UHV flanges, which would be unsuitable for SEM use. Since an EBSD filter does not require an electron gun, it might be possible to make a much smaller unit. As far as we are aware, this has not been attempted.

An alternative design developed by Staib Instruments (2008) was the one used for the experiments described here (Hooghan et al. 2004). In the Staib design, the grid is flat. This has significant advantages for manufacture, especially in a small system suitable for filtering EBSD in the SEM. In order to have the electrons incident on the flat grid at normal incidence, electron lenses are incorporated in front of the grid.

In the Staib design there are two grids. The entrance grid guarantees that there is a field-free region above the sample and that the trajectories of the electrons will be straight lines until they are through the grid. Its function is much like that of the first grid in a LEED system. Following the entrance grid, there are two cylindrical electrodes. The potentials on these two electrodes are set by the operator. The effect is to form electrostatic lenses that focus the electrons, as shown in Fig. 4.3, so that they are incident on the filter grid at normal incidence. In that way the cut-off (produced by the rejection of electrons with energy below the potential on the filter grid) is sharp. In fact with a 20 keV beam it is estimated that the precision of the cut-off is 10 eV. Following the filter grid, the electrons are accelerated back to the beam energy prior to incidence on the fluorescent screen. Between the grid and the fluorescent screen is another cylindrical electrode, the function of which is to minimize distortions in the pattern from edge effects. In practice, the patterns are not very sensitive to the setting of this electrode.

The advantages of this design are that it is compact and can be fitted rather easily into an SEM with a reasonably large port, and that it is simple and easy to operate. A disadvantage is that the capture angle is reduced to 30 degrees. Moreover, the focusing electrodes can make the electrons at the cut-off energy incident on the grid at normal incidence, but electrons at

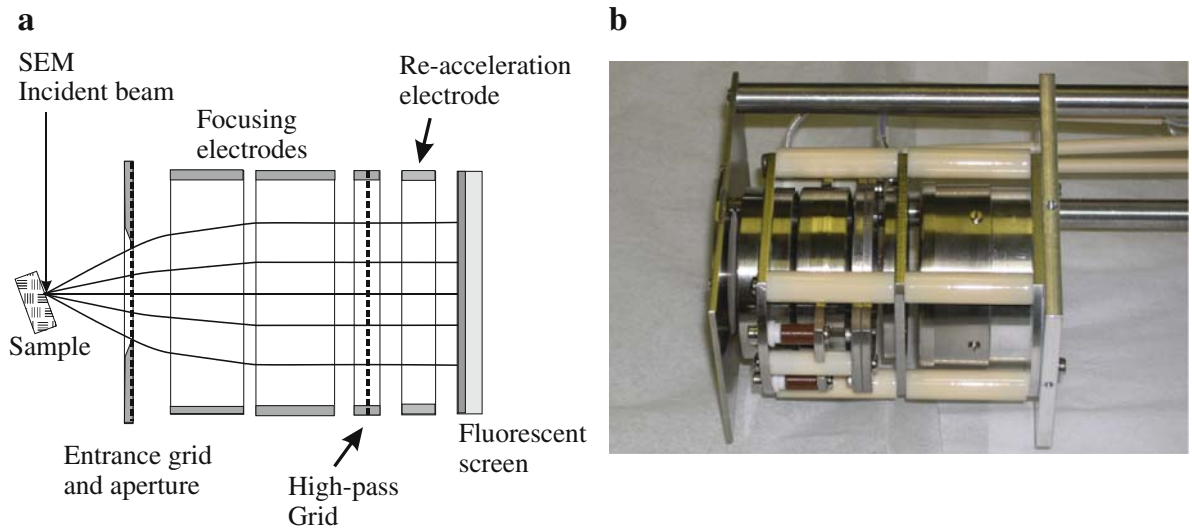


Fig. 4.3 The energy filter used for the experiments described in this chapter. (**a**) A schematic diagram showing the main components of the filter. (**b**) A photograph of the filter at about the same scale and with the components in approximately corresponding positions

higher energies will be focused differently. The lenses will be weaker for electrons of higher energy; this is just chromatic aberration. The filtered patterns will be good representations of the high-pass patterns that are sought only if the filter energy is close to the beam energy. The system has limitations when operated with a wide energy window. The Staib design was originally intended for use in RHEED (reflection high-energy electron diffraction), where—much as in TEM—the range of energies to be filtered is always small compared with the beam energy.

With this system we often had to use long exposure times. This is not intrinsic to the use of an energy filter (though inevitably when filtering, some of the signal is lost); rather it arose from the origins of this filter design for use with RHEED. In RHEED the signal is always huge compared with the signal in EBSD and the filter was not optimized for efficient signal collection.

4.4 Operating the Filter

The filter was mounted on an FEI Dual-Beam FIB, with a Schottky field-emission gun, and all the results described here were obtained with that instrument. It was the only instrument in our laboratory with a port large enough to mount the filter in a suitable configuration, although it is possible to envision future designs for much smaller ports. The axis of the filter is horizontal (at ninety degrees to the beam). The filter has no mechanical alignments. The distance from the axis of the microscope is fixed, as is the height of the filter. The distance from the axis is set by the construction of the device and is within the range of values that the optics can handle. But to operate the filter correctly, it is necessary to move the sample vertically to the focus point for the system of lenses. This is easy to do. Two different methods both find the appropriate height by turning the lens settings away from the values they have for filtration. One method sets the lenses so as to make the illumination on the screen into a small spot and then adjusts the sample height to bring that spot to the center of the screen. Alternatively, if the lens settings are close to optimal, as the cut-off voltage is brought to the beam voltage, the pattern disappears from the screen in some places but not others. This pattern has circular symmetry when the sample is at the right height but not otherwise.

The setting of the lenses is more awkward. There are the two electrodes whose voltages are to be set, but only one basic condition: that the beam at the cut-off energy is normal to the grid. This condition can be detected by sweeping the cut-off energy through the beam voltage. If the lenses are set correctly, the pattern disappears all at the same time. When the voltages are

wrong, some parts of the pattern disappear before others. However, the condition is not unique. If one electrode voltage is changed, the "it all disappears at the same time" condition can be brought back by changing the other voltage (up to a point). Secondary optimization was based on arranging that the pattern did not change size as the cut-off was increased. This was important for the pattern subtraction described below.

Once the lens values have been set at the beam energy, the power-supply electronics scales the lens settings with the cut-off voltage so as to keep a sharp cut-off for all cut-off energies.

4.5 Early Results

Almost as soon as the filter was brought into use, two results were obtained: one surprising and one not. If a pattern that has been filtered is compared with one that has not, there is a marked increase in the contrast of the filtered pattern (Hooghan et al. 2004). That is to say that, if a pattern is made with electrons of all energies from the beam energy down to the detection limit of the phosphor, that pattern has less contrast than a pattern made with only those electrons with energies close to the beam energy (see Fig. 4.4). This is not a surprise since there are several arguments that suggest that low energy electrons will reduce the contrast: Some people have supposed that low energy electrons do not contribute to the Kikuchi diffraction, but just add to the background; low energy electrons will —because of their different wavelengths—put their Kikuchi lines in a different place from those electrons closer to the beam energy; an increased probability of thermal diffuse scatter will increase the background for low energy electrons and thus reduce the contrast (see more on this later).

It is worth noting, however, that we have to be careful when making assertions about contrast. Our

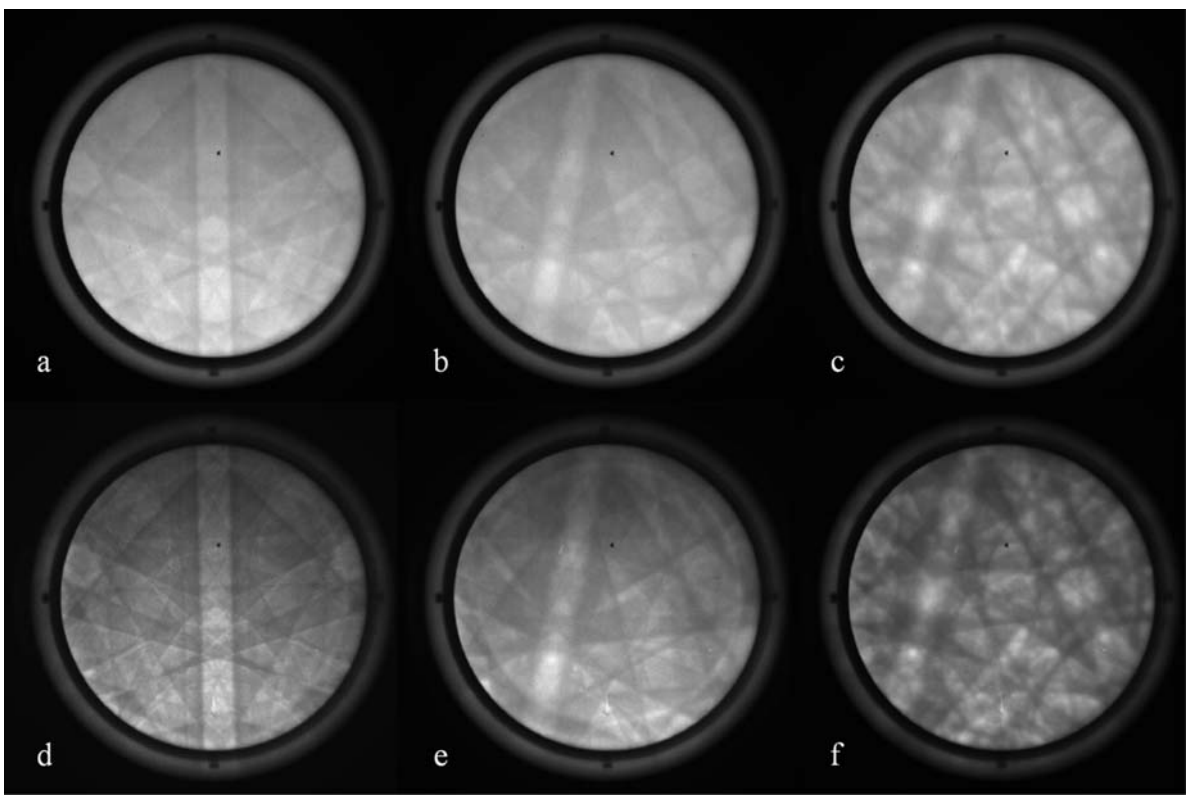


Fig. 4.4 EBSD patterns showing the increase in contrast produced by filtering. The beam energy is 15 keV. **a**, **b,** and **c** are unfiltered patterns from silicon, iron, and iridium. **d**, **e,** and **f** are corresponding patterns with the energy cut-off set to 14.5 keV. Care has been taken to make a fair comparison of the images

microscopes are fitted with knobs labeled "brightness" and "contrast." When comparing the contrast of one image with another we have to be sure that the contrast has not been changed electronically by twiddling the knobs. To calculate the true contrast, defined as:

$$C = \frac{\text{Signal(maximum)} - \text{Signal(minimum)}}{\text{Signal(maximum)}} \quad (4.1)$$

it is necessary to know the absolute values of the signals (or, alternatively, the value of the zero of the signal). Considerable care was taken in all the experiments described in this chapter to do this correctly and to avoid errors associated with the use of image settings.

As can be seen from Fig. 4.5, filtered patterns have a contrast which rises to about twice the contrast of the unfiltered patterns when the filter cut-off is set close to the beam voltage. It might be supposed that this graph implies that the contrast in the Kikuchi lines for electrons at half the beam energy and below is the same as the contrast in the unfiltered patterns, since adding more such electrons to the pattern by lowering the cut-off energy does not change the overall contrast. However, reference to Fig. 4.1 shows that the number of electrons at these energies is very low and therefore adding them to the patterns, regardless of their contrast, is unlikely to make much difference to the overall contrast.

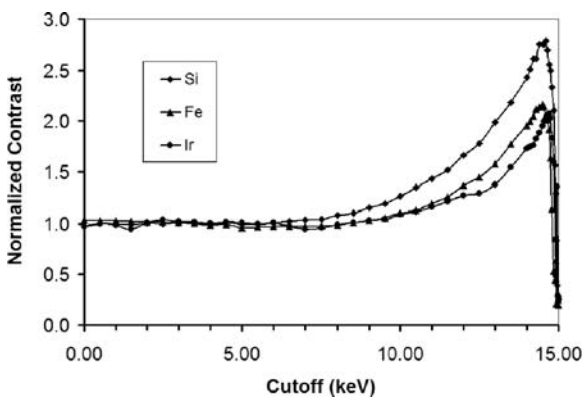


Fig. 4.5 Graph of the band contrast in EBSD patterns as a function of the cut-off energy. The beam energy was 15 keV. Data correspond to the strongest band from single-crystal samples of silicon, iron, and iridium. Each curve has been normalized by dividing the contrast of the pattern by the contrast from an unfiltered pattern of the same material

From this information we can conclude that the strongest contrast in the Kikuchi patterns is produced by electrons that have a little less than the beam energy. We are fortunate that this is also the energy at which there is the largest number of electrons. The drop in contrast as the cut-off energy is lowered (to the left of the peak in Fig. 4.5) may be in part because the diffraction contrast drops as the energy drops due to enhanced thermal scattering, but may also be in part because (owing to the change in wavelength of the electrons) the width of the Kikuchi contrast changes with energy. In this discussion of contrast we should bear in mind that electrons of different energies are not distributed equally across the pattern. Electrons close to the beam energy are more concentrated at the bottom of the screen, while electrons that have lost a lot of energy are more evenly distributed (Deal and Eades 2005). However, the band contrast data are not greatly affected by this since they represent average values.

The surprising early result was that, if the filter is set to accept only electrons with energies very close to the beam energy (within, say, 200 eV of the beam energy), the sharpness of the patterns is reduced (Deal et al. 2008). Making a quantitative measure of sharpness in a pattern is even harder than measuring contrast. David Joy has addressed this problem for SEM images and recommends the use of Fourier transform methods (Joy 2002). However, we were not able to obtain satisfactory results by this means and are forced to present the results of subjective observation. The result, however, does seem to be robust and is systematically obtained over a wide range of samples and operating conditions.

Figure 4.6 shows this effect. Figure 4.6a is a filtered pattern made with electrons down to 500 eV below the beam energy, near where the contrast of the pattern is a maximum. Figure 4.6b is a pattern made with only those electrons within 180 eV of the beam energy. There is a noticeably greater blurriness in the pattern in Fig. 4.6b. We believe that we have an explanation for this result, although it initially took us by surprise.

The starting point for the discussion is the question: How wide is a Kikuchi line? Kikuchi lines arise because of Bragg diffraction; they will appear in positions where the electrons are incident on planes in the crystal at the Bragg angle. But Bragg diffraction describes a physical process, not a mathematical identity. Therefore, there is a range of angles, about the Bragg angle, over which there will be diffraction. A graph of the intensity of the diffracted beam as a func-

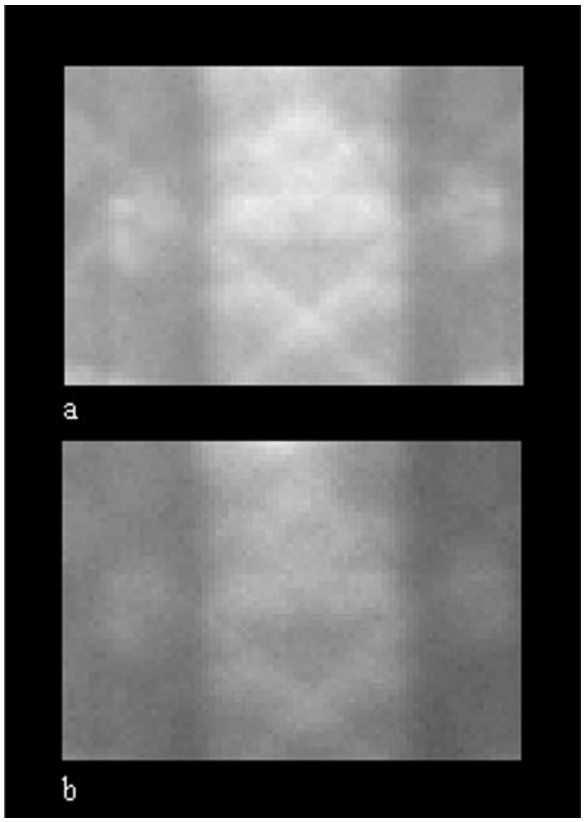


Fig. 4.6 Filtered EBSD patterns from the <114> zone axis of Si, obtained with a 15 s exposure and (**a**) 14.5 keV cut-off, (**b**) 14.82 keV cut-off. Beam energy 15 keV

tion of the angle between the incident electron beam and the crystal planes is called a rocking curve. The width of a rocking curve tells how far you can be from the Bragg condition and still get diffraction from those planes. The width of the rocking curve is thus related to the width of the Kikuchi line.

In the transmission electron microscope, dynamical diffraction is well understood (Williams and Carter 1996), so we can use the transmission microscope as a guide. In the TEM case, it is a well-established result that the width of the rocking curve (under what are called two-beam conditions) is independent of thickness for thicker samples, but for thinner samples the width of the curve is inversely proportional to the thickness (Hirsch et al. 1977). Specifically, the range of angles over which there is diffraction in thicker samples is given by:

$$\Delta\theta = \frac{4}{g\xi_g} \tag{4.2}$$

whereas for thinner samples it is given by:

$$\Delta\theta = \frac{1}{gt} \tag{4.3}$$

where $\Delta\theta$ is the width of the rocking curve, g is the magnitude of **g** diffraction vector, ξ_g is the extinction distance for that reflection, and t is the sample thickness. The latter result is given in Hirsch et al. (1977) as well as in Williams and Carter (1996); while the former is easily derived from the angular range over which the dispersion surface deviates from the free electron sphere, or from the width of simulated rocking curves (Hirsch et al. 1977; Williams and Carter 1996). This means that for sample thicknesses above about $\xi_g/4$ the width of the rocking curve is constant, but below that thickness the rocking curve increases in width as the sample gets thinner. This can be thought of as the effect of imperfect cancellation in the destructive interference of scattering from a smaller number of atoms.

This result can be related to the EBSD case as follows: The electrons that have lost significant energy before they exit the sample may have traveled to a reasonable depth before exiting, and thus will be diffracted in a regime where the width of the rocking curve is the constant value related to the extinction length. However, an electron with an energy very close to the beam energy can have penetrated only a very small distance into the sample; as a result, the diffraction which occurs on exiting the sample is in the regime where the width of the rocking curve depends on the thickness (that is, it depends on how little energy has been lost). This provides a sound explanation for the blurring that is observed.

These early results already provide an important advance in the framework for any discussion of the details of any detailed discussion about the formation of EBSD patterns. We can summarize the conclusions thus:

1. There is good agreement (despite some minor inconsistencies) between the measured distribution of backscattered electron energies and those predicted by Monte Carlo methods (Fig. 4.1). There is no reason to suppose that these results are in error.
2. The strongest contribution to the Kikuchi patterns that are observed in EBSD comes from those electrons near the peak of the electron-energy distribution curve: namely, a few hundred volts below the

beam energy (for a sample tilted to the typical 70 degrees).
3. Any theory or model that is based on the idea that Kikuchi patterns in EBSD are the result of the diffraction of only those electrons whose energy is equal to the beam energy is simply incorrect, although such models may be useful in some cases.

4.6 Patterns at Different Energies

The energy filter used is a high-pass filter. This means that the patterns formed are patterns made with electrons having energies above the limit set by the filter. It is also of great interest to obtain band-pass patterns, that is, patterns made with electrons having energies in a window between two chosen values. This is needed, for example, to see the contribution to the Kikuchi contrast made by electrons of different energies. This cannot be done directly, but can be done in principle by taking two high-pass patterns with different cut-off energies and subtracting one from the other. For example, suppose that the beam energy is 20 keV, then with the cut-off at 18 keV, the pattern is formed by all the electrons above 18 keV, in this case, electrons between 18 and 20 keV. If another pattern is obtained with the cut-off at 17 keV, it will be made with the electrons between 17 and 20 keV. If, finally, the latter pattern is subtracted (pixel by pixel) from the previous pattern, then the result will be the pattern produced by the electrons having energies between 17 and 18 keV.

This procedure has been carried out for single crystals of silicon, iron, and iridium (Deal et al. 2008). The beam energy was 15 keV and subtracted patterns were obtained to show the contributions of the electrons with energies down to 11.5 keV. Before presenting the results of these experiments, we must make it clear that, because of the design of the filter, the experiments are difficult; and the results—although clear—are not as definitive as one would wish. The reason for this is connected with the very high chromatic aberration of the filter, as mentioned above. Because the electrons follow trajectories in the filter which depend on their energy, when the cut-off energy is changed, electrons of the same energies arrive at different places in the pattern. This means that the principle of subtracting patterns is marred by the aberrations of the filter. In order to get the best results possible under these circumstances, very considerable effort was made to find the operating conditions that minimized these unfortunate effects, and, in addition, only very small energy windows were used. If the cut-off was changed by only a small amount, the errors were correspondingly small and the difference pattern could be assumed to be a good representation of the pattern formed by electrons of the chosen energy window. Clearly, care was also taken to normalize the patterns, so that the subtraction of the patterns was legitimate. As can be seen from Fig. 4.1, towards the low energy end of the range explored (i.e., near 12 keV), the number of electrons is already quite small. Thus these patterns were obtained by subtracting two patterns with only a small difference between them. As always, subtracting two large numbers to obtain a small difference is a recipe for large errors and, in this case in particular, a lot of noise.

Results from these experiments are presented in Fig. 4.7. Again, the samples are silicon, iron, and iridium. Two series of band-pass patterns are shown. One set shows patterns made with electrons in the 13–13.5 keV energy window, while the other shows patterns from the 11.5–12 keV energy window. All of the patterns show Kikuchi contrast. We can conclude immediately that backscattered electrons of *all* energies are diffracted to produce a contribution to the Kikuchi lines in the patterns. The unfiltered (normal) EBSD patterns are formed by the sum of the effects of the diffraction of the electrons of all energies.

However, not all energies contribute equally. First, there are fewer electrons at lower energies, so they influence the patterns less. Second, inspection of Fig. 4.7 shows that the Kikuchi contrast is lower at lower electron energies. This may be hard to see since the noise in the lower energy patterns is so much greater, but it is the case. We offer the following tentative explanation for this effect. As the electrons leave the sample and are diffracted, they are subject both to the elastic Bragg diffraction and also to thermal diffuse scattering (the effect of the atoms being displaced from their ideal sites by lattice vibration). The effect of the thermal diffuse scattering, which sends the electrons into random directions, is to reduce the intensity of the Bragg diffraction and to increase the diffuse background. In other words, it reduces the contrast of the signal. Thermal diffuse scattering is small angle scattering, so the effect it has in reducing the contrast will depend on how far below the surface it occurs.

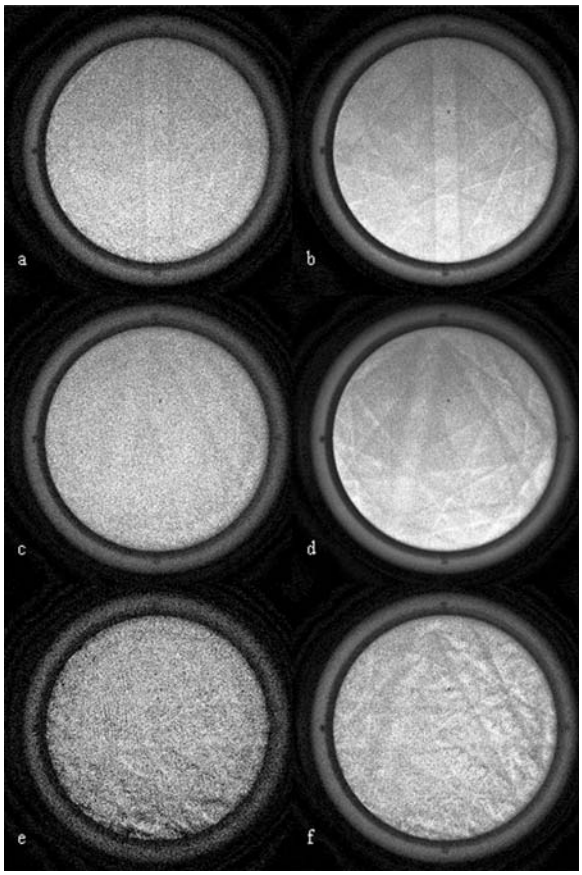


Fig. 4.7 Band-pass EBSD patterns obtained by taking the difference between energy-filtered patterns. Beam energy 15 keV. **a** and **b** are from silicon, **c** and **d** are from iron, **e** and **f** are from iridium. **a**, **c,** and **e** are made by electrons with energies between 11.5 and 12 keV, **b**, **d,** and **f** are made by those with energies between 13 and 13.5 keV

Electrons that have lost more energy can have trajectories subject to diffraction as they leave the sample, starting from deeper inside the crystal. Therefore the thermal diffuse scattering will have a bigger effect and reduce the contrast more markedly on electrons that have lost more energy than electrons that have lost less energy, and which therefore come from closer to the surface.

4.7 Localization of the Signal

At least in a statistical sense, electrons that lose less energy travel a smaller distance in the sample. Thus, if we use a high-pass filter so that the patterns are made with only those electrons close to the beam energy, then we should expect that those electrons will have traveled shorter distances in the sample and will have explored a smaller volume of the sample near the point of incidence. This raises the expectation that filtered patterns would make it possible to determine the orientations of smaller volumes and to make maps of material with smaller grain size. We have performed experiments that confirm these expectations (Bhattacharyya and Eades 2007, and in press).

These experiments involve taking EBSD patterns and deciding whether a Kikuchi band is barely visible or not visible. This is difficult when viewing the patterns on a high quality monitor, but is quite impractical when looking at images on paper. Therefore for this section we are not showing images of the results used. Patterns may be seen (not entirely satisfactorily) in Bhattacharyya and Eades (in press). In addition to inspecting the patterns directly, the relevant results were obtained by measuring the contrast of peaks in the Hough transform of the images. This has the advantage of reducing the noise in the patterns. It also makes possible a statistical estimate of whether a Kikuchi line is present or not, by comparing the difference between the Hough values at the positions of the maximum and minimum of the Hough peak with the variation in the Hough values in adjacent areas where there is no peak from Kikuchi lines.

In one series of experiments, thin films of aluminum were evaporated onto the surface of a silicon single crystal. EBSD patterns were obtained with a large beam size, so that no Kikuchi lines from the aluminum were seen. The aluminum grains were expected to be much smaller than the beam size. Kikuchi lines from the silicon (below the aluminum layer) were studied as a function of the thickness of the aluminum film in both filtered and unfiltered EBSD patterns.

The most interesting case was for aluminum films 15 nm thick. For these films, silicon Kikuchi lines were visible in unfiltered patterns, but not visible in patterns made with electrons close to the beam energy. Careful measurements of detectability in the Hough transform, as described above, were used to assess the cut-off energy in the filter at which the silicon Kikuchi lines just disappeared from the patterns (Table 4.1).

The systematic way in which this limit energy varies with the energy of the incident beam is what might be expected. As the beam energy is reduced, the stopping power of the electrons is increased. Thus, for a given

Table 4.1 Values of the "limit energy"—the cut-off energy of the filter that just caused the disappearance of the Kikuchi lines from a (001) silicon substrate below a 15 nm layer of aluminum

Incident electron beam (keV)	Limit energy (keV)	Difference (keV)
12	11.76 ± 0.04	0.24 ± 0.04
15	14.81 ± 0.03	0.19 ± 0.03
18	17.86 ± 0.01	0.14 ± 0.01

energy loss, electrons of lower beam energy will travel a smaller depth into the sample, and be more likely to remain confined to the aluminum overlayer. Conversely, to penetrate through the overlayer into the substrate, electrons of lower beam energy will need to lose more energy.

In a separate set of experiments, EBSD patterns were obtained as the beam was stepped across a grain boundary in stainless steel. The boundary was oriented across the slope of the sample and the beam was stepped perpendicular to the boundary: down the slope. The beam energy was 15 keV. In a sequence of patterns taken with a shift of 20 nm down the slope between each pattern, when the patterns were not filtered, Kikuchi lines from both grains were visible in four patterns in the sequence. In a similar sequence, when the cut-off energy was set at 14.84 keV, Kikuchi lines were visible from both grains in only a single pattern. Thus, with this (admittedly rather extreme) filtering, the width of the region contributing to the pattern has been reduced by a factor of about four.

4.8 Future Energy Filters in EBSD

Practically speaking, the energy filter used in these studies suffered from a loss of signal, chromatic aberration, a reduced capture angle, and inhibiting geometrical requirements in the SEM. The next generation of filters should be made with great attention to higher efficiency of signal collection. To avoid the problems associated with chromatic aberration, it seems that there would be an advantage in using a filter of LEED geometry, if such a device could be made to fit into the SEM. One possibility is to place the filter extremely close to the sample, so as to minimize its size for a reasonable capture angle. There are difficulties to overcome here: The manufacturing demands on the grids would be severe (they would need to be very precisely made, but still have a high transparency); the voltages to be delivered to the grids would make reducing the size problematic. The filter we used had a fixed geometry and had to be removed from the microscope when not in use. It would be very helpful to make the filter retractable, just as unfiltered EBSD systems are. Some form of alignment, to ensure that the beam intersects the object point of the filter, might also be required.

4.9 Summary and Conclusions

We have performed a series of experiments with an energy filter to obtain EBSD patterns made with only those electrons with energies above a selected cut-off. These results have confirmed, by and large, what might have been anticipated: The Kikuchi contrast is stronger in filtered patterns. The highest contrast is in patterns formed with electrons having an energy somewhat below the beam energy (about 500 eV below, for samples at 70 degrees). Backscattered electrons of all energies are Bragg reflected and hence contribute to the Kikuchi contrast of the patterns. However, not all electrons contribute equally. Electrons very close to the beam energy give less sharp Kikuchi contrast, and electrons far below the beam energy contribute Kikuchi contrast with a higher diffuse background (i.e., with a lower contrast). Filtering the pattern reduces both the depth and the lateral extent of the region contributing to the pattern, and hence opens up the possibility of obtaining maps from materials with a smaller grain size.

Realistically, we do not imagine that an energy-filtered EBSD system will replace the standard system in most cases. For the majority of users, the increase in complexity and the inevitable loss of signal will be too high a price to pay for the improved contrast and improved spatial resolution. However, on the basis of our experience it should be possible to design an improved energy filter that would be both practical and valuable, both for understanding the fundamentals of EBSD and for the mapping of still smaller nanoscale structures.

Acknowledgments We are grateful to (in chronological order): Xiaodong Tao for his important contributions to our work on EBSD prior to the arrival of the energy filter; Philippe Staib

for collaborating on the design of the filter and delivering it promptly; and Aimo Winkelmann for suggestions that improved the text. Support from DOE, under grant DE-FG02-00ER45819, is gratefully acknowledged.

References

Bhattacharyya A, Eades A (2007) Use of an energy filter to improve the depth resolution of electron backscattered diffraction. Microsc Microanal 13(Suppl 2):932–933

Bhattacharyya A, Eades J (in press) A use of an energy filter to improve the spatial resolution of electron backscattered diffraction. Microsc Microanal

Broekman L, Tadich A, Huwald E, Riley J, Leckey R, Seyller T, Emtsev K, Leyb L (2005) First results from a second generation toroidal electron spectrometer. J Electron Spectrosc 144–147:1001–1004

Daimon H, Matsui F (2006) Two-dimensional angle-resolved photoelectron spectroscopy using display analyzer—Atomic orbital analysis and characterization of valence band. Prog Surf Sci 81:367–386

Deal A, Eades A (2005) Energy-dependence of an EBSD pattern. Microsc Microanal 11(Suppl 2):524–525

Deal A, Hooghan T, Eades A (2008) Energy-filtered electron backscatter diffraction. Ultramicroscopy 108:116–125

Goldstein JI, Newbury DE, Echlin P, Joy DC, Lyman CE, Lifshin E, Sawyer L, Michael JR (2003) Scanning electron microscopy and x-ray microanalysis. 3rd ed. Kluwer, New York

Hirsch PB, Howie A, Nicholson RB, Pashley DW, Whelan MJ (1977) Electron microscopy of thin crystals. Krieger, New York (reprinted)

Hooghan TK, Staib P, Eades A (2004) An energy filter for electron backscattering diffraction. Microsc Microanal 10(Suppl 2):938–939

Joy DC (2002) SMART—A program to measure SEM resolution and imaging performance. J Microsc 208:24–34

Mancuso JF, Fama LA, Maxwell WB (1994) Effect of energy filtering on micro-diffraction in the SEM. Proceedings of the microscopy society of America, pp 604–605

Pronin II, Gomoyunova MV (1998) Imaging of near-surface atomic structure by forward-focused backscattered electrons. Prog Surf Sci 59:53–65

Staib Instruments (2008), http://www.staibinstruments.com

van Hove MA, Weinberg WH, Chan CM (1986) Low-energy electron diffraction: experiment, theory, and surface structure determination. Springer-Verlag, Berlin

Wells OC (1999) Comparison of different models for the generation of electron backscattering patterns in the scanning electron microscope. Scanning 21:368–371

Went MR, Winkelmann A, Vos M (in press) Quantitative measurements of Kikuchi bands in diffraction patterns of backscattered electrons using an electrostatic analyzer. Ultramicroscopy

Williams DB, Carter CB (1996) Transmission electron microscopy. Plenum, New York

Chapter 5

Spherical Kikuchi Maps and Other Rarities

Austin P. Day

5.1 Introduction

Spheres, or more accurately, spherical surfaces, are important for electron backscatter diffraction (EBSD). Electron backscatter patterns (EBSPs) and pole figure and misorientation axis data are ideally suited to display on the surface of a sphere.

Spherical Kikuchi maps (SKMs) are a simple means to display the full diffraction pattern for electron backscatter patterns and electron channelling patterns (ECPs). This chapter explains a little of their history, uses, and potential. It also shows new EBSP analysis results on a spherical surface and a spherical Hough transform.

There is also a brief discussion of EBSD detector design, some rarely seen colour forescatter images, and unusual EBSPs with RHEED-like (reflection high-energy electron diffraction) spots and lines.

5.2 Electron Backscatter Patterns

Electron backscatter patterns have a surprisingly long history. The first recognisable EBSPs were taken by Boersch (1937), although Finch and Wilman (1937) also produced high-quality patterns using a more oblique geometry, closer to RHEED (Braun 1999). Boersch used both planar and cylindrical film to produce high-quality diffraction patterns from a wide range of metals and minerals. Figure 5.1 shows an example iron pattern (Boersch 1937), and rock salt and diamond patterns (Finch and Wilman 1937).

5.3 Spherical Kikuchi Maps

Around the 1970s, several laboratories were investigating electron channelling patterns (ECPs; see Joy 1974) and selected area channelling patterns (SACPs). Hutchinson (Stott et al. 1975) and Lloyd (Lloyd and Ferguson 1986) took a large number of channelling patterns, $\sim 15^\circ$ wide and covering a range of orientations, and stuck them onto the surface of large spheres $\sim$37 cm in diameter. Two of these spherical Kikuchi maps are shown in Fig. 5.2.

5.4 EBSP Detectors

An EBSD detector (for example, Fig. 5.3) consists of a planar scintillator with a high sensitivity low-light level camera directly behind it, and either a lens or tapered fibre optic to transfer light to the camera. A vacuum-tight enclosure and an insertion/retraction system are used to position the scintillator in a suitable position.

Most EBSD detectors employ a line-of-sight insertion system, i.e., the detector requires a microscope port that is directly in line with the specimen. However, in the case of the detector shown in Fig. 5.3, a unique bending mechanism was designed by the author to allow the front part of the detector to pass underneath the anti-contamination disk found in some scanning electron microscopes (SEMs). The detector

A.P. Day (✉)
Aunt Daisy Scientific Ltd., Monmouth, Gwent, NP25 3PP; KE Developments, The Mount, Toft, Cambridge, CB23 2RL, UK
e-mail: auntdaisy@btinternet.com

A.J. Schwartz et al. (eds.), *Electron Backscatter Diffraction in Materials Science*,
DOI 10.1007/978-0-387-88136-2_5, © Springer Science+Business Media, LLC 2009

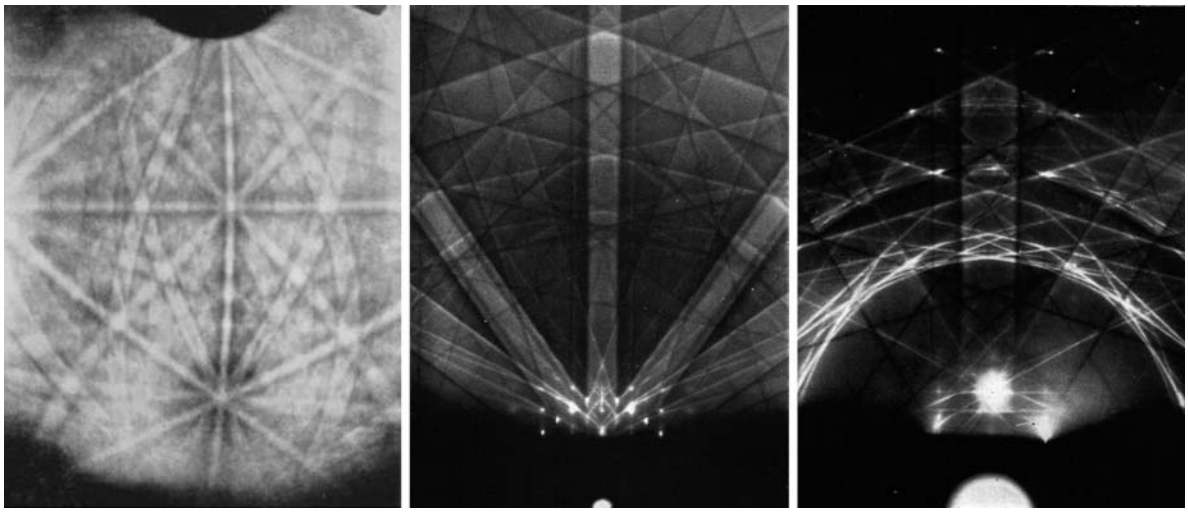


Fig. 5.1 (*Left*) Reflection pattern from iron taken on cylindrical film and covering ∼140° vertically. An <001> zone is just above the centre of the image with a <111> below it, near the bottom. Taken from Boersch (1937). (*Centre*) Reflection pattern from rock salt ∼50 kV, [110] is at the bottom. (*Right*) Reflection pattern from diamond (111) face, angle 60°, 50 kV; <112> is at the bottom and the (–220) plane is vertical with two {311} planes running diagonally. Taken from figures 40 and 29 of Finch and Wilman (1937). With kind permission of Springer Science+Business Media

uses a periscopic mirror system (which can be seen if the detector is partially retracted) to transfer the diffraction pattern to the camera.

To make the detector vacuum-tight, stainless steel bellows or sliding O-rings are commonly used. Bellows give the best vacuum, however, they are large and

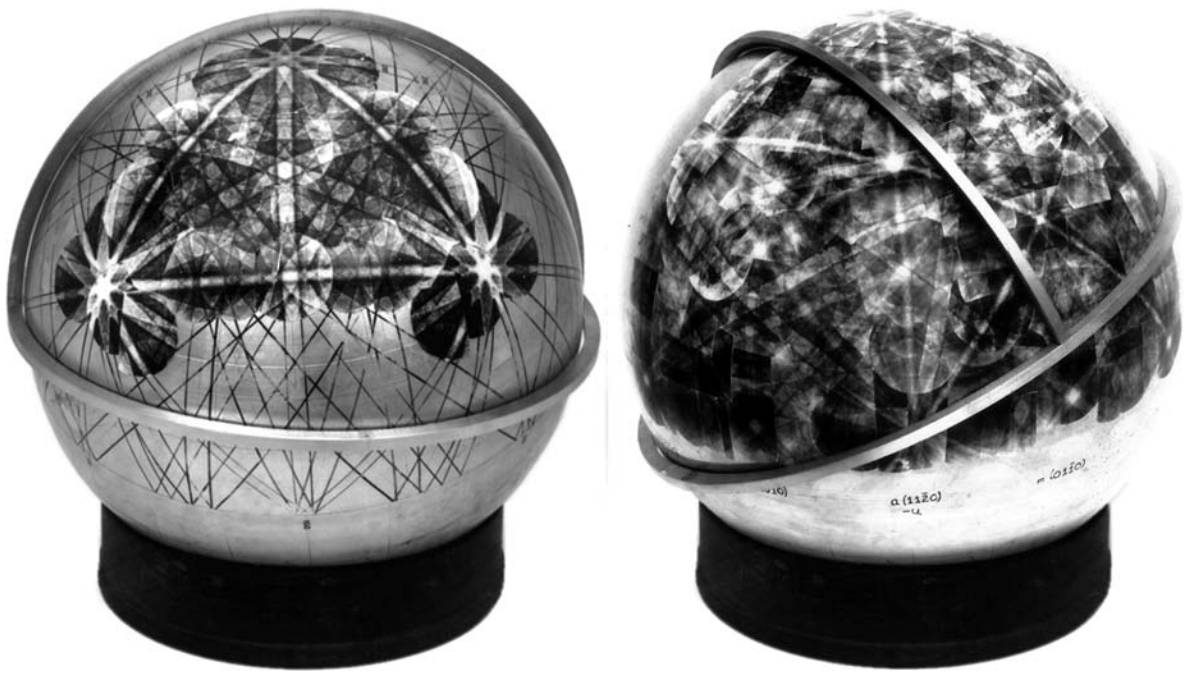


Fig. 5.2 Spherical Kikuchi maps for ferrite (*left*, courtesy of Bevis Hutchinson) and quartz (courtesy of Geoff Lloyd). The composite ECPs cover 1/24th (ferrite) and 1/6th (quartz) of the spherical surface. For the ferrite, the four-fold <001> zone can be seen at the top, and two three-fold <111> zones are at the far left and right, with a two-fold <110> between them. The quartz [0001] zone is at the top of the sphere with the –a axis at the bottom, directly below it

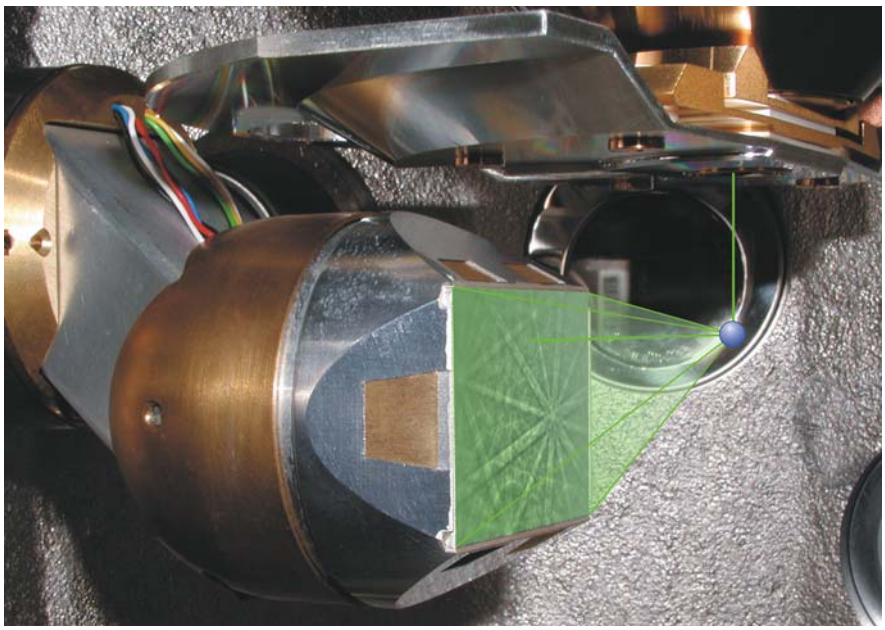


Fig. 5.3 An example of a modern EBSD detector with a planar, rectangular scintillator, as designed by the author. The solid angle over which the EBSP is captured is shown in *green*. Image courtesy of John Bonevich and Mark Vaudin, NIST

may vibrate; and, to avoid microphonic pickup when working at very high magnification, it may be necessary to damp them. A sliding O-ring has the advantage that it is compact; but it is not ideal for high vacuum, and occasional leaks may be observed, especially on larger seals.

For EBSP, the most widely used scintillator materials are P22G (ZnS:Cu, Al, Au, green 540–570 nm, ∼24% efficiency, ∼35 μs decay time), P43 (Gd_2O_2S:Tb, green 545 nm, ∼15%, ∼1.5 ms), and YAG ($Y_3Al_5O_{12}$:Ce, green 550 nm, ∼5%, ∼70 ns). For low kV work, P15 (ZnO:Zn, blue/green 495 nm, ∼7 μs) can be used. It can be difficult to deposit powdered scintillators without producing pinholes or marks, and brushing is usually the best deposition method, although for circular phosphors, sedimentation/spinning is easier; see Yen et al. (2007) and Ozawa (2007) for details. To minimise charging, the phosphor is usually coated with a very thin aluminium layer which also acts as a mirror for light travelling away from the camera, thereby increasing the EBSP signal at the expense of some spatial resolution.

Scintillators are normally circular, square, or rectangular. Circular phosphors are easier and cheaper to produce; however, rectangular ones can be matched to the CCD (charge-coupled device) chip inside the

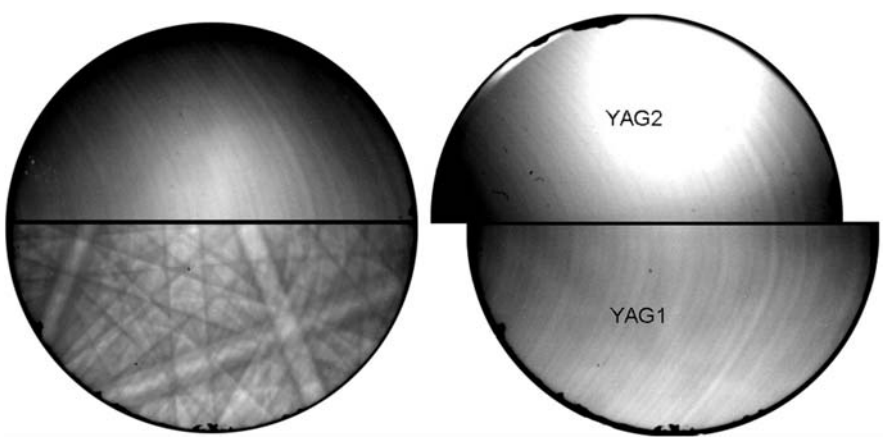


Fig. 5.4 Images from a YAG scintillator showing growth rings (*top left*) and a raw EBSP (*bottom left*). Two different YAG screens (*right*) show almost identical rings, but slightly displaced

camera, so that the whole of the phosphor can be imaged on the full CCD. Compared to circular phosphors, rectangular phosphors use more of the CCD's active area and minimise the shadowing of and potential collisions with other detectors.

Single crystal screens, e.g., YAG (yttrium aluminium garnet), can improve spatial resolution in the EBSP but are an expensive alternative to powdered scintillators. However, some crystals can contain growth rings, which can be seen in the raw diffraction pattern, as shown in Fig. 5.4. Software background correction can be used to remove most artefacts for all types of scintillators.

5.5 EBSP Imaging and Uniformity

Because an EBSP originates from an (almost) point source and is imaged on a planar scintillator, it appears as a gnomonic projection (Randle and Engler 2000) and is highly distorted near the edges and corners. This is particularly noticeable when using a rectangular scintillator.

EBSPs also suffer from non-uniform illumination—their centre is much brighter than their edges. Part of this is due to an inherent variation in the EBSP signal with angle (Reimer 1998); however, there are also contributions from distance effects ($1/d^2$) and vignetting. Vignetting occurs when apertures in the lens or detector housing restrict the angles over which light can be focussed onto parts of the CCD, and results in a lowering of intensity, usually near the EBSP corners/edges.

The use of spherical or cylindrical detection screens would improve illumination uniformity and minimise EBSP distortion; however, they are difficult to produce. In the past, cylindrical film has been used, e.g., Boersch (1937) and Alam et al. (1954), but this is not desirable in a modern, digital microscope.

There are alternatives to the usual phosphor + camera arrangement, and some of the techniques used in transmission electron microscope (TEM) imaging of diffraction patterns can be applied in the SEM. In the TEM, electrons have been imaged by direct exposure of a CCD or sensor array (Roberts et al. 1982; Spence and Zuo 1988; Hawkes 2007). Along with energy filtering, this may lead to direct methods for recording EBSPs and to high-efficiency nonplanar detectors.

5.6 EBSP Simulation

Most EBSD analysis software uses kinematical Kikuchi band intensities (de Graef 2003) to decide which bands are most likely to appear in the EBSP, and employs a look-up table of their interplanar angles to index the EBSP (Wright and Adams 1992). However, there are many structures for which the kinematical model is inadequate. Developments in dynamical diffraction modelling (Spence and Zuo 1992; Winkelmann 2003, 2004; Winkelmann et al. 2007) have allowed high quality EBSPs to be simulated with extraordinary levels of accurate detail. The advantages of being able to accurately simulate EBSPs are:

- Any phase, orientation and EBSD geometry can be simulated. Also, the sensitivity to key parameters can be modelled (Villert et al. 2008; Day 1993).
- Simulations can test and benchmark band detection and indexing algorithms.
- Extremely fine structures can be seen in the simulations that may be blurred in real EBSPs. These features can aid in the identification of complex phases.
- Excess and deficiency lines can be simulated (Winkelmann et al. 2008) to allow accurate fitting of the experimental EBSPs. Alternatively, simple empirical models can be used to introduce asymmetries in near-vertical Kikuchi bands.

Figure 5.5 shows a stereographically projected simulated ferrite EBSP. The dynamical calculations were done using Winkelmann's ECP.EXE program (version 2.90), and took ~5 hours; ~400 beams were used.

5.7 Spherical Kikuchi Maps from EBSPs

The manual assembly of a spherical Kikuchi map from single ECPs, as done by Hutchinson and Lloyd, can also be done with EBSPs (Day 2008). Since EBSPs generally have a larger capture angle than ECPs, fewer patterns are needed to cover the whole sphere, but distortion in the EBSP (e.g., due to the lens), brightness/contrast nonuniformities, and the effects of excess/deficiency lines can become significant factors.

The simplest way to visualise the projection of EBSPs onto a sphere is to imagine a hollow, rubber

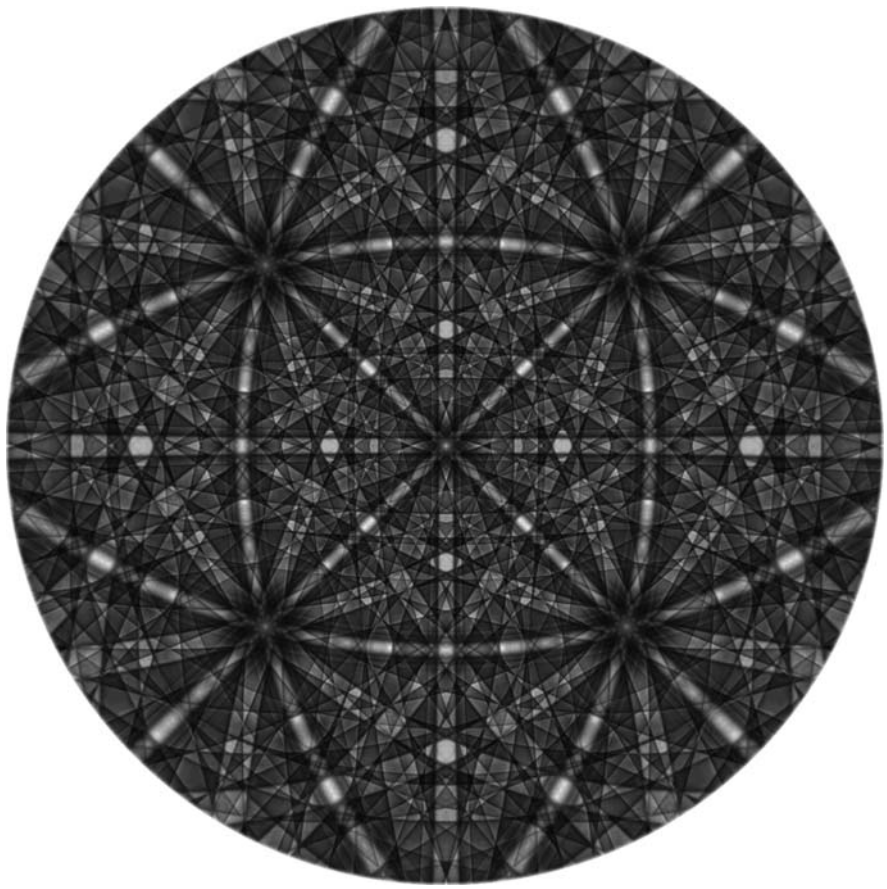


Fig. 5.5 Simulated 20 kV ferrite EBSP with [001] at the centre and four <111> arranged diagonally around it (and looking like snow flakes)

cube with six gnomonically projected EBSPs on its faces; and then to "inflate" it until it is spherical. This process is shown in Fig. 5.6.

Figure 5.7 shows a single EBSP that has been projected onto the surface of a sphere, then repeated using symmetry operations to cover most of the sphere. Part of the SKM is clearly missing around the <111> zones, but this can be patched from EBSPs at other orientations. If the EBSPs are averaged as they are stitched together, then the effects of the excess/deficiency lines can be minimised and measured. Since most EBSD maps produce thousands of diffraction patterns (which are usually thrown away), this is an attractive means to squeeze more information

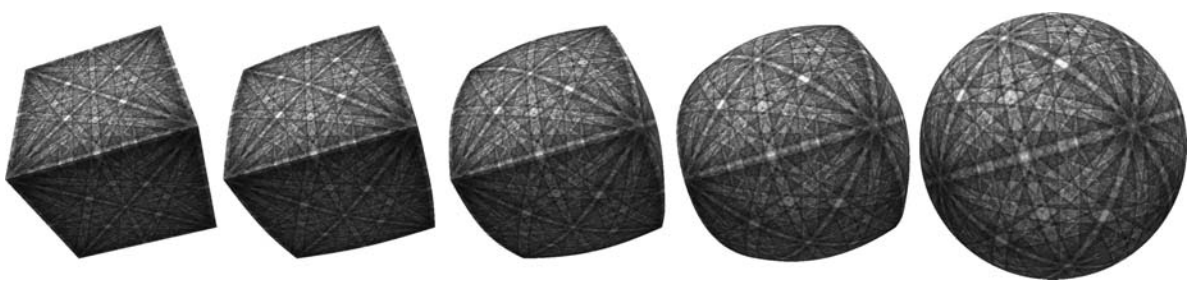


Fig. 5.6 Inflation of a cube to produce a sphere. The process starts with a cube (*far left*) with six gnomonically projected <001> EBSPs on it; the cube is inflated until its faces touch the sphere (*far right*)



Fig. 5.7 Example showing the creation of a spherical Kikuchi map; starting with a single fcc EBSP (*top*); repeating it using symmetry (*left*); and adding in other EBSPs at different orientations with averaging (*right*)

from existing data, particularly as the SKM Kikuchi band intensities, and profiles can be used to improve EBSP indexing.

This form of image mosaicing is frequently used in computer vision systems; see, for example, Hartley and Zissermann (2003) and Capel (2001). For information on image warping, see Heckbert (1989) and Wolberg (1992). Imiya et al. (2005) discuss how standard image processing functions can be applied to spherical images.

For accurate projection of the EBSP onto the spherical surface, it is critical that the EBSP projection geometry and EBSD detector distortion parameters are known—a total of ∼11 independent parameters:

- Pattern centre: the point on the phosphor closest to the specimen.
- Specimen to phosphor distance: sometimes called the detector distance.
- Radial lens distortion: this can be modelled using an odd-termed polynomial.
- Misalignment between the EBSP phosphor and the camera's optic axis.

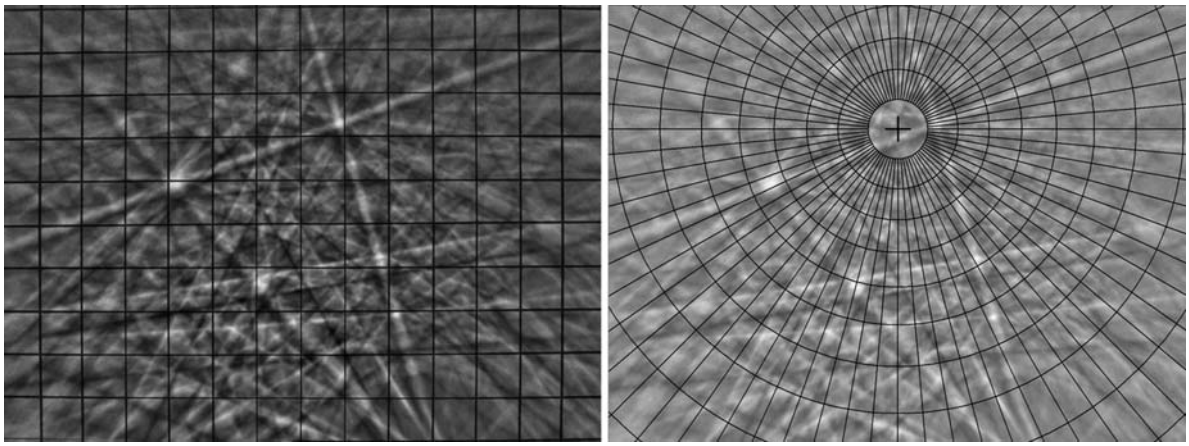


Fig. 5.8 Example EBSP with a grid overlay to show distortion (*left*) and a 5° grid superposed (*right*). From the inwards displacement and diffuseness of the *grid lines* near the EBSP periphery (*left*), there is a degree of distortion and defocus

- Horizontal and vertical skews, EBSP image rotation, and the effective CCD pixel aspect ratio (including nonparallelism of phosphor and CCD).

Since the pattern centre is our "centre" of projection, rotations of the EBSP about it generally are not important. To simplify the model, it can be assumed that the camera's centre of distortion is close to the centre of the image (i.e., the EBSP); which will, in general, not coincide with the pattern centre. Hartley and Zissermann (2003) have detailed information and algorithms for camera calibration.

Figure 5.8 shows an example EBSP with an orthogonal test grid superposed over it to show the distortion in the EBSP. This distortion can partially be corrected for by a change in the projection parameters, particularly the screen to detector distance. Simultaneous, high-precision fitting of many EBSPs using a suitable

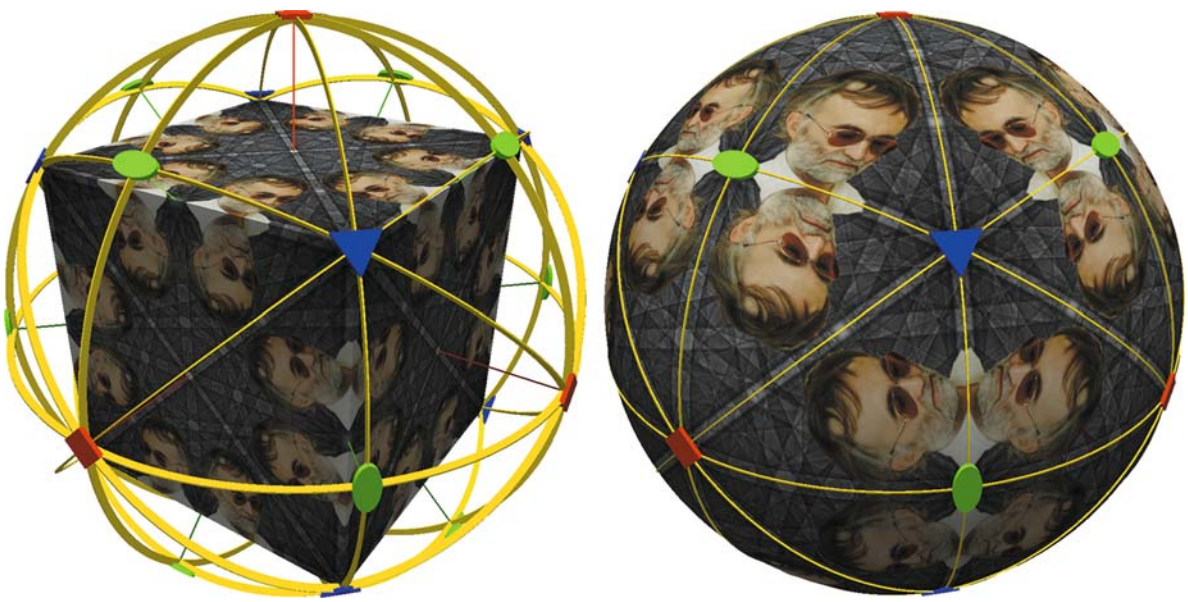


Fig. 5.9 Cubic symmetry on a spherical surface as shown by an asymmetric repeating motif (courtesy Peter Quested, NPL). For cubic materials, a "triangular" motif is repeated a total of 48 times (including reflections) to cover the whole sphere

camera distortion model may be used to measure distortion on most EBSD systems.

To increase the speed of the dynamical and SKM calculations, symmetry may be applied. If the asymmetric effects of excess/deficiency lines are ignored, then for cubic symmetry, only 1/48th of the sphere needs to be calculated. To illustrate this, Fig. 5.9 shows a cube with a symmetrically repeated motif on its surface. The main cube symmetry elements are also shown—mirror planes in yellow, diads (2-fold axes) as green ellipses, triads (3-fold axes) as blue triangles, and tetrads (4-fold axes) as red squares. For more details and examples from other Laue and point groups, see McKie and McKie (1986), de Graef (1998, 2003), and de Graef and McHenry (2007).

5.8 Kikuchi Band Profiles

An EBSP consists of a large number of overlapping Kikuchi bands whose intensities, as a first approximation, are summed together. An experimental Kikuchi band profile (Day 2008) is the intensity averaged along a length of the band as a function of the angle from the Kikuchi band centre. For conventional EBSPs, care has to be taken to correct for the gnomonic projection. Kikuchi band profiles are generally asymmetric, as shown in Fig. 5.10 (left); horizontal Kikuchi bands show the greatest asymmetry.

Kikuchi band profiles have been measured from single EBSPs (e.g., Alam et al. [1954]; Day and Shafirstein [1996]); and calculated using dynamical diffraction (e.g., Reimer et al. [1986]). Relative intensities have been estimated and compared (Prior and Wheeler [1999]; Wright [Schwartz et al. 2000, p 61]) to values calculated using a kinematical diffraction model (Peng et al. 2004). Figure 5.11 shows three ferrite simulations done at 15, 20, and 25 kV, along with cylindrical projections and profiles of selected Kikuchi bands.

Quantitative intensity measurements are not easy to make (Quested et al. 1988; Day and Shafirstein 1996), particularly due to the high level of processing during EBSP capture. This processing consists of:

- Conversion of the (diffracted) electron intensity to light in the scintillator.
- Light capture effects, e.g., lens vignetting or optical taper fibre-pixel mismatch.
- CCD camera gain and offset.
- Background correction (subtraction, division, etc.).
- Contrast stretch and possible reduction to 8 bits.

Even though CCD chips are extremely linear, the other effects may not be. Also, the CCD pixels are generally square when projected back on to the phosphor, but the solid angle that they capture varies depending on where they are relative to the pattern centre. The choice of the start and finish positions for averaging has an effect on the measured profile (see

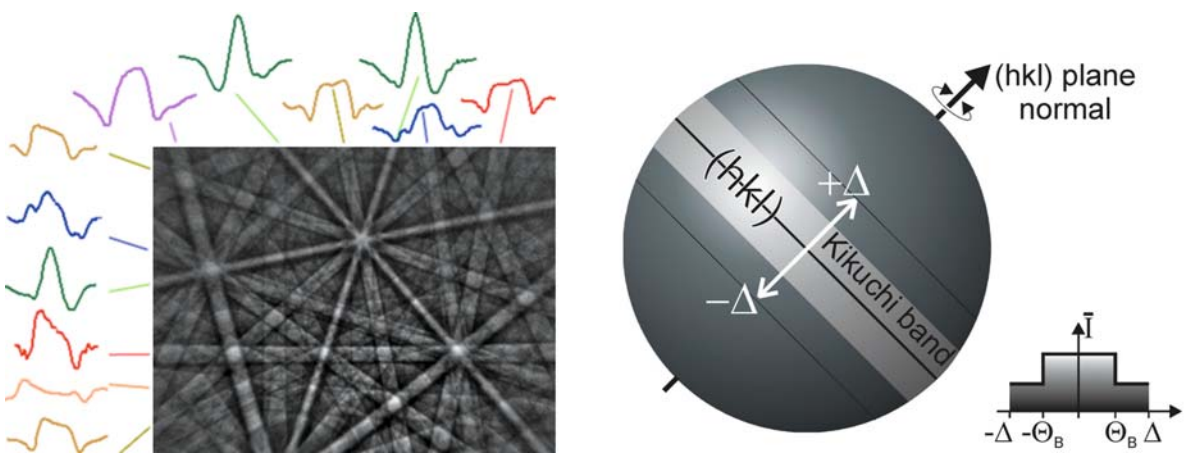


Fig. 5.10 Schematic showing asymmetric Kikuchi band profiles from a real EBSP (*left*); and how to calculate a profile on a spherical Kikuchi map

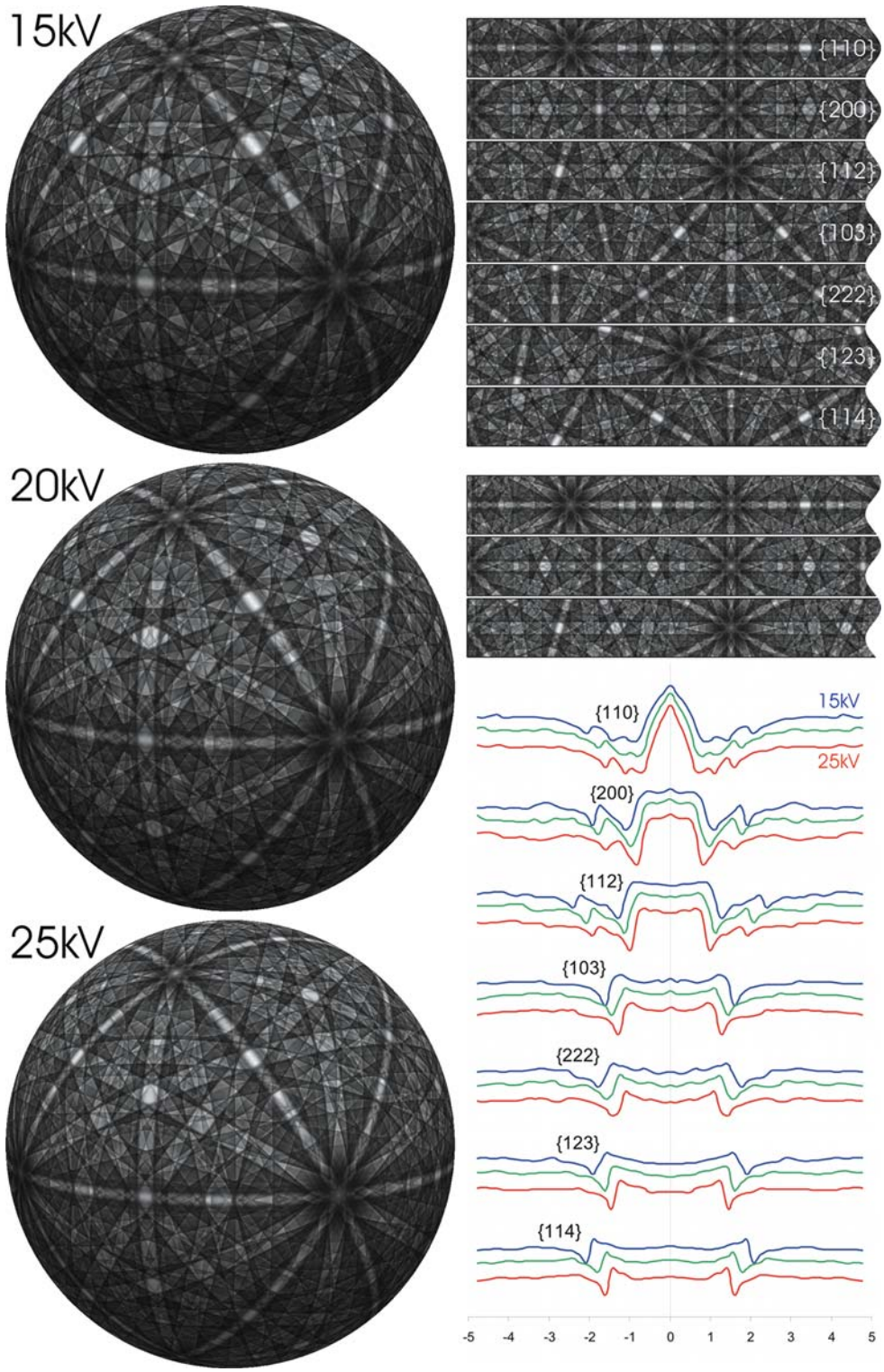


Fig. 5.11 Ferrite simulations, Kikuchi band projections, and profiles for 15, 20, and 25 kV. The Kikuchi band profiles are cylindrical projections

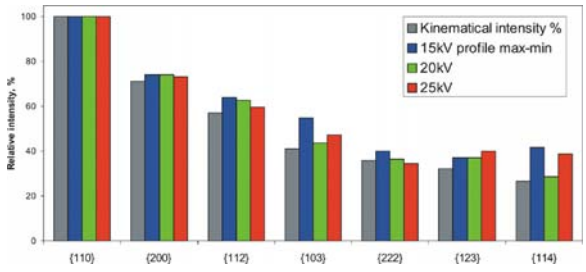


Fig. 5.12 Relative intensities for selected ferrite Kikuchi bands (the profiles are shown in Fig. 5.11) normalised so that the most intense is 100%

Fig. 5.10 *left*), and ideally the whole of the Kikuchi band should be averaged (Fig. 5.10 *right*), although this is difficult without using multiple EBSPs. Reconstructed spherical Kikuchi maps offer a solution to this problem.

A comparison of the relative intensities of bands from Fig. 5.11 to those from a kinematical diffraction model is shown in Fig. 5.12. There are clear intensity differences and, since they are only simple max-min values, these can be more pronounced, depending on the sharpness of features in the dynamical simulation. It appears that when more reflectors are used for computation, then sharper features appear and the discrepancies usually increase. The use of an average band profile, rather than a single "intensity" figure, is clearly more appropriate. Contributions from overlapping Kikuchi bands have a large effect on the average profile, and deconvolution may help to understand and empirically model the "true" profiles.

5.9 Spherical Kikuchi Map Inversion

The Hough transform is used to analyse planar EBSPs, but something different is needed for spherical Kikuchi maps. Imiya et al. (2005) explain how image processing and analysis on spherical images can be done, and Torii and Imiya (2005) introduce a spherical Hough transform, which was developed for catadioptric computer vision systems to provide a mobile robot with a full hemispherical view of its surroundings. By applying a modified algorithm to spherical Kikuchi maps, the Kikuchi bands can be "inverted" so that they become circular disks centred about the plane normal and of a diameter related to the Kikuchi band width. The processing is done in a similar way to the usual Hough transform on flat EBSPs (Hough 1962; Leavers and Boyce 1986; Leavers 1992; Krieger Lassen et al. 1992; Krieger Lassen 1994). To improve the calculation speed on the spherical surface, geographic information systems (GIS) algorithms have been employed (Samet 2006). This transform has been named the "SCRUFF" (spherical correlated randomised Hough) transform, to avoid confusion with the statistical Hough transform and to echo the "Muff" transform (Wallace 1985).

The "inversion" allows high-order Kikuchi bands to be more easily identified by minimising band overlap; it is a partial deconvolution.

A three-parameter SCRUFF transform can be used to more accurately find the Kikuchi band edges in SKMs; the third parameter represents the angle by which the sampling "line" or circle is displaced from the parent plane (Maurice and Fortunier 2008).

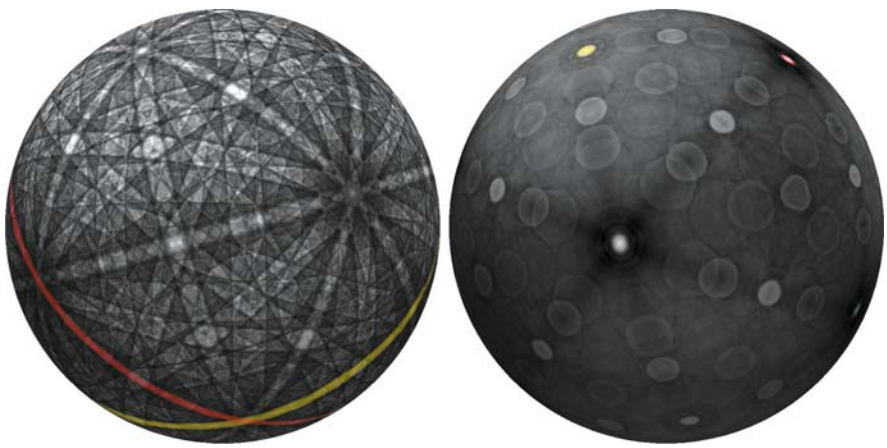


Fig. 5.13 A simulated ferrite SKM and its SCRUFF transform. Two bands and their transforms have been highlighted in *red* and *yellow*

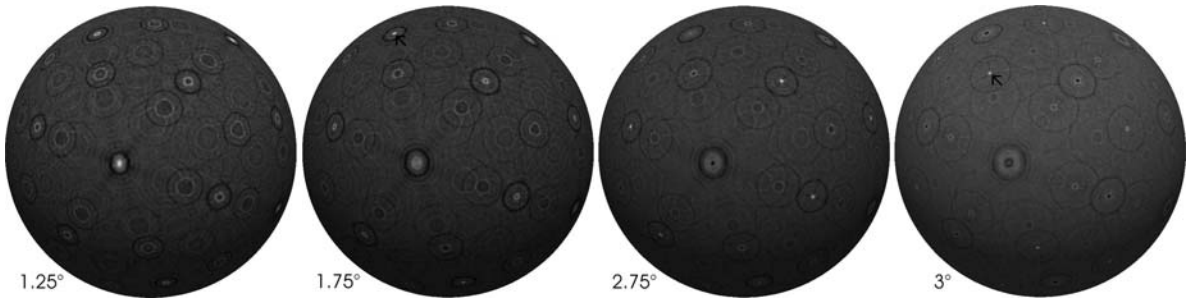


Fig. 5.14 3D SCRUFF transform for selected angles. An intense white peak occurs when both the Bragg angle and plane normal are matched

Figure 5.14 shows example 3D SCRUFF transforms (of the SKM shown in Fig. 5.13), where certain angles (from the Kikuchi band centre) produce a sharp peak, indicating that this is close to the Bragg angle for a particular plane and its normal.

5.10 Uses for Spherical Kikuchi Maps

Spherical Kikuchi maps can be applied to:

- Accurate indexing using calculated or measured Kikuchi band profiles.
- Phase identification—an approach to whole pattern matching.
- Strain measurement for polycrystalline materials—using an SKM from an unstrained specimen as the reference. Wilkinson et al. (2006) and Villert et al. (2008) have shown impressive strain sensitivity for near single crystals; SKMs may help to extend this to polycrystals.
- Indexing of phases for which crystallographic data does not exist —ab initio analysis (see le Page [1992] for TEM details and Day [2008] for an SKM procedure).

Models, possibly empirical ones, for the effects of excess/deficiency lines would be extremely useful (Winkelmann et al. 2008).

For EBSPs, Laue, point, and space group identification has been done manually (Dingley et al. 1995; Michael, in Schwartz et al. 2000); automatically in

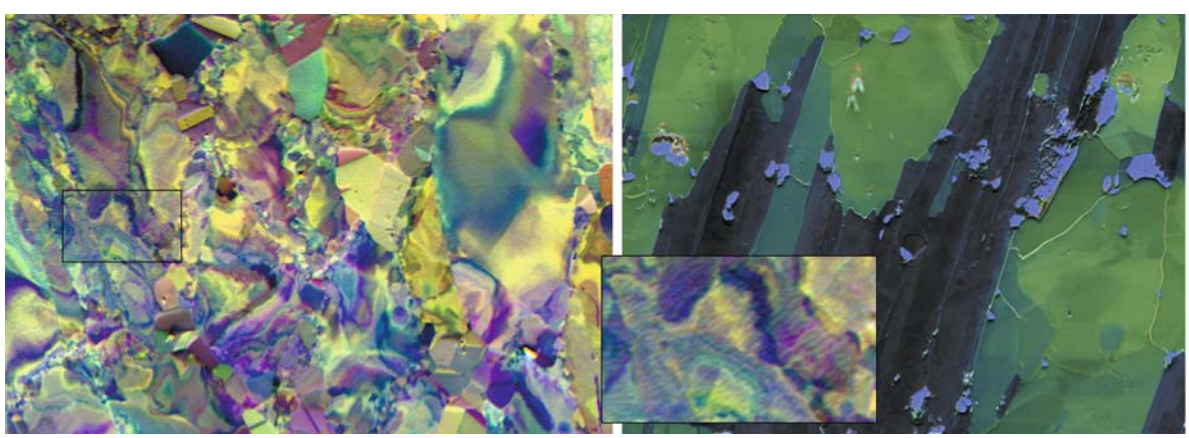


Fig. 5.15 Color forescatter/backscatter images from a compressed Waspaloy specimen (*left* and detail), and a schist thin section specimen containing quartz, plagioclase, biotite, and muscovite (*right*). Images taken using a KE Developments Generation 5 amplifier. Specimens courtesy of Ken Mingard, NPL, and Dave Prior, Liverpool University

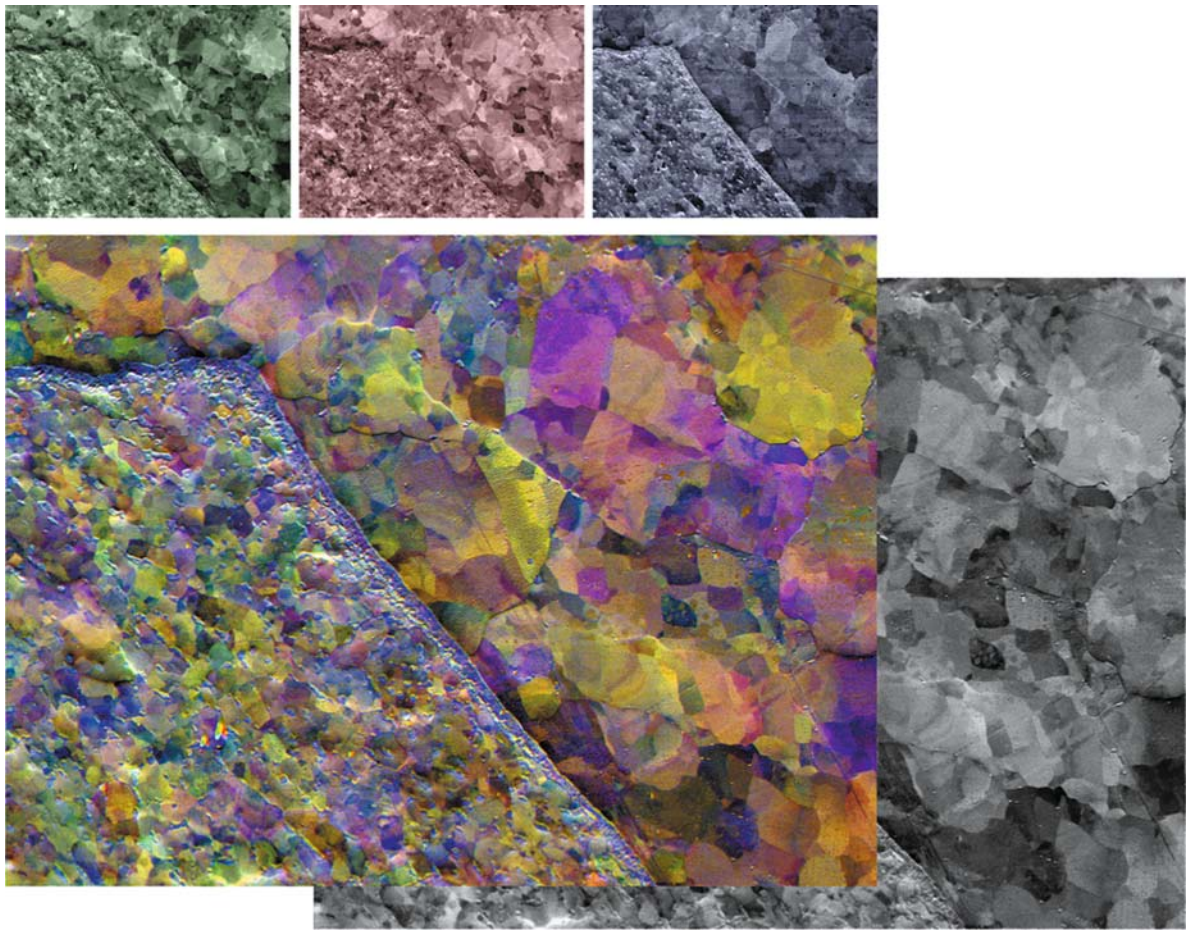


Fig. 5.16 COCI produced by combining signals from three diodes (*top row*); the grey level average is shown at the *bottom right*. Gibeon meteorite, image width ~100 μm. KE Developments Generation 5 amplifier

conjunction with EDX chemical data (Michael and Goehner 1993; Goehner and Michael 1996); and using HOLZ rings (Michael and Eades 2000) from single EBSPs. Methodologies for analysing TEM are more advanced and widely applied; for example, Steeds and Vincent (1983), de Graef (2003), and Peng et al. (2004).

5.11 Colour Orientation Contrast Images

Colour orientation contrast images (COCIs; Day 1993; Day and Quested 1999) are produced from multiple forescatter diode images of the same area of the specimen. Examples are shown in Fig. 5.15. There are usually three diodes and each is assigned a colour (e.g., red, green, or blue), then mixed together. This process is depicted in Fig. 5.16, where the separate forescatter images are shown at the top. It is often easier to see subtle changes in COCIs, compared to greyscale equivalents, and the images take only a few minutes to produce.

5.12 STEM in the SEM

Scanning transmission electron microscopy (STEM) is normally done in the TEM where large accelerating voltages are available. In the SEM, this is also possible using a suitable STEM detector and high sensitivity amplifier. The STEM detector contains solid-

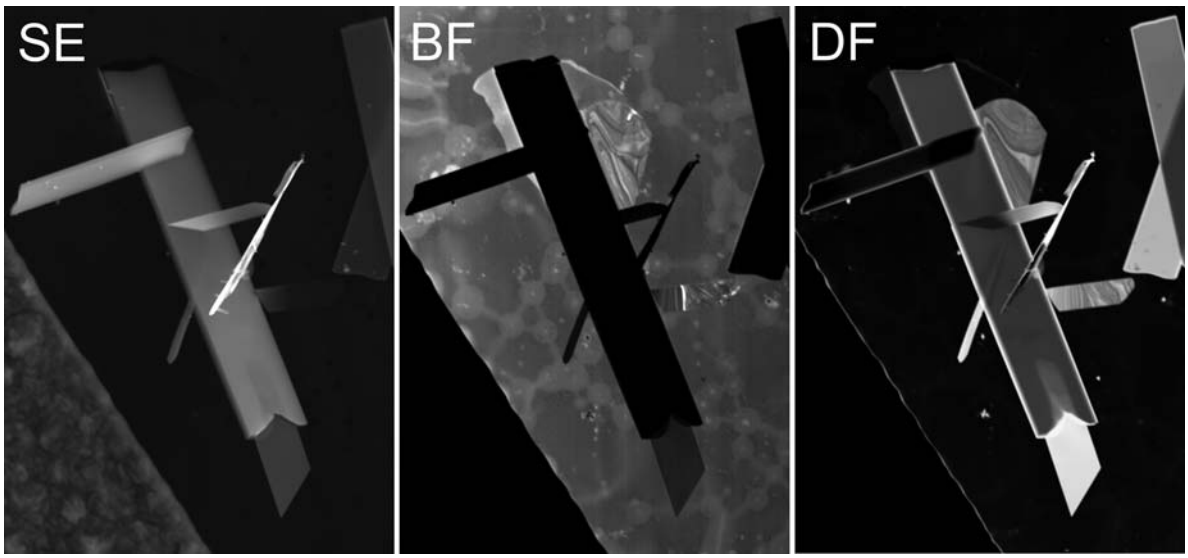


Fig. 5.17 Molybdenum oxide crystals on carbon film—SE: secondary electron image; BF: bright field transmission image; DF: dark field (diffracted) transmission image. Image width ~40 μm. Taken on a CamScan 3200 tungsten filament SEM using KE Developments STEM detector and Generation 5 amplifier. Images courtesy of Jim Greig, CamScan

state diodes, carefully aligned under the beam so that the bright field (BF) image is formed by the undeviated electron beam passing through the specimen onto the small, central diode. The dark field image is detected by larger, offset diodes and shows contrast due to diffraction within the specimen.

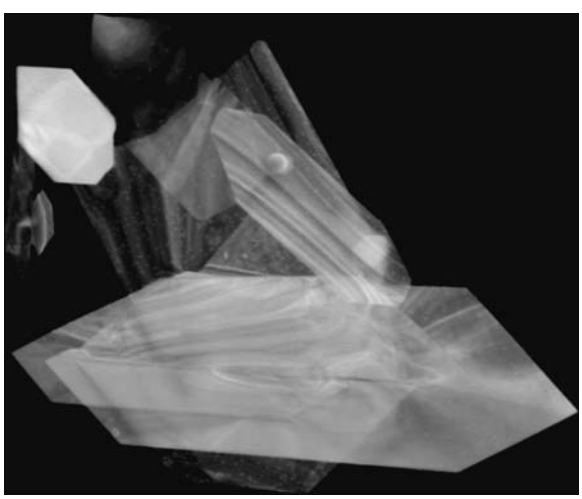


Fig. 5.18 STEM image from molybdenum oxide crystals. Taken on a Supra 40 FEGSEM using a KE Developments STEM detector and Generation 5 amplifier. Largest crystal ~7 μm long. Courtesy of Ken Mingard, NPL

Example STEM images are shown in Figs. 5.17 and 5.18.

Experiments on TEM foils have shown that EBSPs can be produced in most regions; so combined STEM and EBSD should be possible. By building a STEM detector into an EBSD specimen holder, it should be possible both to map crystallographic orientation and to look through the specimen. Adjustment of kV and specimen thickness will probably be necessary. An EBSD detector positioned under the specimen could be used to image a diffraction pattern.

5.13 Unusual Features in EBSPs

Reflection high-energy electron diffraction (RHEED) can be used to monitor surface reconstruction for growing films (Braun 1999; Ichimiya and Cohen 2004). RHEED patterns consist of a set of spots, often with overlapping Kikuchi bands, but the capture angle is smaller than for EBSP.

In conjunction with the Universities of Strathclyde and Halle, we have been investigating the possibility of using RHEED-like spots, observed in GaN EBSPs, to map surface changes; example images are shown in Fig. 5.19. Since the diffraction patterns are produced

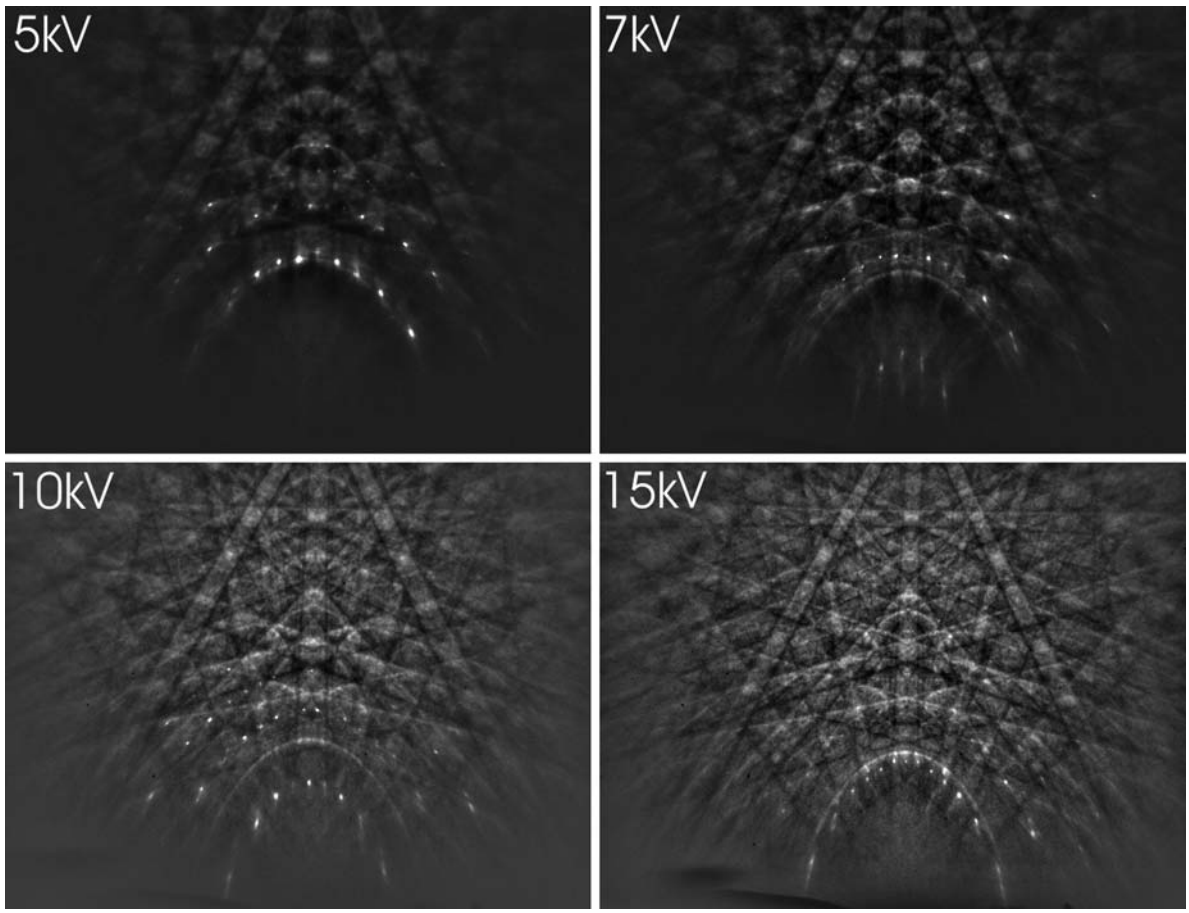


Fig. 5.19 GaN EBSPs at various kVs; RHEED-like spots are apparent. The spots change with kV and when the electron beam is moved over the specimen. Specimen courtesy of Carol Trager-Cowan, University of Strathclyde

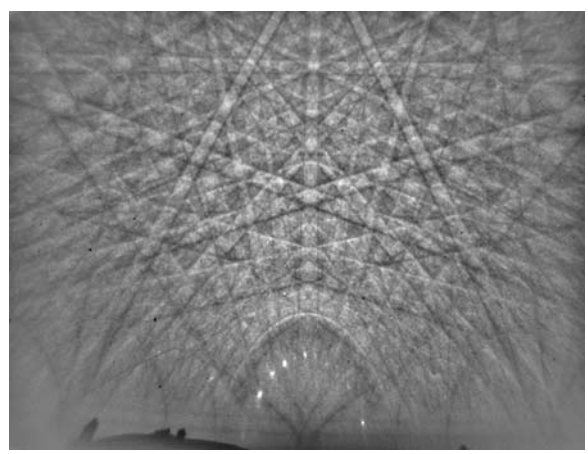


Fig. 5.20 GaN EBSP taken at 26 kV. Note the black whisker-like features radiating from the bottom centre of the image. Note: To allow direct comparison, this series of EBSPs (5–30 kV) were taken using the same image for background correction; as a result of this, some phosphor flaws and specimen surface debris are visible, especially in this image

in a FEGSEM, the vacuum is not at UHV levels and surface contamination is a problem. In slow mapping, it has been observed that the spots disappear after a few minutes. Spots have also been observed in EBSPs from other materials, e.g., SiC, WC, and Si. Other features have also been observed which have been attributed to surface resonance effects as reported in the RHEED literature (Ichimiya and Cohen 2004); see Fig. 5.20. It is interesting to note that these features also appear in Finch and Wilman (1937); see Fig. 5.1.

Acknowledgments The assistance of Dr. Aimo Winkelmann in producing the ferrite EBSP simulations and for providing a copy of his beautiful ECP simulation program is gratefully acknowledged, as are the many contributions, over the decades, of Dr Peter Quested, National Physical Laboratory. Robert Schwarzer is thanked for bringing the 1937 Finch and Wilman paper to my attention, as is Carol Trager-Cowan for many discussions on EBSP, RHEED, and GaN.

References

Alam MN, Blackman M, Pashley DW (1954) High angle Kikuchi patterns. Proceedings of the Royal Society of London Series 221A:224–242

Boersch H (1937) Über Bänder bei Elektronenbeugung, Z Techn Phys 18:574–578

Braun W (1999) Applied RHEED. Springer, Berlin, ISBN 3-540-65199-3

Capel A (2001) Image mosaicing and super-resolution. D. Phil. thesis, Robotics Research Group, Department of Engineering Science, University of Oxford

Day AP (1993) Developments in the EBSP technique and their application to grain imaging. Ph.D. thesis, University of Bristol, UK

Day AP (2008) Spherical EBSD. J Microsc 230(Pt 3):472–486

Day AP, Quested TE (1999) A comparison of grain imaging and measurement using horizontal orientation and colour orientation contrast imaging, electron backscatter pattern and optical methods. J Microsc 195(Pt 3):186–196

Day AP, Shafirstein G (1996) Assessment of local residual strain by electron backscatter patterns and nanoindentation. Mater Sci Tech 12:873

de Graef M (1998) A novel way to represent the 32 crystallographic point groups. J Mater Educ 20:31–42

de Graef M (2003) Introduction to conventional transmission electron microscopy. Cambridge University Press, Cambridge, UK, ISBN 0-521-62006-6

de Graef M, McHenry ME (2007) Structure of materials: An introduction to crystallography, diffraction, and symmetry. Cambridge University Press, Cambridge, UK, ISBN 978-0-521-65151-6

Dingley DJ, Baba-Kishi KZ, Randle V (1995) Atlas of backscattering Kikuchi diffraction patterns. Institute of Physics Publishing, Bristol, UK, ISBN 0-7503-021207

Finch GI, Wilman H (1937) The study of surface structure by electron diffraction. Erg Exakt Naturwiss 16:353–436

Goehner RP, Michael JR (1996) Phase identification in a scanning electron microscope using backscattered electron Kikuchi patterns. J Res Natl Inst Stan 101:301–308

Hartley R, Zissermann A (2003) Multiple view geometry in computer vision, 2nd ed. Cambridge University Press, Cambridge, UK, ISBN 0-521-54051-8

Hawkes PW (ed) (2007) Advances in imaging and electron physics, vol. 145. Academic Press, San Diego, CA, ISBN 0-12-373907-1

Heckbert PS (1989) Fundamentals of texture mapping and image warping. Master's thesis, Department of Electrical Engineering and Computer Science, University of California

Hough PVC (1962) Method and means for recognizing complex patterns. US patent 3,069,654

Ichimiya A, Cohen P (2004) Reflection high energy electron diffraction. Cambridge University Press, Cambridge, UK, ISBN 0-521-45373-9

Imiya A, Sugaya H, Torii A, Mochizuki Y (2005) Variational analysis of spherical images. In: Proceedings of the 11th international conference on computer analysis of images and patterns (CAIP 2005). Springer, Versailles, France, ISBN 032-9743

Joy DC (1974) Electron channelling patterns in the scanning electron microscope. In: Holt DB, Muir MD, Boswarva IM, Grant PR (eds) Quantitative scanning electron microscopy. Academic Press, New York

Krieger Lassen NC (1994) Automated determination of crystal orientations from electron backscattering patterns. Ph.D. thesis, Institute of Mathematical Modelling, The Technical University of Denmark

Krieger Lassen NC, Juul Jensen D, Conradsen K (1992) Image processing procedures for analysis of electron backscatter patterns. Scan Microsc 6:115–121

Le Page Y (1992) Ab initio primitive cell parameters from single convergent-beam electron diffraction patterns: A converse route to the identification of microcrystals with electrons. Microsc Res Techniq 21:158–165

Leavers VF (1992) Shape detection in computer vision using the Hough transform. Springer-Verlag, New York, ISBN 3-540-19723-0

Leavers VF, Boyce JF (1986) An implementation of the Hough transform using a linear array processor in conjunction with a PDP/11 microprocessor. NPL report DITC 74/86

Lloyd GE, Ferguson CC (1986) A spherical electron-channelling pattern map for use in quartz petrofabric analysis. J Struct Geol 8(5):517–526

Maurice C, Fortunier R (2008) A 3D Hough transform for indexing EBSD and Kossel patterns. J Microsc 230(Pt 3): 520–529

McKie D, McKie C (1986) Essentials of crystallography. Blackwell Scientific Publications, Oxford, UK, ISBN 0-632-01574-8

Michael JR, Goehner RP (1993) Crystallographic phase identification in the scanning electron microscope: Backscattered electron Kikuchi patterns imaged with a CCD-based detector. MSA Bull 23:168

Michael JR, Eades JA (2000) Use of reciprocal lattice layer spacing in electron backscatter diffraction pattern analysis. Ultramicroscopy 81:67–81

Ozawa L (2007) Cathodioluminescence and photoluminescence. CRC Press, Boca Raton, FL, ISBN-42005-270-5

Peng LM, Dudarev SL, Whelan MJ (2004) High-energy electron diffraction and microscopy. Oxford Science Publications, Oxford, UK, ISBN 0-19-8500742

Prior DJ, Wheeler J (1999) Feldspar fabrics in a greenschist facies albite-rich mylonite from electron backscatter diffraction. Tectonophysics 303:29–49

Quested PN, Henderson PJ, McLean M (1988) Observations of deformation and fracture heterogeneities in a nickel-base superalloy using electron backscattering patterns. Acta Metall 36:2743–2752

Randle V, Engler O (2000) Introduction to texture analysis: macrotexture, microtexture and orientation mapping. Gordon and Breach, Amsterdam, ISBN 90-5699-224-4

Reimer L (1998) Scanning electron microscopy: physics of image formation and microanalysis, 2nd ed. Springer, Berlin, ISBN 3-540-63976-4

Reimer L, Heilers U, Saliger G (1986) Kikuchi band contrast in diffraction patterns recorded by transmitted and backscattered electrons. Scanning 8:101–118

Roberts PTE, Chapman JN, MacLeod AM (1982) A CCD-based image recording system for the CTEM. Ultramicroscopy 8:385–396

Samet H (2006) Foundations of multidimensional and metric data structures. Morgan Kaufmann, San Francisco, CA, ISBN 0-12-369446-9

Schwartz AJ, Kumar M, Adams BL (2000) Electron backscatter diffraction in materials science. Kluwer Academic, New York, ISBN 0-306-46487-X

Spence JCH, Zuo JM (1988) Large dynamic range, parallel detection system for electron diffraction and imaging. Rev Sci Instrum 59(9):2102–2105

Spence JCH, Zuo JM (1992) Electron microdiffraction. Plenum Press, New York, ISBN 0-306-44262-0

Steeds JW, Vincent R (1983) Use of high-symmetry zone axes in electron diffraction in determining crystal point and space groups. J Appl Cryst 16:317–324

Stott DE, Wise MLH, Hutchinson WB (1975) A distortion-free map for use with electron channelling patterns. J Microsc 105:305–307

Torii A, Imiya A (2005) The randomized Hough transform for spherical images. In: Proceedings of the 11th international conference on computer analysis of images and patterns (CAIP 2005). Springer, Versailles, France, ISBN 032-9743

Villert S, Maurice C, Wyona C, Fortunier R (2008) Accuracy assessment of elastic strain measurement by EBSD. J Microsc in press

Wallace RS (1985) A modified Hough transform for lines. In: Proceedings of the IEEE computer society conference on computer vision pattern recognition. San Francisco, pp 665–667

Wilkinson AJ, Meaden G, Dingley DJ (2006) High-resolution elastic strain measurement from electron backscatter diffraction patterns: New levels of sensitivity. Ultramicroscopy 106:307–313

Winkelmann A (2003) Elektronenbeugungsmethoden zur Strukturanalyse epitaktischer Siliziumkarbidschichten. Dissertation: Jena Universität, Physikalisch-Astronomische Fakultät

Winkelmann A (2008) Dynamical effects of anisotropic inelastic scattering in electron backscatter diffraction. Ultramicroscopy 108:1546–1550

Winkelmann A, Schröter B, Richter W (2004) Electron diffraction methods for the analysis of silicon carbide surfaces and the controlled growth of polytype heterostructures. J Phys-Condens Mat 16:S1555–S1578

Winkelmann A, Trager-Cowan C, Sweeney F, Day AP, Parbrook P (2007) Many-beam dynamical simulation of electron backscatter diffraction patterns. Ultramicroscopy 107(4):414–421

Wolberg G (1992) Digital image warping, 3rd ed. IEEE Computer Society Press, New York, ISBN 0-8186-8944-7

Wright SI, Adams BL (1992) Automatic analysis of electron backscatter diffraction patterns. Metall Trans 23A:759–767

Yen WM, Shionoya S, Yamamoto H (2007) Practical applications of phosphors. CRC Press, Boca Raton, FL, ISBN 1-4200-4369-2

Chapter 6

Application of Electron Backscatter Diffraction to Phase Identification

Bassem El-Dasher and Andrew Deal

6.1 Introduction

The distribution, morphology, and stability of material phases govern the bulk properties of virtually all of the technologically relevant materials used to design engineering components and products. Phase identification and characterization are therefore critical to the development and use of practical materials. In this chapter, we will focus on the application of electron backscatter diffraction (EBSD) to phase identification.

Complete phase identification must include two components that identify the phase uniquely: structure and chemistry. Strictly speaking, unambiguous crystalline phase identification requires determining the exact periodic, atomic arrangement of the unknown phase. This is the information contained in the space group, lattice parameters, and the chemical occupancies of the space group's atomic positions for a given phase. Given its diffraction-based origins, the EBSD technique can directly satisfy the structural determination component of phase identification, but not without limitations. The complete data set of structural information contained within an EBSD pattern is difficult to extract, typically requiring nonstandard set-ups and/or detectors; and space group and lattice parameter determination by EBSD has been accomplished only with meticulous manual scrutiny of the EBSD diffraction patterns (Baba-Kishi and Dingley 1989a, 1989b; Baba-Kishi 1998; Michael and Eades 2000; Dingley and Wright, Phase Identification Through Symmetry Determination in EBSD Patterns, in this volume).

For comprehensive phase identification, EBSD needs to be supplemented with quantitative chemical characterization. Techniques such as energy or wavelength dispersive X-ray spectroscopy (EDS or WDS) are perfect complements to EBSD, as they also require a scanning electron microscope (SEM), allowing for simultaneous diffraction and compositional data collection. When the material pedigree is known, however, this is not necessary, and successful phase differentiation and verification using semi-automated EBSD was demonstrated over a decade ago (Goehner and Michael 1996).

Despite its limitations, there are clear advantages to using EBSD for phase determination. These include spatial resolution, sample requirements, and the convenience/availability of other SEM techniques for phase analysis. EBSD lateral spatial resolution, 0.1–0.01 μm depending on the SEM, is approximately two orders of magnitude higher than conventional (non-synchrotron) X-ray diffraction (XRD) methods and two orders of magnitude lower than TEM, filling the gap between those techniques. Recently available commercial systems capable of processing over two hundred patterns per second have also allowed for EBSD datasets spanning tens of millimeters, effectively sampling an amount of material as statistically relevant as that sampled with XRD. Furthermore, EBSD is a bulk technique, and meticulous preparation, such as that required for electron-transparent thin specimens for TEM, is unnecessary. SEM imaging can also provide morphological information to support an EBSD analysis, and SEMs equipped with EDS or WDS can assess the chemistry of the phase without additional sample preparation or transfer to another instrument.

B. El-Dasher (✉)
Lawrence Livermore National Laboratory, Livermore, CA, USA
e-mail: eldasher2@llnl.gov

A.J. Schwartz et al. (eds.), *Electron Backscatter Diffraction in Materials Science*,
DOI 10.1007/978-0-387-88136-2_6, © Springer Science+Business Media, LLC 2009

Combining all these capabilities with the statistical nature of EBSD also permits the study of previously inaccessible aspects of multi-phase materials such as simultaneous phase distribution, volume fraction, and orientation relationships. Furthermore, coupling EBSD/EDS with a focused ion beam (FIB) and 3D reconstruction allows for a full morphological view that includes phase identification; and chapters by Zaefferer and Wright; by Groeber, Rowenhorst, and Uchic; and by Sintay, Groeber, and Rollett describe this in this volume. While these are advantages over the "traditional" XRD and TEM analyses, this does not imply that EBSD is the preferred alternative to either TEM or XRD, and in many cases, phase identification benefits greatly from the parallel use of these methods.

For a comprehensive review of EBSD's application to studying phase transformation, complete with over 600 references, the reader is directed to a recently compiled review by Gourgues-Lorenzon (2007).

6.2 Considerations for Phase ID with EBSD

There are multiple approaches to using EBSD to assist with phase identification, and these are typically dictated by the specific application. Nevertheless, there are some fundamental considerations that equally apply regardless of approach, including: the use of prior sample knowledge and chemical information, basic manual scrutiny of patterns, and semi-automated database searching to identify an unknown phase. Before we address these, it is important to stress that two experimental requirements are essential to any attempt at phase identification using EBSD, regardless of the approach:

1. accurate and precise geometric calibration,
2. obtaining the highest quality EBSD patterns.

As discussed in other chapters, the calibration of an EBSD system is highly sensitive to sample positioning and especially to the sample-to-detector distance. Thus, the possibility of using a fixed set of calibration parameters (e.g., those established upon installation) for multiple samples is severely hindered by the tolerances of these measurements. For example, EBSD cameras are necessarily retractable, leading to slight inconsistencies in camera placement upon reinsertion, and sample positioning is even less repeatable. In modern SEMs, reported working distances are typically calculations based on ideal alignments and conditions, and they are often rounded to the nearest millimeter. These values are therefore not as precise as needed for placing a sample at exactly the same working distance, as required for EBSD phase identification. Changing the beam conditions on an instrument and refocusing can also result in a slightly different reported working distance (e.g., 0.1 mm or so for those that report this precision), even after degaussing. While this is not an issue for most SEM analyses, it is too imprecise for EBSD phase identification, and changes in sample and/or detector positions will affect all subsequent measurements, manual or automated, for phase identification. It is therefore absolutely critical to confirm or refine the calibration of the EBSD system *for each phase analysis performed*, either with a known, strain-free crystal phase in the sample or with a standard material such as copper or silicon.

Obtaining the highest possible quality EBSD patterns from the phase of interest is just as critical. Typically, this is accomplished by using the CCD camera in its non-binned state to maximize the angular resolution of the pattern, although pixel binning may be necessary if sufficient signal is unobtainable. The quality of flat-fielding (background subtraction) is also important, so care must be taken to ensure that static backgrounds acquired for the procedure are sufficiently free of crystallographic information and representative of the intensity distribution for the region examined. It is also helpful for most analyses to shorten the detector distance to maximize the pattern's angular range and expose as many of the major symmetry elements of the phase as possible. This is particularly valuable for lower symmetry phases and semi-automated EBSD phase identification. Both make use of well-separated Kikuchi bands to determine symmetry.

Generally speaking, an analysis of a completely unknown crystalline sample is a rare event. More often than not, a reasonable amount of prior knowledge will be available to the investigator. This may include the sample's origin, bulk chemistry, thermomechanical history, or even a list of expected phases and morphologies. In many cases, samples are often analyzed in a comparative set such that much of this information can be deduced from a more well-characterized and known variation. Prior sample knowledge should be used to thin down the list of phase possibilities.

For example, commercial engineering materials such as steels, nickel-based superalloys, and titanium-based alloys have been heavily characterized over decades. Consequently, lists of expected phases, morphologies, chemistries, and occurrences can and should be extracted from the literature and other sources for comparison with an unknown sample. This information should be consistent with any EBSD results for the phases in question. If the result of a phase identification experiment does not match what is expected based on prior sample knowledge, the analysis must be scrutinized for possible sources of error. If no sources of error are found, then the existence of the unexpected phase(s) should be weighed against any other outstanding aspects of the sample, such as material properties, for validation. In this way prior sample knowledge can increase the accuracy of an EBSD phase identification analysis. It is therefore extremely important for analysts to collect as much information as possible about the sample prior to the EBSD analysis. This includes imaging the sample at several magnifications to identify the morphology and distribution of phases.

Understanding the chemistry of the phase of interest (and of the bulk sample if unknown) is an important aspect in this approach. Qualitative chemical information can usually be acquired with EDS. EDS is well suited to supplement EBSD phase identification because many modern SEMs are set up for simultaneous acquisition. An initial list of elements present in a phase can be generated with relative ease and reasonable accuracy. A full quantitative analysis is also possible if standards are available and the elemental X-ray peaks are well separated in energy. However, it is important to realize when EDS is inadequate, and when the substantially better energy resolution of WDS may be necessary to distinguish between elements with X-ray peaks close in energy. Similarly, the finer spatial resolution of Auger may be required if the phase size is significantly smaller than one micron. The phase chemistry information obtained with these techniques can often help narrow the field of possible phases. Caution should be used, however, with this approach. Phases in databases are typically reported with a specific stoichiometric composition, with no information about the solubility of other elements. As a simple example, alpha titanium (6/mmm) has a large solubility for aluminum, which will be detected in an EDS analysis of alpha in a Ti alloy. A database will typically list the alpha phase chemistry as pure Ti. Thus, a database search on phases containing both Ti and Al will not necessarily yield the alpha phase. As can be imagined, this problem is compounded for multi-element alloys containing phases with unknown solubility. In these cases, it is often better to investigate the structure before assessing the chemistry.

EBSD patterns contain a wealth of structural information, and manual scrutiny is a good starting point. A detailed review of manual pattern inspection and structure identification is available in the literature (Baba-Kishi 2002). Symmetry elements such as the mirror plane, 2-fold, 3-fold, 4-fold, and 6-fold axes of patterns in Fig. 6.1, may be identified in quality patterns. The presence or absence of symmetry elements can be used to narrow down the structure possibilities. For example, a 6-fold axis indicates that the crystal structure is hexagonal, and means that the number of possible point groups reduces from 32 to 7. On the other hand, it is helpful to acquire multiple EBSD patterns covering a significant amount of Kikuchi space to ensure that a given symmetry element is truly absent. This can be difficult for phases that have a preferential orientation in a single sample (e.g., castings, extrusions), and it may be necessary to analyze orthogonal cross-sections of the material and/or capture EBSD patterns at various stage tilts/rotations to bring different orientations into view. For semi-automated EBSD analysis, identifying the bands in the patterns is vital to the subsequent computer analysis. While manual analysis provides the highest ultimate accuracy (by virtue of providing the most control), automated band detection is of great benefit if large numbers of diffraction patterns are to be analyzed. In such cases, the resolution of the Hough transform should be maximized to correctly identify the band positions.

Once the bands in a high-quality, well-calibrated pattern are identified, automated phase matching can be performed using a phase database. This method is similar to the automated indexing of a single phase, except that the best solutions for multiple phases are compared against each other to find the best identification. Available databases can have thousands of entries, and it is impractical to compare all entries to the unknown phase, even with modern computing power. Consequently, information obtained from prior sample knowledge, morphology, chemistry, and manual scrutiny of the pattern is critical to reduce the list of phase possibilities in the search, and a typical refinement reduces the scope of consideration to a few hundred phases or less. Evidence for correct phase identification should not be limited to a database match

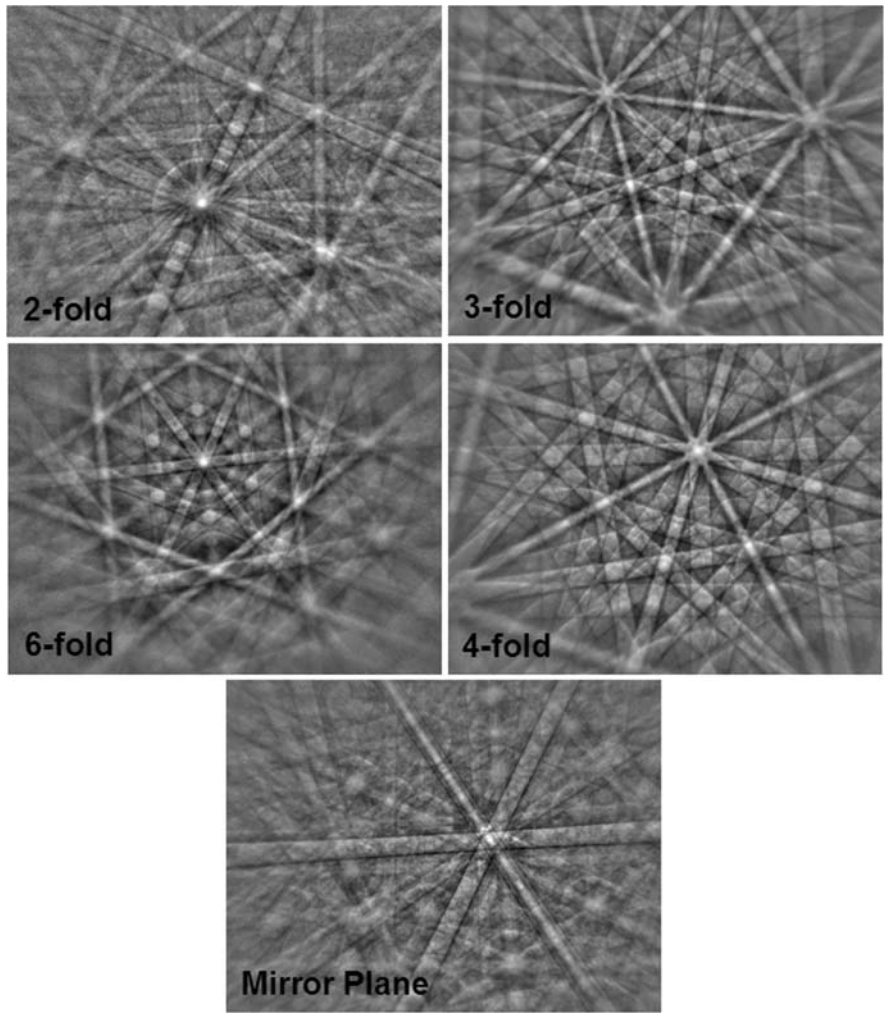


Fig. 6.1 Diffraction patterns of the various symmetry elements that can be used to identify phases

on a single EBSD pattern. Different patterns from the same phase should be compared and produce the same result (be self-consistent), and the identified phase should also be consistent with all the parameters used to refine the search. It should be noted that new phases are constantly discovered, and it is important to supplement a database with any recent phases from the literature that might be present in the unknown sample.

6.3 Case Studies

In this section we present three case studies that are meant to guide the reader through approaches used to solve phase discrimination problems using EBSD. While not representative of all the experiments possible, these case studies are intended to represent typical applications of EBSD phase identification. The first of these shows how compositional differences can be used to discriminate between phases using simultaneous EBSD and EDS acquisition. The second discusses the difficulties in differentiating structurally similar phases on a size scale that is not amenable to simultaneous EBSD/EDS. Finally, the third shows how crystallographic discrimination can be used to yield quantitative statistical results.

We chose a Ni-based superalloy for each case study for several reasons. Ni-based superalloys are a class of engineering materials that have been developed over decades. The unique ability of these materials to

maintain desirable properties at temperatures close to their melting temperatures allow them to be used for gas turbine components for power generation and aircraft. The integrity of these alloys at operating temperatures depends on the distribution and interaction of multiple phases. Consequently, accurate phase identification and characterization are vital to the success and quality control of these materials. Many of these phases are difficult to distinguish from each other based upon structure alone, necessitating the use of complementary analyses to correctly identify the phases.

6.3.1 Simultaneous EBSD/EDS Phase Discrimination

There are several precipitates in superalloys that are difficult to distinguish by EBSD alone. Among these are relatively large, undesirable M(C,N) carbonitride inclusions that form during solidification. These phases are very stable and are difficult to dissolve in subsequent thermomechanical processing. Because of their cubic symmetry they are often confused with the matrix phase during automated EBSD analyses. However, their distinctly different chemistries make phase discrimination possible with simultaneous EDS acquisition and subsequent postprocessing.

A sample of the Ni-based superalloy INCONEL 718 was chosen to demonstrate EBSD/EDS phase discrimination. The sample was metallographically prepared, and subsequent analyses were performed with a Hitachi SU-70 thermal FEG SEM equipped with Oxford INCA X-Act EDS and HKL EBSD. Initial screening of potential phases was accomplished with backscattered electron imaging. Four potentially different phases were identified based on morphology and backscattered electron contrast: the large-grained matrix phase(s); a small elongated light grey phase that was homogeneously dispersed; a large, dark, blocky phase; and a bright, globular phase. Based on the phase morphology and metallurgical knowledge of the alloy, these were expected to be the γ matrix, Nb-rich δ precipitates, and Ti or Nb-rich M(C,N) carbonitrdes, respectively. γ'', a nm scale phase structurally similar to the matrix, was not expected to be discernable in the SEM even if present in the alloy.

A region where all four distinguishable phases existed was chosen for analysis, shown in Fig. 6.2. After careful calibration, unbinned patterns from these phases were taken, as presented in Fig. 6.3. Crystallographic parameters of the four suspected phases, γ-Ni, δ-Ni_3Nb, TiN, and NbC, were taken from the Inorganic Crystal Structure Database (ICSD). TiN and NbC are representative chemistries of the phases, since TiN has solubility for Nb and C and NbC has solubility for Ti and N. The lattice parameters of all three cubic phases did not vary much, ranging from 0.356 to 0.447 nm. Kinematic simulations produced reflector lists for each phase, and the cubic phases had the same strong reflectors with only subtle intensity differences. The strong Kikuchi bands in each pattern were then manually detected. Subsequent automated phase matching with commercial software identified the elongated phase as δ unambiguously. However, differentiation between the other three phases was not conclusive. These phases were all identified as cubic by the software, but indexing between γ, TiN, and NbC was not consistent with the backscattered differentiation of the phases.

To distinguish between the cubic phases in the material, simultaneous EBSD/EDS acquisition was employed while mapping the region of interest with a 15 kV electron beam. The microscope settings were adjusted to obtain a full spectrum X-ray count rate of 35,000 counts per second with a 28% dead time. EBSD indexing speed was slowed to approximately 9 points per second to ensure the collection of good X-ray statistics at each point. The step size for the map was 35 nm over a 914×628 grid. Additionally, since the cubic phases could not be distinguished well structurally, only the γ and δ phases were included for automated differentiation during mapping.

The resulting phase map, together with the Ni, Nb, and Ti elemental maps, are shown in Fig. 6.4(a). The EBSD indexing rate was 97% with only minor misindexing at the grain boundaries. These artifacts (less than 1% of the points) were removed upon initial postprocessing. The γ and δ phases were readily distinguished by the automated phase differentiation, and the high Nb content in the δ phase areas supported the identification of that phase. However, it was very apparent from the EDS maps of Ni, Ti, and Nb that the blocky and globular phases had different chemistry than the matrix. Higher levels of carbon were also detected in these regions. Nitrogen could not be

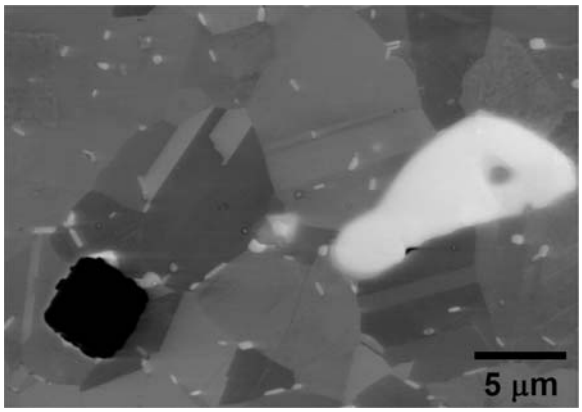


Fig. 6.2 Backscattered electron image of the region of interest

mapped with any accuracy due to an energy overlap with Ti. However, the morphology, detected chemistry, and cubic structure of the globular and blocky phases were consistent with M(C,N) carbonitrides.

By selective thresholding of the EDS maps and Boolean operations it was possible to automatically reassign regions of appropriate chemistry to either the TiN or NbC phases with postprocessing software. The result is shown in Fig. 6.4(b), which is a substantial improvement over phase differentiation by structure alone. A final piece of supporting evidence for the phase assignments was collected when the mapped region was examined optically. Cubic nitrides in Ni-based superalloys are recognizably yellow to orange in color as seen with a light microscope. Similarly, cubic carbides are often grey to lavender (Davis 1997), and the optical image of the region of interest, also shown in Fig. 6.4(b), is consistent with the phases identified.

6.3.2 Distinguishing γ and γ′ in Ni Superalloys

Two phases that are difficult to differentiate structurally with EBSD in many Ni-based superalloys are γ and γ′. The γ′ phase, $Ni_3(Ti,Al)$, is an ordered precipitate that forms coherently from the γ matrix upon the segregation of Ti and Al. Both γ and γ′ phases have cubic crystal structures with lattice parameters that differ by no more than 0.5% in most commercial alloys. This small coherency strain, along with differences in

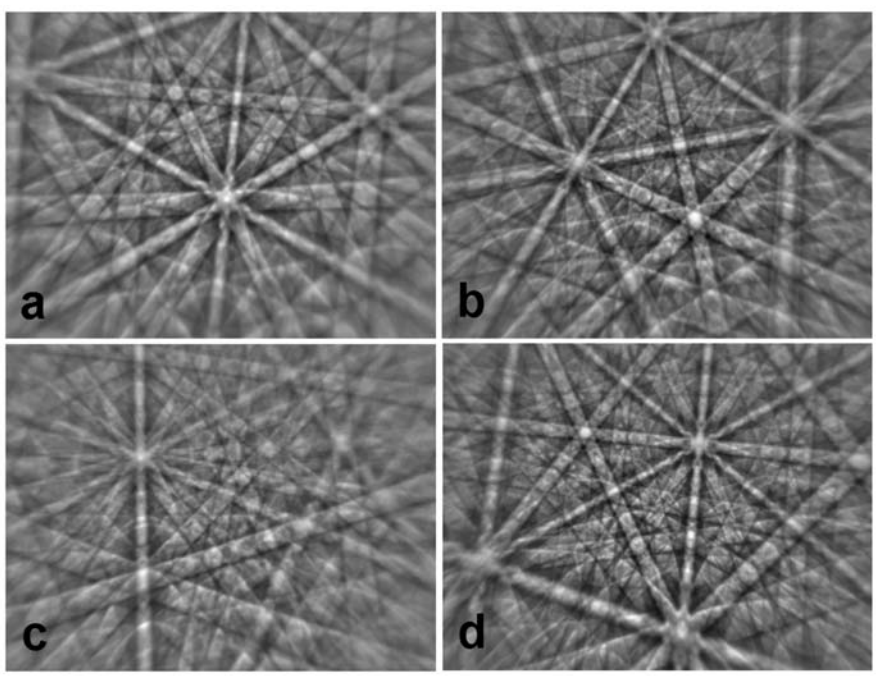


Fig. 6.3 EBSD patterns of four apparent phases in Fig. 6.2: (**a**) matrix grain, (**b**) dark, blocky phase, (**c**) small, elongated phase, (**d**) bright, globular phase

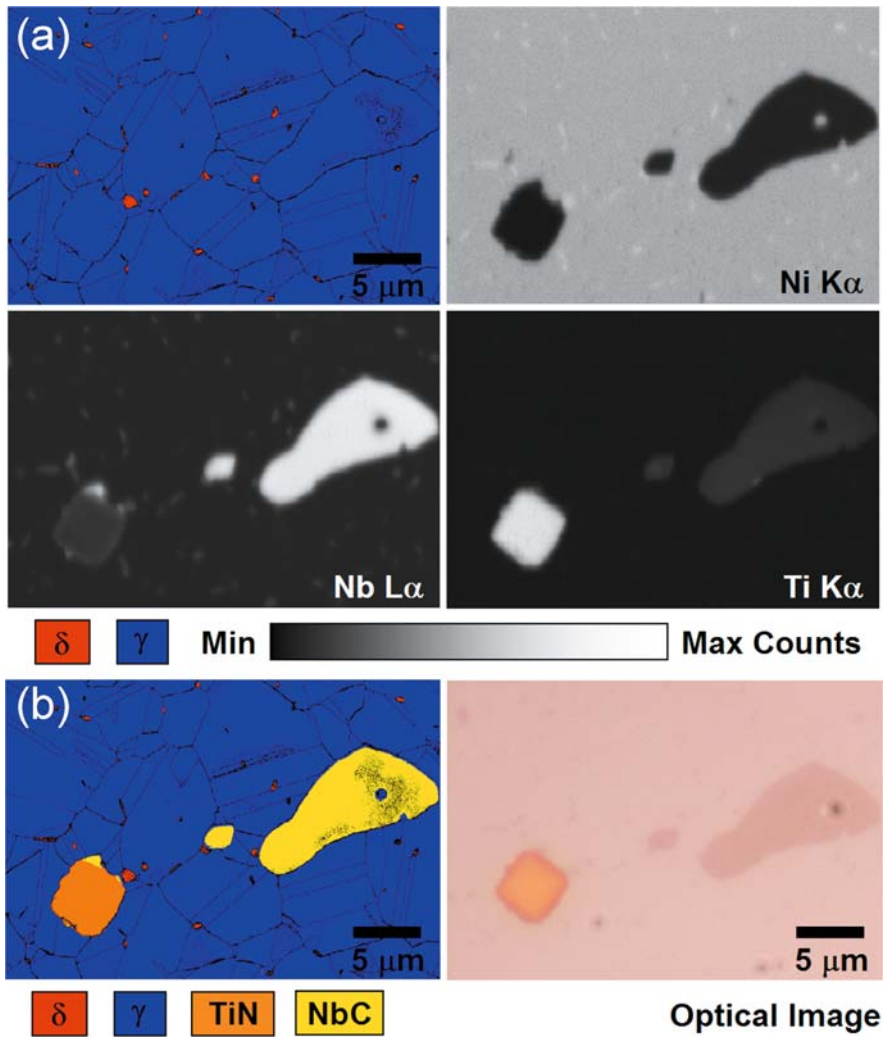


Fig. 6.4 (**a**) EBSD and EDS maps of the region of interest (shown in Fig. 6.2) illustrating the initial resultant phase map, as well as the EDS signal from the Ni Ka, Nb La, and Ti Ka peaks; and (**b**) the phase map obtained after incorporating the EDS information shown in Fig. 6.4(a). Assigned phases are corroborated by the colors observed in the optical microscope image

elastic moduli and atomic ordering between the phases, is a major contributor to the strength of the material.

A sample of commercially available Rene' 88 bar stock was used to test the ability of conventional EBSD to accurately distinguish between γ and γ' under high-resolution SEM conditions. The sample was heat treated to produce globular/blocky submicron γ' in a γ matrix. It was then metallographically prepared for EBSD. Subsequent analyses were performed with the same instrumentation used in the previous case study. Backscattered electron imaging, relying on chemical differences to provide phase contrast, revealed the distribution of γ' shown in Fig. 6.5.

After careful calibration, several pairs of non-binned EBSD patterns were taken from opposite sides of phase boundaries in parent γ grains. Over 30 frames were averaged for each pattern to reduce noise. A representative pair of patterns is presented in Fig. 6.6(a and b). The sister patterns in the figure appear almost identical to the eye. However, subtle differences between the patterns do exist. Figure 6.6(c) is a plot of the contrast in the $\{200\}$ Kikuchi band of both

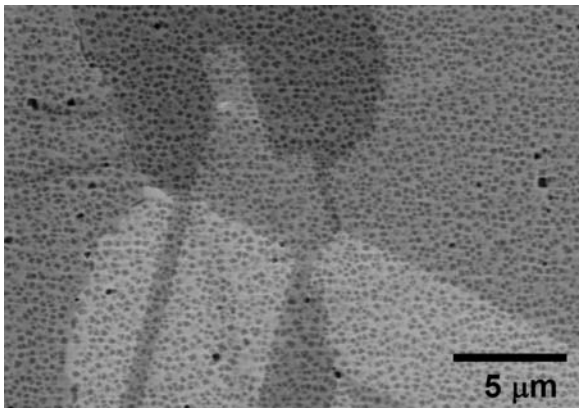


Fig. 6.5 Backscattered electron micrograph revealing the γ′ distribution within the γ′ matrix as *darker shaded* regions

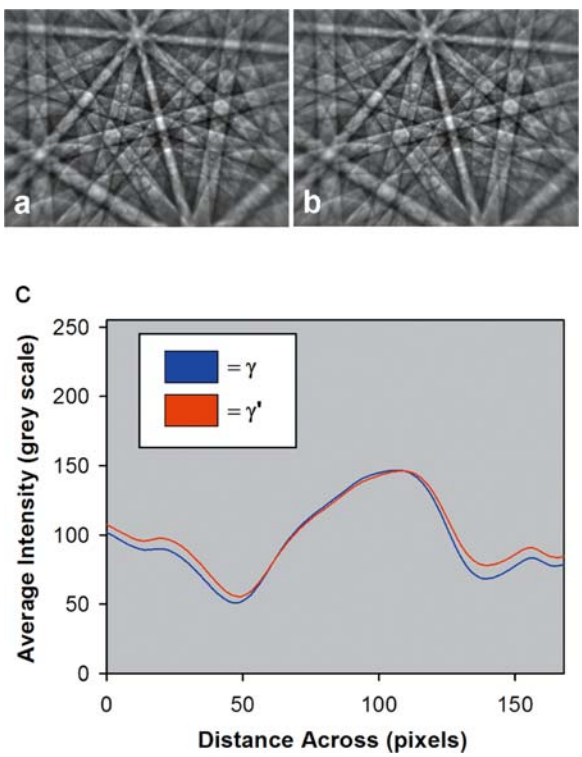


Fig. 6.6 EBSD patterns from (**a**) γ and (**b**) γ′ appear virtually identical. (**c**) Shows the plot of the average grayscale value across the {200} bands, demonstrating the contrast differences between γ and γ′

patterns, demonstrating that the band contrast is slightly stronger for the γ phase than for the γ′.

As a first attempt at differentiation, the γ and γ′ phases were kinematically simulated to establish a reflector list for each phase. There were no appreciable differences in the generated reflector lists, but the γ phase had slightly larger calculated reflector intensities. From these lists, the number of reflectors was refined to represent the bands present in the patterns, and the position of the bands was detected manually for a pair of patterns. Subsequent computer indexing using commercial software could not distinguish between the patterns with any certainty, which was not surprising considering the structural similarities of the two phases.

Automated EBSD indexing and simultaneous EDS acquisition with a 15 kV beam was attempted next. However, even by acquiring over 30,000 counts per second and 500 ms of dwell time per pixel, the phases could not be distinguished from each other. While orientation was easily determined during EBSD mapping, the EDS maps did not show Ni, Ti, or Al segregation above the noise level. This was in part due to the fact that the size of the γ′ approached the resolution of the EDS technique, which is generally on the order of a micron for standard analysis conditions. Detecting statistically significant segregation at a submicron level in this sample with EDS required an enormous number of X-ray counts.

Figure 6.7 shows a successful EDS map taken at 0° tilt without simultaneous EBSD acquisition. The full-spectrum map was acquired continuously over 40 hours and consisted of well over 2 million frames. Stability of the region of interest was maintained with the aid of a stage locking mechanism and drift correction software. While possible in principle to acquire an EBSD map at the same time and obtain phase differentiation, in practice several difficulties prevented such a measurement. At the tilts required for EBSD, sample drift becomes more of a problem, especially with drift correction currently unavailable in commercial EBSD packages. Additionally, extraordinarily long dwell times per pixel would have been required during EBSD to obtain good X-ray statistics, and this would have led to significant local surface contamination that degrades and even destroys the EBSD patterns.

Ultimately, the subtle band contrast between the γ and γ′ proved to be the most useful feature for distinguishing the phases with EBSD. A one micron square region of the sample was selected for automated EBSD mapping that included several γ′ precipitates. Both the γ and γ′ phases were selected for mapping,

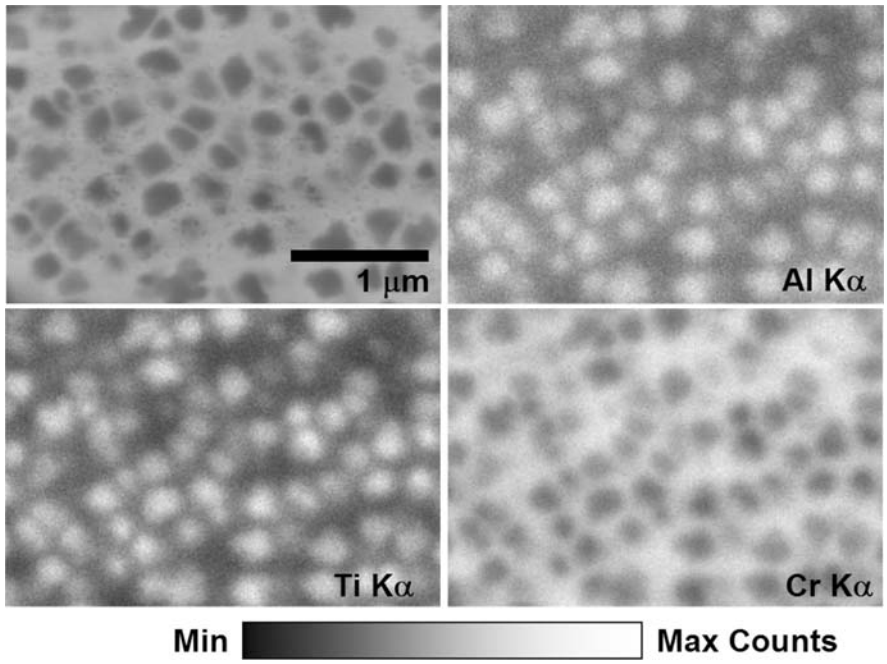


Fig. 6.7 Backscattered electron image of the region mapped using EDS (*top left*) and the associated distributions of Al, Ti, and Cr

and the band detection settings were modified to maximize the subtle difference in band contrast. The map step size was 10 nm. As before, direct phase differentiation based on structure was not possible. Figure 6.8(a and b) shows the backscattered image of the region compared to the indexed phase map. The poor correlation is obvious, as the differentiation was essentially random. However, a band contrast map from the same scan, shown in Fig. 6.8(c), demonstrated the ability of EBSD automated indexing to detect the subtle difference in band contrast between the two phases. By subsequently reassigning the phase of each indexed point based on a threshold value of the band contrast, it was possible to improve the phase differentiation dramatically, as shown in Fig. 6.8(d).

It is important to note that although band contrast thresholding worked well for γ and γ' phase differentiation, it is generally not advisable to distinguish phases using band contrast alone. One reason is that band contrast depends on the phase orientation, since this dictates which Kikuchi bands are present in an EBSD pattern. Consequently, the band contrast difference between two phases may invert for a different set of orientations. This is not a concern in the case discussed, since γ' precipitates coherently with γ. This ensures that within a given parent grain the same Kikuchi bands are present in the EBSD patterns of both phases, so the band contrast is directly comparable.

6.3.3 Volume Fraction Determination in a Multiphase Alloy

By their very nature, EBSD datasets rely on statistics to yield information such as texture, misorientation distributions, and grain size. Using EBSD phase identification capabilities, the type of information yielded from datasets can be extended to include phase relations and quantitative distributions. Such a capability is extremely valuable when studying the material behavior of multiphase systems, and this study is an example of employing such an approach with EBSD phase identification.

For this case, we study Alloy 22 (also referred to as C22 in the literature), a Ni–Cr–Mo alloy that possesses one of the highest corrosion resistance properties of engineering metals. It is primarily specified for use as an outer barrier in long life (>100 year)

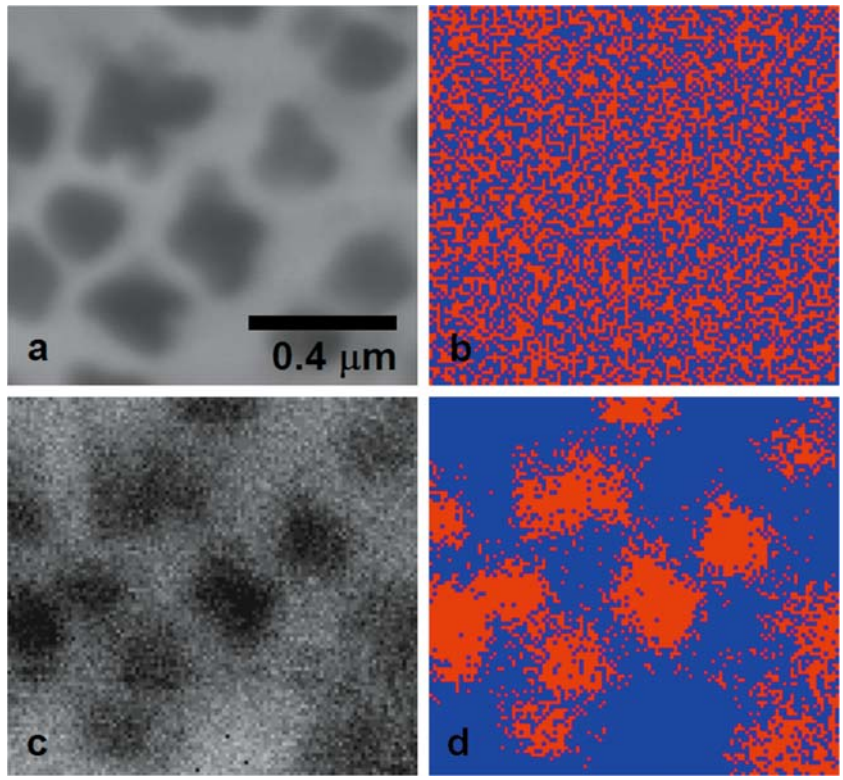


Fig. 6.8 (**a**) Backscattered electron micrograph of the region scanned. The initial phase map from the scan shown in (**b**) illustrates the poor distinguishing ability between the similar g and g' phases. Using the diffraction contrast shown in (**c**) to distinguish the phases, a significantly better phase map results (**d**). The slight positional shift of the phases near the bottom of the EBSD map, seen when comparing (**a**) with (**c** and **d**), was due to sample drift during acquisition

applications where corrosive environments may exist. Due to its composition, however, Alloy 22 has a propensity for forming intermetallic secondary phases (particularly at high temperatures), usually referred to as tetrahedrally or topologically close packed (TCP), that are known to decrease its corrosion performance (Hodge and Kirchner 1976; Heubner et al. 1989). Accurate estimations of the degree of secondary phase formation are therefore necessary to forecast the potential decrease in material performance.

The long timescales involved in Alloy 22 applications dictate that phase stability models are required to predict material behavior, and subsequent validation of these models must then rely on characterization of specimens artificially aged at elevated temperatures. Specifically, the extent of the transformed phases as a function of aging condition must be determined in order for direct comparisons to model predictions to be performed.

Research on the possible intermetallics that may form for a multicomponent alloy rich in Ni, Cr, and Mo indicated that a large number can exist. Fortunately, a sufficient amount of previous work was found in the literature that limited the number of potential phases that may precipitate during the aging treatment to three distinct types: σ, P, and μ (Leonard 1969; Raghavan et al. 1982; Cieslak et al. 1986). While valuable, this information was insufficient on its own to allow for immediate data collection, and two other pieces of information were needed: whether these are the same phases present in *our* material, and what method could be used to distinguish between them (i.e., composition, crystallography, or a combination of both).

To answer these questions, TEM thin sections were made from aged specimens. Three distinct types of secondary phases were observed (Fig. 6.9), and were determined by indexing their respective diffraction patterns to be the three TCP phases reported in the

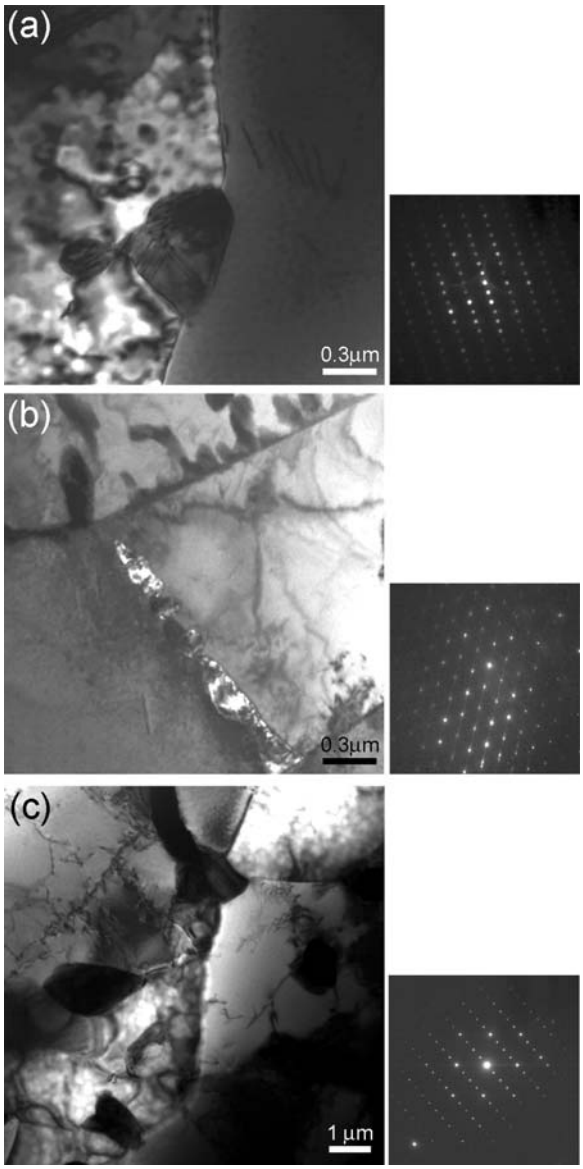


Fig. 6.9 The three types of secondary phases observed in TEM thin sections of aged Alloy 22. These were subsequently identified as (**a**) rhombohedral μ phase, (**b**) orthorhombic P phase, and (**c**) tetragonal σ phase

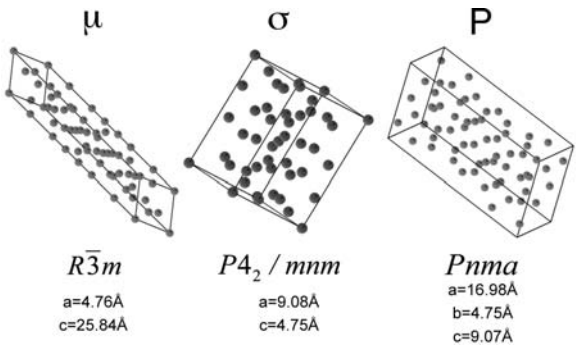


Fig. 6.10 Unit cells and crystal structures of the three TCP phases in aged Alloy 22

literature. Using EDS, compositional differences between the three phases were also measured. While variations existed, these were found to be too small (within 3%) to be useful when performing EDS discrimination on an SEM (due to the larger spot size). Fortunately, the three phases were crystallographically distinct from each other as well as the parent fcc matrix, allowing for direct discrimination between them, and their structures are presented in Fig. 6.10. Armed with this information, we could now attempt to identify the phases using EBSD.

As these phases are atypical, materials files for each needed to be created first (these are the files that contain the information required to calculate the interplanar relations used to index diffraction patterns). The first step to creating these files was looking up the powder diffraction files (PDF) for the prototype compounds for each of the three secondary phases within the International Centre of Diffraction Data (ICDD) database. Within the EBSD data collection software (TSL OIM 4.6, in this case), the crystal structure was defined, and the 25 reflector families (planes families) with the highest intensity reported in the PDFs were entered. While 25 reflector families is a relatively large number (cubic systems need at most 7), consideration of the lower symmetry of the phases as well as the differences in structure factor between X-ray diffraction and electron diffraction meant that we needed to start by considering an artificially high number of reflectors.

A systematic approach was then needed to whittle the number of reflectors down, and this was begun by manual inspection. Patterns were collected from more than 50 individual secondary phase precipitates as well as from the fcc matrix. The highest resolution possible (nonbinned) was used, and the diffraction pattern from the fcc matrix was employed to precisely calibrate the pattern center. As one would expect from three different crystal structures, three distinct types of diffraction patterns were observed, as shown in Fig. 6.11. Since only one TCP structure (μ) possessed a rhombohedral structure, it would be the only one with diffraction patterns with 3-fold symmetry. Restricting

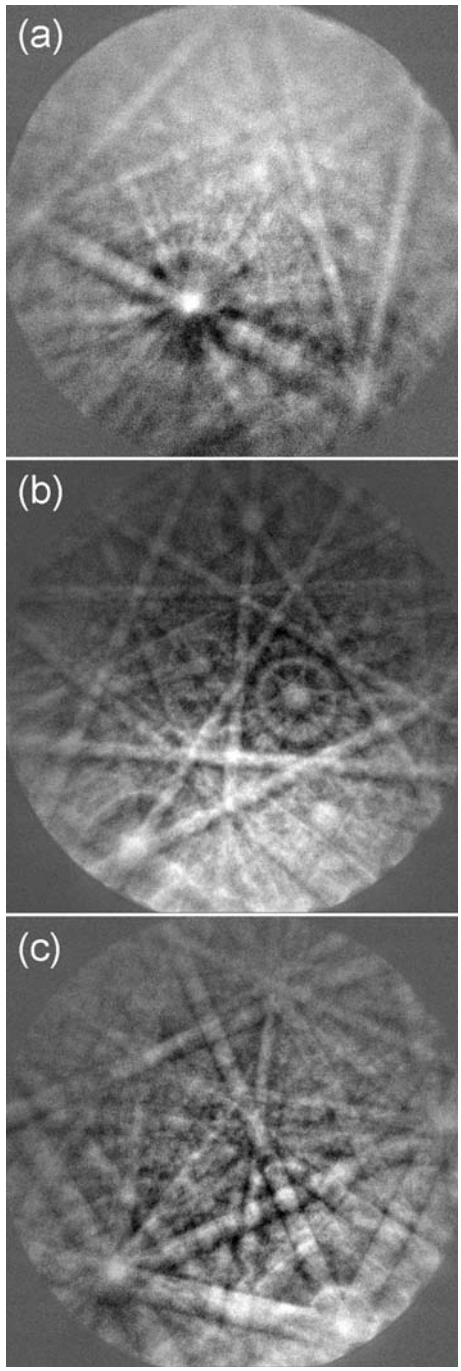


Fig. 6.11 Examples of the three distinct EBSD pattern types obtained from precipitates in aged Alloy 22. These were identified as (**a**) μ phase, (**b**) σ phase, and (**c**) P phase, as described in the text

the possible phases solely to the μ phase, and iteratively down-selecting the number of reflectors, the pattern was indexed to a fit of better than 0.5°.

To distinguish between the P and σ phases was a greater challenge, and the morphology of the precipitates was used. The TEM observations suggested that the σ phase formed only at grain boundaries, and possessed a more rounded (globular) morphology; whereas the P phase tended to form a more elongated crystal, and not necessarily at the boundaries. By limiting the patterns examined to those obtained from rounded precipitates at grain boundaries and solely to the σ phase, we iterated as we had done previously with the μ phase to down-select the reflectors, again ending with an indexed pattern with a fit better than 0.5°.

Comparison between the μ and σ phase diffraction patterns and the third, as of yet unindexed pattern type revealed the presence of significantly stronger higher order rings in the μ and σ patterns (Fig. 6.12), allowing us to then restrict the analysis of the P phase to patterns with either very weak or no rings. Following the same reflector down-selecting procedure as before, the patterns were indexed for the P phase.

Though individual patterns were now successfully indexed, this was accomplished by limiting the possible phases to a single phase during the indexing. During the automated data collection, however, all four phases need to be considered as possible solutions for each pattern. To this end, a final fine-tuning of the reflectors list for each phase was performed, ensuring that patterns previously associated with a specific phase were still indexed as that phase, despite the possibilities of other phase options.

Multiple EBSD scans were then performed on five Alloy 22 samples, each aged at a different condition (Table 6.1), and a total of 10^6 data points per sample was collected to ensure a statistical significance to the quantification of the secondary phase content. A limitation of this approach, however, was immediately apparent when examining the first dataset: some intragranular regions of the scan area that had low image quality (diffraction contrast) were indexed as the matrix (fcc), while others, usually the larger ones, were indexed as the μ phase, as seen in Fig. 6.13. By returning to the area and manually examining the diffraction patterns, it was apparent that these were μ precipitates with sizes less than 0.5 μm, and convoluted patterns were being generated from these areas, consisting

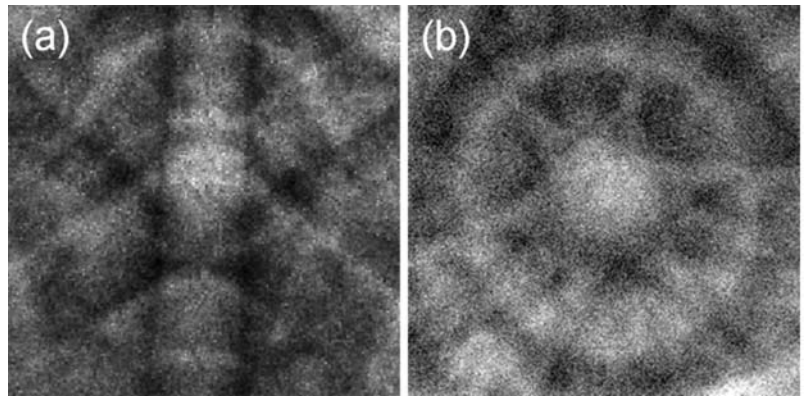


Fig. 6.12 HOLZ rings observed in diffraction patterns from both (**a**) μ phase and (**b**) σ phase particles

Table 6.1 Aging conditions of Alloy 22 samples

Sample	Temp. (°C)	Time (hours)
A	760	1,000
B	760	2,000
C	760	16,000
D	750	10,076
E	800	1,000

of both μ phase and fcc diffraction, and subsequently being indexed as fcc.

To address this issue, a post-scan processing code was written to assign low image quality points indexed as fcc to the μ phase instead (Fig. 6.14), similar to that used in Section 6.3.2. Although no crystallographic information could be assigned to these points, this allowed for an accurate representation of the secondary phase content of the material. It is critical to note that this was possible only because of a combination of excellent polish quality and a well-annealed matrix, since polishing artifacts or defected material regions would also yield low diffraction contrast, rendering this analysis incorrect.

In order to determine whether or not the measurements obtained using this method were accurate, the values were compared to those measured using an image analysis (IA) procedure applied to backscattered electron images captured in the SEM. The IA procedure relies on the contrast difference between the secondary phases and the matrix, such that by applying a threshold to the image, the area fraction (and

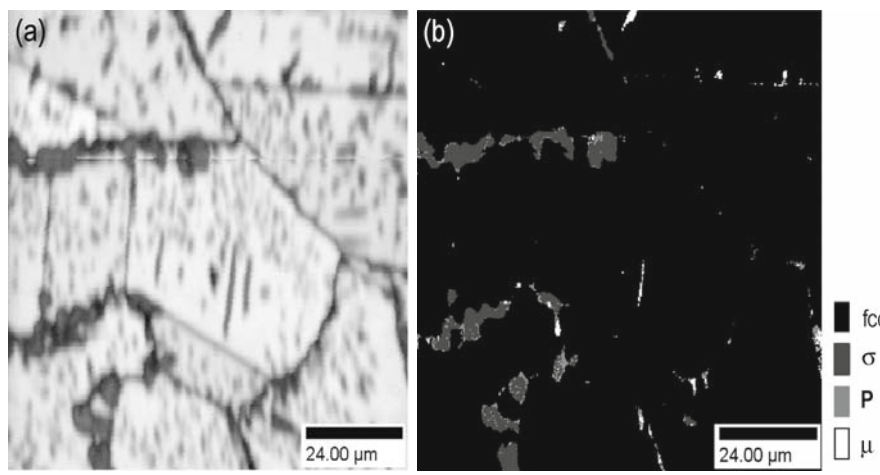


Fig. 6.13 Diffraction contrast map (**a**) illustrating how only the coarse intragrain m phase particles are indexable, as shown in (**b**)

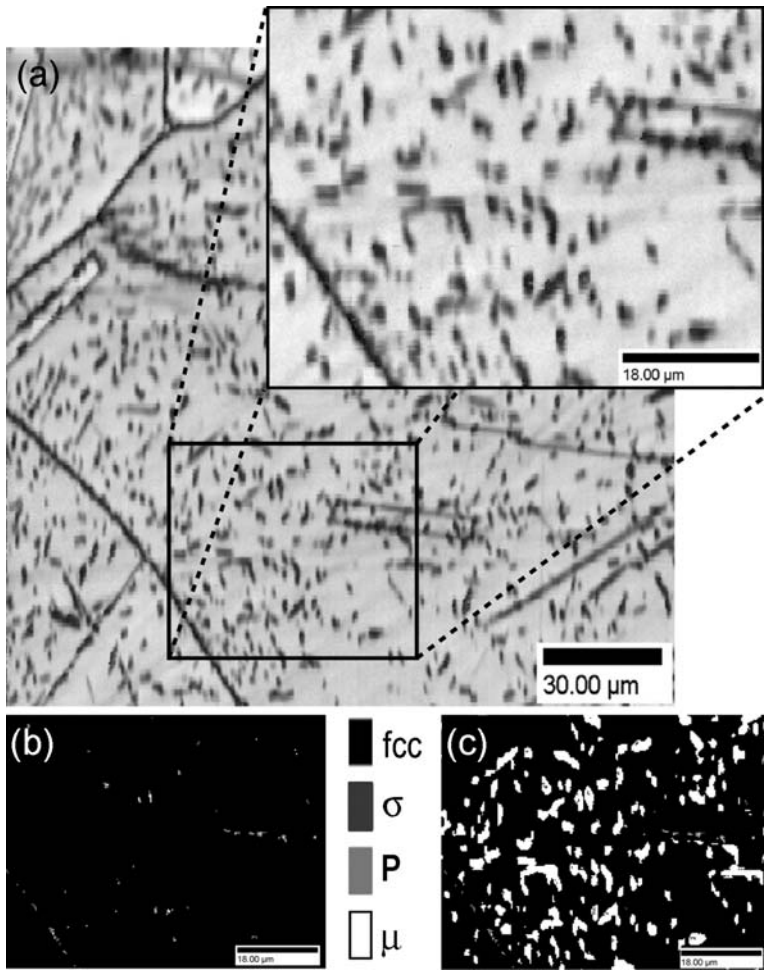


Fig. 6.14 An example of how diffraction contrast is used to correctly adjust the phase information: (**a**) region of interest, (**b**) phase map prior to correction, and (**c**) phase map after correction

Table 6.2 Phase volume fraction determination using EBSD vs. image analysis

	Individual phase volume fraction from EBSD			Total volume fraction	
Sample	μ	σ	P	EBSD	Image analysis
A	6.7	0.2	0.1	7.0	6.3
B	9.4	0.2	0.2	9.9	10.1
C	20.2	1.4	0.5	22.1	22.5
D	16.6	0.5	0.6	17.8	17.9
E	11.9	0.3	0.2	12.5	12.7

subsequently volume fraction) of all the precipitates can be measured.

Comparisons of the total secondary phase volume fraction results using EBSD to those obtained from the IA procedure are shown in Table 6.2. It can be seen that the total volume fraction measured using EBSD is within 10% of that measured using image analysis, validating the approach. More significant, however, is the fact that the use of EBSD has yielded the volume fraction of the specific phases present, and not just a total.

Acknowledgments Part of this work was performed under the auspices of the U.S. Department of Energy by Lawrence Livermore National Laboratory, in part under Contract W-7405-Eng-48 and in part under Contract DE-AC52-07NA27344.

References

Baba-Kishi KZ (1998) Measurement of crystal parameters on backscatter Kikuchi diffraction patterns. Scanning 20: 117–127

Baba-Kishi KZ (2002) Review: Electron backscatter Kikuchi diffraction in the scanning electron microscope for crystallographic analyses. J Mater Sci 37:1715–1746

Baba-Kishi KZ, Dingley DJ (1989a) Backscatter Kikuchi diffraction in the SEM for identification of crystallographic point groups. Scanning 11:305–312

Baba-Kishi KZ, Dingley DJ (1989b) Application of backscatter Kikuchi diffraction in the scanning electron microscope to the study of NiS_2. J Appl Cryst 22:189–200

Cieslak MJ, Headley TJ, Romig AD Jr (1986) The welding metallurgy of HASTELLOY alloys C-4, C-22, and C-276. Metall Trans A 17A:2035–2047

Davis JR (ed) (1997) Heat resistant materials. ASM Specialty Handbook. ASM International, Materials Park, OH

Goehner RP, Michael JR (1996) Phase identification in a scanning electron microscope using backscattered electron Kikuchi patterns. J Res Natl Inst Stand Technol 101:301–308

Gourgues-Lorenzon AF (2007) Application of electron backscatter diffraction to the study of phase transformations. Int Mater Rev 52:65–128

Heubner UL, Altpeter E, Rockel MB et al (1989) Electrochemical behavior and its relation to composition and sensitization of NiCrMo alloys in ASTM G-28 solution. Corrosion 42:249–259

Hodge FG, Kirchner RW (1976) An improved Ni–Cr–Mo alloy for corrosion service. Corrosion 32:332–336

Leonard RB (1969) Thermal stability of Hastelloy alloy C-276. Corrosion 25:222–228

Michael JR, Eades JA (2000) Use of reciprocal lattice layer spacing in electron backscatter diffraction pattern analysis. Ultramicroscopy 81:67–81

Raghavan M, Berkowitz BJ, Scanlon JC (1982) Electron microscopic analysis of heterogeneous precipitates in Hastelloy C-276. Metall Trans A 13A:979–984

Chapter 7

Phase Identification Through Symmetry Determination in EBSD Patterns

David J. Dingley and S.I. Wright

7.1 Introduction

The established use of electron backscatter diffraction (EBSD) is now widespread in orientation determination, orientation mapping (OIM), and when coupled with X-ray energy dispersive chemical analysis (EDS), as a tool for phase discrimination (Schwartz et al. 2000). A look back at the early application of the technique, before full automation, shows that it was used primarily for extracting the symmetry elements of an unknown crystal phase. The approach is detailed in Chapter 3 of *An Atlas of Wide Angle Kikuchi Patterns* (Dingley et al. 1994) and applied extensively to an investigation of an anomalous thin film growing on the surface of a synthetic nickel sulfide crystal (Baba-Kishi and Dingley 1987). Both point group and space group symmetries were extracted. The fundamental limitations that arise from the backscatter diffraction process itself have been discussed by Baba-Kishi (1986) and Dingley et al. (1994). In particular, whereas electron diffraction is exempt from Friedel's law, the peculiarities of the EBSD diffraction process somewhat negate this. Friedel's law states that in X-ray diffraction it is not possible to distinguish between centrosymmetric and noncentrosymmetric crystal structures. In electron backscatter diffraction this should be possible and thus enable identification of the noncentrosymmetric point groups (Baba-Kishi and Dingley 1989).

D.J. Dingley (✉)
H. H. Wills Physics Laboratory, Bristol University, Bristol BS8 1TL, United Kingdom
e-mail: djdingley@hotmail.com

Since retiring from EDAX-TSL in 2006, Professor David Dingley returned to the symmetry determination problem, but now taking advantage of the automation of pattern recognition developed for EBSD as part of the technique for orientation mapping. To complete the work, new computer analysis was needed, and this was accomplished by the co-author of this paper, Dr. Stuart Wright. We present the basis of the new method and a description of its application to test cases where the patterns were from known crystals. They include the cubic, hexagonal, and trigonal systems.

7.2 Basis of the Phase Identification Method

The EBSD pattern is a gnomonic projection of sets of Kossel cones generated by the diffraction of electron waves diverging from a point source in the crystal. When adopted for use in a scanning electron microscope, the source is confined to a small region no more than 20 nm or so beneath the target point where the electron beam strikes the crystal. Two Kossel cones are generated for each set of crystal planes structure factor values withstanding. Each pair of cones has a common axis passing normal to the generator crystal plane and each mirrors the other across the plane. One corresponds to Laue diffraction in the positive *hkl* sense, and the other in the negative *hkl.* The semi-cone angle is equal to $\pi/2$ minus the Bragg angle. It is large because the Bragg angle is typically less than a few degrees, so that the projected cones cut the recording film as a hyperbola only a short distance apart. The lines of intersection of the cones with the film are

A.J. Schwartz et al. (eds.), *Electron Backscatter Diffraction in Materials Science*,
DOI 10.1007/978-0-387-88136-2_7, © Springer Science+Business Media, LLC 2009

referred to as Kikuchi lines and the region between them as Kikuchi or diffraction bands. The respective intensities are a function of the structure factor and the dynamical diffraction process; see, for example, the excellent paper by Winkelmann et al. (2007) in which the theory is described and computer-generated EBSD images are created which are remarkably similar in detail to those in experimental observation. A high quality pattern from silicon is shown in Fig. 7.1. It is deliberately taken with the [011] Kikuchi band cutting the screen vertically to illustrate that the mirror symmetry that exists across this plane in the crystal becomes distorted when projected onto the image plane. It remains, however, quite easily recognizable as a symmetry plane. If the crystal phase and the camera geometry are known, the computer methods can easily extract the true symmetry. The problem that we address here, on the other hand, is one in which the crystal phase is an unknown parameter.

The centerline through each Kikuchi band marks the line of projection onto the screen of the crystal plane giving rise to the paired Kossel cones. The intersection points of these lines are zone axes in the crystal. The arrangement of Kikuchi bands about those zone axes which correspond to symmetry axes will, after taking the gnomonic projection into account, exhibit the exact symmetry of that axis. One can thus immediately construe various methods of extracting this symmetry and thence, by combining the symmetries found about different axes, discover the crystal class. However, no symmetry axes may appear, even though the patterns extend over a wide angular range. This is especially true for low symmetry crystals. We thus have to take advantage of other properties of the pattern. In our considerations it is convenient to consider the pattern as a projection of the low order planes of the crystal lattice. We need to discover the unit cell of this lattice which best describes its symmetry. In fact, any unit cell will suffice at first, because by judicious analysis of any cell the symmetry of the lattice can be found. New reference axes can then be assigned based on the symmetry found and a new unit cell constructed. The new unit cell and its associated symmetry define the crystal phase.

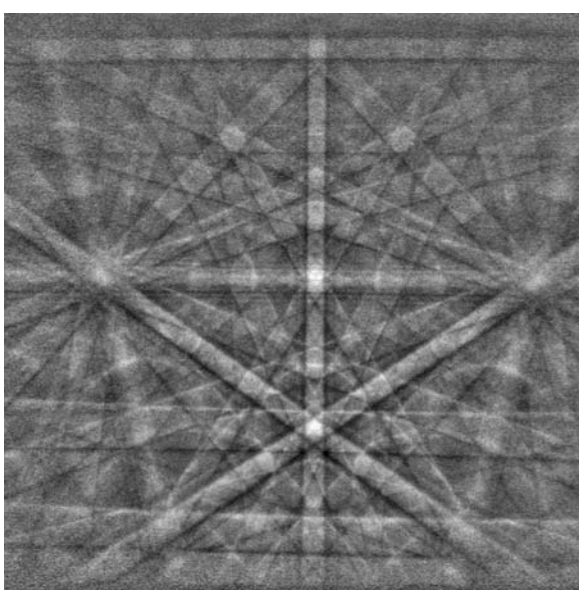


Fig. 7.1 Electron backscatter diffraction pattern from silicon

7.3 Determination of the Crystal Unit Cell

Michael (2000) was the first to outline a methodology for extracting a triclinic unit cell from any EBSD pattern. He used this as his basis for phase discrimination. It is based on extracting three noncoplanar lattice vectors from the pattern from which a triclinic unit cell is constructed. The reduced cell is calculated from this, the volume of which, by definition, is the smallest that can be determined for the particular lattice. The reduced unit cell volume together with chemical data is used to search a database to identify the crystal phase. This is a phase discrimination method rather than a phase identification method, as it ultimately relies on obtaining a match between measured crystal and chemical parameters and entries in a database. Our approach is different in both concept and methodology. The concept is that we aim to determine the crystal phase without reference to a database or requiring any chemical knowledge in assisting the process. The new methodology starts as per the Michael (2000) method, with a requirement to determine first a triclinic unit cell; but differs in that the principal use of the cell is to determine the symmetry elements of the crystal. This cannot be done with sufficient precision using the three noncoplanar lattice vector method of Michael (2000), because in general the precision in

lattice spacing measurement obtained from EBSD patterns is low—typically no better than 5%, and is often considerably worse. In our method we take advantage of the fact that the precision of angles measured between Kikuchi bands in the EBSD pattern can be better than 0.5 degrees, that is 0.2%, especially if the images are recorded at high resolution, 1000 × 1000 pixels; an iterative Hough algorithm is used; and care is taken in the calibration procedure. The accuracy can be judged in TSL OIM DC software from the fit parameter, which is a measure of the average angular difference between calculated line positions and actual positions. A fit value of 0.5 degrees indicates some Kikuchi bands were determined to a higher precision than this. We can thus be confident in the measured shape of the unit cell to this degree. We set one of the vectors of the unit cell to unity. The relative magnitude of the other two is then determined from the interaxis angles. Effectively, by extending the unit cell to form the entire lattice, we can then extract the symmetry. From this, as mentioned above, we determine a new unit cell to better reflect the symmetry of the lattice. This enables an overlay of the EBSD pattern that would be formed from such a lattice to be drawn over the observed pattern. The lattice parameter is now fixed by matching the band widths produced in the overlaid pattern to those observed, a match being required for all bands observed. The method by which all of this is achieved, however, is best described after the details of triclinic cell determination have been presented.

We note first that an infinite number of unit cells can be constructed for any given crystal lattice. It requires the determination of any three noncoplanar lattice vectors. The cell so constructed will in general not be a primitive cell. That is not an important factor at this stage. To find just one of these unit cells, we locate within the EBSD pattern any two zone axes which have at least three Kikuchi bands passing through them, with one band in common. This is illustrated in Fig. 7.2a. The two zone axes in the EBSD pattern are labeled ZA_1 and ZA_2. The common Kikuchi band is band C.

A routine function of all automated EBSD indexing programs is that the crystal plane normals for all detected bands are calculated with respect to an orthonormal set of reference axes, (normally set to the SEM specimen stage axes). For all planes passing through a single zone axis, the plane normals are of course coplanar. The two sets of plane normals for ZA_1 and ZA_2 are shown alongside the EBSD pattern in Fig. 7.2. The two sets are clearly not in the same plane. We assign unit magnitude to the common normal labeled V_{12} for ZA_1 and V_{22} for ZA_2, as unity. The magnitude of the vectors V_{11}, V_{13}, V_{21}, and V_{23} are then determined from trigonometry. They have magnitudes relative to the V_{22} unit vector and, because only

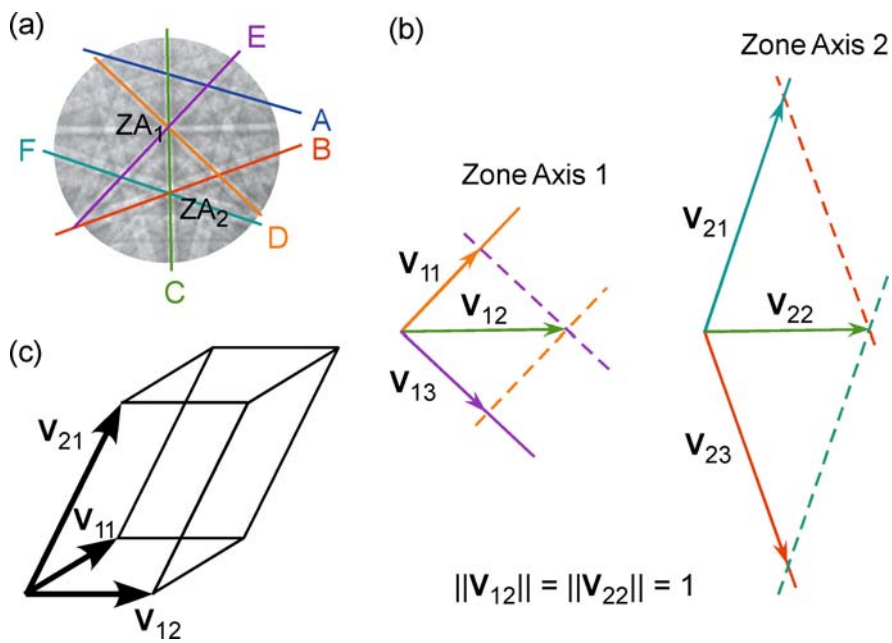


Fig. 7.2 (**a**) Selection of 2 zone axes in an EBSD pattern to construct a triclinic unit cell, (**b**) definition of vector normals for the three planes intersecting at each of the zone axes, (**c**) the constructed three-dimensional triclinic unit cell

trigonometry is employed in their calculation, are precise to the same degree to which the interplanar angles are measured. We next select the common vector and one other from each of the two sets to form the three-dimensional unit cell, as illustrated in Fig. 7.2c. The cell is triclinic.

7.4 Discovering the Lattice Symmetry

The triclinic unit cell determined from selection of three arbitrary noncoplanar planes defines the crystal lattice just as well as any other that could be constructed within the lattice, so it can be used as a basis for indexing the entire EBSD pattern. Of course the indexing will be with respect to the triclinic cell. We utilize the EDAX-TSL OIM computer software to perform the indexing. First a look-up table is generated comprising all the possible interplanar angles for the detected lattice planes within the unit cell. In the OIM software procedure, all possible sets of three Kikuchi bands are next selected from the total detected in the pattern. The plane normals are determined, and for each set the three interplanar angles are compared with theoretically calculated interplanar angles in the look-up table. A consistent match allows the planes to be identified and hence the bands to be indexed. If a crystal possesses any symmetry other than triclinic, then more than one consistent match between experimental and calculated interplanar angles will be found. These solutions are related by the symmetry of the crystal, and arise from the initial choice of reference axes. If the crystal were cubic, for example, the reference axes 1, 2, and 3 could be labeled in 24 different ways, [100] [010] [001]; [010] [001] [100]; [00-1] [010] [100]; etc. The different labeling of a triplet results in different outputs for the orientation of the crystal. The different orientations will again be related to the symmetry possessed by the crystal. In our new procedure the orientation relationship is calculated between all pairs of output orientations. Continuing with our illustration using a cubic crystal, we would expect to find orientation relationships between the different solutions which, when presented in terms of an axis angle pair, included rotation angles of 90°, 180°, and 120°, these being the rotational symmetry values for the 4-fold, 2-fold, and 3-fold symmetry axes of a cubic crystal. The indices of the corresponding axes will be output in terms of the triclinic lattice and thus will be different for each pair of solutions. But that does not matter. We should also find that a 90° axis lies 54.7° from a 120° axis, 90° from another 90° axis, 45° from a 180° axis, etc. Thus a table can be drawn up of rotation axes and angles between them. This table is checked against the set of symmetry relationships that define the conventional crystal systems. The symmetry axes for the conventional crystal systems are given in Table 7.1, and

Table 7.1 Symmetry axes for conventional crystal systems

Crystal symmetry	Symmetry axes
Cubic	Four 90° axes—<100>
	Three 120° axes—<111>
	Six 180° axes—<110>
Tetragonal	One 90° axis—[001]
	Four 180° axes—[100], [010], [110], and [1-10]
Orthorhombic	Three 180° axes—<100>
Hexagonal	One 60° axis—[0001]
	Six 180° axes—$<11\bar{2}20>$ and $<10\bar{1}10>$
Trigonal	One 120° axis—[0001]
	Three 180° axes—$<10\bar{1}10>$
Monoclinic	One 180° axis—[100]

Table 7.2 Angles between symmetry axes for conventional crystal systems

Crystal Symmetry	Symmetry axes	Angle between axes
		90° from other 90° axes
		45° or 90° from 180° axes
Cubic	90° axes	54.7° from 120° axes
Cubic	180°axes	45° or 90° from 90° axes
		60° or 90° from other 180° axes
		35.3° or 90° from 120° axes
Cubic	120°axes	54.7° from 90° axes
		35.3° or 90° from 180° axes
		70.5° from other 120° axes
Tetragonal	90° axis	90° from 180° axes
Tetragonal	180° axes	90° from the 90° axis
		45° or 90° from other 180° axes
Orthorhombic	180° axes	90° from other 180° axes
Hexagonal	60° axis	90° from 180° axes
Hexagonal	180° axes	90° from the 60° axis
		30°, 60°, or 90° from other 180° axes
Trigonal	120° axis	90° from the 180° axes
Trigonal	180° axes	90° from the 120° axis
		60° from other 180° axes
Monoclinic	180° axis	–
Triclinic	–	–

the angles between the axes within each crystal system are given in Table 7.2.

If the symmetry search found all the possible and only the possible symmetries possessed by the lattice, then the problem would be solved. However, because the number of bands detected is limited, and because of the finite precision in angular measurement between crystal planes, ambiguities arise and a voting scheme and weighting procedure have had to be adopted. It is not necessary to describe the details of this procedure, as it is better illustrated by examination of the example cases below.

7.5 Re-Indexing the Pattern According to the Discovered Crystal Class

At the completion of the procedure, in order to discover the symmetry elements possessed by the lattice, a list of potential crystal systems is produced weighted in order of the degree that each satisfies the rules in the tables above. The crystal system at the top of the list is selected first. Let us refer to this as Potential Solution 1, PS_1. We utilize the fact that each symmetry element will be associated with an axis and an angle of rotation. The axis will have a known specific set of *uvw* indices in terms of the triclinic crystal direction. Let us label these as $u_t v_t w_t$. However, at this stage we also know the potential crystal class and thus the rotation axis type associated with each rotation angle. For example, a 120° rotation is associated with a <111> rotation axis. Let us label these as $u_c v_c w_c$. Admittedly there is some ambiguity for the hexagonal system as to which set of 180° axes are labeled $<10\bar{1}0>$ and which $<11\bar{2}0>$, and similarly for the tetragonal system where there is ambiguity in selecting which of the two pairs of 180° axes are labeled <100> and which <110>, but that is an arbitrary choice always made in labeling such crystals. That is, there are always two equivalent and equally valid solutions for these crystals. Convention establishes the one used. For a given crystal the first such symmetry axis found can be assigned any $u_c v_c w_c$ value within the family type. For example, if the crystal system is orthorhombic and the symmetry axis has a rotational symmetry of 180°, then that axis can be assigned [001] or [010] or [100]. All are equivalent. Other symmetry axes in that crystal cannot be assigned with such freedom. However, their specific indices are predictable because the angles between the symmetry axes are also known and we restrict ourselves to a right-handed system. Once three such axes are determined, not necessarily orthogonal, then a transformation matrix T can be calculated relating the triclinic indices $u_t v_t w_t$ to the new crystal indices, $u_c v_c w_c$. The triclinic indexing of all the zone axes can then be transformed into that of the PS_1 system. This permits us to re-index the entire pattern and calculate the orientation in terms of the PS_1 crystal system. Likewise, it becomes possible to calculate the relative lattice spacing of any *hkl* plane in terms of the lattice parameters of PS_1. However, this is not as straightforward. We first use the inverse of the transformation matrix T to calculate the indices $u_t v_t w_t$ in the triclinic system of the three reference directions $u_c v_c w_c$ in the PS_1 crystal system [100], [010], [001]. The vector product of the $u_t v_t w_t$ values corresponding to the $u_c v_c w_c$ values [010], [001] yields the plane normal $h_t k_t l_t$ for the plane [100] in terms of the triclinic system. We calculate similarly the triclinic $h_t k_t l_t$ for the other PS_1 planes (010) and (001). The lattice spacing *d* of these planes is found by substituting respectively their $h_t k_t l_t$ values for *hkl* in the general equation for a triclinic crystal,

$$\frac{1}{d^2} = \frac{1}{V^2}(S_{11}h^2 + S_{22}k^2 + S_{33}l^2 + 2S_{12}hk + 2S_{23}kl + 2S_{13}hl) \tag{7.1}$$

where V is the volume of the unit cell and is given by

$$V = abc(1 - \cos^2\alpha - \cos^2\beta - \cos^2\gamma + 2\cos\alpha\cos\beta\cos\gamma)^{1/2} \tag{7.2}$$

and

$$\begin{aligned} S_{11} &= b^2c^2\sin^2\alpha \quad S_{12} = abc^2(\cos\alpha\cos\beta - \cos\gamma) \\ S_{22} &= a^2c^2\sin^2\beta \quad S_{23} = a^2bc(\cos\beta\cos\gamma - \cos\alpha) \\ S_{33} &= a^2b^2\sin^2\gamma \quad S_{13} = ab^2c(\cos\alpha\cos\gamma - \cos\beta) \end{aligned} \tag{7.3}$$

a, b and *c* are the normalized triclinic lattice parameters illustrated in Fig. 7.2c.

The values of *d* found are thus relative to that of the unit vector used initially in construction of the triclinic unit cell. They are of course the lattice parameters a_c, b_c, and c_c of the PS_1 crystal. If the crystal is cubic, then the lattice spacing values found will be the same.

Otherwise, the ratios a_c:b_c:c_c will be in correct proportion or can be scaled to yield the correct proportions. That is, the correct proportions could be a_c:nb_c:mc_c where n and m are integers. This follows because the original triclinic unit cell may have been a sub-cell of the true unit cell. If this is the case, it is immediately recognizable when a new EBSD overlay is calculated based on the PS_1 lattice, the normalized lattice parameters a_c, b_c, and c_c, and the orientation calculated in terms of the PS_1 crystal. Basically, what happens is that if the incorrect ratios are used to calculate the overlay, the zone axes parallel to the reference crystal axes will fall in the correct positions, while all others will be displaced. Increasing m and n successively by 1 and recalculating the overlay will eventually yield the correct a_c:b_c:c_c ratio, which happens when all zone axes appear in the correct positions. This is illustrated later. A computer routine has been written that makes these adjustments automatically. The program also allows for refinement of the a_c:b_c:c_c ratio to take into account the small measurement errors in calculation of the initial unit cell.

We proceed with three examples to illustrate the procedure. Although in all cases the crystal phase was actually known, this information was not used anywhere in the analysis. In the first example the crystal phase was cubic, in the second case it was hexagonal, and in the third case the crystal phase was trigonal.

7.6 Examples

7.6.1 Case 1, A Cubic Crystal

The EBSD pattern from silicon shown in Fig. 7.1 is used for the first example. It is reproduced in Fig. 7.3. The Kikuchi band positions used to determine the triclinic unit cell were input manually in this case in order to restrict the complexity and clarify the figure. Each band was identified in terms of the generated triclinic lattice and is shown colored in the figure. The triclinic unit cell is shown to the right. The two zone axes used to generate the unit cell are labeled 100 and 001 in the figure. The third axis, 010, lies at the intersection of the 100 and 001 bands and falls to the left and outside the pattern, as indicated by the arrows.

The symmetry relationships found from the pattern are indicated in Fig. 7.4, which is a snapshot of one of

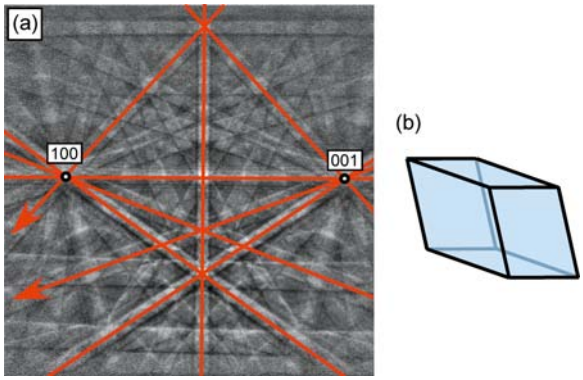


Fig. 7.3 (**a**) Bands selected to construct the triclinic unit cell, (**b**) the triclinic unit cell

Misorientations between axes

A	No.	B	No.	angle
180	0	180	4	89.95
180	1	180	8	58.52
180	2	180	11	89.43
180	2	180	12	61.08
180	2	180	15	59.08
180	3	180	7	31.10
180	3	180	10	30.02
180	3	180	11	59.84
180	4	180	13	60.86
180	5	180	6	59.08
180	6	180	7	88.03
180	6	180	10	89.88
180	6	180	13	61.11
180	7	180	11	58.80
180	9	180	17	88.71
180	10	180	11	29.82

Votes (Triplet votes)

angle	No.	cubic	tetra...	ortho...	hexa..
Total	-	234	2	0	30
179.2	0	7	1	0	0
180.0	1	10	0	0	2
178.0	2	9	0	0	2
179.8	3	2	0	0	4
179.9	4	7	0	0	0
178.3	5	3	0	0	0
179.7	6	5	0	0	2
179.2	7	4	0	0	0

Fig. 7.4 Snapshot from computer program showing symmetries found from examination of the triclinic unit cell, the relationship between these axes, and their compliance with the symmetry of the different crystal systems

the computer program output screens. It is seen that six 180° rotation axes were found, three 90° axes, and two 120° axes. All 180° axes lay within 1° of 60° or 90° from any other 180° axis, 45° and 90° from the 90° axes, and 35° and 90° from 120° axes. This is entirely consistent with what is expected in a cubic crystal. To accumulate votes for a particular crystal system, all possible sets of three rotation axes were selected. Whenever all inter-axis angles within a set were consistent with what was possible for a particular crystal system, that system was credited one vote. This naturally biases the cubic system, so the tally was eventually normalized by dividing by the maximum number of votes possible for that system. In this example, the cubic system achieved an unnormalized total of 234.

Steps in the refinement of the procedure are shown in Fig. 7.5. The voting procedure clearly identified the crystal as cubic. The crystal was re-indexed in terms of the cubic system and a new orientation determined. Figure 7.5a shows the computer-generated overlay in which only the band center lines are shown. The input band positions for the computation were just the eight bands selected in the initial analysis, Fig.7.3a. The computation takes into account the symmetry of the crystal and automatically adds Kikuchi bands that are symmetrically related to any of the eight input bands. A total of 13 bands are included, all of the additional lines corresponding exactly to bands that appear in the image. The band widths, which are still with respect to the normalization procedure adopted for the triclinic cell, are now shown in Fig. 7.5b. As expected, few match. In this case, the widest band of first-order type was selected. These are the (113) type bands shown in blue in the solution overlays in Fig. 7.5b. The lattice parameter was then incremented in units of 0.01 nm until the band width matched that seen in the image. In a later development, this has become an automated process. The result is shown in Fig. 7.5c. Whereas many computer-simulated band widths now

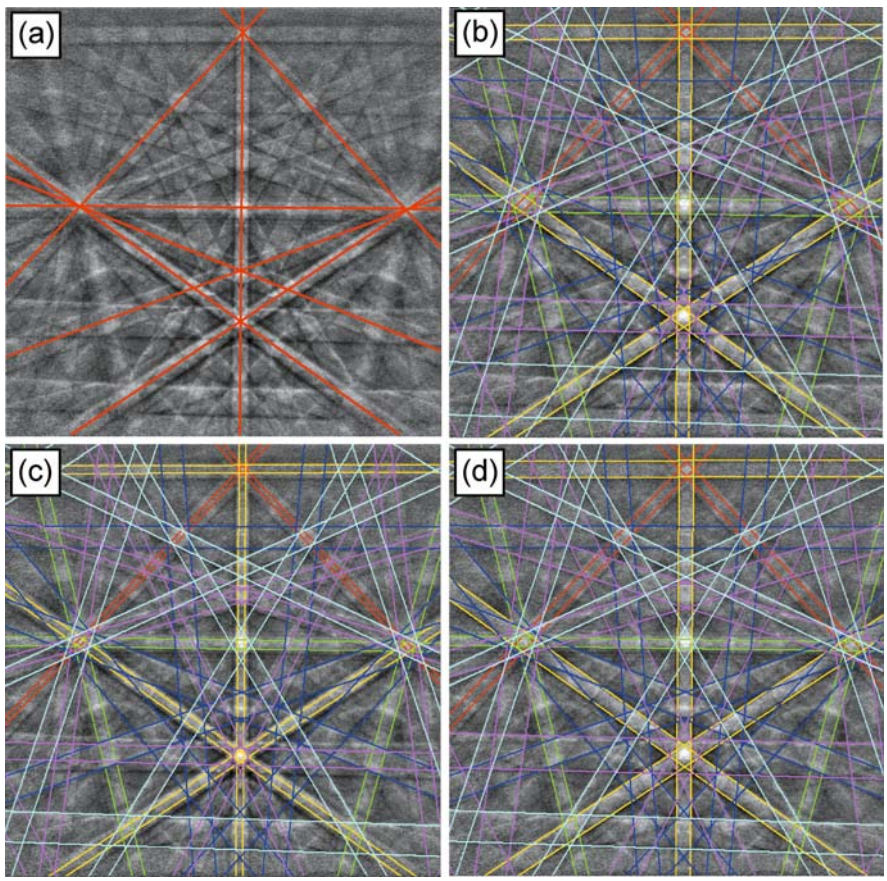


Fig. 7.5 Solution overlays after steps in the lattice parameter refinement process. (**a**) Input bands (in red) and the solution overlay, (**b**) initial solution overlay, (**c**) solution overlay after adjustment of the lattice parameter to match the blue bands in (**b**), and (**d**) solution overlay after increasing the order of the bands which do not match

match those in the image, others don't. As computed, these bands have the following indices: {111} for the green lines, {100} for the red, and {110} for the yellow. The order of reflection was accordingly increased for these bands, with the {111} band width matching correctly when re-indexed as {222}, and likewise for the {100} bands when re-indexed as {400}, and {110} when re-indexed as {220}. The final result is shown in Fig. 7.5d. The overlay is for a lattice parameter of 0.54 nm. (A more careful examination of the {222} band actually shows a contrast change but no distinct line corresponding to the projection of the {111} Kikuchi lines, whilst {333} and {444} lines also appear, though rather faint. However, no {200} lines are detected, as is expected for the space group for this crystal 5_43d. The result gives overwhelming confidence in the correctness of the computer determination of the crystal system.

The Kikuchi bands detected, including those only faintly seen, were {111}, {220}, {131}, {222}, {400}, {331}, {422}, {333}, {115}, and {444}. The indices fit exactly those expected for an fcc Bravais lattice and, with the exception of the appearance of the {222} reflection, to the diamond structure. The observation of the {222} reflection in electron diffraction patterns is normal and results from a double diffraction effect. We have, during this analysis, observed that the {110} axes exhibit 2-fold symmetry, the {100} axes exhibit 4-fold symmetry, and the {111} axes exhibit 3-fold symmetry. This is sufficient to identify the point group symmetry as *m3m.*

7.6.2 Case 2, A Hexagonal Crystal

The second example is the identification of the titanium hexagonal alpha phase. The EBSD pattern used is shown in Fig. 7.6a, overlaid with the Hough detected bands and with two of the reference vectors of the generated triclinic cell labeled [001] and [010]. The third lies outside the range of the image. The ranking provided two solutions with virtually equally good matches between the calculated overlay and the original pattern. They were both hexagonal. The first result is shown in Fig. 7.6b and includes the bands originally detected in the pattern plus those that would appear because of the symmetry and orientation of the crystal. The *a:c* ratio of the lattice parameters resulting directly from the determination of the hexagonal unit cell from the triclinic cell was 1.13. After refinement to adjust for the slight misalignment of the zone axes, the ratio was 1.11. The *a* lattice vector is larger than the *c* vector. The lattice spacing fit in this case was adjusted by setting the computer to increase automatically both *a* and *c* parameters in proportion until a best match of all lines was obtained. The result is shown in Fig. 7.6d. The lattice parameters obtained were $a = 0.49$ nm and $c = 0.448$ nm.

The second solution recorded after the determination of the hexagonal unit cell is shown in Fig. 7.6e. It is in a different orientation. Note that the [0001] zone axis has remained unchanged but, for example, the [-2113] axis has become the [01-1-1] axis. After refinement to better fit the zone axes, and automatic adjustment of band width so that the observed band width and that in the overlay match, the *a:c* ratio is measured as 0.632 and the magnitudes of the vectors *a* and *c* are 0.309 nm and 0.489 nm, respectively.

The above two results are related by a 60° rotation about [0001]. This is precisely the ambiguity referred to in the section on re-indexing the pattern according to the discovered crystal class. We note that the second solution values for the lattice parameters match those for the conventional titanium unit cell quite well. The published figures are $a = 0.295$ nm and $c = 0.468$ nm, respectively, and the ratio $a{:}c = 0.63$. It is seen that the refinement in fitting the calculated positions of the zone axes to those observed, which determines the *a:c* ratio as 0.632, is more precise than the fitting of the band widths. This is as expected and is the reason the new method of determining the triclinic unit cell was adopted.

7.6.3 Case 3, A Trigonal Crystal

The final example is taken from a study of alumina. Three EBSD patterns were investigated and all resulted in a correct identification of the trigonal lattice to which this phase belongs. One of the patterns with the overlay produced after determining the triclinic unit cell is shown in Fig. 7.7a. Analysis of the symmetry identified the lattice as trigonal. After zone axis position refinement and automatic band width matching, the resultant overlay is shown in Fig. 7.7c. The higher-order lines shown were added manually. This analysis

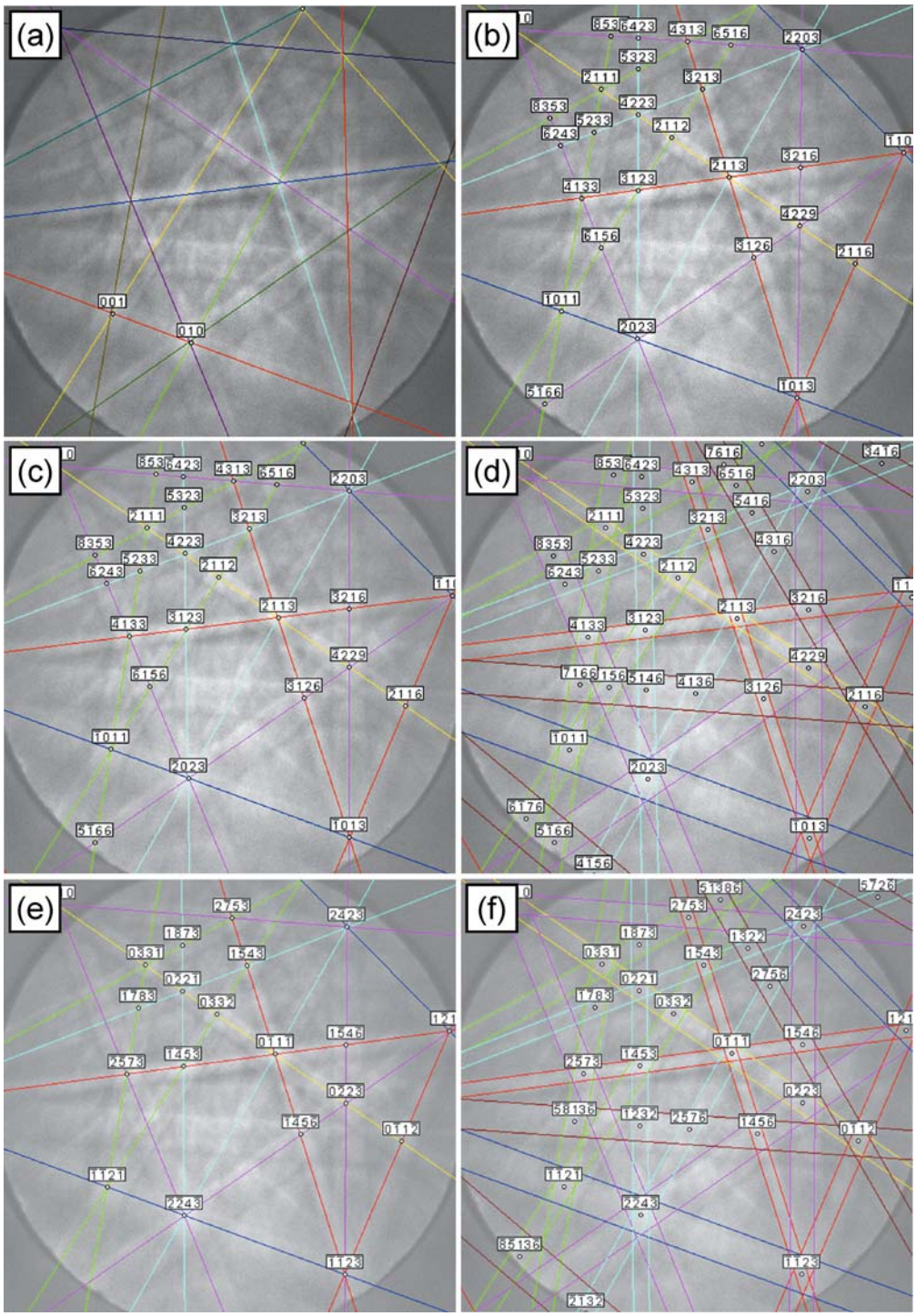


Fig. 7.6 (**a**) Titanium EBSD pattern with bands used for determination of triclinic cell, (**b**) calculated overlay hexagonal crystal, (**c**) result of refining a:c ratio (note in particular the difference in the location of the green overlay lines), (**d**) final overlay with calculated band widths, (**e**) alternative and equivalent indexing solutions for the titanium pattern as a hexagonal crystal, (**f**) final overlay after refinement for alternative indexing

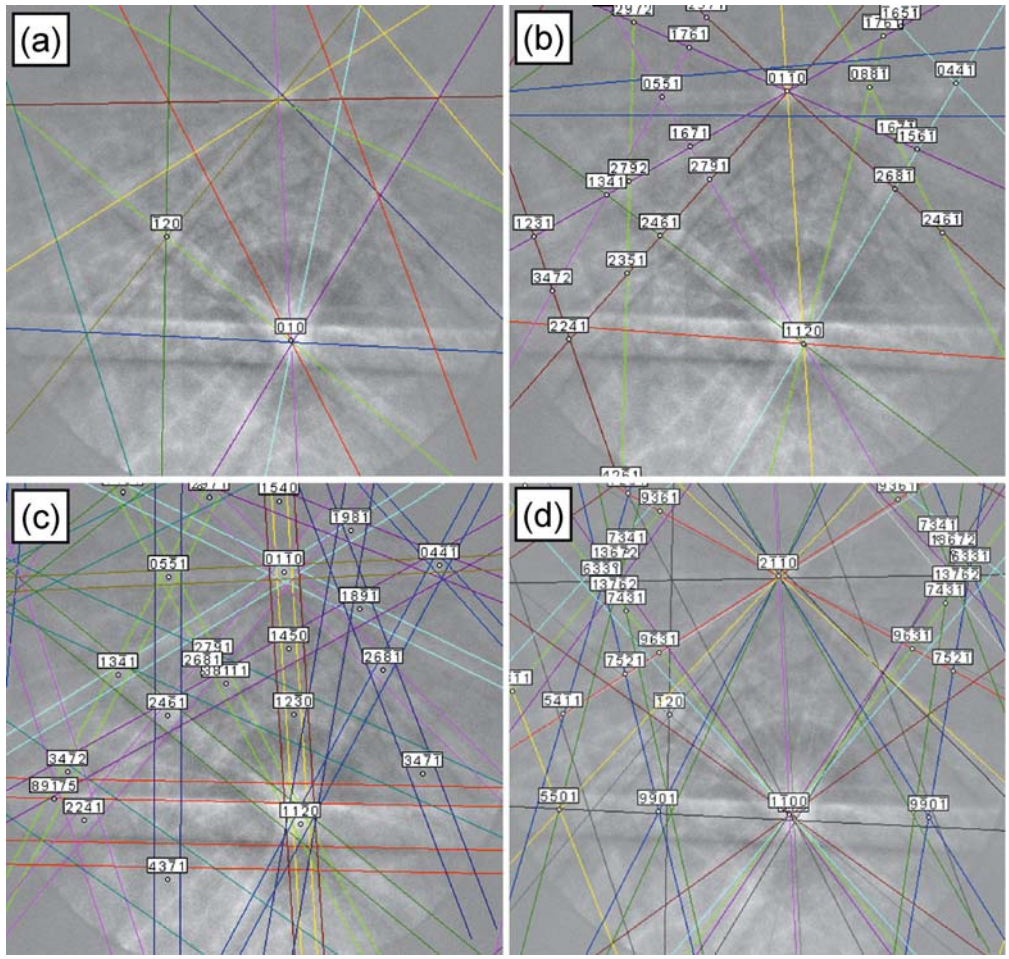


Fig. 7.7 (**a**) Alumina EBSD pattern with bands used to form triclinic cell, (**b**) as computed overlay for a trigonal crystal, (**c**) computer overlay after refinement, (**d**) result of indexing as if the pattern were hexagonal

was straightforward and produced no complications. However, as mentioned in the introduction, because a limited number of bands are considered in the analysis, and because a tolerance of up to two degrees is permitted in interzonal angle measurements, some ambiguity is inevitable. The program in fact lists all potential solutions, though they are ranked to display only those with the best fit between overlay and input bands for each crystal system. In the previous cases we have shown only the result for the overall best fit system. To conclude this case study, we include the result for the second best fit crystal system. It was hexagonal and the result after refinement is shown in Fig. 7.7d. Only the center lines along the bands are shown for clarity. The orientation is the same as when indexed as a trigonal crystal, but the extra symmetry produced by the hexagonal system over that of the trigonal system has introduced additional bands in the overlay that do not exist in the pattern. It demonstrates clearly that this method can resolve these otherwise similar crystal systems.

7.7 Discussion

The above results, produced using a development computer program based on the EDAX-TSL OIM DC software, enabled some 12 patterns, including those shown above, to be analyzed in a few hours. In general, the procedure required little manual input. Special care was needed in acquiring precise calibration values for pattern center and camera length, and each pattern was

inspected prior to launching the analysis to establish that the Hough transform settings had resulted in precise location of the diffraction bands. Where this was not possible, the diffraction bands were located manually. Sometimes the crystal system that accumulated the greatest ranking even after normalization was not the correct one. This was immediately apparent when the computed band positions were calculated and overlaid on the pattern, and hence caused minimal distraction. The second ranked solution was then chosen. Nevertheless, it indicates that there remains a need for improvements in the voting and ranking system. Notwithstanding these anomalies, the results have well proven that the principal of the method is sound.

The two parts of the lattice parameter refinement procedure were found to function with differing precision. The software based on adjusting the ratios of the lattice parameters until the best match between calculated and observed zone axis positions was found gave good results. The precision was found to be on the order of 0.2%. The fitting of band widths, however, was less precise, at 5%. The fitting was done in two parts. First, the unit vector which was used as the base vector in constructing the triclinic unit cell was altered to the value measured from the pattern. All other vectors were then changed in proportion. Next, a small proportional and sequential change was made to all calculated band widths and the quality of overly band widths to observed made by visual inspection. There is clearly room for improvement here, and for automation. The difficulty is that the Kikuchi line profile varies in a nonuniform manner from bright to dark, and is different for the Kikuchi lines on the upper side of the band compared to those on the lower side. It differs also with regard to the type and order of reflection. A possible solution is to make use of the HOLZ rings that are frequently observed surrounding the principal zone axes. These are high-order reflections and are thus considerably more sensitive to lattice spacing than the zero-order lines that make up the majority of the pattern. A computer simulation of these rings would adjust to changes in the lattice parameters with regard to the Kikuchi band widths providing a more precise assessment of when the best fit occurs between the computed overlay and the observed pattern.

References

Baba-Kishi KZ (1986) Crystallographic information from electron back-scattering diffraction patterns. Ph.D. Thesis, Bristol University, Bristol, UK

Baba-Kishi KZ, Dingley DJ (1987) Application of backscatter Kikuchi diffraction in the SEM to studies of NiS. J Appl Crystallogr 22:89–98

Baba-Kishi KZ, Dingley DJ (1989) Backscatter Kikuchi diffraction in the SEM for identification of crystallographic point groups. Scanning 11(6):305–312

Dingley DJ, Baba-Kishi K, Randle V (1994) Atlas of backscatter Kikuchi diffraction patterns. Institute of Physics Publishing, Bristol, UK

Michael, JR (2000) Phase identification using electron backscatter diffraction in the scanning electron microscope. In: Schwartz AJ, Kumar M, Adams BL (eds) Electron backscatter diffraction in materials science. Kluwer Academic/Plenum Publishers, New York

Schwartz AJ, Kumar M, Adams, BL (2000) Electron backscatter diffraction in materials science. Kluwer Academic/Plenum Publishers, New York

Winkelmann A, Trager-Cowan C, Sweeney F, Day AP, Parbrook P (2007) Many-beam dynamical simulation of electron backscatter diffraction patterns. Ultramicroscopy 107: 414–421

Chapter 8

Three-Dimensional Orientation Microscopy by Serial Sectioning and EBSD-Based Orientation Mapping in a FIB-SEM

Stefan Zaefferer and Stuart I. Wright

8.1 Introduction

Conventional EBSD-based orientation microscopy is a 2-dimensional (2D) characterization method, which is applied to plane cuts through a sample. Statistical stereological techniques can be used to gain insight into the 3D aspects of microstructure, as in, e.g., Adams (1986), Adams et al. (1987), and Howard and Reed (1998); see also the web site http://www.liv.ac.uk/fetoxpath/quantoxpath-/stereol.htm. However, there are also a large number of cases where a true 3-dimensional characterisation of a sample volume is critical to a correct understanding of the role the microstructure plays in a particular material property. Also, computer modelling of microstructure formation processes (e.g., deformation or recrystallisation processes) profits greatly from realistic 3-dimensional input data (e.g., Zaafarani et al. 2006; Zaefferer 2008).

Information that is in most cases missing in 2D microstructure observations is the full crystallographic characterisation of interfaces, e.g., grain boundaries. Grain boundaries are characterised by 5 macroscopic parameters, represented by the misorientation across the boundary (3 parameters) and its plane normal (2 parameters). In two-dimensional orientation microscopy, only the misorientation can be determined unequivocally, while only one parameter of the plane normal is accessible. In the case of a microstructure close to thermodynamic equilibrium, grain boundary planes can be determined using a statistical argument: assuming that most grain boundaries will occupy low energy positions, the traces of different grain boundaries will all point to the same grain boundary normal. The type and density of low energy grain boundaries can thus be determined (Rohrer et al. 2004). Nevertheless, in nonequilibrium microstructures, and when local information on the boundary character is needed, a 3D technique is essential.

Principally, 3D-characterisation of microstructures can be performed by two different approaches, either by serial sectioning or by observation with some sort of transmissive radiation. The latter techniques obtain the 3D information from bulk samples, either by reconstruction from a large number of extinction images taken under different beam incidence directions onto the sample, or by a ray-tracing technique. Ray-tracing techniques are suitable for the characterisation of the microstructure of crystalline materials; see, e.g., Poulsen et al. (2001), Yang et al. (2004), and Preusser et al. (2005). The current spatial resolution of these techniques is in the order of volumes of some μm^3, and the method has been shown to enable in situ observations of recrystallisation and deformation processes: for example, Lauridsen et al. (2006) and Margulies et al. (2001).

Significantly simpler than the bulk methods, yet comparably powerful (and partly complementary) methods for the 3D characterisation of crystalline materials are the serial sectioning techniques. The techniques simply comprise the removal of slices of material with some cutting technique, followed by the recording of the structure of the exposed materials surface with an appropriate microscopic technique. Finally the 3D structure is reconstructed, e.g., by

S. Zaefferer (✉)
Max Planck Institute for Iron Research, Max-Planck-Straße 1, D-40237 Düsseldorf, Germany
e-mail: s.zaefferer@mpie.de

A.J. Schwartz et al. (eds.), *Electron Backscatter Diffraction in Materials Science*,
DOI 10.1007/978-0-387-88136-2_8, © Springer Science+Business Media, LLC 2009

stacking of the recorded images. Serial sectioning techniques are applicable to a very wide range of materials and material problems, with the only serious disadvantage being that they are destructive.

For serial sectioning a large number of different methods can be imagined: e.g., mechanical polishing, chemical polishing, or laser or electrical discharge ablation. For the observation of the serial sections, all kinds of microscopic techniques are available: e.g., light optical observations following some etching procedure, or SEM observations using contrast created by backscattered electrons. The main challenge associated with many of the sectioning methods is controlling the sectioning depth, obtaining flat and parallel surfaces, and correctly redetecting and aligning the area of observation. On the observation side, the main obstacle is the nonquantitative contrast of many microscopic techniques, which prevents unique microstructure reconstruction. Finally, most of the serial sectioning methods are extremely laborious. It should be mentioned that, disregarding all these difficulties, Rowenhorst and co-workers devised a powerful 3D system composed of serial sectioning by mechanical polishing and a combination of light optical microscopy and EBSD-based orientation microscopy for section analysis (Rowenhorst et al. 2006).

A technique that avoids, in an ideal way, all of the aforementioned problems with sectioning and imaging is the combination of serial sectioning with a focused ion beam and EBSD-based orientation microscopy in a combined FIB (focused ion beam)-SEM. The focused ion beam usually consists of 30 kV Ga^+ ions. The impact of the beam on a sample leads to localised sputtering of the target material and can be used to perform cuts into the material a few nanometres in width. Irradiating a material surface in grazing incidence allows preparation of smooth surfaces that show little radiation damage: e.g., Prasad et al. (2003), Michael et al. (2003), and Matteson et al. (2002). This technique has been used extensively for the preparation of TEM samples as well as the preparation of flat surfaces for metallographic investigations. By sputtering of subsequent parallel surfaces, serial sections can be created with a precise distance of some 10 nm up to several μm. A number of papers describe such a technique for the preparation of serial sections or TEM samples: e.g., Sheng et al. (1997), Cheng et al. (1998), and Jin et al. (2005).

For observation of the microstructures of the serial sections, EBSD-based orientation microscopy is an excellent method because it actually allows quantitative characterization of crystalline materials where areas (or volumes in 3D) belonging to the same grain in different sections can be easily assembled by their similar orientation and crystallographic structure. Orientation microscopy is therefore the predestined method for three-dimensional microstructure characterisation based on serial sectioning.

The combination of EBSD-based orientation microscopy with serial sectioning is currently under strong development. The papers assembled in a recent viewpoint set in Scripta Materialia (Spanos 2006) give nice examples. Also, the combination of orientation microscopy with serial sectioning by FIB has been described earlier: e.g., Uchic et al. (2004) and Groeber et al. (2006). Fully automated 3D orientation microscopy systems combining FIB and EBSD have been developed in the last few years, first by Mulders and Day (2005). The present author, in collaboration with EDAX/TSL and Zeiss, was probably the second to develop such a system (Zaefferer et al. 2005). An overview on the technique and on investigations that have been done with it was recently published by Zaefferer et al. (2008).

8.2 The Geometrical Set-Up for 3D Characterisation in a FIB-SEM

A typical instrument for FIB-EBSD tomography consists of a SEM with a FIB mounted to its side at an angle of usually 54° from the vertical. The EBSD detector may be mounted either below the FIB column or on the opposite side of it. Both set-ups are sketched in Fig. 8.1. For EBSD the investigated surface is usually tilted 70° from the horizontal position while gracing incidence ion milling of the surface requires the surface to be inclined to 36° (= 90°–54°). In the case that the EBSD detector is mounted to the opposite side of the FIB column, the sample has to be tilted about an axis perpendicular to the electron and ion beam in order to change between the EBSD and the milling position. This set-up is therefore called the "tilt" set-up (Zaefferer et al. 2005, 2008) and is displayed in Fig. 8.1a. In the other case, the sample has to be rotated about an axis positioned at the half angle

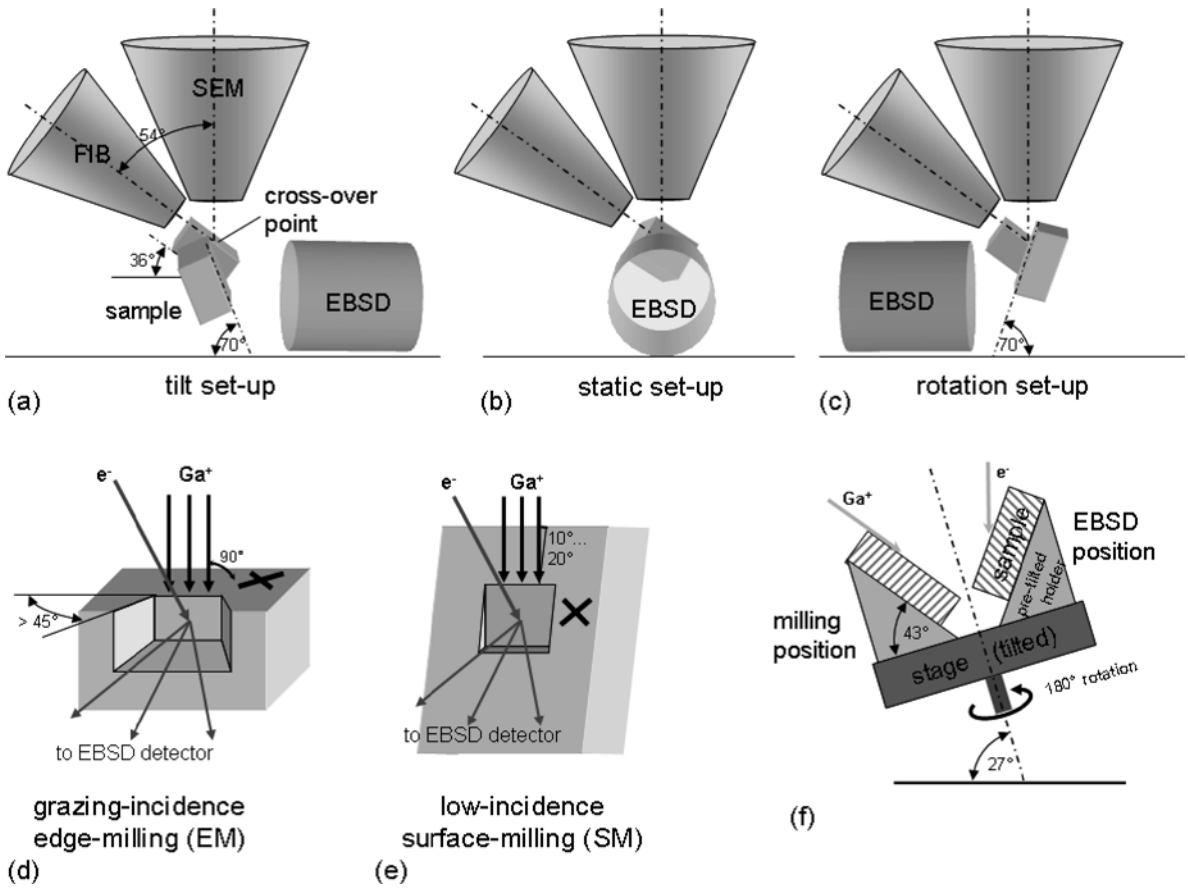


Fig. 8.1 Schematics of the different geometrical set-ups of the EBSD-FIB tomography. (**a**) The tilt geometry—the sample has to be tilted to change between the milling and the EBSD position, (**b**) the static set-up—the sample does not have to be moved at all, (**c**) the rotation set-up—the sample is rotated to change between the positions. Details of this rotation procedure are given in the sketch in figure (**f**). Figures (**d**) and (**e**) show the edge milling (EM) method and the surface milling (SM) method. Both methods can be applied to all tomography set-ups, but most easily for the tilt and static set-ups. For the rotation set-up, different holders are required to switch between EM and SM

between the electron and ion beam (Fig. 8.1c). This set-up is called the "rotation" set-up (Mulders and Day 2005). A third set-up—which has not, to the authors' knowledge, been used yet for 3D serial sectioning but probably offers the most powerful arrangement for 3D EBSD—is sketched in Fig. 8.1b: here the EBSD detector is mounted at 90° to both the electron beam and ion beam direction. If the sample is positioned appropriately, no sample movement between the milling and EBSD position is necessary at all. This set-up is therefore called the "static" set-up.

In tilt geometry a sample tilt between milling and EBSD of 70°–(90°–54°) = 34° is required, as illustrated in Fig. 8.1a. Since the sampled area usually cannot be brought into the eucentric tilt position of the stage, each sample tilt must be combined with an *x-y* translation movement of the stage. For the rotation geometry (Fig. 8.1c and f), on the other hand, the sample is positioned on a pretilted holder which itself is fixed to the pretilted stage. The stage is tilted to half the angle between the EBSD and FIB beam directions, thus to about 27°. The holder on the stage is then additionally inclined 43°, to reach 70°. In order to change between the milling and the EBSD position, the stage is now rotated about the (tilted) axis by 180°, usually followed by a translation in the *x-y* plane. For both geometries the fine tuning of the milling or EBSD position is accomplished by a beam shift. To this end a fiducial marker is applied to the surface. In the case of the tilt set-up this may be, for example, a cross milled into

the surface next to the investigated area. In the case of the rotation set-up two fiducial markers are necessary in order to correct the rotation angle.

Both the tilt and the rotation movement involve inaccuracies (though these are small on modern stage designs) which may limit the resolution obtainable with this technique. The inaccuracies are more severe for the tilt set-up, because the tilt angle cannot be directly controlled using the fiducial marker approach. There are, however, ways to measure and at least partially correct this inaccuracy. The determination of tilt inaccuracy is accomplished by measurement of the misorientation between neighbouring points in successive slices. In the orientation map, the correction of the tilt inaccuracy is easy because the related distortion of the measurement field is purely linear: a wrong tilt angle leads to expansion or compression of the measurement field in the direction perpendicular to the tilt axis. If the angle of tilt is α ($= 70^\circ$ for EBSD) and the tilt inaccuracy is $\Delta\alpha$, then the linear distortion of the measurement area is $(l_0 + \Delta l) / l_0 = \sin\alpha/\sin(\alpha - \Delta\alpha)$, where l_0 denominates the extension of the measurement area in the direction of the ion beam, and Δl is its distortion due to misalignment. For a tilt inaccuracy of 1° (which is larger than the accuracy of modern stages), the distortion of the EBSD map is on the order of 1%. Another effect of the tilt inaccuracy is the appearance of a certain milling depth inaccuracy. In fact, the depth inaccuracy increases with increasing length of the measured area, according to $\Delta l/l = \tan \Delta\alpha$, where l is the distance on the milled surface measured along the beam direction. For a tilt inaccuracy of 1°, this leads to a milling depth inaccuracy of about 1.7% of the milling area length.

For the rotation set-up, another source of inaccuracy has to be considered, which is related to the different working distances which are used for serial sectioning and EBSD observations. Milling is performed at a working distance given by the cross-over point of the ion and electron beam (usually 4–8 mm) while EBSD is usually carried out at a significantly larger working distance of more than 10 mm. Nevertheless, Z-axis movement should be avoided when changing between the two different positions because the Z position cannot be easily controlled or corrected during the process. A wrong Z position results in defocusing of the ion and electron beam. For the tilt set-up, the no-Z-movement requirement is easily satisfied: the noneucentricity of the stage tilt automatically leads to a decrease of the sample height in the EBSD position. For the rotation set-up, however, this condition is more difficult to satisfy. Ways to prevent Z-axis movement here are either to mill outside of the cross-over conditions (which is not convenient); to design the instrument such that the cross-over point is sufficiently low (which sacrifices lateral resolution of the FIB instrument); or to perform EBSD at a rather small working distance (which sacrifices EBSD performance because the EBSD detector is not illuminated under optimum conditions).

The third measurement geometry, the static set-up, of course avoids all problems of sample repositioning because the sample is not moved at all. The sample is positioned at a 70° tilt to allow for an optimum EBSD take-off angle. At the same time, the sample is rotated so that the ion beam illuminates this tilted surface at grazing incidence. Milling then occurs at the edge of the tilted specimen. Despite the favourable condition that the sample does not have to be moved, for this geometry the position of the cross-over point of the instrument also has to be carefully designed, because it is essential here that EBSD and milling are both set up at the cross-over point of the two beams. It is probably advisable to select a cross-over point at a working distance of 10 mm of the SEM.

For all the above mentioned geometries two 3D sectioning strategies are possible. The first, which we term the grazing-incidence edge milling method (EM), is illustrated in Fig. 8.1d. The sample is prepared by mechanical grinding and polishing to produce a sharp rectangular edge. Milling is performed at the grazing incidence to one surface of this sample edge. This method has the advantage of being easy to set up and allowing investigation of large volumes. In contrast, the microstructure to be investigated must be close to the sample edge, which is not always easily achieved or even possible at all. In this case, an alternative method may be applied, the low-incidence surface milling (SM) method, which is illustrated in Fig. 8.1e: the sample is tilted such that the ion beam enters the surface at an angle of $10–20^\circ$. The advantage of this method is that virtually any volume close to the sample surface can be investigated. The disadvantage is that the milling area needs to be significantly larger than in the case of EM in order to avoid shadowing of the EBSD detector. It should be mentioned that both the tilt and the static set-up allow free selection between the EM and SM method. In contrast, for the rotation set-up, the angle of incidence is fixed by

the angle of the pretilted holder. Thus, for each milling situation, a particular holder has to be available.

Besides the geometry of the microscope set-up, it is also important to consider the geometry of the milled volume. The most important point here is that the edges of the milled area may project a shadow onto the EBSD detector if they are too close to the investigated area. Usually it is required that the milled area be bounded by side walls that are inclined at angles larger than 45° on all sides, in order to allow shadow-free diffraction patterns, as shown in Fig. 8.1d. In order to avoid too extensive milling times, it is reasonable to remove the shadowing areas with a large ion beam current and mill only the investigated surface with a small ion current, i.e., a finely focused beam. This may be accomplished by defining a "milling list," which consists of a series of different milling commands with various beam currents.

8.3 Automatic 3D Orientation Microscopy

Automatic serial sectioning and EBSD mapping requires the synchronisation of SEM, FIB, and the camera control hardware. All participating processes are controlled by one 3D measurement program. Once the software is configured, it runs the milling and EBSD cycle until a predefined number of cycles has been reached. For the tilt set-up, a cycle consists of the following steps: (1) The EBSD camera is moved to its position in the chamber. (2) The fiducial marker is detected by image cross-correlation and the sample brought to its reference position using beam shift functions. (3) A reference image is taken in EBSD position. (4) Orientation mapping is performed using the predefined camera and mapping parameters. (5) The camera is retracted, the stage is moved to the predefined milling position, and the FIB gun is switched on if it was off. (6) The microscope is switched to FIB mode and the fiducial marker is detected by cross correlation. A shift of the ion beam brings the milling area into reference position. (7) A reference image is taken using the FIB beam to document the milling progress from the FIB position. (8) The FIB is switched to milling mode, the beam is shifted one serial sectioning step, and the commands in the milling list are carried out. (9) The FIB gun is switched off, if requested, and the stage is moved back to the predefined EBSD position.

Automatic 3D orientation microscopy puts high demands on the measurement process: (1) The stage positioning has to be accurate enough to allow redetection of the marker in each position within the limits of the beam shift controls. (2) The precision of the stage tilt must be high enough to avoid any visible distortion of the field of view. (3) The stage drift after sample repositioning must be minimized and the stage must reliably come to a complete stop within the range of tens of seconds. (4) The position correction algorithm must be precise enough to achieve the desired resolution. (5) The SEM and the FIB must work stably over long measurement times.

8.4 Software for 3D Data Analysis

Software for the data analysis and display of 3D orientation microscopy should, ideally, be able to render a 3-dimensional image of the microstructure and to reconstruct 3D grains and 3D boundaries on the basis of the measured orientations. A software tool that fulfils these requirements has been developed by Rowenhorst et al. (2006). In particular, its boundary rendering algorithms are extremely elaborate. Besides colouring grain boundaries according to the position of the local crystallographic normal vector in a standard orientation triangle, it also renders, for example, boundary curvature.

Another software tool has been presented by Mulders and Day (2005). Their software is able to render 3D orientation images of a microstructure, select individual grains, and deliver stereological data like volume, shape, size, and so on. A well-known public domain software package for 3D rendering is IMOD, which is based on the construction of 3D wire-frame models from 2D cuts (Kremer et al. 1996). We used the software ourselves for the presentation of 3D orientation data (Konrad et al. 2006). The software, however, is not based on orientation data but on colour information in 2D images; in most cases this has turned out to be impracticable for orientation microscopy.

The present authors also developed some so far rather rudimentary software, which will be used to represent our later examples. It presents the measured volume by sequential display of 2D microstructure

images. For preparation of the individual slice images, the batch processing function of the EDAX-TSL OIM Analysis software package is used. This function allows applying similar operations to any number of measured 2D data sets: for example, clean-up, map construction, and saving of images to disk. The 3D software furthermore contains a tool that allows manual selection of grain boundaries or other interfaces. Subsequently, the local grain boundary normals in the sample and crystal reference systems are calculated.

An important precondition for proper rendering of 3D data is the precise alignment of the slices. Although this is achieved to a large extent during the data acquisition process, the data still show misalignment between the slices. We therefore developed an alignment tool which is based on the calculation of a correlation function:

$$C_{ij} = \sum_{i,j} \left| \begin{pmatrix} \varphi_1 \\ \phi \\ \varphi_2 \end{pmatrix}_{r,(x,y)} - \begin{pmatrix} \varphi_1 \\ \phi \\ \varphi_2 \end{pmatrix}_{t,(x+i,y+j)} \right| \quad (8.1)$$

$$\text{for} \quad \Delta R_{r,t,(x,y)} \leq \Delta R_{\max}$$

Here the three Euler angles of an orientation, ϕ_1, Φ, ϕ_2, are interpreted as a Cartesian vector. The Euler vector at a position x, y in the reference orientation map is subtracted from the one at the position $x+i$, $y+j$ in the target map. A term is only added if the misorientation between the two compared points is smaller than a given threshold, $\Delta R_{\max}$, which accounts for the fact that the microstructure might locally change significantly between two subsequent slices. The position in which the sum over all differences C_{ij} is minimum produces the best alignment. Note that before C_{ij} is calculated, the Euler angles must be reduced to a single symmetric variant by multiplication of the orientation matrix by one of the symmetry element matrices of the respective crystal structure.

8.5 Application Examples

The measurement examples described in the following sections have all been collected in the authors' lab on a Zeiss-Crossbeam XB 1540 FIB-SEM, which consists of a Gemini-type field emission gun electron column and an Orsay Physics ion beam column. For EBSD, a DigiView camera of EDAX-TSL was mounted opposite to the FIB column on a motorised and computer-controlled slide. The geometric arrangement is a tilt set-up, as described earlier. The SEM was operated at an acceleration voltage of 15 kV, the FIB at 30 kV. The cross-over point of the system was at 8 mm, the EBSD working distance was about 12–14 mm.

8.5.1 The 3D Microstructure and Crystallography of Pearlite Colonies

Pearlite is a lamellar arrangement of ferrite (α-Fe with bcc lattice structure) and cementite (Fe_3C) that forms in a eutectoid reaction from austenite (γ-Fe with fcc lattice structure). In two-dimensional investigations, pearlite often exhibits characteristic bending of the lamella structure, which is related to a significant orientation change of the ferrite and likely also of the cementite. The occurrence of bending and of the related orientation change is an interesting hint of the physical mechanism of phase transformation. A 3D investigation of the arrangement of pearlite lamellae may yield new and otherwise inaccessible information: First, the direction of the maximum orientation gradients may be determined and spatially correlated with the strength of the lamella curvature. Second, the ferrite-cementite phase boundary might be precisely characterised with respect to the ferrite grain boundary normal.

For the example presented here, a simple high carbon steel Fe 0.49% sample was heated to 950°C and then furnace cooled at a rate of 0.1°C/s. The sectioning was carried out in the EM mode. 50 slices of 30 × 20 μm were milled with a step size of 100 nm. The milling of each slice took 10 min using an ion beam current of 500 pA. Additionally, on each side a coarse milling of 2 min at 2 nA was applied to remove the shadowing material. Orientation mapping was performed using a lateral step size of 100 nm. Only the ferrite phase was indexed, since cementite did not produce any indexable patterns. The time for one complete cycle was approximately 35 min, including 16 min for milling and 15 min for EBSD mapping.

Figure 8.2 displays the results of the measurements in the form of a 3D orientation map where the

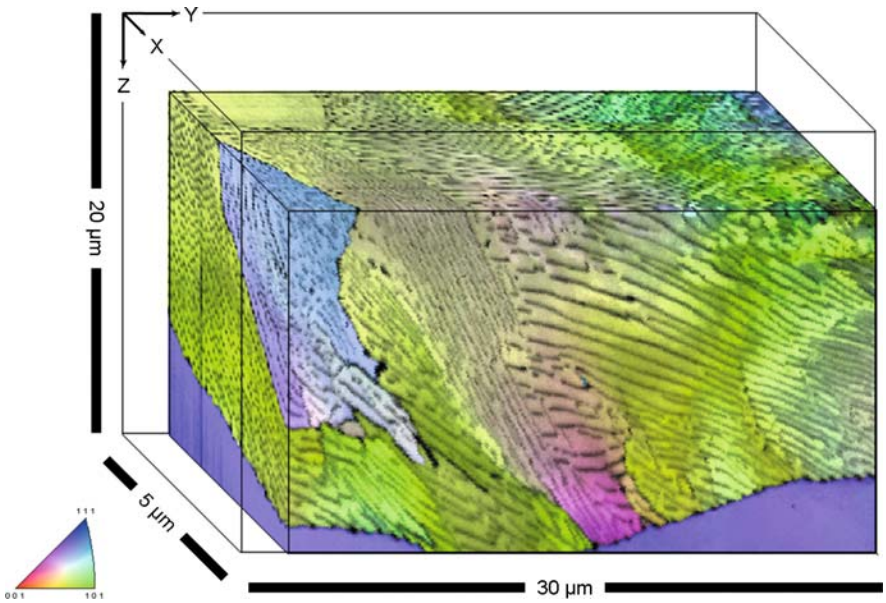


Fig. 8.2 3D orientation map of a pearlite microstructure. The colour is composed of image quality (grey value) and a colour code for the crystal direction parallel to the X-axis of the sample

colour of each voxel (volume pixel) is a combination of the diffraction pattern quality, which defines the brightness of the voxel, and the orientation of the measurement plane normal, which defines the colour according to the inverse pole figure colour triangle. Though cementite could not be indexed, the reduced ferrite diffraction pattern quality indicates the position of the lamellae. The cementite lamellae have a width of 100–200 nm and a distance varying between 200 and 400 nm. The figure shows the good alignment accuracy of the measurement: at many positions, it is possible to track the pearlite lamella through all three dimensions. Nevertheless, in areas where the lamellae are close together, their exact direction is not clear.

One of the most significant advances of 3D orientation microscopy compared to the 2D technique is the opportunity to determine grain or phase boundary planes. Here a semiautomatic tool is applied to measure the position of the boundary planes. From three user-selected points on a plane, the plane normal vector with respect to the sample and crystal coordinate system is calculated. The results are demonstrated in Fig. 8.3. Two sets of pearlite lamellae, 1 to 6 and 7 to 10 have been investigated. As indicated by the pole figures in Fig. 8.3b, in each of the lamellae groups the ferrite crystals continuously rotate about a (1 1 1) plane. The rotation pole, however, is different for each group. The position of the lamellae normals relative to the sample reference frame is displayed in the pole figures in Fig. 8.3c. The crystallographic indices of the ferrite side of the lamellae boundaries are shown in the inverse pole figures in Fig. 8.3d. The inverse pole figures show that the ferrite phase boundary is close to (1 1 1), albeit with a significant deviation of up to 16°. It has been shown by TEM investigations that the atomic habit plane of ferrite-cementite lamellae may be (1 2 5), (1 1 2), or (0 1 1) (see Zhou and Shiflet [1992] and Spanos and Aaronson [1990], for example), depending on the orientation relationship between both phases. While the (1 1 1) plane determined here deviates considerably from these results, it has in fact been shown that there is not necessarily any correspondence between the atomic habit plane and the macroscopic one (Hackney and Shiflet 1986).

8.5.2 Microstructure of "Nanocrystalline" NiCo Deposits

Electrodeposition from aqueous solution has been intensively studied as a method to create metallic films with nanocrystalline microstructure: e.g.,

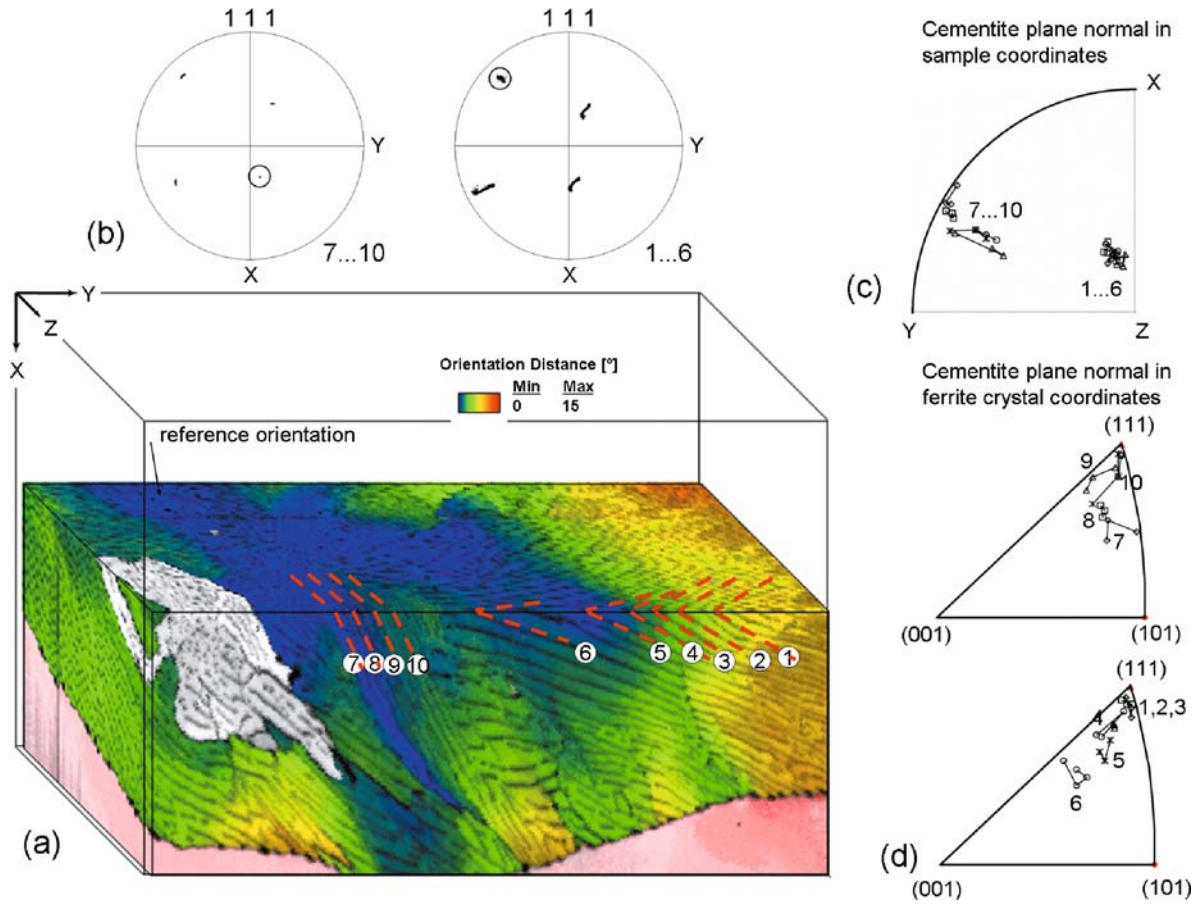


Fig. 8.3 Ferrite-cementite interface analysis on a 3D orientation map. (**a**) Microstructure displayed in reference-orientation coding (reference: orientation of the lamella-free area in the upper back corner; maximum misorientation 15°) with some cementite lamellae marked. (**b**) (111) Pole figure of the area of lamellae 7 to 10 (*left*) and 1 to 6 (*right*) indicating that each pearlite colony is characterised by one common (111) pole as rotation axis. The common pole is marked by a circle. (**c**) Stereographic projection of the cementite lamellae plane normals. (**d**) Inverse pole figure of the crystallographic ferrite plane normals of the cementite lamellae. For figures (**c**) and (**d**) each lamella position has been measured several times, indicated by similar symbols connected by lines

Vicenzo and Cavallotti (2004), Gómez et al. (1998), El-Sherik and Erb (1995), and Wu et al. (2005). The deposition parameters, such as solution composition, current density, and bath movement strongly influence the developing microstructure. The exact mechanisms of microstructure formation are still largely unknown, partly because a precise characterisation of the microstructure has rarely been undertaken. In a recently published work (Bastos et al. 2006) we applied EBSD-based high resolution orientation mapping to obtain a deeper knowledge of the microstructure of electrodeposited thin films of NiCo. Most of the investigated films consist of a large volume fraction of columnar crystals with cross sections in the submicrometer range but lengths on the order of more than 30 μm, as shown in Fig. 8.4a. For all columnar grains the $<1\,1\,\bar{2}\,0>$ direction is close to the growth direction of the crystal column. Only in niches beside these crystals do areas of truly nanocrystalline material exist. It was furthermore found that the elongated crystals are in most cases growing in triples of parallel crystals which are related to each other by a twin orientation relationship. The existence of these triples can be seen on the free grown surface of the electrodeposited material in the form of 3-fold pyramids, as shown in Fig. 8.4b. We suspect that the existence of

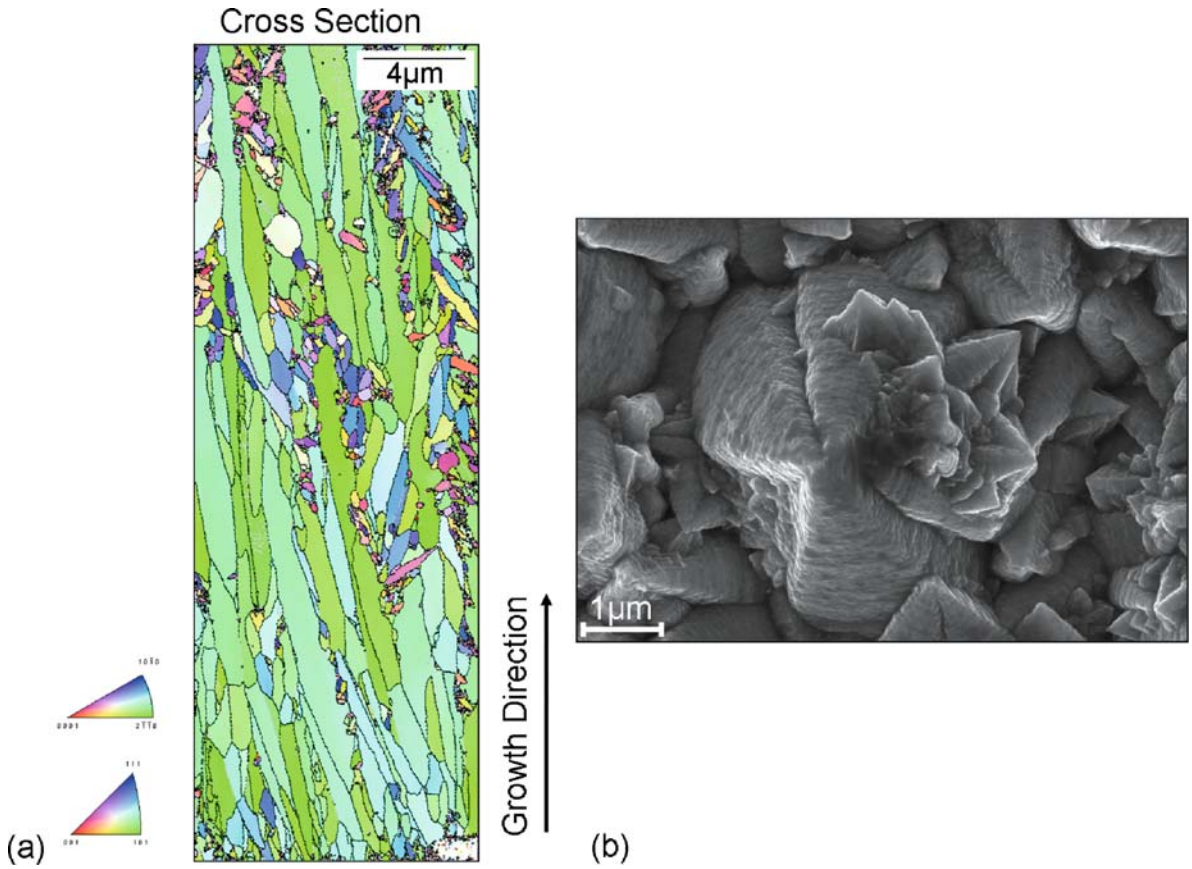


Fig. 8.4 (**a**) Cross section orientation map of the microstructure of columnar-grown NiCo electrodeposited film. (**b**) Surface morphology of the film, showing the formation of 3-fold pyramids

twins stabilizes the growth of columnar grains by the formation of low energy boundaries.

3D orientation microscopy was performed on a full, 100-µm wide cross section of an electrodeposited material. The sample was manually ground and polished on the cross sections to produce a sharp rectangular edge, as shown in Fig. 8.5. 3D orientation microscopy was performed using the EM method. A step size of 100 nm in all dimensions was selected and 60 maps covering a volume of 83 × 16 × 6 µm were measured within less than two days. The results are shown in Fig. 8.6a as a 3D orientation map, coloured according to the inverse pole figure of a direction perpendicular to the growth direction. Random large angle grain boundaries are coloured black, while all possible twin boundaries are displayed as white lines. In the centre of the map a part has been cut out to expose a typical twin-triple consisting of three grains with two 56° $<1\,1\,\bar{2}\,0>$ twin relations between them

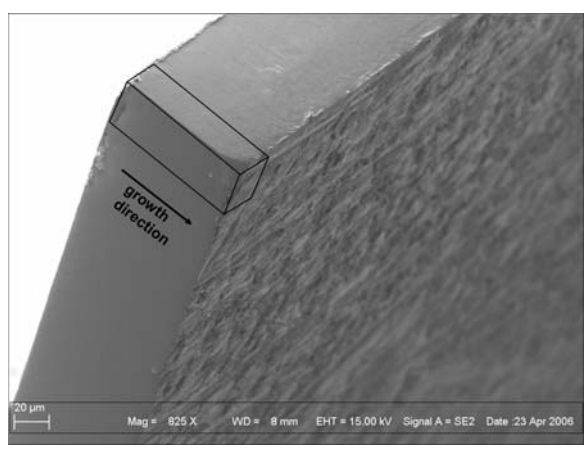


Fig. 8.5 Secondary electron image of the cross section of the NiCo thin film ready for 3D orientation microscopy. The investigated volume is indicated by a black line frame, the growth direction by an arrow. The rectangular edge has been prepared by mechanical grinding and polishing

and an approximately 66° $<1\,1\,\bar{2}\,0>$ relationship on the remaining boundary. In Fig. 8.6b the block is cut along the plane that contains this twin triple. The triple is not growing straight, but is visibly quite heavily curved. Together with this curvature the orientation of the triple changes, as shown by the colour code of the figure, which displays the deviation of the macroscopic growth direction from the $<1\,1\,\bar{2}\,0>$ crystal direction.

From Fig. 8.6b, note that the grains (1) and (2) exist as twins with a sharp 57° $<1\,1\,\bar{2}\,0>$ relation when they first enter into the measurement area (marked as point A in Fig. 8.6b); note also that grain (2) is not visible in the figure as it is on top of grain (1). At point B, grain (3) nucleates and grows for the first approximately 10 μm as a very thin tube parallel to grains (1) and (2). Where the grains reach a position for optimum growth (i.e., $<1\,1\,\bar{2}\,0>$ parallel to the macroscopic GD), grain (3) also expands and grows larger (point C). At this position the grain boundary characteristics are determined in more detail; the results are displayed in Fig. 8.7. Between grains (1) and (2) a $\{1\,0\,\bar{1}\,1\}$ coherent twin boundary is found. Grain (3), although it shows a precise twin orientation relation with grain (2), does not have a coherent boundary with

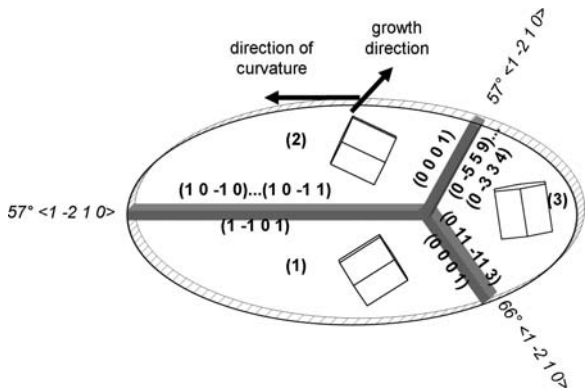


Fig. 8.7 Grain boundary analysis on the twin triple observed above. Crystals (1) and (2) form a coherent 57° $<1\,1\,\bar{2}\,0>$ compression-type twin. Crystal (3) is in a noncoherent twin relation to crystal (2), but it has no special relationship with (1). Grains (2) and (3) and (1) and (3) have basal planes as boundary planes

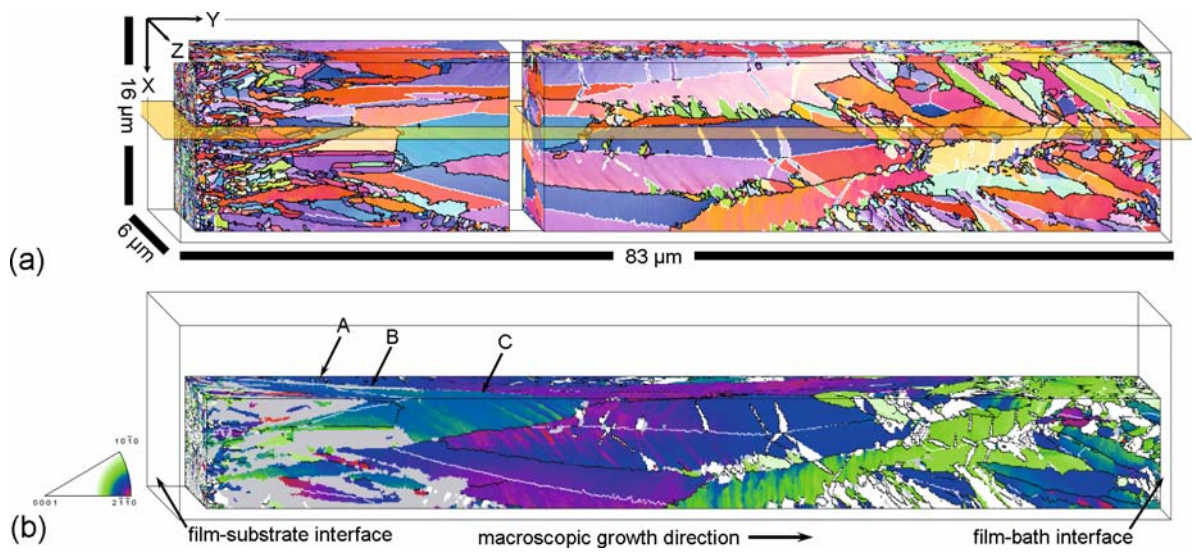


Fig. 8.6 3D orientation maps from a NiCo electrodeposited film. Measurement voxel size 100 × 100 × 100 nm^3. (**a**) The full measured orientation map coloured according to the inverse pole figure of the X-direction. General large angle grain boundaries ($\theta > 15°$) are displayed in black, all kinds of twin boundaries in white. A part is cut-out in the middle to display the position of one twin triple, marked by a circle. (**b**) Orientation map coloured according to the deviation of the crystal $<1\,1\,\bar{2}\,0>$ direction from the macroscopic growth direction Y. Areas in gray indicate crystals with fcc crystal structure. The structure is cut along the plane marked in (**a**). The markers A, B, and C indicate particular positions in the formation of the twin triple. Note that the scattered white pixels on top of the crystal marked A occur due to the twin boundary being almost parallel to the cutting plane

the latter, i.e., the plane indices on both sides of the grain boundary are different, the one of grain (2) being very precisely the (0 0 0 1) basal plane, the other being some quite highly indexed one. The same is true for the boundary with grain (1), although this grain boundary does not even show any typical twin orientation relationship. We conclude that the triple grain arrangement forms low energy boundaries which support the growth of the triples; see Bastos et al. (2008) for more information.

8.6 Discussion

8.6.1 Accuracy and Application Limits

The 3D orientation microscopy system fully preserves the powerful functions of EBSD-based 2D orientation microscopy and extends them into the 3rd dimension. Important parameters to assess the performance of this technique are (i) the spatial resolution, (ii) the angular resolution, and (iii) the maximum size of the observable volumes with regard to the long-term stability of the instrument.

(i)The spatial resolution of the system results from the *lateral* resolution achieved on the 2D sections, the accuracy of alignment of the sections, and the *depth* resolution. The lateral resolution of EBSD-based 2D orientation microscopy is on the order of 30–100 nm on a FEGSEM (e.g., Zaefferer 2007). During measurement, alignment of the serial sections is achieved by recognition of a fiducial marker and positioning it via beam shifts. Additional slice alignment procedures can be applied in a postprocessing step as described above. An important prerequisite for application of the image recognition tool is that the alignment marker lies within the visible image after each stage repositioning. Current stages allow a sufficiently high stage positioning accuracy of at maximum 2 μm in the x and y directions and $< 1^\circ$ for the tilt (see point (ii)).

The *depth* resolution, i.e., the information depth of EBSD, was found to be less than 10 nm for medium atomic number materials (Zaefferer 2007). This value, therefore, defines the lower limit of the achievable 3D depth resolution. This value is inconsequential because the slice cutting is less precise than this: it is, for example, difficult to prepare thin foils for TEM via FIB milling with a thickness below 50 nm. The accuracy of cutting in the automated system is defined mainly by the FIB image resolution and the accuracy of automatic image alignment. The pattern recognition precision is, at best, as good as one pixel in the digital image, provided that image resolution is high enough. For a 50 pA beam, which is usually used for image alignment, image resolution is better than 20 nm. Therefore, for a sufficiently high magnification, it is theoretically possible to reach approximately 20 nm depth resolution. In reality, we found that the image recognition is usually less precise than one pixel, i.e., in the order of three or four pixels. Thus, a FIB image magnification of 20,000 × is required to reliably obtain 50 nm image positioning accuracy. Also, the accuracy of the stage tilt has an influence on the accuracy of milling, as was shown in Section 8.2. A deviation of 1° from the predefined cutting angle results in a deviation of 170 nm at the bottom of a 10-μm long milling field. Usually the tilt accuracy is better, but we believe that a depth resolution value of 50 nm represents the best resolution currently achievable. Most of the studies performed so far have been carried out with 100 nm step sizes in all directions, which gives satisfactory section alignment. The pearlite lamellae shown in Fig. 8.2 display a particularly well-suited structure for testing the resolution of a 3D EBSD system, because the continuity of the lamellae is a particularly critical measure for the accuracy of alignment. In the present example there are areas where the lamellae appear perfectly aligned, particularly on the upper part of the measured block. However, other areas, at the lower part of the milled area in particular, show lamellae which cannot be uniquely grouped together.

(ii) The angular resolution of the 2D EBSD technique is on the order of 0.5° for high speed measurements. On a 3D EBSD tilt set-up system, this value may be larger due to inaccuracy of the stage tilt. By measuring the orientation variation from slice to slice inside a well-recrystallised grain of constant orientation, we found for the authors' instrumentation an average tilt imprecision of 0.5°. For typical orientation microscopy applications, therefore, the angular resolution of 3D EBSD is as good as that of the 2D technique. Since the angular misalignment between two slices affects all pixels in a map in a similar way, the misalignment can be approximately determined—and thus

corrected—by calculation of the average misorientation of all neighbouring points in neighbouring slices, excluding all points that have a misorientation larger than a certain threshold value.

(iii) The maximum size of the observable volume depends mainly on the material and on the time investment one wants to make. While the width of the milled surface is virtually unlimited, the height of the observable surface depends on the sensitivity of the sample material to curtaining. In fact, from a certain distance to the top edge of the milled area, intense ion beam scattering prevents the formation of smooth surfaces and good EBSD patterns, and renders the depth position very imprecise. The distance at which curtaining starts depends strongly on the material, its microstructure and crystal orientation, the quality of the top surface, and the milling current. To date, the largest curtain-free height obtained by the author is larger than 60 μm on an FeNi sample milled with 500 pA beam current. Other authors (West 2007, private communication) reached a milling area height of almost 100 μm on a Ni-base superalloy.

The number and maximum thickness of milled sections are, like the width, in principle unlimited. However, with increasing milling depth, the milled volume has to be increased in order to prevent shadows on the EBSD screen and serious redeposition of milled material on the sides of the milled volume. The volume-limiting parameter is therefore the milling time: a curtain-free area of 20 × 20 μm may be milled 1 μm into a low-alloy steel sample in approximately 15 min with a beam current of 500 pA. The sides of the volume may be milled with a larger beam current at a higher rate, since they don't require any surface quality. We believe that the largest volume accessible with the methods presented here is on the order of $w \times h \times d = 50 \times 50 \times 50$ μm. Other groups have shown that by using a particular sample preparation (e.g., a "finger," prepared by mechanical machining), still larger volumes can be obtained (Groeber et al. 2006).

Large volumes or high resolution measurements require long measurement times and therefore long-term stability of the instrument, in particular, of the FIB gun. The longest successful measurements performed with the authors' equipment lasted about five days. During this time the FIB gun was not continuously switched on but switched automatically off during the EBSD measurements.

8.6.2 Materials Issues

On many metals and intermetallics investigated so far (e.g., various ferritic, austenitic and martensitic steels, nickel, copper, aluminium, FeAl, CuZnAl), excellent diffraction patterns were obtained from milled surfaces, and the microstructures observed on these were similar to those prepared by other methods. Nevertheless, various problems exist. One is the amorphisation of certain materials. We have observed, for example, that Nb-containing Laves-phase precipitates in Fe_3Al, which give sharp diffraction patterns after mechanical preparation, do not give any patterns when prepared by milling (Konrad et al. 2006). Similar effects have been observed on certain carbides. It is known from silicon, that Ga^+ ion beam milling with 30 kV ions creates an amorphous layer of approximately 20 nm thickness (Kato et al. 1999), which is too thick for EBSD. On TEM sample preparation, low-kV ion polishing subsequently reduces the thickness of the amorphous layer significantly. It is possible, but not yet tested, that this would help also with 3D orientation microscopy. A second, serious problem has been observed when milling steels with metastable residual austenite, for example low-alloyed TRIP steels. Here, all austenite transforms under the influence of the ion beam into ferrite. Up to now, this transformation could not be avoided by either small beam currents or by low-kV milling, or by a milling with Ar^+ ions. Finally, we observed that the microstructure of heavily deformed aluminium may be destroyed by intense ion beam irradiation, which can probably be attributed to the formation of a low-temperature melting Al-Ga eutectic.

8.7 Conclusions

Automated 3D orientation microscopy yields a multi-dimensional data vector for each voxel of the measured volume, including the crystal orientation, the crystallographic phase, a value for the lattice defect density, and, if measured by simultaneous EDS analysis, the elemental composition. A volume pixel resolution of $100 \times 100 \times 100$ nm^3 has been obtained as a standard but $50 \times 50 \times 50$ nm^3 seems to be a realistic optimum. Other authors have claimed an even better resolution of $20 \times 20 \times 20$ nm^3 (Mulders and Day

2005). The largest volumes observable are on the order of 50 × 50 × 50 μm. On particular materials (Ni-based superalloys), larger volumes have been reported. The technique works on a large number of materials, but some exceptions have been found where the material's microstructure is significantly changed under Ga^+ ion beam irradiation.

Until recently the measurement time was still long, from about 30 min to more than 1 h per cycle. Recent advances in EBSD camera technology and in the optimisation of milling strategies have shortened these times significantly. The EBSD pattern acquisition rate increased from 70 patterns per second to almost 200 patterns per second. The milling times may be shortened by more than a factor of 2. The time per cycle therefore develops in the direction of 10–30 min.

One main disadvantage of the FIB-EBSD tomography is the fact that it is a destructive technique, thus 3D observations of materials processes can not be performed. However, the introduction of computer simulation tools offers the possibility of investigating the evolution of microstructures. A second serious disadvantage is the relatively small volume that can be observed with the technique. Statistical data, like grain size distributions or textures, thus may be quite questionable and must be carefully checked. Here another powerful technique, the combination of EBSD with serial sections created by mechanical polishing (MP-EBSD tomography), allows a large extension of the observed volume. Unfortunately, this technique (MP-EBSD tomography) is extremely laborious and is, in fact, difficult to be automate fully. In comparison to the newly developed 3D X-ray diffraction techniques, the strength of the FIB-EBSD tomography technique lies in its significantly higher spatial resolution, its applicability also to highly deformed or multiphase structures, and its ease of application.

References

Adams BL (1986) Description of the intercrystalline structure distribution in polycrystalline materials. Metall Trans 17A:2199

Adams BL, Morris PR, Wang TT, Willden KS, Wright SI (1987) Description of orientation coherence in polycrystalline materials. Acta Metall 35:2935

Bastos A, Zaefferer S, Raabe D, Schuh C (2006) Characterization of the microstructure and texture of nanostructured electrodeposited NiCo using electron backscatter diffraction (EBSD). Acta Mater 54:2451–2462

Bastos A, Zaefferer S, Raabe D (2008) 3-Dimensional EBSD study on the relationship between triple junctions and columnar grains in electrodeposited Co-Ni films. J Microsc 230:487–498

Cheng Z, Sakamoto T, Takahashi M, Kuramoto Y, Owari M, Nihei Y (1998) Development of ion and electron dual focused beam apparatus for high spatial resolution three-dimensional microanalysis of solid materials. J Vac Sci Technol B 16:2473–2478

El-Sherik AM, Erb U (1995) Synthesis of bulk nanocrystalline nickel by pulsed electrodeposition. J Mater Sci 30: 5743–5749

Gómez E, Ramirez J, Vallés E (1998) Electrodeposition of Co-Ni alloys. J Appl Electrochem 28:71–79

Groeber MA, Haley BK, Uchic MD, Dimiduk DM, Gosh S (2006) 3D reconstruction and characterization of polycrystalline microstructures using a FIB-SEM system. Mater Charact 57:259–273

Hackney SA, Shiflet GJ (1986) Anisotropic interfacial energy at pearlite lamellar boundaries in a high-purity Fe-0.80-percent C-alloy. Scripta Metall 20:389–394

Howard CV, Reed MG (1998) Unbiased stereology—Three-dimensional measurement in microscopy. Bios Scientific Publications, Oxford

Jin H, Wu PD, Ball MD, Lloyd DJ (2005) Three-dimensional texture determination of 6111 aluminium alloy sheet by precise serial sectioning and EBSD measurement. Mater Sci Technol 21:419–428

Kato NI, Kohno Y, Saka H (1999) Side-wall damage in a transmission electron microscopy specimen of crystalline Si prepared by focused ion beam etching. J Vac Sci Tech A17:1201–1204

Konrad J, Zaefferer S, Raabe D (2006) Investigation of orientation gradients around a hard Laves particle in a warm-rolled Fe3Al-based alloy using a 3D EBSD-FIB technique. Acta Mater 54:1369–1380

Kremer JR, Mastronarde DN, McIntosh JR (1996) Computer visualization of three-dimensional image data using IMOD. J Struct Biol 116:71–76

Lauridsen EM, Schmidt S, Nielsen SF, Margulies L, Poulsen HF, Juul-Jensen D (2006) Non-destructive characterization of recrystallization kinetics using three-dimensional X-ray diffraction microscopy. Scripta Mater 55: 51–56

Margulies L, Winther G, Poulsen HF (2001) In situ measurement of grain rotation during deformation of polycrystals. Science 291:2392

Matteson TL, Schwarz SW, Houge EC, Kempshall BW, Gianuzzi LA (2002) Electron backscattering diffraction investigation of focused ion beam surfaces. J Electron Mater 31:33–39

Michael JR, Schischka J, Altmann F (2003) HKL technology EBSD application catalogue. HKL Technology, Hobro, Denmark

Mulders JJL, Day AP (2005) Three-dimensional texture analysis. Mater Sci Forum 495–497: 237–242

Poulsen HF et al (2001) Three-dimensional maps of grain boundaries and the stress state of individual grains in polycrystals and powders. J Appl Cryst 34:751

Prasad SV, Michael JR, Christenson TR (2003) EBSD studies on wear-induced subsurface regions in LIGA nickel. Scripta Mater 48:255–260

Preusser A, Klein H, Bunge HJ (2005) Texture and microstructure imaging by the moving area detector method. Solid State Phenom 105:41334

Rohrer GS, Saylor DM, El-Dasher BS, Adams BL, Rollett AD, Wynblatt P (2004) The distribution of internal interfaces in polycrystals. Z Metallkd 95:197–214

Rowenhorst DJ, Gupta A, Feng CR, Spanos G (2006) 3D crystallographic and morphological analysis of coarse martensite: Combining EBSD and serial sectioning. Scripta Mater 55:1112016

Sheng TT, Goh GP, Tung CH, Wang LF (1997) Precision transmission electron microscopy sample preparation using a focused ion beam by extraction method. J Vac Sci Technol B 15:610–613

Spanos G (2006) Viewpoint set no. 41 "3D characterization and analysis of materials." Scripta Mater 55:3

Spanos G, Aaronson HI (1990) The interfacial structure and habit plane of proeutectoid cementite plates. Acta Metall Mater 38:2721–2732

Uchic MD, Groeber M, Wheeler R, Scheltens F, Dimiduk DM (2004) Augmenting the 3D characterization capability of the dual beam FIB-SEM. Microsc Microanal 10: 1136–1137

Vicenzo A, Cavallotti PL (2004) Growth modes of electrodeposited cobalt. Electrochim Acta 49:4079–4089

Wu BYC, Ferreira PJ, Schuh CA (2005) Nanostructured Ni-Co alloys with tailorable grain size and twin density. Metall Mater Trans A 36:1927–1936

Yang W et al (2004) Differential-aperture X-ray structural microscopy: A submicron-resolution three-dimensional probe of local microstructure and strain. Micron 35:431

Zaafarani N, Raabe D, Singh RN, Roters F, Zaefferer S (2006) Three-dimensional investigation of the texture and microstructure below a nanoindent in a Cu single crystal using 3D EBSD and crystal plasticity finite element simulations. Acta Mater 54:1863–1876

Zaefferer S (2007) On the formation mechanisms, spatial resolution and intensity of backscatter Kikuchi patterns. Ultramicroscopy 107:254–266

Zaefferer S (2008) 3D EBSD-based orientation microscopy and 3D materials simulation tools: An ideal combination to study microstructure formation processes. In: Luysberg M, Tillmann K, Weirich T (eds) EMC 2008, Vol. 1: Instrumentation and methods. Springer-Verlag, Berlin, pp 641–642

Zaefferer S, Konrad J, Raabe D (2005) 3D-orientation microscopy in a combined focused ion beam (FIB)-scanning electron microscope: A new dimension of microstructure characterisation. Microscopy Conference 2005, Davos, p 63

Zaefferer S, Wright SI, Raabe D (2008) 3D-orientation microscopy in a FIB SEM: A new dimension of microstructure characterisation. Metall Mater Trans 39A:374–389

Zhou DS, Shiflet GJ (1992) Ferrite-Cementite crystallography in pearlite. Metall Trans 23A:1259–1269

Chapter 9

Collection, Processing, and Analysis of Three-Dimensional EBSD Data Sets

Michael A. Groeber, David J. Rowenhorst, and Michael D. Uchic

9.1 Introduction

Three-dimensional (3D) characterization methods are required to completely determine microstructural descriptors such as the true shape and size of features, the number of features, and the connectivity between these features. Experimental methods to characterize microstructure in 3D have undergone dramatic improvements in the past decade, and there now exists a host of methodologies that are capable of determining 3D microstructural information, ranging from counting individual atoms to imaging macro-scale volumes. The state of the art for this field has been reviewed recently in a Viewpoint Set for Scripta Materialia (Spanos 2006).

This chapter focuses on the specific topic of experimental interrogation and analysis of microstructural features such as grains or precipitates in 3D that includes crystallographic orientation data. Currently there are two main experimental pathways to collect such information. Serial sectioning experiments are more commonplace, but consume the sample as part of the experiment; while X-ray methods are nondestructive, but typically require the use of high-intensity X-ray sources. For the X-ray methods, there are a handful of groups world-wide that are working towards spatially-resolved crystallographic analyses of grain structures in 3D using high-intensity X-ray systems (Schmidt et al. 2004; Lauridsen et al. 2006; Budai et al. 2004, 2008; Lienert et al. 2007). These methods have a significant advantage in that the sample remains intact after analysis, allowing for the possibility of time-dependent studies of microstructural changes due to thermal or mechanical input. Nonetheless, these experiments require the high brilliance of a synchrotron source, which puts significant restrictions on the general applicability of the methods.

Therefore, the focus of this chapter is on the collection, processing, and analysis of grain-level data using more universally-accessible serial section experiments, where electron backscattered diffraction (EBSD) maps are used as an integral component of the characterization method. The incorporation of crystallographic maps enables a straightforward approach to defining the individual grains or precipitates that compose aggregate assemblies, and also allows for orientation-based data analysis—for example, determining the disorientation between neighboring grains, or assessing the complete character of grain boundaries (Saylor et al. 2004a; Kim et al. 2006).

The authors of this chapter have assumed that the reader has knowledge of most basic aspects of crystallography and is aware of some of the commercial packages pertaining to EBSD data collection and analysis. We recommend the first volume of this book to anyone interested in additional background information.

9.2 Data Collection

Serial sectioning experiments are comprised of two main tasks—sectioning and data collection—which are repeated until the desired volume of material has been interrogated. The sectioning process involves the removal of a known volume of material, usually with

M.A. Groeber (✉)
Wright Patterson Air Force Base, Dayton, OH 45433, USA
e-mail: michael.groeber.ctr@wpafb.af.mil

A.J. Schwartz et al. (eds.), *Electron Backscatter Diffraction in Materials Science*,
DOI 10.1007/978-0-387-88136-2_9, © Springer Science+Business Media, LLC 2009

the requirement that the newly-exposed surface be as planar as possible. The amount of material removed, i.e., the serial sectioning thickness, is primarily determined by the size-scale of the microstructural features that are to be examined. A typical rule of thumb is to acquire a *minimum* of 10 sections per average feature if feature shape is to be determined. The section thickness is often a compromise between the desire for high-fidelity data and the constraints of both personnel and instrument time to collect the data sets. Note that the serial section thickness is usually uniform throughout the experiment to simplify data processing, but fiducial marks can be added to track differences due to intentional variations or experimental error.

After sectioning, the surface of interest is characterized through standard imaging methods, or other mapping methods such as EBSD. There are a couple of factors that one must consider in order to successfully incorporate EBSD data into a serial sectioning experiment. Obviously, the material sectioning process must be capable of producing a "low damage" surface that allows for the EBSD patterns to be successfully indexed. For example, mechanical sectioning procedures often produce some damage, and so multiple processing steps may be required in order to minimize surface damage at the completion of the sectioning process, such as the combination of mechanical polishing followed by vibratory, chemical, ion, or electropolishing. Also, another practical concern is that EBSD data collection typically adds significant overhead to the time required to complete an experiment, because of the relatively slow data acquisition speed compared to standard electron imaging methods. These time constraints can be addressed by collecting complementary data, for example, both EBSD maps and SEM images, where EBSD data is collected less frequently than the image data (i.e., every *n*th slice) (Rowenhorst et al. 2006).

The combination of serial sectioning via mechanical polishing and EBSD mapping was initially demonstrated by Wall et al. (2001) and Saylor et al. (2001), and later by groups at the Naval Research Laboratory to examine grain aggregate microstructures (Lewis et al. 2006) and martensite precipitates (Rowenhorst et al. 2006). One significant advantage of using mechanical sectioning methods to perform this experiment is that the dimensions of the serial sectioning surface can be very large ($>$1 mm). This allows for the characterization of microstructural features that are typically larger than a few microns in scale. Also, mechanical polishing equipment is usually available in most materials science laboratories, and the procedures for producing high-quality surfaces are well understood. A possible disadvantage is that it may be difficult with mechanical polishing to consistently obtain serial section thickness below a few hundred nanometers in scale, although there are examples in the literature of successful serial mechanical polishing even at this scale (Lund and Voorhees 2002). Also, at present this experiment must be performed manually.

In addition to mechanical sectioning, ion-based micromilling using Focused Ion Beam-Scanning Electron Microscopes (FIB-SEMs) have also been used for EBSD-inclusive serial sectioning studies (Groeber et al. 2004, 2006; Zaafarani et al. 2006). The high precision of FIB milling can produce a finer serial sectioning thickness than can be performed by mechanical polishing, but the limited milling speed of FIB microscopes usually results in a much smaller analysis volume. The surface damage produced by FIB milling using 30 kV Ga ions can be moderate enough to allow for EBSD pattern collection from some materials such as Ni and Fe. It is worth noting that the process for serial sectioning and EBSD pattern collection has been automated on two of the commercial microscope systems. Note that this technique is covered in more detail in the chapter in this book by Zaefferer.

9.3 Processing Strategies

9.3.1 Registration and Alignment of Sections

It is often the case that misalignment between sections occurs during the sectioning experiment and can cause difficulties in the subsequent analysis of the dataset. These misalignments can be minimized through the use of fiducial marks coupled with manual and automated alignment tools during the data collection process, but can rarely be totally avoided. This section will address techniques used to adjust sections after the collection process has completed. First, the generalized alignment solution is discussed and then the special condition involving EBSD data is presented. It is important to note that manual sectioning

processes are typically more susceptible to misalignment errors. Automated processes, such as FIB-OIM data collection, can incorporate procedures for very precise positioning of the sample following movements after sectioning and imaging. In the case of the FIB-OIM, image recognition software has been demonstrated to be able to place the sample to within 0.1 microns and 0.1 degrees of the desired position, removing nearly all misalignment (Groeber et al. 2006).

The most straightforward registration procedures involve applying simple translations and rotations to sections to improve section-to-section alignment. In the general case, this can be done with images and image processing techniques like least-square difference fitting or image convolution. In these procedures, images are translated (generally at multiples of the pixel size) or rotated in the plane of the image until either a minimum difference or maximum product between pixels in consecutive images is obtained.

Often the registration of separate serial sections requires more than simple translations and rotations of the sections to gain proper alignment of the image stack. This is most prevalent when combining data collected by different methods, such as micrographs from a light optical microscope and EBSD scans from a SEM, where there may be different coordinate orientations, and scaling between pixels. However, these same techniques can be applied to remove distortions or drift during data collection within a set of serial EBSD scans.

The alignment of the images begins by identifying a number of point features (examples would include the centers of grains, or triple junctions). One then must choose a reference frame to which the image is aligned, either a SEM/EBSD image that is relatively free of drift, or an optical image (hereby noted as X', Y'). The points in the EBSD scan (X, Y) should then be brought into coincidence with the reference frame. The transformation from the EBSD image to the reference optical image is given by:

$$\begin{bmatrix} X' \\ Y' \\ 1 \end{bmatrix} = T \begin{bmatrix} X \\ Y \\ 1 \end{bmatrix}, \tag{9.1}$$

where T is a two-dimensional transformation matrix of the form:

$$T = \begin{bmatrix} t_{11} & t_{21} & t_{31} \\ t_{12} & t_{22} & t_{32} \\ 0 & 0 & 1 \end{bmatrix}.$$

In the most general case, T describes an affine transformation. An affine transformation is a transformation that preserves colinearity and the ratio of distances, but not necessarily angles. Affine transformations can be considered as linear combinations of image rotation and independent scaling and shearing in each direction, combined with a translation. The components of the affine transformation matrix, T, can be solved using the pseudo inverse matrix (a least squares fit to a system of linear equations).

However, by allowing shearing of the images, it is not possible to independently determine the rigid rotation of the two coordinate frames, which is necessary to correct the measurement of the crystallographic orientations between each section. Therefore a limited transformation matrix can be used that allows only independent scaling in the x-direction and y-direction, S; translations in the x-direction and y-direction, P; and finally an image rotation normal to the sectioning plane, R. Thus:

$$T = RPS, \tag{9.2}$$

where:

$$R = \begin{bmatrix} \cos(\theta) & -\sin(\theta) & 0 \\ \sin(\theta) & \cos(\theta) & 0 \\ 0 & 0 & 1 \end{bmatrix}; P = \begin{bmatrix} 1 & 0 & P_x \\ 0 & 1 & P_y \\ 0 & 0 & 1 \end{bmatrix};$$

$$S = \begin{bmatrix} S_x & 0 & 0 \\ 0 & S_y & 0 \\ 0 & 0 & 1 \end{bmatrix}.$$

The terms in the transformation matrix are then determined by a least-squares optimization.

As mentioned, errors associated with translations and rotations in the plane orthogonal to the sectioning direction can be corrected in image space by processes such as least-square difference fitting, image convolutions, and Fourier transforms. However, these methods may not utilize all of the data in an image equally, and image conditions can vary significantly between sections. EBSD data for consecutive sections enables the use of all data points equally, and generally provides a more invariant parameter to follow between sections.

The misorientation between a data point and the corresponding data point on a neighboring section can be calculated for all points in a given section. A parameter (Ψ) can then be created to define the amount of misalignment between the two sections. The sections can be translated to locate the position of minimum Ψ. The definition of Ψ is given by:

$$\Psi(k) = \sum_{j=0}^{y_{\max}} \sum_{i=0}^{x_{\max}} \Psi(i, j, k), \tag{9.3}$$

where $x_{\max}$ and $y_{\max}$ are the total number of data-points in the corresponding directions, and $\Psi(i, j, k)$ is given by:

$$\Psi(i, j, k) = \begin{cases} 1 & \text{if } M[P(i, j, k), P(i, j, k-1)] \geq 5^\circ \\ 0 & \text{otherwise} \end{cases},$$

where $M[P(i, j, k), P(i, j, k-1)]$ is the misorientation between points *i,j,k* and *i,j,k*-1.

Following completion of the alignment procedures, the data set exists in the form of a 3D volume made up of voxels. Each voxel contains at a minimum the following characteristics: the x, y, and z positions within the array, and quantities that describe the local orientation, such as the three Euler angles $\{\phi_1,\Phi,\phi_2\}$.

9.3.2 Segmentation of Grains

Segmentation of individual grains is necessary to allow for the measurement of each grain as a separate feature. Additionally, identifying and separating microstructural constituents provides the ability to investigate features removed from their surroundings. Grain segmentation is greatly aided by the quantitative orientation information provided by the EBSD maps, as local orientation information is the most direct means to group voxels and thus reduce issues of image contrast, thresholding, and feature identification. During segmentation, grains are identified as groups of voxels that share a similar orientation. An algorithm for identifying these groups of voxels has been presented previously (Groeber et al. 2008; Bhandari et al. 2007). Commercial analysis packages (TSL, HKL) likewise use a similar approach to identifying grains. The major steps of the algorithm are outlined in this section.

The initiation of each identified grain is the selection of a seed voxel. Generally, it is a useful idea to select a voxel that has been deemed to be of "good" quality. Quality is defined by the EBSD data collection software and refers to the sharpness of the pattern, which is often correlated with confidence in the assigned orientation. Usually the highest quality data tends to lie within the center of a grain, and these voxels serve as a reliable point to begin grain segmentation. A grain is then defined as the set of voxels contiguous to and with the same orientation as the seed voxel. The requirement of the voxels to have the same orientation (within a defined tolerance) is based on the fact that all regions within a grain should share a similar orientation. A list of voxels assigned to the grain is created, which initially contains only the seed voxel. The voxels that neighbor the seed voxel are checked to determine whether they have a similar orientation. The misorientation is measured to evaluate the orientation difference between the seed voxel and each of its neighbors. The value of the misorientation is given by the following equation:

$$\theta = \min \left| \cos^{-1} \left(\frac{tr(O_c g_A g_B^{-1} O_c) - 1}{2} \right) \right|, \tag{9.4}$$

where O_c is the crystal symmetry operator and g_A and g_B are the rotation matrices of voxel A and B, given by:

$$g_i = \begin{pmatrix} \cos\varphi_1 \cos\varphi_2 - \sin\varphi_1 \sin\varphi_2 \cos\Phi & \sin\varphi_1 \cos\varphi_2 + \cos\varphi_1 \sin\varphi_2 \cos\Phi & \sin\varphi_2 \sin\Phi \\ -\cos\varphi_1 \sin\varphi_2 - \sin\varphi_1 \cos\varphi_2 \cos\Phi & -\sin\varphi_1 \sin\varphi_2 + \cos\varphi_1 \cos\varphi_2 \cos\Phi & \cos\varphi_2 \sin\Phi \\ \sin\varphi_1 \sin\Phi & -\cos\varphi_1 \sin\Phi & \cos\Phi \end{pmatrix},$$

where $(\varphi_1,\Phi,\varphi_2)$ are the Euler angles of the voxel. If the misorientation is less than the defined tolerance (i.e., $\sim 5^\circ$), then that voxel is added to the list of voxels of the grain being segmented. Each voxel on the list undergoes the process of checking its neighboring voxels until no new voxels are added to the list. After the list is complete, a new seed point is generated and the voxel assignment is repeated for the next grain. An option during segmentation is to terminate the process when no unassigned voxels remain above a

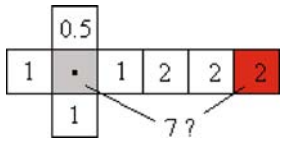


Fig. 9.1 Schematic illustrating the possibility of accumulated misorientation. If a tolerance of 5° was chosen to segment voxels, the *red* and *grey* voxels would be assigned to the same grain, due to the lack of a 5° boundary between immediately neighboring voxels. However, the *red* and *grey* voxels could be misoriented by as much as 7°. If a second criterion was used, where the misorientation between an immediate neighbor voxel (the *red* voxel) and the initial seed voxel (the *grey* voxel) also had to be below 5°, then accumulated misorientation would be limited to 5° as well

data quality tolerance. This ensures that no grains can be formed that include only low quality voxels. Techniques for subsequent treatment of the remaining low quality points will be discussed in the section on data clean-up.

Note that the relative degree of misorientation that "defines" a grain should be carefully considered. For example, if misorientation is determined by comparing any given voxel with only its immediate neighbors, rather than also comparing this voxel with the original seed point, it is possible that systematic rotations could result in misorientations inside a feature that are larger than the defined tolerance allowable between any two neighboring voxels, as shown in Fig. 9.1. This effect could become important in a deformed structure, where the lack of an abrupt change in misorientation could allow many voxels to be assigned to the same grain. Application of a second misorientation tolerance, referring to the misorientation with the original seed voxel, will set a limit on accumulated misorientation.

9.3.3 Clean-Up Routines

There are inevitably data points that are assigned incorrect orientations during data collection, as well other microstructural features that currently cannot be identified by the EBSD software. Incorrect orientations are generally either a result of data points falling very near a grain boundary, where the generated pattern may be composed of information from both grains, or a layer of mechanical damage on the surface of the sample "blurring" the pattern. As a result, the EBSD pattern for the data point is not likely to match well with any orientation. Other features, such as precipitates or pores, may also return low quality values because these features return either no EBSD pattern or the crystal structures are not selected for use in pattern fitting.

Ideally data clean-up should be performed in 3D rather than 2D. Processing each section individually blinds the cleaning procedure from what is occurring directly above and below the section, which may change the interpretation of "problematic" data. The following subsections will discuss processing options used to clean and reassign portions of the EBSD data. Figure 9.2 shows some examples of reconstructed and processed data sets obtained from FIB-based sectioning and manual polishing.

9.3.3.1 Filtering of Low Quality Data

The segmentation procedure described previously may produce "grains" that are wholly comprised of low quality data. These "grains" are often small and may result from the presence of a pore, carbide, or local surface condition. Also, there may be voxels that are unassigned during the segmentation process, if the termination condition mentioned previously is used. These low quality or unassigned voxels should be examined a second time and potentially reassigned, but care must be taken to ensure that their addition does not significantly alter the grain morphologies of the good quality grains. There are multiple strategies that can be used in reassigning these points.

One option is to rerun the segmentation process for selected voxels with an increased misorientation tolerance (for example, from 5° to 10°). Often these low quality points correspond to data that are adjacent to a grain boundary. It is sometimes the case that these points produce overlapping EBSD patterns (from the two grains) and are indexed only slightly off their true orientation. However, the misorientation tolerance of 10° is still relatively small and not likely to cause points to be arbitrarily assigned to grains.

A second option is to determine the number of contiguous low quality points. This number is important in providing some understanding of the cause of the poor quality data. For example, if there is a grouping of low confidence points located together, then it is likely that these voxels correspond to a microstructural feature that could not be indexed successfully (i.e., a void or

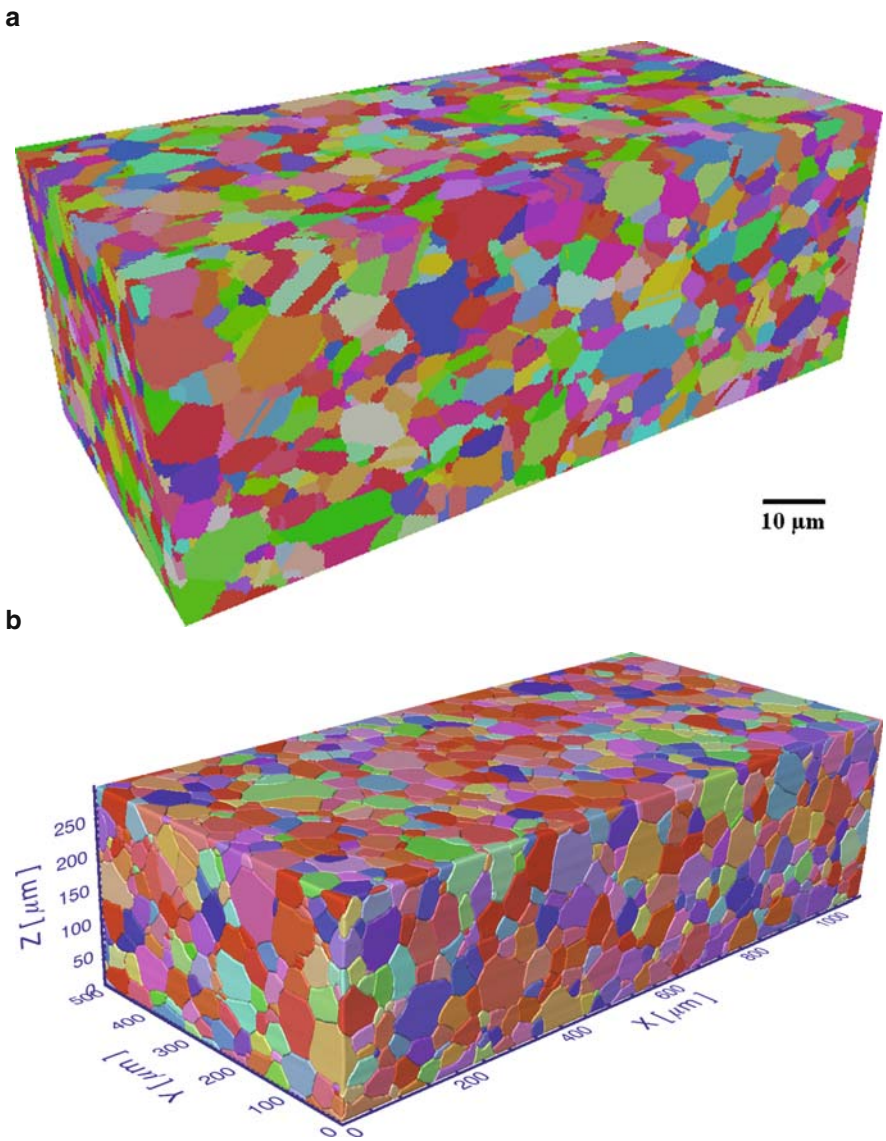


Fig. 9.2 Sample reconstructions of (*top*) a nickel-base superalloy obtained through FIB-based sectioning and (*bottom*) a titanium alloy obtained by manual mechanical polishing

a secondary phase that was not included in the indexing scheme). If the number of voxels that correspond to this feature exceed the minimum grain size criteria (see the next section), then these voxels do not need to be reassigned and can be segmented as with grain segmentation. The feature may not correspond to a grain, but it is a microstructural feature that may be of interest for later inspection.

Any remaining low quality voxels should still be assigned to neighboring grains to create a fully dense structure. The low quality voxels can be left unassigned if there is a desire to track such areas of low quality. There are multiple options for deciding how to assign these remaining points, each of which has advantages and disadvantages. The remaining low quality points can be assigned to the grain with which they share the most surface area, to the grain which owns the highest quality neighbor of the unassigned voxel, or to the largest grain which they neighbor.

9.3.3.2 Removal of Small Grains

A minimum grain size criterion can be used to filter any extremely small grains. A grain which contains less than a defined number of voxels can be dissolved and its voxels reassigned to neighboring grains in a fashion similar to the low quality points in the previous section. The main motivation to remove extremely small grains is the inability to accurately characterize features made of so few voxels. However, if the "true" grain shape is of importance, it may be more prudent to treat the data set as is and not dissolve small grains; rather simply omit them from the analysis. The minimum size should be carefully defined and not selected arbitrarily. One important factor in selecting the minimum size is the number of voxels needed to generate a reasonable description of grain shape. Another factor is the fraction of grains that will be removed by the filter. Generally, it is undesirable to remove a large percentage of grains with any one filter. If more than a few percent of the grains are removed due to the minimum size criteria, it may be an indication that the resolution of the data is insufficient.

9.3.3.3 Additional Data Processing Possibilities

There are a variety of additional data processing procedures that can be applied to the 3D EBSD data, many of which are simple extensions of the 2D filters supplied in commercial EBSD analysis programs. For example, the average orientation of each grain can be calculated and assigned to all the voxels that constitute that grain. The average orientation is the orientation that minimizes the total misorientation with all the voxels in a grain. The average orientation can be solved for numerically, as shown by Barton and Dawson (2001). Generally, an adequate initial estimate of the average orientation can be obtained by transforming the orientation of each voxel into a single fundamental zone and finding the center of mass of the resultant point cloud in orientation space. Additionally, the data set can be scanned for grains are that are fully contained within another grain and as a result have only one neighbor. These grains could potentially be small subgrains that are misoriented only slightly beyond than the misorientation tolerance. Data sets may also contain grains with special boundaries (i.e., twin boundaries) that can be identified and omitted from certain analyses if desired. Grains sharing these special misorientations can be merged together to leave only general grain boundaries in the data set. These processing possibilities are provided as selected examples and not meant to comprise a full list of the options available to further process 3D EBSD data.

9.4 Analysis Capabilities

The direct measurement of microstructural parameters in 3D allows one to describe these features without the need for stereological interpolation, and also enables a higher order characterization (i.e., distributions and correlations). Additionally, if each individual constituent of the microstructure (i.e., grains) is characterized independently, this allows one to develop distributions of parameters, rather than simply average values. This more detailed description can provide information about the higher order moments of the distributions. Segmented grains coupled with EBSD data provide the opportunity to quantify a number of parameters that define the morphology and crystallography of a material. In this section, examples of some morphological and crystallographic parameters will be presented as they relate to a variety of materials.

As an aside, it should be mentioned that there are a number of factors to consider when undertaking a statistical analysis of grain structure, in order to ensure that the results are not biased by the analysis procedure. These issues have been discussed in the peer-reviewed literature, and it is highly recommended that anyone interested in such an analysis should first review this work (Zhang et al. 2004; Humphreys 1999; Kral et al. 2000; Ralph and Kurzylowski 1997).

9.4.1 Morphological Descriptors

9.4.1.1 Grain Size and Volume

Grain volume can be calculated simply by summing the number of voxels that are assigned to each grain. Each voxel has an associated volume given by:

$$V_{voxel} = \delta\varepsilon^2, \tag{9.5}$$

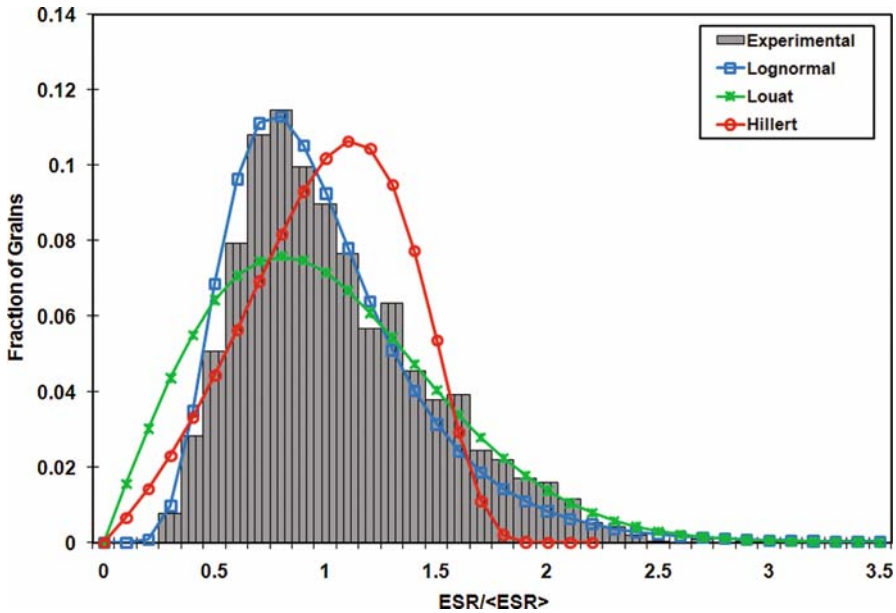


Fig. 9.3 Plot of equivalent sphere radius (ESR) for a nickel-base superalloy along with three fit theoretical distributions

where δ is the section thickness and ε is the step size of the 2D EBSD map. The grain volume is calculated by:

$$V_{grain} = N_v \cdot V_{voxel}, \tag{9.6}$$

where N_v is the number of voxels in the grain. In addition to measuring the true grain volume, the equivalent sphere radius (*ESR*) can be calculated (Groeber et al. 2008). The distribution of *ESRs* is useful for comparison with classical descriptions of grain size (or radius), which often involved some extrapolation from 2D. Additionally, various theoretical distributions have been developed to fit the *ESR* distribution (Zhang et al. 2004; Feltham 1957; Hillert 1965; Louat 1974). Figure 9.3 shows a sample distribution of *ESR* for a nickel-base superalloy along with fit theoretical distributions.

9.4.1.2 Grain Shape

The irregular geometries that are typical of grains in some materials make grain shape a difficult parameter to describe unambiguously. This is especially true because of the lack of general shape descriptors, in which most descriptions of shape involve combining groups of size parameters to generate a unitless value (Russ 1998). Examples of possible shape descriptors include: length/width (aspect ratio), area/convex area (solidity), and length/fiber length (curl). A common practice is to fit an ellipsoid (or ellipse in 2D) to the grain (Saylor et al. 2004b; Brahme et al. 2006). While there are obvious objections to the ellipsoid representation (mainly the lack of dense packing), the ellipsoid has been accepted as one of the current standards. Other dense packing polygons (i.e., the Kelvin polyhedron) do fill space, but generate separate issues relating to their size and neighbor distributions. A systematic method of generating ellipsoidal inclusions from voxel data obtained by serial-sectioning has also been developed (Li et al. 1999). In this method, the zeroth-order moment (I0), first-order moments (Ix, Iy, Iz), and second-order moments (Ixx, Iyy, Izz) are first calculated for each grain by adding the contribution of each voxel belonging to an identified grain. The coordinates of the centroid for the best-fit ellipsoid are computed from the zeroth- and first-order moments as:

$$x_c = \frac{I_x}{I_0}, \quad y_c = \frac{I_y}{I_0}, \quad z_c = \frac{I_z}{I_0}. \tag{9.7}$$

Next, the principal directions, corresponding to the principal axes of the ellipsoid are calculated

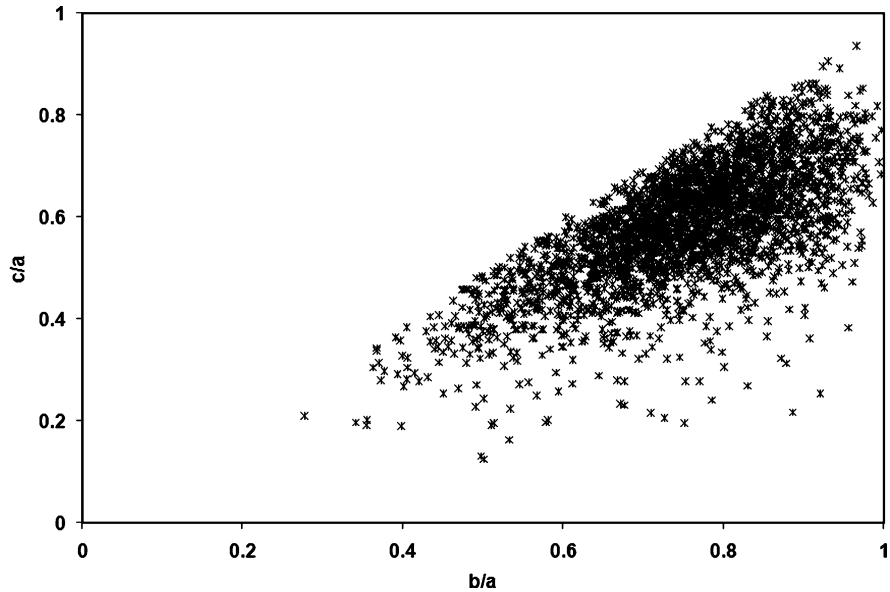


Fig. 9.4 Plot of the distribution of grain aspect ratios for a nickel-base superalloy

from the eigenvalues and eigenvectors of the second-order moments $I_{i,j}$, $i, j = 1, 2, 3$. The major axis (2a), minor axis (2c), and intermediate axis (2b) of the ellipsoidal grain are solved from the relations of the principal second moments of inertia as:

$$a = \left[\frac{A^4}{B \cdot C}\right]^{\frac{1}{10}}, b = \left[\frac{B^4}{A \cdot C}\right]^{\frac{1}{10}}, c = \left[\frac{C^4}{A \cdot B}\right]^{\frac{1}{10}}, \tag{9.8}$$

where A, B, and C are given by:

$$A = \left(\frac{15}{4\pi}\right) \cdot \left(\frac{I_1 + I_2 - I_3}{2}\right),$$
$$B = \left(\frac{15}{4\pi}\right) \cdot \left(\frac{I_1 + I_3 - I_2}{2}\right),$$
$$C = \left(\frac{15}{4\pi}\right) \cdot \left(\frac{I_2 + I_3 - I_1}{2}\right),$$

In some, if not most, cases the ellipsoidal representation of grains is an oversimplification and the error should be quantified. Correspondingly, an accuracy indicator in the ellipsoidal representation can be developed (Groeber et al. 2008). The best-fit ellipsoid based on the moment analysis is scaled slightly to be of the same volume as the grain, with the same aspect ratios and orientation. The fraction of the grain's voxels that lie within the best-fit ellipsoid is calculated. If the grain is perfectly ellipsoidal, then the value of this quantity would be very near 1 (with the voxel size controlling the nearness to 1). Decreasing values indicate more complex and likely concave shapes that are poorly represented by an ellipsoid. Figure 9.4 shows a sample plot of the distribution of grain aspect ratios for a nickel-base superalloy. It is important to note that the further investigation of 3D data sets may likely lead to more sophisticated measures of grain shape. However, at present, the ellipsoid representation has been selected as a starting point, and the measurement of the associated errors has been attempted.

9.4.1.3 Number of Neighbors

In addition to the shape of grains, the number of nearest neighbors is another example of a parameter that cannot be determined directly from 2D measurements, but is easily determined in 3D. The grain IDs, which are assigned during the previously described segmentation process, allow this process to be easily automated. Here, all the voxels belonging to a grain are checked to see if they neighbor another grain. The grain IDs of each voxel's neighboring voxels are checked. If a neighboring voxel has a differing ID (i.e., belongs to a different grain), then the two grains are neighbors.

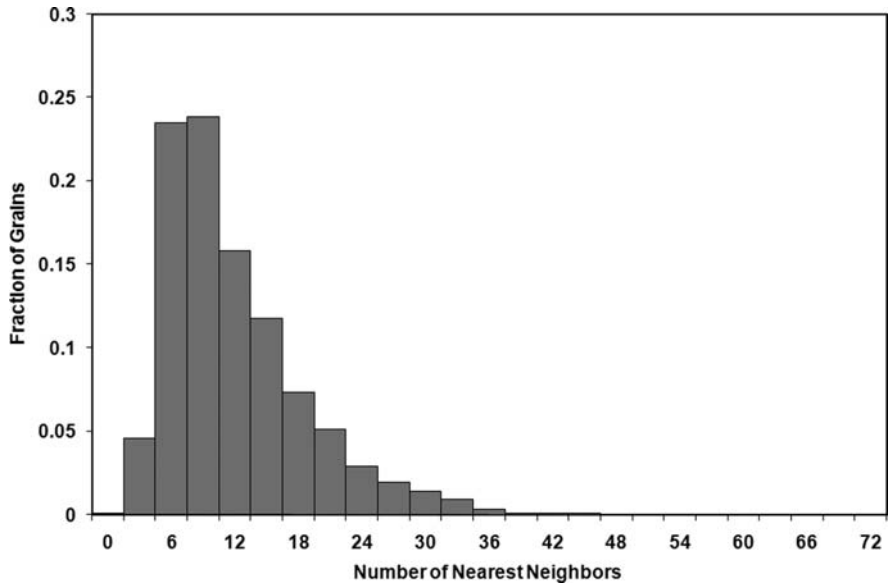


Fig. 9.5 Distribution of the number of neighbors for grains in a nickel-base superalloy

This process is exceedingly useful because it not only determines the number of neighbors, but it identifies the grain connectivity in the structure, which allows for further automated investigation of any parameter involving neighbor interactions. Note that when checking neighboring voxels, only voxels that share a common face, not a common edge or corner, are considered. This requires that the grains share some actual area and avoids counting grains that meet only at an edge or a point. Figure 9.5 shows a sample plot of the number of neighbors distribution for a nickel-base superalloy.

9.4.1.4 Correlations Between Parameters

The correlation or mutual relationship between parameters is important because it provides additional information regarding the morphology and spatial arrangement of grains. The grain connectivity coupled with the parameters of each individual grain allows for the relationships between parameters as well as the clustering of critical grains to be studied. It is desirable to quantify the degree of correlation between two selected parameters. A quantity called the correlation ratio, η^2, can be used for this purpose (Kenney and Keeping 1947). The correlation ratio is a preferred metric in comparison to the correlation coefficient, r, because it can be used with nonlinear relationships. The correlation ratio is the square of the correlation coefficient (r^2) if the relationship is linear. If the relationship is nonlinear, the magnitude of the correlation ratio is larger, but retains a value between 0 and 1. The formula for the correlation ratio is given by:

$$\eta^2 = \frac{\sum_{b=0}^{N_b} n_b \left(\bar{y}_b - \bar{y}\right)^2}{\sum_{i=0}^{N_g} \left(y_i - \bar{y}\right)^2}, \tag{9.9}$$

where N_g is the total number of grains, N_b is the number of bins, n_b is the number of observations in a given bin b, and

$$\bar{y}_b = \frac{\sum_{i=0}^{n_b} y_{bi}}{n_b}, \quad \bar{y} = \frac{\sum_{b=0}^{N_b} n_b \bar{y}_b}{\sum_{b=0}^{N_b} n_b}.$$

The correlation ratio can be thought of as the percent of the total variance of the dependent variable accounted for by the variance between groups of the independent variable. It is evident from the equation that if there is a large difference between the mean of

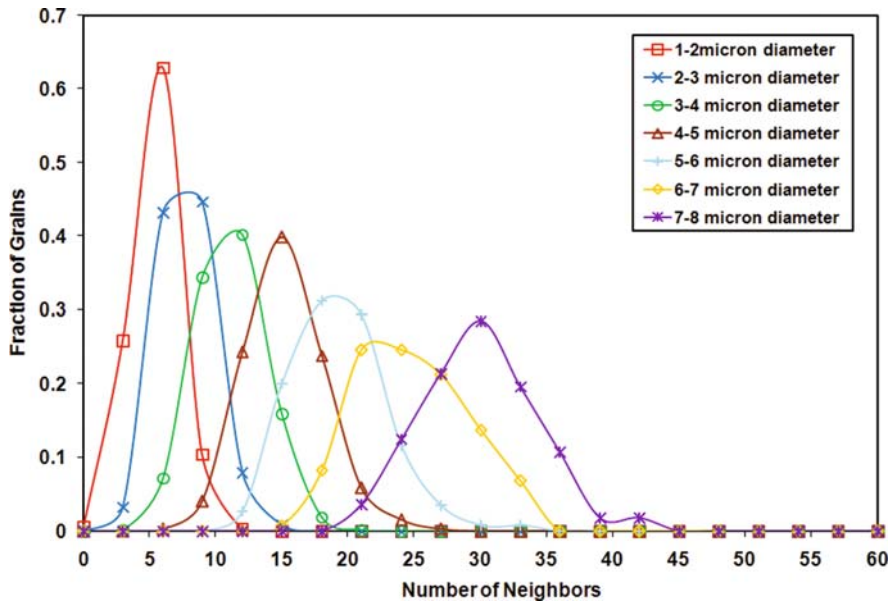


Fig. 9.6 Plot showing the correlation between number of neighboring grains as a function of grain diameter for a nickel-base superalloy

the whole data set and the means of the individual bins, then the correlation ratio will be high. Figure 9.6 shows a correlation plot relating number of neighbors to grain size for a nickel-base superalloy.

9.4.2 Crystallographic Descriptors

9.4.2.1 Classical Measurements

Many of the traditional analyses of 3D EBSD data are directly analogous to the traditional two-dimensional counter analyses. For example, the volume fraction of a particular phase is analogous to the orientation distribution function (ODF), since the area fraction is exactly equal to the volume fraction for a random section through a material. However, the 3D analyses can often add information to the 2D analyses; for example, only through a 3D analysis can the preferred morphological orientation, such as that measured by the ellipsoid of fit, be correlated with the crystallographic texture measured in the ODF.

Other measurements have 2D to 3D analogs related through stereological relationships that give a statistical equivalence of the properties. An example of this would be the distribution of misorientations across grain boundaries in a material. In a random 2D section the crystallographic misorientations across the grain boundary can be easily measured. Ideally, the distribution is weighted by the surface area of a grain boundary per unit volume; the 2D section only reveals the grain boundary length. However, if a large number of boundaries are collected in one 2D section with a similar misorientation, one can apply the stereological relation, $S_V = 4B_A/\pi$, where S_V is the grain boundary surface area per unit volume, and B_A is the grain boundary length per unit area as measured on a random 2D slice through the microstructure (Russ and DeHoff 1986). Note that a very large number of grain boundaries are required in the 2D section in order to obtain a statistically significant number of boundaries for each misorientation type for this analysis to be valid. In the case of a 3D reconstruction, the measurement of the misorientation distribution is relatively straightforward since, as discussed above, the grain nearest neighbor misorientation and the grain boundary areas can be directly calculated from the 3D reconstruction; thus the misorientation distribution function can be directly measured without assumption.

9.4.2.2 Fundamentally 3D Measurements

There are many analyses that can only be measured directly through 3D reconstruction of the material. In a very general sense, these analyses can be seen as the correlation of a specific 3D geometry with the crystallographic orientation. One of the most relevant applications of this is the determination of crystallographic interface orientations, which requires directly correlating the crystallographic orientation of an object with the local interface normal.

One of the most common visualization techniques for 3D objects is to form a surface mesh of the object so that its exterior interface is described as a 3D mesh of discrete interconnected triangles. The conversion from a regularly gridded 3D array of data (such as a stack of images) is most often accomplished using a fast-marching cubes algorithm that converts the volumetric regular array data form to a surface mesh (Lorenson and Cline 1987). Often it is necessary to apply some degree of surface smoothing in order to remove pixel-like artifacts from the surface mesh.

Once the surface is described in terms of a set of triangles, the properties of these triangles can be used to quantify the interfaces of the 3D reconstruction, particularly the local interface normal. The normal $\hat{n}$ and the area A of each triangle in the surface mesh is given by:

$$\hat{n} = \frac{\vec{e}_1 \times \vec{e}_2}{\left|\vec{e}_1 \times \vec{e}_2\right|}; A = \left|\vec{e}_1 \times \vec{e}_2\right|/2, \tag{9.10}$$

where $\vec{e}_1$ and $\vec{e}_2$ are the two edge vectors of the triangle.

One powerful construction that can be formed from this type of data is the interface normal distribution (IND; Kammer et al. 2006). The IND is constructed by first placing the collection of all the interface normal vectors onto a unit sphere. The normals are then binned (weighted by the surface areas of the triangles) according to orientation, then normalized by a random distribution of orientations. Therefore, an orientation on the spherical histogram that has a strong intensity corresponds to a large surface area that shares that orientation. This spherical histogram is then projected to a 2D plot using a stereographic projection (typically along the +z direction, but this is a matter of how one wants to represent the data), preserving the angular relationships between the orientations in the plot producing the IND plot. It should be noted that if the binning of the data occurred on the projected data space of the stereoplot, rather than on the unit sphere, the intensities of the histogram would be altered by the nonequal-area nature of the stereographic projection. Because the binning of the data occurs on the unit sphere, this artifact is avoided and a randomly distributed shape (like a sphere) would have a flat intensity. For INDs that contain peaks, the exact shape of the peaks on the stereoplot would still be slightly altered by the projection, especially close to the center poles and edges of the stereoplot. The stereographic projection has extremely large distortions for orientations that have a $-z$ component. To avoid this, often it is necessary to project each hemisphere separately; however, this can be avoided if there is crystallographic symmetry, which allows the plot to be compressed to a stereographic triangle.

The inclusion of the local crystallographic orientation along with the local interface normal means that the interface normals can be expressed in the crystallographic coordinate system as well, creating a crystallographic interface normal distribution (CIND). The only variation in the construction of the CIND is that before the normals are binned on the unit sphere, they are rotated to the crystallographic coordinate system using the Euler angles of the object in question. There are two analyses that especially lend themselves to this type of construction: the examination of individual objects and the examination of the overall crystal interface texture in a sample, which we will briefly review.

Rowenhorst et al. (2006) used the CIND analysis to examine the facet planes on individual coarse martensite crystals. Using mechanical serial sectioning with optical micrographs, combined with EBSD scans every 10th section, they formed a 3D reconstruction of several coarse martensite variants, including their average crystal orientation (see Fig. 9.7a). For each individual crystal in the reconstruction, a CIND was produced, which revealed three distinct peaks within the CIND. These peaks corresponded to three facets on the martensite crystals (see Fig. 9.8). The average crystallographic normal for each facet was determined by fitting a plane (representing a single normal value) to each one of the peaks. The CIND plots revealed that not only were the shapes of the martensite variants similar, but also the variants formed similar facet planes. This article also introduced a unique visualization technique in which the interfaces of the martensite crystals were colored according to the local interface crystallographic normal. The coloring scheme is

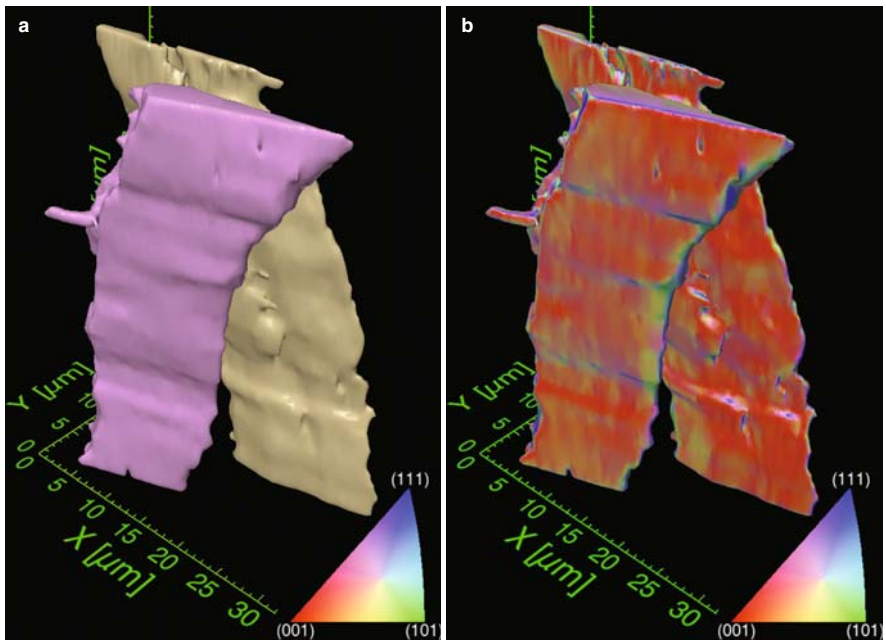


Fig. 9.7 Reconstruction of two coarse martensite crystals in HSLA-100 steel. (**a**) *Color* indicates the crystallographic direction that is parallel with the Z-axis. The difference in color indicates that the martensite crystals represent separate martensite variants. (**b**) *Color* indicates the crystallographic orientation of the local interface normal at each local patch of the interface. Note that while the crystals represent different variants, the crystal facets have similar crystallographic normals

similar to that used to create an inverse pole figure (IPF). In an IPF each point in the image is colored (using the standard triangle color legend) according to the crystallographic direction that points along the direction normal to the image plane. In the reconstruction, each point on the 3D interface was colored according to the crystallographic direction that is parallel with the surface normal (see Fig. 9.7b). This visualization contains essentially the same information as the CIND construction, with the advantage of directly showing how the crystallographic normal of an interface corresponds to specific morphological features, but lacking the quantitative nature of the CIND plots.

Saylor et al. (2004a) significantly expanded on the CIND construction to include not only the interface distribution of grain boundaries in polycrystalline MgO, but to include the full five parameter space of the grain boundaries, constructing the grain boundary character distribution (GBCD). By examining the full five parameter space, they were able to determine not only the interface texture for the system, but also the interface texture for particular grain misorientations. Since this initial study, the GBCD has been determined for many more materials systems including Al, Ni, Cu, Brass, and Ti-6-4 (Saylor et al. 2004a; Randle et al. 2008a, 2005, 2008b).

9.5 Summary

This chapter discusses the collection, processing, and analysis of 3D data from serial-sectioning experiments of grain-level microstructures, where the experiments included the collection of crystallographic information via electron backscatter diffraction (EBSD). Importantly, the collection of EBSD maps enables the unsupervised segmentation of grains—a process that can be very difficult in experiments that contain only image data. Furthermore, the 3D morphology of grains can be linked to the crystallography in a way that allows the grain surfaces to be investigated in a very robust manner. These are two very important advancements made possible by EBSD.

In particular, this chapter has focused on key issues that arise when undertaking a serial sectioning experiment and in subsequent postprocessing and analysis of

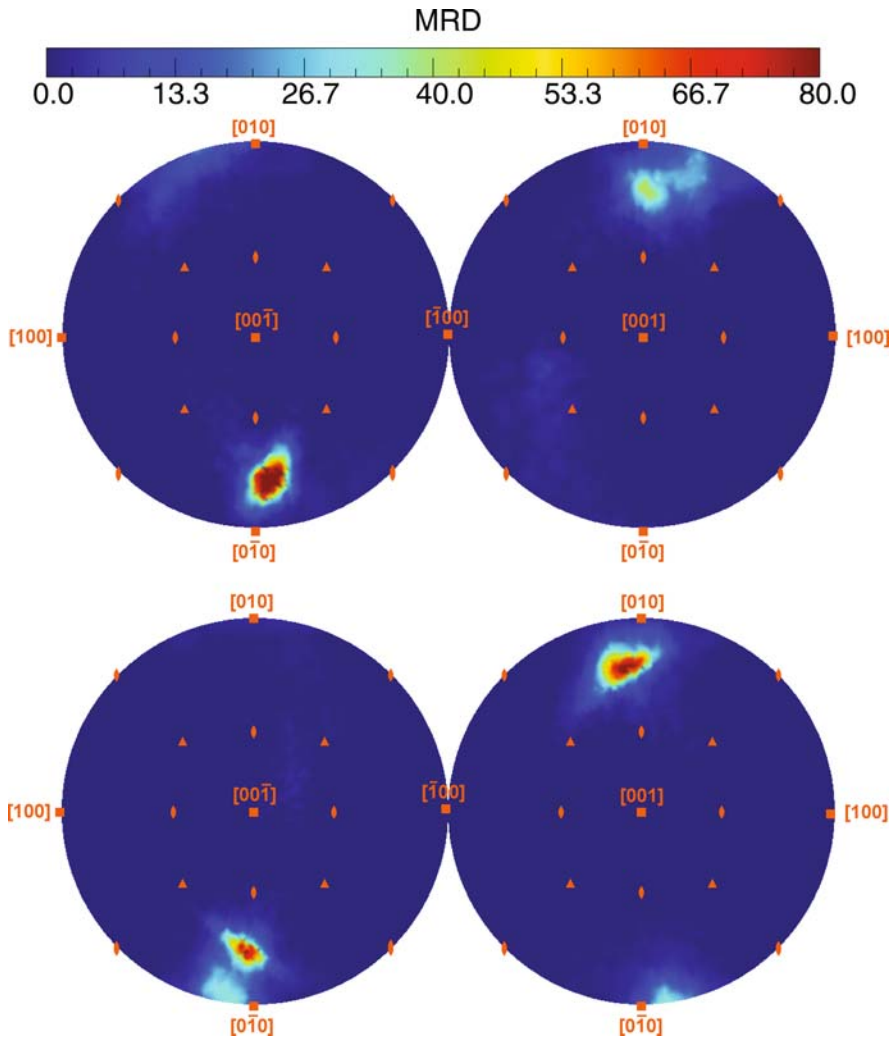


Fig. 9.8 Crystallographic interface normal distribution (CIND) plots of the martensite crystals shown in Fig. 9.7, where the upper and lower CINDs correspond respectively to the *purple* and *yellow* crystals in Fig. 9.7a. The peaks in the CIND indicate the average orientation of the facet planes of the crystals; peak intensities indicate multiples of a random distribution (MRD)

the data. Important factors such as stack alignment and registry, feature segmentation, and data clean-up have been discussed. Selected analysis techniques have also been presented to characterize the geometric properties of individual grains and their boundaries. The quantitative analysis of 3D microstructural data is a topic of contemporary interest, and the field is developing at a rapid pace. The authors have attempted to provide a current snapshot of their own research, although admittedly these advances have only scratched the surface with regards to the wealth of potential information that can be garnered from these robust data sets.

References

Barton NR, Dawson PR (2001) A methodology for determining average lattice orientation and its application to the characterization of grain substructure. Metall Trans A 32: 1967–1975

Bhandari Y, Sarkar S, Groeber M, Uchic M, Dimiduk D, Ghosh S et al (2007) 3D polycrystalline microstructure reconstruction from FIB generated serial sections for FE analysis. Comp Mater Sci 41:222–235

Brahme A, Alvi MH, Saylor D, Fridy J, Rollett AD et al (2006) 3D reconstruction of microstructure in a commercial purity aluminum. Scr Mater 55:75–80

Budai JD, Yang W, Larson BC, Tischler JZ, Liu W, Weiland H, Ice GE et al (2004) Three-dimensional micron-resolution

x-ray laue diffraction measurement of thermal grain-evolution in aluminum. Mater Sci Forum 467–470: 1373–1378

Budai JD, Liu W, Tischler JZ, Pan ZW, Norton DP, Larson BC, Yang W, Ice GE et al (2008) Polychromatic x-ray micro- and nanodiffraction for spatially-resolved structural studies. Thin Solid Films 576:8013–8021

Feltham P (1957) Grain growth in metals. Acta Metall 5:97–105

Groeber MA, Haley B, Uchic MD, Ghosh S et al (2004) Microstructural characterization using 3-D orientation data collected by an automated FIB-EBSD system. In: Ghosh S, Castro J, Lee JK (eds) Proceedings of NUMIFORM 2004, AIP Publishers Melville, New York

Groeber MA, Haley BK, Uchic MD, Dimiduk DM, Ghosh S et al (2006) 3D reconstruction and characterization of polycrystalline microstructures using a FIB-SEM system. Mater Charact 57:259–273

Groeber MA, Uchic MD, Dimiduk DM, Ghosh S et al (2008) A framework for automated analysis and simulation of polycrystalline microstructures, part 1: statistical characterization. Acta Mater 56:1257–1273

Hillert M (1965) On the theory of normal and abnormal grain growth. Acta Metall 13:227–238

Humphreys FJ (1999) Quantitative metallography by electron backscattered diffraction. J Microsc 195:170–185

Kenney JF, Keeping ES (1947) Mathematics of statistics. Van Nostrand, Princeton, NJ

Kim C-S, Rollett AD, Rohrer GS et al (2006) Grain boundary planes: new dimensions in the grain boundary character distribution. Scr Mater 54:1005–1009

Kral MV, Mangan MA, Spanos G, Rosenberg RO et al (2000) Three-dimensional analysis of microstructures. Mater Charact 45:17–23

Kammer D, Mendoza R, Voorhees PW et al (2006) Cylindrical domain formation in topologically complex structures. Scr Mater 55:17–22

Lund AC, Voorhees PW (2002) The effects of elastic stress on coarsening in the Ni-Al system. Acta Mater 50:2085–2098

Lauridsen EM, Schmidt S, Nielsen SF, Margulies L, Poulsen HF, Juul Jensen D et al (2006) Non-destructive characterization of recrystallization kinetics using three-dimensional x-ray diffraction microscopy. Scr Mater 55:51–56

Lewis AC, Bingert JF, Rowenhorst DJ, Gupta A, Geltmacher AB, Spanos G et al (2006) Two- and three-dimensional microstructural characterization of a super-austenitic stainless steel. Mater Sci Eng A 418:11–18

Li M, Ghosh S, Richmond O, Weiland H, Rouns TN et al (1999) Three dimensional characterization and modeling of particle reinforced metal matrix composites, part 1: quantitative description of microstructure morphology. Mater Sci Eng A A265:153–173

Lienert U, Almer J, Jakobsen B, Pantleon W, Poulsen HF, Hennessey D, Xiao C, Suter RM et al (2007) 3-dimensional characterization of polycrystalline bulk materials using high-energy synchrotron radiation. Mater Sci Forum 539–543:2353–2358

Lorenson WE, Cline HE (1987) Marching cubes: a high resolution 3D surface construction algorithm. Comput Graphics 21:163–169

Louat NP (1974) On the theory of normal grain growth. Acta Metall 22:721–724

Ralph B, Kurzylowski KJ (1997) The philosophy of microscopic quantification. Mater Charact 38:217–227

Randle V, Hu Y, Rohrer GS, Kim C-S et al (2005) The distribution of misorientations and grain boundary planes in grain boundary engineered brass. Mater Sci Technol 21: 1287–1292

Randle V, Rohrer GS, Hu Y et al (2008a) Five-parameter grain boundary analysis of a titanium alloy before and after low-temperature annealing. Scr Mater 58:183–186

Randle V, Rohrer GS, Miller H, Coleman M, Owen G et al (2008b) Five-parameter grain boundary distribution of commercially grain boundary engineered nickel and copper. Acta Mater 56:2363–2373

Rowenhorst DJ, Gupta A, Feng CR, Spanos G et al (2006) 3D crystallographic and morphological analysis of coarse martensite: combining EBSD and serial sectioning. Scr Mater 55:11–16

Russ JC, DeHoff RT (1986) Practical stereology. Springer, New York

Russ JC (1998) The Image processing handbook. CRC Press, Boca Raton, FL

Saylor DM, Morawiec A, Cherry KW, Rogan FH, Rohrer GS, Mahadevan S, Casasent D et al (2001) Crystallographic distribution of grain boundaries in magnesium oxide. In: Gottstein G and Molodov DA (eds) Proceedings of the first joint international conference on grain growth. Springer Verlag, Aachen, Germany 449–454

Saylor DM, El-Dasher BS, Rollett AD, Rohrer GS et al (2004a) Distribution of grain boundaries in aluminum as a function of five macroscopic parameters. Acta Mater 52:3649–3655

Saylor DM, Fridy J, El-Dasher BS, Jung KY, Rollett AD et al (2004b) Statistically representative three-dimensional microstructures based on orthogonal observation sections. Metall Trans A 35A:1969–1979

Schmidt S, Nielsen SF, Gundlach C, Margulies L, Huang X, Juul Jensen D et al (2004) Watching the growth of bulk grains during recrystallization in deformed metals. Science 305: 229–232

Spanos G (2006) Foreword: scripta materialia viewpoint set on 3D characterization and analysis of materials. Scr Mater 55:3

Wall MA, Schwartz AJ, Nguyen L (2001) A high-resolution serial sectioning specimen preparation technique for application to electron backscatter diffraction. Ultramicroscopy 88:73–83

Zaafarani N, Raabe D, Singh RN, Zaefferer S et al (2006) Three-dimensional investigation of the texture and microtexture below a nanoindent in a Cu single crystal using 3D EBSD and crystal plasticity finite element simulations. Acta Mater 54:1863–1876

Zhang C, Suzuki A, Ishimaru T, Enomoto M et al (2004) Characterization of three-dimensional grain structure in polycrystalline iron by serial sectioning. Metall Trans A35A: 1927–1932

Chapter 10

3D Reconstruction of Digital Microstructures

Stephen D. Sintay, Michael A. Groeber, and Anthony D. Rollett

10.1 Motivation

The main motivation for this chapter is a decidedly practical one, in that many questions can be asked about the effect of microstructure on materials' response. Often, the use of simple average quantities such as "grain size" is inadequate; instead one may need to consider the possibility that the full three-dimensional (3D) microstructure is important. Calculations by hand being self-evidently impracticable, computers must be used, and thus a digital microstructure is required in which all relevant microstructural features are fully described. We find sufficient complexity in materials with predominantly single-phase grain structures, perhaps containing dispersions of second phase particles. Other chapters, however, describe more complex microstructures based on, e.g., titanium alloys. Reconstructing polycrystalline, single-phase microstructures in 3D is thus the main focus of this chapter. The statistics required to perform the numerical procedures raises some interesting issues and a more general motivation to prove that the general stereological problem of reconstructing 3D microstructures is solvable, based on limited cross-sectional information. Our conclusion is that, notwithstanding the known difficulties associated with the general problem (Cruz-Orive 1976a, 1976b), the constraint imposed by the fully space-filling nature of grains means that the dimensionality of the problem is reduced, which allows the numerical fitting procedures to produce meaningful results.

There are many ways to tackle the challenge of generating three-dimensional representations of microstructure based on EBSD, even setting aside other approaches such as synchrotron-based microscopy. The obvious approach, and one that is the focus of other chapters in this book, is to generate direct images with serial sectioning and reconstruct the 3D image, either from the stacks of EBSD scans, or from some mix of more traditional images from secondary or backscatter electron imaging. In this chapter, however, we present a summary of how to generate synthetic microstructures that are based on EBSD data in order to obtain the required information on grain shape, orientation, and grain boundary character. The motivation for such an approach is the ability to generate many different representative microstructures, all of which match statistically the measurements on the material of interest to a predetermined degree of accuracy.

10.2 Background

Clearly, matching all aspects of a microstructure in a single procedure is unrealistic, and so the procedures outlined here represent various degrees of coordination between, say, grain shape and orientation or grain boundary character.

10.2.1 2D–3D Inference

The statistical reconstruction method described here is based on limited cross-sectional information from

S.D. Sintay (✉)
Department of Materials Science and Engineering, Carnegie Mellon University, Pittsburgh, PA 15213, USA
e-mail: ssintay@andrew.cmu.edu

A.J. Schwartz et al. (eds.), *Electron Backscatter Diffraction in Materials Science*,
DOI 10.1007/978-0-387-88136-2_10, © Springer Science+Business Media, LLC 2009

a given material; it is essential, however, that cross sections are made on more than one sectioning plane, and preferably in three orthogonal planes. Statistical methods for reconstructing microstructures have been developed in a number of fields, especially for modeling geological materials (Fernandes et al. 1996; Oren and Bakke 2002, 2003; Sundararaghavan and Zabaras 2005; Talukdar et al. 2002a, 2002b, 2002c, Talukdar and Torsaeter, 2002) . Saylor et al. proposed a method of constructing 3D polycrystalline models of materials based on the microstructural features observed in three orthogonal sections (Saylor et al. 2004b). In this report the microstructural features of interest include size and shape of grains, misorientation distribution, orientation distribution, and the relative placement of grains with respect to size. The procedure outlined by Saylor, along with adaptations for elongated grain shape noted by Brahme et al. (2006) is the basis for one of the procedures described here. Groeber (2007) also offers a methodology for inferring 3D structure from 2D measurements.

There is a substantial literature on the general stereological problem of reconstructing 3D microstructures based on limited section information. When treating microstructures as collections of general particles whose size, shape, and orientation are to be reconstructed (without regard to their packing), the problem is known to lack a solution (Cruz-Orive 1976a). However, for particles that are monodisperse (in size and shape), this problem is well known and has semi-analytical solutions for which the names Cahn and Saltykov are well known in the materials literature (Cahn and Fullman 1956; Saltykov 1958). For a historical overview, see Underwood (1970). In contrast to these more general cases, polycrystalline grain structures have an added constraint, since grains are not independent particles (i.e., low volume fraction), because they fill space. This constraint enhances the ability to accurately reconstruct a 3D distribution from 2D observations (Przystupa 1997). This chapter will attempt to address the previously less investigated problem of space-filling particles (i.e., grains).

10.2.2 3D Polycrystal Microstructure Generation

A number of authors have proposed methods for generating synthetic or reconstructed 3D digital microstructures and provided examples of their operations. Saylor et al. (2004b) focused their efforts on single-phase, nearly equi-axed polycrystals. Brahme et al. (2006) extended this work to build microstructures with highly elongated grains in one direction to match microstructures in as-rolled metals. Here the application was to simulate the recrystallization process where heterogeneous nucleation on the prior grain boundaries was important. Dawson's group has also proposed methods for instantiating polycrystal and polyphase microstructures (Han and Dawson 2005). Recently, Groeber et al. have proposed an alternative approach to the problem of packing ellipsoids in order to match microstructural characteristics (Groeber et al. 2008b). Again, we emphasize that these approaches are focused on space-filling polycrystalline microstructures, in contrast to the broad range of previous work that has focused almost entirely on (porous) composites; see, e.g., the text by Torquato (2001). It is also important to acknowledge the extensive effort that has been made to model materials properties in two dimensions, notably the OOF project (García et al. 2004). The OOF project provides tools for converting (2D) images to a mesh that describes the geometry of the microstructure, which in turn provides the basis for finite element modeling of materials behavior such as (thermo-)elasticity.

10.3 Data Collection and Analysis

10.3.1 Data Sources

Data collection is the foundation of all reconstruction attempts. The techniques and parameters should be selected appropriately to accurately capture the distribution of the features of interest. For example, if grain size and shape in a deformed microstructure are of interest, then a relatively coarse step size might be appropriate; but if the grain boundary normal distribution is the key feature, then a finer step size will be needed to capture the distribution of the inclination of the grain boundary planes. There are a number of techniques that can be utilized when collecting microstructure data. Standard imaging methods and specialized mapping methods all offer a view of the grain and particle structure of a sample. As mentioned previously,

the investigatory technique should be selected with consideration of both the goal of the collection and analysis process, and the structure of the material itself. Standard imaging techniques (i.e., optical, SEM, or ion imaging) are relatively fast and generally produce high resolution images. However, these techniques can struggle with producing images suitable for easy feature identification, depending on the material. In contrast, mapping methods like EBSD provide a quantitative and correlated data form that enables straightforward, automated feature segmentation, albeit with longer acquisition times and lower resolution. There are some examples of combining these different methods. For example, optical microscopy and EBSD maps have been used in conjunction to reconstruct serial section data (Rowenhorst et al. 2006; Dillard et al. 2007).

10.3.2 Identifying Features

Feature identification is a critical step in any characterization or representation process. Precise segmentation is important to ensure accurate quantification of features, and automation of the process is vital to limit bias and make segmentation of large data sets practical. The data format collected is generally the largest factor in dictating the feature identification technique(s) used. Images are an older form of data and have fueled an entire field of research regarding image segmentation. Many researchers have developed techniques for segmenting images with various goals, and the book by Russ (2006) provides an overview of the possibilities and complications of image segmentation. Data from mapping methods like EBSD is a newer data form and has been shown by a number of researchers to be a pathway to fast, automated segmentation (Humphreys 1999; Groeber et al. 2008a; Saylor et al. 2004b; Lewis et al. 2006). The 3D EBSD chapter by Groeber et al. in this book describes an algorithm for the development of an automated segmentation routine utilizing the data obtained by EBSD.

10.3.3 Statistical Description of Features

Segmented grains coupled with EBSD data provide the opportunity to quantify a number of parameters that define the morphology and crystallography of a material. The microstructure reconstruction methods that are presented in this chapter are predicated on the statistical description of grains. In this work, the grains and/or particles are represented by ellipses in the 2D scans and are assumed to be sections through ellipsoidal grains in 3D. While there are obvious objections to the ellipsoid representation (mainly the inability to fill space), the ellipsoid has been accepted as one of the current standards. Dense packing with monosized polygons (i.e., the Kelvin polyhedron) can fill space, but there are challenges to work with if a range of sizes and neighbor distributions is required, as is self-evident in modeling realistic polycrystals. Once the grains are segmented, each grain is essentially a group of pixels identified as belonging to the same feature. An ellipse can be fit to each group of pixels by the method(s) described by Li et al. (1999); Saylor et al. (2004); and Groeber et al. (2008a) and can also be found in many commercial software programs (e.g., Image J). Following the ellipse fitting process, the various parameters that define the ellipse can be used to define aspects of the grain's morphology. For example, the area of the grain can be obtained directly from the area covered by the group of pixels, but the lengths, ratio, and orientation of the principal axes obtained from the fit ellipse better describe the grain morphology. In addition, the number of neighboring features and the crystallographic differences between them can also be quantified. It should be noted that while the methods presented here have been developed for the ellipse-ellipsoidal grain shape assumption, it is conceivable that similar methods could be developed for other geometrical representations. The availability of simple analytical expressions for calculating the separation and overlap between pairs of ellipsoids, as well as the reasonable fit to the experimental grains, led to the choice of the ellipsoidal grain shape assumption.

10.4 Methods for 3D Structure Inference

This section will describe two possible methods for the generation of a probable set of ellipsoids, based on the experimental measurements of orthogonal 2D sections. The two methods were applied to two different microstructures, which can be seen in Fig. 10.1.

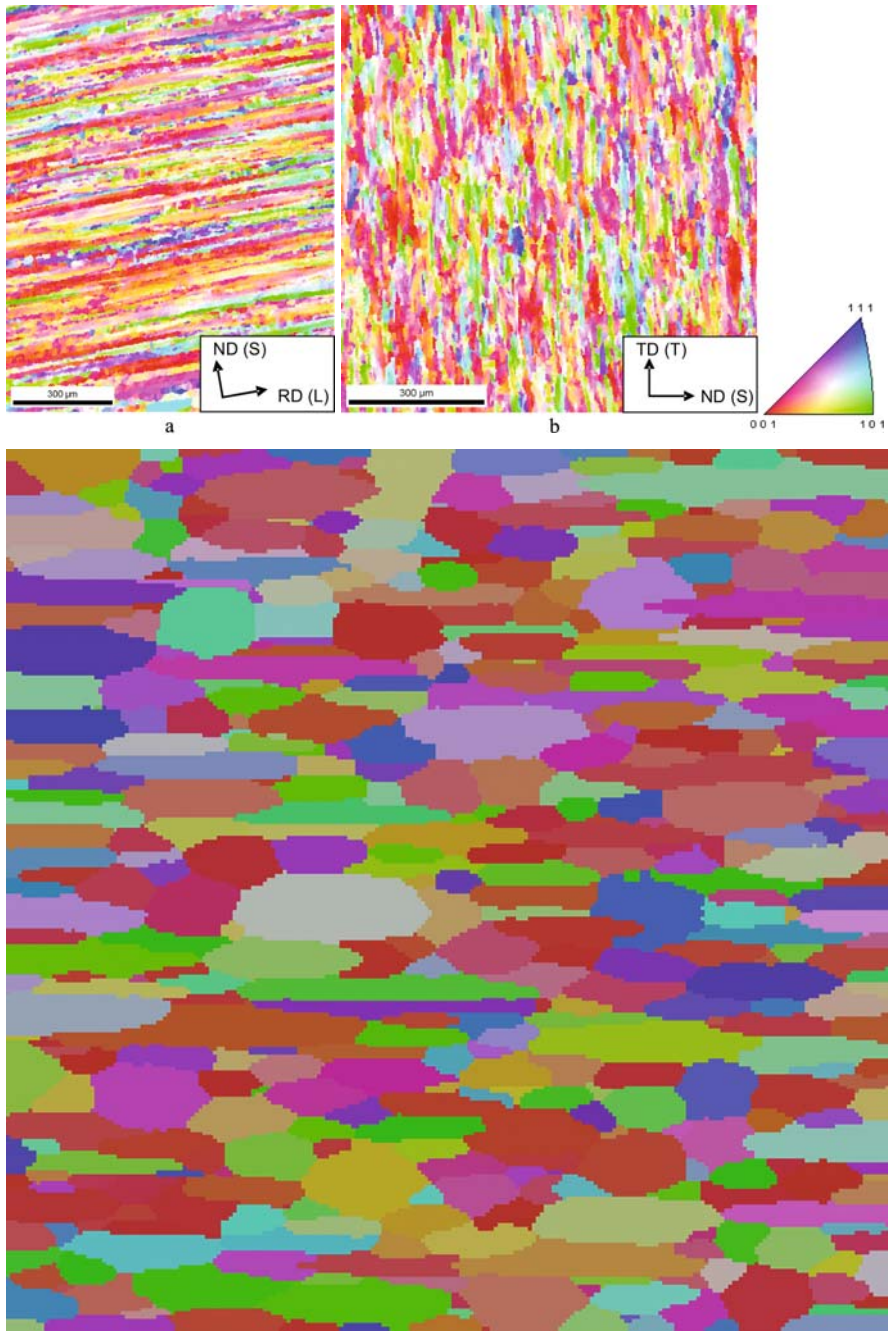


Fig. 10.1 Representative images of 2D microstructures used to generate 3D synthetic structures by means of *top* Monte Carlo-based histogram fitting and *bottom* observation-based domain constraint. Figure 10.1Aa shows the RD–ND section and 10.1Ab shows the ND–TD section of a 7075 aluminum alloy. The microstructure shown in the *top* images was experimentally measured, while the microstructure seen in the *bottom* image is the result of a section through a synthetically generated 3D microstructure

10.4.1 Monte Carlo-Based Histogram Fitting

In this section we give an example of generating a set of 3D (ellipsoidal) grains using statistical distributions calculated on three 2D, orthogonal, EBSD-based micrographs of the material. The grain size distributions for the three orthogonal planes of a rolled aerospace aluminum alloy are shown in Fig. 10.2. Matching the statistics in the generated 3D structure to the measured 2D statistics is accomplished through a multi-step process that includes: (1) generating representative ellipsoids (in terms of size and shape distributions), (2) placing those ellipsoids into a volume, (3) allowing that volume to be filled with voxels that are grouped as grains, and (4) modifying the grain structure by use of a (isotropic) Monte Carlo grain growth (Rollett and Manohar 2004). The first step in this process is the focus of this section, while the latter steps will be discussed in the following sections.

The first step in creating a synthetic microstructure is to generate a set of 3D ellipsoids based on the orthogonal 2D grain size distributions as seen in Fig. 10.2. The transition from 2D to 3D is accomplished by assuming that the grain shape is that of an ellipsoid and considering that the observations on the 2D sections are only a portion of the true size and shape of the actual grain. The probability distribution functions (PDFs) of the ellipse dimensions obtained from the sliced ellipsoids are given as:

$$f'(a),\ f'(b), \tag{10.1}$$

where a and b are the semi-axes of an ellipse, and the prime accent indicates that it is from a slice. In this case the ellipse dimensions are assumed to be independent, and that $a > b$. References to the cumulative distribution function, CDF, utilize the same notation but with a capital "F." Figure 10.2 also shows a complication in the 2D observations (for this material) in that the grain size in the RD dimension is larger than the image. In this particular example, optical microscopy gives

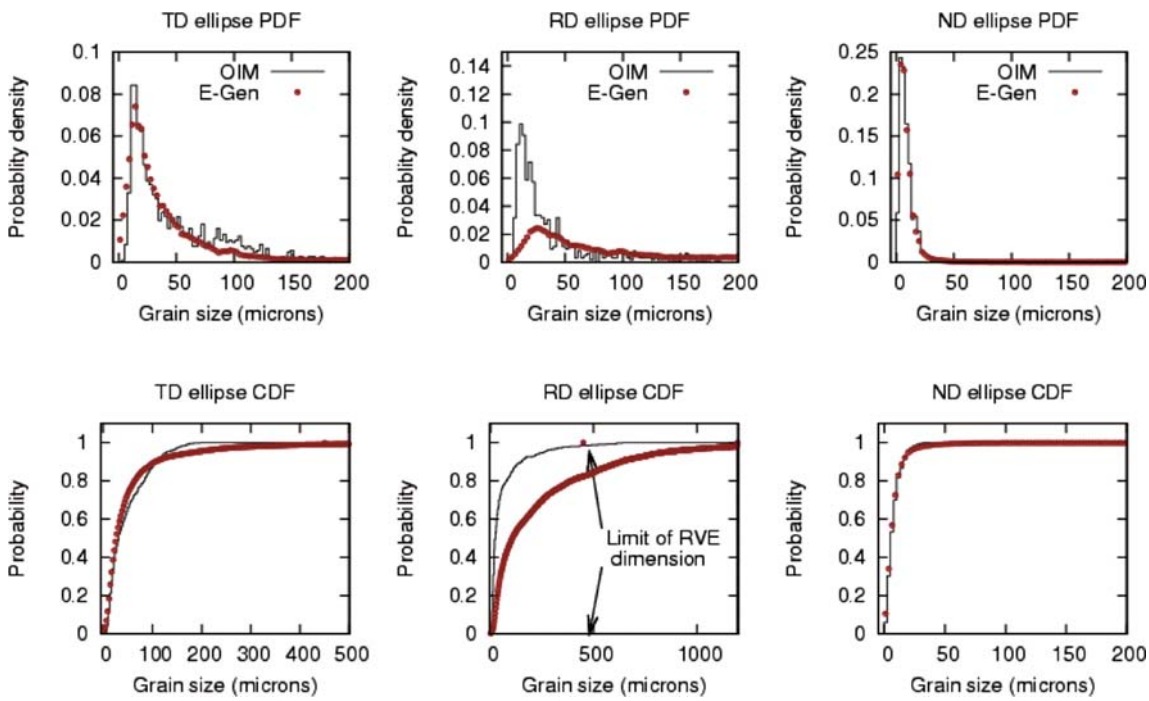


Fig. 10.2 Here a set of PDFs and CDFs compare the grain size distributions from the OIM data and from the ellipsoids generated to represent the data. In the upper series of images PDFs are shown to compare the grain size in the TD, RD, and ND directions respectively. In the lower series of images CDFs of the same are shown. The data for the generated ellipsoids is obtained from a list of 10,000 representative ellipsoids

an average grain length of 2 mm. Thus an accurate description of the grain size in the RD is not available from conventional EBSD. To deal with this limitation, a grain aspect ratio of RD:ND = 12:1 was assumed, which allows the reconstruction to proceed appropriately.

The purpose of ellipsoid generation is to create a set of ellipsoids that can be packed into a desired volume. The ellipsoids should have an appropriate shape and size with respect to each other and with respect to the volume that they are being placed within. The first step of the process is to define the actual size of each of the three semi-minor axes of the representative ellipsoid. Multiple strategies are available, as discussed elsewhere in this chapter. They range in complexity, and the measure of accuracy is ultimately determined by the size and shape of the grains in the final digital microstructure.

In the first strategy, the lognormal nature of the data is emphasized and the dimensions are chosen based on sampling a lognormal distribution repeatedly. In the reconstruction of the rolled alloy, a form of the distribution of grain size in ND is normalized and programmed directly. It is then sampled to obtain the ND dimension of a representative ellipsoid. The TD and RD dimension are then obtained by multiplying the ND dimension by a value chosen from a distribution of the aspect ratios, where the TD direction distribution has a mean value of 4.0 and the RD direction distribution has a mean value of 12.0. This simple strategy relies on the observation of a mean value of the aspect ratios to completely define an ellipsoid, which represents a grain in the volume. There is, however, no attempt to check if the final size and shape distributions of the ellipsoids generated are actually representative of the input grain size and shape distributions. In this approach the ellipsoid shape and size is normalized, as is the volume that they are placed within. They must be rescaled by selecting an appropriate microns/voxel ratio in the final step of structure generation. The total number of ellipsoids generated is actually determined by the size and shape of the volume that they are placed within.

In the second strategy the input data is used directly to create a CDF (i.e., $F(TD)$) of grain size where the range of the CDF is 0 to 1 and the domain is scaled in micrometers. In this case the ND and TD data are used directly and the RD is simulated by multiplying the ND distribution by the chosen RD:ND aspect ratio, 12.0. To select the ellipsoid size from the CDFs, a value from 0 to 1 is chosen as a sample along the ordinate of the distribution. Then the appropriate value from the abscissa is read as depicted in Fig. 10.3. The distribution for each direction is sampled and multiplied by an arbitrary constant to account for the fact that that the CDF is generated from a 2D section. In this approach the total number of ellipsoids generated is specified as input to the program and it proceeds to optimize the list such that they are a good match to the input data. The optimization is accomplished iteratively and the first step is to create an initial list of ellipsoids and then slice each of them many times and extract the 2D CDFs of grain size on each section. The RMS error between the list and the input data is computed such that

$$\text{error} = \sqrt{\sum_{i=1}^{3} (F_i\_\text{list} - F_i\_\text{data})^2}, \qquad (10.2)$$

where i is an index on the semi-axis. The initial list is then modified by generating a new ellipsoid in the same manner as before and then randomly choosing an ellipsoid to replace from the list. The ellipsoid is replaced only if the new ellipsoid lowers the error

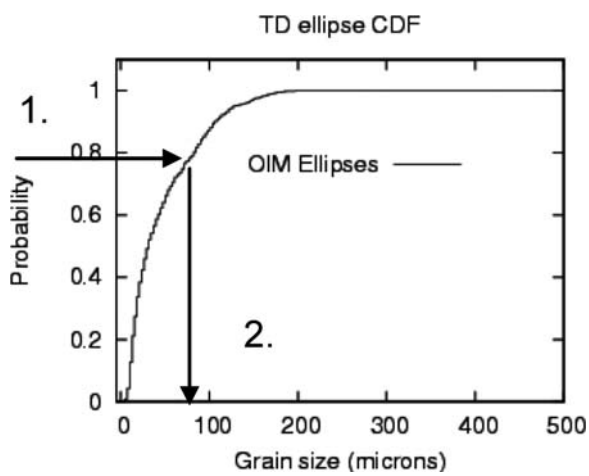


Fig. 10.3 Sampling of the CDF to generate an ellipsoid using the properties of the CDF of the ellipses as obtained from OIM data is shown here. In the first step (1.) a value from 0 to 1 is chosen along the ordinate, and in the second step (2.) the appropriate value of the grain size is read from the abscissa

of the system. The program completes when it has performed the number of user-specified iterations. The result of this method can be observed directly by comparing the PDFs and CDFs of the data and the simulated ellipsoids directly as can also be seen in Fig. 10.2. The distributions in both the ND and TD directions are well matched to the input data.

10.4.2 Observation-Based Domain Constraint

The elemental assumption of this method is that the entire (and infinite) set of all possible ellipsoids can be bounded by observations of ellipses on experimentally collected, orthogonal 2D sections to leave a "most probable" set of ellipsoids. Factors such as the distributions of size, shape, and orientation of the ellipses on the 2D sections are used to assign probabilities to groups of ellipsoids. This type of approach is fundamentally different from the analytical developments made by Cruz-Orive (1976b) and DeHoff (1962), in that an exact solution is not the goal; rather, a probable set is desired. An initial description of this technique is introduced by Groeber (2007).

In order to assign probabilities to groups of ellipsoids, the infinite domain of ellipsoids must be initially truncated and discretized. A five-dimensional space is created to define the ellipsoids. Three dimensions correspond to the orientation of the principal axes of the ellipsoid and are inherently bounded by the finite dimensions of Euler space, which describe the orientation of the ellipsoid (i.e., its principal axes). The other two dimensions correspond to the two aspect ratios of the ellipsoid. The aspect ratio dimensions are not inherently bounded, but can be truncated by using the 2D observations to make assumptions about reasonable upper and lower bounds. By definition, the upper limit of the two aspect ratio dimensions is 1 (i.e., a sphere) and the lower limit can be set to be the smallest aspect ratio observed in the 2D sections. In practicality, the accuracy of the estimated lower limit will be directly related to the number of observations and thus, it may be prudent to reduce the minimum observed value by an additional 25–50%. The volume of the ellipsoids is treated only as a distribution within each discrete bin in the 5D space, not as its own dimension. This is because volume only isotropically scales the dimensions of an ellipsoid and any resultant elliptic section, which has no effect on the following process.

The development of a probable set of ellipsoids is undertaken as an iterative process because of the inability to decouple the influences of ellipsoid shape (aspect ratios) and orientation on the resultant distribution of ellipses. The iterative process initiates by calculating a probable orientation distribution for the ellipsoids with an assumed uniform shape distribution. Then the shape distribution is updated using the calculated orientation distribution. Iteratively, each distribution is updated using the most recently calculated instance of the other distribution until a level of convergence is reached. Some details of the calculations are offered here, as well as the process of extrapolation of the individual ellipses.

Calculation of a probable orientation distribution requires sectioning a large number of ellipsoids within each discrete orientation bin and observing their resultant elliptic sections. Each ellipsoid is assigned a set of aspect ratios in accordance with the shape distribution, which is initially uniform. A two-dimensional histogram of resultant ellipse orientation and resultant ellipse aspect ratio is created for all ellipsoids in each of the orientation bins. An example histogram is shown in Fig. 10.4. The histograms for each bin are then compared to the same histogram made from the actual observations on the experimental 2D sections. The simulated histograms are fit to the experimental histogram by a least squares method to determine the probability of each orientation bin.

Upon calculating the orientation probability distribution, the shape distribution can be updated by sectioning a large number of ellipsoids within each discrete shape bin, represented by a set of aspect ratios. Each ellipsoid is assigned an orientation in accordance with the previously calculated orientation distribution. A two-dimensional histogram of resultant ellipse aspect ratio and resultant ellipse normalized size is constructed for all ellipsoids in each of the shape bins. The normalized size is the area of the resultant ellipse divided by the average resultant ellipse area. An example histogram is shown in Fig. 10.5. The histograms for each bin are then compared to the same histogram made from the actual observations on the experimental 2D sections. The simulated

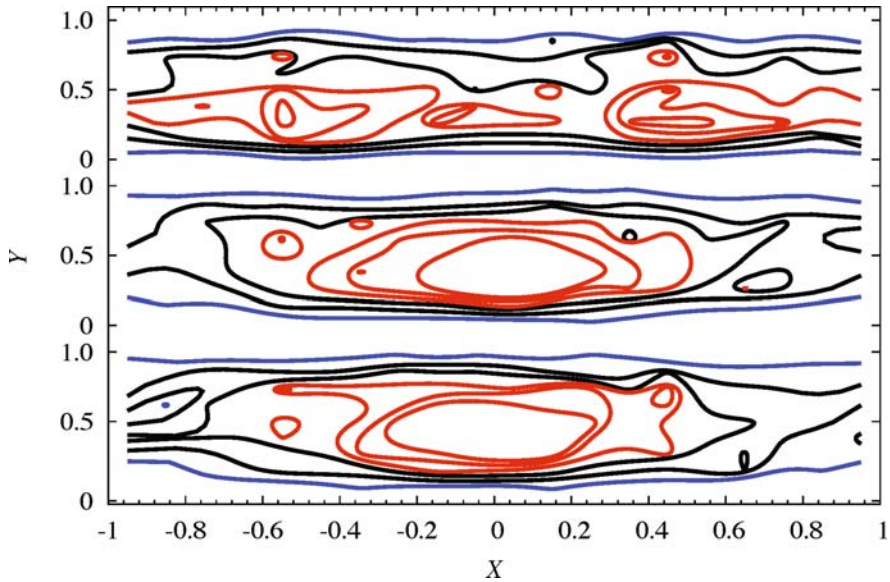


Fig. 10.4 Density plot of ellipse principal axis orientation vs. aspect ratio. The *top* third of the plot shows ellipses on the plane normal to the z-direction, the *middle* third shows ellipses on the plane normal to the y-direction, and the *bottom* third shows ellipses on the plane normal to the x-direction. The x-axis refers to the x-component of a unit vector oriented along the major axis of the ellipse. The y-axis is the aspect ratio (b/a) of the ellipse

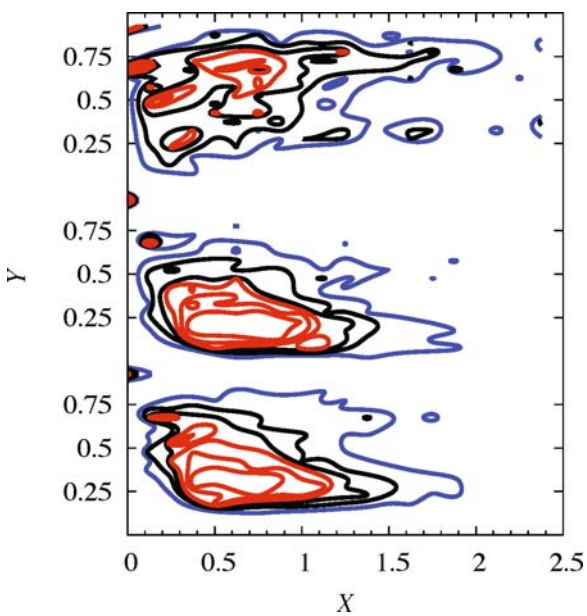


Fig. 10.5 Density plot of ellipse normalized size vs aspect ratio. The *top* third of the plot shows ellipses on the plane normal to the z-direction, the *middle* third shows ellipses on the plane normal to the y-direction, and the *bottom* third shows ellipses on the plane normal to the x-direction. The x-axis is the ellipse area divided by the average ellipse area. The y-axis is the aspect ratio (b/a) of the ellipse

histograms are fit to the experimental histogram by a least squares method to determine the probability of each shape bin.

While sectioning the ellipsoids to determine a probable orientation and shape distribution, the distribution of fractional section size is constructed for each shape bin. The fractional section size is defined as the resultant ellipse area divided by the maximum possible resultant ellipse area for a given ellipsoid. The fractional section size distribution is used to extrapolate the individual experimental ellipses. The shape of each experimental ellipse's parent ellipsoid is predicted by the probability of an ellipsoid of a given shape producing the experimental ellipse (i.e., its normalized size and aspect ratio). Once the parent ellipsoid's shape is assumed, the distribution of fractional section size for that shape can be used to convert the experimental section's area to the maximum possible section area for the parent ellipsoid. With an assumed shape and maximum possible section size, everything necessary to fully define the parent ellipsoid is available. This process is carried out for each experimental ellipse, resulting in a set of "probable" ellipsoids whose statistics can be used to generate synthetic 3D volumes. Figure 10.6 shows the results of the observation-based domain constraint process for a sample microstructure.

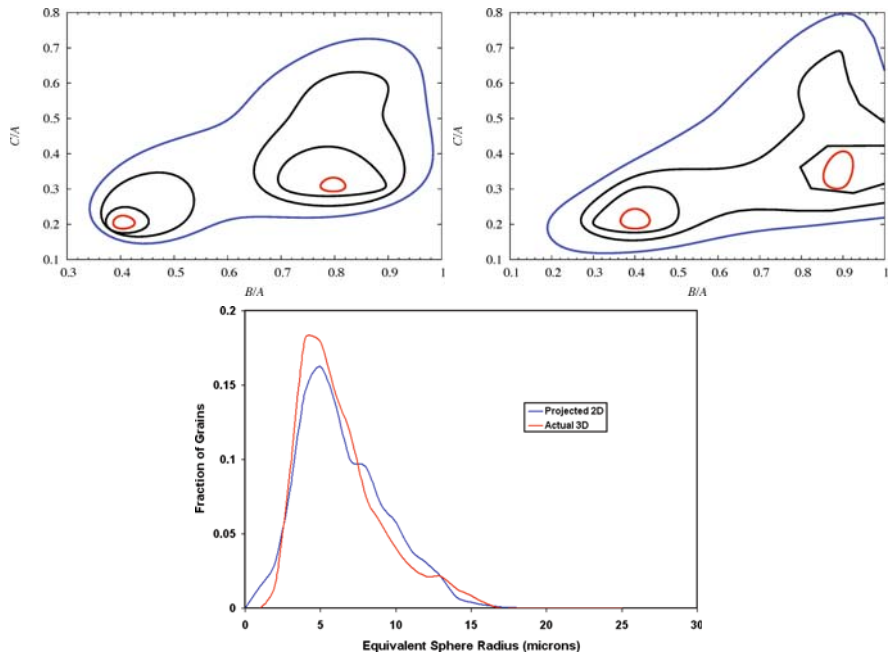


Fig. 10.6 Results of the observation-based domain constraint method. The *upper right* image is the true 3D shape distribution (ellipsoid aspect ratios). The *upper left* image is the "probable" shape distribution calculated by the method. The lower image is a comparison of the true 3D grain size distribution (equivalent sphere radius) and the calculated "probable" size distribution

10.5 Generation of 3D Structure

10.5.1 Packing of Ellipsoids

After generating a set of ellipsoids that is representative of the 3D grains and/or particles, the focus must be shifted to the placement of the ellipsoids in the volume. There are multiple issues to consider when packing the ellipsoids. The density of the objects represented by the ellipsoids is one of the largest factors in developing the packing algorithm. For example, ellipsoids representing particles of a low volume fraction phase will certainly be placed differently than ellipsoids representing grains in a fully dense polycrystalline material. In the fully dense grain example, care must be taken to pack the volume as densely as possible, but minimize overlap between ellipsoids in order to retain each ellipsoid's prescribed shape. In both cases, the local neighborhood of the ellipsoid (i.e., neighboring ellipsoids) must also be addressed during placement. The low volume fraction particles should be spaced equivalently to the experimental/reference data and the densely packed grains should neighbor grains of similar sizes and shapes as seen in the experimental/reference data.

Two inherently different, but viable options for ellipsoid packing will be discussed here. The first approach involves overpopulating the volume with a large number of ellipsoids. This approach is presented in greater detail elsewhere (Saylor et al. 2004b; Brahme et al. 2006). A large set of representative ellipsoids, generated by either of the methods discussed in the previous section, are placed into the model volume. The ellipsoids should have a total volume much larger than the volume to be filled and are allowed to overlap and extend outside of the volume. A simulated annealing procedure can then be employed to determine an "optimal" set of ellipsoids. An optimal set of ellipsoids would maximize space-filling, while minimizing overlap of ellipsoids. Saylor et al. (2004b) and Brahme et al. (2006) outline the development of a penalty function that promotes optimal space filling. It is easy to imagine the adjustment of this function to address the less dense packing of the distant particle case. At present, only the space-filling nature of

the ellipsoids is addressed in this technique, and not the local neighborhood of an ellipsoid. However, it is conceivable that penalty functions could be developed to encourage the desired clustering or spacing of ellipsoids of given sizes or shapes. Once an active set of ellipsoids is selected by this method, a voxelized structure is generated using cellular automata (CA), where the centroid for each ellipsoid is a seed point in the simulation and voxels are added starting at this seed point until the entire structure is filled. The growth is constrained initially such that only those voxel locations that are located inside the ellipsoids are added. When each ellipsoid is completely filled, then the constraint is dropped and the remaining free volume is consumed.

A second approach to the ellipsoid packing problem is to sequentially place the ellipsoids while using statistical descriptors from the experimental/reference data as constraints. One such implementation of this approach is presented by Groeber et al. (2008b). Here, the set of representative ellipsoids should have a total volume much nearer to the model volume than the first approach. The ellipsoids are allowed to extend outside the volume, as in the first approach, and thus the total volume should be some small amount above the model volume. Each ellipsoid is randomly placed in a sequential fashion and checked against a number of constraints to determine if its current position is acceptable. Constraints can include, but are not limited to: overlap limits, number of neighboring ellipsoids, and size distributions of neighboring ellipsoids. This approach generally yields optimal space-filling through the overlap limits, and produces realistic neighborhoods by constraining placement to locations that improve the surroundings of previously placed grains. Though this technique presents some advantages over the previous, there are complications that arise as well. In any sequential process there should be concerns about a failure to locate a suitable position, especially near the end of the process. Generally, the process is more efficient and successful when the largest grains are placed first,

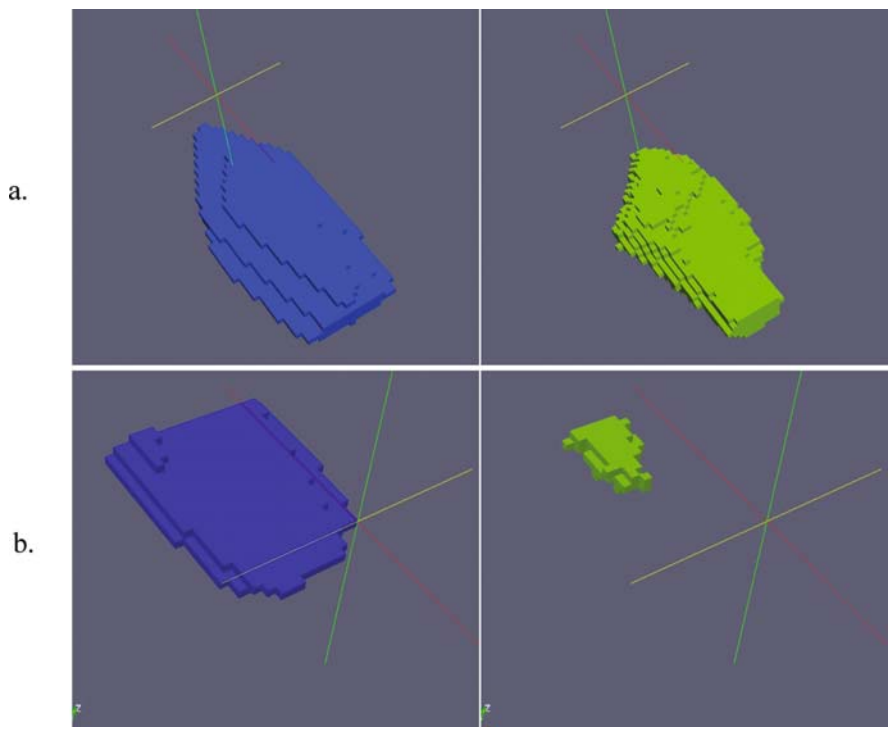


Fig. 10.7 The effect of MC relaxation on grain shapes and sizes is illustrated with two examples of before and after images. (**a**) In the *upper pair* of images, a grain changes shape to accommodate its neighbors. (**b**) In the *lower pair*, a very thin grain rapidly shrinks in response to a large curvature driving force

when there is sufficient room left for their placement. Additionally, the number of constraints greatly affects the feasibility of locating a suitable position, and thus should be optimized.

10.5.2 Relaxation of Boundaries

An artifact of the constrained CA process and the sequential grain placement process is that the grains are very close in shape to the ellipsoids used to model the grains, which means that the triple lines and quadruple points where boundaries intersect will deviate from the equilibrium dihedral angle. Therefore the grain shapes are relaxed using an isotropic Monte Carlo (MC) grain growth model (Rollett and Manohar 2004). Figure 10.7 depicts a series of images that highlight the effect of the MC procedure on the shape of individual grains. In the upper series the grain shape and size have both changed, but the changes are moderate as compared to the lower series where the entire grain is nearly consumed during MC relaxation. In general MC relaxation will relax the ellipsoid geometry, allow the grain boundaries to become more natural, and allow the grain size distribution to become more natural; but it will also cause the grains to quickly lose their anisotropic shape.

10.6 Quality Analysis

10.6.1 Size Distribution Comparison

Measuring the "size" of a grain may appear to be a simple matter at first sight. Even in 2D sections, however, computing the circle-equivalent diameter yields a (slightly) different result than the average linear intercept (Underwood 1970). In 3D, one must be concerned with all three dimensions, of which measuring the volume and surface area of a grain is intuitively obvious. Less obvious is how best to measure the linear dimension of a grain, since there are so many possibilities (linear intercept, sphere-equivalent radius, etc.). The recent publication by MacPherson and Srolovitz (2007) on the theory of grain growth has, however, pointed out to the materials science community that

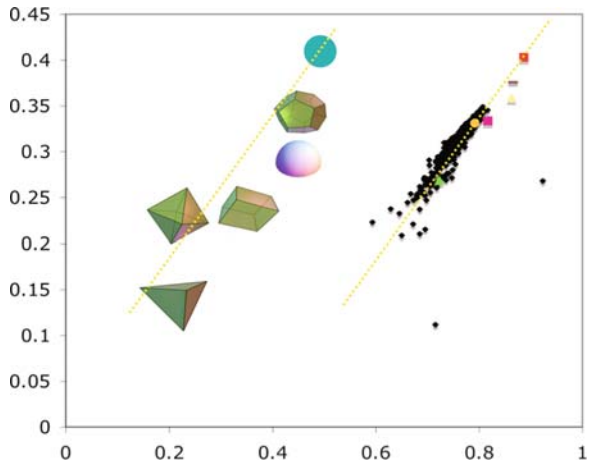


Fig. 10.8 Plot correlating the ratio of square root of surface area and mean width (x-axis) to the ratio of cube root of volume and mean width (y-axis). For reference, some basic geometric structures (i.e., the tetrahedron, the octahedron, etc.) are plotted as well. This type of analysis serves to offer some basic information about typical grain shapes (Uyar et al. 2008)

"mean width" is not only a useful measure of integral curvature of objects such as grains, but is also unique in its property of additivity. Hadwiger (1957) showed that there is only one measure in each dimension that has the property of additivity, which means that the volume/area/mean width of the union of two overlapping objects is the sum of the separate quantities, minus the volume/area/mean width of the overlapping region. This suggests that the distributions of the three basic quantities (volume, area, and mean width) should be part of the validation of a digital microstructure. Moreover, ratios between pairs of these quantities, as shown in Fig. 10.8, also provide basic information on the shape of objects (Uyar et al. 2008). Fitting to distributions of such ratios may also be part of the development of grain geometry in 3D models.

10.6.2 Shape Distribution Comparison

A typical approach to quantifying the shape of grains is to fit an ellipsoid and report the aspect ratios (Groeber et al. 2008a; Saylor et al. 2004b). This approach is useful in describing the distribution of the amount

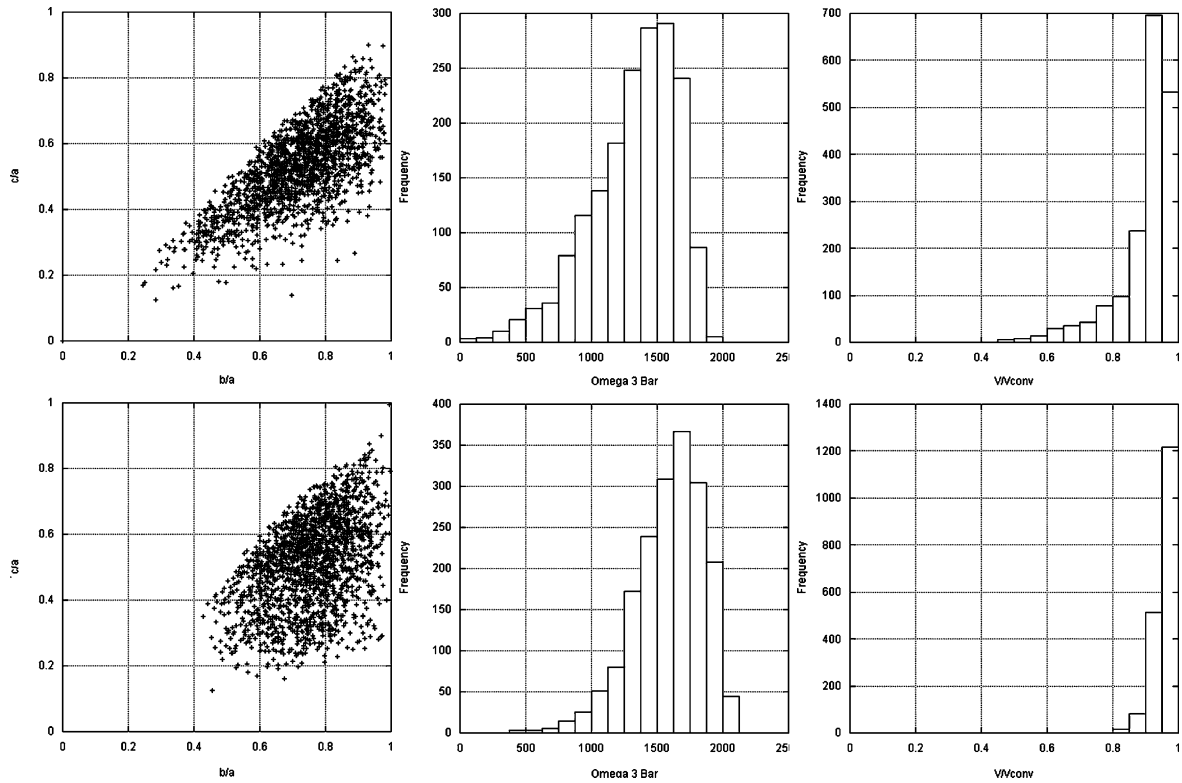


Fig. 10.9 Example of results from a moment invariant analysis. The *upper set* of plots is from an experimentally collected volume (Groeber et al. 2008). The *lower set* of plots is from a synthetic microstructure generated with the goal of matching the experimental volume's statistics, using methods presented by Groeber et al. (2008). The analysis highlights the need (and ability) to look past lower order descriptors like aspect ratios

of elongation of the grains. However, aspect ratios are ambiguous in reference to many aspects of shape. For example, it is possible for an ellipsoid and a rectangular prism to have the same set of aspect ratios. The local curvatures of grain boundaries are often disregarded when a "simple" geometric feature is fit to represent a grain. It is this issue that makes shape one of the more complicated parameters to describe.

MacSleyne et al. (2008) have presented a method for distinguishing shapes by using higher order moments and moment invariants. The moment invariant technique creates a three-dimensional moment invariant space to represent a grain's shape rather than the limited two-dimensional space defined by a pair of aspect ratios. In the moment invariant space, shapes with similar aspect ratios lie on the same arc, but are separated along the third dimension, Ω_3. Additionally, combinations of the calculated moments can yield interesting insights into the types of shapes present in the structure. An example of a moment invariant analysis is shown in Fig. 10.9. The analysis provides the distribution of aspect ratios, which appears roughly equivalent for the two structures. However, when the value of Ω_3 is compared, there is a noticeable shift in the distribution between the two structures. Finally, the largest difference between the two structures can be seen in the comparison of the distribution of V/V_{conv}. V_{conv} is the volume of the convex hull of the grain and V is the volume of the grain itself. The ratio of these two volumes is bounded by 0 and 1 and compares the relative concavity of the grain. It should be clear that the aspect ratio comparison alone does not accurately highlight many of the differences between the shapes of the two structures.

10.6.3 Neighborhood Comparison

The local neighborhood of a grain can be a complicated aggregate of features that can be described by a number of different parameters. For example, the morphological descriptors of the neighboring features could be reported, or their crystallographic relationship to the reference grain could be of more interest. Additionally, the approach to describing the local neighborhood of a grain is likely to vary with the type of microstructure and data being investigated. A grain structure which has been segmented is likely to have a known connectivity of grains and contiguous neighbors can be characterized. In the case of low volume fraction second-phase particles, the nearest neighbors may not be known, and a two-point statistics approach (Tewari et al. 2006) may be better suited.

For describing the morphology and connectivity of a grain's neighborhood, there are multiple distributions that can be created. First, the distribution of the number of neighbors can be generated for all grains, as well as correlated to grain size by grouping grains of similar size. In addition to number of neighbors, the size distribution of the neighboring grains can also be considered. The size distribution of neighbors, when correlated to the size of the reference grain, offers insights into the tendency of grains of certain sizes to cluster together (i.e., the Aboav-Weaire law). The shapes of neighboring grains can be correlated to the reference grain's shape to quantify the clustering of similar shaped grains, which may evolve during recrystallization or deformation.

The crystallographic description of individual boundaries will be discussed in the next section, but there are other parameters that describe the crystallography of local grain aggregates to varying degrees. The misorientation distribution function (MoDF) can be calculated for the entire structure, which gives some insight into the local textures present in the material. However, the MoDF does not provide any knowledge of the spatial distribution of the misorientations in the MoDF. The known connectivity of the grains allows for the spatial description of the misorientations. For example, one could calculate the fraction of a grain's neighbors that have a critical misorientation value, be it high, low, or special. This approach could then be expanded to include secondary neighbors (i.e., neighbors of neighbors) and would ultimately offer a more local estimate of the clustering of grains with similar orientation. Two-point statistics can also be employed to describe distributions of orientations as well.

10.6.4 Boundary Structure Comparison

In order to generate a complete 3D microstructure, one must add grain (crystal lattice) orientations to the description. The current state of the art is that the grain geometry is created first and then a set of orientations is optimized with respect to texture and grain boundary misorientation (Saylor et al. 2004b; Groeber et al. 2008b). The procedure relies on simulated annealing and is computationally straightforward on modern personal computers. This procedure has at least two significant limitations, however. The first is that it assumes that size and shape are uncorrelated with orientation. This is not always the case; however, Bozzolo et al. (2005) have demonstrated that in titanium that has been deformed and then recrystallized there are texture components that are more dominant in the small grains and vice versa. The second limitation is that it ignores the fact that grain boundary properties depend on the interface normal as well as the lattice misorientation across them. The full description of grain boundary character requires, in fact, five macroscopic parameters, as discussed in detail by Rohrer and Randle in Chapter 16 of this volume. Fitting orientations to include both texture and misorientation and interface normal distributions needs to be developed. Implementing such an algorithm in voxel-based representations requires some method to compute the local interface normal (Bullard et al. 1995). Alternatively, interface normals can be straightforwardly computed in a surface or volumetric mesh representation of a microstructure.

10.7 Thoughts on Current Conditions and Future Work

Everything that has been described up to this point deals with grain size and shape, grain orientation (texture), and intergrain misorientation. There are several important aspects of microstructure that have not yet

been addressed. Grain boundaries require five parameters to describe their macroscopic degrees of freedom (crystallographically), which are addressed by Rohrer and Randle in this volume. Polycrystals are known to exhibit strong preferences for certain interface normals (Saylor et al. 2004a). A more complete fitting procedure for grain orientations in synthetic microstructures will account for the complete five-parameter grain boundary character. Deformed solids and even annealed polycrystals exhibit orientation gradients within grains. Mechanical properties can depend on the presence of such gradients, as seen in strain gradient theories of solid mechanics, for example. Recrystallization during annealing occurs when boundaries move in response to differences in stored energy, and orientation gradients can give rise to such differences. Yet another issue that will need to be addressed is that of grain shape. It is convenient to use the ellipsoid as a surrogate for actual grains, but real grains are far from ellipsoidal in reality. It would be useful to be able to work with more sophisticated surrogates for shape as presented by MacSleyne et al. (2008).

References

Brahme A, Alvi MH, Saylor D, Fridy J, Rollett AD (2006) 3D reconstruction of microstructure in a commercial purity aluminum. Scripta Mater 55:75–80

Bozzolo N, Dewobroto N, Grosdidier T, Wagner F (2005) Texture evolution during grain growth in recrystallized commercially pure titanium. Mater Sci Eng A Struct Mater 397:346

Bullard JW, Garboczi EJ, Carter WC, Fuller ER (1995) Numerical methods for computing interfacial mean curvature. Comp Mater Sci 4:103–116

Cahn JW, Fullman RL (1956) On the use of lineal analysis for obtaining particle size distribution functions in opaque samples. Trans Metall Soc AIME 206: 610–612

Cruz-Orive LM (1976a) Correction of stereological parameters from biased samples on nucleated particle phases, part 1: nuclear volume fraction. J Microsc 107:1–18

Cruz-Orive LM (1976b) Particle size-shape distributions: the general spheroid problem. J Microsc 107:235–253

Dehoff RT (1962) The determination of the size distribution of ellipsoidal particles from measurements made on random plane sections. Trans Metall Soc AIME 224:474–486

Dillard SE, Bingert JF, Thoma D, Hamann B (2007) IEEE T Vis Comput Graph 13:1528–1535

Fernandes CP et al (1996) Multiscale geometrical reconstruction of porous structures. Phys Rev E 54:1734–1741

García RE et al (2004) Microstructural modeling of multifunctional material properties: the OOF project. In: Raabe D (ed) Continuum scale simulation of engineering materials. Wiley-VCH, Weinheim, Germany; http://www.ctcms.nist.gov/oof/index.html

Groeber MA (2007) Ph.D. Thesis, The Ohio State University

Groeber MA, Uchic MD, Dimiduk DM, Ghosh S (2008a) A framework for automated analysis and simulation of 3D polycrystalline microstructures, part 1: statistical characterization. Acta Mater 56:1257–1273

Groeber MA, Uchic MD, Dimiduk DM, Ghosh S (2008b) A framework for automated analysis and simulation of 3D polycrystalline microstructures, part 2: synthetic structure generation. Acta Mater 56:1274–1287

Hadwiger H (1957) Vorlesungen über inhalt, oberfläche und isoperimetrie. Springer, Berlin

Han TS, Dawson PR (2005) Representation of anisotropic phase morphology. Model Simul Mater Sci Eng 13: 203–223

Humphreys FJ (1999) Quantitative metallography by electron backscattered diffraction. J Microsc 195:170–185

Lewis AC, Bingert JF, Rowenhorst DJ, Gupta A, Geltmacher AB, Spanos G (2006) Two- and three-dimensional microstructural characterization of a super-austenitic stainless steel. Mater Sci Eng A 418:11–18

Li M, Ghosh S, Richmond O, Weiland H, Rouns TN (1999) Three dimensional characterization and modeling of particle reinforced metal matrix composites, part 1: quantitative description of microstructure morphology. Mater Sci Eng A A265:153–173

MacPherson RD, Srolovitz DJ (2007) The von neumann relation generalized to coarsening of three-dimensional microstructures. Nature 446:1053

MacSleyne J, Simmons JP, DeGraef M (2008) On the use of moment invariants for the automated analysis of 3-D particle shapes. Model Simul Mater Sci Eng 16:045008

Oren PE, Bakke S (2002) Process based reconstruction of sandstones and prediction of transport properties. Transport Porous Med 46:311–343

Oren PE, Bakke S (2003) Reconstruction of berea sandstone and pore-scale modeling of wetability effects. J Petrol Sci Eng 39:177–199

Przystupa MA (1997) Estimation of true size distribution of partially aligned same-shape ellipsoidal particles. Scripta Mater 37:1701–1707

Rollett AD, Manohar P (2004) The monte carlo method. In: Raabe D (ed) Continuum scale simulation of engineering materials. Wiley-VCH, Weinheim, Germany

Rowenhorst DJ, Gupta A, Feng CR, Spanos G (2006) 3D crystallographic and morphological analysis of coarse martensite: combining EBSD and serial sectioning. Scripta Mater 55:11–16

Russ JC (2006) The Image Processing Handbook. (5 ed.). CRC Press, Boca Raton, FL

Saltykov SA (1958) Stereometric metallography, Metallurgizdat, Moscow

Saylor DM, El-Dasher BS, Adams BL, Rohrer GS (2004a) Measuring the five-parameter grain boundary distribution from observations of planar sections. Metall Mater Trans 35A:1981–1989

Saylor DM, Fridy J, El-Dasher BS, Jung KY, Rollett AD (2004b) Statistically representative three-dimensional microstructures based on orthogonal observation sections. Metall Mater Trans A 35A:1969–1979

Sundararaghavan V, Zabaras N (2005) Classification and reconstruction of three-dimensional microstructures using support vector machines. Comp Mater Sci 32:223–239

Talukdar MS, Torsaeter O (2002) Reconstruction of chalk pore networks from 2D backscatter electron micrographs using a simulated annealing technique. J Petrol Sci Eng 33:265–282

Talukdar MS, Torsaeter O, Ioannidis MA (2002a) Stochastic reconstruction of particulate media from two-dimensional images. J Colloid Interf Sci 248:419–428

Talukdar MS, Torsaeter O, Ioannidis MA, Howard JJ (2002b) Stochastic reconstruction, 3D characterization and network modeling of chalk. J Petrol Sci Eng 35:1–21

Talukdar MS, Torsaeter O, Ioannidis MA, Howard JJ (2002c) Stochastic reconstruction of chalk from 2D images. Transport Porous Med 48:101–123

Tewari A, Spowart JE, Gokhale AM, Mishra RS, Miracle DB et al (2006) Characterization of the effects of friction stir processing on microstructural changes in DRA composites. Mater Sci Eng A 428:80–90

Torquato S (2001) Random heterogeneous materials: Microstructure and macroscopic properties. Springer-Verlag, New York

Underwood E (1970) Quantitative Stereology, Addison-Wesley, New York

Uyar F, Wilson S, Gruber J, Rollett AD, Srolovitz DJ (2008) Int J Mater Res (submitted)

Chapter 11

Direct 3D Simulation of Plastic Flow from EBSD Data

Nathan R. Barton, Joel V. Bernier, Ricardo A. Lebensohn, and Anthony D. Rollett

11.1 Introduction

Given high quality EBSD scans of microstructures, researchers naturally wish to assess the properties and performance of the material. For virtually all aspects of material behavior, this involves a model for the material's response, and considerable uncertainty in the predictions arises from uncertainties in both model form and model parameters. Classical crystal viscoplasticity is often used to assess the plastic flow behavior of polycrystalline materials (Kocks et al. 1998); but more sophisticated approaches are under active development. For example, Arsenlis et al. (2004) have included the effects of detailed dislocation density evolution, including dislocation flux terms that capture heterogeneity in the flow; and Acharya and Beaudoin (2000) have examined interactions between lattice curvature and hardening. Once a modeling framework has been chosen, including both the material model and the method for solving the boundary value problem, a key consideration becomes the numerical accuracy of the solution. Ideally, observations should not be influenced appreciably by inadequacies in the implementation of the model or convergence of the results. However, even relatively simple material models can require substantial computational resources to achieve proper convergence of the results. Here we focus on a relatively simple material model and a particularly challenging microstructure to illustrate some of the current limitations in analysis. The degree to which a model captures heterogeneous material response depends directly on the microstructural discretization.

A crystal-based restricted slip rigid-viscoplastic material model is used to predict the steady-state plastic flow in the microstructure. The multiphase microstructures in titanium alloys motivate most of the simulations, with variations in the thermomechanical processing path producing a wide variety of microstructures for these materials (Lüetjering and Williams 2003). Heterogeneity of the flow in lamellar microstructures has been studied previously (Barton and Dawson 2002). Even for microstructures without lamellar features, complex heterogeneous plastic flow arises from the strong plastic anisotropy in the α phase and the relative geometric softness of the β phase. Here we examine microstructures with equiaxed α grains, with some attention paid to heterogeneities of the sort that might be associated with the creation of defects such as voids and cracks. Creation of such defects is of ongoing interest (Sinha et al. 2007). It is well known that compressive deformation modes in materials with highly anisotropic microstructural constituents can produce substantial tensile hydrostatic stresses (Dao et al. 1996) that are implicated in the formation of defects. For comparison of finite element-based and Fourier transform-based modeling approaches, a single-phase microstructure of a BCC material is also considered.

Three-dimensional calculations are desirable for accurate treatment of realistic microstructures, and researchers are actively exploring methods for three-dimensional microstructure creation, given experimental measurements from EBSD scans and other sources. See Chapter 10 by Sintay, Groeber, and Rollett in this volume for discussion of three-dimensional

N.R. Barton (✉)
Lawrence Livermore National Laboratory, Livermore, CA 94550, USA
e-mail: barton22@llnl.gov

A.J. Schwartz et al. (eds.), *Electron Backscatter Diffraction in Materials Science*,
DOI 10.1007/978-0-387-88136-2_11, © Springer Science+Business Media, LLC 2009

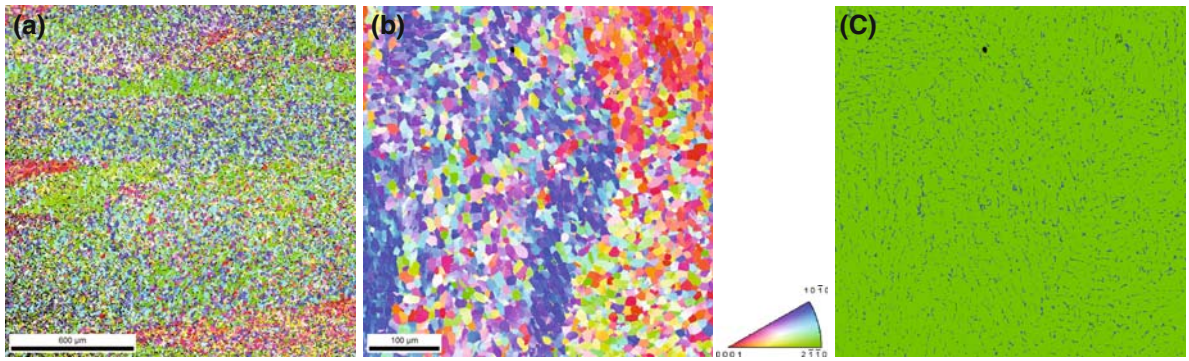


Fig. 11.1 Data from EBSD scans of Ti-6Al-4V covering (**a**) 1.725 mm on a side with 3.5-micron step size, and (**b**) on a perpendicular face 0.5 mm on a size with 0.5-micron step size. For parts (**a**) and (**b**), lattice orientations in the α phase are colored according to the crystallographic axis aligned with direction normal to the scan plane. Part (**c**) shows the phase distribution for the scan in part (**b**) with α being *green* and β being *blue*

microstructure reconstruction. In some cases, investigators wish to build a computational mesh with elements conforming to grain boundaries (Maniatty et al. 2008). This is likely to increase the rate of convergence with mesh refinement, and may have distinct advantages if stress concentrations in the elastic loading range are of interest. To simplify examination of mesh convergence, we use logically regular grids with serrated grain boundaries and mixed-material elements at phase boundaries. This seems to be adequate for examination of behavior under steady plastic flow. Note that in general the rate of convergence with mesh refinement depends significantly on the quantity of interest, with overall response converging in many cases more quickly than subgrain deformation features (Barton and Dawson 2001a, 2001b).

11.2 Material and Microstructural Model

In general, the slip and twinning modes in titanium alloys depend strongly on alloying and temperature (Paton et al. 1973). While twinning is of interest in commercial purity titanium (Bozzolo et al. 2007, for example), alloys such as Ti-6Al-4V do not tend to produce appreciable amounts of twinning during deformation at room temperature and quasi-static strain rates. While this simplifies analysis in some regards, considerable complexity remains in the observed microstructures. Figure 11.1 shows EBSD scans of a relatively simple Ti-6Al-4V microstructure. Long-range correlation of the orientations of the α phase can be observed, presumably correlated to the prior high temperature β grain structure. Figure 11.2 shows a scan for a sample with a different final heat treatment. Direct numerical simulation of three-dimensional microstructures such as the one in Fig. 11.2 are currently beyond generally available computational resources, and one must resort to modeling assumptions to treat deformation partitioning in such structures. We will examine direct numerical simulations of a microstructure such as the one in Fig. 11.1, but with a somewhat larger volume fraction of β phase

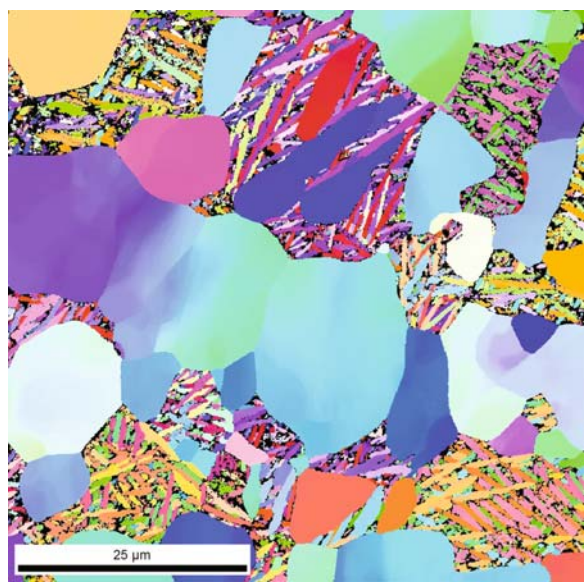


Fig. 11.2 Data from a different heat treatment than the one shown in Fig. 11.1, using the same color mapping as in Fig. 11.1. A relatively small fraction of β phase points were indexed and it is assumed that index failures occur preferentially in the β phase

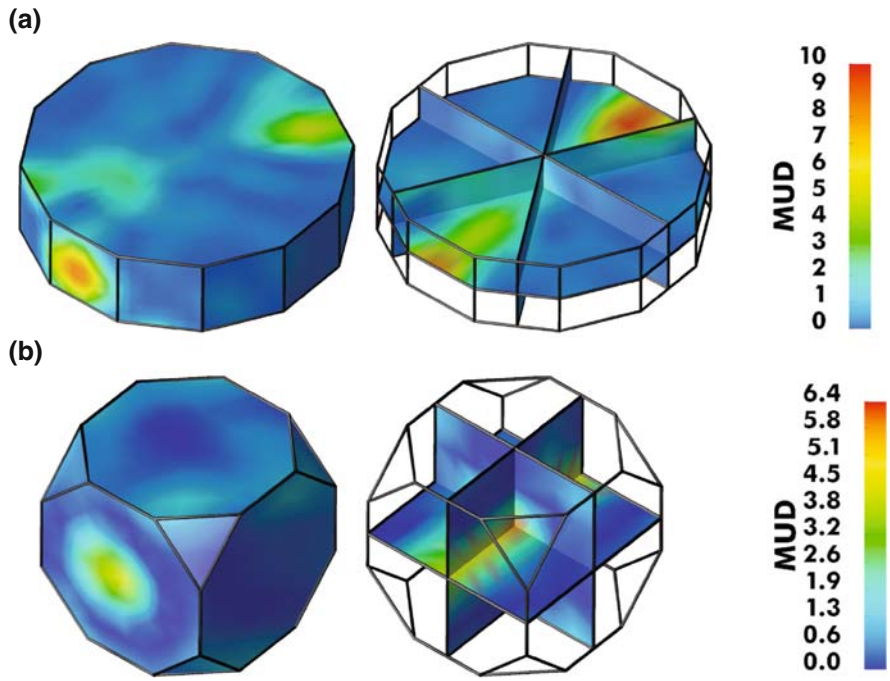


Fig. 11.3 Lattice orientation distribution functions for (**a**) α and (**b**) β phases, plotted as multiples of a uniform distribution

in order to examine effects of interest for connected or nearly connected soft phases.

Orientation distribution functions for the α and β phases can be determined from data shown in Fig. 11.1(a). Due to the long-range spatial correlations in the lattice orientations, these EBSD data are supplemented by bulk X-ray diffraction using high energy X-rays from the Advanced Photon Source at the Argonne National Laboratory. Surface and bulk diffraction data are consistent, and the orientation distribution functions reduced from X-ray diffraction data, using pole figure inversion techniques based on finite element discretizations in Rodrigues space (Barton et al. 2002; Bernier et al. 2006), are shown in Fig. 11.3.

11.2.1 Three-Dimensional Microstructure Generation

Three-dimensional microstructures are generated by matching certain experimentally measured distributions. Grain size distributions from the EBSD scans are sampled to generate grains, and these grains are then packed into a spatial domain larger than the desired computational domain. Various heuristics are used in the particle packing process and in subsequent manipulations in order to generate morphologies and final phase volume fractions of interest. By packing particles in order from largest to smallest, tighter packings may be achieved. Once a packing of grain centroids has been generated, standard convex hull analysis packages can be used as the basis for construction of full microstructures. The tessellation algorithm employed takes account of the grain size data used in the original packing of grains. These techniques are not the focus of this chapter, and might best be replaced by direct measurement of three-dimensional microstructures. The three previous chapters in this volume contain a more detailed discussion of microstructure generation techniques. Here we are interested in behavior of the models under challenging computational scenarios, and somewhat idealized microstructures are adequate. For models that require periodic boundary conditions, microstructure generation from distributions of microstructural features is likely to remain of interest. One such modeling framework is based on fast Fourier transform (FFT) algorithms and will be discussed below. For synthetic microstructure generation, multi-point correlation functions have some desirable properties (Yeong and Torquato 1998).

Figure 11.4 shows one instance of the microstructure used in most of the calculations here. Plots in Fig. 11.4 are from a logically regular finite element mesh with 128 elements per side (2097152 elements

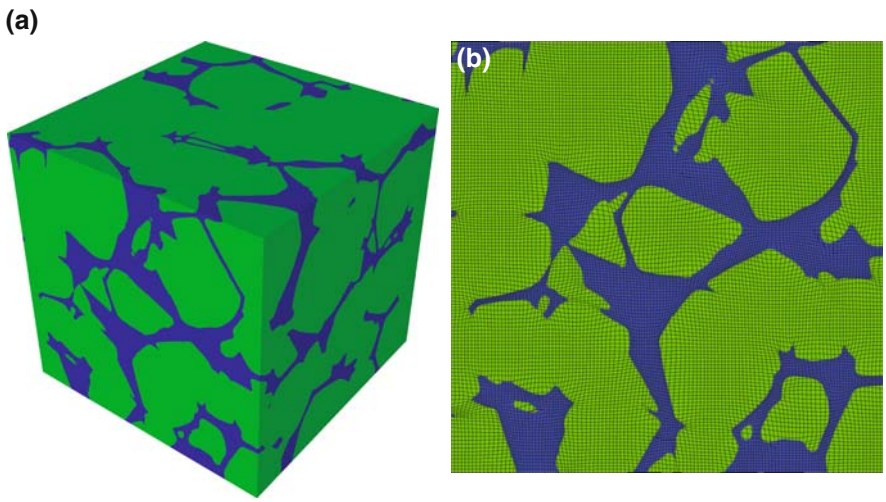


Fig. 11.4 Phase distributions in an idealized multiphase titanium microstructure with α and β being *green* and *blue*, respectively; β volume fraction is roughly 15%. The plot in (**b**) shows the finite element mesh on one face of the domain, indicating the degree to which elements are preferentially located in the β phase

total). To capture localization of the deformation in the β phase, elements are preferentially placed in the β phase. A standard arbitrary Lagrangian-Eulerian advection scheme accomplishes this task (Benson 1992, 1998). Use of advection here effectively allows us to hold the material and microstructure fixed while distorting the mesh to pull elements preferentially into the geometrically softer β phase. Because mesh connectivity does not change during this process, mesh distortions limit the achievable relative size of elements in the β. The efficacy of this local refinement method is demonstrated in Fig. 11.5, which shows results on a regular Cartesian mesh (Fig. 11.5[a]) and on an advected mesh (Fig. 11.5[b]). The advected mesh with more elements in the thin β phase regions captures more strain localization and detailed features of the response with the same number of computational degrees of freedom. Advection may be used during the simulation of the deformation with crystal level material models (Barton et al. 2004), perhaps with elements preferentially advected based on plastic shearing rates. However, the computational framework used here cannot at this time combine advection with boundary conditions appropriate to quasi-static deformation. As discussed below, adaptive mesh refinement may be a better technique for capturing localization in high fidelity simulations.

11.2.2 Micromechanical Model

The model employs standard restricted slip crystal plasticity described in considerable detail elsewhere (Hosford 1993; Kocks et al. 1998; and the references contained therein). That is, plastic deformation occurs by a linear combination of shearing modes on a set of slip systems defined with respect to the crystal lattice. The specific formulation here is similar to those described by Barton and Dawson (2002) and Barton et al. (2004, 2008). While the rigid-viscoplastic response is of interest for steady plastic flow, the formulation includes elasticity, and the elastic degrees of freedom are driven to steady state using a specialized algorithm. Lattice orientations and state variables associated with material hardness are all held constant as the steady plastic flow solution is determined. All slip systems follow power law kinetics with a rate sensitivity of 0.05. The β phase deforms plastically using 12 $\{110\}\langle 111\rangle$, 12 $\{112\}\langle 111\rangle$, and 24 $\{123\}\langle 111\rangle$ slip systems. Plastic deformation in the α phase occurs by slip on 3 basal $\{0001\}\langle 11\bar{2}0\rangle$, 3 prismatic $\{10\bar{1}0\}\langle 11\bar{2}0\rangle$, and 12 pyramidal $\{10\bar{1}1\}\langle \bar{1}\bar{1}23\rangle$ slip systems. All slip systems other than the α pyramidal slip systems are assumed to have the same strength, with the pyramidal systems five times stronger. These strengths are consistent with the range of values deduced from experimental results for multiphase titanium alloys (Bieler and Semiatin 2002).

As noted below, rigid-viscoplastic material models create challenges related to incompressibility and numerical conditioning—the solution of the elasto-viscoplastic problem is typically less challenging. However, the solution of the rigid-viscoplastic problem allows for direct comparison between FFT- and

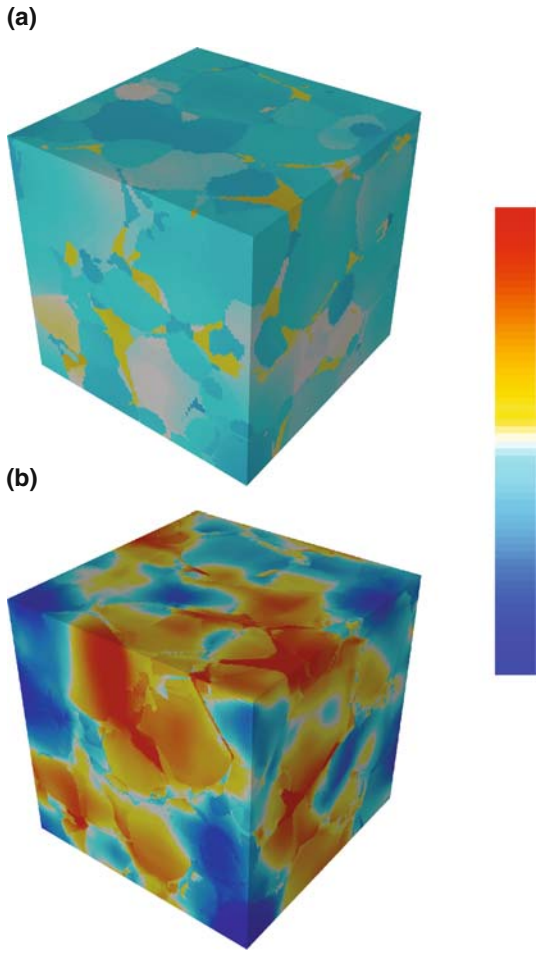


Fig. 11.5 Plots of total slip system activity for (**a**) a uniform Cartesian mesh and (**b**) an advected mesh, both having 96 elements per side. Slip activity is normalized by the average rate, so that the average becomes *white* on the indicated color map. Blue indicates zero slip activity, and values greater than or equal to twice the average are plotted in *red*

finite element-based methods and allows for evaluation of the response of a fixed as-measured microstructure.

11.2.3 Finite Element Model

Various finite element formulations are in use for micromechanical simulations of the sort performed here. See Benson (1998) for a discussion of the use of formulations with advection capabilities in micromechanics simulations. Other methods also use shaping of microstructures and mixed material elements to circumvent some of the challenges in discretizing microstructures (Barbe et al. 2001). In the formulation used here, mixed material elements employ a uniform strain partitioning assumption among the material volume fractions, and material volume fractions are computed accurately from the underlying microstructural description.

Elastic effects in the material model tend to regularize the behavior, but the convergence rate of the parallel iterative linear system solver does diminish as the simulation approaches steady plastic flow, adding substantially to the computational expense. The linear solver is based on an algebraic multi-grid technique, as described by Henson and Yang (2002). The solver shows good performance versus system size over the range examined here—computational cost is nearly linear in the total number of degrees of freedom. The formulation with elastic effects also proves useful in low symmetry materials, such as $CaIrO_3$ post-perovskite (Miyagi et al. 2008), with a paucity of plastic deformation mechanisms.

Direct simulation of the rigid-viscoplasticity problem is conducted elsewhere using hybrid finite element formulations to improve numerical behavior (Beaudoin et al. 2000; Sarma and Dawson 1996; Beaudoin et al. 1993), and specialized finite elements have in some cases been employed to improve treatment of the flow of an incompressible fluid (Mika 1999; Dawson et al. 2002). In general, crystal rigid-visocplasticity solutions are a challenge to obtain, particularly in the face of highly anisotropic constituents and multiple phases with disparate effective strengths.

11.3 Simulation Results

Simulation results in this section focus on the isochoric compression of the microstructure shown in Fig. 11.4. In all plots, the compression direction is vertical. All exterior faces are forced to remain planar, though velocity components in the plane need not be zero. Periodic boundary conditions are not currently available in the computational framework used here—see for example the work of Maniatty et al. (2008) for an example of the use of periodic boundary conditions in finite element simulations of polycrystals.

Even with the use of advection to concentrate elements in the geometrically softer β phase, most features of the microstructural response do not show convergence with 128 elements on a side of the cube. Figure 11.6 shows volume averages for the axial component of the deviatoric stress and for phase-specific average slip activity. Slip activity is defined as the sum of the magnitudes of shear rates over a phase or slip system type. With mesh refinement, simulated deformation becomes more localized and the average stress magnitude diminishes. The finite element formulation strictly enforces compatibility and naturally tends to be closer to an upper bound result when there are insufficient degrees of freedom. Note that due to the nonlinearity of the viscoplastic response, average slip activity can increase even as average stress magnitude decreases. In this case peak slip rates increase substantially with mesh refinement, as shown in Fig. 11.7. In this and other plots of slip system activity, values are scaled by the average activity in the simulation with 128 elements on a side. The mesh refinement studies are not continued to higher mesh refinement because of computational costs. The simulation with 128 elements on a side required 159 hours on 200 processors running at 2.2 MHz. Obtaining a converged steady plastic flow solution requires 25 time steps with typically three iterations per time step and typically 1500 to 2000 iterations in each execution of the iterative linear system solver. In light of these computational demands, current efforts are focused on more effective preconditioners for the system solve and on more robust finite element formulations. Spurious fluctuations in the pressure field persist over the range of mesh refinement examined here, and a specialized formulation may produce marked increases in convergence rate with mesh refinement.

Note from Fig. 11.7 that mesh refinement produces both a sharpening of features existing at coarser refinements and the introduction of localization features not observed at coarser refinements. The introduction of new localization features is in fair measure due to resolution of fine details in the idealized microstructure. This points to the potential importance of high-resolution microscopy for materials that potentially contain such features.

The amounts of basal and non-basal slip activity in the α phase are shown in Fig. 11.8. Data such as these may be useful in assessing the propensity of given microstructural features to initiate damage such as microstructural level cracks and voids. Higher

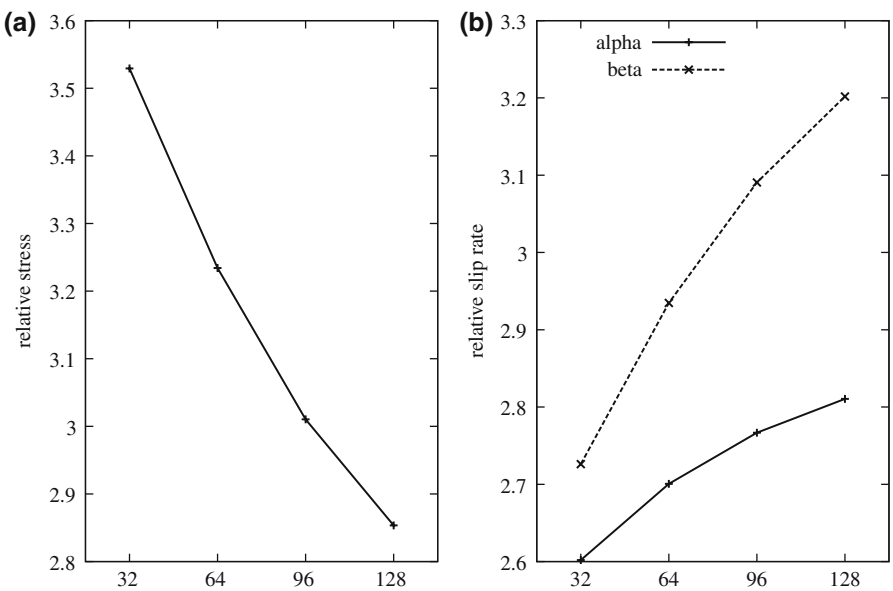


Fig. 11.6 Volume averages versus mesh refinement; with (**a**) showing axial deviatoric compressive stress and (**b**) showing phase specific slip system activities. Slip activity is relative to the applied macroscopic deformation rate. Stress is scaled by the strength of the nonpyramidal slip systems

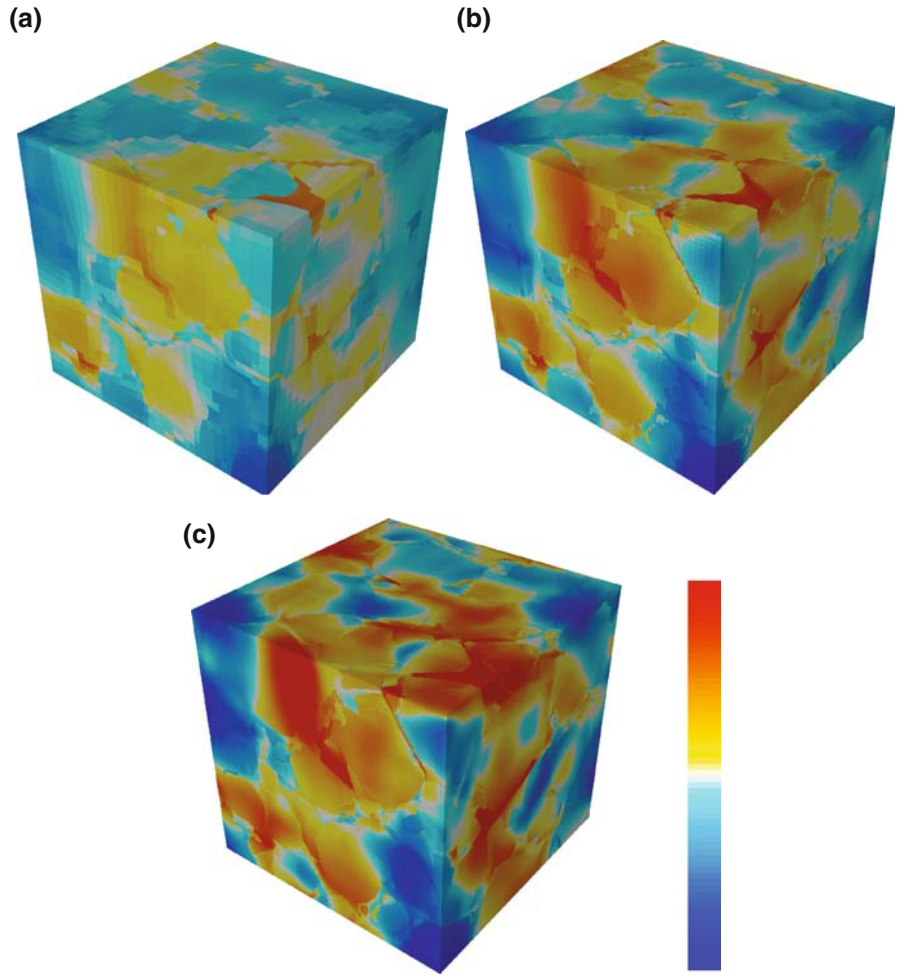


Fig. 11.7 Total slip system activities as a function of mesh refinement for (**a**) 32, (**b**) 64, and (**c**) 128 elements per side; using the same color mapping as in Fig. 11.5

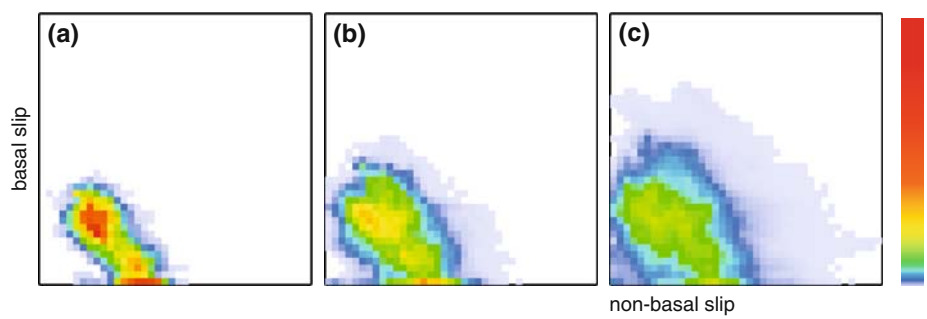


Fig. 11.8 Probability density for basal slip activity versus non-basal slip activity in the α phase, with axes scaled to cover a range up to six times the nominal deformation rate; versus mesh refinement for (**a**) 32, (**b**) 64, and (**c**) 128 elements per side. Mapping from probability to color emphasizes lower probabilities, as shown in the color map; bins without contributions are shown in *white*

probabilities along the horizontal axis, corresponding to negligible basal slip, are attributed to basal slip contributing only three of the eighteen total slip systems. That is, the material contributing to the horizontal axis is deforming by a combination of prismatic and pyramidal slip with negligible basal slip. Increased mesh refinement captures substantially broader dispersion in the slip rates. As with the total slip activity data, the spatial distribution (not shown) of the relative amount of basal slip shows both refinement of features and the development of new features with mesh refinement. At higher mesh refinement, the solution includes appreciable amounts of material deforming almost exclusively by slip on basal systems, and these types of features in distributions could have implications for damage initiation on the basal planes in the α phase. Even in compression, tensile hydrostatic stresses on the order of the effective flow strength or higher can be produced in materials with highly anisotropic constituents, such as the one examined here. Such effects are worth detailed examination employing methods that are not prone to spurious fluctuations in the pressure field. Assuming converged solutions may be obtained, predicted distributions of features in the mechanical response might come to play an important role in assessments of as-measured microstructures.

11.4 Directions for Further Computational Development

Given the computational expense of using general-purpose finite element programs to solve rigid-viscoplasticity problems, alternative approaches are attractive. One promising approach is based on FFT (Moulinec and Suquet 1998; Lebensohn 2001; Lebensohn et al. 2004), which generally scales better with problem size than finite element implementations. The computational framework is also dramatically simpler given the special purpose nature of the code base and the use of a Cartesian regular grid. These benefits come with some sacrifice in flexibility—one cannot, for example, examine details of incipient plasticity in advance of fully developed plastic flow.

Direct comparison of results from FFT and finite element simulations is hampered by differences in boundary conditions. The FFT method must employ periodic boundary conditions, and many finite element codes, including the one used here, do not implement equivalent boundary conditions. Some comparison can however be made by invoking Saint Venant's principle (von Mises 1945) for columnar geometries and surrounding the lateral faces of the domain in the FFT simulation by "void" cells. In this way, microstructures under uniaxial tension may be simulated. The serial FFT implementation is, however, bound by memory constraints, and the simulation shown in Fig. 11.9 is limited to roughly two million FFT points. Thus the domain has 512 points along the axis and 64 points across each lateral dimension. In both lateral dimensions, there are void points to simulate traction-free lateral surfaces, leaving 60 points for resolving the microstructure. Adequately resolved and converged simulations should show similar responses in the middle section of the computational domain, even though the boundary conditions at the ends differ in

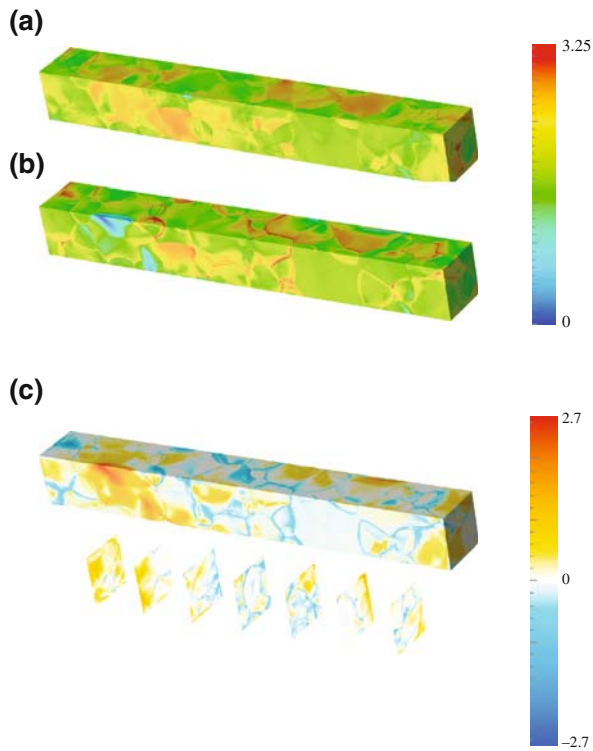


Fig. 11.9 Magnitudes of the deviatoric stress from (**a**) FFT- and (**b**) finite element method-based simulations, with the color map ranging from 0 to 3.25. Differences are shown over the surface and on interior slices in (**c**) with the color map ranging from -2.7 to 2.7. All values and differences are relative to the slip system strength

their details between the FFT- and finite element-based simulations.

For these tensile simulations, the microstructure is composed of single phase BCC material with twelve slip systems all having the same strength. This relatively low anisotropy material system is used because mesh refinement limitations in the tensile geometry do not allow for adequate resolution of deformation heterogeneity in highly anisotropic and multi-phase materials. The FFT-based method does not treat mixed material cells, and so both the FFT- and FEM-based simulations are performed without mixed material zones. That is, the grain boundaries are stair-stepped.

While some of the features observed in Fig. 11.9 are similar, it is clear that more mesh resolution and perhaps better convergence is needed before definitive comparison may be made. Parallel FFT methods are available, and use of these methods in the rigid-viscoplastic polycrystal context is actively being pursued. Elasto-viscoplastic FFT formulations are also actively being pursued, and the availability of such methods would greatly ease comparison between FFT and FEM techniques, given the challenges associated with solving rigid-viscoplasticity problems. As shown in Fig. 11.10, the results are more similar with stronger enforcement of incompressibility of the flow in the FEM method. In the figure, the penalty refers to a scaling of the bulk modulus to more strictly enforce incompressibility. Mathematically, this is equivalent to a dramatic increase in the time-step size and tends to speed the approach to a steady plastic flow. However, penalization to enforce incompressibility is limited by the performance of the iterative parallel linear system solvers employed here.

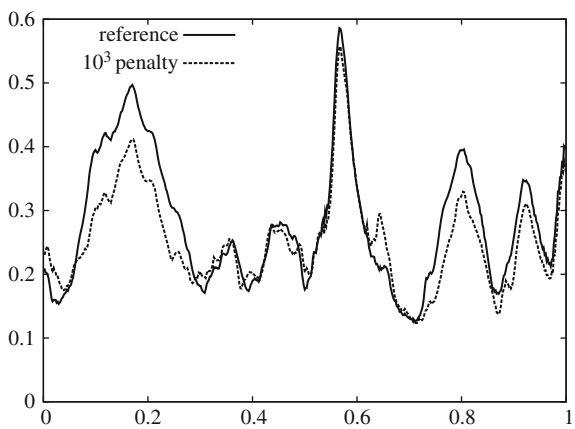


Fig. 11.10 Normalized differences between FFT and FEM results as a function of position along the long axis of the sample. FEM results in Fig. 11.9 are for the 10^3 penalty case

Some of the differences are due to oscillations in the FFT results (Fig. 11.9[a]), with these oscillations tending to diminish with mesh refinement. The remaining differences are concentrated at grain boundaries and at exterior surfaces. The strongest differences are associated with regions in the FEM calculation having relatively large volumetric deformation rates (incompressibility errors), but not all differences may be correlated with these errors. Given the stair-stepped nature of the boundaries, these effects are worth pursuing with finite element meshes that conform to grain boundaries (Maniatty et al. 2008).

Differences may also be due to the manner in which stress equilibrium and compatibility are enforced. As noted above, the finite element formulation enforces compatibility by construction. Stress equilibrium is enforced in a weak sense. Within the discretization error, stress equilibrium is enforced quite accurately—the solution procedure achieves quadratic convergence using a Newton-Raphson approach combined with consistent tangent stiffness matrices from the material model implementation. The biggest weakness in the FEM approach here for rigid-viscoplasticity is the difficulty in strictly enforcing incompressibility (or equivalently, in finding the true steady flow solution).

In contrast, the FFT model used here (based on the augmented Lagrangian algorithm of Michel et al. [2000]) consists in an iterative search of a compatible strain-rate field and a stress field in equilibrium. Both fields are related at each Fourier point by a rigid-viscoplastic local constitutive relation. The convergence of the method is achieved when the compatibility and equilibrium conditions are fulfilled within a certain threshold (see Michel et al. [2000] and Lebensohn et al. [2008] for details). Overall, differences in the results from the two methods may be attributed to differences in the strategies for solving the challenging rigid-viscoplasticity problem. The two methods may well be converging to the same solution, but along different paths, given the differences in how the conditions are enforced. It is worth noting that the FFT method enjoys a strong advantage in computational performance, with the FFT calculation requiring three orders of magnitude less processor time than the FEM calculation. This advantage would likely diminish substantially in comparison to a more specialized

finite element program, especially one better suited to incompressibility.

Adaptive mesh refinement (AMR) offers another attractive avenue of pursuit. Within the context of more general purpose finite element implementations, this would allow resolution of detailed features of the microstructural response without limitations on relative grid size from mesh distortions attendant upon the advection-based technique employed in the previous section. However, substantial effort is required for implementation of AMR in an implicit finite element code, and such capabilities are not widely available. The movement toward scientific software development for enhanced interoperability (Kumfert et al. 2006) will hopefully help facilitate the union of computational capabilities evolving out of distinct specialty areas. Use of interoperability strategies combined with sharing of code bases could aid substantially in advancing capabilities for simulations in micromechanics.

Ultimately, the mechanics community is looking toward multi-scale embedding techniques to enhance the fidelity of simulations at the scale of engineering components. Capabilities are being developed which can inform constitutive models directly from experimental measurement of microstructural features, with most of the capabilities focused on measured distri-

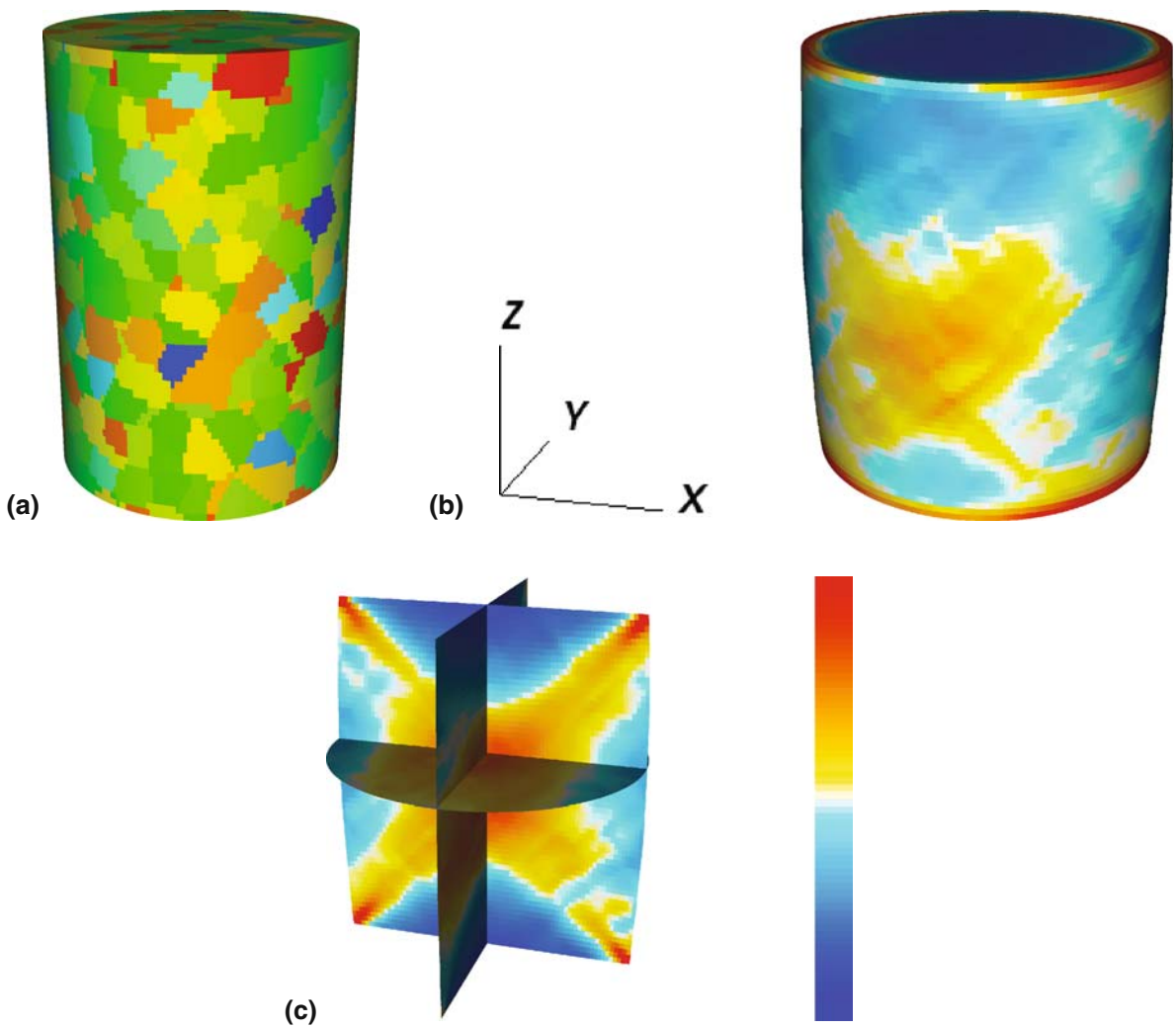


Fig. 11.11 Embedded multi-scale simulation using adaptive sampling to embed a polycrystal plasticity calculation. Orientation of the fine-scale distribution functions is indicated in part (**a**); parts (**b**) and (**c**) show effective plastic strain rates

butions, such as lattice orientation distribution functions (Dawson et al. 2005; Maudlin et al. 1996). There is, however, the possibility of moving toward direct multi-scale embedding of as-measured microstructures. Direct embedding with full computation of the fine-scale microstructure at every coarse-scale integration point is quite expensive (Han and Dawson 2007). Adaptive sampling techniques largely circumvent the expense of direct embedding while maintaining good error control (Barton et al. 2008); and work is under way to combine them with fine-scale simulations of polycrystal plasticity, which could include as-measured morphological information of the sort obtained from EBSD scans. Parallel implementations of FFT-based methods may prove particularly attractive as the embedded fine-scale model.

As an example of the adaptive sampling-based embedding technique, we show results for simulations based on measured orientation distribution functions for Ti-6Al-4V, similar to those shown in Fig. 11.3. Current simulation results are based on a uniform strain assumption in the polycrystal. As such, they are known to be deficient in capturing deformation heterogeneity; but they do capture some aspects of anisotropic response in the polycrystal, leading to a propensity to form long-range strain localizations. The actual orientation distribution functions are obtained from a windowed portion of the EBSD scan shown in Fig. 11.1, with fine-scale evaluations using 1302 α and 600 β weighted crystal orientations. Use of this windowed region captures some aspects of the long-range ordering of the lattice orientations. These fine-scale orientation distributions are then embedded into the coarse-scale model with perturbations that tend to smear the texture in a way that reproduces the measured bulk distributions (Fig. 11.3). As shown in Fig. 11.11(a), these perturbations are ordered over lengths in the coarse-scale sample corresponding roughly to the long-range ordering which is assumed to arise from prior β grain size. The compression specimen shown in Fig. 11.11(a) is 1/3 inch in diameter and 1/2 inch high. The coarse-scale mesh contains roughly 350,000 finite elements with 8-point quadrature. With 1902 distinct crystal orientations effectively informing each quadrature point, there are more than $5.3 \cdot 10^9$ crystals in the calculation. The power of the adaptive sampling technique lies in the fact that only a small fraction of the polycrystal level calculations must be performed over any given time step.

As shown in the figure, strain localizations form at multiple scales over the specimen. Longer-range localization arises from the frictional contact between the compression specimen and the platens. Shorter-range localizations are correlated with the assumed prior β grain size. Localizations at this scale are observed during compression tests of this material. Multi-scale embeddings of this kind are effective for a variety of applications (Barton et al. 2008; Bernier et al. 2008; Knap et al. 2008). We hope that with active development, more details of as-measured microstructure may be used to efficiently inform engineering scale computations. Even with efficient embedding techniques, the desire for high fidelity engineering scale simulations serves to highlight the need for efficient computational methods at the polycrystalline scale.

11.5 Conclusions

As in previous investigations, the use of an elasto-viscoplastic crystal model allows for polycrystal calculations in a finite element formulation without specialized element types. However, results for steady plastic flow calculations point to the need for more widespread use of formulations that can treat the flow of nearly incompressible materials. Calculation of the response at fixed microstructure is a particularly challenging case, and the presence of elasticity in the model improves numerical behavior considerably when the material is allowed to harden and reorient, forming grain substructure as the deformation progresses.

Given a reasonable desire to assess fixed as-measured microstructures, it is worth further pursuit of specialized methods. Enhancements in computational abilities and speeds could also directly benefit efforts aimed at high fidelity multi-scale embedding. Even with significant improvement in computational abilities, lath-type microstructures will remain challenging for some time to come, given the number of degrees of freedom needed to resolve the microstructural details (Barton and Dawson 2002). Many issues remain in the model forms appropriate to such microstructures, with slip system behavior potentially being influenced by reductions in dislocation mean free path due to the preponderance of domain boundaries. In this context, it is worth pursuing specialized linking assumptions that

homogenize with an accounting for the geometry of the fine microstructural details (Lebensohn 1999).

Techniques for microstructural characterization, including full three-dimensional characterization, will continue to provide opportunities to test and inform modeling frameworks (Spanos et al. 2008). Detailed EBSD scans offer one avenue of pursuit with the potential for comparison with models that can account for detailed dislocation interactions (Kysar et al. 2007; Arsenlis et al. 2004). X-ray-based techniques using high brilliance third generation synchrotron sources are now able to determine full three-dimensional orientations and lattice stretches nondestructively (Larson et al. 2004; Yang et al. 2004). Resolution and collection times for these techniques continue to improve. For example, these methods are now able to collect grain scale lattice stretch data from in situ loading, and to observe changes in lattice stretches in parent and product domains as twins form. X-ray methods may soon be able to observe variations in the strengths of slip and twinning modes in situ as a function of temperature and alloying, and thus help to fill a long recognized need (Brechet et al. 1994). Such developments are for now best viewed as complimentary to EBSD-based measurements, given the advantages retained by EBSD in spatial resolution.

Acknowledgments The work of NRB and JVB was performed under the auspices of the U.S. Department of Energy at Lawrence Livermore National Laboratory under Contract DE-AC52-07NA27344 (LLNL-JRNL-405176); the support of the LDRD program is gratefully acknowledged. This work builds on contributions from many collaborators, particularly Richard Becker and Michael King for the finite element simulation results. Support from the User Productivity Enhancement and Technology Transfer (PET) of the High Performance Computing Modernization Office for ADR is gratefully acknowledged. Use of facilities by ADR provided by the MRSEC at CMU under NSF grant number DMR-0520425 is also gratefully acknowledged.

References

Acharya A, Beaudoin J (2000) Grain-size effect in FCC viscoplastic polycrystals at moderate strains. J Mech Phys Solids 48:2213–2230

Arsenlis A, Parks DM, Becker R, Bulatov VV (2004) On the evolution of crystallographic dislocation density in non-homogeneously deforming crystals. J Mech Phys Solids 52:1213–1246

Barbe F, Decker L, Jeulin D, Cailletaud G (2001) Intergranular and intragranular behavior of polycrystalline aggregates. Part I: F. E. Model. Int J Plasticity 17:513–536

Barton NR, Dawson PR (2001a) On the spatial arrangement of lattice orientations in hot-rolled multiphase titanium. Model Simul Mater Sci Eng 9:433–463

Barton NR, Dawson PR (2001b) A methodology for determining average lattice orientation and its application to the characterization of grain substructure. Metall Mater Trans A 32: 1967–1975

Barton NR, Dawson PR (2002) Lattice misorientations in titanium alloys: modeling the origins of defects. Int J Forming Process 5:191–203

Barton NR, Boyce DE, Dawson PR (2002) Pole figure inversion using finite elements over Rodrigues space. Text Microstruct 35:113–144

Barton NR, Benson DJ, Becker R (2004) Crystal level simulations using Eulerian finite element methods. In: Materials processing and design: modeling, simulation and applications. AIP Conference Proceedings, vol. 712, pp 1624–1629

Barton NR, Knap J, Arsenlis A, Becker R, Hornung RD, Jefferson DR (2008) Embedded polycrystal plasticity and adaptive sampling. Int J Plasticity 24:242–266

Beaudoin AJ, Mathur KK, Dawson PR, Johnson GJ (1993) Three-dimensional deformation process simulation with explicit use of polycrystal plasticity models. Int J Plasticity 9:833–860

Beaudoin AJ, Acharya A, Chen SR, Korzekwa DA, Stout MG (2000) Considerations of grain-size effect and kinetics in the plastic deformation of metal polycrystals. Acta Mater 48:3409–3423

Benson DJ (1992) Computational methods in Lagrangian and Eulerian hydrocodes. Comput Methods Appl Mech Eng 99:235–394

Benson DJ (1998) Eulerian finite element methods for the micromechanics of heterogeneous materials: dynamic prioritization of material interfaces. Comput Methods Appl Mech Eng 151:343–360

Bernier JV, Miller MP, Boyce DE (2006) A novel optimization based pole-figure inversion method: comparison with WIMV and maximum entropy methods. J Appl Cryst 39: 697–713

Bernier JV, Barton NR, Knap J (2008) Polycrystal plasticity based predictions of strain localization in metal forming. J Eng Mater Technol 130:021020

Bieler TR, Semiatin SL (2002) The origins of heterogeneous deformation during primary hot working of Ti-6Al-4V. Int J Plasticity 18:1165–1189

Brechet YJM, Dawson P, Embury JD, G'sell C, Suresh S, Wenk H-R (1994) Recommendations on modeling polyphase plasticity: conclusions of panel discussions. Mater Sci Eng A175:1–5

Bozzolo N, Dewobroto N, Wenk H-R, Wagner F (2007) Microstructure and microtexture of highly cold-rolled commercially pure titanium. J Mater Sci 42:2405–2416

Dao M, Kad BK, Asaro RJ (1996) Deformation and fracture under compressive loading in lamellar TiAl microstructures. Philos Mag A 74:569–591

Dawson PR, Mika DP, Barton NR (2002) Finite element modeling of lattice misorientations in aluminum polycrystals. Scripta Mater 47:713–717

Dawson PR, Boyce DE, Hale R, Durkot JP (2005) An isoparametric piecewise representation of the anisotropic strength of polycrystalline solids. Int J Plasticity 21:251–283

Han T-S, Dawson PR (2007) A two-scale deformation model for polycrystalline solids using a strongly-coupled finite element methodology. Comput Method Appl Mech Eng 196: 2029–2043

Henson VE, Yang UM (2002) BoomerAMG: a parallel algebraic multigrid solver and preconditioner. Appl Numer Math 41:155–177

Hosford WF (1993) The Mechanics of crystals and textured polycrystals. Oxford University Press, Oxford

Knap J, Barton NR, Hornung RD, Arsenlis A, Becker R, Jefferson DR (2008) Adaptive sampling in hierarchical simulation. Int J Numer Meth Eng DOI: 10.1002/nme.2339

Kocks UF, Tomé CN, Wenk H-R (1998) Texture and anisotropy: preferred orientations in polycrystals and their effect on materials properties. Cambridge University Press, Cambridge

Kumfert G, Bernholdt DE, Epperly TGW, Kohl JA, McInnes LC, Parker S, Ray J (2006) How the common component architecture advances computational science. J Phys Conf Ser 46:479–493 DOI:10.1088/1742-6596/46/1/066

Kysar JW, Gan YX, Morse TL, Chen X, Jones ME (2007) High strain gradient plasticity associated with wedge indentation into face-centered cubic single crystals: geometrically necessary dislocation densities. J Mech Phys Solids 55: 1554–1573

Larson BC, Yang W, Tischler JZ, Ice GE, Budaia JD, Liub W, Weiland H (2004) Micron-resolution 3-D measurement of local orientations near a grain-boundary in plane-strained aluminum using X-ray microbeams. Int J Plasticity 20: 543–560

Lebensohn R (1999) Modelling the role of local correlations in polycrystal plasticity using viscoplastic self-consistent schemes. Modell Simul Mater Sci Eng 7:739–746

Lebensohn RA (2001) N-site modeling of a 3D viscoplastic polycrystal using fast Fourier transform. Acta Mater 49:2723–2737

Lebensohn RA, Liu Y, Ponte Castañeda P (2004) On the accuracy of the self-consistent approximation for polycrystals: comparison with full-field numerical simulations. Acta Mater 52:5347–5361

Lebensohn RA, Brenner R, Castelnau O, Rollett AD (2008) Orientation image-based micromechanical modelling of subgrain texture evolution in polycrystalline copper. Acta Mater 56:3912–3926

Lüetjering G, Williams JC (2003) Titanium. Springer-Verlag, Berlin

Maniatty AM, Littlewood DJ, Lu J (2008) Polycrystal simulations investigating the effect of additional slip system availability in a 6063 aluminum alloy at elevated temperature. J Eng Mater Technol 130:021019

Maudlin PJ, Wright SI, Kocks UF, Sahota MS (1996) An application of multisurface plasticity theory: yield surfaces of textured materials. Acta Mater 44:4027–4032

Michel JC, Moulinec H, Suquet P (2000) A computational method based on augmented Lagrangians and fast Fourier transforms for composites with high contrast. CMES-Comp Model Eng Sci 1:79–88

Mika DP (1999) Polycrystal plasticity modeling of deformation microstructures. Ph. D. Thesis, Cornell University

Miyagi L, Nishlyama N, Wang YB, Kubo A, West DV, Cava RJ, Duffy TS, Wenk H-R (2008) Deformation and texture development in CaIrO3 post-perovskite phase up to 6 GPa and 1300 K. EPSL 268:515–525

Moulinec H, Suquet P (1998) A numerical method for computing the overall response of nonlinear composites with complex microstructure. Comput Method Appl Mech Eng 157:69–94

Paton NE, Williams JC, Rauscher GP (1973) The deformation of α-phase titanium. In: Jaffee RI, Burte HM (eds) Titanium science and technology, vol. 2, pp 1049–1069

Sarma GB, Dawson PR (1996) Effects of interactions among crystals on the inhomogeneous deformations of polycrystals. Acta Mater 44:1937–1953

Sinha V, Mills MJ, Williams JC (2007) Determination of crystallographic orientation of dwell-fatigue fracture facets in Ti-6242 alloy. J Mater Sci 42:8334–8341

Spanos G, Rowenhorst DJ, Lewis AC, Geltmacher AB (2008) Combining serial sectioning, EBSD analysis, and image-based finite element modeling. MRS Bull 33:597–602

von Mises R (1945) On Saint Venant's principle. Bull Am Math Soc 51:555–562

Yang W, Larson BC, Tischler JZ, Ice GE, Budai JD, Liu W (2004) Differential-aperture X-ray structural microscopy: a submicron-resolution three-dimensional probe of local microstructure and strain. Micron 35:431–439

Yeong CLY, Torquato S (1998) Reconstructing random media. Phys Rev E 57:495–506

Chapter 12

First-Order Microstructure Sensitive Design Based on Volume Fractions and Elementary Bounds

Surya R. Kalidindi, David T. Fullwood, and Brent L. Adams

12.1 Introduction

Prior chapters of this book have focused largely on the experimental aspects of EBSD technique. We shift our attention here to a mathematical framework for establishing invertible linkages between the mesoscale internal structure of the material and the macroscale properties exhibited by the material. It is noted that the current practice in engineering design does not pay adequate attention to the internal structure of the material as a continuous design variable. The design effort is often focused on the optimization of the geometric parameters of the component being designed using robust macroscale numerical simulation tools, while the material selection is typically relegated to a relatively small database. Furthermore, material properties are usually assumed to be isotropic, and this significantly reduces the design space. Since the majority of commercially available metals used in structural applications are polycrystalline and often possess a nonrandom distribution of crystal lattice orientations (as a consequence of complex thermomechanical loading history experienced in their manufacture), they should be expected to exhibit anisotropic properties.

A new mathematical framework called microstructure sensitive design (MSD) has been developed recently to facilitate a rigorous consideration of the microstructure as a continuous variable in engineering design and optimization. In this chapter, we will limit our attention to 1-point statistics (i.e., volume fractions) of lattice orientation (also called the orientation distribution function, or ODF; see also Chapter 13) in fcc and hcp polycrystals and the first-order bounding theories for estimation of the macroscopic elastic and plastic properties of these materials. Consequently, the theories discussed in this chapter are referred to as first-order MSD. Consideration of higher-order details of the internal structure together with higher-order composite theories for improved estimates of the macroscopic properties will be presented in the next chapter.

First-order MSD aims to optimize the performance of structural components made from polycrystalline metals through an efficient consideration of the complete set of all theoretically feasible crystallographic textures. It is fully acknowledged that a large number of these crystallographic textures are not yet achievable in practice by currently known manufacturing options. Salient features of first-order MSD include: (1) construction of texture hulls (Adams et al. 2001, 2004; Kalidindi et al. 2004; Proust and Kalidindi 2006; and Wu et al. 2007) that represent the complete set of theoretically feasible crystallographic textures, and (2) delineation of first-order property closures (Adams et al. 2004; Knezevic and Kalidindi 2007a; Lyon and Adams 2004; Proust and Kalidindi 2006; and Wu et al. 2007) that identify the complete set of theoretically feasible combinations of macroscale properties of interest in a given application (e.g., for a selected first-order bounding theory). The primary advantages of the MSD approach lie in its (a) consideration of anisotropy of the properties at the local and component length scales, (b) exploration of the complete set of relevant microstructures (due to the use of microstructure hulls and property closures) leading to global optima, and (c) invertibility of the microstructure-property

S.R. Kalidindi (✉)
Department of Materials Science and Engineering, Drexel University, Philadelphia, PA 19104, USA
e-mail: skalidin@coe.drexel.edu

A.J. Schwartz et al. (eds.), *Electron Backscatter Diffraction in Materials Science*,
DOI 10.1007/978-0-387-88136-2_12, © Springer Science+Business Media, LLC 2009

relationships (due to the use of spectral methods in representing these linkages).

12.2 Quantification of Microstructure

The local state space describing the set of distinct orientations relevant to a selected class of textures is referred to as the fundamental zone (FZ) (Bunge 1993). The fundamental zones in the Euler space (using Bunge-Euler angles: φ_1, Φ, φ_2 [Bunge 1993]) for selected classes of textures are described below. In the convention used here, the first symmetry refers to the symmetry at the crystal level (resulting from the atomic arrangements in the crystal lattice), while the second refers to symmetry at the sample scale (resulting from processing history). Examples include the following.

Cubic-Orthorhombic:

$$\mathrm{FZ} = \left\{ \begin{array}{l} g = (\varphi_1, \Phi, \varphi_2) | 0 \leq \varphi_1 < \frac{\pi}{2}, \\ \\ \cos^{-1}\left(\dfrac{\cos\varphi_2}{\sqrt{1+(\cos\varphi_2)^2}}\right) \leq \Phi \leq \frac{\pi}{2}, \\ \\ 0 \leq \varphi_2 \leq \frac{\pi}{4} \end{array} \right\} \tag{12.1}$$

Hexagonal-Orthorhombic:

$$\mathrm{FZ} = \left\{ g = (\varphi_1, \Phi, \varphi_2) \,\middle|\, 0 \leq \varphi_1 \leq \tfrac{\pi}{2}, 0 \leq \Phi \leq \tfrac{\pi}{2}, \; 0 \leq \varphi_2 \leq \tfrac{\pi}{3} \right\} \tag{12.2}$$

Hexagonal-Transversely Isotropic:

$$\mathrm{FZ} = \left\{ g = (\Phi, \varphi_2) \,\middle|\, 0 \leq \Phi < \frac{\pi}{2}, 0 \leq \varphi_2 < \frac{\pi}{3} \right\} \tag{12.3}$$

In this chapter, our interest will be limited to 1-point statistics of microstructure. For single-phase polycrystalline metals, the relevant 1-point statistics are those of the lattice orientations of the constituent grains and are efficiently captured as an orientation distribution function (also commonly referred to as crystallographic texture. or sometimes simply as texture). The ODF, denoted as $f(g)$, reflects the normalized probability density associated with the occurrence of the crystallographic orientation g in the sample (Bunge 1993) as:

$$f(g)dg = \frac{V_g}{V}, \int_{FZ} f(g)dg = 1 \tag{12.4}$$

In Eq. (12.4), V denotes the total sample volume and V_g is the sum of all sub-volume elements in the sample associated with a lattice orientation that lies within an incremental invariant measure, dg, of the orientation of interest, g. The lattice orientation, g, is usually defined by a set of three angles called the Bunge-Euler angles (Bunge 1993), i.e., $g = (\phi_1, \Phi, \phi_2)$. The Bunge-Euler angles define a specific sequence of three rotations that would bring the crystal and sample reference frames into coincidence. The local properties depend strongly on the local crystallographic orientation, and therefore the overall behavior of the material is strongly influenced by the distribution of the crystallographic orientations inside the polycrystalline material.

12.3 Microstructure Sensitive Design Framework

MSD (Adams et al. 2001, 2004; Kalidindi and Houskamp 2007; Kalidindi et al. 2004; and Sintay and Adams 2005) starts with efficient spectral representations of the microstructure distribution functions. For example, the ODF can be expressed in a Fourier series using generalized spherical harmonics (GSH), $T_l^{\mu v}(g)$, as:

$$f(g) = \sum_{l=0}^{\infty} \sum_{\mu=1}^{M(l)} \sum_{v=1}^{N(l)} F_l^{\mu v} T_l^{\mu v}(g) \tag{12.5}$$

Note that it is customary to place a certain arrangement of dots on top of the T in conveying the specific symmetries being implicitly invoked in the selection of an appropriate Fourier basis. In this chapter, we will add those descriptions whenever needed (especially in the discussion of the case studies). Equation (12.5) facilitates visualization of ODF as a point in Fourier space whose coordinates are given by $F_l^{\mu v}$. Recognition of the fact that ODF provides information only about the volume fraction of the various orientations present in the polycrystalline sample permits an alternate mathematical description as:

$$f(g) = \sum_k \alpha_k \, \delta\left(g - g^k\right), \quad 0 \le \alpha_k \le 1, \sum_k \alpha_k = 1 \tag{12.6}$$

The Dirac-delta function $\delta\left(g - g^k\right)$ in Eq. (12.6) represents the ODF of a single crystal of orientation g^k, and α_k denotes its volume fraction in the polycrystal. Let ${}^k F_l^{\mu v}$ define the Fourier coefficients of the single-crystal ODFs. It is then possible to define a convex and compact texture hull (Adams et al. 2001), M, as:

$$M = \left\{ F_l^{\mu v} \,\middle|\, F_l^{\mu v} = \sum_k \alpha_k {}^k F_l^{\mu v}, {}^k F_l^{\mu v} \in M^k, \alpha_k \ge 0, \sum_k \alpha_k = 1 \right\}, \tag{12.7}$$

where

$$M^k = \left\{ {}^k F_l^{\mu v} \,\middle|\, F_l^{\mu v} = \tfrac{1}{(2l+1)} \overline{T_l^{\mu v}}\left(g^k\right) g^k \in FZ \right\} \tag{12.8}$$

The bar on top of the GSH in Eq. (12.8) denotes the complex conjugate. It should be recognized that M represents the complete set of all theoretically feasible ODFs, several of which have not yet been realized in practice or even targeted for manufacture by materials specialists. Examples of texture hulls, projected into selected subspaces, are presented in Figs. 12.1 and 12.2. It is important to recognize that all textures that can be physically conceived will have representations inside these hulls. Just as important is the notion that points outside these hulls do not correspond to any physically conceivable textures.

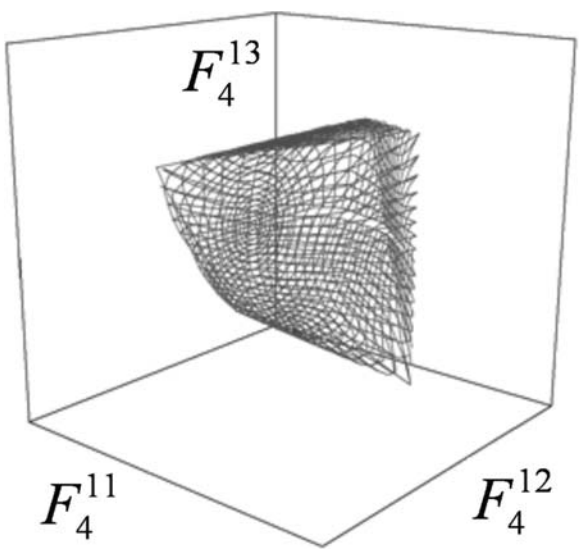


Fig. 12.1 The texture hull in the first three dimensions of the Fourier space for the cubic-orthorhombic textures (Kalidindi et al. 2004)

The first-order bounds for certain components of the macroscopic elastic stiffness tensor, C^*_{ijkl}, in the sample reference frame can be expressed as (Hill 1952, 1963; Paul 1960; Proust and Kalidindi 2006):

$$\left(\langle S\rangle\right)^{-1}_{ijij} \le C^*_{ijij} \le \left\langle C_{ijij}\right\rangle \tag{12.9}$$

$$\max\left(\left\langle C_{iijj}\right\rangle, \left(\langle S\rangle\right)^{-1}_{iijj}\right) - \sqrt{\Delta_i \Delta_j} \le C^*_{iijj} \le \min\left(\left\langle C_{iijj}\right\rangle, \left(\langle S\rangle\right)^{-1}_{iijj}\right) + \sqrt{\Delta_i \Delta_j}, \quad \text{when } i \ne j, \; with \; \Delta_i = \langle C_{iiii}\rangle - \left(\langle S\rangle\right)^{-1}_{iiii}, \tag{12.10}$$

where S_{ijkl} denotes the components of the local elastic compliance tensor, $\langle . \rangle$ denotes the volume average, and $\left(\langle S\rangle\right)^{-1}_{ijkl}$ denotes the components of the inverse of the volume-averaged elastic compliance tensor. These bounds can be used to delineate property closures, which identify the complete set of theoretically achievable combinations of selected macroscale properties in a given material system through a consideration of the complete set of textures (i.e., all elements of the texture hull). All of the volume-averaged quantities needed in these expressions can be computed highly efficiently using spectral representations of microstructure-property linkages.

As a specific example, consider the computation of the volume-averaged compliance tensor components. The local elastic compliance tensor in the sample reference frame is defined using a coordinate transformation law for fourth-rank tensors as:

$$S_{ijkl} = g_{ip} g_{jq} g_{kr} g_{ls} S^c_{pqrs}, \tag{12.11}$$

where S^c_{pqrs} is the local elastic compliance tensor in the local crystal reference frame, and g_{ij} are the components of the transformation matrix defined in terms of the Bunge-Euler angles (Bunge 1993). The $S_{ijkl}(g)$ functions defined in Eq. (12.11) can be represented in a Fourier series using GSH functions as:

$$S_{abcd}(g) = \sum_{l=0}^{4} \sum_{\mu=1}^{N(l)} \sum_{v=1}^{M(l)} {}_{abcd} S_l^{\mu v} T_l^{\mu v}(g), \tag{12.12}$$

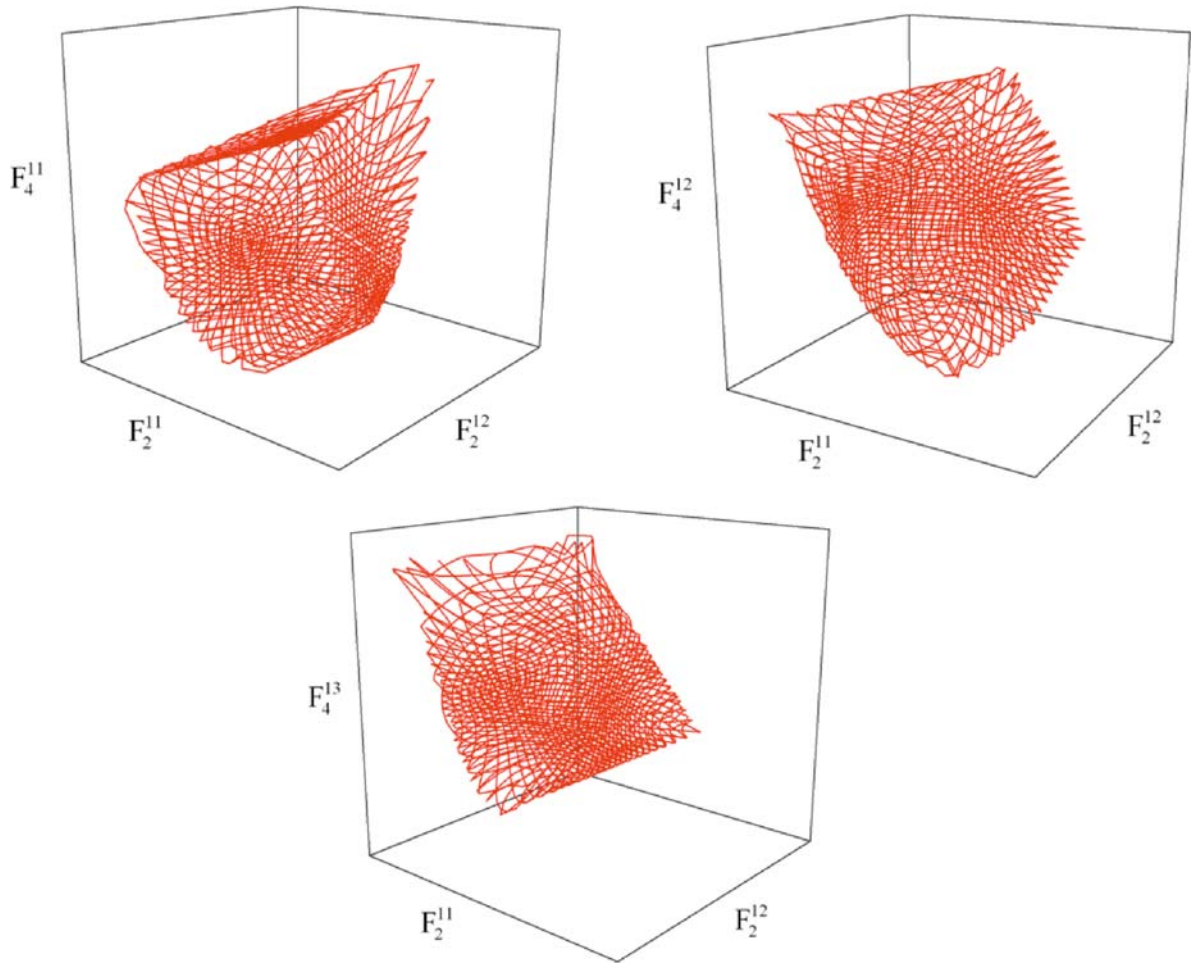


Fig. 12.2 Selected three-dimensional projections of the texture hull for hexagonal-orthorhombic materials. The sections represented are: (**a**) $(F_2^{11}, F_2^{12}, F_4^{11})$, (**b**) $(F_2^{11}, F_2^{12}, F_4^{12})$, and (**c**) $(F_2^{11}, F_2^{12}, F_4^{13})$

where ${}_{abcd}S_l^{\mu v}$ are referred to as the elastic Fourier coefficients, and the details of their computation have been reported in the published literature (Wu et al. 2007). The volume-averaged value is then computed by exploiting the orthogonality of the Fourier basis as:

$$\begin{aligned}\langle S_{abcd}\rangle &= \oint S_{abcd}(g) f(g) dg \\ &= \sum_{l=0}^{4} \sum_{\mu=1}^{N(l)} \sum_{v=1}^{M(l)} \frac{1}{(2l+1)}\, {}_{abcd}\overline{S_l^{\mu v}} F_l^{\mu v}\end{aligned} \tag{12.13}$$

Equations (12.8) and (12.13) embody one of the central features of MSD. They provide an efficient linkage between the complete set of feasible ODFs and the corresponding feasible combinations of macroscale elastic properties. Of particular significance is the fact that unlike the Fourier representation of the ODF, the representation for properties often extends to only a finite number of terms in the Fourier expansion. As shown in Eqs. (12.12) and (12.13), in consideration of elastic properties the only relevant Fourier coefficients are those that correspond to $l \leq 4$. The main advantage of the spectral methods described herein lies in the fact that we are able to formulate highly efficient structure-property relationships. The ideas presented here have also been successfully extended to plastic properties of polycrystalline fcc and hcp metals (Proust and Kalidindi 2006; Wu et al. 2007).

12.4 Property Closures

Property closures delineate the complete set of theoretically feasible effective (homogenized) anisotropic

property combinations in a given material system, and are of tremendous interest in optimizing the performance of engineering components. Let P and Q denote two effective anisotropic elastic-plastic properties of interest at the macroscale. The delineation of the first-order closures for (P,Q) can be visualized through the following sequence of computations. We start by identifying the subset of textures (regions inside the texture hull) that are theoretically predicted to correspond to a selected value of one of the effective properties of interest (say, $P = \tilde{P}$), based on the elementary bounding theories (by solving equations of the type shown in Eq. [12.13]). Restricting our attention to this subset of textures, we evaluate the maximum and minimum values of Q that are theoretically feasible. This step often requires the use of sophisticated optimization algorithms. Let Qmax and Qmin represent these values, respectively. Note that ($\tilde{P}$, Qmax) and ($\tilde{P}$, Qmin) constitute two of the points on the boundary of the property closure sought. By exploring $\tilde{P}$ between its own theoretically feasible maximum and minimum values, one can delineate the complete first-order property closure. It should be noted that these computations can be fairly involved and may require substantial computational time and effort. Further details of these procedures can be found in the published literature (Knezevic and Kalidindi 2007b; Knezevic et al. 2008; Proust and Kalidindi 2006; Wu et al. 2007).

Figure 12.3 depicts an atlas of $\left(C^*_{1111}, C^*_{1313}\right)$ closures that have been produced for a broad range of cubic materials. The shaded areas inside the closures represent all of the possible combinations of the selected elastic stiffness components that can be obtained according to the first-order bounding theories for the particular material. Figure 12.3 reveals that the shapes of the property closures shown can be broadly classified into two groups. These correspond to materials with the $A = 2C_{44}\,/(C_{11} - C_{12})$ ratio being greater and smaller than 1, respectively. For example, Mo and LiO exhibit values of $A < 1$, while all of the other materials in Fig. 12.3 exhibit values of $A > 1$. Note also the relative (normalized) size of the closure scales with the magnitude of (A-1). For example, Tungsten, with an A ratio close to 1.0, exhibits the smallest closure; while $MgAl_2O_3$, with an A ratio of 2.43, exhibits one of the larger closures obtained. Obviously, with larger closures there exists a higher potential for improvement of performance in a given design application.

As an example of a closure of plastic properties, we present in Fig. 12.4 the $\left(R_1, \sigma_{y1}/s\right)$ closure computed for fcc metals using the MSD methodology. The R-ratio represents the ratio of the true width strain to the true thickness strain in a tensile test, and is an example of an effective plastic property of the metal that is typically of interest in metal shaping operations. The R_1 value corresponds to tensile loading in the $\mathbf{e}_1$-axis; σ_{y1}/s denotes the tensile yield strength along the $\mathbf{e}_1$-axis normalized by the slip resistance (assumed to be the same for all slip systems in fcc polycrystals).

As a final example, we present in Fig. 12.5 the first-order closure for the ultimate tensile strength (σ_{UTS}) and the yield strength (σ_{y1}). Note that the evaluation of

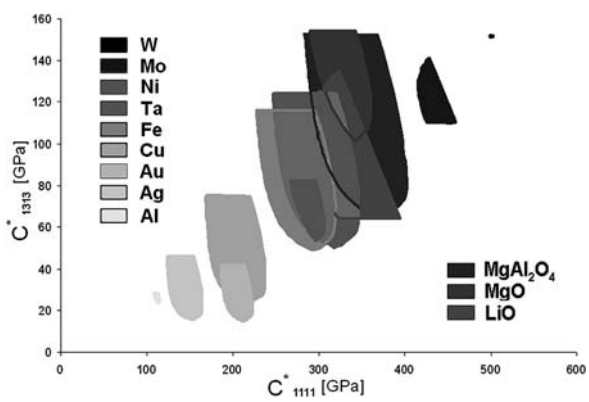


Fig. 12.3 Atlas of $\left(C^*_{1111}, C^*_{1313}\right)$ closures for a broad selection of cubic materials

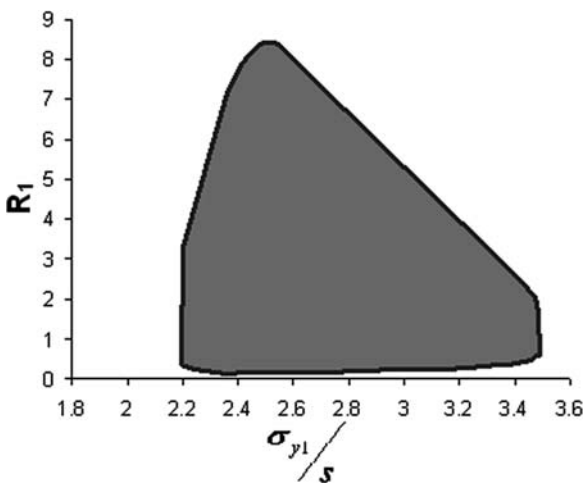


Fig. 12.4 $\left(\mathrm{R}_1, \sigma_{y1}/s\right)$ closure for all fcc metals

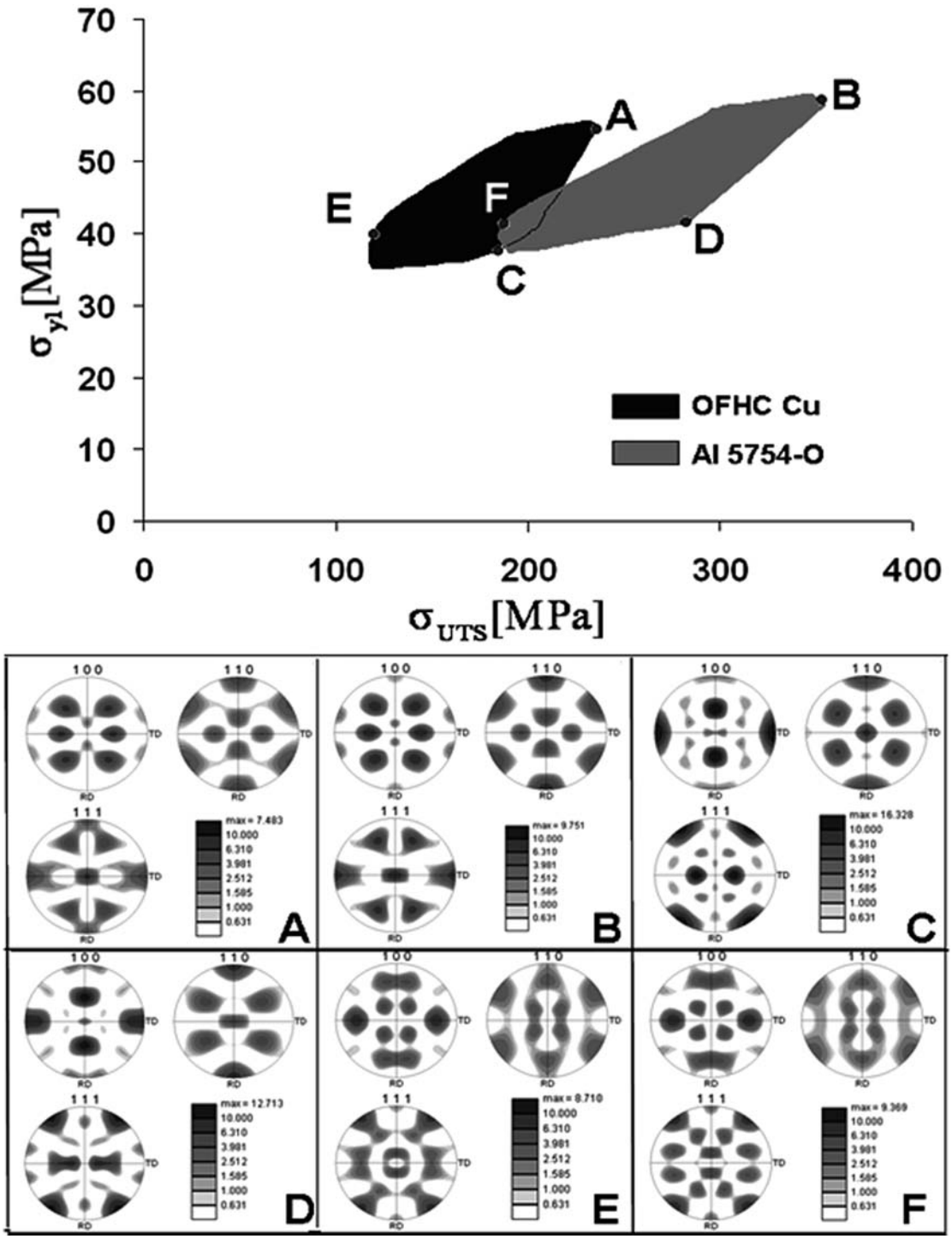


Fig. 12.5 First-order closures for the ultimate tensile strength (σ_{UTS}) and the yield strength (σ_{y1}) in OFHC Cu and 5754-O Al, based on Taylor-type models and a consideration of all theoretically possible textures (i.e., the elements of the texture hull). The textures that are theoretically predicted to correspond to salient points of interest on the boundary are depicted. Textures A, C, and E are for OFHC Copper, while textures B, D, and F are for 5754-O Al

σ_{UTS} requires simulation of large plastic strains in tension, while capturing the details of texture evolution. This was accomplished using a simple Taylor-type model in computing the closure presented in Fig. 12.5. It is observed that the closures for the two metals selected in this study are strongly influenced by the strain-hardening parameters.

The examples described above clearly demonstrate the ability of the first-order MSD to facilitate solutions to inverse problems in microstructure design in which the goal is to identify the textures that are theoretically predicted to satisfy a set of designer specified criteria on anisotropic macroscale properties and/or performance. More recently, the ability to interface the MSD framework with the finite element (FE) modeling tools used typically by the designers has also been demonstrated (Houskamp et al. 2007). This new MSD-FE framework facilitates a rigorous consideration of microstructure in a broad class of mechanical problems involving elastic-plastic design and optimization.

Acknowledgements Financial support for this work was provided by the Army Research Office, Proposal No. 46886 MS, Dr. David Stepp, Program Director.

References

Adams BL, Henrie A, Henrie B, Lyon M, Kalidindi SR, Garmestani H (2001) Microstructure-sensitive design of a compliant beam. J Mech Phys Solids 49(8):1639–1663

Adams BL, Lyon M, Henrie B (2004) Microstructures by design: linear problems in elastic-plastic design. Int J Plasticity 20(8–9):1577–1602

Bunge H-J (1993) Texture analysis in materials science. Mathematical methods. Morris PR (trans) Cuvillier Verlag, Göttingen

Hill R (1952) The elastic behavior of a crystalline aggregate. Proc R Soc Lond A 65:349–354

Hill R (1963) Elastic properties of reinforced solids: some theoretical principles. J Mech Phys Solids 11:357–372

Houskamp JR, Proust G, Kalidindi SR (2007) Integration of microstructure sensitive design with finite element methods: elastic-plastic case studies in FCC polycrystals. Int J Multiscale Comput Eng 5:261–272

Kalidindi SR, Houskamp JR (2007) Application of the spectral methods of microstructure design to continuous fiber reinforced composites. J Compos Mater 41:909–930

Kalidindi SR, Houskamp JR, Lyons M, Adams BL (2004) Microstructure sensitive design of an orthotropic plate subjected to tensile load. Int J Plasticity 20(8–9):1561–1575

Knezevic M, Kalidindi SR (2007a) Fast computation of first-order elastic-plastic closures for polycrystalline cubic-orthorhombic microstructures. Comput Mater Sci 39(3): 643–648

Knezevic M, Kalidindi SR (2007b) Fast computation of first-order elastic-plastic closures for polycrystalline cubic-orthorhombic microstructures. Comput Mater Sci 39: 643–648

Knezevic M, Kalidindi SR, Mishra RK (2008) Delineation of first-order closures for plastic properties requiring explicit consideration of strain hardening and crystallographic texture evolution. Int J Plasticity 24:327–342

Lyon M, Adams BL (2004) Gradient-based non-linear microstructure design. J Mech Phys Solids 52(11): 2569–2586

Paul B (1960) Prediction of elastic constants of multiphase materials. T Metall Soc AIME 218:36–41

Proust G, Kalidindi SR (2006) Procedures for construction of anisotropic elastic-plastic property closures for face-centered cubic polycrystals using first-order bounding relations. J Mech Phys Solids 54(8):1744–1762

Sintay DS, Adams BL (2005) Microstructure design for a rotating disk: with application to turbine engines. 31st Design automation conference (IDETC/CIE), Long Beach, California

Wu X, Proust G, Knezevic M, Kalidindi SR (2007) Elastic-plastic property closures for hexagonal close-packed polycrystalline metals using first-order bounding theories. Acta Mater 55(8):2729–2737

Chapter 13

Second-Order Microstructure Sensitive Design Using 2-Point Spatial Correlations

David T. Fullwood, Surya R. Kalidindi, and Brent L. Adams

13.1 Introduction

In this chapter we are concerned with second-order interrelations between structure, properties, and processes of materials. Structure can be described in many different ways. The most common metrics of structure involve "first-order" (volume fraction) information: for example, the orientation distribution function. Such metrics serve well as the basis for property relations that do not depend significantly upon the geometrical placement of the material constituents. However, many properties (such as those relating to failure) depend critically upon the geometrical distribution of particular material components, and hence benefit enormously from knowledge of the "higher order" structure.

Examples of higher order structure information include clustering, periodicity, and connectedness. These all describe geometrical relations between material components. In order to be applicable to structure-property relations, these abstract terms must be tied to quantifiable structure metrics. Many such metrics are available, such as nearest-neighbor measures, chord-length, etc. (Torquato 2002). One particularly useful system of metrics is that of n-point correlations. These constitute a hierarchy of metrics that begin at the 1-point (volume fraction) level, and can be extended to arbitrary levels of sophistication in geometrical information. Loosely, an n-point function describes the probability (or probability distribution) of finding a chosen set of local material states (or constituents) at the n vertices of a chosen polytope that is thrown randomly into a material sample. A more rigorous definition will be given in the next section.

For practical purposes, information concerning the structure of real materials is generally captured in digital form—i.e., at a finite number of points. Hence it is clear that for a large enough value of n, the n-point correlations will contain all of the structure data. However, the amount of data required to define higher order correlations becomes prohibitive. If the number of local states of interest in the material is N and the number of points in the discrete material domain is S, then we require on the order of $(8S)^{n-1}N^n$ data points to fully define the correlations (before reducing this number by considering interrelations between the functions). Thus one typically deals with correlations of the minimal order required to provide relevant statistical information. It should be noted that the n-point functions of a given order contain all of the information for correlation functions of lower order. In this chapter we devote our attention almost exclusively to 2-point correlation functions. These represent a huge gain in usable information over the 1-point statistics, without being too numerically cumbersome.

It is worth stating clearly the limitations of the information contained in the 2-point correlation functions. While they can be shown to contain useful clustering and periodicity information, they contain very little directly accessible connectedness information. One may infer some connectedness information from reconstructed structures, although in general this will involve making certain assumptions about the structure which may or may not be reasonable.

D.T. Fullwood (✉)
Department of Mechanical Engineering, Brigham Young University, Provo, UT 84602-4201, USA
e-mail: dfullwood@byu.edu

A.J. Schwartz et al. (eds.), *Electron Backscatter Diffraction in Materials Science*,
DOI 10.1007/978-0-387-88136-2_13, © Springer Science+Business Media, LLC 2009

In the sections below we define the 2-point statistics and demonstrate the structure information contained in the statistics; we discuss how to collect these statistics for practical purposes and then apply them to structure-property relations.

13.2 Definition and Properties of the 2-Point Correlation Functions

In order to define 2-point correlation functions we first introduce the microstructure function (Adams et al. 2005; Fullwood et al. 2007). This will form the basis for a definition of correlation functions in general. Consider a material representative volume element (RVE) with position vector, $\mathbf{x}$, and a single local state variable, $h \in H$; for example, H might represent the set of all possible orientations that a crystalline structure might take, in which case h would represent the orientation at a given point. Then the microstructure function $m(\mathbf{x}, h)$ is a distribution function on the local state space for each point in the RVE:

$$m(\mathbf{x}, h)\, dh = \frac{dV_h}{V} = f(h)|_{\mathbf{x}}\, dh \tag{13.1}$$

where dV_h represents the volume of material in volume element V that is in a state which lies in a neighborhood dh of h. Such a description allows for a continuous state space (such as orientation), but also permits multiple states to exist at a single "point" (or measurement region) of the sample. In the case that only a single state is present at each point, the structure is termed an eigen-microstructure; such is the case for most studies of material structure in the literature. The connection with $f(h)|_{\mathbf{x}}$ allows us to interpret the microstructure function simply as a spatially resolved 1-point distribution.

The motivation for this definition stems from the fact that material information is generally derived from data gathered in a neighborhood, rather than a single point. This is obvious for a local state such as orientation, which is in fact defined in terms of relative positions of atoms in a neighborhood; but it is also true that instruments gather information from an area or volume determined by their resolution rather than from a single point. This definition also leads to a concise definition for the 2-point correlation function in the RVE, Ω:

$$f_2(h, h'|\mathbf{r}) = \frac{1}{Vol(\Omega)} \int_{\Omega} m(\mathbf{x}, h) m(\mathbf{x} + \mathbf{r}, h') \mathrm{d}\mathbf{x} \tag{13.2}$$

It will be noted immediately that the term on the right hand side of this equation is a convolution of the two functions $m(\mathbf{x}, h)$ and $m(\mathbf{x}, h')$. Thus we may use the usual convolution theorem of Fourier analysis to determine the function f_2 as is often used for autocorrelations (Rust and Donnelly 2005).

In order to subsequently benefit from the efficiencies of fast Fourier transforms (FFTs), we first discretize the function $m(\mathbf{x}, h)$ in the real space, $\Re^n$. This is consistent with many characterization techniques that read data from a discrete grid of the material sample. The state space, H, is also often discretized, but this is not necessary to accomplish our current goal. Thus, let us suppose that the real space is discretized into a regular grid, with individual bins enumerated by $s = 0 \ldots S-1$. We will write $m_s^h = m(\mathbf{x}_s, h)$. The vectors $\mathbf{r}$ will also take discrete values, enumerated by t, such that $f_t^{hh'} = f_2(h, h'|\mathbf{r}_t)$.

To simplify the index notation we will momentarily assume that the RVE is a 1D space, but it will be obvious how to generalize to higher dimensions. Then Eq. (13.2) becomes:

$$f_t^{hh'} = \frac{1}{S} m_s^h m_{s+t}^{h'} \tag{13.3}$$

where $\mathbf{r}_t$ take values on a lattice of the same spacing as $\mathbf{x}_s$ and the summation convention is assumed on repeated indices within the same term (in this case, on s) throughout this chapter, unless specified otherwise. If we take the Fourier transform of both sides and use the convolution theorem, then (no summation on k):

$$F_k^{hh'} = \overline{M_k^h} M_k^{h'} \tag{13.4}$$

where $F_k^{hh'}$ and M_k^h are the Fourier transforms of $f_t^{hh'}$ and m_s^h, respectively; the overbar indicates a complex conjugate; and there is no summation over the ks on the right hand side. The result is that in practice we may efficiently obtain the 2-point correlation function using pointwise multiplication of the FFTs of the microstructure function, and an inverse FFT. This is dramatically more efficient than a brute force approach.

For completeness, we briefly mention that all higher order correlation functions may be calculated in a similar manner. For example, the 3-point correlations may be calculated as (no summation on k or k'):

$$F_{kk'}^{hh'h''} = \overline{M_k^h} M_{k-k'}^{h'} M_{k'}^{h''} \tag{13.5}$$

13.2.1 Boundary Conditions

Using FFTs to calculate correlation functions implicitly assumes periodic boundary conditions. A different boundary condition may be applied by using padding (see, for example, Walker[1996] for a discussion of padding). One commonly used definition of the 2-point correlation function that does not involve periodic boundary conditions is given by (Adams et al. 2005):

$$f_2\left(h, h'|\mathbf{r}\right) = N_{\Omega|\mathbf{r}} \int_{\Omega|\mathbf{r}} M\left(\mathbf{x}, h\right) M\left(\mathbf{x}+\mathbf{r}, h'\right) d\mathbf{x} \tag{13.6}$$

where $\Omega|\mathbf{r} = \{\mathbf{x} \in \Omega | \mathbf{x}+\mathbf{r} \in \Omega\}$. In the continuous case the normalization factor is given by $N_{\Omega|\mathbf{r}} = \frac{1}{V_{\Omega|\mathbf{r}}}$. In the discrete 1D case of S points, the normalization factor is given by 1/(number of points sampled); i.e., $N_{\Omega|\mathbf{r}} = 1/(S-t)$ where t takes the integer values from 0 to S-1. If we pad our discrete 1D example with S-1 zeros then the resultant calculation for f_2 effectively calculates the integral in Eq. (13.6) without the normalization factor; hence the FFT results must be normalized by 1/(S-t). Note that one issue with these boundary conditions is that the values of $f_2\left(h, h'|\mathbf{r}\right)$ for larger values of $|\mathbf{r}|$ are sampled with significantly less frequency than those for smaller values of $|\mathbf{r}|$; nevertheless, they are given equal importance. For example, in the discrete 1D case, the vector between the first and last point on the domain is only sampled once. To deal with this issue, it may be assumed (for example) that values of $|\mathbf{r}|$ above $\frac{1}{2}$ the size of the domain should be ignored, as being insufficiently sampled to be statistically meaningful (the value of $\frac{1}{2}$ is an arbitrary value that may be chosen more carefully, depending upon the level of statistical confidence required). If this same approach is taken in the case of the unpadded FFT, it will also reduce the effect from the assumed periodicity, since the smaller $\mathbf{r}$-vectors will cross the boundary of the domain for a smaller proportion of the S sample points.

13.2.2 Properties of the 2-Point Functions

From the definition of the 2-point functions it is clear that $f_t^{hh'} = f_{-t}^{h'h}$ where the index "-t" refers to the negative of the vector $\mathbf{r}_t$. For a discrete state space, H, $\sum_{h'} f_t^{hh'} = f^h$ where f^h is the usual (1-point) distribution function.

For eigen-microstructures it is clear that $f_0^{hh'} = \begin{cases} f^h \text{ if} h = h' \\ 0 \text{ otherwise.} \end{cases}$ For a random medium, it is also true that $f_{t\to\infty}^{hh'} = f^h f^{h'}$.

13.2.3 Visualization of the 2-Point Functions

Recent advances in orientation imaging microscopy (OIM) and related techniques now enable ready determination of the 2-point statistics without undue effort (Gao et al. 2006). 2-point data is often collected from 2D sections of material samples. For example, suppose that we collect OIM data and subsequently generate a grain map as shown in Fig. 13.1a. We may bin the grain sizes and choose a particular bin as relating to local state, h (see Fig. 13.1b). Then the 2-point correlation function f_t^{hh} (also known as an auto-correlation function, since it is the correlation between a certain state and itself) is shown in Fig. 13.1c. Note the inversion symmetry in the plot. One should also note that the "hot-spot" in the center of the figure captures the average shape and size of the grains included in our selection of local state.

The complexity of dealing with data captured by 2D contour plots or 3D plots has led to a common representation of the 2-point data using a reduced function $f_2\left(h, h'|r\right)$ which may be visualized using a line-plot. In this view the correlation functions are defined with respect to vector magnitude r, thus ignoring all directional information. One may obtain the line plot by taking data along rays from the center of Fig. 13.1c and then averaging over all such rays. An example for

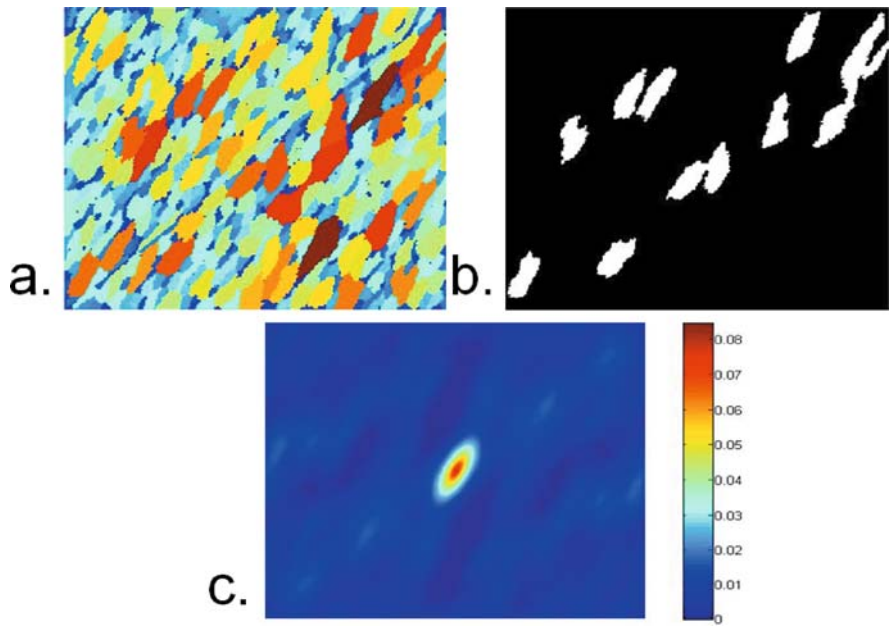


Fig. 13.1 (**a**) Grain map for rolled steel (created from OIM data); (**b**) grains within a selected size range; (**c**) contour map of 2-point statistics for the autocorrelation of the selected grain size

a 2-phase composite is given in Fig. 13.2b. Various structure properties may be read from the graph. The value at a radius of zero gives the volume fraction of the phase. The first minimum indicates the diameter of the average fiber (for this carbon fiber composite), and the first maximum indicates the spacing between the fibers. These interpretations of maximum and minimum points do not necessarily work well for other structures, but happen to define a good metric for the particular structure in Fig. 13.2a.

13.2.4 Metrics from 2-Point Correlations

Various rigorous metrics may be extracted from the 2-point correlation functions that relate to the material structure. These are generally easiest to define on the directionless statistics just defined. For example (Tewari et al. 2004), L_0 may be defined as the point at which the slope of the line is 1/10th of the original slope; L_∞ may be defined as the point where the line plot comes within 2% of its asymptotic value; and λ_∞ may be defined as the wavelength of the dominant frequency of the line plot at large values of *r*. These metrics all relate to clustering of the material constituents. Other metrics are available (see, for example, Torquato 2002); we merely mention here that they exist.

13.2.5 Collecting 2-Point Correlations from Material Samples

The process of collecting 2-point correlation data from a 2D sample of material is straightforward from the definition of the functions. However, the collection of 3D data using 2D characterization methods requires more thought. We wish to fairly sample vectors $\mathbf{r}_t$ in all three dimensions using data obtained from 2D planes. The most obvious cutting scheme to provide such sampling is to determine an axis in the sample frame and cut along a number of planes that contain the axis. Tewari et al. (2004) assert that three such planes (at 60° to each other) are generally sufficient to obtain an unbiased estimator of the 3D 2-point correlations. The number of such planes required will, however, clearly depend upon the anisotropy of the medium.

One issue with such a cutting scheme is that it does not provide an unbiased set of 3-point statistics should the engineer wish to extract such functions from the data later. 3-point functions can clearly be extracted from planes of data, since any three points must lie in a plane. An alternative cutting scheme that gives better 3-point data might be arrived at by requiring that the plane normals give an optimal covering of the unit sphere. An example of such a cutting scheme is given in Fig. 13.3a, with normals to the planes shown on the unit sphere in Fig. 13.3b (Homer et al. 2006). Example

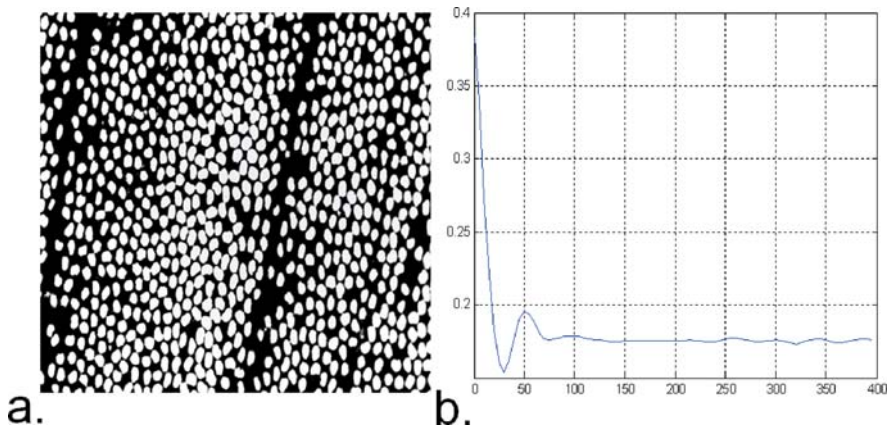


Fig. 13.2 (**a**) Cross section of carbon fiber composite; (**b**) autocorrelation for directionless 2-point statistics. The units along the x-axis are in pixels from the original image

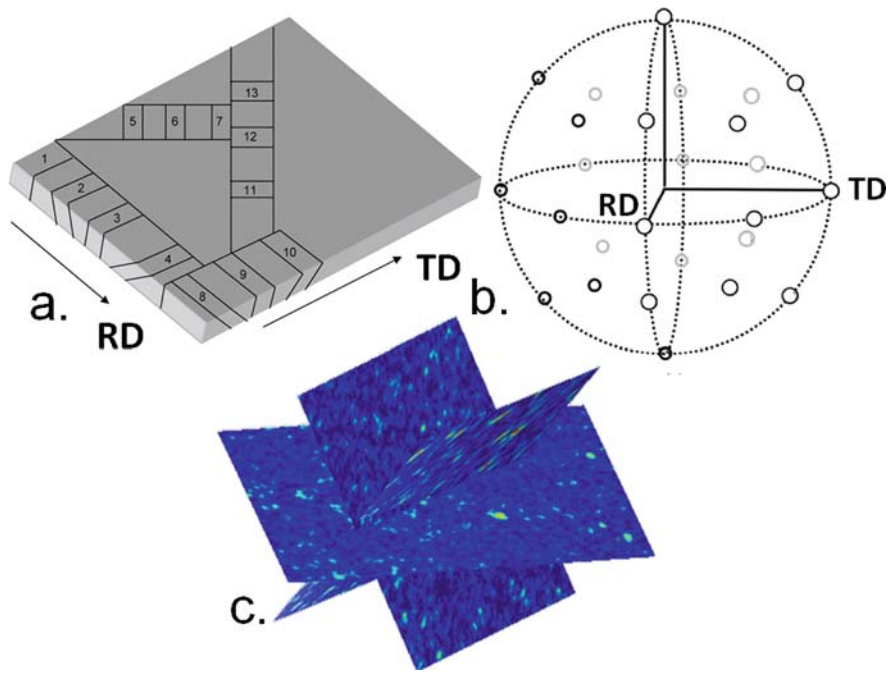


Fig. 13.3 (**a**) Cutting scheme to arrive at planes whose normals best cover the unit sphere (**b**); (**c**) example of 2-point cross correlations taken from 3 planes of OIM maps of silicone steel cut according to this scheme

2-point correlations for three of the planes are shown in Fig. 13.3c.

13.3 Structure Property Relations

Homogenization relations, linking a material's properties at the mesoscale to those at the macroscale, are fundamental tools for design and analysis of microstructure. Such relations are often achieved through perturbation expansions (Beran 1968; Dederichs and Zeller 1973; Phan-Thien and Milton 1982; Willis 1981). Recent advances in this field have successfully applied spectral techniques to Kroner-type perturbation expansions for polycrystalline and composite materials to provide efficient inverse relations for materials design.

The Green's function solution often used in these methods provides a natural link between terms of the series expansion and correlation functions that contain different orders of geometrical information. Such a framework may be applied to a range of material properties with the same basic equations; these include fluid flow, diffusion, electricity, magnetism, and elasticity (Milton 2002). In this chapter we focus on

elasticity, and in particular the stiffness tensor of a material; other properties may be obtained by an analogous route. In keeping with standard notation we will write the stress, strain, and displacement within the material as $\boldsymbol{\sigma}$, $\boldsymbol{\varepsilon}$, and $\mathbf{u}$, respectively; the local stiffness tensor is $\mathbf{C}(\mathbf{x})$, and the reference stiffness tensor for the perturbation analysis is $\mathbf{C}^R$.

13.3.1 Localization Tensors

We employ an additive decomposition of the strain field in the sample into an average quantity and a perturbation from the average as:

$$\boldsymbol{\varepsilon}(\mathbf{x}) = \langle \boldsymbol{\varepsilon} \rangle + \boldsymbol{\varepsilon}'(\mathbf{x}), \quad \langle \boldsymbol{\varepsilon}' \rangle = \mathbf{0} \tag{13.7}$$

The angled brackets indicate ensemble averaging, which is taken to be equivalent to volume averaging using the ergodic assumption for homogeneous material. The local perturbation in the strain field can be expressed in terms of a fourth-rank polarization tensor, $\mathbf{a}$, that we will refer to as the localization tensor:

$$\boldsymbol{\varepsilon}'(\mathbf{x}) = \mathbf{a}(\mathbf{x}) \langle \boldsymbol{\varepsilon} \rangle, \quad \langle \mathbf{a} \rangle = \mathbf{0} \tag{13.8}$$

Then using $\varepsilon_{ij} = \left(u_{i,j} + u_{j,i}\right)/2$ and $\boldsymbol{\sigma}(\mathbf{x}) = \mathbf{C}(\mathbf{x})\boldsymbol{\varepsilon}(\mathbf{x})$, the conservation principle $\nabla \cdot \boldsymbol{\sigma} = 0$ leads to a differential equation that we may solve using the Green's function method to obtain:

$$\mathrm{a}_{\mathrm{klmn}}(\mathbf{x}) = \int_{\mathrm{V}} \frac{1}{2}\left(\mathrm{G}_{\mathrm{ki,l}}\left(\mathbf{x}-\mathbf{x}'\right) + \mathrm{G}_{\mathrm{li,k}}\left(\mathbf{x}-\mathbf{x}'\right)\right) \left[\mathrm{C}'_{\mathrm{ijmn}}\left(\mathbf{x}'\right) + \mathrm{C}'_{\mathrm{ijpq}}\left(\mathbf{x}'\right)\mathrm{a}_{\mathrm{pqmn}}\left(\mathbf{x}'\right)\right]_{,\mathrm{j}} \mathrm{d}\mathbf{x}' \tag{13.9}$$

where $\mathbf{C}'(\mathbf{x}) = \mathbf{C}(\mathbf{x}) - \mathbf{C}^R$, $\mathbf{G}$ is the Green's function tensor, and commas before indices indicate differentiation with respect to the subsequent index. The value for "**a**" can be repeatedly substituted into the right hand side of the equation to obtain a series that may be written in condensed form as:

$$\mathbf{a} = -\boldsymbol{\Gamma}\mathbf{C}' + \boldsymbol{\Gamma}\mathbf{C}'\boldsymbol{\Gamma}\mathbf{C}' - \ldots \tag{13.10}$$

where $\boldsymbol{\Gamma}$ is the integral operator containing the Green's function. Note that the Green's function has a singularity ($\mathrm{G}_{\mathrm{ki,l}}\left(\mathbf{x}-\mathbf{x}'\right) \to \infty$ as $\mathbf{x}-\mathbf{x}' \to 0$). A common approach to dealing with this issue is to evaluate the integral in Eq. (13.9) using integration by parts over a volume $\tilde{V}$ that lies between two spherical surfaces centered at $\mathbf{x}-\mathbf{x}'=0$ with radii approaching 0 and ∞, respectively. Expanding only the first term of the series in Eq. (13.10) (the other terms follow in a similar manner):

$$\mathbf{a}(\mathbf{x}) = \mathbf{E}\left\langle \mathbf{C}' \right\rangle - \mathbf{E}\mathbf{C}'(\mathbf{x}) - \int_{\tilde{\mathrm{V}}} \boldsymbol{\Phi}\left(\mathbf{x}-\mathbf{x}'\right)\mathbf{C}'\left(\mathbf{x}'\right)\mathrm{d}\mathbf{x}' + \ldots \tag{13.11}$$

where the first term on the right is an approximation for the integral on the outer sphere in the case that the local states are randomly distributed at infinity, and the second term gives the integral on the vanishingly small sphere. Clearly the first term is zero if $\mathbf{C}^R = \langle \mathbf{C} \rangle$. The tensors $\mathbf{E}$ and $\boldsymbol{\Phi}$ gather the Green's function terms:

$$E_{klij} = \underset{\tilde{\mathrm{x}}\to 0}{Lim}\left(\int_{\mathrm{S}} \frac{1}{2}\left(\mathrm{G}_{\mathrm{ki,l}}\left(\mathbf{x}-\mathbf{x}'\right) + \mathrm{G}_{\mathrm{li,k}}\left(\mathbf{x}-\mathbf{x}'\right)\right) n_{\mathrm{j}}\mathrm{d}S\right)$$

$$\boldsymbol{\Phi}_{klij}\left(\mathbf{x}-\mathbf{x}'\right) = \frac{1}{2}\left(\mathrm{G}_{\mathrm{ki,lj}}\left(\mathbf{x}-\mathbf{x}'\right) + \mathrm{G}_{\mathrm{li,kj}}\left(\mathbf{x}-\mathbf{x}'\right)\right) \tag{13.12}$$

For an isotropic reference tensor defined by parameters μ and λ, it may be shown that $\boldsymbol{\Phi}$ is given by (Torquato 2002 p 533; Kröner 1986 p 260):

$$\boldsymbol{\Phi}_{ijkl} = \frac{-1}{8\pi\mu(\lambda+2\mu)r^3} \left[\begin{array}{l} (\lambda+\mu)\left(\delta_{ij}\delta_{kl} - 3\delta_{ij}n_k n_l - 3\delta_{kl}n_i n_j + \right. \\ \left. 15 n_i n_j n_k n_l\right) - \mu\left(\delta_{ik}\delta_{jl} + \delta_{il}\delta_{jk}\right) - \\ \frac{3}{2}\lambda\left(\delta_{ik}n_j n_l + \delta_{il}n_j n_k + \delta_{jk}n_i n_l + \delta_{jl}n_i n_k\right) \end{array}\right] \tag{13.13}$$

where $\mathbf{n} = \mathbf{r}/|\mathbf{r}|$. Also, $\mathbf{E}$ is given by:

$$E_{\mathrm{ijkl}} = \frac{1}{15\mu}\left\{\frac{\lambda+\mu}{\lambda+2\mu}\delta_{ij}\delta_{kl} - \frac{3\lambda+8\mu}{\lambda+2\mu}I_{ijkl}\right\} \tag{13.14}$$

where $\mathbf{I}$ is the fourth-order symmetrized tensor identity:

$$I_{ijkl} = \frac{1}{2}\left(\delta_{ik}\delta_{jl} + \delta_{il}\delta_{jk}\right) \tag{13.15}$$

The Kroner type expansions are commonly used to provide effective medium properties. However, in the form given in Eqs. (13.8, 13.11) they may be used to determine local strain fields from a knowledge of the applied macroscopic strain, and the local material structure. By considering the effect of material structure on the local stress and strain fields, it is possible to determine patterns in the structure that may lead to local "hot spots." Furthermore, the resultant stress and strain distributions may be studied for input into failure analysis frameworks, for example. Such analysis may be undertaken with much greater efficiency if the integrals are written in spectral form.

13.3.1.1 Spectral Form

Consider the formula for the localization tensor as given in Eq. (13.11). Let us assume that $\mathbf{C}^R = \langle \mathbf{C} \rangle$ so that we can ignore the first term on the right hand side. Equations of this type have benefited from rewriting in spectral form in various previous studies (Adams et al. 2005; Fullwood et al. 2008). One benefit of a spectral formulation is the ability to split material data from structure data for efficient design studies. Another immediate benefit may be seen in the calculation of the final term of the equation. The convolution can be efficiently calculated using fast Fourier transforms if the data is in discrete form. Let us combine the $\mathbf{E}$ and $\mathbf{\Phi}$ terms back into a single term, $\mathbf{\Gamma}$, as in Eq. (13.10), for simplicity of notation. Discretize the values of this integrand on a regular grid as follows (normalized to remove the requirement for an extra normalization term on the integrals):

$$\mathbf{\Gamma}(\mathbf{r}) \approx \frac{1}{\boldsymbol{\delta}^3} \mathbf{\Gamma}_t \boldsymbol{\chi}_t(\mathbf{r}), \quad \mathbf{\Gamma}_t = \int_{R(\boldsymbol{\Omega})} \mathbf{\Gamma}(\mathbf{r}) \boldsymbol{\chi}_t(\mathbf{r}) \, d\mathbf{r} \tag{13.16}$$

where $\chi_t(\mathbf{r})$ is the indicator function for the spatial cell around discrete point $\mathbf{r}_t$, taking the value 1 for vectors lying in the cell, and 0 for vectors lying outside it; and $\boldsymbol{\delta}^3$ is the volume of one of these uniformly sized cells. If values of $\mathbf{x}$ are defined on a discrete grid (obviously of the same spacing as $\mathbf{r}$) and enumerated by s, then (summation on t):

$$\mathbf{a}_s = -\mathbf{\Gamma}_t \mathbf{C}'_{s-t} \tag{13.17}$$

From the definition of the microstructure function, m, we may write $\mathbf{C}'_{s-t} = \mathbf{C}'^h m^h_{s-t}$, allowing us to rewrite the localization relation with the structure (m) and material ($\mathbf{\Gamma}$, $\mathbf{C}$) parameters separated:

$$\mathbf{a}_s = \mathbf{\Gamma}_t \mathbf{C}'^h m^h_{s-t} \tag{13.18}$$

Taking the Fourier transforms of both sides and using Plancherel's theorem and the convolution theorem (no summation on k):

$$\mathbf{A}_k = \sum_j \tilde{\mathbf{\Gamma}}_k \left(\tilde{C}^j\right)^* M^j_k = \sum_j Z^j_k M^j_k \tag{13.19}$$

where $\tilde{C}^j$ is the FFT of $\mathbf{C}'^h$, $\tilde{\mathbf{\Gamma}}_k$ is the FFT of $\mathbf{\Gamma}_t$, and $M^j_k = \Im_s\left(\Im_h\left(m^h_s\right)\right)$; $\Im_h$ indicates FFT with respect to variable n, and the asterisk indicates complex conjugation. This is a very efficient way to calculate the localization tensor for each point in the material. Not only does it dramatically cut down the number of operations involved in the original convolution (in the spatial dimensions), but it also enables dramatic compression of the data in the material (j) dimension(s).

Figure 13.4 demonstrates the results for local strain using the localization tensor calculated via the method above. In Fig. 13.4a the cubic model used in the comparison is shown. The sample consists of two isotropic phases with a low contrast (of order 1.5) between the stiffnesses of the two, and with 75% volume fraction of the stiffer phase. The strain in individual cells as calculated using finite element analysis is compared with the result from the localization tensor in Fig. 13.4b, and the distribution of strains as calculated via the two methods is shown in Fig. 13.4c. In this exercise care has been taken to accurately calculate the integrals of the Green's function in the region of the singularity (using Monte Carlo integration). Only the first term in the series was used; higher accuracy would result from taking a higher number of terms from the series in Eq. (13.10). Nevertheless, the results give good correlation with the FE calculations (within around 4% error).

13.3.1.2 Calibration Techniques

One method of avoiding the issues associated with the Green's function singularity is to take the form of the Green's function solution and calibrate the variables to finite element (FE) results using a set of "basis"

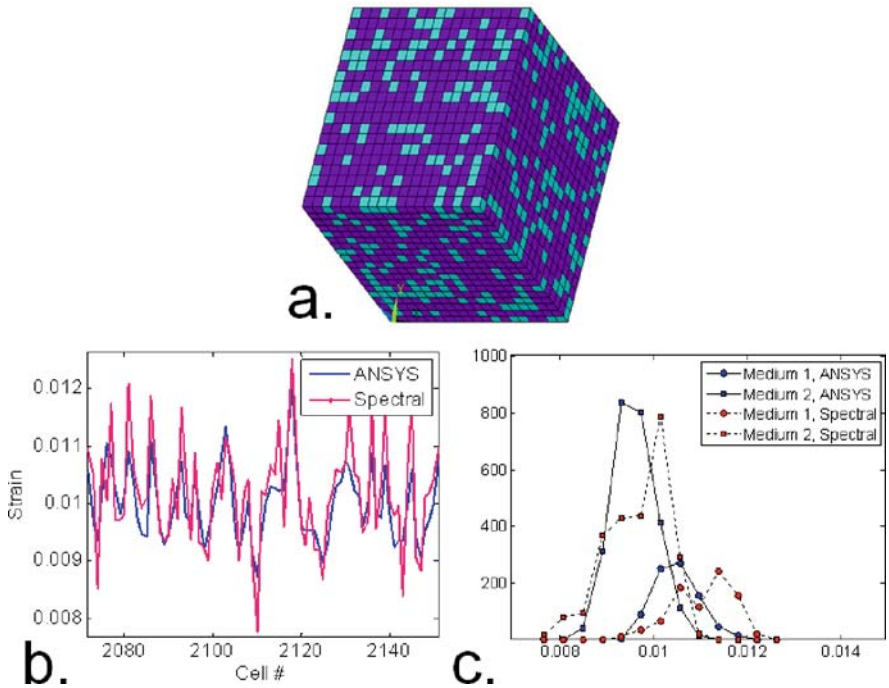


Fig. 13.4 (**a**) Cubic structure comprised of two isotropic phases with 75% volume fraction of the stiffer phase and applied strain of 1% in the z-direction; (**b**) FE results of strain in individual cells vs. results from the spectral model developed above; (**c**) distributions of strain in the stiff and soft phases as calculated by FE and the spectral method

geometries that represent a range of real structures. The form of the equations is given by (Binci et al. 2008):

$$\mathbf{a}_{\S} = \mathbf{I} - \mathbf{J}^{h}_{\hat{s}s} m^{h}_{s} + \mathbf{L}^{hh'}_{\hat{s}ss'} m^{h}_{s} m^{h'}_{s'} - \ldots \tag{13.20}$$

where the J and L terms are calibrated to FE results. Such an approach gives excellent results for a range of microstructures, as demonstrated in Fig. 13.5.

13.3.2 Effective Tensors

As mentioned earlier, the perturbation expansions developed above are typically used to produce relations for effective property tensors. If we use the relation for effective stiffness tensor, $\mathbf{C}^{*}$:

$$\begin{aligned} \mathbf{C}^{*}\langle\boldsymbol{\varepsilon}\rangle =& \langle\mathbf{C}\boldsymbol{\varepsilon}\rangle = \left\langle\mathbf{C}\left(\boldsymbol{\varepsilon}' + \langle\boldsymbol{\varepsilon}\rangle\right)\right\rangle = \left\langle\mathbf{C}\boldsymbol{\varepsilon}'\right\rangle \\ &+ \langle\mathbf{C}\rangle\langle\boldsymbol{\varepsilon}\rangle = \langle\mathbf{C}\mathbf{a}\rangle\langle\boldsymbol{\varepsilon}\rangle + \langle\mathbf{C}\rangle\langle\boldsymbol{\varepsilon}\rangle \\ &\Rightarrow \mathbf{C}^{*} = \langle\mathbf{C}\mathbf{a}\rangle + \langle\mathbf{C}\rangle \end{aligned} \tag{13.21}$$

This leads to the usual Kroner-type expansion for the effective elastic stiffness tensor $\mathbf{C}^{*}$ in terms of the local property, $\mathbf{C}$, and often written as (Kröner 1967):

$$\mathbf{C}^{*} = \langle\mathbf{C}\rangle - \left\langle\mathbf{C}'\boldsymbol{\Gamma}\mathbf{C}'\right\rangle + \left\langle\mathbf{C}'\boldsymbol{\Gamma}\mathbf{C}'\boldsymbol{\Gamma}\mathbf{C}'\right\rangle - \ldots \tag{13.22}$$

If the series is truncated after the first term, we have the usual upper bound theory in terms of the volume fraction of the local states. The subsequent terms introduce increasingly higher order geometrical statistics.

Splitting the Green's function operator as for the localization tensor, we may rewrite Eq. (13.22) as (Fullwood et al. 2007):

$$\begin{aligned} \mathbf{C}^{*} =& f^{h}\mathbf{C}^{h} - f^{h}\left(\mathbf{C}'^{h}\right)\mathbf{E}\left(\mathbf{C}'^{h}\right) \\ &+ \int\limits_{R(\boldsymbol{\Omega}),r\neq 0} f^{hh'}(\mathbf{r})\left(\mathbf{C}'^{h}\right)\boldsymbol{\Phi}(\mathbf{r})\left(\mathbf{C}'^{h'}\right)d\mathbf{r} + \ldots \end{aligned} \tag{13.23}$$

where $\mathbf{r} = (\mathbf{x} - \mathbf{x}')$.

Consider the formula for effective stiffness as given in Eq. (13.23). The correlation functions, *f,* may be calculated rapidly using FFTs. For the other terms, the idea is to gather function values into arrays that may take some time to compute, but once available, lead to rapid computation of relations, hence making optimization algorithms (with repeated function calls) possible. This facilitates determination and search of the property closure. For the tensor, $\boldsymbol{\Phi}$, we derive a spectral form analogous to that for $\boldsymbol{\Gamma}$ in Eq. (13.16). Then:

$$\begin{aligned} \mathbf{C}^{*} \approx\ & f^{h}\mathbf{C}^{h} - f^{h}\left(\mathbf{C}'^{h}\right)\mathbf{E}\left(\mathbf{C}'^{h}\right) \\ &+ \left\{f^{hh'}_{t}\right\}\left(\mathbf{C}'^{h}\right)\boldsymbol{\Phi}_{t}\left(\mathbf{C}'^{h'}\right) + \ldots \end{aligned} \tag{13.24}$$

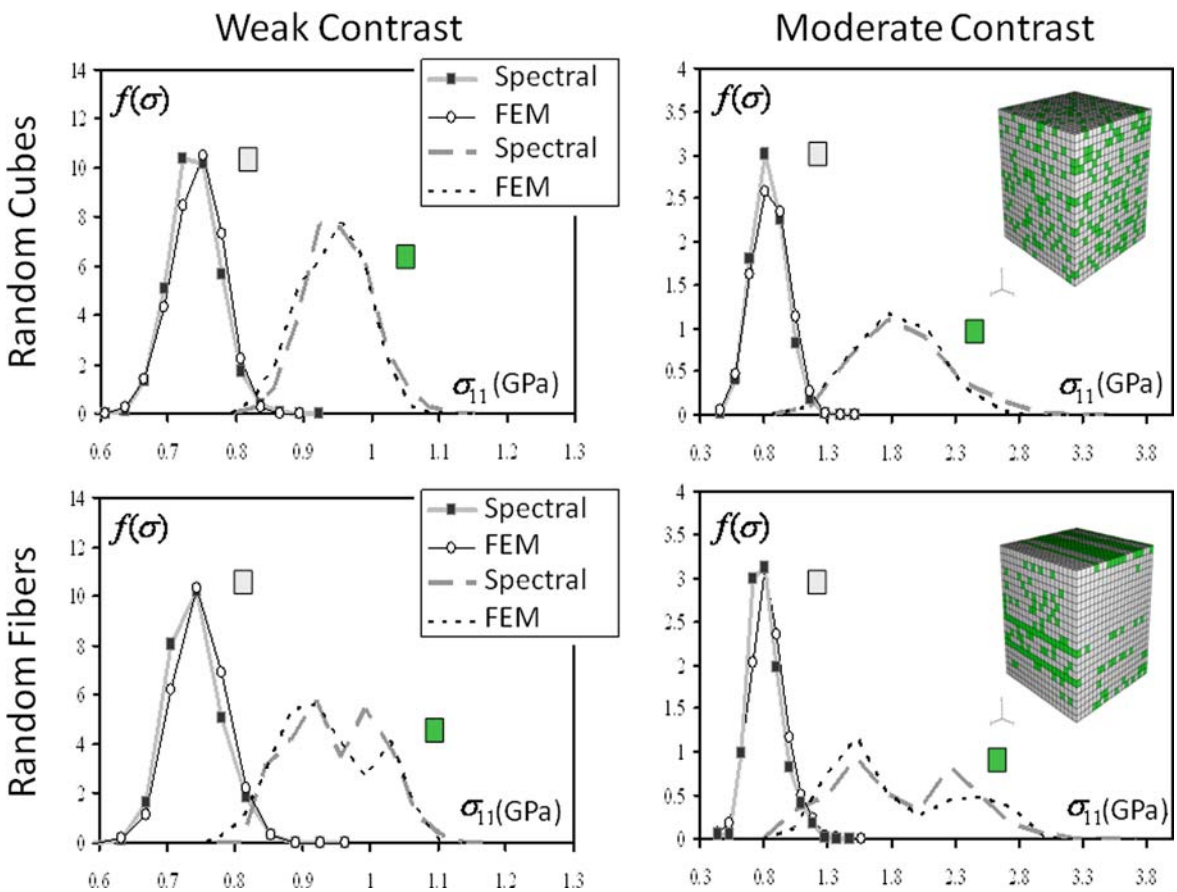


Fig. 13.5 Distributions for strain in the stiff and soft phases of two isotropic materials distributed in different structural arrangements (as shown), for both weak and moderate contrast between the properties of the isotropic phases, as calculated using FE and using the spectral calibration method

We may collect the terms that are constant for the given material:

$$\mathbf{\Lambda}^h = \left(\mathbf{C}'^h\right)\mathbf{E}\left(\mathbf{C}'^h\right), \quad \mathbf{\Pi}_t^{hh'} = \left(\mathbf{C}'^h\right)\mathbf{\Phi}_t\left(\mathbf{C}'^{h'}\right) \tag{13.25}$$

Then we have what amounts to an algebraic expression for $\mathbf{C}^*$ with the material information effectively separated from the geometry data contained in the correlation functions, *f:*

$$\mathbf{C}^* \approx f^h\mathbf{C}^h - f^h\mathbf{\Lambda}^h + \left\{f_t^{hh'}\right\}\mathbf{\Pi}_t^{hh'} + \ldots \tag{13.26}$$

Optimization of material properties may be efficiently performed by searching over either the material or geometry space represented by these terms.

When using regular grid points to evaluate these integrals, particular care must be taken in the region

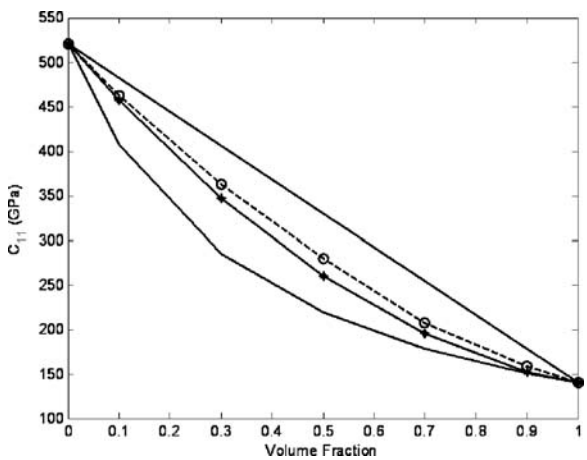


Fig. 13.6 Upper and lower bounds (*straight lines*) and estimates calculated using FE (*asterisks*) and the spectral method (*circles*) for a random mixture of isotropic phases of varying volume fraction. The contrast in stiffness between the phases is just over 3 (as seen from the extremes of the plot)

of the origin. For example, in Eq. (13.26) the cell relating to $t = 0$ must be included, and may require Monte Carlo integration about the point $\mathbf{r} = 0$ for an accurate result. For other values of t, regular grid points may be used if chosen carefully. The reference tensor is often taken to be the average stiffness tensor in the material. If the component stiffness tensors are not isotropic, one may use various techniques to assign an isotropic stiffness as close as possible to the average of these tensors (Gazis et al. 1963; Norris 2006). An alternative strategy is to choose a tensor "midway" between the extremes of the stiffness tensors of the material components (Kalidindi et al. 2006). Using this method resulted in good approximations for effective tensors of structures composed of two isotropic components of weak and medium contrast and varying volume fraction and heterogeneity, as shown in Fig. 13.6.

13.4 Microstructure Design

First-order microstructure sensitive design (MSD) was introduced in the previous chapter. The concepts may readily be extended to higher orders, based upon the

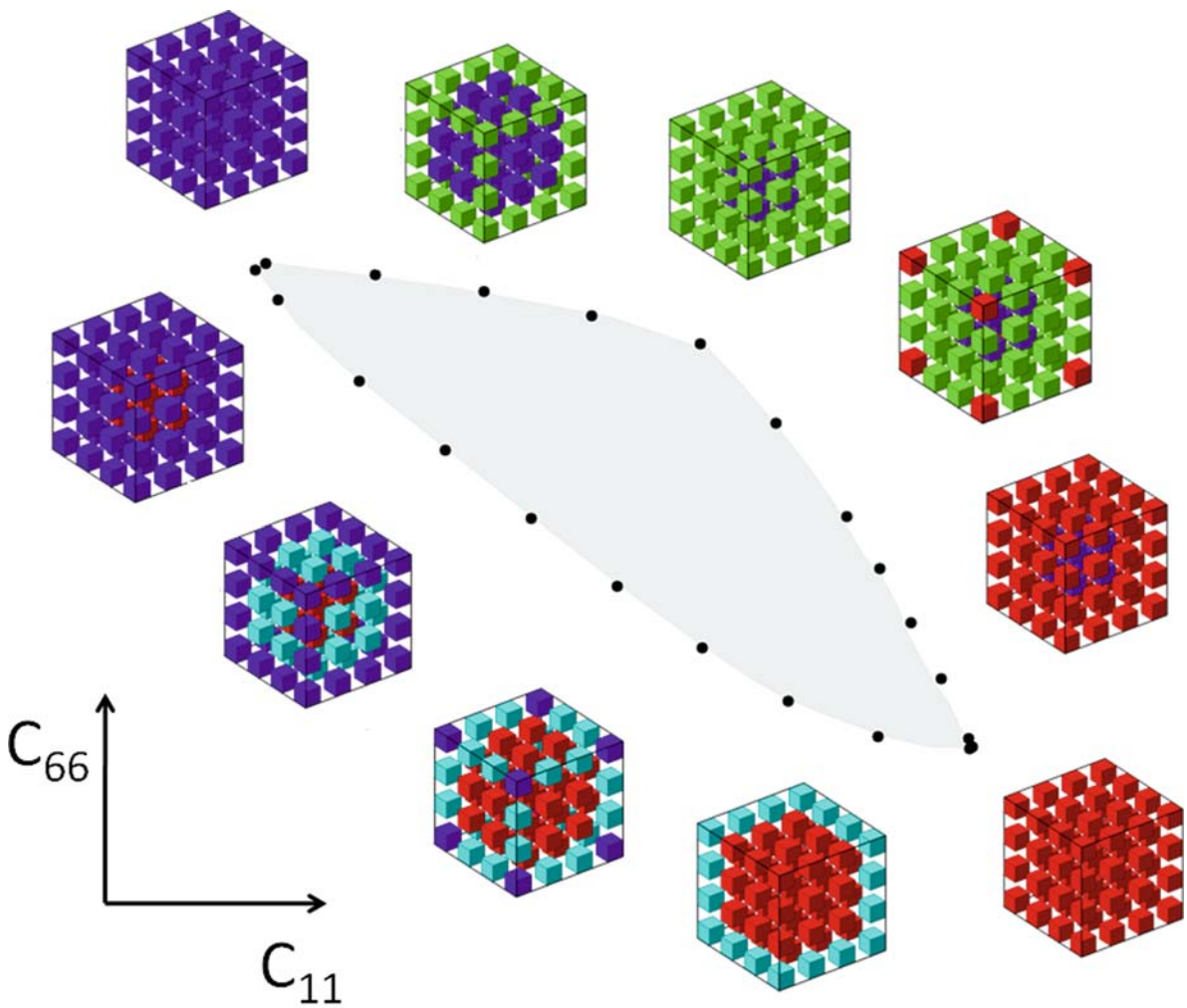


Fig. 13.7 Cubic structures that give properties at various points on the boundary for the C11 vs. C66 property closure for copper; the various colors represent 4 different orientations of the copper crystals

framework described above (Fullwood et al. 2007; Kalidindi et al. 2006). Second-order property closures may be created by truncating the series for effective properties at the second-order as the basis of the map from the microstructure hull to the property space. The efficiency of the calculations using the spectral methods described in this chapter enables the map to be inverted as the basis for structure design.

Using the notation introduced above, the hull of all possible microstructures is given by the usual set of constraints on the microstructure function (in the discrete space):

$$\sum_h m_s^h = 1,\ 0 \le m_s^h \le 1 \tag{13.27}$$

If spectral analysis is used during the design process, these constraints may be translated into a set of constraints in the relevant Fourier space (see, e.g., Niezgoda et al. 2008).

To produce a closure we must determine a pair of properties of interest (for a 2D closure; higher dimension closures may of course be defined), with equations analogous to Eq. (13.26). Then, using the Pareto front or other optimization techniques (Fullwood et al. 2007), the microstructure hull may be searched for the boundaries of the property closure.

The property closures are then used to resolve the inverse design problem for optimal properties. Various examples have been solved in the literature (Adams et al. 2001. 2004; Fullwood et al. 2007; Kalidindi et al. 2004). In Fig. 13.7 we demonstrate a series of structure designs that correspond to points on the boundary of a property closure for C_{11} and C_{66} of a single-phase copper material with four possible crystal orientations. Once an ideal property combination has been identified within the closure by a designer, a structure (almost certainly nonunique) that corresponds to the given properties may be identified using linear combinations of structures already identified on the boundary.

By using the efficient spectral methods developed above, and the 2-point correlations, a powerful framework is available for materials analysis and design.

Acknowledgments SK and DF acknowledge financial support for this work from the Office of Naval Research, Award No. N000140510504 (Program Manager: Dr. Julie Christodoulou). BA acknowledges funding provided by ARO, David Stepp, Program Manager.

References

Adams BL, Gao X, Kalidindi SR (2005) Finite approximations to the second-order properties closure in single phase polycrystals. Acta Mater 53(13):3563–3577

Adams BL, Henrie A, Henrie B, Lyon M, Kalidindi SR, Garmestani, H (2001) Microstructure-sensitive design of a compliant beam. J Mech Phys Solids 49(8):1639–1663

Adams BL, Lyon M, Henrie B (2004) Microstructures by design: linear problems in elastic-plastic design. Int J Plasticity 20(8–9):1577–1602

Beran MJ (1968) Statistical continuum theories. John Wiley Interscience, New York

Binci M, Fullwood D, Kalidindi SR (2008) A new spectral framework for establishing localization relationships for elastic behavior of composites and their calibration to finite-element models. Acta Mater 56(10):2272–2282

Dederichs PH, Zeller R (1973) Variational treatment of the elastic constants of disordered materials. Z Phys A 259:103–116

Fullwood DT, Adams BL, Kalidindi SR (2007) Generalized Pareto front methods applied to second-order material property closures. Comput Mater Sci 38(4):788–799

Fullwood DT, Adams BL, Kalidindi SR (2008) A strong contrast homogenization formulation for multi-phase anisotropic materials. J Mech Phys Solids 56(6):2287–2297

Gao X, Przybyla CP, Adams BL (2006) Methodology for recovering and analyzing two-point pair correlation functions in polycrystalline materials. Metall Mater Trans A 37(8): 2379–2387

Gazis DC, Tadjbakhsh I, Toupin RA (1963) The elastic tensor of given symmetry nearest to an anisotropic elastic tensor. Acta Crystallogr 16:917–922

Homer ER, Adams BL, Fullwood DT (2006) Recovery of the grain boundary character distribution through oblique double-sectioning. Scripta Mater 54:1017–1021

Kalidindi SR, Binci M, Fullwood D, Adams BL (2006) Elastic properties closures using second-order homogenization theories: Case studies in composites of two isotropic constituents. Acta Mater 54(11):3117–3126

Kalidindi SR, Houskamp JR, Lyons M, Adams BL (2004) Microstructure sensitive design of an orthotropic plate subjected to tensile load. Int J Plasticity 20(8–9):1561–1575

Kröner E (1967) Elastic moduli of perfectly disordered composite materials. J Mech Phys Solids 15:319–329

Kröner E (1986) Statistical modelling. In: Gittus J, Zarka J (eds) Modeling small deformation in polycrystals. Elsevier, Amsterdam

Milton GW (2002) The theory of composites. Cambridge University Press, Cambridge

Niezgoda SR, Fullwood DT, Kalidindi SR (2008) Delineation of the space of 2-point correlations in a composite material system. Acta Mat 56(18) 5285–5292

Norris AN (2006) The isotropic material closest to a given anisotropic material. J Mech Mater Struct 1(2):231–246

Phan-Thien N, Milton GW (1982) New bounds on effective thermal conductivity of n-phase materials. Proc R Soc Lond A 380:333–348

Rust B, Donnelly D (2005) The fast Fourier transform for experimentalists part III: Classical spectral analysis. Comput Sci Eng 7(5):74–78

Tewari A, Gokhale AB, Spowart JE, Miracle DB (2004) Quantitative characterization of spatial clustering in three-dimensional microstructures using two-point correlation functions. Acta Mater 52:307–319

Torquato S (2002) Random heterogeneous materials. Springer-Verlag, New York

Walker JS (1996) Fast Fourier transform. CRC Press, Boca Raton, FL

Willis JR (1981) Variational and related methods for the overall properties of composites. Adv Appl Mech 21:1–78

Chapter 14

Combinatorial Materials Science and EBSD: A High Throughput Experimentation Tool

Krishna Rajan

14.1 Introduction

The impact of EBSD in combinatorial experimentation lies in its value as a nondestructive focused probe for high throughput screening of materials libraries via backscattered diffraction. The types of information gathered by EBSD are of course well documented (especially in the present and the previous companion volume [Schwartz et al. 2000]). From the perspective of high throughput screening EBSD:

- the symmetry of the backscattered diffraction patterns provides orientation information (assuming one knows the crystal structure), and of course serves as the foundation for texture analysis;
- the symmetry information, when coupled with the measurement of the spacing of the Kossel type lines associated with EBSD, can help to serve as a phase identification, or more accurately a phase *selection* tool, in those cases where we have some a priori knowledge of the phases likely to occur (Laigo et al. 2008; Zaldívar-Cadena and Flores-Valdés 2007; Perez et al. 2006; Fischer et al. 2006; Silva et al. 2006); and
- orientation imaging can be used to delineate grain boundaries and, when integrated into edge detection algorithms, can serve as a rapid grain size assessment tool

The mechanics of texture analysis and phase identification are discussed elsewhere and will not be the topic of this chapter. We will instead focus on the challenges associated with combining accuracy and high throughput methods in order to fully advance EBSD in the field of combinatorial methods. This discussion will begin by defining the terms "combinatorial" and "combinatorial experiments," followed by some examples of the use of EBSD in chemical and processing libraries. Using selected works in the literature as examples, we then discuss the types of advances in EBSD research that are needed to fully exploit EBSD in high throughput experimentation.

14.2 Introduction to Combinatorial Methods

Combinatorial materials science offers an exciting experimental strategy for rapidly surveying a wide array of materials chemistries and process variables coupled to their screening structure and properties. Adapting approaches used in synthetic organic chemistry for applications such as pharmaceutical sciences and chemical discovery, materials scientists have developed a variety of approaches to create solid-state libraries in the attempt to rapidly examine a broad range of materials characteristics, with the hope of accelerating the discovery of new materials and/or new materials properties (Rajan 2008). The concept of combinatorial libraries in the area of solid state has been popularized over the last decade, by borrowing from similar work in the field of organic chemistry (Liu and Schultz 1999). The goal of combinatorial

K. Rajan (✉)
Department of Materials Science and Engineering, Iowa State University, Ames, IA 50011–2300, USA
e-mail: krajan@iastate.edu

A.J. Schwartz et al. (eds.), *Electron Backscatter Diffraction in Materials Science*,
DOI 10.1007/978-0-387-88136-2_14, © Springer Science+Business Media, LLC 2009

experimentation in engineering is to recreate the diversity in the chemistry and structure, and hence the properties, of materials found in nature. The literature in this field is vast and continues to grow rapidly as different approaches to generating combinatorial libraries are explored and adapted to address a variety of materials systems and materials properties (Seyler et al. 2007; Kim and Maier 2006; Lin et al. 2007; Martin et al. 2008; Lu et al. 2006; Lu 2006; Bhat and Genzer 2006; Guerrero-Sanchez et al. 2006; Chen et al. 2008; Chambers and Taylor 2007; He et al. 2007; Ludwig et al. 2007; Guo et al. 2007; Yoo et al. 2007; Miller et al. 2007; Cooper and McGinn 2006; Behrens et al. 2006; Garoli et al. 2006; Laurila et al. 2004; Sambandam et al. 2006; Adomaitis 2007). The concept of generating combinatorial libraries is some respects is simple, but the implementation is not trivial because different experimental strategies have to be developed that are specific to the class of materials being studied and the properties being measured. One illustrative example is the work of Jayaraman and Hillier (2005), who developed a method for synthesis of multicomponent gradient libraries for combinatorial catalyst discovery. They used a "gel-transfer" synthesis method that involved localized diffusion of aqueous precursor metal salts into a hydrated gel to establish spatially varying concentration fields. Electrodeposition was then used to transfer the gradient in metal precursors to a surface. An optical screening technique based upon the pH-sensitive fluorescence of quinine was used to visualize the spatial onset of reactivity on the ternary catalyst gradient (see Fig. 14.1).

The logic of examining these resulting chemical arrays is to associate the signal of the property or characteristics used in the screening technique to that of the known variations in chemistry that are produced in the combinatorial experiments. The appeal of combinatorial arrays lies in the fact that this association between property and chemistry can be made very quickly. Such chemistry-property associations are predicated on the fact that the probes used to make such measurements can be focused onto the specific areas of the combinatorial spread. The same applies to probing structure, and hence the advent of EBSD as a focused probe for diffraction information makes it another valuable tool in the field of combinatorial materials science.

The reader is directed to a number of recently published review articles that also provide a large bibliography of information (Xiang 1999; Xiang and Takeuchi 2003; Cawse 2003; Journal of Measurement Science and Technology 2005; Zhao 2006; Potyralio and Maier 2007; Narasimhan et al. 2007). Irrespective of the type of materials systems used, libraries of materials in thin film, particulate, or bulk forms can be created.

Whatever form the material is in, combinatorial libraries fall into two broad geometrically based categories, "discrete" and "continuous" (Fig. 14.2). The former involves spatially resolved variations in chemistry resulting in 1-dimensional (1D) or 2-dimensional (2D) arrays, very similar to the microarrays used in organic chemistry. Apart from having discrete wells or containers for each chemistry (which may be generated by a number of means, for example, robotic deposition), one can also generate a variety of discrete patterns on a substrate by lithographic techniques, or by assisting self-assembly processes that result in discrete arrays. A good example is shown in the work of Saalfrank and Maier (2004) in the field of catalysis, in which they used liquid phase synthesis to prepare libraries using pipetting robots. These discrete arrays were subjected to reacting gases and the simultaneous evaluation of catalytic activity on materials, emissivity-corrected infrared thermography was chosen. With infrared thermography, the heat of reactions is monitored and this provides excellent information on the relative catalytic activity of all the materials on a catalyst library. Continuous libraries effectively capture unbroken gradients in chemistry or other materials attributes (e.g., microstructure), which can be achieved in a number of ways depending on the material, ranging from thickness gradients to thermal and thermomechanical gradients. In this chapter, we present selected examples of how EBSD can be applied to rapidly track orientation, phase formation, and/or grain size in discrete or gradient microstructures resulting from both chemical and processing libraries; and discuss the data analysis challenges associated with high throughput EBSD.

14.2.1 High Throughput EBSD Screening

14.2.1.1 Analysis of Chemical Libraries

Diffusion couples provides one method of creating phase libraries, and EBSD has been used as a means of rapidly screening the local changes in the microstructure to identify phase formation associated

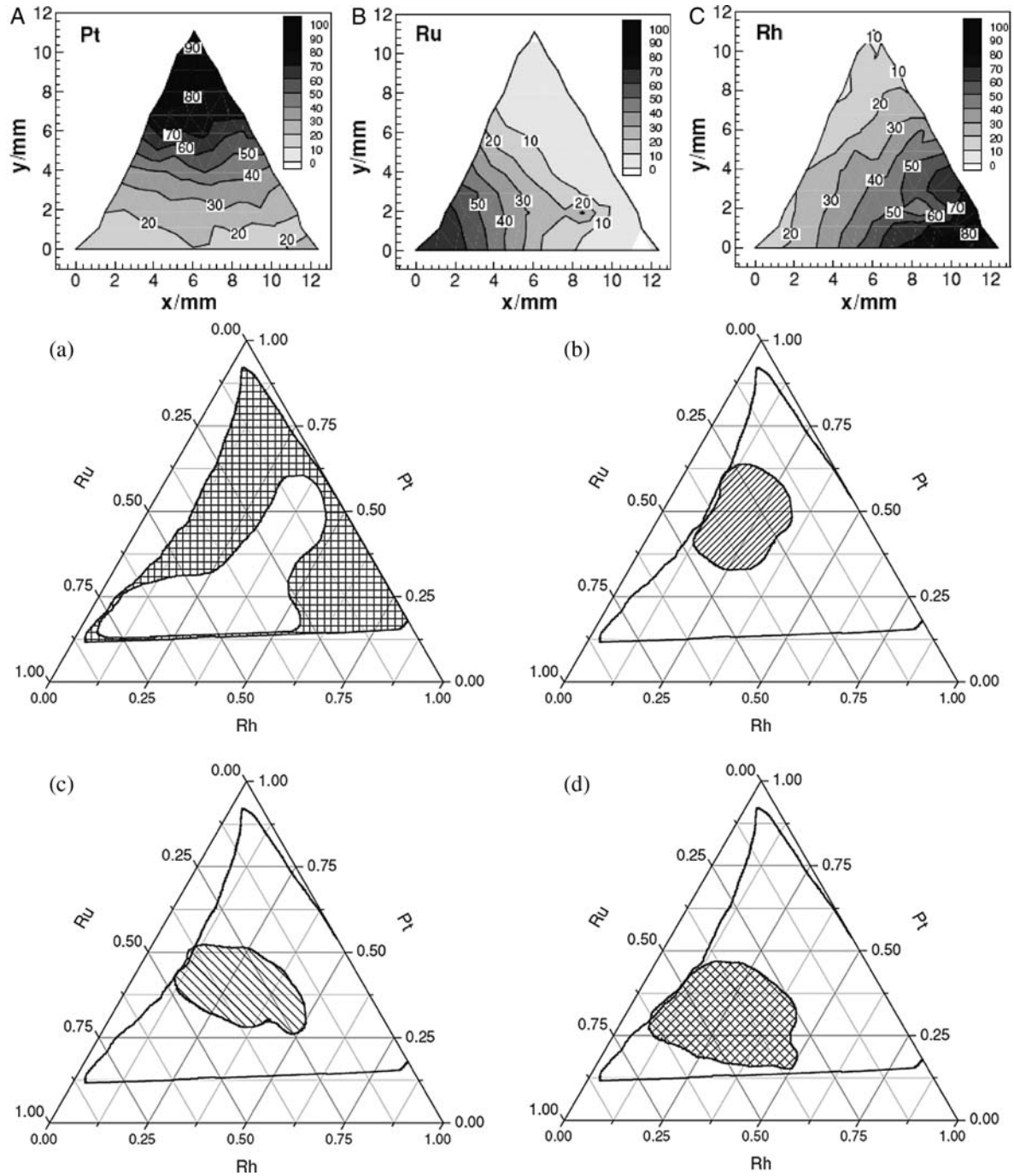


Fig. 14.1 (**a**) Composition of the $Pt_xRu_yRh_z$ gradient as a function of the distance in x and y directions: (**a**) Pt, (**b**) Ru, and (**c**) Rh, shown as contour maps. Compositions at numerous points along the gradient surface were measured using X-ray energy dispersive spectroscopy (EDS) to construct these maps (from Jayaraman and Hillier 2005). (**b**) Summary of results showing the regions of lowest onset potentials for various fuels: (**a**) H_2, (**b**) CO, (**c**) methanol, and (**d**) ethanol. The solid outline indicates a mapping of the gradient sample onto this ternary composition diagram. Regions outside this outline were not present in the sample gradient (from Jayaraman and Hillier 2005)

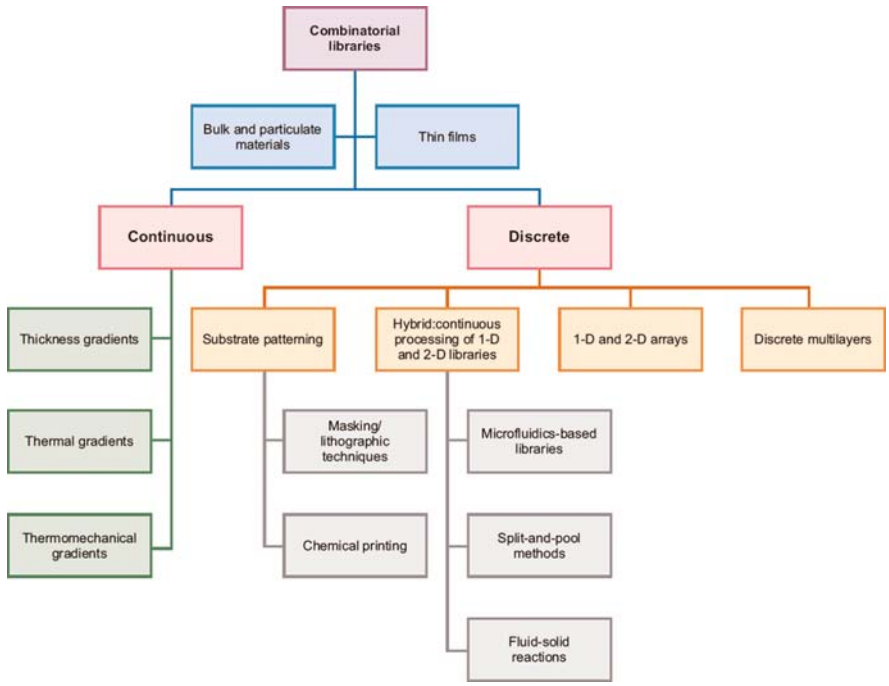


Fig. 14.2 A classification chart of experimental methods for generating combinatorial libraries for bulk, particulate, and thin-film materials (from Rajan 2008)

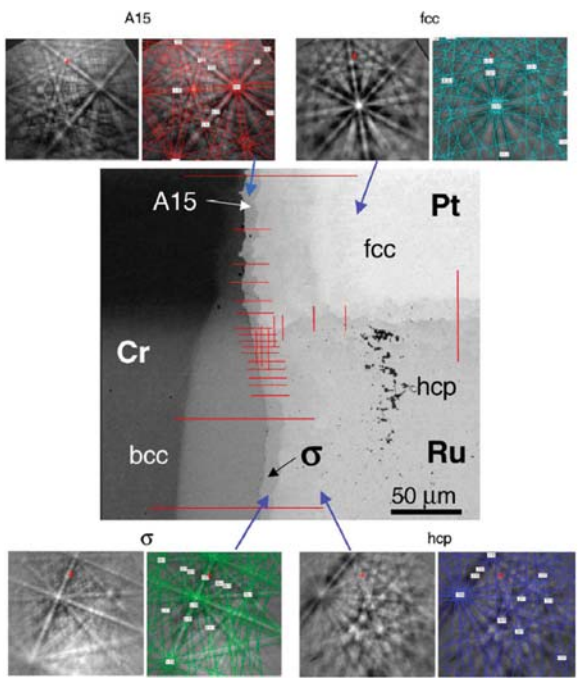


Fig. 14.3 EBSD identification of phases in the Cr-Pt-Ru ternary system in the diffusion multiple. The EBSD analysis also helps locate the interface between the A15 and the σ phases—the SEM image alone cannot differentiate them (Zhao et al. 2004)

with interdiffusion (Zhao et al. 2003, 2004a, 2004b). As shown in Fig. 14.3, EBSD has been used to identify phases in the Cu-Pt-Ru ternary system, and also to help locate the interface between phases, via solid-solid diffusion couples. Phase identification is accomplished by a direct match of the diffraction bands in an experimental EBSD pattern with simulated patterns generated using known structure types and lattice parameters. This approach has also been used to screen diffusion couples as a way to develop phase diagrams. It should be emphasized that such an approach requires that the EBSD data be coupled with other microanalytical techniques such as EPMA to map elemental chemistry across these diffusion couple-based combinatorial libraries. EBSD can thus potentially be used to develop phase diagrams; and when coupled to spatially resolved property screening, one can in principle generate structure-property libraries via combinatorial experimentation (Zhao 2004).

Cha et al. (2006) have used EBSP combined with detailed thermochemical calculations to quantitatively assess phase equilibria at liquid-solid interfaces. Their work provides a good example of how, through carefully controlled experiments, EBSD can serve as a powerful tool to map phase equilibria (Fig. 14.4). They show how different types of titanium oxide phases can be distinguished (Fig. 14.5).

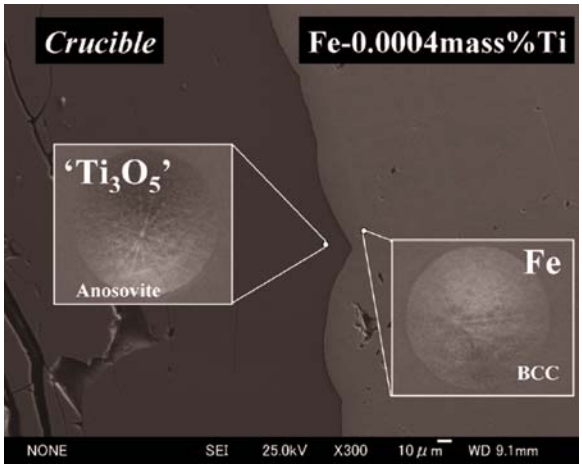


Fig. 14.4 Typical EBSD patterns across phase boundaries in combinatorial chemical library (Zhao et al. 2003)

While bulk diffusion couples can be viewed as gradient chemical libraries, EBSD has also shown to have value as a high throughput screening tool for thin films. For instance, Davydov et al. (2004) have used EBSD to track orientation effects associated with thin film combinatorial arrays related to chemistry and film thickness. They used this approach to explore the structural quality of the Au and Ni single- and bi-layered combinatorial library on a GaN/sapphire substrate. This was investigated as a function of the metal ratios and thickness using XRD, EBSD and TEM. For the best structural quality, it was found advantageous to first deposit a thin layer of nickel onto the GaN.

14.2.1.2 Microstructural Gradients

There are numerous studies reported in the literature which have used EBSD to track spatial variations in microstructure due to processing. While they are not called "combinatorial," such studies in fact address some of the challenges in sampling and analysis of data in a high throughput manner. In the following discussion, we provide some illustrative examples.

This example of gradients in bulk materials can be juxtaposed with the work of Bastos et al. (2008) on thin films. They have linked high throughput EBSD with microstructural variations in 3D using focused ion beam techniques (Fig. 14.7). They were thus able to establish growth mechanisms for columnar grains. The work of Mateescu et al. (2007), however, has pointed out that the use of a FIB can influence the quality of EBSD patterns and should be taken into consideration during the sample preparation process (Fig. 14.8).

Mingard et al. (2007) have used EBSD to rapidly gather information on grain size and related parameters. As they note, the automated nature of EBSD can provide a much greater amount of information which is less susceptible to experimental uncertainties due to etching or identification of twin boundaries or illumination effects. Using deformation-induced microstructural gradients associated with nickel-based superalloys, they showed, for instance, that EBSD could be used to distinguish twins and resolve much smaller grains, resulting in a difference of up to 50% in detailed optically measured grain size (Fig. 14.6).

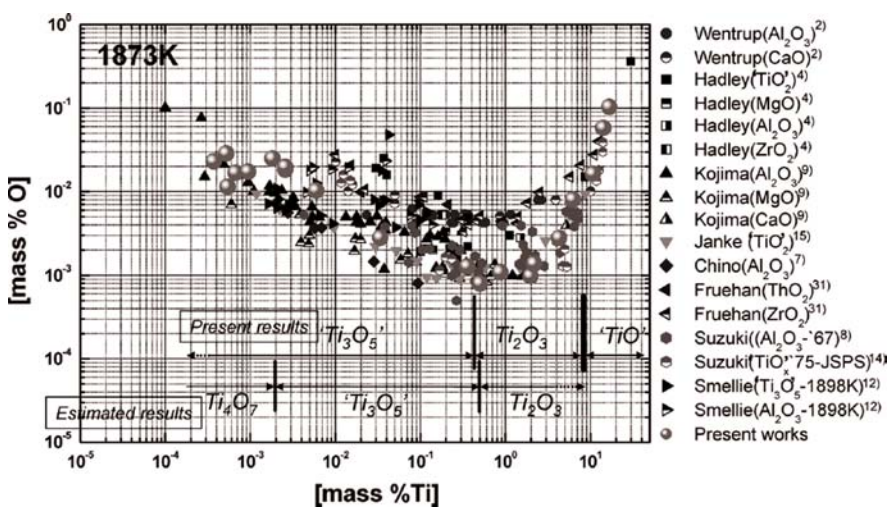


Fig. 14.5 Equilibrium relations between Ti and O in liquid iron, comparing EBSD results (indicated by *large grey dot*) with conventional thermodynamic measurements (Cha et al. 2006)

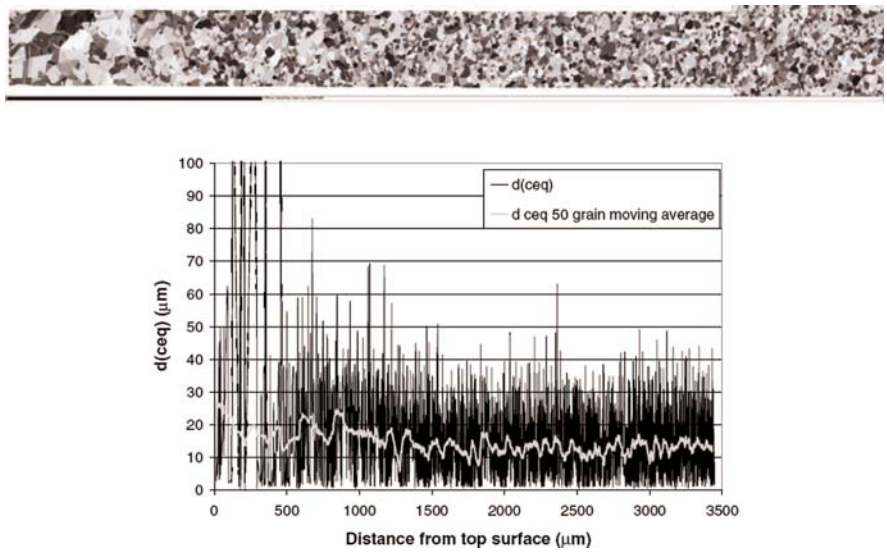


Fig. 14.6 EBSD map of grain orientation in a section of a uniaxially compressed nickel-based superalloy sample (*top*), and corresponding fluctuations in mean grain size ($d_{(ceq)}$) (Mateescu et al. 2007)

14.2.2 Informatics and Data

The role of data analysis is an integral part of high throughput analysis via EBSD. While the examples provided above are illustrative of the experimental issues, we conclude this chapter with a discussion on some of the data analysis and information processing (informatics) issues that are important to consider.

One needs to couple EBSD not only to other experimental data, but also to microstructural simulation data. One of the challenges in doing this is the size of the data sets that can result from such an analysis. For example, Lewis et al. (2008) described the quantitative 3D analysis of the correlations between real (experimentally determined) microstructural features in a stainless steel alloy and the mechanical response. The three-dimensional grain structure of the austenite phase in this alloy was determined using serial sectioning techniques which combined optical microscopy with electron backscattered diffraction (EBSD). The spatial and crystallographic information was incorporated into a 3D reconstruction of the microstructure, and each individual grain and twin was assigned crystallographic properties based on the averaged orientation values for each grain, as measured by EBSD. A volume measuring 243 × 243 × 158 μm was reconstructed, containing 138 individual grains. This dataset was used as input for image-based finite element simulations. The volume analyzed here consists of 312,500 voxels measuring 3.6 × 3.6 × 3.3 μm each, representing a total volume of 9.3×10^6 μm^3. Using algorithms developed for microstructural analysis and visualization, grains and twins can be viewed individually, and sections or ''slices" of the microstructure can be viewed in any orientation (Fig. 14.9).

Due to the large size of these datasets and the number of different variables to be examined, scientific visualization techniques alone do not give sufficient insight into the relationship between mechanical response and microstructure. Instead, visualization techniques can be used to provide a qualitative

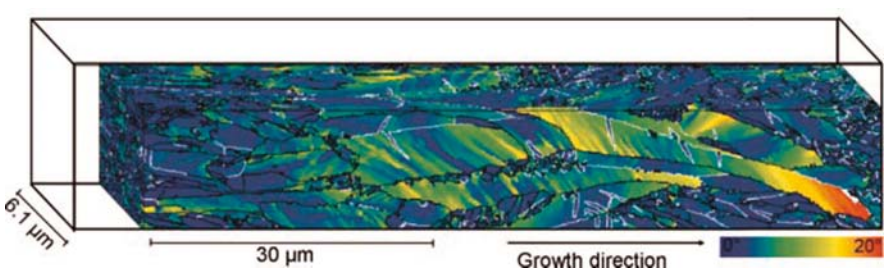


Fig. 14.7 Three-dimensional orientation gradient map for a maximum gradient of 20° from the grain average orientation. Possible twin boundaries are shown in *white,* high-angle grain boundaries in *black*, and low-angle grain boundaries in *grey* (Mateescu et al. 2007)

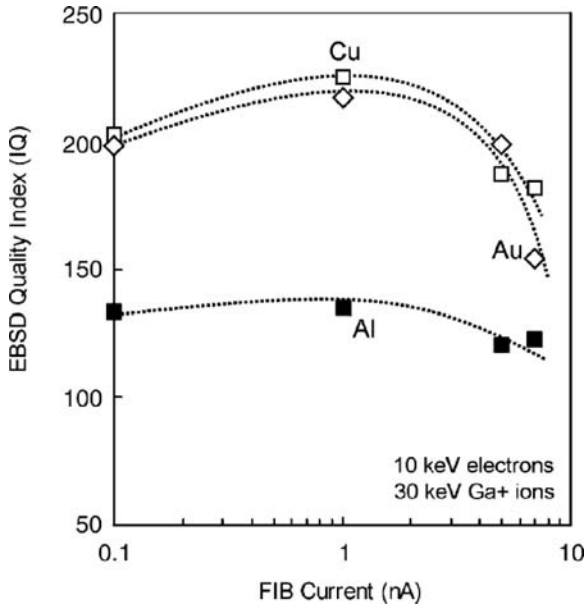


Fig.14.8 Influence of FIB milling current on EBSD image quality (IQ) for Al, Cu, and Au (Mateescu et al. 2007)

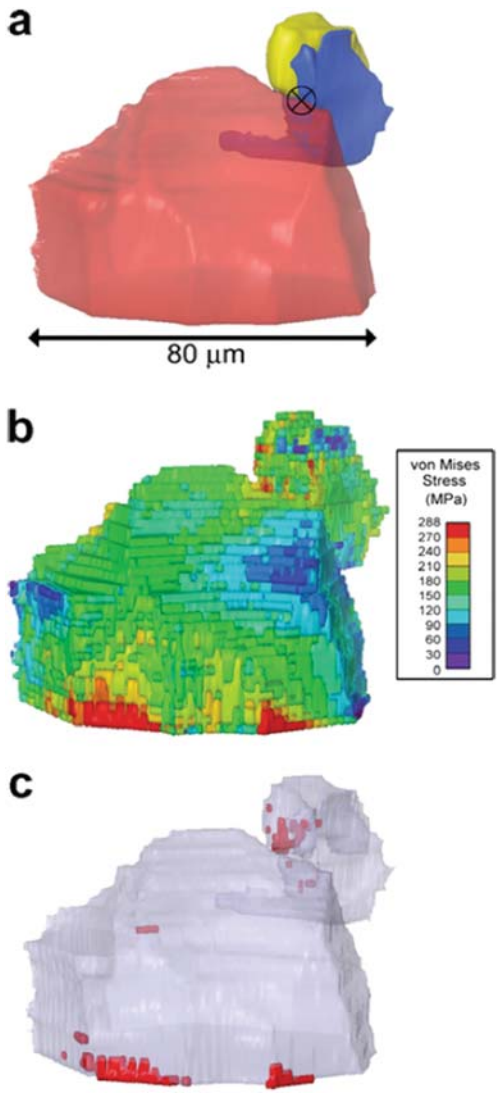


Fig. 14.9 3D reconstruction of three grains in the microstructure. (**a**) Location of high-stress triple junction (marked by "x"). (**b**) Contour of von Mises stress from the simulation superimposed on grain reconstruction. (**c**) Locations of all points with von Mises stress >288 MPa (shown in *red*) (Lewis et al. 2008)

understanding of trends and correlations, which can subsequently be examined more quantitatively using feature tracking and image-based data mining techniques (Fig. 14.10).

In the 3D microstructure studied here, it was determined that a uniaxial stretch condition resulted in high-stress regions associated with proximity to grain boundaries; whereas for an imposed simple shear, high values of von Mises stress occurred within the grain interiors. In addition, by discriminating between edge and interior points in a 3D reconstruction, artifacts resulting from boundary conditions were identified. This example serves to show how data mining/informatics methods are critical to analyzing EBSD-based data sets that involve large amounts of data.

Another application of data mining occurs when one has to screen large numbers of individual EBSD patterns. It is important to remind ourselves that one of the major reasons for the wide adoption of EBSD as a standard analytical tool in materials characterization has been its ability to gather data in a high throughput manner. Hence EBSD qualifies itself as a high throughput experimentation (HTE) technique. With this high speed data acquisition come new challenges that need to be addressed. For instance, as noted by Trimby et al. (2002), high throughput can come at the expense of high accuracy. They conducted systematic studies to explore the impact of speed of data acquisition on the accuracy of analysis. They showed that for routine texture, grain size, and high angle boundary misorientation, there was minimal penalty on the statistics. However, when needing to resolve very low angle boundaries, then the data collected at

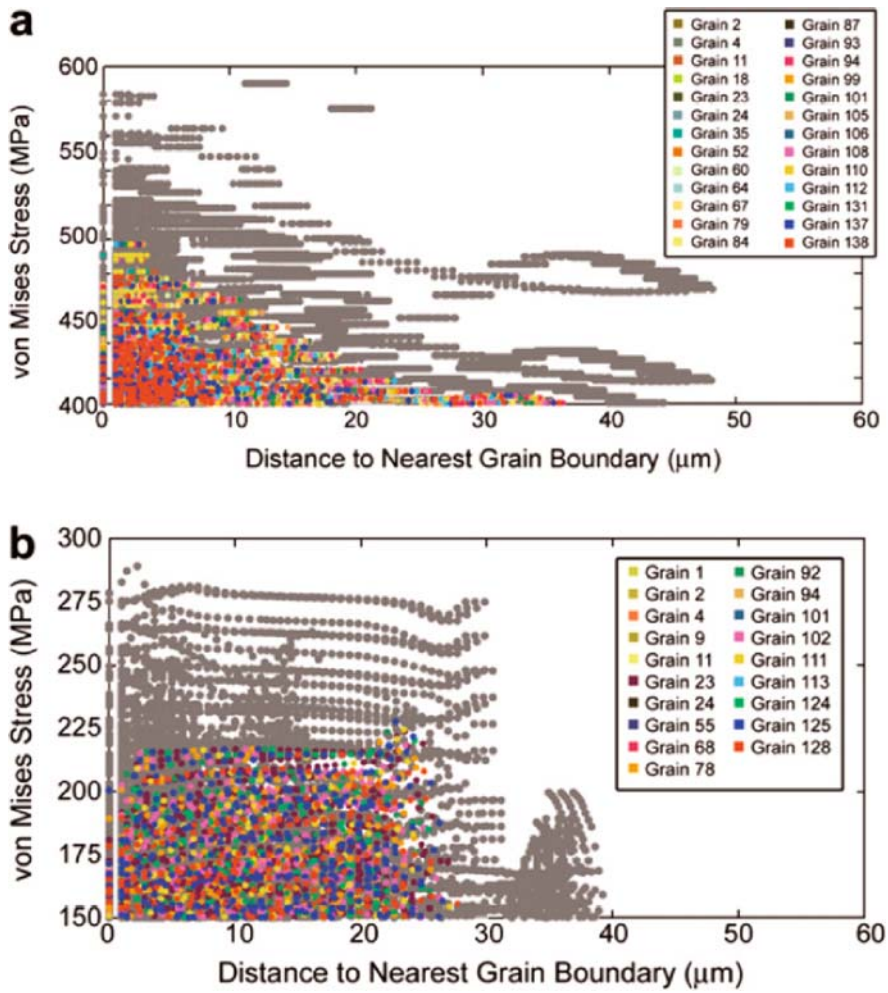


Fig. 14.10 Von Mises stress vs. distance from nearest grain boundary for all data in 3D simulation. Points on the edge of the reconstructed volume are shown in *grey;* "interior" points are shown in a different color for each grain. For simplicity, a 50% sampling of points is shown. (**a**) Uniaxial stretch, x-direction, (**b**) simple shear (e_{zy}) (Lewis et al. 2008)

slower rates significantly improved the accuracy (e.g., 2000 points/hour vs. 84,000 points/hour).

Brewer et al. (2008) have significantly explored this issue much further by quantifying the impact of uncertainty due to specific contributions of the EBSD pattern. As they have noted, a high rate of pattern collection, combined with complications due to EBSD patterns with missing information, incorrectly indexed information, and/or overlapping EBSD patterns (due to small grain size), makes it a challenge to identify the key components of the microstructure (e.g., phase identification, orientation) that can help extract accurate information. Techniques such as principal component analysis (Suh et al. 2006; Rajan 2005; Sieg et al. 2007; Brewer et al. 2008) reduced a large set (thousands) of individual EBSD patterns into a core set of statistically derived component EBSD patterns that could subsequently be indexed. They also showed that these patterns are higher in signal-to-noise ratio than any given single pattern, and can be used to distinguish phases with similar crystal structures. Mathematically, principal component analysis (PCA) relies on the fact that most of the descriptors are interrelated, and that these correlations in some instances are high. PCA is used to make new variables (principal component: PC) from linear combinations of existing variables (Fig. 14.11).

14.3 Summary

The integration of EBSD techniques into combinatorial experiments is still an evolving field. In this

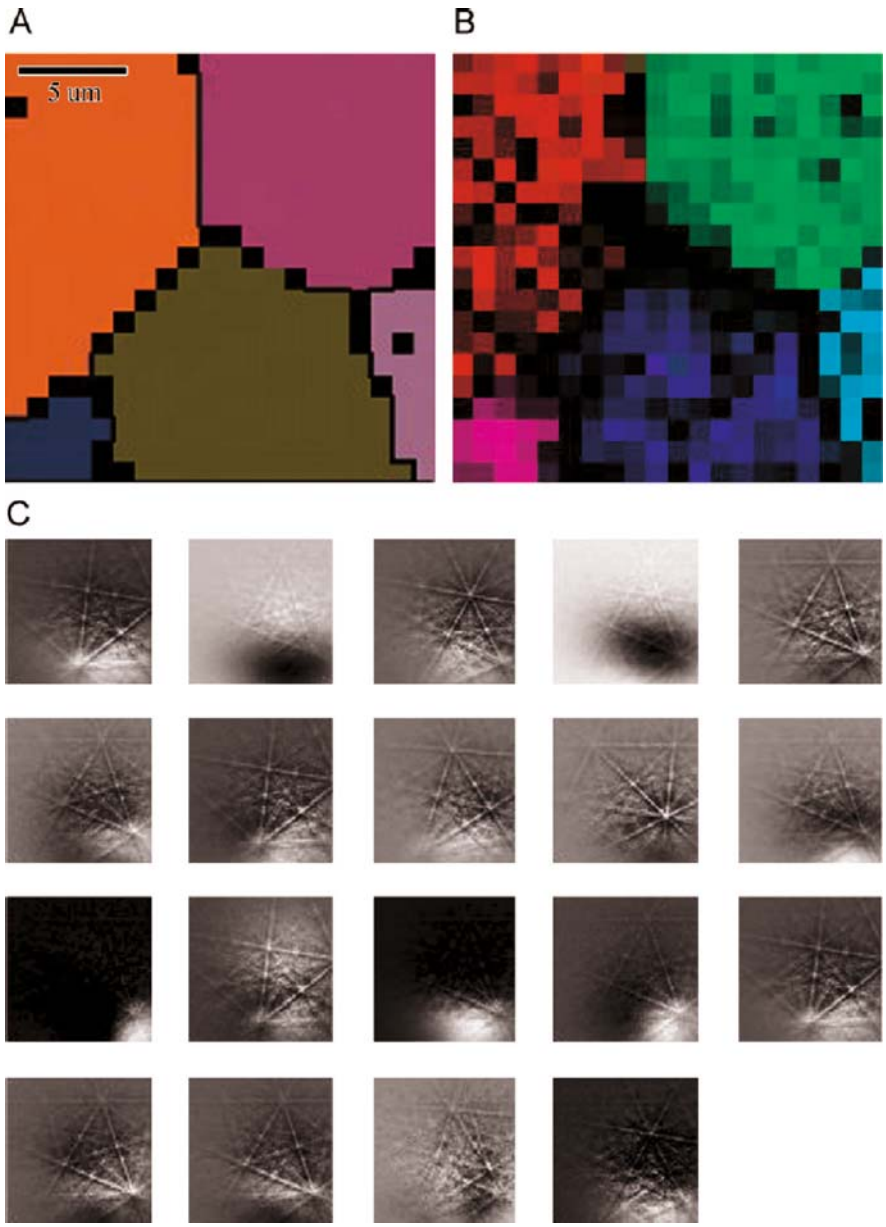


Fig. 14.11 Spectrum images from polycrystalline Al sample: (**A**) Euler orientation map; (**B**) EBSD component map using the five unique, actual EBSD pattern contributions to the signal; (**C**) all EBSD components generated by multivariate analysis (Brewer et al. 2008)

chapter, we have provided examples of how it is used for screening structure, orientation, and grain size. The definition of "combinatorial" has been broadened to include any method by which discrete or gradient changes in chemistry, orientation, or other microstructural metrics are created. The role of EBSD in all cases is to systematically track in two or three dimensions these various microstructural characteristics. By linking this information to other spatially resolved probes that can assess properties, EBSD becomes a critical technique in the establishment of structure-property combinatorial libraries. The broader impact of EBSD and combinatorial experimentation is its advancement as a tool for high throughput experimentation that generates large amounts of data at a very rapid rate. The challenges are then how to develop data analysis techniques that can assist in the analysis and interpretation of such data in a rapid manner. It is here that informatics-based methods using data mining, for instance, offer powerful solutions.

Acknowledgements The author acknowledges support from the National Science Foundation International Materials Institute Program for the Combinatorial Sciences and Materials Informatics Collaboratory (CoSMIC-IMI), grant # DMR-0833853; Office of Naval Research, grant # N00014–06–1-0310; and the Air Force Office of Scientific Research, grant # FA95500610501.

References

Adomaitis RA (2007) Intentionally patterned and spatially non-uniform film profiles in chemical vapor deposition processes. Surf Coat Tech 201:9025–9029

Bastos A, Zaefferer S, Raabe D (2008) Three-dimensional EBSD study on the relationship between triple junctions and columnar grains in electrodeposited Co-Ni films. J Microsc 230(Pt 3):487–498

Behrens M, Tomforde J, May E, Kiebach R, Bensch W, Häußler D, Jäger W (2006) A study of the reactivity of elemental Cr/Se/Te thin multilayers using X-ray reflectometry, in situ X-ray diffraction and X-ray absorption spectroscopy. J Solid State Chem 179:3330–3337

Bhat RR, Genzer J (2006) Combinatorial study of nanoparticle dispersion in surface-grafted macromolecular gradients. Appl Surf Sci 252:2549–2554

Brewer LN, Kotula PG, Michael JR (2008) Multivariate statistical approach to electron backscattered diffraction. Ultramicroscopy 108:567–578

Cawse JN (2003) Experimental design for combinatorial and high throughput development. Wiley Interscience, Hoboken, NJ

Cha W-Y, Takahiro M, Yasushi S, Mitsutaka H (2006) Identification of titanium oxide phases equilibrated with liquid Fe-Ti alloy based on EBSD analysis. ISIJ Int 46:(7): 987–995

Chambers BD, Taylor SR (2007) The high throughput assessment of aluminum alloy corrosion using fluorometric methods, Part II—a combinatorial study of corrosion inhibitors and synergistic combinations. Corros Sci 49:1597–1609

Chen W, Liu Q, Liu Q, Zhu L, Wang L (2008) A combinatorial study of the corrosion and mechanical properties of Zn-Al material library fabricated by ion beam sputtering. J Alloy Compd 459:261–266

Cooper JS, McGinn PJ (2006) Combinatorial screening of thin film electrocatalysts for a direct methanol fuel cell anode. J Power Sources 161:330–338

Davydov AV, Bendersky LA, Boettinger WJ, Josell D, Vaudin MD, Chang K-S, Takeuchi I (2004) Combinatorial investigation of structural quality of Au/Ni contacts on GaN. Appl Surf Sci 223(1–3):24–29

Fischer R, Eleno LTF, Frommeyer G, Schneider A (2006) Precipitation of Cr-rich phases in a Ni–50Al–2Cr (at %) alloy. Intermetallics 14(2):156–162

Garoli D, Monaco G, Frassetto F, Pelizzo MG, Nicolosi P, Armelao L, Mattarello V, Rigato V (2006) Thin film and multilayer coating development for the extreme ultraviolet spectral region. Radiat Phys Chem 75:1966–1971

Guerrero-Sanchez C, Paulus RM, Fijten MWM, de la Mar MJ, Hoogenboom R, Schubert US (2006) High-throughput experimentation in synthetic polymer chemistry: from RAFT and anionic polymerizations to process development. Appl Surf Sci 252:2555–2561

Guo K-T, Scharnweber D, Schwenzer B, Ziemer G, Wendel HP (2007) The effect of electrochemical functionalization of Ti-alloy surfaces by aptamer-based capture molecules on cell adhesion. Biomaterials 28:468–474

He T, Kreisler E, Xiong L, Ding E (2007) Combinatorial screening and nano-synthesis of platinum binary alloys for oxygen electroreduction. J Power Sources 165:87–91

Jayaraman S, Hillier AC (2005) Electrochemical synthesis and reactivity screening of a ternary composition gradient for combinatorial discovery of fuel cell catalysts. Meas Sci Tech 16:5–13

Journal of Measurement Science and Technology—special issue (2005) Combinatorial and high throughput, Materials Research 16(1):296–301

Kim DK, Maier WF (2006) Combinatorial discovery of new auto reduction catalysts for the CO_2 reforming of methane. J Catal 238:142–152

Laigo J, Christien F, Le Gall R, Tancret F, Furtado J (2008) SEM, EDS, EPMA-WDS and EBSD characterization of carbides in HP type heat resistant alloys. Mater Charact 59:1580–1586

Laurila T, Vuorinen V, Kivilahti JK (2004) Analyses of interfacial reactions at different levels of interconnection. Mat Sci Semicon Proc 7:307–317

Lewis AC, Suh C, Stukowski M, Geltmacher AB, Rajan K, Spanos G (2008) Tracking correlations between mechanical response and microstructure in three-dimensional reconstructions of a commercial stainless steel. Scripta Mater 58:575–578

Lin N, Drzal PL, Lin-Gibson S (2007) Two-dimensional gradient platforms for rapid assessment of dental polymers: a chemical, mechanical and biological evaluation. Dent Mater 23:1211–1220

Liu DR, Schultz PG (1999) Generating new molecular function: a lesson from nature. Angew Chem Int Edit 38:36–54

Lu Y (2006) A combinatorial approach for automotive friction materials: effects of ingredients on friction performance. Compos Sci Tech 66:591–598

Lu G, Cooper JS, McGinn PJ (2006) SECM characterization of Pt-Ru-WC and Pt-Ru-Co ternary thin film combinatorial libraries as anode electrocatalysts for PEMFC. J Power Sources 16:106–114

Ludwig A, Cao J, Savan A, Ehmann M (2007) High-throughput characterization of hydrogen storage materials using thin films on micromachined Si substrates. J Alloy Compd 446–447:516–521

Martin TP, Chan K, Gleason KK (2008) Combinatorial initiated chemical vapor deposition (iCVD) for polymer thin film discovery. Thin Solid Films 516:2130–2137

Mateescu N, Ferry M, Xu W, Cairney JM (2007) Some factors affecting EBSD pattern quality of Ga^+ ion-milled face centered cubic metal surfaces. Mater Chem Physics 106(1):142–148

Miller DC, Herrmann CF, Maier HJ, George SM, Stoldt CR, Gall K (2007) Thermo-mechanical evolution of multilayer thin films: part II. Microstructure evolution in Au/Cr/Si microcantilevers. Thin Solid Films 515:3224

Mingard KP, Roebuck B, Bennett EG, Thomas M, Wynne BP, Palmiere EJ (2007) Grain size measurement by EBSD in complex hot deformed metal alloy microstructures. J Microsc 227(Pt 3):298–308

Narasimhan B, Mallapragada SK, Porter MD (2007) Combinatorial materials science. Wiley Interscience, Hoboken, NJ

Perez MG, Kenik EA, O'Keefe MJ, Miller FS, Johnson B (2006) Identification of phases in zinc alloy powders using electron backscatter diffraction. Mater Sci Eng A 424(1–2):239–250

Potyralio R, Maier WF (2007) Combinatorial and high-throughput discovery and optimization of catalysts and materials. Taylor, New York

Rajan K (2005) Materials informatics. Mater Today 8:38–45

Rajan K (2008) Combinatorial materials science. Annu Rev Mater Res 38:299–322

Saalfrank JW, Maier WF (2004) Doping, selection and composition spreads, a combinatorial strategy for the discovery of new mixed oxide catalysts for low-temperature CO oxidation. C R Chim 7:483–494

Sambandam SN, Bhansali S, Bhethanabotla VR, Sood DK (2006) Studies on sputtering process of multicomponent Zr-Ti-Cu-Ni-Be alloy thin films. Vacuum 80:406–414

Schwartz AJ, Kumar M, Adams BL (2000) Electron backscatter diffraction in materials science. Kluwer Academic, New York

Seyler M, Stoewe K, Maier WM (2007) New hydrogen-producing photocatalysts—a combinatorial search. Appl Catal B-Environ 76:146–157

Sieg SC, Suh C, Schmidt T, Stukowski M, Rajan K, Maier WF (2007) Principal component analysis of catalytic functions in the composition space of heterogeneous catalysts. QSAR Comb Sci 26:528–535

Silva F, Lopes NIA, Santos DB (2006) Microstructural characterization of the C-Mn multiphase high strength cold rolled steel. Mater Charact 56(1):3–9

Suh C, Rajan K, Vogel BM, Eidelman N, Cabral JT, et al (2006) Informatics methods for combinatorial materials science. In: Mallapragada SK, Narasimhan B, Porter MD (eds) Combinatorial materials science. Wiley, Hoboken, NJ

Trimby P, Day A, Mehnert K, Schmidt N-H (2002) Is fast mapping good mapping? A review of the benefits of high-speed orientation mapping using electron backscatter diffraction. J Microsc 205:259–269

Xiang XD (1999) Combinatorial materials synthesis and screening: an integrated materials chip approach to discovery and optimization of functional materials. Annu Rev Mater Sci 29:149–171

Xiang X-D, Takeuchi I (2003) Combinatorial materials synthesis. Marcel Dekker, New York

Yoo YK, Xue Q, Chu YS, Xu S, Hangen U, Lee H-C, Stein W, Xiang, X-D (2006) Identification of amorphous phases in the Fe-Ni-Co ternary alloy system using continuous phase diagram material chips. Intermetallics 14:241–247

Zaldívar-Cadena AA, Flores-Valdés A (2007) Prediction and identification of calcium-rich phases in Al-Si alloys by electron backscatter diffraction, EBSD/SEM. Mater Charact 58(8–9):834–841

Zhao J-C (2004) Reliability of the diffusion-multiple approach for phase diagram mapping. J Mater Sci 39:3913–3925

Zhao J-C (2006) Combinatorial approaches as effective tools in the study of phase diagrams and composition-structure-property relationships. Prog Mater Sci 51:557–631

Zhao J-C, Jackson MR, Peluso LA (2003) Determination of the Nb-Cr-Si phase diagram using diffusion multiples. Acta Mater 51:6395–6405

Zhao J-C, Jackson MR, Peluso LA (2004a) Mapping of the Nb-Ti-Si phase diagram using diffusion multiples. Mater Sci Eng A 372(1–2):21–27

Zhao J-C, Jackson MR, Peluso LA (2004b) Evaluation of phase relations in the Nb-Cr-Al system at 1000 degrees C using a diffusion-multiple approach. J Phase Equilib Diff 25: 152–159

Chapter 15

Grain Boundary Networks

Bryan W. Reed and Christopher A. Schuh

15.1 Introduction

Statistical information about grain orientations within a polycrystal has been available to materials researchers for many decades. In particular, the orientation distribution, or crystallographic texture information, has been measured using X-ray diffraction techniques since about 1950. Consequently, the role of texture in materials performance and design is widely appreciated and commonly taught in the core Materials Science curriculum. However, texture data represent only "one-point" statistics, and do not capture microstructural geometry or topology.

The landmark achievement of EBSD was the ability not only to measure crystal orientations, but to map them spatially. This technology dramatically expanded the amount of statistical information available about microstructures. Notably, the one-point distribution of grain orientations can be expanded to include two-point, three-point, or higher-order correlations among grain orientations; we may construct not only distributions of orientations, but of pairs or triplets of them, for example. Indeed, so overwhelming is the possible space of statistical information available from a single EBSD dataset that the field has yet to develop common techniques and tools for managing and analyzing it. This will remain an active area of materials research for the foreseeable future.

B.W. Reed (✉)
Lawrence Livermore National Laboratory, Livermore, CA 94550, USA
e-mail: reed12@llnl.gov

EBSD provides two broad classes of combined orientation and spatial information. First, traditional geometrical aspects of the grain structure, such as grain size and shape distributions, can not only be measured from EBSD data, but augmented by local grain-specific knowledge of their orientation. This information may be used to predict or understand, e.g., volumetrically averaged bulk properties such as effective elastic constants. The use of EBSD data in these applications is discussed elsewhere in this volume (see Chapters 12 and 13).

Second, the coverage of a large section of microstructure with EBSD permits study of the topological aspects of the microstructural elements, and connectivity among elements related by their orientations or crystallography. For example, clusters of grains related by specific misorientations, or networks of grain boundaries of related symmetries can be identified and quantified using, e.g., neighbor distribution information, number of faces per grain, or distributions of branching features such as triple junctions and quadruple nodes. These elements of the microstructure tend to be especially relevant for properties involving path dependence, as for transport or damage propagation across a specimen. Such topological issues of microstructure, and their analysis with EBSD, are the focus of this chapter.

Concurrently with—and spurred by—the development of EBSD, materials scientists have increasingly focused attention on the importance of microstructural topology in governing materials properties. Examples in this regard include the development of polycrystalline high-T_c superconductors, in which a network of grains related by low-angle misorientations is required to pass supercurrent, or grain-boundary engineered metals that resist intergranular damage propagation

A.J. Schwartz et al. (eds.), *Electron Backscatter Diffraction in Materials Science*,
DOI 10.1007/978-0-387-88136-2_15, © Springer Science+Business Media, LLC 2009

by incorporating a high fraction of "special" damage resistant grain boundaries (Frary and Schuh 2003b; Gaudett and Scully 1994; Krupp et al. 2005; Randle 2004; Schuh et al. 2003a; Schwartz et al. 2006; Wells et al. 1989). This shift in focus has also led to the integration of statistical physics concepts into materials science, including notions borrowed from percolation theory and network science (Basinger et al. 2005; Bouchaud 1997; Fullwood et al. 2006; McGarrity et al. 2005; Meinke et al. 2003; Nichols et al. 1991a, 1991b; Romero et al. 1996; Schuh and Frary 2006; Schuh et al. 2003c; Van Siclen 2006; Wells et al. 1989). This represents a potentially revolutionary paradigm for materials design, as the "universal" concepts from statistical physics may unify our view of disparate materials and properties.

In the following sections, we briefly review some of the local microstructural elements that are amenable to analysis and quantification by EBSD, and progress to the study of their connectivity and topological characteristics. We then address the issue of connecting these microstructural measures with properties, and conclude with some comments on the frontier areas of research in this field.

15.2 Measurement and Classification of Local Network Elements

15.2.1 General Definitions for Single Boundaries

In specifying the mathematical elements of a grain boundary network, we will start with some definitions. A *grain* is a contiguous three-dimensional region consisting of a single phase with a crystalline orientation constant to within some tolerance (typically $\sim$1–2° for a well-annealed polycrystal), while a *grain boundary* is a contiguous two-dimensional region where two grains meet. This definition of grains does not distinguish between grains and subgrains; what would often be called a twin subgrain of a larger grain is considered here to be a separate grain.

Two-dimensional cross sections of grains, and the corresponding one-dimensional cross sections of grain boundaries with triple junctions at their end points, are easy to identify in high-quality EBSD data sets. The tolerance is typically set to be compatible with the point-to-point experimental uncertainty in the orientation, which varies with the signal-to-noise ratio in the measurement. Transitivity is usually enforced, i.e., if pixels A and B belong to the same grain, and B and C belong to the same grain, then so do A and C, even if the misorientation between A and C exceeds the tolerance. This avoids the situation represented in Fig. 15.1. As a result, boundary identification algorithms never find isolated boundaries nor boundaries that abruptly end in the middle of grains; all boundaries end either at triple junctions or at the edge of the measured region. Various algorithms exist for identifying and dropping out single-pixel noise, and it is highly recommended that these be applied prior to any grain boundary network analysis, lest single-pixel grains dominate the statistics. A simple method is to identify pixels that (1) have poor signal quality and (2) are surrounded by pixels of significantly different orientation, and then to overwrite each such pixel with the orientation from its best-quality neighbor.

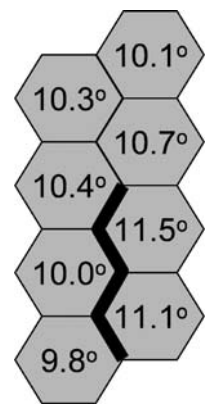


Fig. 15.1 An example of what it means to enforce transitivity in grain identification. Each pixel in an EBSD scan is labeled with an angular orientation (simplified to a single angle for purposes of the figure; real grain orientations are three dimensional), with a random error $\sim$0.5°. A local grain-boundary-finding algorithm with a 1° threshold would identify the bold edges as grain boundaries. A global algorithm would take the output of the local algorithm and enforce minimal transitivity. Under the global algorithm, the bold edges would not be considered grain boundaries, and it is impossible for a boundary to end in the middle of a grain. The pictured situation can arise from both statistical measurement fluctuations and localized plastic deformation. Analysis of grain boundary network topology usually uses some version of the global algorithm and is typically performed on well-annealed polycrystals that rarely exhibit this problem in any case

The categorization of grain boundaries is described elsewhere in this volume and will be briefly summarized here. Suppose each grain A, B, C, ... has its orientation represented as a rotation *A, B, C,* ... (which may be a matrix, a quaternion, a Rodriguez vector, or a set of Euler angles; see Chapter 3). Then the *misorientation* is a rotation specified in the reference frame of one of the grains by, for example, $M_{AB} = A^{-1}B$ (this convention, and the alternate convention $M_{AB} = BA^{-1}$, are both widely used; either is acceptable so long as consistency is maintained).

For a given grain boundary, the misorientation is usually almost constant as a function of space and time and is typically considered a property of the *entire* grain boundary rather than of one localized piece of it at a given time. This is important, as this property is not shared by the grain boundary plane normal $\hat{n}_{AB}(\vec{r}, t)$, which can vary extremely rapidly for a highly faceted, fast evolving boundary. Thus, while it is recognized that both M_{AB} and $\hat{n}_{AB}$ are important for the atomic structure, energy density, and mobility of a boundary, for purposes of studying the network topology the attention of the field has traditionally focused almost exclusively on M_{AB}. There is also a practical concern, as the M_{AB} are much easier to determine from EBSD scans than are the $\hat{n}_{AB}$ (see Chapter 16 by Rohrer and Randle).

The misorientation between two adjacent EBSD pixels will fall into one of the following categories:

1. Subthreshold: smaller than the $\sim 1^\circ$ threshold described above. In this case the two pixels are part of the same grain.
2. Low-angle boundary (LAB): greater than the threshold but smaller than some moderately small angle, typically set at $\sim 15^\circ$, above which the dislocation cores making up the boundary are considered to overlap (Read and Shockley 1950).
3. Coincident-site-lattice (CSL) boundary, with M_{AB} within some acceptable error (such as the Brandon criterion [Brandon 1966] $\theta_{\max} = 15^\circ / \Sigma^{1/2}$) of a low-$\Sigma$ CSL misorientation.
4. Otherwise unique or symmetric non-CSL high-angle boundary, which can occur in some materials (Lejcek and Paidar 2005; Randle 2006; Zhao et al. 1988).
5. General high-angle boundary (GHAB), i.e., anything not covered by the above categories.

For any given material, some misorientations correlate to significantly enhanced properties with respect to impurity segregation and embrittlement, cracking, coarsening, diffusion, or other properties associated with grain-boundary-mediated failure and material property degradation. These misorientations, and the boundaries that have them, are termed *special,* while other boundaries are *general.* "Special" does not necessarily mean that a boundary *does* have enhanced properties, but rather that portions of it *could* have enhanced properties, should their boundary planes fall into the right orientations.

15.2.2 Structures with More than One Boundary

A key insight of grain boundary network analysis is that often the properties of a single boundary are relevant to material performance only in the context of a network. There are two complementary ways in which the network is important. First, there are many situations in which we are concerned with, e.g., transport or damage propagation along contiguous paths of grain boundaries. These are called "direct lattice" properties. Second, many problems involve the complementary issue of transport *across* grain boundaries. Examples include electrical conductivity or superconductivity, where general boundaries are more disruptive to current flow than are special ones. These are called "dual lattice" properties, as they involve connectivity not among the grain boundaries directly, but among grain centers. A cartoon illustrating the direct and dual lattices for a hexagonal grain boundary network is shown in Fig. 15.2.

In a later section, we will clarify the connection between the structure of the boundary network, the dual network, and various properties that rely upon them. Central to understanding the structure-property connection are the rules by which grains and grain boundaries can connect together in the network. The basic elements of boundary connectivity are the *triple junctions,* the one-dimensional edges of grain boundaries where three grains and three boundaries meet; and the *quadruple nodes,* the zero-dimensional points where four grains, six boundaries, and four triple junctions meet.

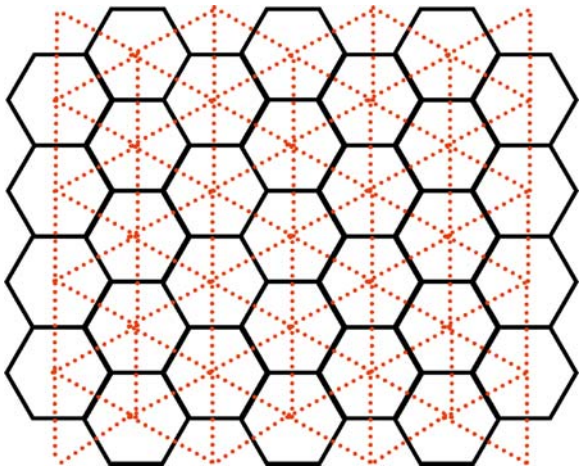


Fig. 15.2 Illustration of a hexagonal lattice (*solid black lines*) that represents a network of grain boundaries in a 2D section of a polycrystal, and the corresponding "dual lattice" (*dashed red lines*) that defines the topology of transgranular paths

Triple junctions and quadruple nodes cannot be constructed arbitrarily; they are subject to constraints (see Fig. 15.3). For example, consider the Σ combination rule (Gertsman 2001b; Miyazawa et al. 1996). If three CSL boundaries (Σ*a,* Σ*b,* and Σ*c*) in a cubic material meet at a junction, their Σ numbers must satisfy the relation $ab = m^2c$, where m is a common factor of a and b. Thus Σ3-Σ3-Σ9 and Σ9-Σ9-Σ9 triple junctions are allowed, while Σ3-Σ3-Σ3 and Σ3-Σ5-Σ7 triple junctions are crystallographically impossible. The rules are relaxed somewhat when deviations from the ideal cases are considered (Frary and Schuh 2003a), but the ideal CSL boundaries are rigidly constrained.

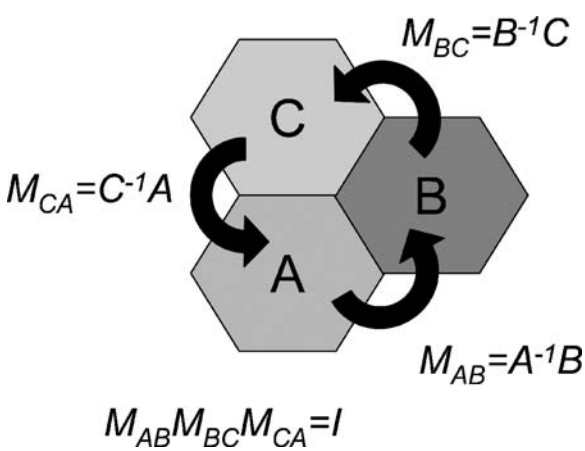


Fig. 15.3 Three grains (A, B, and C) at a triple junction with orientations A, B, and C, have a necessary connection among their misorientations M_{AB}, M_{BC}, and M_{CA}, even if the orientations themselves are completely uncorrelated. The triple junction is a triangle in the dual network of Fig. 15.2

Note the immediate practical implication: The strongest boundaries in many cubic materials are the Σ3 twin boundaries, but since it is impossible for three such boundaries to come together in a triple junction, it is impossible to make a nontrivial grain boundary network entirely out of the strongest boundaries; weaker boundaries *must* be included in the mix.

Beyond the triple junction constraint in Fig. 15.3, there are potentially an infinite number of higher-order constraints analogous to the Σ combination rule. While some of these constraints will be redundant, the examples in Fig. 15.4 show a trend: as we make the network more complex, the locally-derived constraints from one level of complexity never exactly capture all of the constraints for the next higher level. In the first row of Fig. 15.4, we see a triple junction that satisfies the Σ combination rule, yet is mathematically impossible because we have overspecified the crystallographic boundary types. In the second row, we see a quadruple node in which every triple junction is valid, yet the quadruple node is illegal (Gertsman 2001a). The third row shows a cluster of five grains in which every quadruple node is legal, yet the greater structure is disallowed (Reed et al. 2004). In short, we may identify a hierarchy of local constraints on the way that different boundary types may be combined into a network. In the next section we shall see how some of these constraints imply a degree of short- and long-range correlation in the boundary networks of real materials.

15.3 Geometry of the Network Structure

The assignment of grain boundaries as either "special" or "general" arose historically as a means of simplifying the overwhelmingly complex grain boundary network into a simple statistical description, in which the fraction of special grain boundaries becomes the essential state variable. This binary description leads naturally to the use of tools from statistical physics, most notably percolation theory, which is extremely well developed for binary systems (Grimmett 1989; Stauffer and Aharony 1994). Consequently, much of

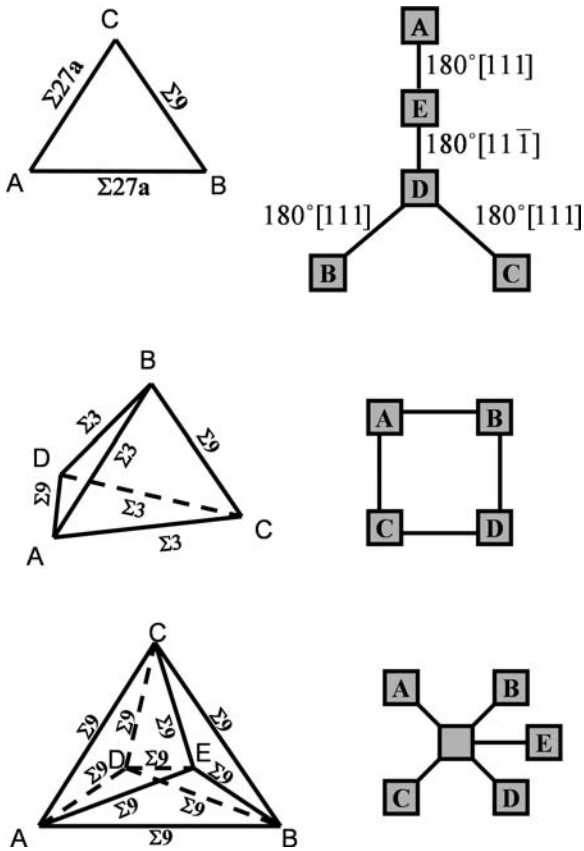


Fig. 15.4 Examples of impossible constructions in a cubic polycrystal. *Left column:* Dual network. *Right column:* $\Sigma 3^n$ connectivity diagram (each node is a potential grain orientation and each link is a single $\Sigma 3$ operation [Reed et al. 2004]). *First row:* The Σ combination rule is satisfied, but the construction is still impossible because there is no allowable assignment of specific $\Sigma 3$ operators to each link. The pictured assignment (which is forced, modulo an arbitrary choice of convention, by the $\Sigma 27a$ boundaries) fails because node D links to two different nodes (B and C) through the same $\Sigma 3$ operator. *Second row:* Even though every triple junction in the $4\Sigma 3 - 2\Sigma 9$ quadruple node satisfies the Σ combination rule, the global construction is impossible because it implies that the $\Sigma 3^n$ diagram must have a loop, which is illegal for this group. *Third row:* A cluster of five mutually-adjacent grains with all $\Sigma 9$ boundaries. Even though all of the quadruple nodes are perfectly legal, the global construction is impossible because it forces one node to have five neighbors when there are only four distinct fundamental $\Sigma 3$ operations. Adapted from Reed et al. (2004)

our understanding of grain boundary network structure is built upon the concepts of percolation theory. In this section we briefly review the standard geometrical percolation problem as it applies to grain boundary networks, focusing upon what this approach teaches us about the clustering of grain boundaries. We then review the effects of crystallographic constraints as described previously, and how these affect the structure of grain boundary clusters and the percolation transition.

15.3.1 Percolation Measures of the Grain Boundary Network

As noted above, the basic state variable used in grain boundary percolation problems is the fraction of special boundaries in the network. Conventionally a number fraction, *p,* is used to appreciate the statistics of grain boundary connectivity (although EBSD software more routinely outputs a length fraction). The basic components of percolation theory include the percolation threshold and a set of scaling relationships. These can be understood most easily by considering what happens in a microstructure if we begin from a network comprising only general boundaries ($p = 0$), and progressively substitute in special boundaries (progressively increase p). For now, let us imagine that the special boundaries are placed randomly into the network.

For low values of *p,* the special boundaries will tend to be isolated from one another, and only rarely connect together. As p rises, gradually the special boundaries become connected into small contiguous groups, or clusters. These clusters grow in size and in topological complexity as p increases. Put another way, the average cluster radius of gyration increases, or the mean connectivity length of the special boundaries rises with *p.* In fact, in percolation problems it is established that the connectivity length, ξ, increases as a power-law:

$$\xi \propto (p_c - p)^{-\nu}. \tag{15.1}$$

This power law diverges to infinity at a critical value of *p,* called the percolation threshold, p_c. This critical point thus separates those microstructures which have an infinitely connected path of special boundaries (at high p) from those that do not (at low p). There is also a complementary power law and percolation threshold for the general boundaries, the fraction of which is $q = 1–p$, with q_c the percolation threshold for general boundary connectivity.

Equation (15.1) is just one of many similar power-law scaling relationships that describe the statistics of grain boundary clusters and their properties. Related equations describe the distribution of cluster sizes, the strength or size of the largest percolating cluster, the fractal nature of clusters, and other statistical properties of the boundary network. Interestingly, the power-law equations that capture all of these details are considered "universal" for all geometrical percolation problems, and numerical values for the power-law exponents are known and tabulated. The power-law exponents do not change with details of the grain structure, including grain size or shape, but only with the dimensionality of the microstructure.

Grain boundary cluster statistics have been quite thoroughly studied in two dimensions. For example, Frary and Schuh (2005b) used computer simulations of various microstructures to explore percolation and scaling of special and general grain boundaries. Complementary experimental studies (Schuh et al. 2003a, 2003b) have provided software tools that analyze boundary clusters directly from EBSD datasets. Percolation, clustering, and scaling laws have also been addressed in three-dimensional simulated structures in Frary and Schuh (2005a, 2005b), and three-dimensional experimental data are also beginning to emerge (King et al. 2008).

The scaling laws and percolation threshold offer a simple statistical means of assessing how connected the special and general boundaries are in a given microstructure or family of microstructures. This has important implications for the structure-property relationship of polycrystals, as we will discuss in a later section.

15.3.2 Crystallographic Constraints

In the above discussion of percolation and scaling, it was convenient to envision grain boundary types being randomly distributed in the network. In reality, they are not randomly distributed, and in fact can never be randomly distributed by virtue of the correlations described earlier; misorientation conservation rules govern the assembly of boundary clusters. Some of the early EBSD studies of grain boundary connectivity drew attention to this specific issue, by looking at, e.g., the coordination of special grain boundaries at triple junctions.

Figure 15.5 illustrates the so-called *triple junction distribution* for a variety of FCC metals, as measured using EBSD in Schuh et al. (2005). This plot indicates what fraction of the triple junctions, J_i, are coordinated by i special boundaries, given a special boundary fraction p. Shown for comparison are expectation curves for a boundary network assembled at random; the deviation of the experimental data from these curves illustrates the effects of crystallographic constraints on the local clustering of boundaries at their nearest-neighbor connection points.

The basic trend in Fig. 15.5 is seen repeatedly in polycrystals, even when the definition of boundary specialness is changed. For example, in networks differentiated only on the basis of low vs. high disorientation angles, a similar triple junction distribution is found (Frary and Schuh 2004). In general, it seems that crystallography tends to suppress pairs of special boundaries (J_2), in favor of triplets (J_3) or "dangling ends" (J_1). There is an intuitive reason for this: special misorientations tend to be related to one another, so that the product of two special misorientations has an enhanced probability of being special itself. Conversely, general boundaries tend to collect in pairs at triple junctions. This amounts to a bias in the types of grain boundary clusters that form in polycrystals, which is readily seen upon inspection of the network. For example, Fig. 15.6 compares two simulated grain boundary networks from Frary and Schuh (2004); the network on the left was assembled at random, without heed of crystallographic constraints, while that on the right is a realistic microstructure where the boundary types were based on misorientation calculations of the crystal orientations. In each figure, only general boundaries are shown; the assembly of these into clusters is clearly affected by the crystallographic constraints, which favor the formation of longer, stringier clusters.

Similar analyses of grain boundary clusters have led to a more sophisticated understanding of the microstructures produced by multiple twinning. Many materials exhibit simple twinning patterns, in which individual "parent" grains are segmented into parallel bands alternating between two twin-related orientations (Fig. 15.7 [a]); that is, the parent grain contains twin subgrains separated by $\Sigma 3$ twin boundaries. This kind of simple back-and-forth twinning

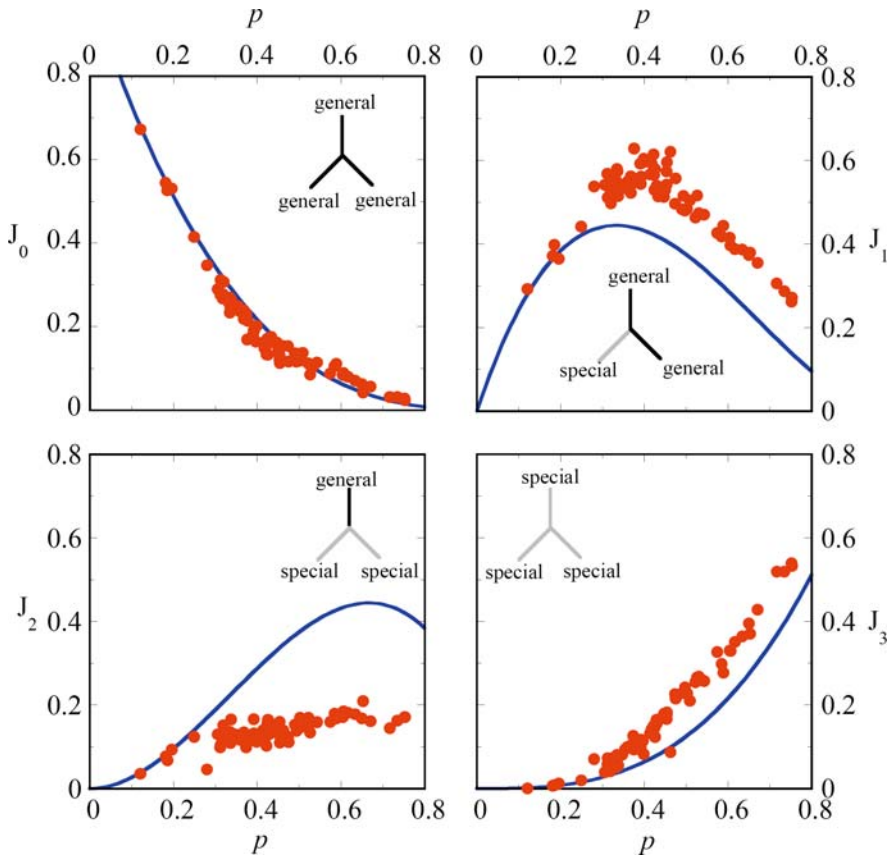


Fig. 15.5 Experimental data acquired by EBSD on 70 different FCC metals, including aluminum, copper, nickel, and iron alloys, showing the distribution of triple junction types in the microstructure. The value of J_i indicates the fraction of triple junctions with i special boundaries, given a special boundary fraction p. The *blue solid curves* show the expected trends for a network assembled at random; the deviation of the experimental data from these trendlines is an effect stemming from crystallographic constraints, which generally dictate that when two special boundaries meet at a junction, they are very likely to be mated with a third special boundary. After Schuh et al. (2005)

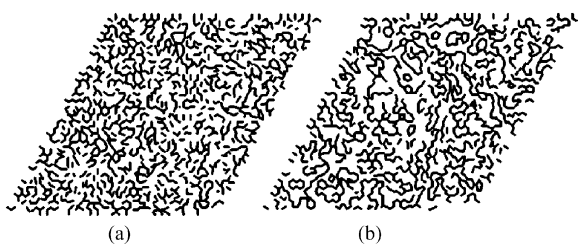


Fig. 15.6 Simulated grain boundary networks reproduced from Frary and Schuh (2005b). Both networks have 50% special boundaries ($p = 0.5$), but only the general boundaries are shown here. The network shown in (**a**) is random, meaning that no crystallographic constraints are enforced, while that shown in (**b**) enforces complete crystallographic constraints. The resulting cluster topologies are quite different, with general boundaries favoring longer and stringier clusters when crystallographic effects are included

is common in many deformation scenarios, with a strong bias towards twinning in certain orientations. While the parent grain/subgrain description is convenient for such microstructures, it becomes more awkward for the complex twin-related grain clusters that can occur in some grain boundary engineered materials (Fig. 15.7[b]), where twinning occurs on many different boundary planes, and boundaries of type $\Sigma 81$ or higher can arise from the indirect interaction of $\Sigma 3$ misorientations. These clusters have been referred to as twin-related domains (TRDs; Reed and Kumar 2006), and they can be identified as clusters of $\Sigma 3^n$ boundaries in the dual network (Gertsman and Henager 2003; Kopezky et al. 1991). Any two grains in the TRD will have a $\Sigma 3^n$ misorientation. Usually this misorientation very closely approximates the theoretical ideal, because the TRDs typically grow from a sequence of annealing twinning events, each of which usually creates a nearly perfect $\Sigma 3$ misorientation. Conversely, the boundaries *between* TRDs are usually general, which accounts for the extended, "stringy" appearance of large general boundary clusters in these materials. The literature suggests that TRDs define a characteristic length scale in the cluster size distributions (Reed et al. 2008) and that percolation behaviors approach universality above this scale.

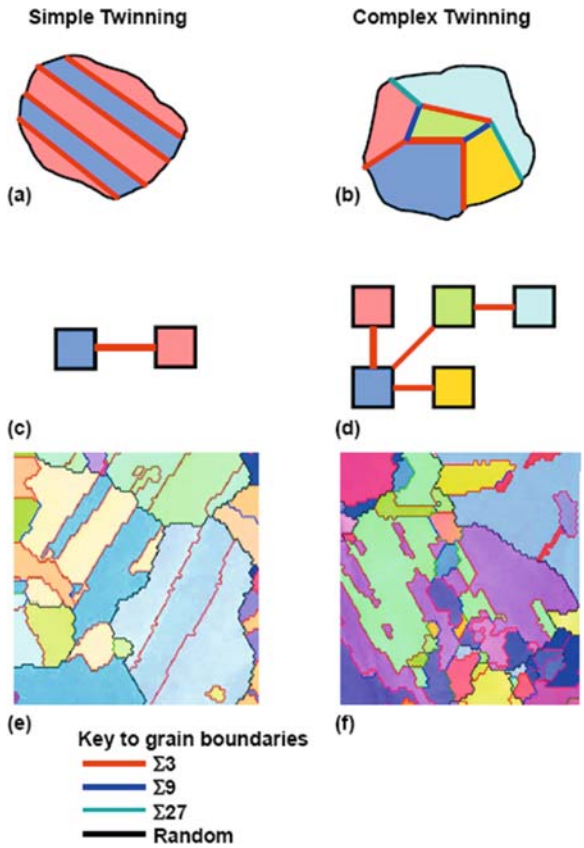


Fig. 15.7 Examples of twinned microstructures. (**a**) Schematic of a typical grain-subgrain geometry dominated by back-and-forth twinning on parallel {111} planes. The associated twin subgrain boundaries generally play a negligible role in the larger network connectivity. (**b**) Schematic of a complex twin-related domain with each grain twinning more or less isotropically on different {111} planes. This results in a complex intra-TRD network that can play a decisive role in breaking up the larger scale random boundary clusters. (**c**, **d**) $\Sigma 3^n$ connectivity diagram (see Fig. 15.4) for the microstructures in (**a**, **b**). The complexity of the *right hand column* is of an entirely different order. (**e**, **f**) Example EBSD inverse pole figure maps of each type of microstructure

Methods have been developed for identifying TRDs and for characterizing their internal crystallographic relationships with a simple graphical representation (Fig. 15.7[c, d]; Reed and Kumar 2006; Reed et al. 2004). In this representation, each grain orientation is a node (color coded to match the grains in Fig. 15.7[a, b]), each link is a $\Sigma 3$ misorientation, and two nodes separated by n links have a misorientation of $\Sigma 3^n$. The rules for drawing the graphs ensure that all crystallographic constraints are satisfied within the TRD.

Crystallographic constraints require some modification to the percolation-theory description of the boundary network. In general, because crystallographic constraints promote longer and stringier clusters of general boundaries, they tend to favor percolation of general boundaries at lower general boundary fractions, q. Conversely, crystallographic constraints generally lead to clumping of special boundaries in relatively compact cluster structures, which means that larger special fractions, p, are required to achieve percolation.

The percolation thresholds of grain boundary networks have been well studied both in two and three dimensions, and for different crystallographic textures, and with various definitions of boundary specialness. A recent compilation of the resulting percolation thresholds is provided by Frary and Schuh (2005a), from which Table 15.1 is taken. In general, all of these studies reveal that grain boundary networks, as compared with randomly assembled networks, require a greater fraction of special boundaries to effect percolation transitions. For practitioners of "grain boundary engineering," this has important implications as to what special fraction, p, constitutes success in the exercise of microstructure design. This issue will be made clearer in the following section, where we discuss how the grain boundary network structure impacts the properties of polycrystals.

15.4 Microstructure-Property Connections

The connection between the grain boundary network structure and the properties of a polycrystal can generally be regarded as a composite problem, where we wish to develop a proper "average" of the properties of the grain boundaries in the network. In a simple binary classification scheme using special vs. general grain boundaries, these "average" or "effective" properties are a function of the fractions of these two species, as well as their topological arrangements. Much of the development on this topic is mathematically focused and therefore beyond our immediate scope. Instead, our purpose is to briefly highlight some of the major defining features of microstructures and their properties, and the methods used to quantitatively connect them.

Table 15.1 A compilation of percolation thresholds after Frary and Schuh (2005a) for grain boundary networks in both 2D and 3D, and with different textures and rules for boundary specialness. The thresholds for both special and general boundaries are listed

	2D networks		3D networks	
	$q_{c,general}$	$p_{c,special}$	$p_{c,special}$	$q_{c,general}$
Randomly assembled	0.653	0.653	0.775	0.775
Fiber textured	0.601	0.689	0.711	0.842
General textured	0.676	0.663	0.818	0.835
Multiply twinned	0.659	0.666	0.789	0.801

15.4.1 Composite Averaging vs. Percolation Theory

In the introduction, it was hinted that some properties are strongly dependent upon the topology of the grain boundary network (or the dual network), while others are more amenable to simple composite averaging schemes. The main consideration that separates these classes of properties is the *property contrast,* or the degree to which special and general grain boundaries differ in a given property. For example, there are some material/property combinations for which low-Σ boundaries differ by many orders of magnitude from their high-Σ counterparts, e.g., diffusion, diffusional sliding, or intergranular cracking rates in FCC metals (Lim and Raj 1984; Watanabe 1983). Such properties are said to have "high contrast." Conversely, for other properties such as fatigue cracking the Σ number appears to have only a subtle effect, i.e., the system is "low contrast" (Gao et al. 2007).

In general, when properties exhibit low contrast, they are less dependent upon microstructural topology; when the properties of any two boundaries are similar, the details of how they connect have a relatively small influence on the average properties of the network. In the limit where special and general boundaries have the same properties, their relative spatial arrangements are arbitrary as far as the average system properties are concerned. Low contrast systems are thus relatively simple to model from a structure-property connection perspective, and usually quite simple effective medium approaches give remarkably reasonable results.

An example of a low contrast situation on a simple two-dimensional grain boundary network is shown in Fig. 15.8 (a), which represents a concentration gradient for simulated diffusion across a network of grain boundaries (Chen and Schuh 2006). Here the system has about 30% special grain boundaries ($p = 0.3$), through which impurities diffuse ten times more slowly than they do through the general boundaries. The diffusivity contrast ratio of 10 is considered low, and the resulting diffusion profile is quite planar; as a result, one can easily define an average concentration gradient, and by extension an average diffusivity for the entire network. Figure 15.8(c) shows the net, or effective, diffusivity of such a network, as the fraction of special boundaries is varied over the full range. Because the contrast is low, a straightforward effective medium-type average yields an excellent fit to the data (shown by the solid line).

Because grain boundaries have such a broad range of possible structures, it is more common that they exhibit high contrast in properties. The same example from above, using a more realistic diffusivity contrast of 10^8, reveals new complexities in the structure-property connection. Figure 15.8(b) shows the concentration profile for such a network, again given 30% slow-diffusing special boundaries ($p = 0.3$). Due to the high contrast, the concentration gradient cannot be simply described with an average plane, because the local undulations and variations across the network are of the scale of the entire gradient. This interesting effect speaks to the importance of topology: for high contrast systems, details of connectivity dominate the effective properties of the grain boundary network. In this case, effective medium models are insufficient to describe the average properties because they do not properly capture the percolation threshold of the system. The corresponding effective diffusivity of the network from Fig. 15.8(b) is shown in Fig. 15.8(d), showing a rapid change in diffusivity at the percolation threshold at $\sim$65% general boundaries. For such high contrast systems, percolation theory can be used to reasonably capture the structure-property connection. Much like the geometrical properties of the grain

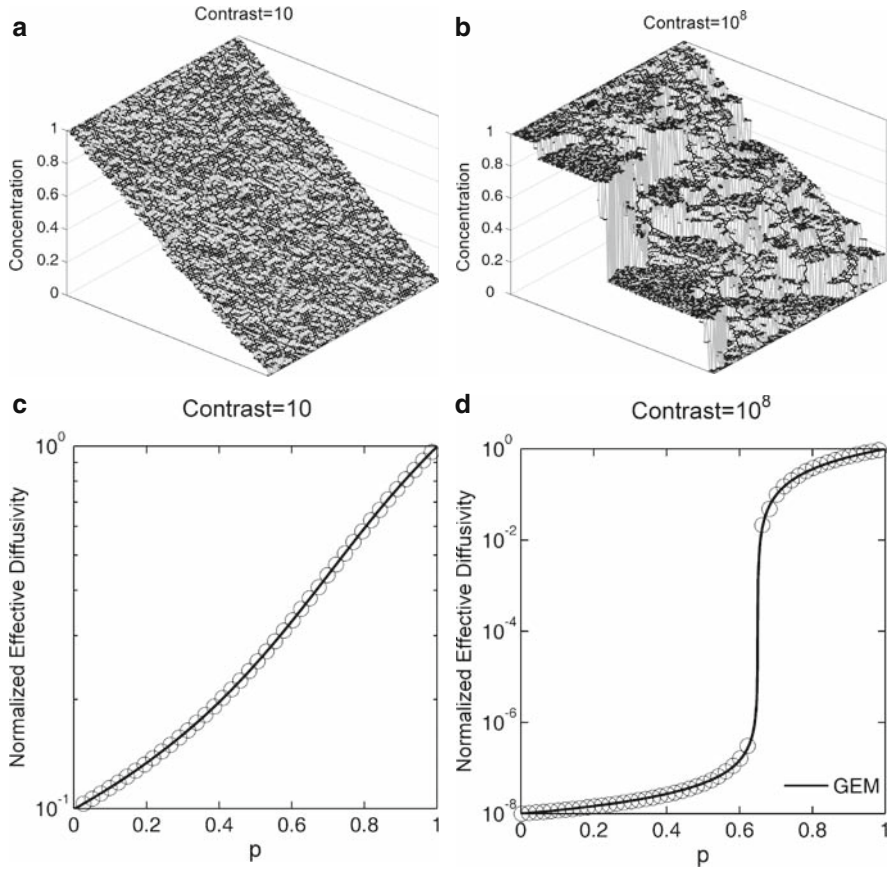


Fig. 15.8 Illustration of the role of property contrast in the structure-property relationships of polycrystals. These simulation data are from Chen and Schuh (2006), and consider intergranular diffusion on a simple 2D boundary network. In (**a**) and (**c**), the situation of low property contrast is considered, where the special boundaries are only 10 times more slowly diffusing than the general ones. As a result, the concentration gradient is on average quite linear (**a**), and the effective diffusivity of the network varies smoothly with the special boundary fraction, p (**c**). In (**c**) the predictions of standard effective medium theory are shown as a *solid line,* and match the simulations quite well. In (**b**) and (**d**), the high contrast case is shown, for which the situation is less well behaved and the effect of a percolation threshold is seen. In (**d**) the line shown is the prediction of a generalized effective medium theory that incorporates a percolation threshold. After Chen and Schuh (2006)

boundary clusters described earlier, the physical properties also generally scale as power laws in $(p\text{-}p_c)$, and equations taking the form of Eq. (15.1) generally describe the effective properties of networks with excellent accuracy.

The introduction of percolation concepts into grain boundary network analysis provides a necessary conceptual underpinning for the practice of grain boundary engineering. As noted earlier, for many properties including intergranular cracking and corrosion, superconductivity, and creep, "grain boundary engineered" materials often exhibit improved properties by large margins (e.g., up to orders of magnitude) as compared with nonengineered counterparts of the same composition (Krupp et al. 2003, 2005; Lehockey et al. 1998a, 1998b; Michiuchi et al. 2006; Shimada et al. 2002; Spigarelli et al. 2003). As suggested by Fig. 15.8(d), grain boundary engineering can be so remarkably effective because of the presence of a percolation threshold; a small change in microstructure (an increase in the fraction of special boundaries) can yield a large property change only in the vicinity of the threshold, for a high contrast system. In short, grain boundary engineering permits one to shut down long-range damage pathways, or open long-range conduction pathways, through microstructures.

A beautiful mathematical feature of percolation theory is that the direct and dual lattices are intimately related, and understanding percolation on one of these is tantamount to understanding it on both. In two-dimensional situations in particular, the percolation thresholds are simply complementary, i.e., $p_c^{direct} + p_c^{dual} = 1$. Thus, there is great generality in grain boundary network studies; those that study an intergranular process are relevant to transgranular properties, and vice versa.

The question remains as to how to identify the high and low contrast regimes, and how to handle systems intermediate to these two limiting cases. Figure 15.9 shows the general effect of contrast on the structure-property relationship, as studied for the case of diffusion in two-dimensional networks in Chen and Schuh (2006). Here the goodness-of-fit (R^2) of analytical models based on effective medium theory and percolation theory to numerical simulation data are presented. The main point of this graph is the complementary nature of these two modeling approaches: for low contrast systems, topology is apparently unimportant and the effective medium theory is exact; while at high contrast, topology dominates the problem and the scaling laws of percolation theory become essentially exact. Outside of these regimes, either theory quickly loses accuracy. Figure 15.9 can be used as a general guideline for the choice of a model to connect structure and properties in GB networks.

For the intermediate range, there are some proposed models that combine percolation theory with more traditional composite averaging schemes to provide a structure-property prediction that spans all possible property contrast ratios. One example that has proven valuable for simulated grain boundary networks is the so-called generalized effective medium (GEM) theory of Mclachlan (1987). This model empirically adapts the effective medium theory to incorporate the percolation threshold and critical scaling exponents of percolation theory. As shown in Fig. 15.9, such a model can be quantitatively descriptive for virtually any grain boundary network. Further, this type of model can be extended beyond the simple binary "special" vs. "general" approach to include a broader spectrum of grain boundary types. In Chen and Schuh (2006), the GEM model was extended to an arbitrary number of different grain boundary types, and validated against simulations on ternary grain boundary networks.

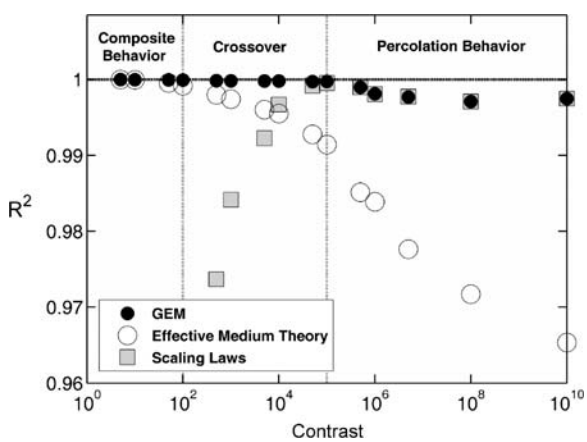


Fig. 15.9 The general effect of property contrast on the structure-property relationships of grain boundary networks, showing the coefficient of determination, R^2, which describes the degree of accuracy with which a given model represents the true effective properties of a network. At low contrast, simple effective medium theories (composite averages) are remarkably accurate; while at high contrast, percolation theory scaling equations are more useful. Generalized effect medium theories (GEM) combine features of both models and capture both types of behavior, at all contrast levels. After Chen and Schuh (2006)

15.4.2 Crystallographic Correlations

The crystallographic correlations described at length above tend to shift the percolation threshold by promoting connectivity among special grain boundaries. Fortunately, however, these correlations are short-range, and they do not alter the critical scaling laws associated with percolation (Frary and Schuh 2005b). This is good news for modeling the structure-property connection, because although the specific numerical value of the percolation threshold shifts due to crystallographic effects, the shapes of the effective property curves are unchanged. An example of this is illustrated in Fig. 15.10 for the case of grain boundary diffusional creep, from Chen and Schuh (2007). Here the effective creep viscosity is plotted for both a randomly assembled network and one with proper crystallographic correlations. Although the percolation threshold is different, the same scaling laws apply near the threshold (i.e., the same curvatures are present in the sigmoid), and the same analytical model can be used to describe both curves.

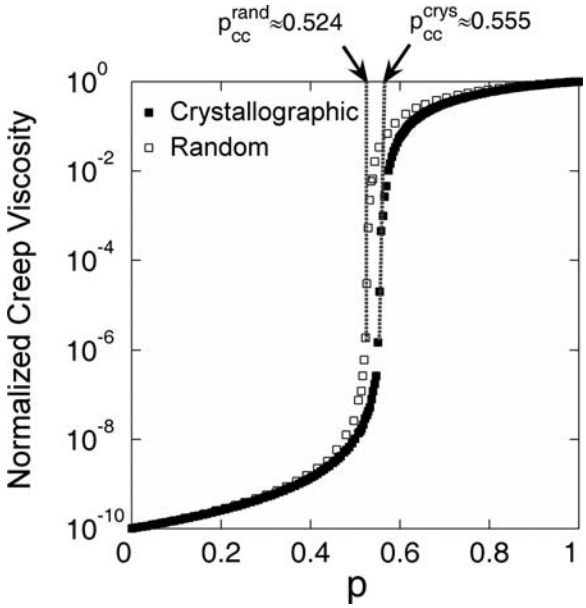


Fig. 15.10 Example of percolation data for grain boundary networks, illustrating the role of crystallographic constraints. These data for Coble (diffusional) creep are from computer simulations on 2D hexagonal grain boundary networks. The effect of crystallographic constraints is to shift the percolation threshold somewhat, but the shapes of the *curves* (and the exponents of the power laws that describe them) are unchanged. After Chen and Schuh (2007)

15.5 Conclusions and Future Outlook

The field of grain boundary network analysis is moving quickly; not many years ago, there were very few practitioners in this particular subfield, but there seems to be a growing realization about the importance of correlated percolation in the performance of a material. Thus we conclude with a few observations about the possible future course of the field:

- Most published experimental studies of grain boundary network statistics rely exclusively on two-dimensional cross sections via EBSD. Yet the boundary networks in most materials are irreducibly three-dimensional, which introduces significant complexity. Advances in serial sectioning and digital reconstruction techniques, as well as advanced X-ray diffraction methods, now permit access to fully three-dimensional data sets completely describing the grain structure of a material. Percolation problems change subtly going from two to three dimensions; it is quite possible that both the special boundaries and the general boundaries may percolate over a very wide range of special boundary fractions. The three-dimensional structure of twin-related domains also remains somewhat mysterious, and could be elucidated with such new tools.
- Early in this chapter we introduced a classification scheme for grain boundaries, much as the field has always done in order to simplify the description of the boundary network. Future advances in this field will rely upon progressively adding more details to this classification scheme, including boundary plane inclinations, orientation of boundaries with respect to, e.g., an external stress axis, and thermodynamic state variables such as the degree of boundary relaxation. Although some of the effective medium type modeling approaches laid out in this chapter can be extended from the binary case to include more differentiation in boundary properties, there is a significant experimental challenge to assess connectivity among boundaries that are not merely special or general, but which lie on a multidimensional spectrum of structure and properties.
- Whereas some properties are primarily concerned with connectivity on the direct lattice (intergranular pathways) and others are more appropriately treated on the dual (transgranular paths), many properties involve both lattices simultaneously. For example, stress corrosion cracking is one of the best-known examples of a property that can be manipulated broadly through grain boundary engineering, and it implicitly involves intergranular damage propagation coupled to a force transmission network across the grain boundaries. In percolation theory correlated problems are relatively common, but correlations between direct and dual lattices are essentially unstudied. The aims of the materials science community therefore require study of this new statistical physics problem.

These problems represent some of the most immediate needs of the community working on grain boundary networks. As always, access to improved experimental tools based on EBSD will drive continued progress on these problems.

References

Basinger JA, Homer ER, Fullwood DT, Adams BL (2005) Two-dimensional grain boundary percolation in alloy 304 stainless steel. Scripta Mater 53(8):959–963

Bouchaud E (1997) Scaling properties of cracks. J Phys-Condens Mat 9(21):4319–4344

Brandon DG (1966) Structure of high-angle grain boundaries. Acta Metall 14(11):1479

Chen Y, Schuh CA (2006) Diffusion on grain boundary networks: Percolation theory and effective medium approximations. Acta Mater 54(18):4709–4720

Chen Y, Schuh CA (2007) Coble creep in heterogeneous materials: The role of grain boundary engineering. Phys Rev B 76(6):064111

Frary M, Schuh CA (2003a) Combination rule for deviant CSL grain boundaries at triple junctions. Acta Mater 51(13):3731–3743

Frary M, Schuh CA (2003b) Nonrandom percolation behavior of grain boundary networks in high-T-c superconductors. Appl Phys Lett 83(18):3755–3757

Frary M, Schuh CA (2004) Percolation and statistical properties of low- and high-angle interface networks in polycrystalline ensembles. Phys Rev B 69(13):134115

Frary M, Schuh CA (2005a) Connectivity and percolation behaviour of grain boundary networks in three dimensions. Philos Mag 85(11):1123–1143

Frary M, Schuh CA (2005b) Grain boundary networks: Scaling laws, preferred cluster structure, and their implications for grain boundary engineering. Acta Mater 53(16): 4323–4335

Fullwood DT, Basinger JA, Adams BL (2006) Lattice-based structures for studying percolation in two-dimensional grain networks. Acta Mater 54(5):1381–1388

Gao Y, Stolken JS, Kumar M, Ritchie RO (2007) High-cycle fatigue of nickel-base superalloy Rene 104 (ME3): Interaction of microstructurally small cracks with grain boundaries of known character. Acta Mater 55(9):3155–3167

Gaudett MA, Scully JR (1994) Applicability of bond percolation theory to intergranular stress-corrosion cracking of sensitized Alsl 304 stainless-steel. Metall Mater Trans A 25(4):775–787

Gertsman VY (2001a) Coincidence site lattice theory of multicrystalline ensembles. Acta Crystallogr A 57:649–655

Gertsman VY (2001b) Geometrical theory of triple junctions of CSL boundaries. Acta Crystallogr A 57:627–627

Gertsman VY, Henager CH (2003) Grain boundary junctions in microstructure generated by multiple twinning. Interface Sci 11(4):403–415

Grimmett G (1989) Percolation. Springer-Verlag, New York

King A, Johnson G, Engelberg D, Ludwig W, Marrow J (2008) Observations of intergranular stress corrosion cracking in a grain-mapped polycrystal. Science 321(5887):382–385

Kopezky CV, Andreeva AV, Sukhomlin GD (1991) Multiple twinning and specific properties of Sigma = 3n boundaries in FCC crystals. Acta Metall Mater 39(7):1603–1615

Krupp U, Kane WM, Liu XY, Dueber O, Laird C, McMahon CJ (2003) The effect of grain-boundary-engineering-type processing on oxygen-induced cracking of IN718. Mater Sci Eng A 349(1–2):213–217

Krupp U, Wagenhuber PEG, Kane WM, McMahon CJ (2005) Improving resistance to dynamic embrittlement and intergranular oxidation of nickel based superalloys by grain boundary engineering type processing. Mater Sci Tech 21(11):1247–1254

Lehockey EM, Palumbo G, Lin P (1998a) Improving the weldability and service performance of nickel- and iron-based superalloys by grain boundary engineering. Metall Mater Trans A 29(12):3069–3079

Lehockey EM, Palumbo G, Lin P, Brennenstuhl A (1998b) Mitigating intergranular attack and growth in lead-acid battery electrodes for extended cycle and operating life. Metall Mater Trans A 29(1):387–396

Lejcek P, Paidar V (2005) Challenges of interfacial classification for grain boundary engineering. Mater Sci Tech 21(4):393–398

Lim LC, Raj R (1984) Effect of boundary structure on slip-induced cavitation in polycrystalline nickel. Acta Metall 32(8):1183–1190

McGarrity ES, Duxbury PM, Holm EA (2005) Statistical physics of grain-boundary engineering. Phys Rev E 71(2):026102

Mclachlan DS (1987) An equation for the conductivity of binary-mixtures with anisotropic grain structures. J Phys C 20(7):865–877

Meinke JH, McGarrity ES, Duxbury PM, Holm EA (2003) Scaling laws for critical manifolds in polycrystalline materials. Phys Rev E 68(6):066107

Michiuchi M, Kokawa H, Wang ZJ, Sato YS, Sakai K (2006) Twin-induced grain boundary engineering for 316 austenitic stainless steel. Acta Mater 54(19):5179–5184

Miyazawa K, Iwasaki Y, Ito K, Ishida Y (1996) Combination rule of Sigma values at triple junctions in cubic polycrystals. Acta Crystallogr A 52:787–796

Nichols CS, Cook RF, Clarke DR, Smith DA (1991a) Alternative length scales for polycrystalline materials 1. Microstructure evolution. Acta Metall Mater 39(7):1657–1665

Nichols CS, Cook RF, Clarke DR, Smith DA (1991b) Alternative length scales for polycrystalline materials 2. Cluster morphology. Acta Metall Mater 39(7):1667–1675

Randle V (2004) Twinning-related grain boundary engineering. Acta Mater 52(14):4067–4081

Randle V (2006) "Special" boundaries and grain boundary plane engineering. Scripta Mater 54(6):1011–1015

Read WT, Shockley W (1950) Dislocation models of crystal grain boundaries. Phys Rev 78(3):275–289

Reed BW, Kumar M (2006) Mathematical methods for analyzing highly-twinned grain boundary networks. Scripta Mater 54(6):1029–1033

Reed BW, Kumar M, Minich RW, Rudd RE (2008) Fracture roughness scaling and its correlation with grain boundary network structure. Acta Mater 56:3278–3289

Reed BW, Minich RW, Rudd RE, Kumar M (2004) The structure of the cubic coincident site lattice rotation group. Acta Crystallogr A 60:263–277

Romero D, Martinez L, Fionova L (1996) Computer simulation of grain boundary spatial distribution in a three-dimensional polycrystal with cubic structure. Acta Mater 44(1): 391–402

Schuh CA, Frary M (2006) Correlations beyond the nearest-neighbor level in grain boundary networks. Scripta Mater 54(6):1023–1028

Schuh CA, Kumar M, King WE (2003a) Analysis of grain boundary networks and their evolution during grain boundary engineering. Acta Mater 51(3):687–700

Schuh CA, Kumar M, King WE (2003b) Connectivity of CSL grain boundaries and the role of deviations from exact coincidence. Z Metallkd 94(3):323–328

Schuh CA, Kumar M, King WE (2005) Universal features of grain boundary networks in FCC materials. J Mater Sci 40(4):847–852

Schuh CA, Minich RW, Kumar M (2003c) Connectivity and percolation in simulated grain-boundary networks. Philos Mag 83(6):711–726

Schwartz AJ, King WE, Kumar M (2006) Influence of processing method on the network of grain boundaries. Scripta Mater 54(6):963–968

Shimada M, Kokawa H, Wang ZJ, Sato YS, Karibe I (2002) Optimization of grain boundary character distribution for intergranular corrosion resistant 304 stainless steel by twin-induced grain boundary engineering. Acta Mater 50(9):2331–2341

Spigarelli S, Cabibbo M, Evangelista E, Palumbo G (2003) Analysis of the creep strength of a low-carbon AISI 304 steel with low-Sigma grain boundaries. Mater Sci Eng A 352(1–2):93–99

Stauffer D, Aharony A (1994) Introduction to percolation theory, rev 2nd ed. Routledge, London

Van Siclen CD (2006) Intergranular fracture in model polycrystals with correlated distribution of low-angle grain boundaries. Phys Rev B 73(18):184118

Watanabe T (1983) Grain-boundary sliding and stress-concentration during creep. Metall Trans A 14(4):531–545

Wells DB, Stewart J, Herbert AW, Scott PM, Williams DE (1989) The use of percolation theory to predict the probability of failure of sensitized, austenitic stainless-steels by intergranular stress-corrosion cracking. Corrosion 45(8):649–660

Zhao JW, Koontz JS, Adams BL (1988) Intercrystalline structure distribution in alloy 304 stainless-steel. Metall Trans A 19(5):1179–1185

Chapter 16

Measurement of the Five-Parameter Grain Boundary Distribution from Planar Sections

Gregory S. Rohrer and Valerie Randle

16.1 Introduction: Grain Boundary Planes and Properties

Although EBSD is essentially a surface measurement technique, strategies have been developed to extend its capabilities to the characterisation of microstructure in three dimensions. These developments have been realised because advances in both EBSD technology and computing power have rendered the collection of large data sets a routine matter. There are several scientific motivations for characterizing the three-dimensional structure of polycrystals by EBSD. In this chapter, we describe the application of EBSD to the measurement of internal interface planes by application of both serial sectioning and also a stereological technique known as the "five-parameter analysis."

An interface (referred to as a grain boundary where it exists between crystals of the same phase) has five geometric degrees of freedom, as described below. Usually, three independent parameters are used to describe the misorientation between grains, and two independent parameters describe the orientation of the boundary plane (Wolf and Lutsko 1989). Whereas the misorientation is accessed readily by EBSD performed on a single section through the specimen, the boundary plane orientation is not so readily available, because the boundary surface itself is buried. Furthermore, a single grain boundary, having by definition a fixed misorientation, usually consists of many differently oriented boundary plane segments, as illustrated in Fig. 16.1. For these reasons measurement of boundary plane crystallography has tended to be neglected. However, both atomistic simulations and a slowly increasing amount of experimental evidence demonstrate that boundary plane crystallography has a fundamental influence on grain boundary properties such as energy, mobility, corrosion resistance, and segregation (Randle 1997). A few modern examples, which demonstrate these links, are:

- The effect of grain boundary orientation on energy has been illustrated in NiAl (Amouyal et al. 2005). The boundary energy was found to vary with inclination, and twist boundaries had higher energies than tilt boundaries. The data were obtained from 43 grain boundaries via a combination of EBSD, serial sectioning, thermal grooving, and scanning probe microscopy.

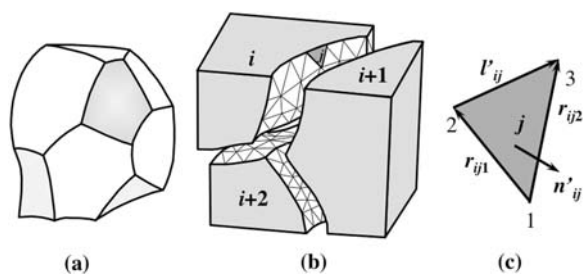


Fig. 16.1 (**a**) Schematic shape of a single grain from a dense polycrystal. (**b**) Representation of a three-grain junction within a polycrystal. The view is exploded so that the internal interfaces can be seen. The external surfaces are *shaded* and the internal surfaces are *triangulated.* The *j*th triangular facet on the *i*th grain is *shaded* and an enlarged view of this facet is shown in (**c**) (Rohrer et al. 2004)

G.S. Rohrer (✉)
Department of Materials Science and Engineering, Carnegie Mellon University, Pittsburgh, PA 15213, USA
e-mail: gr20@andrew.cmu.edu

A.J. Schwartz et al. (eds.), *Electron Backscatter Diffraction in Materials Science*,
DOI 10.1007/978-0-387-88136-2_16, © Springer Science+Business Media, LLC 2009

- In directionally solidified pure copper it was found that the corrosion resistance of grain boundaries was correlated to the interplanar spacing at the boundary, but not the Σ-value, for [110] tilt boundaries (Miyamoto et al. 2004). This work was carried out on 26 grain boundaries in tricrystals, by X-ray back reflection Laue diffraction combined with atomic force microscopy measurements on corrosion grooves.
- In bicrystals of an Fe-Si alloy, grain boundaries with [100] tilt misorientations, symmetric tilt boundaries, and asymmetric boundaries formed with a (110) plane were found to be resistant to segregation (Lejcek et al. 2003).
- Studies of grain boundary wetting by liquid copper in an iron alloy indicated that the propensity for wetting increased with the grain boundary free volume and the atomic roughness of the surfaces comprising the boundary (Wynblatt and Takashima 2001). The data were obtained by EBSD and serial sectioning from 975 boundaries.
- A different experimental approach to the study of grain boundary planes is to adapt EBSD to measure the indices of intergranular fracture surfaces. Using this method it was found that in TiO_2 there was reduced segregation to low energy boundary planes (Pang and Wynblatt 2005).

Boundaries which have improved properties compared to those of a random boundary have come to be known as "special" boundaries. It used to be thought that special boundaries were low-Σ coincidence site lattice (CSL) boundaries. Now it is realised that the orientation of the boundary plane has a greater influence on properties than does the misorientation (Rohrer et al. 2004).

16.2 Serial Sectioning

Unless the component grain boundaries in a specimen have a predefined or easily measurable geometry, such as bicrystals, tricrystals, columnar grains, thin films, fracture surfaces, etc., a serial sectioning procedure has in the past been used to obtain the orientation of the boundary plane. Figure 16.2 illustrates the parameters required to specify the orientation of a single boundary plane. The sample reference frame is *xyz,* the grain boundary trace vector on the specimen surface is $\boldsymbol{l'}_{ij}$, the grain boundary plane normal is $\boldsymbol{n'}_{ij}$, the "trace angle" and the "inclination angle" as illustrated in Fig. 16.2 are α and β, respectively, and the section depth is t. Also required is a means of calibrating accurately the depth of section removed, and ensuring accurate registration between successive sections. If these parameters are obtained manually, data sets tend to be small because these operations are tedious. In the 1990s information on the crystallographic indices of planes from several metals was obtained (Randle 1995, 1997).

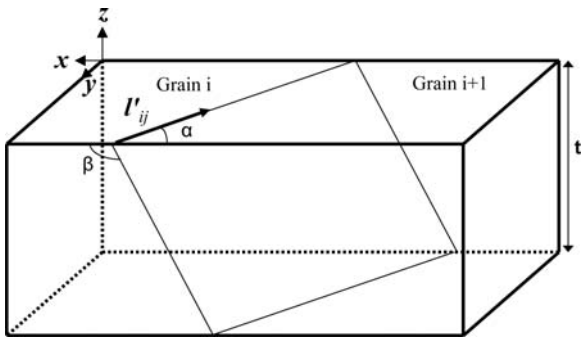


Fig. 16.2 The parameters required to specify the crystallographic orientation of a single boundary plane (*thin lines*). The sample reference frame (*thick lines*) is *xyz* and the grain boundary trace vector on the specimen surface is $\boldsymbol{l'}_{ij,}$ the "trace angle" and the "inclination angle" are α and β, respectively, and the section depth is t

More comprehensive analysis of serial section data has made it possible to determine the inclinations of many thousands of grain boundaries, and therefore determine the five-parameter grain boundary character distribution (GBCD; Saylor et al. 2003, 2004a). Each grain boundary trace on a two-dimensional section plane is approximated by a series of short tangent lines. When traces from the same interfaces are located on two adjacent layers, the interface can be represented by a series of triangles joining two pixels on one layer with a third pixel on an adjacent layer, as illustrated in Fig. 16.3. The normal of each triangle is therefore known, and as long as the grain orientations have been measured by EBSD, it is also possible to determine the misorientation. With information from a sufficient number of triangles, the GBCD can be calculated.

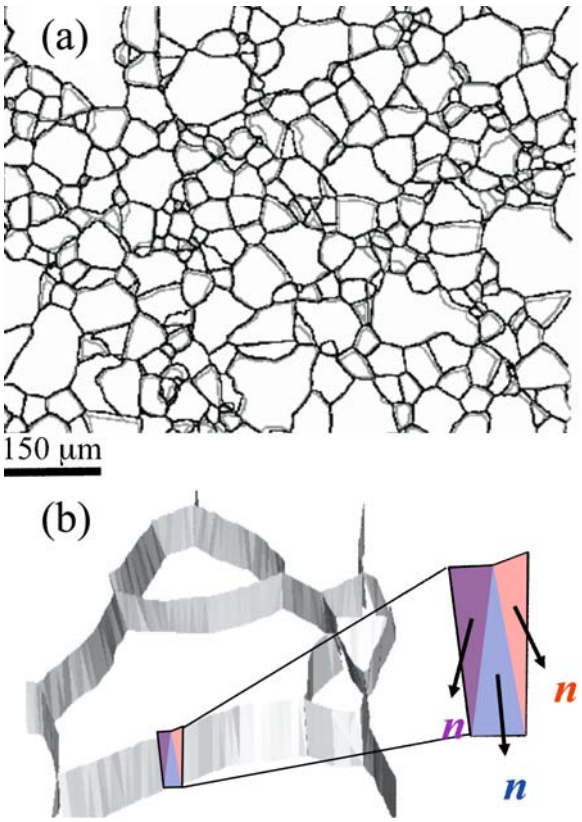


Fig. 16.3 (**a**) A superposition of the grain boundary traces from adjacent layers in the microstructure of MgO. The vertical separation is about 5 μm. (**b**) Illustration of the formation of triangles between traces on adjacent layers, with known lattice misorientation and orientation

16.3 Single-Surface Trace Analysis

More recently, interest has been generated in exploiting the information provided from the grain boundary trace direction on the specimen surface, and dispensing with the serial sectioning step. This is because there are unavoidable geometrical errors involved in serial sectioning and three-dimensional reconstruction. For example, the assumption has to be made that the interface is planar within the section depth. These errors are an order of magnitude greater than errors in a single section plane. Serial sectioning is also laborious and time consuming.

The crystallographic boundary trace direction plus the misorientation between neighbouring grains provides four out of the five boundary parameters. The "trace vector" $\boldsymbol{l'}_{ij}$ (Fig. 16.2) can be calculated from EBSD data in the coordinate systems of both interfacing grains, where it is referred to as $\boldsymbol{l}_{ij}$ (note that throughout this chapter, primed vectors denote the sample reference frame and unprimed vectors denote the crystal frame). Because $\boldsymbol{l}_{ij}$ lies in the grain boundary plane it is orthogonal to the boundary plane normal vector $\boldsymbol{n}_{ij}$ and it must be true that $\boldsymbol{l}_{ij} \bullet \boldsymbol{n}_{ij} = 0$. This condition can be used to check if the boundary plane normal could be $<111>$, for example, in one or both grains. If $\boldsymbol{l}_{ij} \bullet <111> \neq 0$, then the boundary cannot be $\{111\}$. On the other hand if $\boldsymbol{l}_{ij} \bullet <111> = 0$, then the boundary plane might be on $\{111\}$. If the condition applies in both interfacing grains, then it is likely that the boundary is either a coherent twin (if the boundary is a $\Sigma 3$), or a $\{111\}$ twist boundary (if the boundary has some other misorientation about [111]). This calculation therefore supplies valuable information about the boundary plane crystallography: what the plane cannot be and what it is likely to be (Randle, 2001). In previous work where the method was rigorously tested and validated, for $\Sigma 3$ boundaries analysed in brass, only 10% of the cases were ambiguous in terms of recognising the type of $\Sigma 3$ (coherent or incoherent) by the single-surface trace analysis compared to a full serial sectioning analysis (Randle and Davies 2002).

The methodology for identifying the possibility of twinning in this way has been automated by use of an algorithm, which extracts the boundary trace position from EBSD orientation maps. This algorithm has been used to investigate twinning in zirconium, nickel, and copper (Wright and Larsen 2002) and to study the relationship between precipitate-free zone width and grain boundary type in an aluminium alloy (Cai et al. 2007). More significantly, it is used as part of the procedure to determine automatically all five boundary parameters from a single section (see Section 16.4).

The automated boundary trace reconstruction routine works on an orientation map in which grains have been identified as groups of similarly oriented points, from which grain boundaries are defined according to a preset tolerance. Triple junctions can then be located and a first attempt at reconstructing a boundary trace is made by joining the two neighbouring triple junctions, as shown in Fig. 16.4a. However, the grain boundary is rarely a straight line between the two junctions, and so the reconstructed trace needs to be segmented to follow more closely the true boundary. This is done by locating the point on the true boundary furthest from the reconstructed boundary. If the perpendicular distance

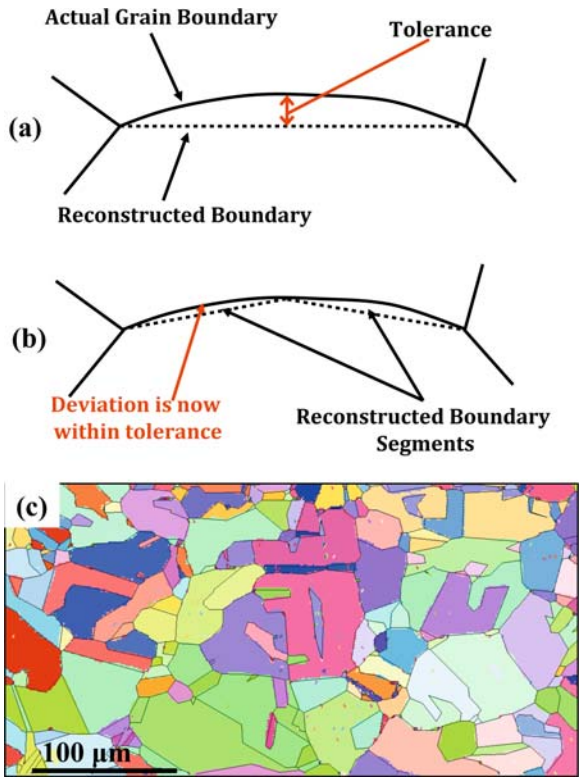


Fig. 16.4 Illustration of the boundary trace reconstruction routine. (**a**) First reconstruction attempt, by joining adjacent triple junctions. (**b**) Segmentation of the reconstructed trace. (**c**) Small map wherein reconstructed boundaries are superimposed on true boundaries. Grains are coloured randomly

between this point and the reconstructed boundary exceeds a predefined tolerance, then the reconstructed boundary is split into two line segments, as shown on Fig. 16.4b. This procedure is repeated until all points on the reconstructed boundary are within the tolerance distance of the true boundary.

Figure 16.4c shows a small map wherein reconstructed boundaries are superimposed on true boundaries. To minimise errors, a small step size needs to be used to generate the EBSD map in order to reproduce the boundary positions as faithfully as possible, given the discrete nature of the measurement grid. Then the segmenting process must aim to reproduce the true boundary, rather than any "noise" on the boundary length. It is therefore essential that a small tolerance, e.g., twice the map step size, is chosen to reconstruct boundaries. The expected error for a boundary of length six times greater than the scan step size would be $\pm 2^\circ$ (Wright and Larsen 2002). Finally, an average orientation from each neighbouring grain is associated with each segment of the reconstructed boundary trace. Measurement points between one and five steps from the boundary are used in the averaging.

16.4 Five-Parameter Stereological Analysis

16.4.1 Parameterization and Discretization of the Space of Grain Boundary Types

For evaluation of the five-parameter GBCD, we choose lattice misorientation (Δg) and grain boundary plane orientation ($\boldsymbol{n}$) to parameterize the function $\lambda(\Delta g,\boldsymbol{n})$, which is the relative areas of grain boundaries within a polycrystal distinguished by Δg and $\boldsymbol{n}$. For all of our calculations, we parameterize the lattice misorientation using three Eulerian angles ϕ_1, Φ, and ϕ_2. However, for display of the data, we choose the angle/axis system θ/[uvw], which is more intuitive. The grain boundary plane orientations are parameterized using spherical angles θ and ϕ in both the calculations and the display of the data. In the complete domain, these five angular parameters, ϕ_1, Φ, ϕ_2, θ, and ϕ range from 0 to 2π, π, 2π, π, and 2π, respectively. For most crystal systems, this complete domain contains many indistinguishable, symmetrically related parameter configurations. Therefore, one can choose a sub-domain that reduces some, but not all, of the degeneracy in the calculations. In our calculations, we use a sub-domain in which the misorientation parameters range from zero to $\pi/2$, $\pi/2$, and $\pi/2$ for ϕ_1, Φ, and ϕ_2, respectively. This sub-domain is 1/64th of the entire range of possibilities and is a convenient choice because it is the smallest volume that contains an integer number of fundamental zones and can still be partitioned in a simple way. For the cubic system, there are 36 general equivalent grain boundaries for any particular set of parameters in the subdomain (Moraweic 2004, Rohrer et al. 2004).

To partition the misorientation subdomain into cells of equal volume, we equally partition ϕ_1, $\cos(\Phi)$, and ϕ_2. In this case, there are D^3 cells with $\Delta\phi_1 = \Delta\phi_2 = \pi/2D$ and $\Delta\cos\Phi = 1/D$. The cells in Euler space can

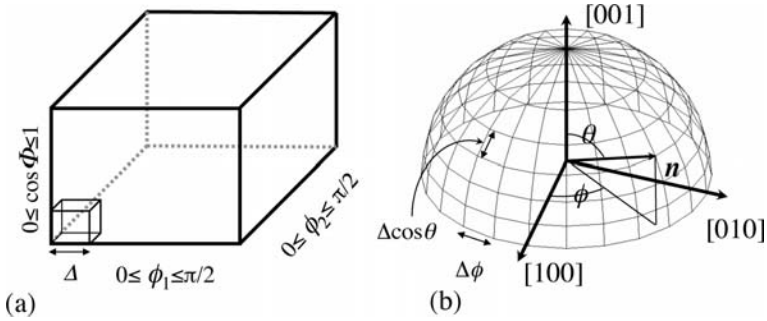


Fig. 16.5 The parameterization of $\lambda(\Delta\gamma, \boldsymbol{n})$ into (**a**) three lattice misorientation parameters and (**b**) two boundary plane orientation parameters. (**b**) Definition of the spherical angles used to parameterize $\boldsymbol{n}$. The range of $\boldsymbol{n}$ is partitioned so that all of the cells have the same width in ϕ and $\cos\theta$ and the same area on the surface of the hemisphere. In the misorientation space, there are D^3 cells and for each of these cells, there is a hemisphere of boundary plane normals with $4D^2$ cells

be visualized as a three dimensional rectangular parallelepiped, as illustrated in Fig. 16.5a. For each cell in the misorientation space, there is also a distribution of grain boundary normals, $\boldsymbol{n}$. For centrosymmetric crystals, the two spherical angles (θ and ϕ) in the range between 0 and $\pi/2$ and 0 and 2π, respectively, reproduce the domain of $\boldsymbol{n}$ (it is assumed to have a center of symmetry and only the upper hemisphere of surface orientation space is considered). So that each cell has the same area on the surface of a unit sphere, the domain of $\boldsymbol{n}$ is parameterized by $\cos\theta$ and ϕ, as illustrated in Fig. 16.5b. If there are D cells for every $\pi/2$ radians, then there will be a total of $D \bullet 4D$ cells, each with the size $\Delta\cos\theta = 1/D$ and $\Delta\phi = 2\pi/4D$. With the five-dimensional grain boundary parameter space divided into cells of equal volume, each cell has the same probability of being populated by a random choice of parameters.

Based on the parameterization described above, there are $4D^5$ equal volume cells in the subdomain. The appropriate resolution for the five-dimensional space should lie in the range between 5° and 10°. The rationale for this is that grain boundary properties are known to vary over intervals smaller than 10°, but measuring grain boundary plane orientations with an accuracy greater than 5° is currently difficult because of the number of required observations. With a resolution of 5°, $D = 18$ and with 10°, $D = 9$ and for these choices, there are 7.5×10^6 and 2.4×10^5 cells in the subdomain. For the cubic case, the number of distinguishable cells is 2.1×10^5 and 6.5×10^3, respectively. This provides guidance for the number of observations required to reliably determine the GBCD. Because the number of distinguishable bins at 5° resolution is 32 times that at 10°, many more observations are needed at higher angular resolution.

16.4.2 Measurement of the Grain Boundary Characterization Distribution

Hilliard was the first to describe a stereology to measure the distribution of interface normals in the sample reference frame (Hilliard 1962). Adams later generalized this approach in his description of the "intercrystalline structure distribution function" (Adams 1986). The method was first applied to study cavitation damage in polycrystalline Cu (Field and Adams 1992) and has more recently been adapted to the misorientation reference frame (Homer et al. 2006). The common feature of these methods is the representation of the interface plane distribution function as a finite harmonic series whose coefficients are determined from the observations of boundary traces from multiple oblique sections. Saylor and Rohrer described an alternate approach for determining interface distributions in the crystal reference frame and used this to measure grain shapes in a composite (Saylor and Rohrer 2002). The method was extended to the misorientation reference frame to measure $\lambda(\Delta g, \boldsymbol{n})$ (Saylor et al. 2004b). In this work, the grain boundary plane distribution is represented as a discrete quantity in the misorientation reference frame and a statistical procedure is used to reconstruct the true distribution from the observations.

In contrast to the earlier work, it is assumed that grain orientations are randomly distributed so that data from a single section plane can be used. Larsen and Adams showed that using the same assumption, the original stereology based on a harmonic series representation could also be used to reconstruct the grain boundary plane distribution using data from a single section plane (Larsen and Adams 2004). Since this time, the series method has been applied to study an Al-Zn-Mg alloy (Cai et al. 2007) and the discrete approach has been applied to a wide range of materials (Rohrer et al. 2004); in the section below, the discrete approach is described.

Stereological measurements of $\lambda(\Delta g, \boldsymbol{n})$ begin with a set of boundary trace vectors, $\boldsymbol{l'}_{ij}$, defined as the trace where the *j*th boundary tangent plane on the *i*th grain meets the surface. Traces on a real micrograph are shown on Fig. 16.4c and the geometry of a single trace is represented schematically in Fig. 16.6a. While each $\boldsymbol{l'}_{ij}$ can be associated with a specific misorientation in the five-parameter space, $\boldsymbol{n'}_{ij}$ is not well defined. However, as implied above in the section 16.3 on the analysis of twin boundaries, it must be true that the actual grain boundary plane belongs to a set of planes that includes the surface trace and obeys the condition $\boldsymbol{l'}_{ij} \bullet \boldsymbol{n'}_{ijk} = 0$, where the vectors $\boldsymbol{n'}_{ijk}$ are a set of C unit normals to the possible grain boundary planes (see Fig. 16.6b). Therefore, each observed trace can be used to generate a set of vectors perpendicular to possible boundary planes ($\boldsymbol{n'}_{ijk}$) that can be transformed to the misorientation reference frame to produce the vectors $\boldsymbol{n}_{ijk}$ (see Fig. 16.6c). The vectors $\boldsymbol{n}_{ijk}$ specify C cells into which the trace length, $|\boldsymbol{l}_{ij}|$, is added. In the end, we would like to know the fractional length of line segments crossing each plane, since this is equal to the fractional area of each plane.

If there are N observations of traces from indistinguishable bicrystals, then we can be certain that for this misorientation, we have accumulated N correct boundary normal orientations and $N(C–1)$ incorrect assignments. It is worth noting that the bicrystals sampled should have a random orientation distribution with respect to the sample reference; preferred orientations bias the distribution and will lead to unreliable results. To get the line length crossing each boundary type, we have to remove the incorrect assignments. To do this, it must be realized that the incorrect assignments are not distributed randomly. If there is a peak in the real distribution of grain boundary planes, then orientations very close to this pole will have more incorrectly assigned

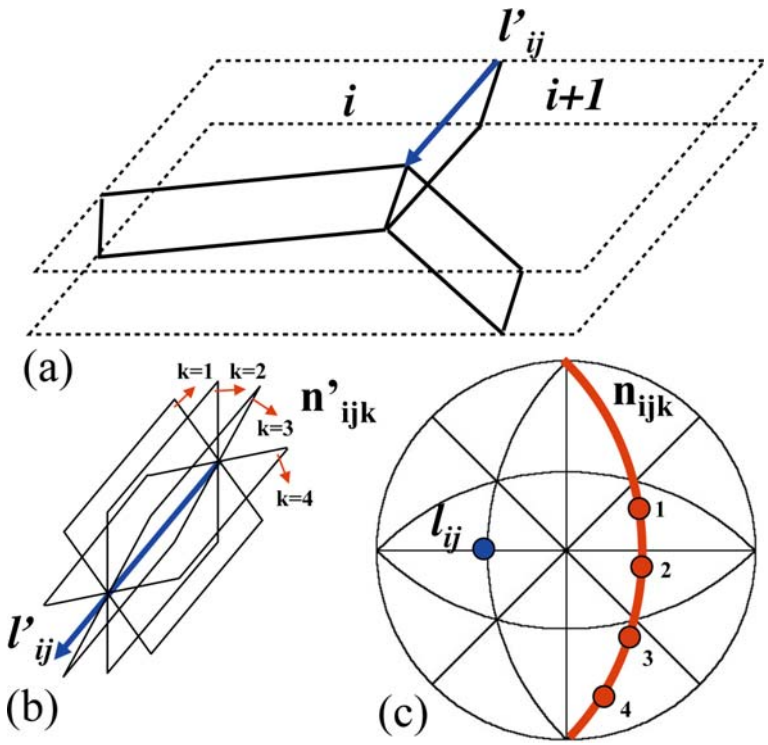


Fig. 16.6 Schematic of interpretation of boundary traces. (**a**) A trace between crystals *i* and *i* + 1 in the sample reference frame is identified. (**b**) The grain boundary normal is one of the set $\boldsymbol{n'}_{ijk}$. (**c**) Represented on a stereogram in the grain boundary reference frame, the boundary trace is a point and the set of possible planes is a great circle

lengths than others. This is because these neighboring cells have a greater probability of being in the zone of the peak orientation than an orientation further away. Conversely, orientations far from the maximum are less likely to share a zone with the most highly populated orientation and will accumulate less incorrectly assigned lengths. By making an approximation for this inhomogeneous distribution, it is possible to subtract the incorrectly assigned lengths. This procedure has been described in detail elsewhere (Saylor et al. 2004b).

When using this stereology to make GBCD measurements, the factors that influence the accuracy are the discretization for the parameters, the accuracy of the line segment orientations, and the number of observations. The discretization of the system influences the discrimination of closely spaced features in the distribution and the magnitudes of the peaks. If, for example, there are two peaks separated by less than the spacing of the cells, they will be merged to a single peak. Features that are sharper than the cell size will also be broadened and have reduced intensity. The discretization also influences how the peak values are interpreted. For example, the upper limit of the population, measured in multiples of random distribution (MRD), is equal to the number of distinguishable cells (this can be reached only when all of the observations fall into a single cell). For example, in a cubic system with $D = 9$ (cell size of approximately 10°), there are 6561 distinguishable cells. It was recently reported that with $D = 9$, the peak of the distribution for a Ni specimen occurred with a value of 1428 MRD at the position of the coherent twin (Randle et al. 2008b). This implies that at least 22% (1428/6561) of the grain boundary area is made up of coherent twins. Because the distribution of coherent twins is expected to be narrower than the 10° cell size, the actual fractional boundary area may be larger. For the remainder of the discussion, we will focus on cubic systems with a 10° ($D = 9$) cell size.

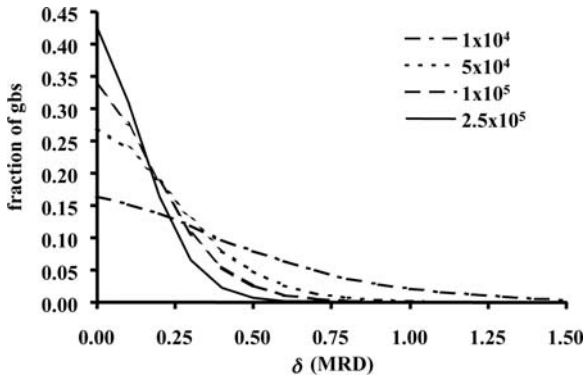


Fig. 16.7 The distribution of the differences, δ (absolute value), between the recovered and actual GBCD from data sets consisting of 1×10^4, 5×10^4, 1×10^5, and 2.5×10^5 simulated boundaries (Saylor et al. 2004b)

16.4.3 Performance of the Stereological Analysis

The agreement between the stereologically measured distribution and a true (simulated) distribution has been shown to depend on the number of observations. If only 10^4 grain boundary traces are used, then there are errors of greater than 0.5 MRD in a large fraction of the cells (see Fig. 16.7). However, if 2.5×10^5 boundaries are measured, then less than 1% of the cells have an error this large. If 5×10^4 traces are used, fewer than 5% of the cells have errors greater than 0.5 MRD. Balancing the desire for accuracy against the time required to make the observations, it was concluded that 5×10^4 traces are sufficient and this standard has been used in the majority of the work that has followed (Saylor et al. 2004b). However, it must be noted that the errors are most likely to occur at the maxima in the distributions and it is frequently these maxima that are interpreted. In comparative studies, it is essential to understand how different two distributions need to be before it can be concluded that they are actually different. This question has been addressed by simulations and these results are described in the remainder of this section.

In simulating experimental observations, it is important to recognize that the boundary traces are not permitted to have a continuous range of orientations in the sample reference frame. Because of the discrete nature of the EBSD map, the end points of grain boundary traces are confined to the nodes of a two-dimensional honeycomb lattice. The relevant scale for this is the ratio of the EBSD step size to the average grain diameter. The allowed ranges of orientation become more continuous as the grain size to pixel ratio increases.

Simulations were carried out to determine how the number of observations and the grain size to pixel ratio influence the observed distribution of grain boundary

planes. To begin, a model GBCD was designed to mimic the distribution observed for $SrTiO_3$ (Saylor et al. 2004a). The GBCD has a small enhancement of low angle grain boundaries and peaks at the positions of {100} planes. The value of each cell was defined by its proximity to the misorientation of 2° about [100] and to the {100} grain boundary plane orientation. For each type of boundary, the amplitude of the GBCD (A) was given by the combination of a misorientation determined component (A_1) and a grain boundary plane determined component (A_2).

$$A = A_1 + (A_2 \bullet A_1) \tag{16.1}$$

The misorientation determined component is:

$$A_1 = 1 + A_m \exp\left[-(\theta_m/W_m)^2\right], \tag{16.2}$$

where $A_m = 1.5$, θ_m is the disorientation between the current cell and the 2°/[100] misorientation, and W_m, the width of the distribution, is 10°. This leads to an MDF that has a weak maximum for low misorientation boundaries and is constant elsewhere. The grain boundary plane orientation determined component of the amplitude is given by:

$$A_2 = A_o \exp\left[-(\theta_o/W_o)^2\right], \tag{16.3}$$

where $A_o = 400$, θ_o is the angle between the normal to {100} and the plane of interest, and W_o, the width of the distribution, is 10°.

This distribution is used to generate simulated data in the following way. First, a random misorientation and grain boundary plane orientation are selected. If they are consistent with the distribution, the observation is kept and if not, it is discarded and another is selected. Whenever an observation is kept in the distribution, a random direction within the grain boundary plane is selected (to simulate the observation of a boundary trace). At this point, the domain of trace orientations is continuous. To simulate the effect of the grid, the closest line segment on a finite, 2D hexagonal lattice is selected, and this is saved as a simulated observation. The process is repeated as many times as necessary to generate simulated data and can then be used to determine the GBCD.

To test the influence of the number of line segments on the extreme points in the distribution, simulation data sets containing 5×10^3, 1×10^4, 2.5×10^4, 5×10^4, 1×10^5, 2.5×10^5, and 5×10^5 traces were created and the GBCD was calculated. For these simulations, the grain size to pixel ratio was 50, which is assumed to closely approximate a continuous distribution and eliminate this factor from the analysis. The distribution of grain boundary planes at the misorientation of 45° about the [100] axis was selected as a characteristic example. The results in Fig. 16.8 show the maximum and minimum of the distribution as a function of the number of traces and the grain boundary plane distribution for three cases. Note that the reference frame defined in the caption is used throughout this chapter. If the distribution determined from 5×10^3 segments is excluded, then the average of the maxima is 3.25 MRD with a standard deviation of 0.3 MRD, or about 10% of the maximum. While the value of the maximum determined from 1×10^4 traces is within 10% of that determined from a larger number of traces, it is also clear that not all features in the distribution are represented. Specifically, the peaks along the vertical axis, corresponding to tilt boundaries, are not reproduced. The distribution from 5×10^4 traces, on the other hand, is nearly the same as the one from ten times as many

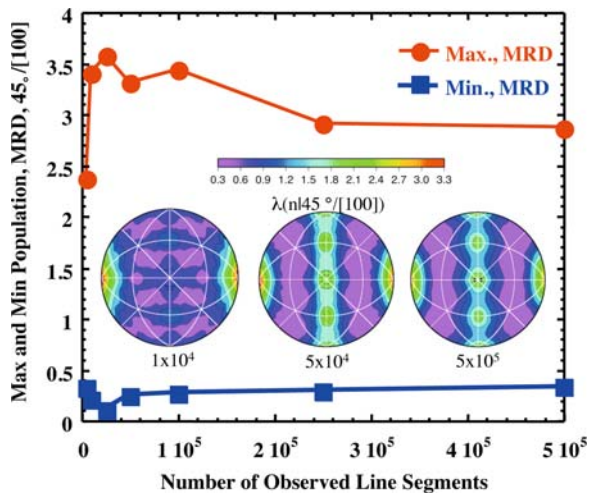


Fig. 16.8 Results from the stereological analysis of simulated data sets comprised of varying numbers of boundary traces. The *circles* and *squares* indicate the maximum and minimum values of the distribution for the 45°/[100] misorientation, and the inset shows the grain boundary plane distributions for three of the data sets. The reference frame of these and other projections in the chapter has [001] perpendicular to the plane of the paper and [100] pointing horizontally to the right. The distribution computed from 5×10^4 traces is not significantly different from that determined from 5×10^5 traces

segments. We therefore conclude that 5×10^4 traces are sufficient to reproduce the distribution.

One can also ask how reproducible the values of the peak positions are. When four different randomly generated sets of data were analyzed, each containing 5×10^4 line segments, the peak for the distribution of planes for a misorientation of 45° about [100] ranged from 2.76 MRD to 3.33 MRD. The four values had an average of 3.10 MRD and a standard deviation of 0.27 MRD. Therefore, we conclude that the maxima of the distribution are reproducible within a range of about 10%.

To examine the effect of the step size, we consider a constant set of 5×10^4 traces, confined to 2D, S×S, hexagonal lattices where S = 3, 5, 10, and 50. The results shown in Fig. 16.9 illustrate that there is a negligible difference in the maxima for the distributions determined with 10 and 50 steps per grain diameter. Furthermore, the shapes of the distributions at these two lattice resolutions are nearly identical. Based on this, we conclude that 10 orientation points per grain diameter is sufficient to determine the distribution and that fewer lattice points will lead to underestimates of the maxima.

The results of the simulations described above allow us to provide some practical guidelines for the acquisition and analysis of the EBSD data used to determine the GBCD. The first is that the resolution of the EBSD mapping should be at least 10 points per grain diameter. The second point is that when comparing two GBCDs, differences of less than 10% should be considered insignificant. The third is that at least 5×10^4 grain boundary traces should be recorded to determine the GBCD. This estimate assumes that they are relatively evenly distributed. Note that if too many of the segments arise from a single type of misorientation, then there will be grain boundary configurations that are not sampled. For example, if one third of all the boundaries are coherent twins, then 1.7×10^4 traces will fall in one cell and 3.3×10^4 will be distributed among the remaining 6560 cells. While the grain boundary plane distribution will be well determined for the twin misorientation, it will be underdetermined for all of the other misorientation types.

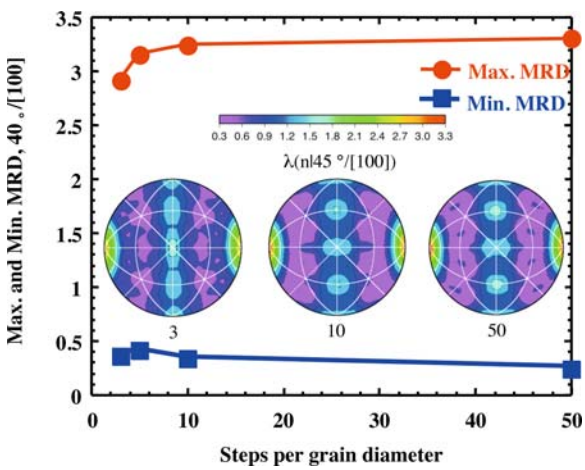


Fig. 16.9 Results from the stereological analysis of simulated data sets with grain boundary traces confined to discrete lattices of different sizes. The *circles* and *squares* indicate the maximum and minimum values of the distribution for the 45°/[100] misorientation and the inset shows the grain boundary plane distributions for three of the data sets. The distribution computed from the 10×10 and 50×50 lattices are nearly identical

16.4.4 Comparison GBCDs Measured Stereologically and by Serial Sectioning in the Dual Beam FIB

Recently, the dual-beam focused ion beam (FIB) scanning electron microscope (SEM) has been used to automate the collection of serial sections of electron backscatter diffraction maps (Konrad et al. 2006; Uchic et al. 2006). Determining the GBCD from such data has been accomplished only recently (Dillon and Rohrer 2008). One of the principal challenges of determining the GBCD from 3D orientation data is the voxelization of the interfaces, which leads to discrete boundary orientations in the sample reference frame. One approach to this problem is to use the grain boundary traces extracted from the individual layers, as described in the previous section. After complementary segments have been identified on adjacent layers, the two end points from one layer and one of the end points from an adjacent layer can be used to form triangular areas that represent the grain boundary. These areas are classified according to their lattice misorientations and grain boundary plane orientations as described above. This approach gives results that are similar to the results of the stereological analysis. This is demonstrated in Fig. 16.10, which shows the distribution of grain boundary planes for the Σ3

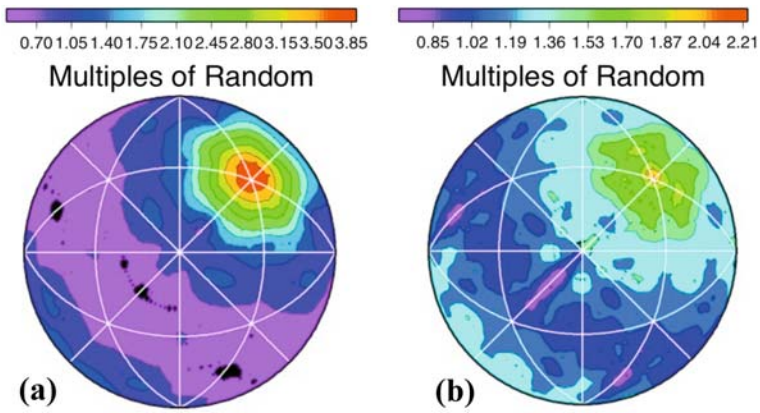


Fig. 16.10 The distribution of grain boundary planes for the Σ3 (60°/[111]) grain boundary in Y_2O_3 computed (**a**) using the conventional stereology and (**b**) from 3D data

(60°/[111]) grain boundary in Y_2O_3 derived by the two techniques. Both methods produce peaks at the position of the (111) twist boundary and are therefore qualitatively similar, but there is a quantitative difference in the intensity. The origin of the difference in the quantitative results is currently being investigated.

16.5 Examples of Five-Parameter Analyses

The five-parameter analysis has been used to measure the misorientation and grain boundary plane distributions of a number of materials and processing variants. These include a range of ceramics, e.g., MgO, NaCl, $SrTiO_3$, TiO_2, WC, $MgAl_2O_4$ (Saylor et al. 2003, 2004a, 2004c; Pennock et al. 2008; Pang and Wynblatt 2005; Kim et al. 2008); and metals, e.g., Al, Cu, Ni, brass, austenitic steels, Ti (Saylor et al. 2004d; Randle et al. 2006, 2008a, 2008b; Downey et al. 2007; Jones et al. 2008). We will describe some of these as illustrations of the five-parameter analysis technique.

The five-parameter grain boundary distribution has been measured on a slightly deformed NaCl (rock salt) specimen, which contained a small quantity of intergranular brine (Pennock et al. 2008). This specimen was of interest because in planar sections the NaCl specimen featured distinct square shaped grains for a wide range of deformation and annealed conditions. A study of grain boundary traces using EBSD showed that the traces of the square shaped grains were within 12° of the trace of {100} planes (Pennock et al. 2006). Figure 16.11 shows a plot of the distribution of boundary planes for the entire sample population, as measured by the five-parameter method. There are peaks at {100}. More information on the distribution of planes is gleaned if sections through the five-parameter space are viewed. For the NaCl distribution low-index, high symmetry misorientation axes [100], [110], and [111] were chosen in addition to [123], which was chosen to represent a low symmetry axis. Figure 16.12 shows the 20° misorientation angle section for these four axes. The misorientation axis is marked on each plot in Fig. 16.12. For each misorientation there are distinct peaks, with maxima for the planes distribution in the range 3.5–4.2 MRD.

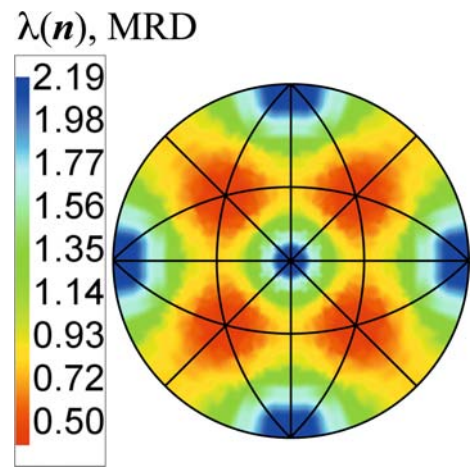


Fig. 16.11 Stereographic projection of grain boundary plane normals from a lightly deformed, wet rock salt specimen

In Fig. 16.12a there are both twist boundaries and asymmetric tilt boundaries along the (100) zone. The distribution of planes along the (100) zone shows that

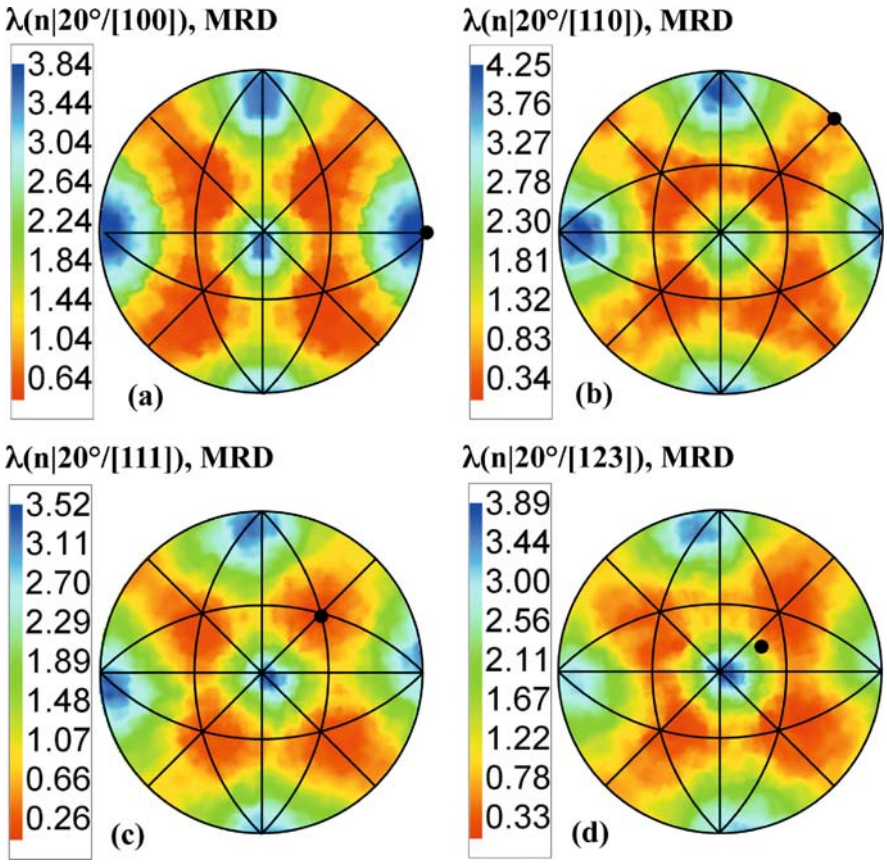


Fig. 16.12 Stereographic projection of grain boundary plane normals from a lightly deformed, wet rock salt specimen for the (**a**) 20°/[100], (**b**) 20°/[110], (**c**) 20°/[111], and (**d**) 20°/[123] misorientations. In each case, the misorientation axis is marked with a *black dot*

one of the interfacing planes is (100) and the counterpart plane in the neighbouring grain is 20° displaced (which it is geometrically required to be) on the (100) zone. The 20°/[110] misorientation section shows no twist or asymmetrical tilt boundaries (Fig. 16.12b). Rather, the planes are close to $\{100\}$, with some spread indicating the presence of the geometrical counterpart to the $\{100\}$ plane on the other side of the interface. A similar result is seen for the 20°/[111] and 20°/[123] sections. It is clear that in these data there is a very strong propensity for $\{100\}$ boundary planes. Previous five-parameter data collected from MgO, using the serial sectioning method, showed similar trends to the data for NaCl (Saylor et al. 2003).

Figure 16.13 shows an example of the five-parameter analysis performed on an alloy with an hcp crystal structure, Ti-6%Al-4%V (Randle et al. 2008a). The alloy had been deformed 10% by cold rolling, and therefore contained deformation twins. Figure 16.13a shows the planes distribution in the deformed specimen for Σ13b, 57.4°/[2 $\bar{1}$ $\bar{1}$ 0]. There is a single, very pronounced maximum of 120 MRD located at the (0 1 $\bar{1}$ 1) plane. It corresponds to the {1 0 $\bar{1}$ 1}< $\bar{1}$ 0 1 2 > twin system of the Σ13b CSL, which is the deformation twin. Figure 16.13b shows the

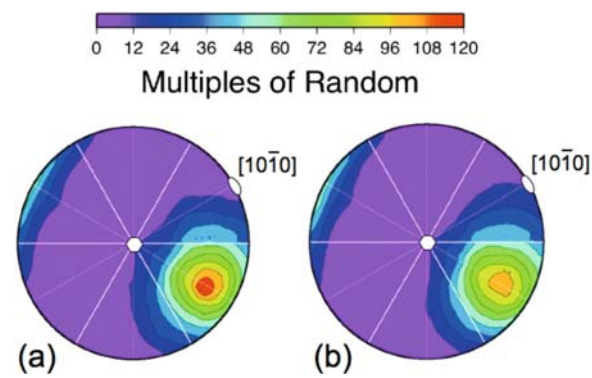


Fig. 16.13 Grain boundary plane distributions for the Σ13b, 57.4°/[2$\bar{1}\bar{1}$0], grain boundaries in deformed Ti-6%Al-4%V specimens (**a**) before and (**b**) after annealing. The [0001] direction is indicated by a *hexagon* and the [10$\bar{1}$0] direction is indicated by an *oval*

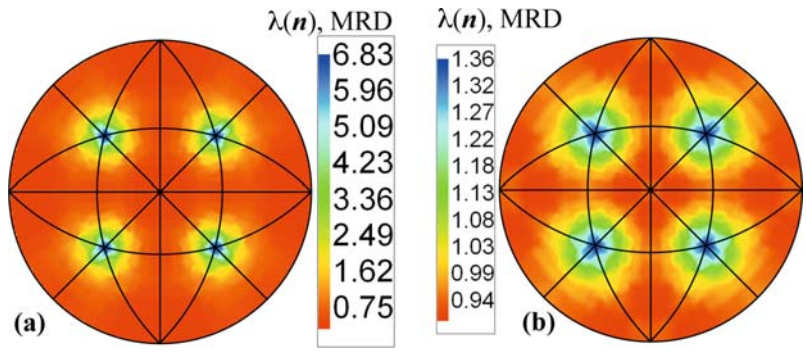


Fig. 16.14 Stereographic projection of grain boundary plane normals from an annealed copper specimen. (**a**) All grain boundaries included. (**b**) All grain boundaries other than Σ3

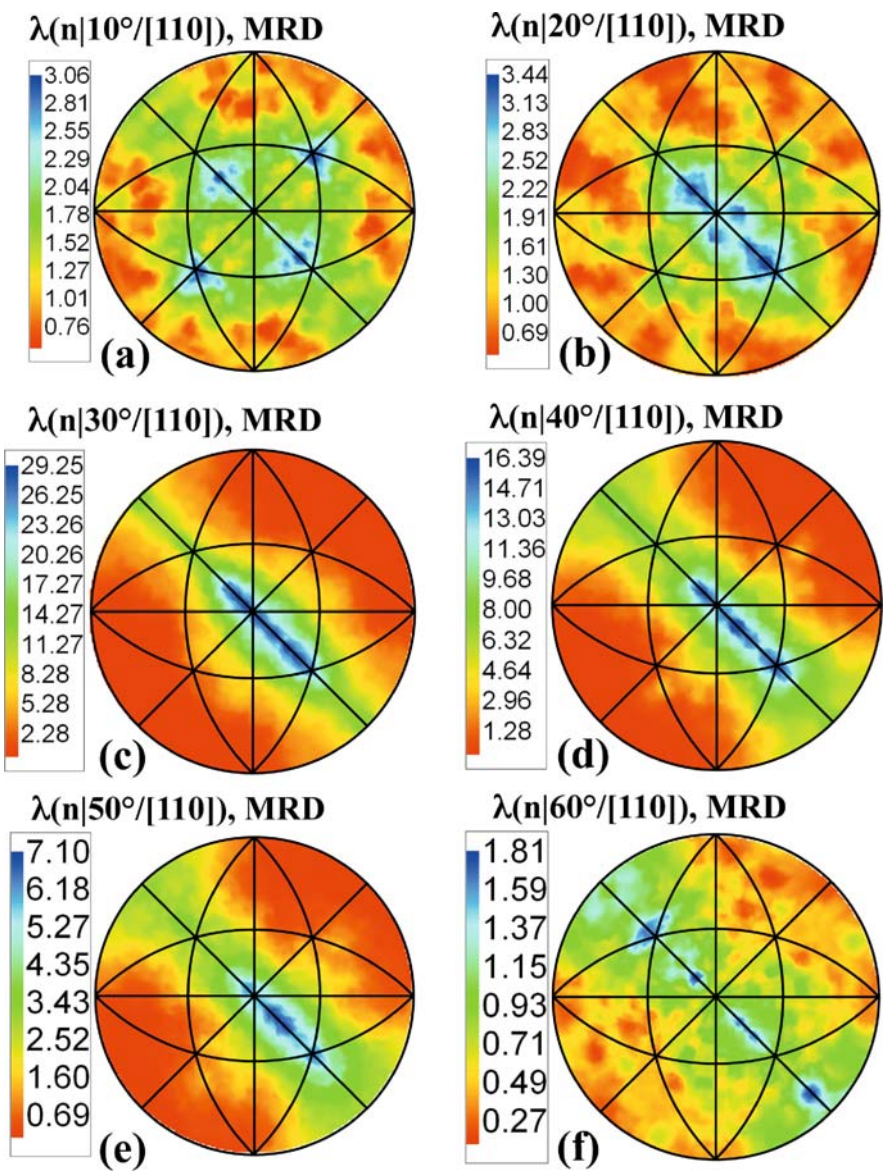


Fig. 16.15 Stereographic projection of grain boundary plane normals from an annealed copper specimen for misorientations about [110], in 10° increments

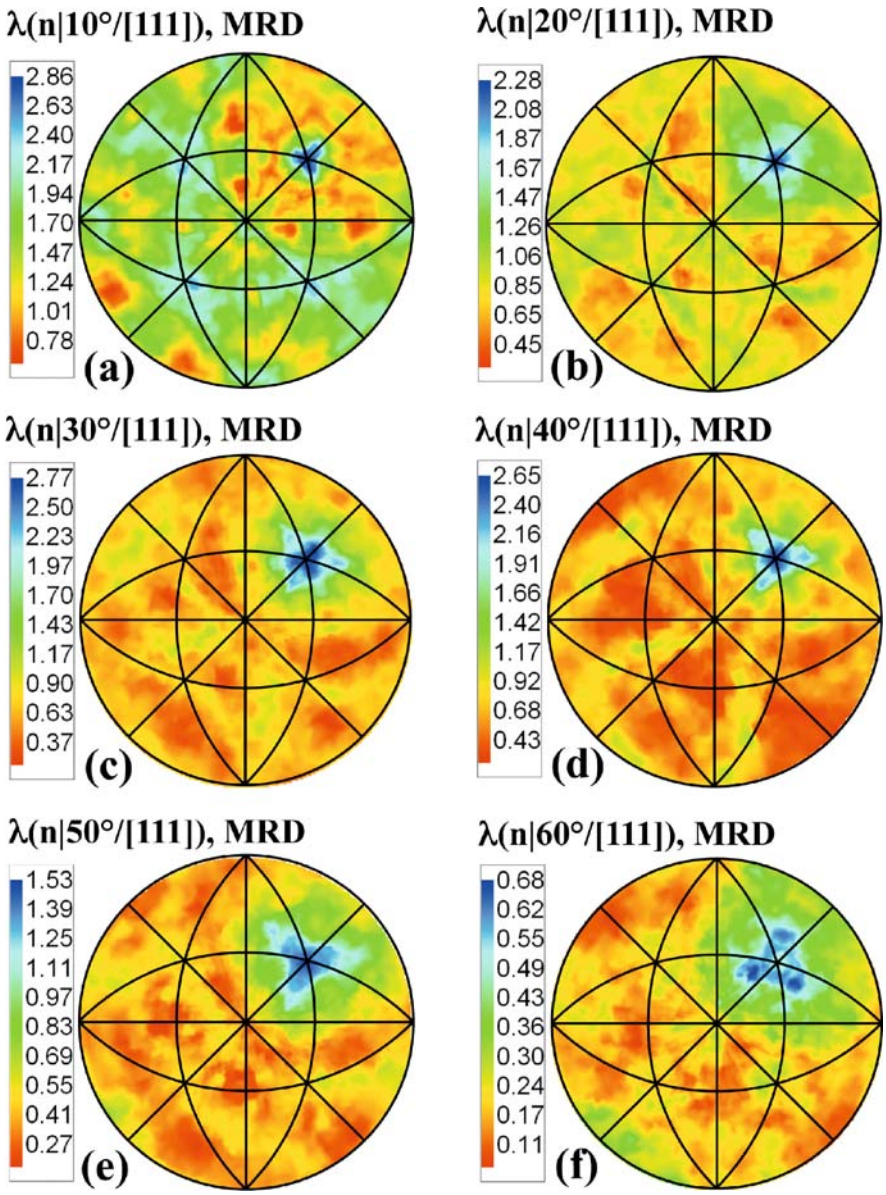


Fig. 16.16 Stereographic projection of grain boundary plane normals from an annealed copper specimen for misorientations on [111], in 10° increments. Σ3 grain boundaries have been excluded from these data and, therefore, the 60° projection is not meaningful

same distribution after annealing. The peak associated with the plane of the deformation twin has decreased marginally.

The five-parameter stereology has been applied extensively to fcc metals and alloys. An example is shown here of annealed copper. Figure 16.14a shows the distribution for all boundaries. There is a strong peak at $\{111\}$, which is largely due to the presence of many coherent annealing twins, where the habit plane is $\{111\}$. 61% of the total interface length was Σ3. However, when all Σ3 boundaries are removed from the data set (Fig. 16.14b), there is still a small peak at $\{111\}$, with a value of 1.36 MRD. Figure 16.15 shows the planes distribution for the <110> misorientation axis, for the entire misorientation angle range (10°–60°). The planes of high angle boundaries are mostly spread along the (110) zone, i.e., they are [110] asymmetrical tilt boundaries. The maxima have high

MRD values, especially in the 30° and 40° sections, which correspond to Σ27 and Σ9 boundaries, respectively. These boundaries are generated as a result of multiple twinning. Figure 16.16 shows the planes distribution for the [111] misorientation axis. On the whole there is a tendency for (111) twist boundaries to predominate, i.e., there are maxima at (111). In both Figs. 16.15 and 16.16, Σ3 boundaries have been omitted. The planes distribution for the [100] misorientation axis is not presented here, because plane densities with values of only one MRD or less were recorded.

There are some striking similarities between all the fcc metals examined so far; for example, the overall planes distribution is always dominated by {111}, even when Σ3 misorientations have been extracted. Also, there are some significant differences depending on the processing route and specific material parameters (Randle et al. 2006, 2008b). The five-parameter data acquired has contributed to our knowledge and understanding of grain boundaries in polycrystals. In particular, the analysis of these and previous results from ceramic materials has led to the suggestion that "special" boundaries are those which terminate on low-index boundary planes (Rohrer et al. 2004). This is in contrast to previous, misorientation-based definitions of a special boundary.

Acknowledgments The work at Carnegie Mellon University was supported primarily by the MRSEC program of the National Science Foundation under Award Number DMR-0520425. The work at Swansea was partially supported by the Engineering and Physical Sciences Research Council.

References

Adams BL (1986) Description of the intercrystalline structure distribution in polycrystalline materials. Metall Trans 17A:2199–2207

Amouyal Y, Rabkin E, Mishin Y (2005) Correlation between grain boundary energy and geometry in Ni-rich NiAl. Acta Mater 53:3795–3805

Cai B, Adams BL, Nelson TW (2007) Relation between precipitate-free zone width and grain boundary type in 7075-T7 Al alloy. Acta Mater 55:1543–1553

Dillon S, Rohrer GS (2008) Characterization of the grain boundary character and energy distributions of yttria using automated serial sectioning and EBSD in the FIB. J Am Ceram Soc (submitted)

Downey ST II, Bembridge N, Kalu PN, Miller HM, Rohrer GS, Han K (2007) Grain boundary plane distributions in modified 316 LN steel exposed at elevated and cryogenic temperatures. J Mater Sci 42:9543–9547

Field DP, Adams BL (1992) Interface cavitation damage in polycrystalline copper. Acta Metall Mater 40:1145–1157

Hilliard JE (1962) Specification and measurement of microstructural anisotropy. T Metall Soc AIME 224:1201–1211

Homer ER, Adams BL, Fullwood DT (2006) Recovery of the grain boundary character distribution through oblique double sectioning. Scripta Mater 54:1017–1021

Jones R, Owen G, Randle V (2008) Carbide precipitation and grain boundary plane selection in overaged type 316 austenitic stainless steel. Mater Sci Eng A496:256–261

Kim C-S, Massa TR, Rohrer GS (2008) Interface character distributions in WC-Co composites. J Am Ceram Soc 91:996–1001

Konrad J, Zaefferer S, Raabe D (2006) Investigation of orientation gradients around a hard Laves particle in a warm-rolled Fe_3Al-based alloy using a 3D EBSD-FIB technique. Acta Mater 54:1369–1373

Larsen RJ, Adams BL (2004) New stereology for the recovery of grain-boundary plane distributions in the crystal reference frame. Metall Trans 35A:1991–1998

Lejcek P, Hofmann S, Paidar P (2003) Solute segregation and classification of [100] tilt grain boundaries in α-iron: consequences for grain boundary engineering. Acta Mater 51:3951–3963

Miyamoto H, Ikeuchi K, Mimaki T (2004) The role of grain boundary plane orientation on intergranular corrosion of symmetric and asymmetric [110] tilt grain boundaries in directionally solidified pure copper. Scripta Mater 50:1417–1421

Moraweic A (2004) Orientation and rotations: Computations in crystallographic texture. Springer Verlag, Berlin

Pang Y, Wynblatt P (2005) Correlation between grain-boundary segregation and grain-boundary plane orientation in Nb-doped TiO_2. J Am Ceram Soc 88:2286–2291

Pennock GM, Drury MR, Spiers CJ (2006) Grain boundary populations in wet and dry NaCl. Mater Sci Tech 22:1307–1315

Pennock G, Coleman M, Drury M, Randle V (2008) Grain boundary plane populations in minerals; the example of wet NaCl after low strain deformation. Contrib Mineral Petr (in press)

Randle V (1995) Crystallographic characterisation of planes in the scanning electron microscope. Mater Charact 34:29–34

Randle V (1997) The role of the grain boundary plane in cubic polycrystals. Acta Mater 46:1459–1480

Randle V (2001) A methodology for grain boundary plane assessment by single trace analysis. Scripta Mater 44:2789–2794

Randle V, Davies H (2002) A comparison between three-dimensional and two-dimensional grain boundary plane analysis. Ultramicroscopy 90:153–162

Randle V, Rohrer G, Kim C, Hu Y (2006) Changes in the five-parameter grain boundary character distribution in alpha-brass brought about by iterative thermomechanical processing. Acta Mater 54:4489–4502

Randle V, Rohrer G, Hu Y (2008a) Five-parameter grain boundary analysis of a titanium alloy before and after low temperature annealing. Scripta Mater 58:183–186

Randle V, Rohrer GS, Miller HM, Coleman M, Owen GT (2008b) Five-parameter grain boundary distribution of com-

mercially grain boundary engineered nickel and copper. Acta Mater 56:2363–2373
Rohrer GS, Saylor DM, El Dasher B, Adams BL, Rollett AD, Wynblatt P (2004) The distribution of internal interfaces in polycrystals. Z Metallkd 95:197–214
Saylor DM, Rohrer GS (2002) Determining crystal habits from observations of planar sections. J Am Ceram Soc 85:2799–2804
Saylor DM, Morawiec A, Rohrer GS (2003) Distribution of grain boundaries in magnesia as a function of five macrosopic parameters. Acta Mater 51:3663–3674
Saylor DM, El Dasher B, Sano T, Rohrer GS (2004a) Distribution of grain boundaries in $SrTiO_3$ as a function of five macroscopic parameters. J Am Ceram Soc 87:670–676
Saylor DM, El Dasher B, Adams BL, Rohrer GS (2004b) Measuring the five-parameter grain-boundary distribution from observations of planar sections. Metall Mater Trans A 35:1981–1989
Saylor DM, El Dasher B, Pang Y, Miller HM, Wynblatt P, Rollett AD, Rohrer GS (2004c) Habits of grains in dense polycrystalline solids. J Am Ceram Soc 87:724–726
Saylor DM, El Dasher B, Rollett AD, Rohrer GS (2004d) Distribution of grain boundaries in aluminium as a function of five macrosopic parameters. Acta Mater 52:3649–3655
Uchic MD, Groeber MA, Dimiduk DM, Simmons JP (2006) 3D microstructural characterization of nickel superalloys via serial-sectioning using a dual beam FIB-SEM. Scripta Mater 55:23–31
Wolf D, Lutsko JF (1989) On the relationship between tilt and twist grain boundaries. Z Kristallogr 189:239–262
Wright SI, Larsen RJ (2002) Extracting twins from orientation imaging microscopy scan data. J Microsc 205:245–252
Wynblatt P, Takashima M (2001) Correlation of grain boundary character with wetting behaviour. Interface Sci 9:265–273

Chapter 17

Strain Mapping Using Electron Backscatter Diffraction

Angus J. Wilkinson, David J. Dingley, and Graham Meaden

17.1 Introduction

In this chapter we review the progress that has been made toward elastic strain (i.e., stress) mapping using electron backscatter diffraction. In particular we focus on development of an analysis method based on using cross-correlation to determine small shifts in the EBSD patterns with respect to a reference pattern. The pattern shifts are determined at many subregions dispersed across the wide angular span of the EBSD pattern, and the magnitude and angular distribution of shifts allows the strain and rotation tensor to be determined. Pattern shifts at a resolution of ± 0.05 pixels, or in some cases even better, have been reported, which corresponds to a sensitivity of $\sim \pm 10^{-4}$ in the components of the strain and rotation tensor.

17.1.1 The Need for Local Strain Assessment

The need to know the local state of stress and strain in a region of material is of the utmost importance in a wide range of applications, from semiconductor structures and devices to structural engineering components. In strained-Si devices local strain states are purposely designed into the active channel region so as to provide performance benefits. However, in other situations, such as near various isolation structures, the strains must be kept small so as to prevent generation of dislocations which can catastrophically degrade the device response. In structural materials local strain enhancements near microstructural features, such as inclusions, precipitates, and grain boundaries, need to be studied if the deformation and failure process are to be understood. The desire for experimental methods with which to measure and map localised strain distributions is pervasive in the materials sciences.

17.1.2 Competing Strain Mapping Techniques

Figure 17.1 shows the approximate length scales and strain sensitivities achieved by a variety of strain measurement techniques.

Hole drilling and other material removal techniques have been widely used by engineers in the macroscopic regime; they rely on the monitoring of strain

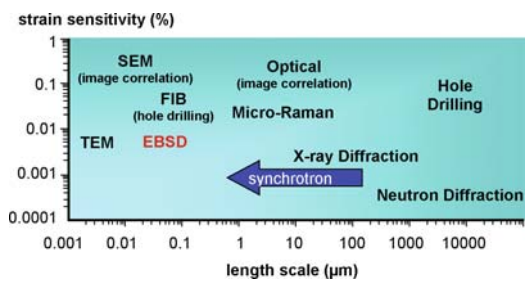


Fig. 17.1 Approximate length scales and strain sensitivities offered by a range of strain analysis techniques. Those towards the *bottom left* combine superior spatial resolution with superior strain sensitivity

A.J. Wilkinson (✉)
Department of Materials, University of Oxford, Parks Road, Oxford OX1 3PH, UK
e-mail: angus.wilkinson@materials.ox.ac.uk

A.J. Schwartz et al. (eds.), *Electron Backscatter Diffraction in Materials Science*,
DOI 10.1007/978-0-387-88136-2_17, © Springer Science+Business Media, LLC 2009

or displacements that are induced in components due to relaxation of residual stresses generated at newly exposed free surfaces. This approach has recently been adapted to the micro- and nanoscale by using a focused ion beam (FIB) for the material removal and SEM or FIB imaging to monitor the resulting displacements (Kang et al. 2003; Sabate et al. 2006).

X-ray diffraction is perhaps the most well developed of techniques for internal strain measurement (see, e.g., Bowen and Tanner 1995). Lattice parameters and hence strains of the order of 1 part in 10^5 can be determined using X-rays; however, the spatial resolution of laboratory based experiments is at best on the order of 100 microns. The use of synchrotron sources can lead to considerable improvement in spatial resolution; however, users have to bear the expense and inconvenience of a large central facility (e.g., Tamura et al. 2002; Di Fonzo et al. 2000). Neutron diffraction also offers high strain sensitivity, and unlike X-rays, can be used to sample volumes of material deep within the sample (Stone et al. 1999). However, the spatial resolution is generally below the length scale of the microstructure or device to be investigated, so that only volume-averaged strain values can be obtained.

A range of powerful spectroscopic techniques has been used for analyzing strain in semiconductor and polymeric structures. These methods rely on a strain-induced shift of peaks in luminescence (Yamaguchi et al. 1990) or micro-Raman (Dietrich et al. 1993; Young 1997) spectra, and as such are indirect measurements of strain, which generally do not lend themselves to determination of the entire strain tensor. In addition, these techniques are often limited by diffraction to spatial resolutions of a little less than a micrometer.

The image correlation method can be used with images obtained by a variety of microscopic imaging methods, most typically optical and SEM (which offers a higher spatial resolution). In early work the strain sensitivity was estimated to be only 1 part in 100 (Davidson 1991; Kinaev et al. 1999), but more recently improved algorithms have enhanced the sensitivity by about an order of magnitude (Da Fonseca et al. 2005). However, because strains are determined by comparing the relative positions of features in a pair of images, the method cannot determine strains caused by processing or loading that occurred prior to the capture of the first image.

The strong interaction between electrons and matter, coupled with the ability to make fine electron beams, naturally leads to electron-based methods having good spatial resolution. TEM-based diffraction methods offer a powerful combination of very high spatial resolution and good strain sensitivity. Convergent beam electron diffraction (CBED) has perhaps been the most widely employed technique, (Maier et al. 1996).

However, the need for a thin foil is a major limitation that is very difficult to overcome. The stress state in the thin foil is often highly relaxed compared to the original bulk sample, and it is at best difficult to undertake in situ loading with any real degree of control.

This chapter will show that EBSD can provide a means of determining local strains with an attractive combination of high spatial resolution and good strain sensitivity. Furthermore, EBSD does not suffer from the need for a thin foil that limits the CBED method.

17.1.3 Review of Applications of EBSD to Analysis of Elastic Strains

Despite early attempts to obtain elastic strain information from EBSD patterns by Troost et al. (1993) and Wilkinson (1996, 1997) over a decade ago, progress has been relatively slow. However, there are clear signs that there is much more activity in this area in the last few years.

Many researchers have attempted to use a simple measurement of the Kikuchi band width to determine the Bragg angle, and through that, the lattice plane spacing. Such an approach has been implemented in the analysis of electron channelling patterns (ECPs) in which higher order features can be seen (Madden and Hren 1985; Kozubowski et al. 1991). However, Wilkinson (1997) noted that such high order features tend not to be present in EBSD patterns, and so the approach cannot attain the precision required to enable strain measurement.

Keller et al. (2004) used EBSD to investigate strain fields near the tip of an oxidation front produced along an $Al_{0.98}Ga_{0.02}As$ layer within an $Al_{0.98}Ga_{0.02}As/GaAs$ multilayer in a VCSEL laser prototype structure. They too concluded that measurement of Kikuchi band widths could only achieve a strain sensitivity

of ∼0.2%, but noted that severe elastic strain gradients caused blurring and reduction in contrast in the patterns. They then used the pattern quality index within commercial EBSD software to determine the spatial extent of the severe strains and strain gradient fields caused by the volume increase associated with the layer oxidation, finding agreement with finite element simulations. Luo et al. (2006) tried to follow the approach of Keller et al. in analyzing strain gradients in MOCVD-grown GaN films on sapphire using cross-sectional samples. Wu et al. (2007) and Fan et al. (2007) have also examined pattern quality variation in cross-sectioned semiconductor heterostructures (wafer-bonded GaN on GaAs, and epitaxial InGaAsP/InP, respectively) in attempts to image the spatial extent of severely strained material. Of these studies, that of Keller et al. is the most convincing and correctly emphasizes the point that it is strain gradients within the diffracting volume, rather than the mean strain, that are significant for pattern blurring. Quantification will always remain difficult with this approach, and is exacerbated by effects from surface topography frequently encountered in cleaved cross sections of heterostructures, changes in material (atomic number, Debye-Waller factors, etc.), and surface contamination.

An interesting approach to extracting higher resolution measurements from EBSD patterns and Kossel patterns has been made by Maurice and Fortunier (2008). They have suggested modifying the two-dimensional Hough transform conventionally employed in orientation measurements to a three-parameter Hough transform which accounts for the hyperbolic nature of the Kikuchi band edges. Working on simulated EBSD patterns, they demonstrate that this three-dimensional Hough transform allows greater precision in locating the Kikuchi bands, and so allows measurement of the distortion of the lattice away from the expected lattice parameters and angles. They state that strain imposed on the simulated patterns can be measured to $\sim 2 \times 10^{-4}$. Measurements on real patterns are yet to be reported, but possible factors that may affect such measurements include noise, especially as the analysis makes use of derivatives of the EBSD patterns, and intensity asymmetries across the bands (see Chapter 2 by Aimo Winkelmann) not accounted for in the semi-empirical pattern simulations used. These factors are likely to reduce the strain sensitivity found in their proof of concept analysis, but the methodology is novel and shows promise.

The most mature EBSD strain measurement methodology is the cross-correlation-based pattern shift analysis. This approach had its beginnings in the early work by Troost et al. (1993) and Wilkinson (1996, 1997), and has culminated in the development of a general and user friendly tool in the work of Wilkinson et al. (2006a, 2006b). The approach relies on the fact that elastic strains and small rotations cause small shifts in features, such as zone axes, within the EBSD patterns and that these can be measured using cross-correlation techniques and related to the strain and rotation tensor.

The approach is described in detail in Section 17.2 below, but here we briefly review the literature relating to the method.

Initial work made use of a large specimen-to-screen distance to enhance the angular resolution to the level required to enable strain measurement. This resulted in a small capture angle for the EBSD system so that the pattern shifts had to be measured one zone axis at a time. This necessitated the use of simplifying assumptions about the nature of the strain state in order to mitigate against the experimental difficulties of making multiple scans of the same region of the sample after reorienting it to bring different zone axes onto the EBSD detector. Although Wilkinson (2000a) presented the analysis for the general case of an arbitrary rotation and strain tensor requiring measurements of pattern shifts at four distinct regions of the pattern, measurements were essentially limited to consideration of the simplified cases of tetragonal distortion (Wilkinson 1996), and generalized plane strain (Wilkinson 2000b). Early implementations of the method used a small capture angle geometry. Making measurements at four distinct regions of the pattern therefore required collecting patterns from the same region with the sample in four different orientations. This led to considerable errors in some of the components of the displacement gradient tensor, as is evident in the data presented in Wilkinson (2000c).

Wilkinson (2001) returned to the more common large capture angle EBSD geometry and showed that it was possible to use cross-correlation analysis to determine small angle misorientations to 0.02°, an improvement of over an order of magnitude from Hough transform-based analysis. Furthermore, the misorientation axis was also retained to ±2° for misorientations

above about 0.5° in angle. This is markedly better than the situation for the Hough-based analysis, for which little information concerning the axis is available for misorientations below ~5° (Prior 1999). Bate et al. (2005) gave an analytical relationship showing the rapid increase in the error in determining the direction of the misorientation axis that results as the misorientation angle is decreased at some fixed orientation measurement error; this fits well with experimental data. They also implemented a cross-correlation analysis, similar to that of Wilkinson (1999, 2001), and used it to determine the rotations within grains of deformed and recovered Al samples.

Tao and Eades (2005) have also explored cross-correlation measurement of shifts in both EBSD patterns and their Hough transforms, although they did not relate these shifts to strains and rotations within the sample. They claimed that implementing the cross-correlation analysis in the ρθ Hough transform space had advantages over analysis of the patterns directly. However, avoidable artifacts were present in their cross-correlation functions generated by analysis of the patterns directly, which were suppressed when using the Hough transform of the patterns. This appears to have led them to a false conclusion. The current authors, and Bate et al. (2005), have independently examined cross-correlation of the Hough transforms, and can find no advantage in it over direct comparison of the EBSD patterns; however, one clear disadvantage is apparent, namely, the considerable increase in computation time.

Landon et al. (2008) have implemented the method described by Wilkinson et al. (2006). Their interest is in the deformation of metals and in recovery of the geometrically necessary dislocation (GND) density, using their extension of the analyses by Nye (1953) and Kröner (1958). They confirm the strain and rotation sensitivity reported by Wilkinson et al. (2006a, 2006b); and from measurements on well annealed Ni using 40 nm steps, they show that this can lead to recovery of the GND content to a level of 2×10^{-7} m^{-2}.

Miyamoto et al. (2007) have produced a variant of this method using phase correlation rather than cross-correlation to determine the pattern shift. Although to date the sensitivity achieved is a little lower, it is clearly much more sensitive than the conventional Hough-based analysis. They successfully used the method to measure the lattice curvature and strains induced by martensitic transformations in various model ferrous systems chosen to represent different martensite morphologies.

Several other groups are now using the CrossCourt software developed by Wilkinson et al. (2006a, 2006b). Ishido et al. (2007) have reported some of their measurements on cross-sectional samples of various and AlGaN/GaN heterostructures grown by MOCVD on Si substrates. In one sample, a multilayer consisting of 50 repeats of 5 nm AlN and 25 nm GaN was used to improve the quality of the subsequently grown thick 800 nm GaN layer. Strain variations between these layers are evident across the 50 repeats of the multilayer, giving strong evidence that high spatial resolution is achieved. The amplitude of the strain variation between the layers has not been corrected for the difference in c/a ratio for the unrelaxed, stress-free, AlN, compared to the reference GaN pattern used.

Vaudin et al. (2008) have made measurements of residual strains near indents in Si. These test samples have allowed direct and detailed comparison of EBSD with micro-Raman measurements. The micro-Raman measurements allow access to only the in-plane biaxial stress, though by varying the wavelength of the incident illumination, different depths can be probed within the sample. Results from the two methods converge as the sampling depth of the micro-Raman method is reduced. Such comparisons help provide confidence in the comparatively new EBSD method.

17.2 Cross-Correlation-Based Analysis of EBSD Patterns

17.2.1 *Geometry: Linking Pattern Shifts to Strain*

Figure 17.2 shows how an arbitrary strain and rigid body rotation changes a direction **r** in the reference crystal to **r** ín the strained crystal. Let **A** be the strain gradient tensor describing the deformation mapping **r** onto **r**,́so that

$$\mathbf{A} - \mathbf{I} = \begin{pmatrix} \frac{\partial u_1}{\partial x_1} & \frac{\partial u_1}{\partial x_2} & \frac{\partial u_1}{\partial x_3} \\ \frac{\partial u_2}{\partial x_1} & \frac{\partial u_2}{\partial x_2} & \frac{\partial u_2}{\partial x_3} \\ \frac{\partial u_3}{\partial x_1} & \frac{\partial u_3}{\partial x_2} & \frac{\partial u_3}{\partial x_3} \end{pmatrix}, \qquad (17.1)$$

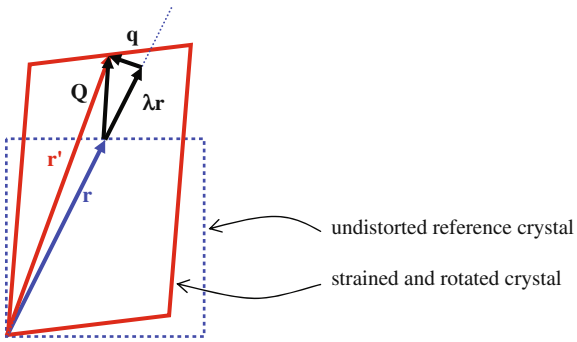


Fig. 17.2 Schematic diagram showing how a strain and rotation (exaggerated) act to alter a zone axis direction **r** shifting across the EBSD screen by **q**

and

$$\mathbf{r}' = \mathbf{A}\mathbf{r}, \tag{17.2}$$

where u_i and x_i are respectively the components of the displacements and positions along the *i*th axis. The displacement caused by the strain and rotation is shown as **Q** in Fig. 17.2 and is related to **A** by:

$$\mathbf{Q} = \mathbf{r}'—\mathbf{r} = (\mathbf{A} - \mathbf{I})\mathbf{r} \tag{17.3}$$

However, the EBSD technique only measures the projection of **Q** perpendicular to the direction **r** for which we find it convenient to work with the vector denoted by **q** in Fig. 17.2. We can write:

$$\mathbf{q} = \mathbf{Q}—\lambda\,\mathbf{r} = \{\mathbf{A}—(\lambda + 1)\mathbf{I}\}\mathbf{r}, \tag{17.4}$$

where λ is an unknown scalar. Thus measurement of **q** for a given **r** gives three equations from which λ can be eliminated to leave two equations in eight variables:

$$r_2 r_3 \left[\frac{\partial u_2}{\partial x_2} - \frac{\partial u_3}{\partial x_3}\right] + r_1 r_3 \frac{\partial u_2}{\partial x_1} + r_3^2 \frac{\partial u_2}{\partial x_3} - r_1 r_2 \frac{\partial u_3}{\partial x_1} - r_2^2 \frac{\partial u_3}{\partial x_2} = r_3 q_2 - r_2 q_3 \tag{17.5a}$$

$$r_1 r_3 \left[\frac{\partial u_1}{\partial x_1} - \frac{\partial u_3}{\partial x_3}\right] + r_2 r_3 \frac{\partial u_1}{\partial x_2} + r_3^2 \frac{\partial u_1}{\partial x_3} - r_1^2 \frac{\partial u_3}{\partial x_1} - r_2 r_1 \frac{\partial u_3}{\partial x_2} = r_3 q_1 - r_1 q_3 \tag{17.5b}$$

Measuring **q** for four widely spaced directions, **r** then allows the values of $\frac{\partial u_1}{\partial x_2}$, $\frac{\partial u_2}{\partial x_1}$, $\frac{\partial u_1}{\partial x_3}$, $\frac{\partial u_3}{\partial x_1}$, $\frac{\partial u_3}{\partial x_2}$, $\frac{\partial u_2}{\partial x_3}$, $\left[\frac{\partial u_1}{\partial x_1} - \frac{\partial u_3}{\partial x_3}\right]$ *and* $\left[\frac{\partial u_2}{\partial x_2} - \frac{\partial u_3}{\partial x_3}\right]$ to be determined. However, measurement of **q** for additional directions does not provide the information necessary to separate the terms $\frac{\partial u_1}{\partial x_1}$, $\frac{\partial u_2}{\partial x_2}$, *and* $\frac{\partial u_3}{\partial x_3}$. This is because the final degree of freedom in the tensor A is the hydrostatic dilatation or contraction of the lattice. This cannot be obtained directly using the current method, since a simple change of lattice parameter generates no change in the angles between different zone axes and so does not cause any shifts in the EBSD pattern. This last degree of freedom can be recovered by imposing boundary conditions required from the simple mechanical concept of equilibrium. EBSD measurements come from very close to the free surface of the sample (within, say, 10–20 nm), where it is reasonable to assume that the proximity of the free surface ensures that the stress σ33 normal to the surface is brought to zero to meet equilibrium conditions. If we impose this condition and use Hooke's law to write the stress in terms of strains and elastic stiffness constants C_{ij}, then we have a further equation allowing separation of all three normal strains. This gives full determination of the displacement gradient tensor (i.e., strains and rotations), assuming that the elastic constants are known for the crystal under investigation.

In most of our work, we measure the pattern shift q at many more (typically 15 to 20) than the minimum four directions r required, and use least squares methods to obtain a "best fit" solution for the displacement gradient tensor A. This approach reduces the noise somewhat and also provides a means of assessing the quality of the measurement. This is done by using the best fit solution to calculate the expected angular shift at each of the selected subregions of the pattern. The absolute difference between the measured and expected angular shifts is then averaged over all the subregions to give a mean angular error for the measurement. In most instances, good quality patterns, obtained using a ~1 megapixel camera at full resolution, allow a mean angular error of 10^{-4} radians or less to be obtained.

17.2.2 Pattern Shift Measurement

At the heart of the method is the use of cross-correlation analysis to determine pattern shifts, i.e., relative positions of common diffraction contrast features

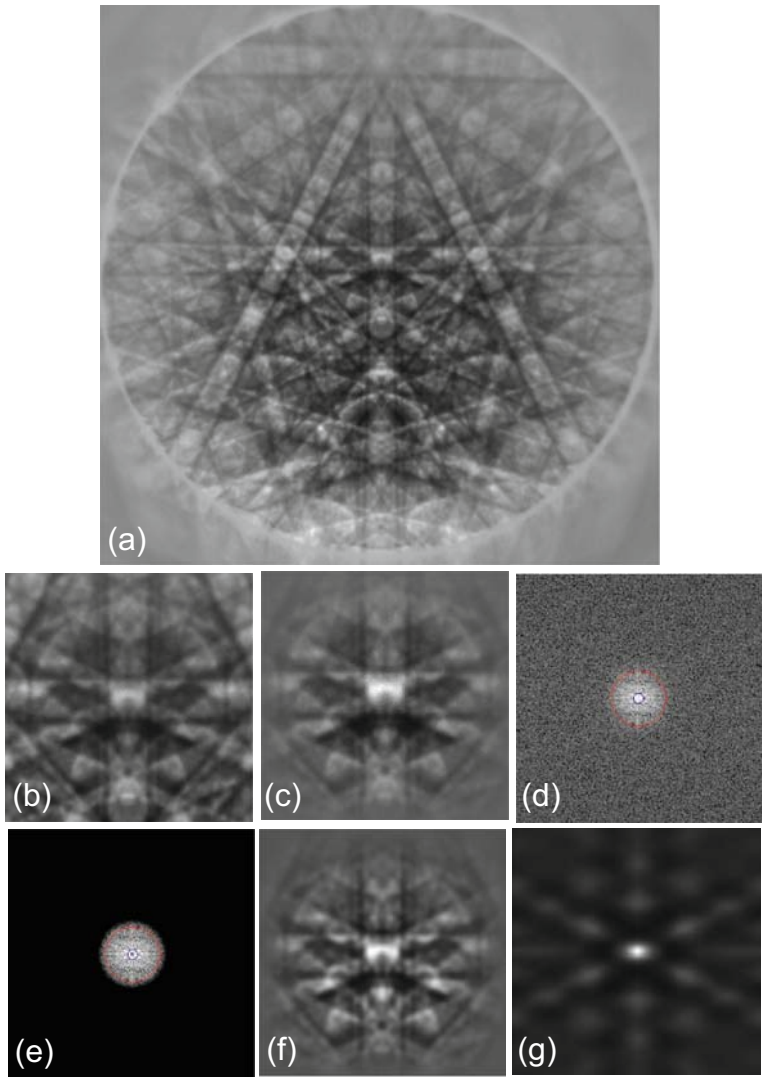


Fig. 17.3 (**a**) EBSD pattern recorded from GaN, (**b**) subregion extracted for analysis, (**c**) intensity and contrast brought smoothly to zero at edges using weighting function (Equation 17.6), (**d**) Fourier transform of weighted subregion, (**e**) application of band pass filter to Fourier transform, (**f**) back transform of filtered Fourier transform, (**g**) cross-correlation with second pattern (after similar preprocessing)

in the test EBSD pattern compared to a reference pattern. These pattern shifts are obtained at subpixel resolution, which is in line with the use of cross-correlation for image matching in other fields (e.g., Da Fonseca et al. 2005; Fincharm and Spedding 1997). The steps are outlined in Fig. 17.3.

The cross-correlation functions were calculated at numerous widely-dispersed subregions of pairs of EBSD patterns extracted at exactly the same place in the CCD camera image. The size of the subregions can be varied, but we typically used subregions measuring 256×256 pixels. For each subregion the mean intensity is first determined, and then subtracted from every pixel, so as to bring the new mean to zero. The resulting intensities were then multiplied by the following weighting function:

$$f(x, y) = \cos\left(\frac{\pi x}{256}\right) \cos\left(\frac{\pi y}{256}\right), \qquad (17.6)$$

where x and y give the pixel position relative to an origin at the centre of the subregion. This brings intensities smoothly to zero at the edges of the subregion and helps prevent aliasing/leakage problems when fast Fourier transforms of each subregion are calculated. The weighting function also means that the pattern shift measurement is dominated by the central part of the subregion, i.e., its effective size is rather smaller than is at first apparent (compare b and c in Fig. 17.3). The cross-correlation function is then the inverse Fourier transform of the product of the Fourier transform of one subregion and the complex conjugate of the Fourier transform of the second subregion. Use of Fourier transforms in calculating the cross-correlation function is computationally faster than direct calculation, given the size of the subregions used here. In Fig. 17.3 g the cross-correlation function is represented as an intensity distribution in which the ordinates are in pixels. The intensity at a point in the distribution represents the degree of correlation between the first (undisplaced) image and the second (displaced) image. The magnitude and direction of the displacement is given by the vector defining the point with respect to the centre of the image. The point with maximum intensity is that of maximum correlation between the two images.

Although not required to calculate the strain and rotation, the height of the cross-correlation peak is useful in assessing the quality of the data produced. In our analysis we use the peak height information as follows. For a given subregion, the peak heights are normalised to bring the peak height for the reference pattern (auto-correlation) to unity. The geometric mean of normalised peak heights for all subregions on a pattern then gives a useful parameter indicating the quality of the match to the reference pattern. Where patterns are of poor quality because of surface contamination or severe plastic deformation, or where they show shadowing from surface topography, the mean peak height is low. Mean peak height values below $\sim$0.25 are indicative of problems with the test pattern. Data sets can of course be filtered, by comparing the mean peak heights to a threshold value.

Care must be taken to remove the influence of defects in the phosphor screen from the EBSD pattern, because such features remain in exactly the same position from pattern to pattern regardless of strain in the sample, and so can lead to artifacts in the analysis. We therefore "flat field" all the patterns using standard background subtraction methods. However, we also may take advantage of the fact that the Fourier transforms of the subregions are calculated in determining the cross-correlation functions, and can use filtering in the frequency domain to improve our results. Removing high frequency components from the analysis has been shown (Wilkinson et al. 2006a) to reduce the scatter in the pattern shift measurements by removing random noise from the patterns.

The CrossCourt software[1] also allows for removal of low frequency components and this has proved useful in situations where pattern overlap is encountered at grain boundaries (Clarke 2008), or where surface topography causes changes in the background intensity variation.

17.2.3 Sensitivity Analysis

We have been careful to assess the sensitivity of the method in several ways. The first of these tests is to simply deflect the incident beam across the surface of a high quality single crystal sample and to note that this should induce a shift of the entire pattern across the scintillator screen. Measurement of pattern shifts at many subregions should yield a mean pattern shift that varies linearly with the distance through which the incident beam is deflected, and the deviation in shifts measured at all subregions of a given pattern gives an indication of the extent of scatter in the measurements. Fig. 17.4 shows the mean of pattern shifts measured at 20 subregions of EBSD patterns obtained from a GaAs single crystal as the beam is displaced by $\pm 10\,\mu$m in 1 μm steps. Error bars indicate the standard deviation in shifts measured at the different subregions of each pattern and are on average 0.02 pixels, which corresponds to an angle of 4×10^{-5} rads at the pattern centre. The improvement compared to the somewhat larger value initially reported by Wilkinson et al. (2006a) is simply due to the better signal-to-noise ratio in the patterns analyzed here. Indeed, Wilkinson et al. (2006a) discuss the influence of noise, filter settings, and size

[1] Further information concerning CrossCourt software is available from BLG Productions Ltd, Bristol, UK (www.blgproductions.co.uk)

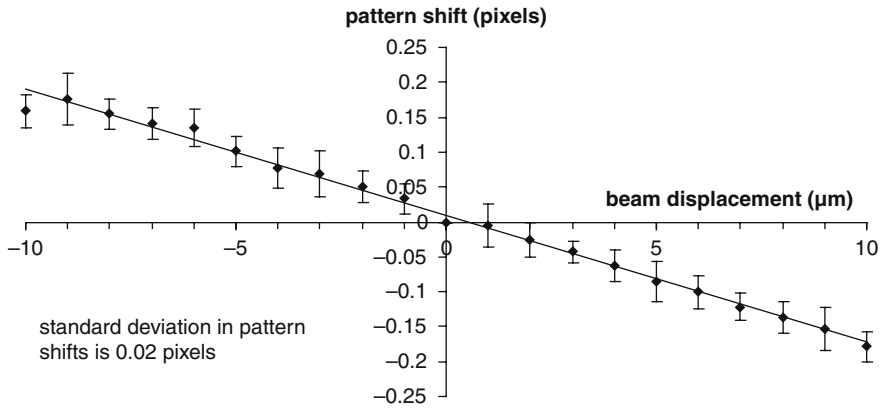


Fig. 17.4 Sub-pixel pattern shifts induced by displacement of incident electron beam across a GaAs single crystal

of the subregions on the resulting scatter in the pattern shift measurements.

It should be noted that the pattern shifts induced by the incident beam displacement are uniform across the whole EBSD pattern, while strains and rotations will cause shifts that vary across the pattern. In general there will be some variation in the pattern shift across each of the subregions, which may tend to reduce the resolution of the average pattern shift for a given subregion. We have also therefore used externally applied rotation of an unstrained single crystal as a further test of the method. Figure 17.5 shows results from such an experiment on a GaAs single crystal that was rotated about its surface normal (the x_3 axis) from –5° to 0° in 0.5° steps and then on to +5° in 1° steps. At each sample orientation a set of 11 patterns were taken from the sample using the full resolution of the camera. Figure 17.5 shows the results obtained using shifts measured at 15 subregions on each pattern. The mean values show the dominant rotation component is as expected w_{12}, and that the measured values are close to the nominal applied ones. The other two rotation components remain much smaller, and the slight variations are probably due to inaccuracies in aligning the sample within the SEM. Perhaps more important is the lower plot in Fig. 17.5 which shows the extent of scatter in the measured rotations, which increases from $\sim 5\times10^{-5}$ rads at zero rotation to $\sim 1.5\times10^{-4}$ rads for applied rotations as large as 5° (87 mrad). Also shown on this lower plot is the mean angular error associated with the best fit solution. This too increases with the size of the applied rotation from $\sim 6\times10^{-5}$ rads at zero rotation to $\sim 6\times10^{-4}$ rads at 5° rotation. Further studies of this kind indicate that the pattern shift measurements begin to become unreliable if the applied rotation is larger than ~8°. Such rotations generate large shifts and changes in the intensity distributions within the EBSD patterns, and the cross-correlation analysis begins to fail in some of the subregions, leading to erroneous results, which are made obvious by a significant increase in the mean angular error.

The sensitivity of the results to calibration parameters in the EBSD projection geometry (i.e., pattern centre and specimen-to-screen distance) has also been examined. For example, Fig. 17.6 shows the effects of altering the x position of the pattern centre location on rotations measured using the cross-correlation-based analysis. The plots are for four different nominal rotations of 0°, 0.5°, 1°, and 2° applied to a single crystal Si sample. It is seen that very large calibration errors are required to make any significant impact on the rotation measurements. A 10% change in the pattern centre location induces changes in the measured rotation angles that are less than 1% of the expected value. Calibration using Hough-based analysis within an iterative scheme aimed at minimizing the errors in interplanar angles typically results in pattern centre determination to better than ±1%. Systematic errors from detector geometry are thus seen to be smaller than random errors from the pattern shift measurement, for the regime of small angle rotation and elastic strains that is of most significance for the application of this method.

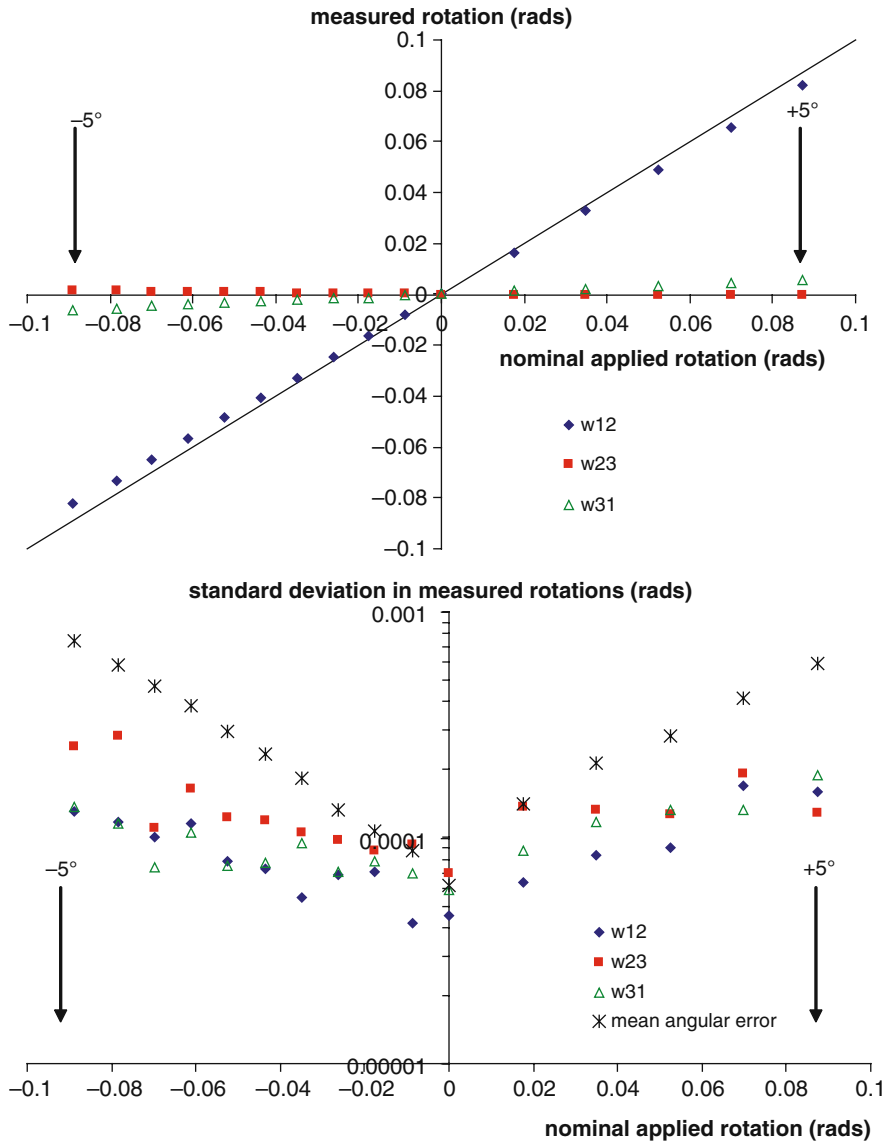


Fig. 17.5 Measurements of applied rotations to a GaAs single crystal. *Upper plot:* mean values from 11 patterns per nominal orientation. *Lower plot:* scatter in results and mean angular error in best fit solution

17.2.4 Illustrative Applications

Here we give two example applications of the technique to illustrate the type of information obtainable.

The first example is of semiconductor structures consisting of a 200 nm thick $Si_{0.85}Ge_{0.15}$ epilayer grown on a (001) Si substrate patterned with shear-sided raised mesas (Wilkinson 2006). The mesas were rectangular, with lengths 400 μm along the [1–10] directions and widths from 15 μm to 1 μm along the [110] direction. Line scans were conducted on the top surface of mesas of various widths using a JEOL JSM6500F at a beam energy of 15 keV, a beam current of ∼16 nA, and a sample tilt of 60°. The strains and rotations reported here are referred to the following Cartesian axes system: x_1 along the width of the mesa, i.e., $[110]_{Si}$; x_2 along the mesa stripe direction, i.e., $[1–10]_{Si}$; and x_3 along the wafer surface normal, i.e., $[001]_{Si}$. A reference pattern was

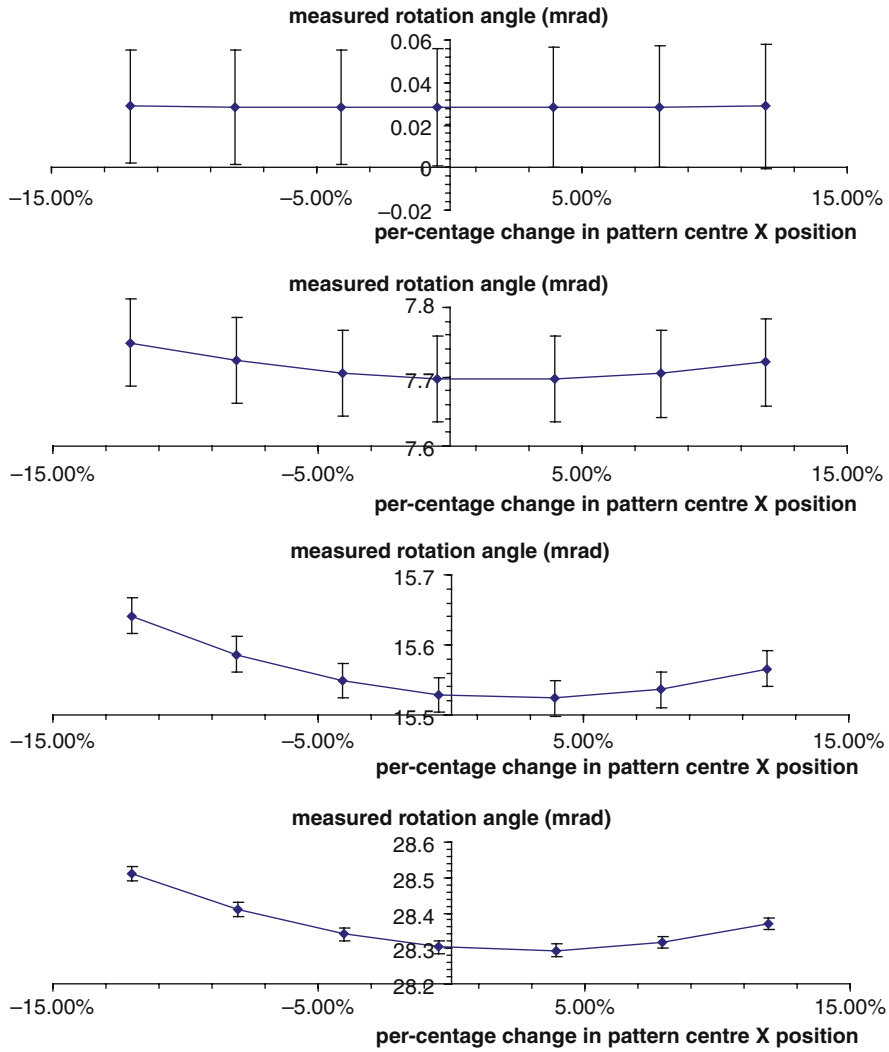


Fig. 17.6 Effects of large changes to assumed pattern centre × position on the measured rotation for applied rotations of 0°, 0.5°, 1°, and 2°. Points show averages of 5 measurements and error bars are ±1 standard deviation

obtained at the centre of the largest mesa, with width 15 μm, where it was assumed that the strain was that of the unrelaxed epilayer (i.e., $e_{11} = e_{22} = -6.2 \times 10^{-3}$, $e_{33} = +4.8 \times 10^{-3}$).

Figure 17.7 shows the variation of each of the strain and rotation components measured across one of these mesas. There are significant rotations w_{13} about the x_2 axis parallel to the long axis of the mesa (see Fig. 17.7a). Over the outer ~0.5 μm at each mesa edge, the lattice rotates as the epilayer expands outwards because of the removal of the lateral constraint at the edge of the mesa. The rotations are of equal magnitude, but in the opposite direction at the two mesa edges. No significant rotations w_{23} and w_{12} about the x_1 and x_3 axes are observed, which is in accord with the expected response given the sample symmetry.

The sample symmetry should also constrain the e_{12} and e_{32} shear strain components to zero, while the equilibrium condition that σ_{31} should be zero and the orthotropic symmetry of the elastic constant should constrain e_{31} to zero. The experimental results (Fig. 17.7b) confirm these constraints, as all three shear strains remain essentially zero. Over

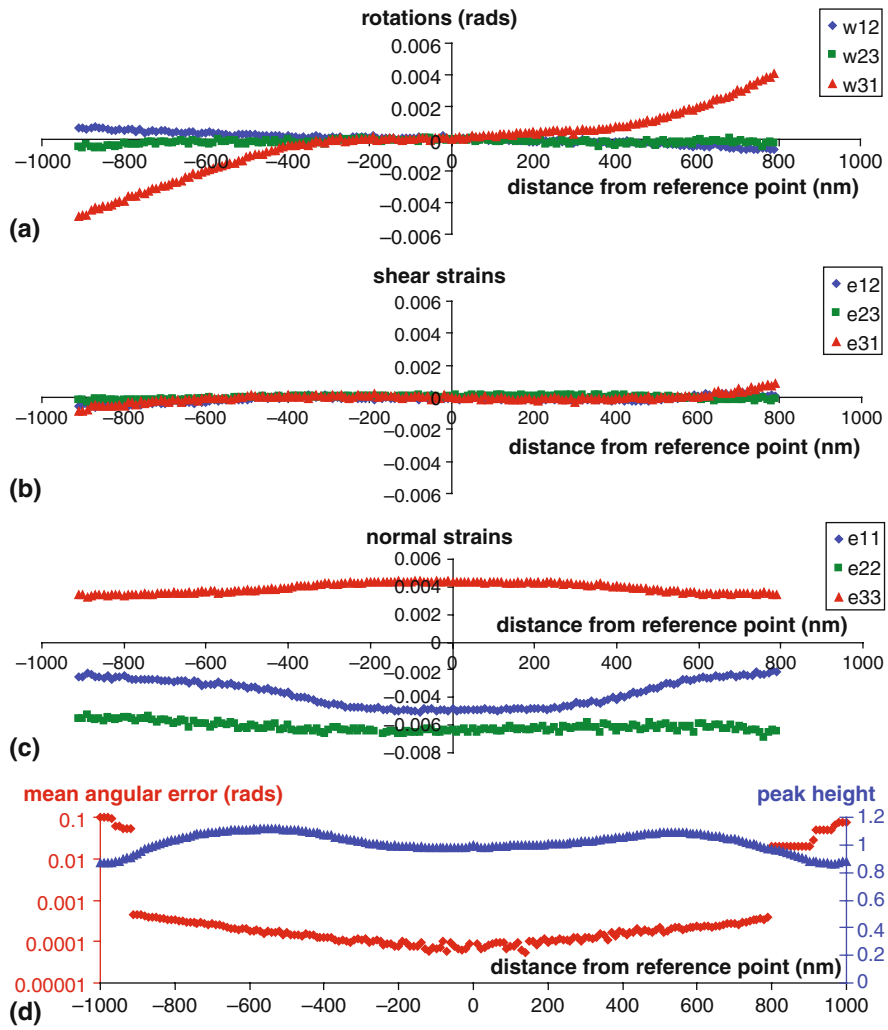


Fig. 17.7 Strain and rotation distributions across the width of a narrow SiGe/Si mesa stripe. (**a**) rotations, (**b**) shear strains, (**c**) normal strains, and (**d**) mean angular error and peak height parameters used to assess quality of measurements

the central 400 nm of the mesa the standard deviation in each of the shear strain components is $\sim 7 \times 10^{-5}$, confirming previous assessments of the technique's sensitivity.

The normal strain components (Fig. 17.7c) show the most significant variations. The e_{22} component remains close to the misfit strain of -6.2×10^{-3} expected for an unrelaxed blanket film of $Si_{0.85}Ge_{0.15}$. However, the e_{11} component shows significant relaxation away from this value because of the removal of the lateral constraint along the x_1 axis. This relaxation is strongest at the mesa edges, but some relaxation extends into the central region of the mesa.

Also shown in Fig. 17.7 are the normalized cross-correlation peak height values (discussed in Section 17.2.2). Generally these values remain high within this data set, even as the electron beam is displaced over the mesa edges. The variation in peak height values is due to subtle changes in pattern intensities as the beam breaks through the sidewalls of the mesa stripe. A further important check on the quality of the measurements is the mean angular error (discussed in Section 17.2.1). This is seen to increase abruptly, by almost two orders of magnitude, as the electron beam is displaced over the edges of the mesa structure. Indeed, these step changes in the mean angular error were used to define

the edges of the mesa stripes; and previous plots of rotations and strains were limited to the central region, where measurements came from the top surface of the mesa. Here the mean angular error is 1.7×10^{-4} averaged over the width of the mesa, compared to 8×10^{-5} over the central 400 nm. The significant rotations and strain variations described above are clearly well above the mean angular error.

The extent of elastic relaxation at the centre of the mesa stripes was studied as a function of mesa width. The strains at the mesa centres were used, along with single crystal elastic constants, to calculate the normal stress σ_{11} across the mesa width. Figure 17.8 shows these experimental data and compares them to the theory of Luryi and Suhir (1986), which is seen to give good predictions of stress at the mesa centres.

The second example concerns localized deformation caused by nanoindentation in a metallic sample (Randman 2006).

A Fe-0.01wt %C polycrystal, with a mean grain size of ~50 μm, was polished to 1 μm diamond and then electropolished in an electrolyte of 10% perchloric acid and 90% acetic acid at 19 V and ~20°C for 45 s. Indents were made with a diamond Berkovich indenter tip using an MTS Nanoindenter XP, and results here come from an indent made to a final depth of 500 nm. The EBSD measurements were made on the indented surface in a JEOL JSM 6500F FEG SEM operated at 20 keV, and a probe current of ~2 nA. Figure 17.9 shows a secondary electron image of the indent, and strain and rotation maps generated from the EBSD analysis. The mean peak height map (Fig. 17.9b) shows that the shadowing of patterns obtained from within the indent itself leads to poorer quality data. All other maps have been filtered so that results are only shown if the mean peak height is above 0.2. Such filtering successfully removes points with large mean angular error; and Fig. 17.9c shows that the mean angular error reaches values up to $\sim10^{-3}$ rads close to the indent, but falls to much lower values ($\sim10^{-4}$ rads) further away from the indent. It should be noted that the colour scale spans a range an order of magnitude larger for the rotation and strain maps compared to the mean angular error map.

Rotations (Fig. 17.9d, e, f) are generally large compared to the mean angular errors. Near the face denoted A in the secondary electron image, Fig. 17.9a, we expect the plastic flow away from the indenter face to cause lattice rotations w_{23} that are predominantly about the x_1 axis, and that is seen to be the case (Fig. 17.9e). The other two components w_{31} about the x_2 axes normal to the edge of the indent (Fig. 17.9f), and w_{12} about the sample surface normal (Fig. 17.9d), are both generally smaller than w_{23} and vary considerably with their position along face A, even changing sign from one end to the other. The w_{23} rotations are smaller near faces B and C than near face A. The indenter has mirror symmetry along the plane bisecting face A parallel to the x_2 axis; however, this symmetry is not maintained in the distribution of w_{23} rotations. This loss of the indenter symmetry is even more marked for the w_{12} and w_{12} components of rotation, and is presumably due to the specific alignment of the available Burgers vectors and slip planes in the indented crystal.

The strains (Fig. 17.9 g, h, l) are generally smaller than for the rotations, and so these maps appear a little noisier and, in some regions very close to the indenter, become comparable to the mean angular error (Fig. 17.9c). However, systematic elastic strain variations above the noise and sensitivity limit of the method are clearly resolved for some strain components. For example, near face A the e_{11} strain is clearly tensile (Fig. 17.9j) while e_{22} is compres-

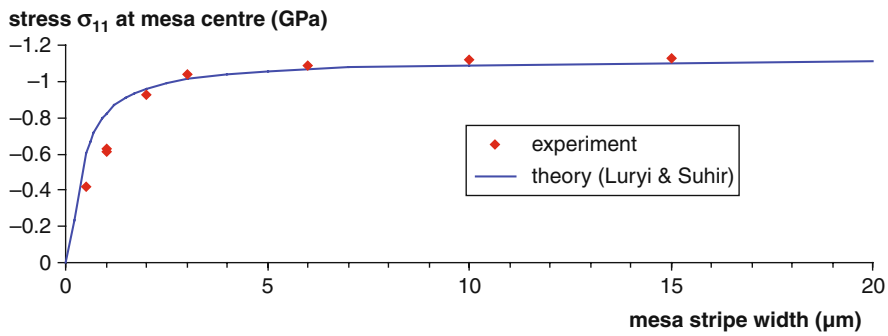
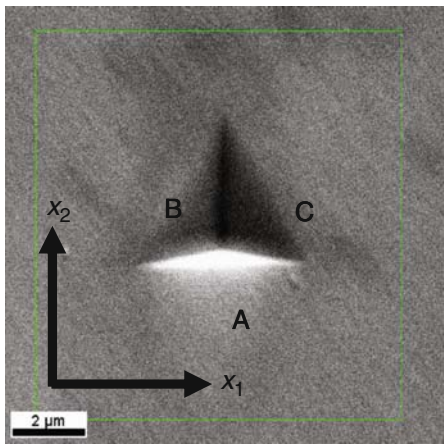
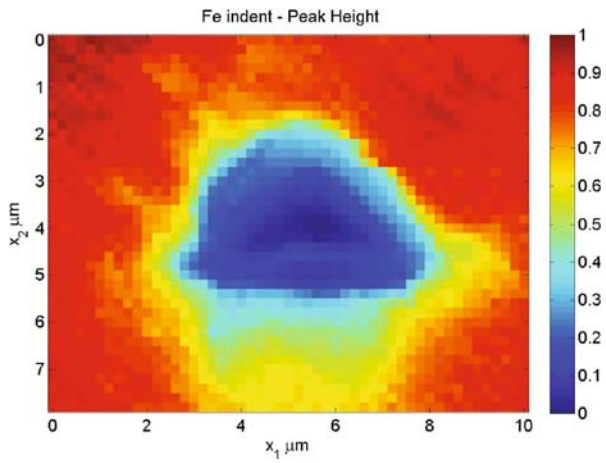


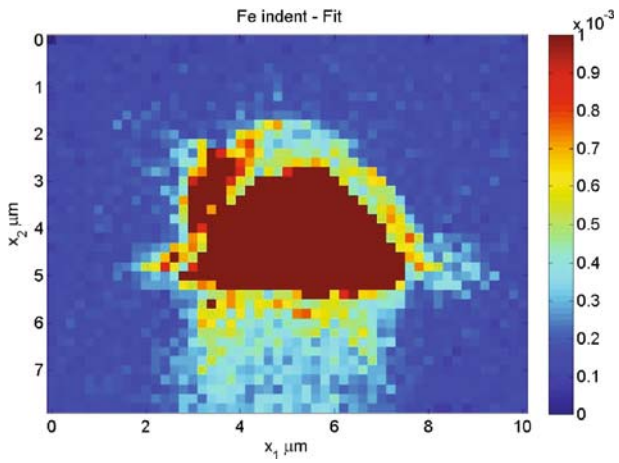
Fig. 17.8 Stress at centre of mesa stripe as a function of width



(a) Secondary electron image

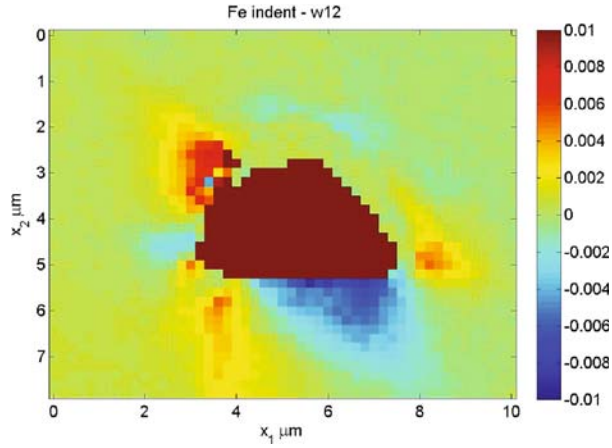


(b) Geometric mean of normalise cross correlation peak heights

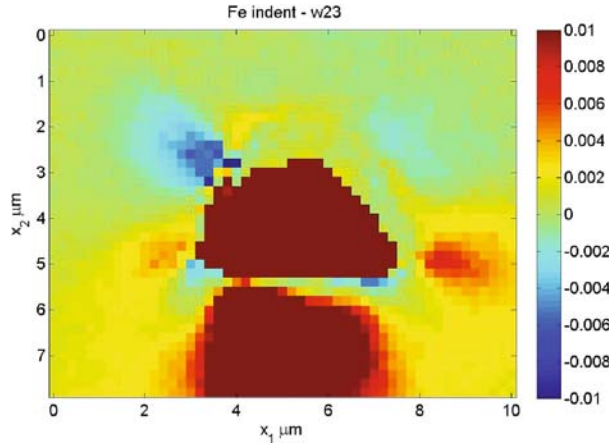


(c) Mean angular error in best fit solution for strains and rotation.

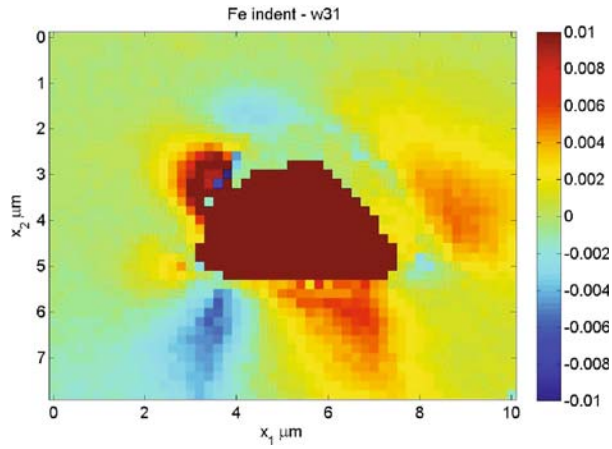
Fig. 17.9 Secondary electron image and EBSD generated maps of rotation and elastic strain fields near a 500 nm deep Berkovich indent in an Fe-0.019wt %C sample



(d) Rotation w_{12} about surface normal

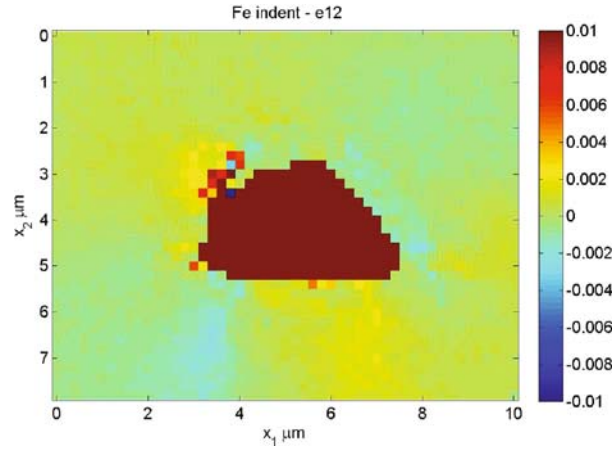


(e) Rotation w_{23} about horizontal axis

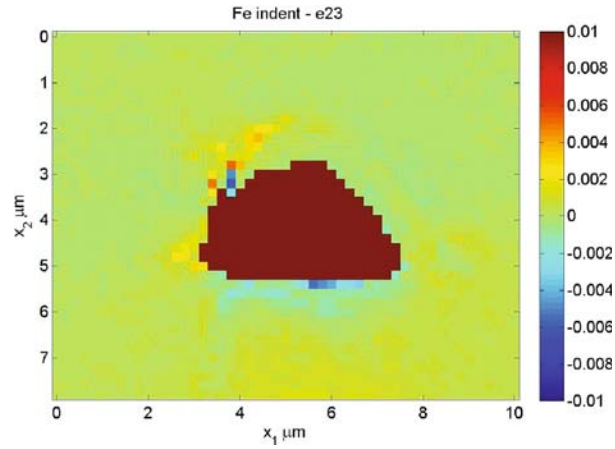


(f) Rotation w_{31} about vertical axis

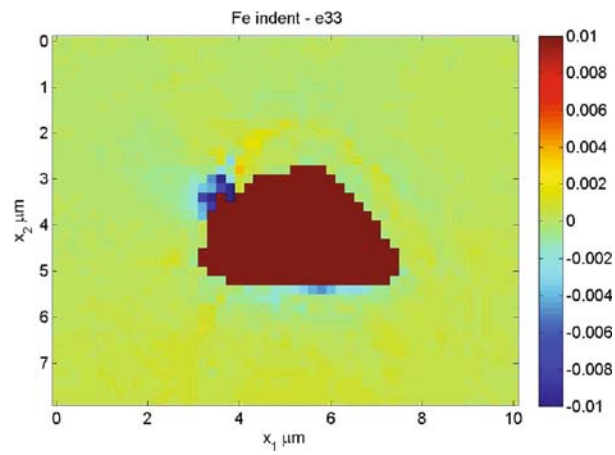
Fig. 17.9 (continued)



(g) Shear strain e_{12} within surface plane.

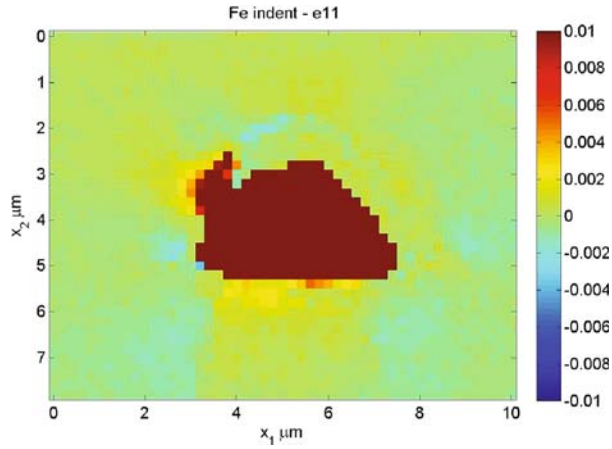


(h) Shear strain e_{23} out of surface

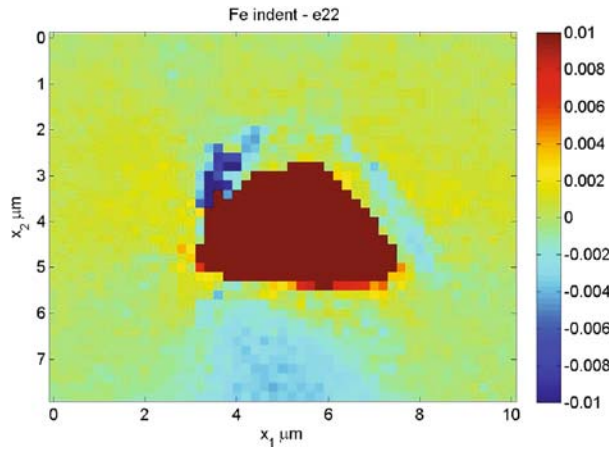


(i) Shear strain e_{31} out of surface

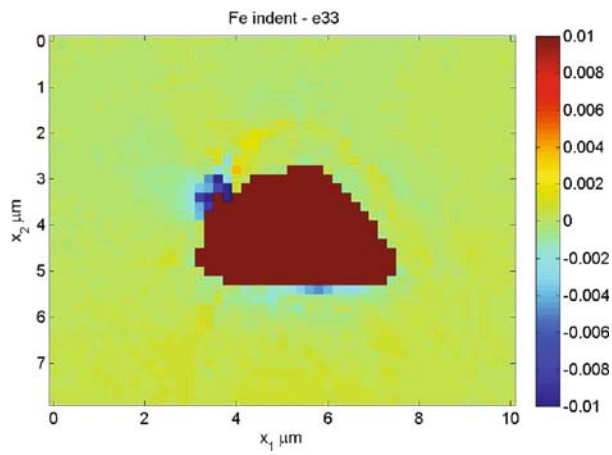
Fig. 17.9 (continued)



(j) Normal strain e_{11} along horizontal axis.



(k) Normal strain e_{22} along vertical axis.



(l) Normal strain e_{33} along surface normal.

Fig. 17.9 (continued)

sive (Fig. 17.9 k), which is in good accord with expectations based on hoop and radial strains near an expanding cavity.

From comparison of the maps shown in Fig. 17.9 it is clear that rotations dominate over elastic strains. This is a result of the significant plastic strain generated close to the indent. In such circumstances it is reasonable to use Nye's analysis to estimate the geometrically necessary dislocation (GND) content near the indenter. From knowledge of the three rotation components (Fig. 17.9d, e, f) on the surface plane, it is possible to calculate six of the nine lattice curvatures that are required to form Nye's dislocation tensor. The three missing curvatures concern the change of rotation with depth into the sample and thus are not directly accessible, though analysis on a FIB/SEM instrument may in the future allow these terms to be determined as well. In Fig. 17.10 a map is presented which shows a lower bound estimation for the GND distribution near this indent. This is a lower bound density for two reasons: firstly, because it is calculated on the assumption that three unknown curvatures are zero (which is unlikely to be the case); and secondly, because the crystallographic constraints and ambiguities concerning possible Burgers vectors and line directions are ignored in favour of what Sun et al. (2000) term a "simple cubic deconstruction." This simple cubic deconstruction ignores the specifics of the sample crystallography and instead considers nine types of GNDs, generated by having possible line directions and Burgers vectors lie along the three Cartesian reference axes, i.e., x_1, x_2, and x_3. GND densities of $\sim 2\times 10^{14}\,\mathrm{m}^{-2}$ are found in some regions close to the indent.

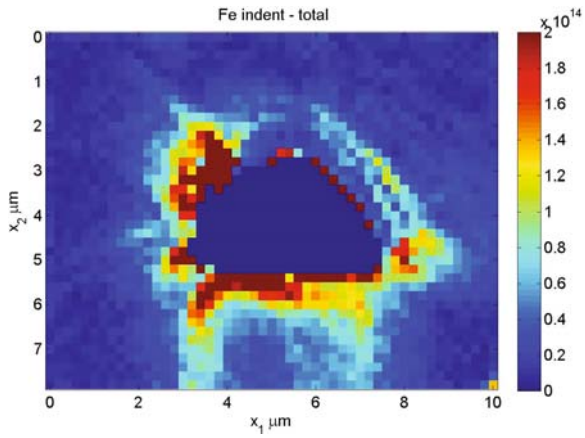


Fig. 17.10 Lower bound estimate of geometrically necessary dislocation distribution near indent in Fe-0.019wt %C. GND density is in lines/m^2

17.3 Concluding Remarks

EBSD has become an indispensable tool for the characterization of grain size, texture, grain boundary type distributions, and many related quantitative descriptions of polycrystalline microstructures. Development of cross-correlation-based analysis of EBSD patterns has come to fruition over the last few years; and software is now commercially available (BLGproductions Ltd, UK, www.blgproductions.co.uk) that can deliver strain measurements at a sensitivity of $\sim 10^{-4}$. The method gives access to variations in the full strain and rotation tensor at the high spatial resolution offered by EBSD. This, coupled with the relative ease of use and wide availability of EBSD systems on FEG SEMs, is likely to lead to a considerable increase in research activity in this area over the next 10 years or so.

Acknowledgments The authors are grateful to Dr. Mark Vaudin (NIST), Mr. Teruki Ishido (Matsushita Electric Industrial Co.), Dr. Cathy Vartulli (Texas Instruments), Mr. Benjamin Britton (Oxford University), Mr. David Randman (Oxford University), and Dr. Eleanor Clarke (Oxford University) for enjoyable and insightful discussion during development and application of this technique.

References

Bate PS, Knutsen RD, Brough I, Humphreys FJ (2005) The characterization of low-angle boundaries by EBSD. J Microsc 220:36–46

Bowen DK, Tanner BK (1995) A method for the accurate comparison of lattice parameters. J Appl Crystallogr 28:753–760

Clarke EE (2008) Internal stresses and dislocation densities generated by phase transformations in steel. D. Phil. Thesis, University of Oxford

Da Fonseca JQ, Mummery PM, Withers PJ (2005) Full-field strain mapping by optical correlation of micrographs acquired during deformation. J Microsc 218:9–21

Davidson DL (1991) Measurement of microdisplacements by machine vision photogrammetry (DISMAP). Rev Sci Instrum 62:1270–1279

Di Fonzo S, Jark W, Lagomarsino S, Giannini C, De Caro L, Cedola A, Muller M (2000) Non-destructive determination

of local strain with 100-nanometre spatial resolution. Nature 403:638–640

Dietrich D, Bugiel E, Osten HJ, Zaumseil P (1993) Raman investigations of elastic strain relief in Si1-xGex layers on patterned silicon substrate. J Appl Phys 74:7223–7227

Fan LX, Guo DL, Ren F, Xiao XH, Cai GX, Fu Q, Jiang CZ (2007) The use of electron backscatter diffraction to measure the elastic strain fields in a misfit dislocation-free InGaAsP/InP heterostructure. J Phys D Appl Phys 40: 7302–7305

Fincharm AM, Spedding GR (1997) Low cost, high resolution DPIV for measurement of turbulent fluid flow. Exp Fluids 23:449–462

Ishido T, Matsuo H, Katayama T, Ueda T, Inoue K, Ueda D (2007) Depth profiles of strain in AlGaN/GaN heterostructures grown on Si characterized by electron backscatter diffraction technique. IEICE Electron Expr 4:775–781

Kang KJ, Yao N, He MY, Evans AG (2003) A method for in situ measurement of the residual stress in thin films by using the focused ion beam. Thin Solid Films 443:71–77

Keller RR, Roshko A, Geiss RH, Bertness KA, Quinn TP (2004) EBSD measurement of strains in GaAs due to oxidation of buried AlGaAs layers. Microelectron Eng 75:96–102

Kinaev NN, Cousens D, Atrens A (1999) The crack tip strain field of AISI 4340: Part I: Measurement technique. J Mater Sci 34:4909–4920

Kozubowski JA, Keller RR, Gerberich WW (1991) Effects of tetragonal distortion in thin epitaxic films on electron channelling patterns in scanning electron microscopy. J Appl Crystallogr 24:102–107

Kröner E (1958) Kontinuumstheorie der Versetzungen und Eigenspannungen. Ergebnisse der Angewandten Mathematik, Vol. 5. Springer-Verlag, Berlin. English: Raasch I, Hartley CS (trans) Continuum theory of dislocation and self stresses. United States Office of Naval Research, Washington, DC

Landon CD, Adams BL, Kacher J (2008) High-resolution methods for characterizing mesoscale dislocation structures. J Eng Mater-T ASME 130:021004

Luo JF, Ji Y, Zhong TX, Zhang YQ, Wang JZ, Liu JP, Niu NH, Han J, Guo X, Shen JD (2006) EBSD measurements of elastic strain fields in a GaN/sapphire structure. Microelectron Reliab 46:178–182

Luryi S, Suhir E (1986) New approach to the high-quality epitaxial-growth of lattice-mismatched materials. Appl Phys Lett 49:140–142

Madden MC, Hren JJ (1985) Fine structure in electron channeling. J Microsc 139:1–17

Maier HJ, Keller RR, Renner H, Mughrabi H, Preston A (1996) On the unique evaluation of local lattice parameters by convergent beam electron diffraction. Phil Mag A 74: 23–43

Maurice C, Fortunier R (2008) A 3D Hough transform for indexing EBSD and Kossel patterns. J Microsc 230:520–529

Miyamoto G, Shibata A, Maki T, Furuhara T (2007) Precise measurement of accommodation strain in austenite surrounding martensite by electron backscatter diffraction. Proceedings 1st International Symposium on Steel Science, The Iron & Steel Institute of Japan

Nye JF (1953) Some geometrical relations in dislocated crystals. Acta Metall 1:153–162

Prior DJ (1999) Problems in determining the misorientation axes, for small angular misorientations, using electron backscatter diffraction in the SEM. J Microsc 195:217–225

Randman D (2006) A nanoindentation study of slip transfer at grain boundaries. Part II thesis, Department of Materials, University of Oxford

Sabate N, Vogel D, Gollhardt A, Keller J, Cane C, Gracia I, Morante JR, Michel B (2006) Measurement of residual stress by slot milling with focused ion-beam equipment. J Micromech Microeng 16:254–259

Stone HJ, Withers PJ, Holden TM, Roberts SM, Reed RC (1999) Comparison of three different techniques for measuring the residual stresses in an electron beam-welded plate of WASPALOY. Metall Trans A 30:1797–1808

Sun S, Adams BL, King WE (2000) Observations of lattice curvature near the interface of a deformed aluminium bicrystal. Philos Mag A 80:9–25

Tamura N, Celestre RS, MacDowell AA, Padmore HA, Spolenak R, Valek BC, Chang NM, Manceau A, Patel JR (2002) Submicron X-ray diffraction and its applications to problems in materials and environmental science. Rev Sci Instrum 73:1369–1372

Tao X, Eades A (2005) Measurement and mapping of small changes of crystal orientation by electron backscattering diffraction. Microsc Microanal 11:341–353

Troost KZ, van der Sluis P, Gravesteijn DJ (1993) Microscale elastic-strain determination by backscatter Kikuchi diffraction in the scanning electron microscope. Appl Phys Lett 62:1110–1112

Vaudin MD, Gerbig YB, Stranick SJ, Cook RF (2008) Comparison of nanoscale measurements of strain and stress using electron back scattered diffraction and confocal Raman microscopy. Appli Phys Lett 93:193116

Wilkinson AJ (1996) Measurement of elastic strains and small lattice rotations using electron backscatter diffraction. Ultramicroscopy 62:237–247

Wilkinson AJ (1997) Methods for determining elastic strains from electron backscatter diffraction and electron channelling patterns. Mater Sci Tech 13:79–84

Wilkinson AJ (1999) Measurement of small misorientations using electron backscatter diffraction. Proceedings of the electron microscopy and analysis.group conference. Inst Phys Conf Ser 161:115–118

Wilkinson AJ (2000a) Measuring strains using electron backscatter diffraction. In: Schwartz AJ, Kumar M, Adams BL (eds) Electron backscatter diffraction in materials science. Kluwer Academic/Plenum Publishers, Dordrecht, The Netherlands

Wilkinson AJ (2000b) Advances in SEM based diffraction studies of defects and strains in semiconductors. J Electron Microsc 49:299–310

Wilkinson AJ (2000c) Electron backscatter diffraction: Probing strains at high spatial resolution. Proceedings of the sixth international conference on residual stresses, Oxford, July 2000, vol. 1, pp 625–632, IOM Communications, London

Wilkinson AJ (2001) A new method for determining small misorientations from electron backscatter diffraction patterns. Scripta Mater 44:2379–2385

Wilkinson AJ (2006) High resolution measurements of strain and tilt distributions in SiGe mesas using electron backscatter diffraction. Appl Phys Lett 89:241910

Wilkinson AJ, Meaden G, Dingley DJ (2006a) High resolution elastic strain measurement from electron backscatter diffraction patterns: New levels of sensitivity. Ultramicroscopy 106:303–313

Wilkinson AJ, Meaden G, Dingley DJ (2006b) High resolution mapping of strains and rotations using electron backscatter diffraction. Mater Sci Technol 22:1271–1278

Wu D, Guo X, Gu X-L, Li Y-B, Shen G-D (2007) Strain field in GaAs/GaN wafer-bonding interface and its microstructure. Chinese Phys Lett 24:3481–3484

Yamaguchi M, Tachikawa M, Sugo M, Kondo S, Itoh Y (1990) Analysis for dislocation density reduction in selective area grown GaAs films on Si substrates. Appl Phys Lett 56: 27–29

Young RJ (1997) Analysis of composites using Raman and fluorescence microscopy—a review. J Microsc 185: 199–205

Chapter 18

Mapping and Assessing Plastic Deformation Using EBSD

Luke N. Brewer, David P. Field, and Colin C. Merriman

18.1 Plastic Deformation Effects on the EBSD Pattern and Orientation Map

This chapter reviews approaches for mapping and assessing plastic deformation using EBSD. This discussion will be focused on the approaches based upon EBSD pattern rotation. Pattern rotation can be mapped or quantified in terms of straight orientation change, local misorientation, average misorientation, or the calculation of geometrically necessary dislocation densities. In polycrystals, the misorientation can be mapped using several different kinds of metrics to visualize plastic deformation around cracks, indentations, and inside deformed grains. We will discuss a number of average misorientation metrics that have been developed to quantify the correlation between plastic deformation and EBSD data. Finally, we will survey the more recent work in the measurement and display of geometrically necessary dislocations and their connection to deformation structures in metals.

Electron backscatter diffraction (EBSD) is sensitive to the collective effects of dislocations that accumulate in the lattice during deformation. These dislocations can be divided into two categories: those which are termed "geometrically necessary" dislocations (GNDs—also called excess dislocations by some researchers), and which give rise to curvature in the lattice; and those which are "statistically stored" (statistically stored dislocations, SSDs), and which do not result in lattice rotation. It is somewhat imprecise to say that EBSD is "measuring plasticity." Instead, EBSD measures the effects of plasticity upon the crystallite lattice in the form of lattice bending (GNDs) and lattice imperfection (GNDs and SSDs). Much work has been done to correlate various kinds of EBSD measurements with the imparted plastic strain on polycrystals, but for the most part, these measurements are still correlations. However, these correlative measurements can be valuable for understanding the interplay between microstructure and plastic deformation in materials. We will use the phrase "assessing plastic deformation" throughout this chapter, but it is important to remember that we are actually assessing changes in polycrystals that are the result of plastic deformation, not the "percent plasticity" itself.

The many kinds of EBSD experiments for assessing plastic deformation and visualizing it in microstructures can be organized into a type of family tree (Fig. 18.1). At the first branch, experiments analyze either EBSD pattern degradation or pattern rotation as a function of plastic deformation level. In each of the branches, the analyst then analyses either the EBSD pattern directly or some transform of the pattern, usually the Hough transform in automated analyses. Pattern degradation can be measured in a variety of ways, with researchers showing some limited success in relating these measures to local plastic deformation. Methods for pattern degradation have included fast Fourier transform analysis of individual patterns (Wilkinson and Dingley 1991) and mapping of the "image quality" (IQ) parameter across microstructures (Wright and Nowell 2006). This chapter will not further discuss pattern degradation approaches.

One of the more important connections between the plasticity mechanics and EBSD is the use of

L.N. Brewer (✉)
Sandia National Laboratories, Albuquerque, NM 87123–1411, USA
e-mail: lnbrewe@sandia.gov

A.J. Schwartz et al. (eds.), *Electron Backscatter Diffraction in Materials Science*,
DOI 10.1007/978-0-387-88136-2_18, © Springer Science+Business Media, LLC 2009

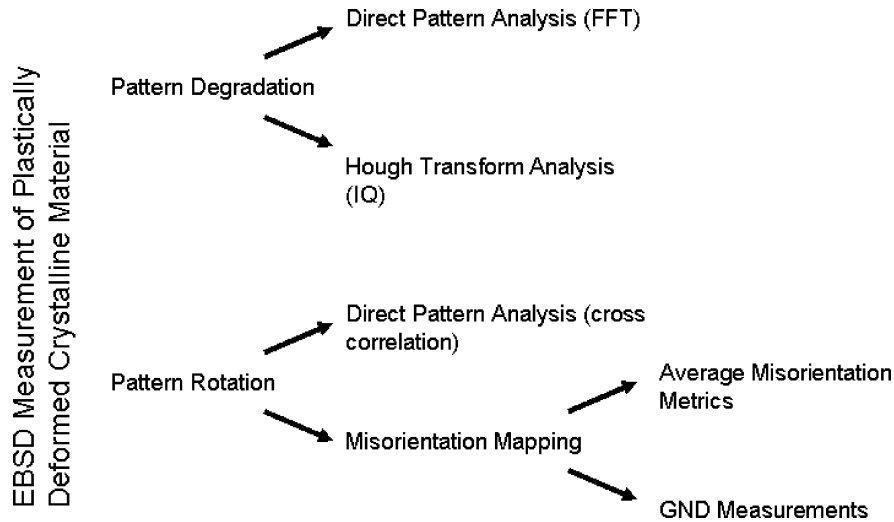


Fig. 18.1 Tree of EBSD experiments for assessing and visualizing plastic deformation

continuum descriptions of dislocations in describing crystal plasticity. This work was begun by Nye in the 1950s and furthered by Ashby and others in the 1970s (Ashby 1970; Nye 1953). A good summary paper of these treatments is found in the work of Arsenlis and Parks (1999). The direct connection of GND determination to EBSD was pioneered in the last several years in the work of Adams (Adams 1997; El-Dasher et al. 2003; Sun et al. 2000) and has been continued by several authors (Field et al. 2005; Pantleon 2008).

Dislocation behavior at this microstructural length scale can be most simply summarized as the ability of dislocation networks to support a strain gradient. Nye first noted that a strain gradient necessitates the creation of dislocation networks to maintain the geometric continuity of the material in the deformed state (Nye 1953). Ashby coined the term "geometrically necessary dislocation" to describe this set of continuum-level dislocations (Ashby 1970). It is important to note that pure, uniform shear will not generate GNDs; instead, they are the result of gradients in strain, which rotate the continuum field from point to point (Fig. 18.2). The result of this rotation is an overall Burgers vector, which explains the deformation from point to point at the continuum scale. Under special conditions (e.g., single crystals, specific loading geometries) materials can plastically deform without a strain gradient. Dislocations are still involved in this process, but they produce no observable overall Burgers vector at the continuum scale. Ashby

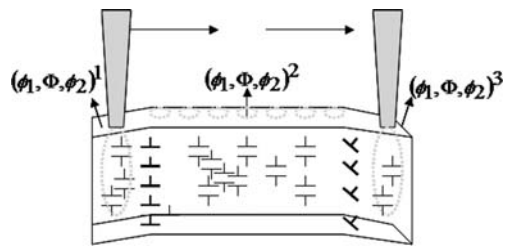


Fig. 18.2 Schematic of change in orientation (as represented by Euler angles: ϕ1, Φ, ϕ2) as the electron beam scans across the surface of a crystallite. Note that the orientation changes only when the beam crosses an array of dislocations that has a net non-zero Burgers vector

described these dislocations as "statistically stored." Even polycrystalline materials under generalized loading can have grain interior regions that possess dislocations (SSDs) without any measurable GND densities or resultant change in orientation (Fig. 18.2).

By definition, there is a direct connection between GNDs and the orientations measured in EBSD. The orientation of a point on the surface of the material can be measured as g_{ij}, represented as an orientation matrix. We generally assume Bunge's notation and convention with the triplet of Euler angles (ϕ_1, Φ, ϕ_2) that are a direct result of the indexing of an individual EBSD pattern at a point (x,y) on the surface of the sample. The change in orientation between two adjacent points can be expressed as the spatial gradient of the orientation, $g_{ij,k}$. We can then write down the

connection between the Nye dislocation tensor, α_{ij}, and this misorientation gradient (El-Dasher et al. 2003):

$$\alpha_{ij} = e_{ikl} g_{jl,k}, \tag{18.1}$$

where e_{ikl} is the permutation tensor.

Nye's work connects the dislocation tensor to the density of dislocations of different types.

$$\alpha_{ij} = \sum_{k=1}^{K} \rho^k b_i^k z_j^k, \tag{18.2}$$

where ρ is the scalar dislocation density and the couple of $b_i^k z_j^k$ specifies a particular dislocation type where b is the Burgers vector and z is the line direction. For a simple cubic system, there are nine components comprising α and nine types of dislocations; so the equation can be solved in a completely deterministic fashion. FCC metals, however, have 36 types of dislocations (including positive and negative dislocations separately and both edge and screw components). BCC metals also have many more slip systems than are available in the simple cubic structure. This plethora of dislocation types results in an underdetermined system of equations. In order to determine the dislocation densities for these systems, it is necessary to perform some sort of optimization calculation. Since the solution is not unique, the dislocation densities calculated are those which give the minimum total dislocation densities required to achieve the observed lattice rotation. Arsenlis and Parks discuss the use of two different norms which minimize either the total number of dislocations required or the total line length (Arsenlis and Parks 1999). If standard two-dimensional EBSD maps are used, these norms are equivalent.

18.2 Pattern Rotation Approaches

Plasticity in polycrystalline materials usually results in local crystal rotation, which EBSD is well designed to measure. Typical values for misorientation resolution using standard EBSD platforms are on the order of 0.5° (Wilkinson 2001). Using direct pattern analysis methods, angular resolutions down to 0.01–0.02° can be achieved (Wilkinson 2001; Brough et al. 2006). Compared to this sensitivity, plastic deformation in metals can easily cause several degrees of intragranular rotation, and EBSD is therefore a useful technique for measuring microscale crystal rotation and connecting it with plastic deformation. We will divide our discussion of crystal/EBSD pattern rotation measurement in EBSD into three sections: (1) orientation and misorientation mapping, (2) averaged misorientation measurements, and (3) GND measurements.

18.2.1 Mapping Orientations and Misorientations

In its most basic form, EBSD is used to map crystal orientations. So much so, that one of the main products in EBSD is called orientation imaging microscopy (Wright 1993). As described in Section 18.1, deformation of a crystalline solid usually results in the internal rotation of the crystal. For single crystals, it is instructive to study the plastic deformation by mapping the crystal orientation itself. For polycrystals, orientation mapping is less useful as a measure of plasticity, since the field of view is usually made up of many grains with possibly random orientations.

An example of the ability of orientation maps to show deformation in single crystals is the work of Field et al. (2005) on the rate-sensitive compression of single-crystal metals. In this work, two single-crystal samples of high purity aluminum were deformed and characterized using EBSD. One crystal was deformed at room temperature using channel die compression to 15% height reduction. The second crystallite was deformed in uniaxial compression at a high strain rate. As can be seen in Fig. 18.3, a map of the orientation with respect to the compression direction shows a very different crystalline response to the imposed deformation. The channel die compression results in bands of spatially abrupt rotation, while the high strain rate deformation produces a gradual rotation across a much larger area of the crystal. Interestingly, the average dislocation content for both of these areas is approximately the same, but the distribution of GNDs and the consequent crystal rotation is strikingly different.

Misorientation mapping is useful for studying plastic deformation in both single crystals and polycrystals. As described in Section 18.1 of this chapter, the spatial gradient in orientation can be directly related to the lattice curvature, which in turn is related to the plastic deformation in the crystal by way of the Nye dislocation tensor, α. A common metric for change in

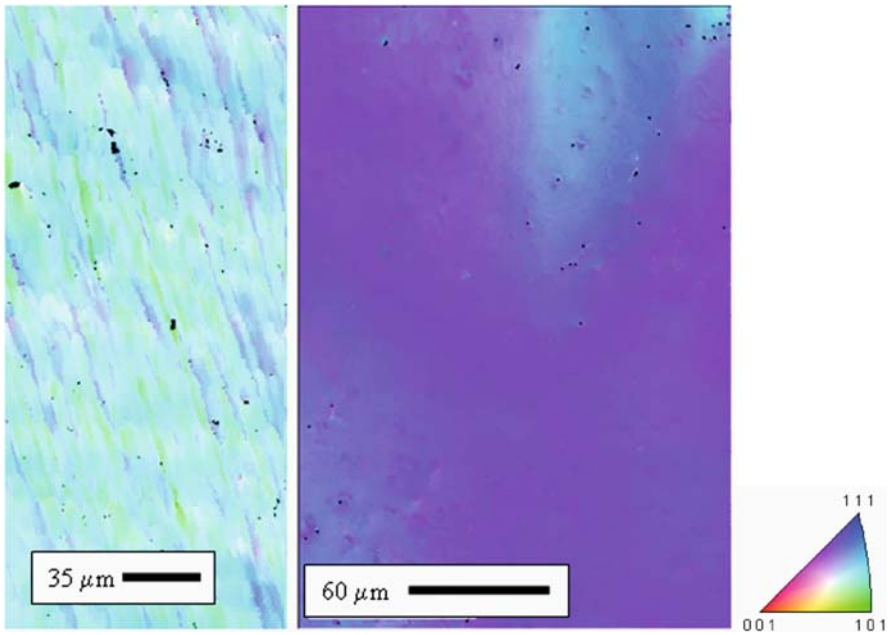


Fig. 18.3 Orientation images of the Al single crystals for (**a**) the specimen deformed in a channel die at 15% strain, and (**b**) the specimen deformed at high strain rate. The orientation-shading key with respect to the compression direction is shown at *right*. Figure from Field et al. (2005)

orientation is the axis-angle pair (<u,v,w>,θ) description of misorientation. Commonly, only the scalar rotation angle portion of the description is used when describing misorientation. Here we will use the scalar definition of the misorientation angle, θ, sometimes termed the "disorientation."

Although misorientation is one of the most basic quantities from an EBSD measurement, there are many ways of quantifying and visualizing misorientation or quantities related to it. It is important to remember that misorientation is a referential number; that is, it is a misorientation with respect to some other orientation. The choice of this reference orientation really changes the nature of the measurement or the visualization quite a bit.

The most basic measurement and visualization of misorientation is grain boundary mapping. Grain boundaries in EBSD are determined as locations at which the scalar misorientation between adjacent pixels is greater than some critical value. For the high angle grain boundaries (HAGB) that demarcate the grains in a polycrystal, this critical misorientation value is generally between 7° and 15°. However, one can also plot the density of low angle grain boundaries (LAGBs) with misorientations between 1 and 10°, for example. These maps will show a higher density of these LAGBs in areas of deformation. In fact, the number or line density of LAGBs for a given area can be easily quantified. In Fig. 18.4, we can see that the density of LAGBs in the grains surrounding a fatigue crack tip in stainless steel is much higher than in the grains further away from the crack tip (Brewer et al. 2006b). Note that by using the scalar misorientation, noth-

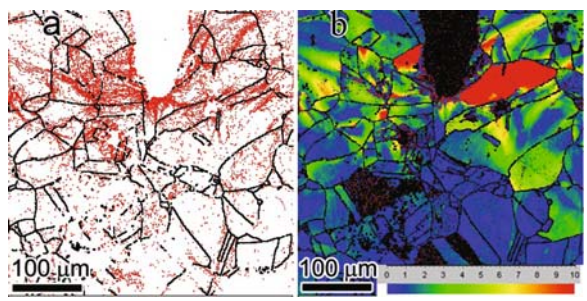


Fig. 18.4 EBSD maps from a region around an air fatigue crack tip in 304 stainless steel. Scale bar is 100 μm. (**a**) Grain boundary map: *black lines* are high-angle boundaries (θ>10°), *red lines* are low-angle boundaries 2°<θ<10°). (**b**) Misorientation map, rainbow scale: *blue* represents 0° misorientation from reference, *red* represents 10° misorientation. Figure from Brewer et al. (2006b)

ing is being said about the nature of the small angle boundaries. One reason for this lack of detail is that the definition of the misorientation axis becomes more and more poorly defined as the misorientation angle becomes smaller (Prior 1999). A potential drawback to the use of GB maps is that this signal is differential, that is to say that LAGB maps show the local sources of misorientation, but not their net effect across the grain. For this reason, LAGB maps can be quite noisy. This situation is similar to the difference between a map of point charges and the resultant electric field maps. The electric field maps should be much smoother than the charge density maps themselves.

Another form of misorientation map is the kernel average misorientation (KAM). In this approach, the arithmetic mean of the scalar misorientation between groups of pixels, or kernels, is calculated and mapped. There is a strong similarity between this approach and grain boundary maps, except that the KAMs are two-dimensional and can extend beyond adjacent pixels (e.g., next-nearest neighbors). The downside of this approach is the same noisiness mentioned for grain boundary maps. The usefulness of KAM really depends upon the question being asked. Is the question, "Are there areas of the sample in which the very local misorientation is high?" (KAM is useful.) Or is the question, "Does this grain deform from one end with respect to the other?" (KAM is less useful.)

There are many other approaches to misorientation mapping that are based upon mapping misorientation across an entire grain with respect to some reference pixel. Earlier work by Wright et al. (1993) showed misorientation maps based upon the average Euler angles for the grain. This type of map works very well for single crystals and is readily interpretable. However, when studying polycrystals, the meaning of this sort of map is less clear. Kamaya et al. (2005) and Brewer et al. (2006b) both published integrated misorientation maps that use a local kernel as the reference point for the map. In the case of Brewer, the reference point is chosen essentially by the KAM method using nearest neighbors. The kernel with the smallest average misorientation becomes the reference for the entire grain. In the work of Kamaya, the kernel for each point extends over the entire grain. The kernel with the minimum summed misorientation is the reference. Both of these methods result in maps which are qualitatively helpful in visualizing the intragranular rotation caused by plastic deformation. Both methods can also be used to quantitatively compare one data set to another. However, both methods also suffer from a choice of kernel which is not altogether physically clear. It might be better to further interrogate the kernel reference point choice by performing essentially a derivative check to determine if the kernel of interest is a maximum in intragrain misorientation or a minimum.

An example comparing some of these techniques can be seen in Fig. 18.5. In this example, a tensile bar of pure, polycrystalline nickel was elongated to 1%, 5%, and 10% strain. At each deformation state, the bar was removed from the tensile rig, and EBSD orientation maps were collected on three regions of interest. In Fig. 18.5a, we see that orientation maps qualitatively show the formation of deformation bands within the grains as the strain increases. One can also see that some grains are rotating more than others, most likely because of their Schmid factor with respect to the loading direction (x-axis). The grain boundary map (Fig. 18.5b) does show an increased density of LAGBs as the strain level increases, but only the 10% level really shows a marked increase in LAGB density. At the 10% level, one can even see LAGBs that suggest the beginning of subgrain formation. The KAM maps in Fig. 18.5c show features which look like subgrains as the strain increases. The KAM for the 1% level seems to show only the noise threshold, but the 5% and 10% KAM maps definitely show intragrain networks of highly localized misorientation. These KAM maps serve as the starting point for the integrated misorientation maps in Fig. 18.5d. This last representation displays the net effect of these internal networks of misorientation. By close inspection, one can see that the regions of highest internal misorientation in Fig. 18.5d correspond somewhat to the regions of highest misorientation network density in Fig. 18.5c. However, the intensity in the KAM maps is relatively uniform for each grain, while the level of misorientation in the integrated misorientation maps varies more from grain to grain as is seen in the orientation maps of Fig. 18.5a.

18.2.2 Average Misorientation Approaches

Average misorientation measurements have been used as a way to connect some sort of average

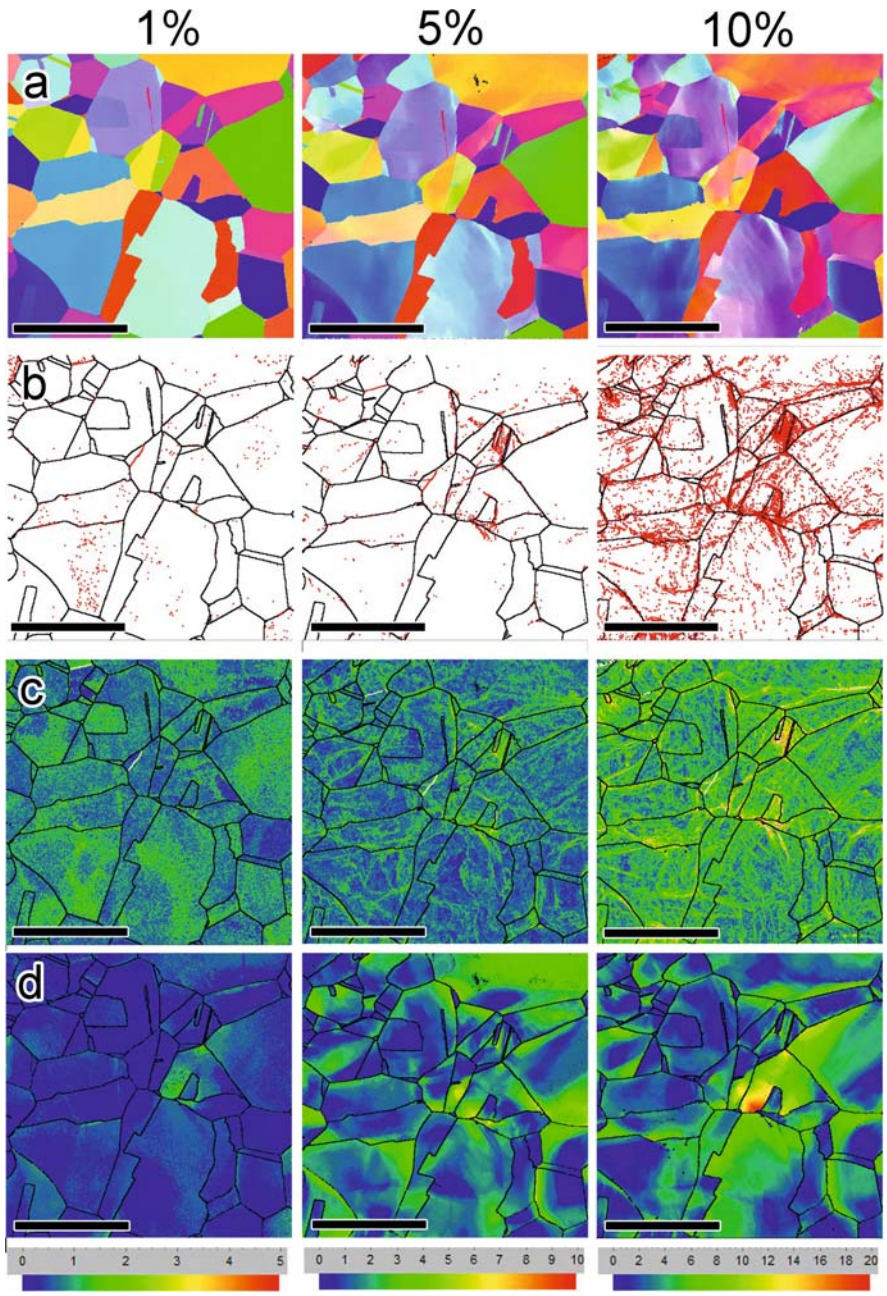


Fig. 18.5 Different mapping algorithms applied to a data set from an interrupted tensile test on polycrystalline nickel. Scale bar on all figures is 50 μm. (**a**) Orientation: inverse pole figure with respect to x-axis (loading axis). (**b**) Grain boundary map: *black lines* are high-angle ($\theta > 10^\circ$) boundaries, *red lines* are low-angle ($1^\circ < \theta < 10^\circ$) boundaries. (**d**) Average kernel misorientation map: 0–1.5°, *blue-red,* cluster (3×3 pixels) misorientation. (**f**) Integrated misorientation map (rainbow scale in degrees)

microstructural misorientation to macroscale plastic deformation in the material. There are many ways of calculating these metrics and many names for them; this list is not exhaustive but attempts to catalog the major types of metrics: grain orientation spread (GOS) (Alvi et al. 2004; Barton and Dawson 2001; Cheong and Weiland 2007; Wright 1999), grain average misorientation (GAM) (Wright 1999), integrated

angular misorientation density (IMD) (Lehockey et al. 2000), average intragrain misorientation (AMIS) (Sutliff 1999), and modified crystal deformation (MCD) (Kamaya et al. 2005, 2006), amongst others. These various methods differ in two major ways: the choice of using spatially correlated versus uncorrelated misorientation and the choice for the reference orientation.

The simplest among these approaches is the simple arithmetic mean of all, uncorrelated misorientations amongst measured pixels, referred to as either GOS (Wright 1999) or AMIS (Sutliff 1999). Various researchers have employed the generic term "scalar orientation spread" (SOS), which should be used generally. In this review chapter we will refer specifically to either AMIS or GOS as used in the various studies cited. SOS is a calculation of the mean, uncorrelated misorientation within grains, either segments in one dimension or grain areas in two dimensions. For a line of N measurements taken from each of M grains, SOS is calculated as follows:

$$SOS = \frac{\sum_{i}^{M} \left(\frac{\frac{1}{2} \sum_{j}^{N} \sum_{k}^{N-1} \theta_{jk}}{N_i} \right)_{grain-i}}{M}, \qquad (18.3)$$

where θ is the misorientation between any two points within a grain, not just the nearest neighbors. In addition, this misorientation calculation is only performed for non-degenerate pairs of orientation measurements.

The IMD approach is based upon the integration of the misorientation distribution over a given area (Lehockey et al. 2000). This measure was developed and discussed in the first volume of this text and will not be further defined in this work. This sort of calculation has also been called grain average misorientation (GAM) in the literature (Wright 1999), but both methods calculate the arithmetic mean of the misorientation between *adjacent* pixels in a set of N pixels over M grains.

The current definition for the grain orientation spread (GOS) is different from the preceding metrics because of its definition of the reference orientation from which the misorientation is calculated (Barton and Dawson 2001; Cheong and Weiland 2007; Wright 1999). The current versions of GOS calculate the reference orientation from the average orientation of a grain from an *orientation or misorientation space* analysis. A general formulation for the GOS is given by:

$$GOS = \frac{1}{N} \sum_{A=1}^{N} \times \left\{ \min \left[\cos^{-1} \left(\frac{\text{trace} \left[g_{ave} \left(h_i g^A \right)^{-1} \right] - 1}{2} \right) \right] \right\}, \qquad (18.4)$$

where g_{ave} is the orientation matrix for the average orientation in the grain, h is an element of the symmetry group for the given crystal structure, and g^A is the orientation matrix for a given data point in the grain. The inverse cosine function calculates the scalar misorientation, θ, that was used in the SOS and IMD methods.

Another pair of average misorientation metrics are the crystal deformation (CD) (Kamaya et al. 2005) and the modified crystal deformation (MCD) developed by Kamaya et al. (2006). The CD differs from the previous metrics in its definition of the reference orientation. As mentioned above, the CD approach uses a spatially derived misorientation kernel in which the summed misorientation of each pixel with respect to every other pixel in the grain is calculated. The cluster with the minimum total misorientation is chosen as the reference orientation. Once this reference kernel or cluster is chosen, the CD is calculated as the mean misorientation between every other pixel in the grain and the reference orientation for a set of M grains. The MCD metric is similar to the GOS in that it first calculates the "average" orientation of the grain and then calculates the mean misorientation of every other pixel in the grain with respect to the calculated average orientation. However, the MCD is calculated using the mean of the log-normal distribution of the misorientations as given by:

$$MCD = \exp \left[\frac{\sum_{k=1}^{M} \left(\sum_{i=1}^{N} \ln \{\theta(g_{ave}, g_i)\} \right)}{\sum_{k=1}^{M} N} \right], \qquad (18.5)$$

where θ is the scalar misorientation between the average orientation, g_{ave}, and the orientation of every other point in the grain, g_i. This mean misorientation is calculated for all N points in M grains, resulting in one scalar value of misorientation for a given microstructural area or test line.

One of the consistent and intriguing findings of these sorts of methods is the strong, linear correlation between the applied plastic strain (primarily tensile testing) and the measured, average misorientation metrics. Lehockey found this linear correlation for nickel-based alloy 600 (FCC structure) (Lehockey et al. 2000), as did Sutliff for Cu and austenitic stainless steels (Angeliu et al. 1999; Sutliff 1999). Young et al. (2002) summarized the correlation between AMIS and applied tensile strain for four different FCC structured metals (Fig. 18.6) and showed that while all had a linear slope, the magnitude of the slope varied between alloys. Lehockey's work showed a difference in slope in the same alloy 600 material for plane view versus cross-sectional specimens, as well as in "C"-ring specimens. The application of the CD and MCD (similar to GOS) to tensile strained samples of 304 stainless steel and alloy 600 also showed these linear relationships, and were shown to be relatively insensitive to EBSD collection parameters such as the type of SEM used, the step size of the map, and the electron beam conditions (Kamaya et al. 2006).

While the potential for these average misorientation metrics to be correlated with plastic strain levels seems promising, great care needs to be taken in order not to misuse these correlations. Lehockey makes the point that IMD will not give the sense of the strain (i.e., compression versus tension) and that any calibration between an IMD value and plastic strain level seems to be specific to the type of deformation applied. Attempts to calibrate average misorientation metrics to plastic strain levels should only be attempted when the deformation process used for the calibration is the same as the deformation process used in the measurement of the unknown, e.g., a calibration made by uniaxial tensile testing at room temperature should probably not be used to measure "plastic strain levels" produced by hot rolling of the same material. The average misorientation values might very well still correlate to applied rolling strain levels, but the absolute accuracy of the plastic strain values will be highly questionable.

Despite these concerns, a number of applications have been made in which average misorientation metrics have been useful in studying plastic deformation in metals. Angeliu et al. used the AMIS approach to examine residual plasticity in the heat-affected zones of welds in stainless steels (Angeliu et al. 1999). By taking line scan measurements parallel to the weld line, the authors showed that average misorientation systematically decreased as a function of distance away from the weld and that this decay was related to the type of weld. Work by Brewer et al. (2006a) examined the use of the AMIS parameter for characterizing surface machining damage in superalloys. This work showed that higher levels of AMIS strongly correlated with higher levels of surface machining damage (Fig. 18.7) (Brewer et al. 2006). These measurements were made in conjunction with synchrotron X-ray diffraction and compared favorably.

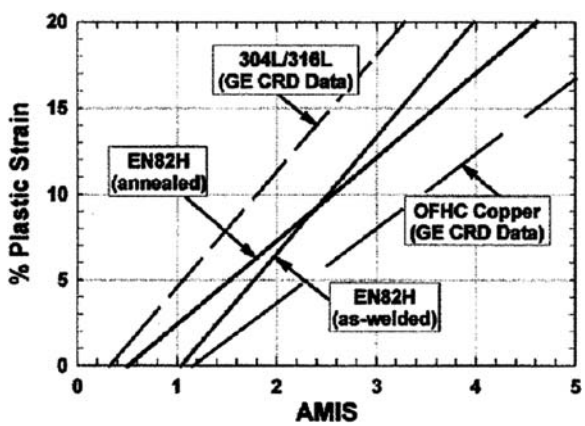


Fig. 18.6 Comparison of AMIS and percent plastic strain calibration curves for super alloys, stainless steels, and pure copper (uniaxial tensile tests performed at room temperature). From Young et al. (2002)

18.2.3 Measurement and Calculation of GND Densities

EBSD has also been used to measure GND densities in deformed metals (El-Dasher et al. 2003; Field et al. 2005; Sun et al. 2000) and geologic materials (Reddy et al. 2007). As described above, the central input into the calculation of these densities is the orientation gradient calculated from an orientation map. One of the challenges to these experiments is the two-dimensional nature of traditional EBSD. Until quite recently, little information was available for the orientation gradient with respect to the Z-direction. The orientation gradient either had to be controlled by the sample geometry or the deformation geometry, or by the assumption that these gradients could safely be neglected. The

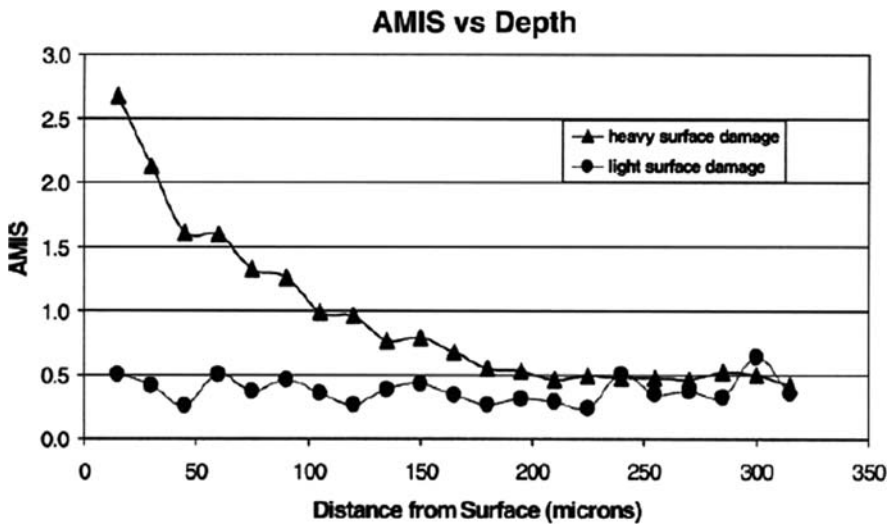


Fig. 18.7 AMIS as a function of depth from the surface of machined components. From Brewer et al. (2006a)

work of Sun et al. (2000) and Field et al. (2005) used mechanical deformation experiments such as channel die compression to precisely control the strain gradients in specific directions. The work of El-Dasher et al. (2003) used directionally solidified, columnar-grained Al in order to neglect the orientation gradient in the Z-direction.

Figure 18.8 shows the progression of orientation images obtained from a given area of a commercial purity Al sample deformed in channel die compression (Merriman et al. 2008). The sample was split with a pseudo-internal polished surface that was re-examined by EBSD after deformations of 5, 10, and 15%. The undeformed orientation image shows a recrystallized structure of the thick plate sample with virtually no lattice curvature being apparent in the undeformed material. The Taylor factor was calculated for {001}<100> orientations to be 2.4 for the given deformation state, while {011}<01–1> and {111}<01–1> grains each had a Taylor factor of ~4.0. This would indicate that the {011} and {111} grains should not deform until the {001} grains had hardened sufficiently to initiate slip in the grains of higher Taylor factor. Ultimately the higher Taylor factor grains would have a higher excess dislocation density due to the increased slip necessary for unit strain in these grains. Figure 18.9 shows

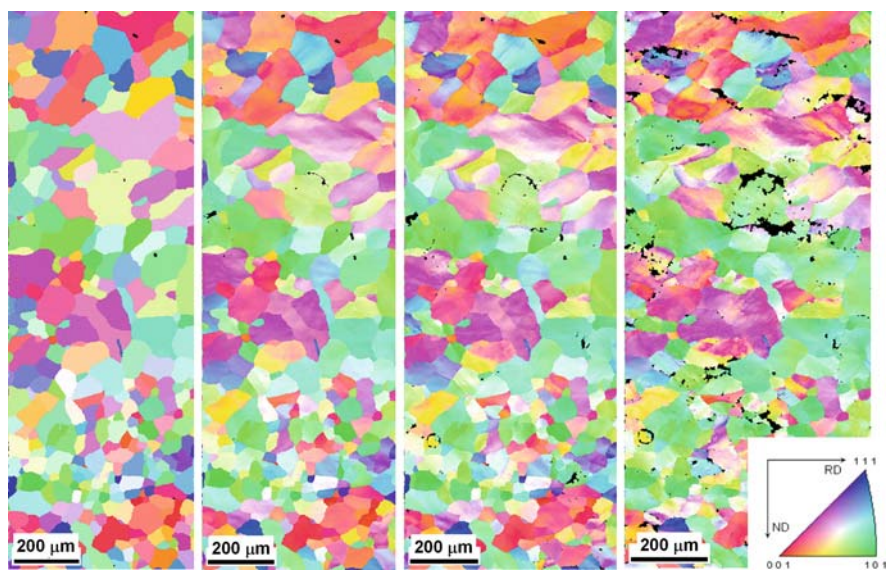


Fig. 18.8 Orientation images (inverse pole figure maps), from *left* to *right,* of undeformed, 5%, 10%, and 15% reduction in a split channel die specimen

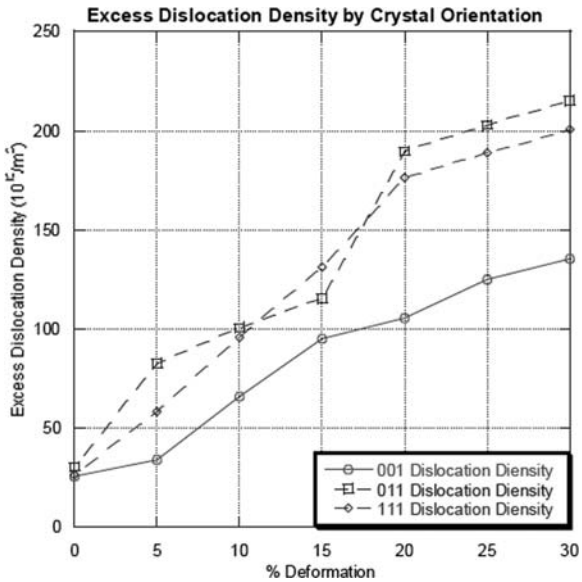


Fig. 18.9 Geometrically necessary dislocation density by orientation, {001}<100>, {011}<01–1>, and {111}<01–1> as a function of channel die reduction percentage

the calculated dislocation densities as determined from EBSD measurements on the plane section and Nye's dislocation density tensor. There is an obvious orientation dependence on the evolution of dislocation density, as might be expected, with the low Taylor factor {001} orientations developing significantly fewer GNDs than the higher Taylor factor grains.

Of course, working on the two-dimensional surface of a deformed material yields only partial information on the dislocation density tensor. Extension to three-dimensional observations has been reported by Larson and co-workers using microbeam X-ray techniques (Larson et al. 2007) and has been recently shown using EBSD measurements by Merriman (2007). The details of general three-dimensional EBSD measurements are discussed by Zaefferer and Wright in Chapter 8 of this book.

The ability to map and assess plastic deformation in three dimensions has several important consequences. Firstly, this approach will allow for the full determination of the Nye dislocation tensor, Eq. (18.1), and the calculation of GND densities. As noted above, most of the work on GND density determination has required samples or mechanical test geometries that allow assumptions to be made about the misorientation gradient in the z-direction. Three-dimensional measurements remove the need for these assumptions.

The complications of surface effects on the measurements of GND densities measured by EBSD can be illustrated by comparing the same measurement with synchrotron X-ray diffraction. A Cu single crystal was deformed by uniaxial compression to about 10 percent nominal strain (Florando et al. 2007). This specimen was split into two parts, with the adjoining faces being analyzed for dislocation content, one by EBSD and one by a method employing orientation measurements from a high energy X-ray source. The X-ray diffraction analyses were done on beam line 7.3.3 of the Advanced Light Source at the Lawrence Berkeley National Laboratory (ALS/LBNL). This particular instrument was well suited for these studies because of the high brilliance of its synchrotron source, the focusing optics that produce an ultrafine beam size (on the order of 0.5 μm), its "white beam" capabilities, and the positioning stages that allow the beam to be swept with a microscale step size over relatively large regions. The EBSD measurements were done on a Schottky source FESEM at 20 keV. The specimen surface was prepared metallographically with the final polish being a 5-hour vibratory-polish using a 0.02 μm colloidal silica suspension solution. Figure 18.10 displays orientation images from each type of analysis, Fig. 18.10a being from the X-ray technique and Fig. 18.10b from EBSD measurements. The color coding shows the misorientation angle from the nominal {2 9 20} orientation of the deformed crystal. These images are roughly the same scale, but appear quite distinct from one another. The deformation appears as sharp bands in the X-ray images, but diffuse in the EBSD maps. The range and positioning of misorientation is approximately the same, and the overall dislocation densities were calculated to be similar (on the order of $10^{13}/m^2$). The X-ray technique has an information volume several orders of magnitude greater than that of the EBSD technique, but the angular resolution of the X-ray measurement is an order of magnitude better than that achievable by EBSD. The more well-defined substructure seen by X-ray measurements is presumed to be a more accurate depiction of the average dislocation structure over a volume of several thousand cubic nanometers. The diffuseness of the structure is seen using the EBSD technique, but not the X-ray, because the EBSD measurement is more sensitive to the specimen surface with a depth resolution

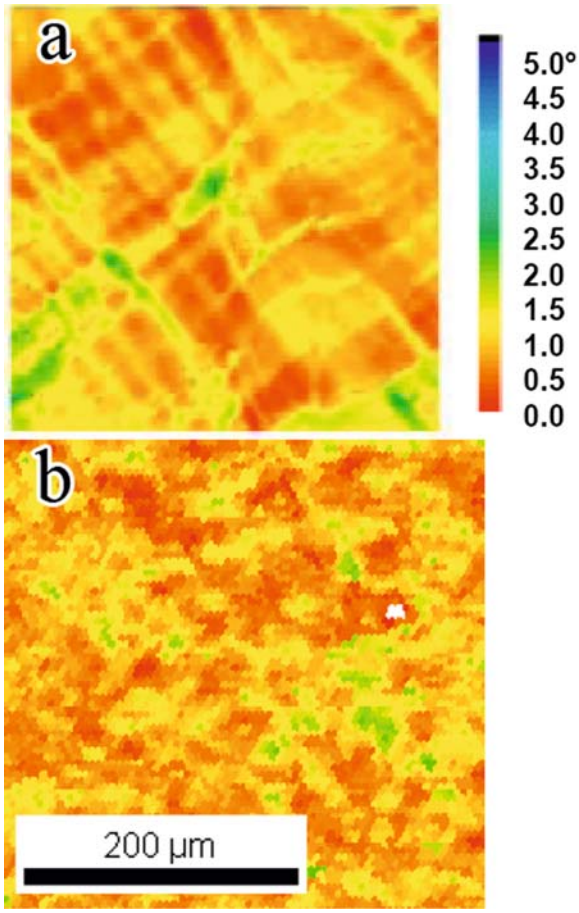


Fig. 18.10 Representative images showing the orientation of a Cu single crystal deformed 10% in uniaxial compression. (**a**) The image (300×300 μm; courtesy of K Magid and JW Morris, UC Berkeley) was obtained from measurements using a high-energy X-ray source. (**b**) A misorientation map from EBSD at the same step size. The color scale for both images shows 0–5 degrees misorientation from the nominal orientation of the single crystal before deformation

usually on the order of tens of nanometers or less (Ren et al. 1998). Dislocation structures may be influenced by the polishing procedure, and certainly tend to relax at the free surface. Simple discrete dislocation dynamics calculations show that a sharp dislocation wall composed of mixed dislocations will relax with the dislocation wall becoming diffuse to a depth of about 50 nm below the surface, but remains with little relaxation between the dislocations at a depth lower than 50 nm. This relaxation is seen in the EBSD measurements, but not by the X-ray technique, which probes over 1 μm below the specimen surface where the dislocation structure has not relaxed.

Several researchers, including the authors of this chapter, have shown tight dislocation walls in deformed Cu and have shown dislocation structures similar to those observed in TEM specimens from EBSD measurements on TEM foils. The difference must be in the character of the dislocation structures observed. Those presented herein are from relatively small plastic deformation, and the dislocation structures are more likely to relax in comparison with structures that have well-established locks or walls that will not as easily relax near a free surface. Definition of these structures and a complete description of what is seen by EBSD measurements is beyond the scope of the present chapter. It suffices to point out that EBSD measurements should not be assumed to always give a true representation of the bulk character of the microstructure. Further combination of the synchrotron measurements described above with three-dimensional EBSD-FIB sectioning and detailed dislocation dynamics calculations applied to specimens with well-characterized deformation structures will be vital to understanding the bounds of applicability for EBSD to detailed crystalline plasticity measurement.

One final note concerns the resolution of EBSD measurements in relation to the dislocation density calculations. Assuming the standard angular resolution cited for EBSD (~0.5 degrees), a significant error in the calculations can be expected; and the error will increase as the step size decreases (since the curvature tensor goes as dq/dx with dx being the step size of the EBSD scan). Our work has shown that smoothing or averaging of the data has little benefit in obtaining correct results; and that for cell-forming materials, the step size should be on the order of the dislocation cell size for the most accurate results. Recent work by Landon, Adams and Kacher (2008) develops a mathematical framework and incorporates the resolution refinement of Wilkinson et al. (2006) to obtain reliable results from 3D measurements. This is another area of interest that should receive considerable attention from plasticity researchers in the coming years.

Acknowledgments The authors wish to thank S. Wright of EDAX-TSL and C. Parish of Sandia National Laboratories for helpful discussion about this chapter. LNB was supported by Sandia National Laboratories, a multiprogram laboratory operated by Sandia Corporation, a Lockheed Martin Company, for the United States Department of Energy (DOE) under contract DE-AC0494AL85000.

References

Adams BL (1997) Orientation imaging microscopy: Emerging and future applications. Ultramicroscopy 67:11–17

Alvi MH, Cheong S, Weiland H, Rollett AD (2004) Recrystallization and texture development in hot rolled 1050 aluminum. Mater Sci Forum 467–470:357–362

Angeliu TM, Andresen PL, Hall E, Sutliff JA, Sitzman S, Horn RM (1999) Intergranular stress corrosion cracking of unsensitized stainless steels in BWR environments. In: Bruemmer S, Ford P, Was G (eds) Ninth international symposium on environmental degradation of materials in nuclear power systems-water reactors. TMS—Minerals, metals and materials society, Newport Beach, CA

Arsenlis A, Parks DM (1999) Crystallographic aspects of geometrically-necessary and statistically-stored dislocation density. Acta Mater 47:1597–1611

Ashby MF (1970) The deformation of plastically non-homogeneous materials. Philos Mag A 21:399–424

Barton NR, Dawson PR (2001) A methodology for determining average lattice orientation and its application to the characterization of grain substructure. Metall Mater Trans A 32: 1967–1975

Brewer LN, Othon MA, Gao Y, Hazel BT, Buttrill WH, Zhong Z (2006a) Comparison of diffraction methods for measurement of surface damage in superalloys. J Mater Res 21:1775–1781

Brewer LN, Othon MA, Young LM, Angeliu TM (2006b) Misorientation mapping for visualization of plastic deformation via electron backscattered diffraction. Microsc Microanal 12:85–91

Brough I, Bate PS, Humphreys FJ (2006) Optimising the angular resolution of EBSD. Mater Sci Tech 22:1279–1286

Cheong S, Weiland H (2007) Understanding a microstructure using GOS (grain orientation spread) and its application to recrystallization study of hot deformed al-cu-mg alloys. Mater Sci Forum 558–559:153–158

El-Dasher BS, Adams BL, Rollett AD (2003) Viewpoint: Experimental recovery of geometrically necessary dislocation density in polycrystals. Scripta Mater 48:141–145

Field DP, Trivedi PB, Wright SI, Kumar M (2005) Analysis of local orientation gradients in deformed single crystals. Ultramicroscopy 103:33–39

Florando JN, LeBlanc MM, Lassila DH (2007) Multiple slip in copper single crystals deformed in compression under uniaxial stress. Scripta Mater 57:537–540

Kamaya M, Wilkinson AJ, Titchmarsh JM (2005) Measurement of plastic strain of polycrystalline material by electron backscatter diffraction. Nucl Eng Des 235:713–725

Kamaya M, Wilkinson AJ, Titchmarsh JM (2006) Quantification of plastic strain of stainless steel and nickel alloy by electron backscatter diffraction. Acta Mater 54:539–548

Landon CD, Adams BL, Kacher J (2008) High-resolution methods for characterizing mesoscale dislocation structures. J Eng Mater Tech 130:021004–1-021004–021004–5

Larson BC, El-Azab A, Wenge Y, Tischler JZ, Wenjun L, Ice GE (2007) Experimental characterization of the mesoscale dislocation density tensor. Philos Mag 87:1327–1347

Lehockey EM, Lin Y, Lepik OE (2000) Mapping residual plastic strain in materials using electron backscatter diffraction. In: Schwartz AJ, Kumar M, Adams BL (eds) Electron backscatter diffraction in materials science. Kluwer Academic, New York

Merriman CC (2007) Orientation dependence of dislocation structure evolution of aluminum alloys in 2-D and 3-D, MS Thesis, Washington State University, Pullman, Washington, DC

Merriman CC, Field DP, Trivedi P (2008) Orientation dependence of dislocation structure evolution during cold rolling of aluminum. Mat Sci Eng A 494:28–35

Nye JF (1953) Some geometrical relations in dislocated crystals. Acta Metall 1:153–162

Pantleon W (2008) Resolving the geometrically necessary dislocation content by conventional electron backscattering diffraction. Scripta Mater 58:994–997

Prior DJ (1999) Problems in determining the misorientation axes, for small angular misorientations, using electron backscatter diffraction in the SEM. J Microsc 195:217–225

Reddy SM, Timms NE, Pantleon W, Trimby P (2007) Quantitative characterization of plastic deformation of zircon and geological implications. Contrib Mineral Petrol 153: 625–645

Ren SX, Kenik EA, Alexander KB, Goyal A (1998) Exploring spatial resolution in electron backscattered diffraction experiments via Monte Carlo simulation. Microsc Microanal 4: 15–22

Sun S, Adams BL, King WE (2000) Observations of lattice curvature near the interface of a deformed aluminium bicrystal. Philos Mag A 80:9–25

Sutliff JA (1999) An investigation of plastic strain in copper by automated EBSD. In: Bailey GW, Jerome WG, McKernan S, Mansfield JF, Price RL (eds) Microscopy and microanalysis. Springer-Verlag, Berlin

Wilkinson AJ (2001) A new method for determining small misorientations from electron backscatter diffraction patterns. Scripta Mater 44:2379–2385

Wilkinson AJ, Dingley DJ (1991) Quantitative deformation studies using electron backscatter patterns. Acta Metall 39: 3047–3055

Wilkinson AJ, Meaden G, Dingley DJ (2006) High-resolution elastic strain measurement from electron backscatter diffraction patterns: New levels of sensitivity. Ultramicroscopy 106:307–313

Wright SI (1993) A review of automated orientation imaging microscopy (OIM). J Comput Assist Microsc 5:207–221

Wright SI (1999) Quantification of recrystallized fraction from orientation imaging scans In: Szpunar JA (ed) ICOTOM 12, Proceedings of the Twelfth International Conference on Textures of Materials (ICOTOM 12), Montreal, Canada, Edited by Jerzy A. Szpunar, NRC Research Press, Ottawa, 1999

Wright SI, Nowell MM (2006) EBSD image quality mapping. Microsc Microanal 12:72–84

Young GA, Lewis N, Battige CK, Somers RA, Penik MA, Brewer L, Othon M (2002) Quantification of residual plastic strains in Ni-Cr-Mn-Nb GTAW welds via electron backscatter diffraction. ASM proceedings of the international conference: Trends in welding research, p 912

Chapter 19

Analysis of Deformation Structures in FCC Materials Using EBSD and TEM Techniques

Oleg V. Mishin, Andrew Godfrey, and Dorte Juul Jensen

19.1 Introduction

In a large number of industrially important metals and alloys, a fraction of the dislocations generated during deformation remain trapped and arranged into well-defined dislocation boundaries (Bay et al. 1992; Hansen and Juul Jensen 1999; Hughes and Hansen 2000; Li et al. 2004). Extensive investigations using the transmission electron microscope have established that these dislocation boundaries separate volumes of different crystal orientations, and that two classes of dislocation boundaries can be defined (Liu et al. 1998; Hansen 2001). Individual cells are delineated by boundaries referred to as incidental dislocation boundaries (IDBs). These dislocation cells are grouped into cell-blocks, delineated by long planar dislocation boundaries, referred to either as extended planar boundaries or geometrically necessary boundaries. Two of the key quantitative parameters for describing the deformed microstructure are therefore the misorientation angle across each boundary, and the spacing between adjacent dislocation boundaries. This description of the deformed microstructure has proved very useful both in providing information to understand the underlying processes taking place during plastic deformation, and in providing quantitative data that can be used to assess both the mechanical properties and the thermal stability of a deformed sample.

O.V. Mishin (✉)
Risø National Laboratory for Sustainable Energy, Materials Research Department, Center for Fundamental Research: Metal Structures in Four Dimensions, Technical University of Denmark, DK-4000, Roskilde, Denmark
e-mail: oleg.mishin@risoe.dk

Until the advent of the electron backscatter diffraction (EBSD) technique, almost all detailed quantitative investigations of deformed microstructures were carried out using the transmission electron microscope (TEM). Investigations in the TEM allow a complete characterization of deformed microstructures with both a high spatial resolution and a high angular resolution. However, the measurement of crystal orientations in the TEM is in general a slow process, though a semi-automated technique has been developed (Liu 1995), and some work has been carried out to develop a system for fully automated orientation measurements in the TEM (Zaefferer 2000; Fundenberger et al. 2003; Rauch and Veron 2005).

The very high measurement speed possible using EBSD (currently more than 300 measurements per second), combined with the fact that deformation microstructures consist of dislocation cells and subgrains, provides therefore a strong motivation for the use of this technique for investigation of deformed metals and alloys. However, when using EBSD to investigate deformation microstructures, difficulties can be encountered due to the presence of dislocation boundaries with very low misorientation angles and with potentially very narrow spacing (Huang and Juul Jensen 2000).

The capability of the EBSD technique to provide quantitative data describing deformed microstructures is limited therefore by both the spatial and angular resolution of the technique (Humphreys et al. 1999; Humphreys and Brough 1999). Of these, the limited angular resolution presents the most serious problem, as it prevents the detection of boundaries with misorientation angles below a certain value, typically either 1.5° or 2°, and restricts accuracy in the determination of the boundary rotation axis for boundaries of

A.J. Schwartz et al. (eds.), *Electron Backscatter Diffraction in Materials Science*,
DOI 10.1007/978-0-387-88136-2_19, © Springer Science+Business Media, LLC 2009

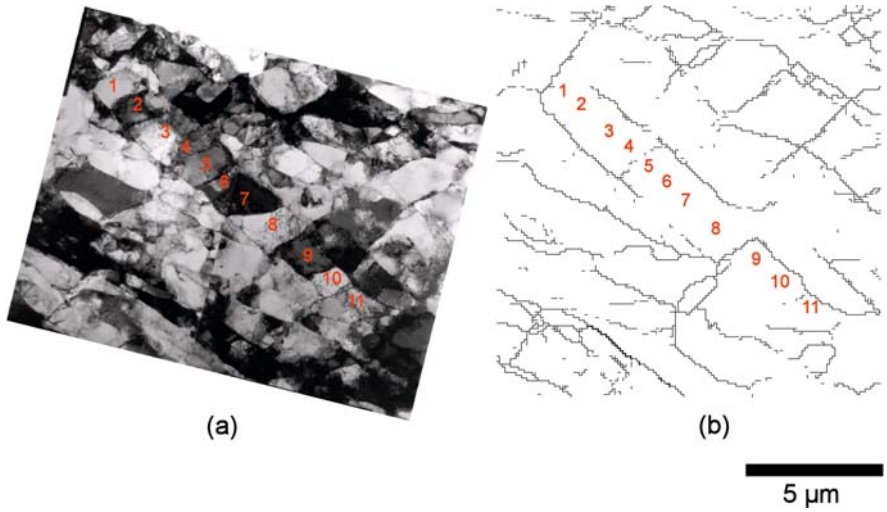


Fig. 19.1 A region in commercially pure aluminum cold-rolled ~50% sampled using (**a**) TEM and (**b**) EBSD techniques. In (**b**) *thin gray lines* show low angle (1.5–15°) misorientations; *bold lines* indicate high angle (>15°) boundaries. The *numbers* indicates the correspondence between the TEM and EBSD data

less than 5° (Prior 1999). This limitation is illustrated in Fig. 19.1, showing the microstructure of commercially pure aluminum cold-rolled to a strain of 0.7. The same region of this sample has been examined both in the TEM and in a field emission gun scanning electron microscope (FEG-SEM) using EBSD. Most of the boundaries in this region are low angle boundaries with misorientations <15°. Moreover, there are many boundaries with very low misorientations. An orientation map constructed to show boundary misorientations of greater than 1.5° reveals only a small fraction of the boundaries present in the microstructure. For instance, along the line of dislocation cells numbered 1 through 11, only three boundaries are seen in the EBSD map, and only one of these (boundary 8–9) is seen as an intact boundary.

Although the fraction of low angle boundaries in a deformed microstructure will in general decrease with increasing strain, TEM investigations show that regardless of the strain, deformed metals always contain a certain population of boundaries with very low misorientation angles. For example, in FCC metals, even after cold-rolling to a strain of $\varepsilon = 2$, the average misorientation for the boundaries identified as IDBs is typically only 2°–4° (Hughes and Hansen 2000; Liu et al. 2002). A complete description of the deformation microstructure is not possible if these boundaries cannot be identified.

The difficulty in reliable detection of very low misorientations is also a problem for investigating microstructural refinement during deformation processes designed to impart large plastic strains. Information about the presence of low angle boundaries is important to assess the effectiveness of the many suggested deformation process variations. For this purpose, the fraction of high angle boundaries (f_{HAB}) is often used as a parameter to characterize the extent of microstructural refinement (usually defined as the fraction of boundaries with misorientation angles greater than 15°). Although this parameter can be useful, it is important to recognize that the EBSD technique cannot in general measure the true value of this parameter, for the simple reason that the technique is not able to detect boundaries below a certain misorientation angle.

The detection of very low misorientations is also important for analysis of the uniformity of microstructural refinement during plastic deformation. Here the EBSD technique offers the advantage of providing orientation data gathered from relatively large areas, but caution must be taken to ensure that the data collected are interpreted in a sensible manner.

In the following, we first examine the way in which the angular resolution affects EBSD data, and then discuss the use and limitations of orientation averaging filters as a means to improve the angular resolution of data collected from deformed samples. In the final part of the chapter, we describe some of the ways in which EBSD data can be used to examine heterogeneity in microstructural refinement, even when misorientations below some angle cannot be detected.

19.2 Orientation Noise in EBSD Data

19.2.1 A Quantitative Description of Orientation Noise

The angular resolution of EBSD data is best considered in a statistical manner and can be thought of as arising from a combination of a number of different parameters. These include the physical resolution limits associated with the EBSD detector, the software routines used to detect and index the patterns, variations in the sample surface quality, the crystal orientation of the volume sampled by the electron beam, and variations in the local density of loose dislocations (those not arranged into boundaries). These effects can be examined in part by collecting a large number of EBSD measurements in a region of an undeformed single crystal. Such measurements give a spread of orientations, with the width of the spread being greater than would be seen from an X-ray investigation of the same sampled volume, and with the orientation spread centered about the true crystal orientation (Humphreys et al. 1999; Demirel et al. 2000; Godfrey et al. 2006). The orientation noise can be quantified by calculating the misorientation angle $\theta_{i,j}$ between adjacent EBSD measurements in such a mapped region, taking the minimum angle among the crystallographically equivalent descriptions for each misorientation. For a perfect undeformed single crystal all misorientations between adjacent measurements should be 0°, hence the distribution of adjacent pixel misorientations, $P(\theta_{i,j})$, can be directly attributed to the noise in the data. Example data taken from two recrystallized single grains within an aluminum sample are shown in Fig. 19.2a. The difference between the two curves highlights the fact that the orientation noise also varies with the crystal orientation. In most cases it has been found that the distribution $P(\theta_{i,j})$ takes the form of a Rayleigh distribution. This is illustrated in Fig. 19.2b where the data are replotted as average normalized distributions. The mean value $\overline{\theta}_{i,j}$ provides therefore a convenient parameter to quantify the orientation noise.

It should be pointed out that this procedure can only be carried out using undeformed samples, as the analysis relies on the assumption that $\theta_{i,j}$ should be 0° everywhere, and hence any non-zero values of $\theta_{i,j}$ can be attributed to the presence of orientation noise in the data. Values as low as $\overline{\theta}_{i,j} = 0.3°$ can be obtained for maps from fully recrystallized samples.

In deformed metals the orientation noise is worse because of a higher dislocation density in the microstructure, leading to lower EBSD pattern qualities and also in some cases to problems with EBSD pattern overlap. In heavily deformed samples these problems may result in a significant number of non-indexed pixels in the final EBSD map, corresponding to locations where the software was not able to assign an orientation to the sampled volume. Commercial EBSD systems provide data cleaning procedures to allow orientations to be assigned to such pixels, based on an analysis of the neighboring pixel orientations. These procedures will not be discussed further here, other than to note that caution should be applied when using such procedures, particularly when clusters of non-indexed sites are present in the microstructure.

In general, the level of orientation noise in an EBSD data set taken from a deformed sample is still estimated on an ad hoc basis: in most investigations of deformed metals the lower limit for reliable detection of boundary misorientations is taken as either 1.5° or 2°. As described in the next section, postprocessing filtering

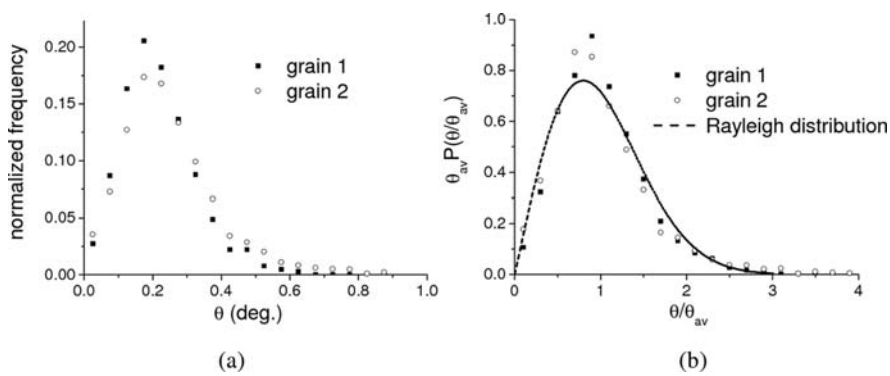


Fig. 19.2 Distributions of adjacent pixel misorientations ($\theta_{i,j}$) in EBSD maps taken in a sample of recrystallized aluminum: (**a**) data for grains of two different crystal orientations; (**b**) average normalized distributions. The distributions can be described approximately as a Rayleigh distribution

operations can be used to reduce the amount of orientation noise; however, such filtering can also introduce artifacts into the data, and the number of such artifacts depends also on the amount of orientation noise in the original data set.

19.2.2 Postprocessing Orientation Filtering Operations

Because the orientation noise results in a measured orientation spread centered around the true orientation, the data quality can be improved, in principle, by the use of an orientation averaging process: for example, assigning the orientation of each pixel as the average orientation of all pixels within a region centered on the pixel of interest. However, care must also be taken to avoid carrying out such averaging calculations over regions where real orientation differences are present in the microstructure. For this reason, the use of a modified edge-preserving Kuwahara filter has been suggested for filtering of EBSD data (Humphreys et al. 2001).

The basic idea of the filter is as follows. For each pixel in the EBSD map a square grid of side length (2*N*-1) is considered, centered on the pixel of interest. Each grid is then divided into 4(*N*-1) subgrids, each of size $N \times N$, such that each subgrid extends to the edge of the main grid. The filter grid construction is illustrated in Fig. 19.3a. For simplicity, orientations are represented by a single number, rather than as an Euler triplet. The mean orientation and variance of each subgrid are calculated, and then the center pixel is assigned the orientation corresponding to the mean orientation of the subgrid with the smallest variance—but only if no pixel in the chosen subgrid is misoriented to the center pixel by more than some chosen value, θ_{ab}. The filtering process is applied to each pixel in turn in the EBSD map, and the orientation values for all pixels are updated simultaneously. The mean and variance can be conveniently calculated using a quaternion parameterization of the crystal orientation, in which the mean orientation is obtained from renormalization

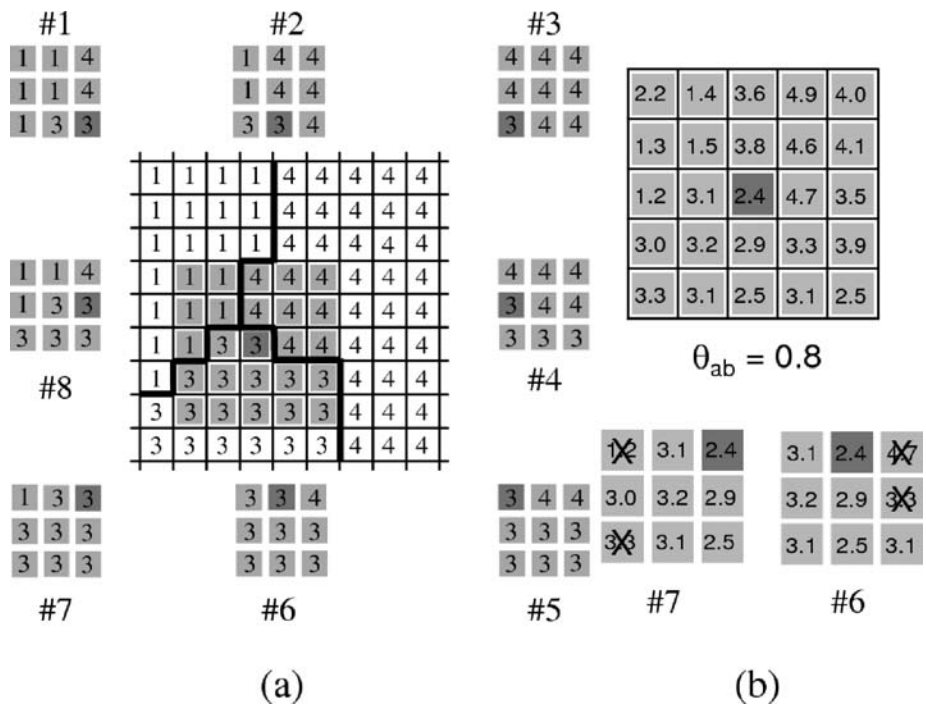


Fig. 19.3 Illustration of the orientation filtering procedure: (**a**) A 5×5 filter centered at a grain triple junction, showing the eight 3×3 subgrids. (**b**) Operation of the MSMV filter. The value at each grid point is adjusted with respect to Fig. 19.3(a) to represent the effect of orientation noise on the data. Of the eight subgrids, #6 and #7 both contain just 2 pixels misoriented by more than θ_{ab} (= 0.8°) to the center pixel (these pixels are shown crossed out in the figure). The filtered orientation is taken as the average orientation with the lowest variance from these two subgrids (in this case #7)

of the quaternion vector sum for the given orientations, and the variance is inversely proportional to the length of the quaternion vector sum (Humphreys et al. 2001). Suitable care must be taken to ensure that all orientations are in a similar region of orientation space prior to calculation of the quaternion vector sum.

A further modification of the filter, the maximum subgrid–minimum variance (MSMV) filter, has been suggested (Godfrey 2004), leading to greater ease of use and to improved filter performance for typical deformed microstructures. This filter consists of the following steps:

1. for each subgrid the number of pixels misoriented to the center pixel by less than or equal to θ_{ab} is determined, and the maximum value of this parameter, K_{max}, is recorded;
2. the mean orientation and variance are calculated only for those subgrids containing K_{max} pixels misoriented to the center pixel by less than θ_{ab}—pixels misoriented by more than θ_{ab} to the center pixel are ignored in the calculation of the mean and variance;
3. the centre pixel is finally reassigned with the mean orientation of the subgrid with the minimum variance.

An additional parameter f_{ab} can also be used, defined such that the averaging process is aborted if the value of K_{max}/N^2 is less than f_{ab} (i.e., this parameter sets a requirement for the minimum number of pixels to use for the averaging calculation). The operation of the MSMV filter is illustrated in Fig. 19.3b. As previously, the orientation associated with each pixel is represented by a single number. Noise has been added to the ideal orientation data by adding values taken randomly from a Gaussian distribution with vanishing mean and standard deviation of $\sigma = 0.5$. For the case of $\theta_{ab} = 0.8$, two subgrids (#6 and #7) have the maximum number of pixels deviated by less than θ_{ab} to the center pixel. Of these, subgrid #7 has the lowest variance, and hence the average of this subgrid (ignoring pixels deviated by more than θ_{ab}) is assigned as the post-filtering orientation of the center pixel.

An example of the operation of the MSMV filter, using simulated EBSD map data, is shown in Fig. 19.4. Initially, each grain in the structure (Fig. 19.4a) is assigned an orientation such that the mean boundary misorientation is 2.2° and the boundary misorientation distribution has the form of a Rayleigh distribution (Pantleon 1998). Orientation noise is then simulated by adjusting the orientation of each pixel within each grain according to $\mathbf{g}_{\mathrm{w/n}} = \mathbf{g}_{\mathrm{old}}.\mathbf{R}_{\mathrm{X}}.\mathbf{R}_{\mathrm{Z}}$.

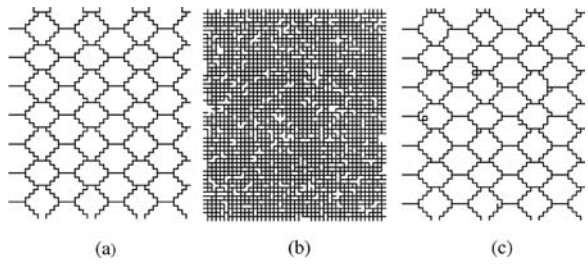


Fig. 19.4 Demonstration of the effect of the MSMV filter using simulated EBSD data: (**a**) original structure (average boundary misorientation = 2.2°); (**b**) misorientation map at $\theta^* = 0.25°$ after addition of orientation noise to the data; (**c**) misorientation map at $\theta^* = 0.25°$ after additional MSMV filtering of the data (filtering parameters described in main text)

Here $\mathbf{g}_{\mathrm{old}}$ is the underlying ideal grain orientation, and $\mathbf{g}_{\mathrm{w/n}}$ is the pixel orientation after the addition of orientation noise. The matrices $\mathbf{R}_{\mathrm{X}}$ and $\mathbf{R}_{\mathrm{Z}}$ are rotations about the sample X and Z axes, in which the rotation angles are taken independently from a Gaussian distribution with mean $\mu = 0$ and a value of the standard deviation σ such that $\overline{\theta}_{i,j} = 1.77\sigma$ (Godfrey et al. 2002, 2006). For the data shown here a value of $\overline{\theta}_{i,j} = 0.44$ was used.

Figure 19.4b shows a misorientation map of the simulated EBSD data (with noise) at $\theta^* = 0.25°$, where θ^* is the boundary angle definition. For this boundary angle definition, the structure is completely obscured by the effects of the orientation noise.

After filtering (using one pass of a 7×7 filter with $\theta_{ab} = 0.9°$ and $f_{\mathrm{ab}} = 0.5$) the orientation noise is greatly reduced (Fig. 19.4c) such that the underlying grains can again be imaged, with just minor distortions.

It is important to note, however, that Kuwahara-type filters work by forcing pixels into blocks of very similar orientation (a comparison between different filters can be found elsewhere: Mishin and Godfrey 2007). Hence artifacts that may be mistaken for dislocation cells or subgrains will appear if the boundary angle definition (θ^*) is taken below a certain value. The main difficulty in using such filtering lies therefore in choosing the optimum filtering parameters (the filter size and the value of θ_{ab}), and then in choosing the lowest value of θ^* for the EBSD map. It is clear, however, that post-processing filtering has the potential to give a

significant improvement in the EBSD data quality. In the next section we examine the effectiveness of such filtering in more detail by comparing orientation measurements made in the same area, both in the TEM and using EBSD.

19.3 Quantitative TEM–EBSD Comparison

The limitations of the EBSD technique for the detection of low angle boundaries can be examined in more detail via the examination of the same deformed microstructure both using EBSD and in the TEM. Here we describe the results of such an investigation performed on a thin foil sample taken from the centre of a friction stir weld nugget in an Al 6082 profile (Mishin et al. 2006). The area examined in the TEM is shown in Fig. 19.5. Note that because of the sensitivity of diffraction contrast to the crystal orientation, not all of the dislocation boundaries in this region are visible in this image. In order to ensure that all dislocation boundaries were identified, the region was examined at a range of tilt angles before any orientation measurements were made, enabling different diffraction contrast conditions. A sketch was then made of the microstructure based on the observations from multiple tilting of the sample.

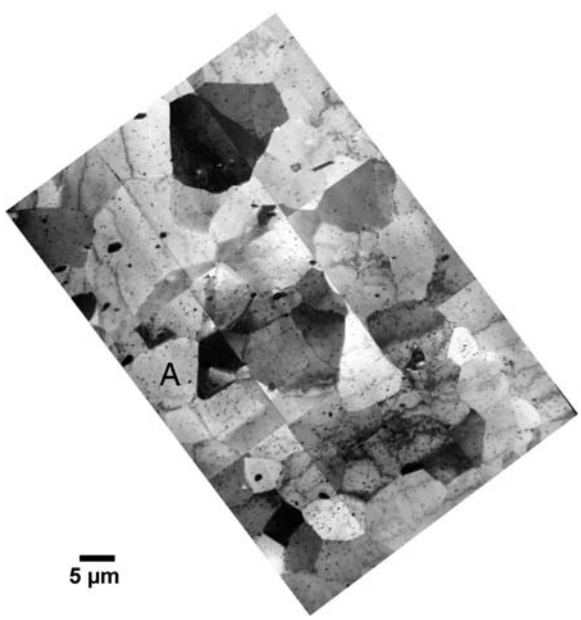


Fig. 19.5 TEM montage showing a region of a friction stir welded (FSW) aluminum 6082 sample that has also been investigated using the EBSD technique. Label "A" is given for reference

The orientations of the dislocation cells in the region were measured in the TEM using a Kikuchi-based method (Liu 1995). Sample tilting was not necessary for measurement of low misorientations, and hence the accuracy in the misorientation angle measurements for low angle boundaries is estimated to be better than $\pm 0.3^\circ$. The sample was subsequently examined in a FEG-SEM, and ESBD measurements were made in a rectangular map covering the same region using a step size of 0.4 μm. A limited amount of data cleaning was carried out, to assign orientations to pixels in the map where indexing was not possible. The EBSD data were additionally postprocessed using the MSMV filter described in the previous section. Two passes of the filter were applied, in each case using a 7×7 ($N = 4$) kernel and a setting of $\theta_{ab} = 1.5^\circ$.

Orientation maps obtained using both the filtered and non-filtered EBSD data are shown in Fig. 19.6a, b, c, d. In Fig. 19.6a one of the cells is marked "A" to facilitate comparison of the TEM and EBSD images. A map of the unfiltered data constructed using a minimum misorientation angle definition of $\theta^* = 1.5^\circ$ (within the range of typical values used for investigations of deformed microstructures) misses a significant number of dislocation boundaries (Fig. 19.6a). Lowering the value of θ^* to 0.5° reveals some additional boundaries, but also results in a very large increase in the orientation noise in the map (Fig. 19.6b). Figure 19.6c shows the misorientation map obtained using $\theta^* = 0.5^\circ$ for the MSMV filtered data. A considerable improvement in the data quality is seen compared with the unfiltered data. The filtering process also results, however, in the introduction of some artifacts. For example, the horizontal segment in the small cell near the top-center of Fig. 19.6c does not correspond to a real boundary in the microstructure. At $\theta^* = 0.4^\circ$ more of the low angle boundaries are visible. This improvement is accompanied though by a further increase in the number and extent of artificial extended boundary segments. These results are shown more clearly in Fig. 19.7 for the smaller area investigated in detail in the TEM. In this figure solid black lines represent real dislocation boundaries that are seen by a given technique under a given set of conditions, solid gray lines represent boundaries that exist but are

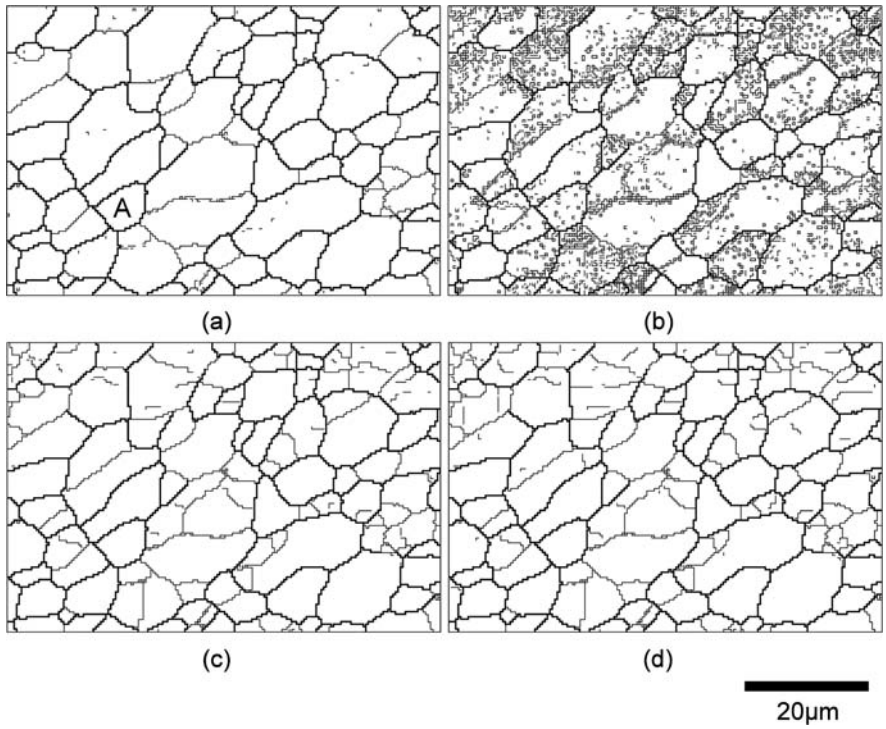


Fig. 19.6 EBSD maps of the FSW sample region shown in Fig. 19.5: (**a**) unfiltered EBSD map, $\theta^* = 1.5^\circ$; (**b**) unfiltered EBSD map, $\theta^* = 0.5^\circ$; (**c**) filtered map, $\theta^* = 0.5^\circ$; and (**d**) filtered map, $\theta^* = 0.4^\circ$. *Bold lines* indicate high angle ($>15^\circ$) boundaries; *thin lines* correspond to low angle misorientations. Label "A" shows the same dislocation cell in both the TEM sketch and EBSD maps. Note that in the EBSD maps, dislocation cell shapes are slightly distorted compared to the TEM image

not seen, and black dotted lines represent artifacts that do not exist in the real microstructure.

A quantitative analysis of the data reveals further complications. The average cell size (given as the average value of the equivalent circle diameter, d_{ECD}), for the cells detected using a grain reconstruction process (Humphreys 2001) as a function of the minimum misorientation angle definition θ^*, is shown in Fig. 19.8a. It should be noted that in deformed materials, each reconstructed "grain" may in fact either consist of a number of dislocation cells or represent an individual cell. Note also that the EBSD data shown in this figure were calculated only for the region sampled in the TEM and not for the entire map. The dashed line in this graph gives the average cell size as measured from the TEM investigation. The dislocation cell size is underestimated in both the unfiltered and the filtered data, even up to large values of θ^*. The reason for this underestimation is the presence of small, mostly single-pixel artifacts in the data. Because the average cell area is calculated as a simple average of the area of all detected cells, the presence of a small number fraction of such single-pixel features can have a dramatic impact on the measured cell size. For orientation maps in which, as is the case for the current study, the EBSD map step size is considerably smaller than the average cell size, these small artificial cells can be safely ignored in the calculation of the average cell size (Cao et al. 2003a). The variation of the average cell size with θ^*, ignoring any features with area $< 1\ \mu m^2$ (<6 pixels at the step size used), is also shown in Fig. 19.8a. After ignoring the artificial features, the filtered data yield values slightly above the true cell size.

Another parameter that is often reported in EBSD studies of deformed samples is the fraction of high angle boundaries, f_{HAB}. This parameter is calculated as the total length of misorientation boundary greater than θ_{HAB} (taken here as 15°), relative to the total length of all boundaries in the map. In practice, this parameter is usually calculated from the number fraction of adjacent pixel misorientations, i.e., $f_{\mathrm{HAB}} = N(>\theta_{HAB})/N(>\theta^*)$.

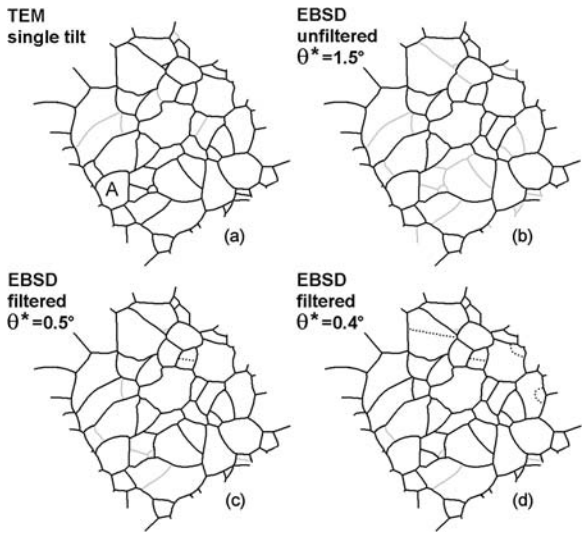


Fig. 19.7 Sketches highlighting the differences to the microstructure revealed in the TEM by multiple tilting of the foil: *solid black lines* show boundaries observed in: (**a**) the single-tilt TEM image in Fig. 19.5; (**b**) the unfiltered EBSD map at θ^*=1.5°; (**c**) the MSMV filtered map at θ^*=0.5°; and (**d**) the MSMV filtered map at θ^*=0.4°. *Gray lines* indicate boundaries missed in a given map, while the *dashed lines* show artifacts produced as a result of the MSMV orientation-averaging procedure. Note that the EBSD maps were used to identify which boundaries/artifacts were visible at different θ* values. Therefore, the sketches are not direct tracings of the EBSD maps. The slight distortion of the structure in the EBSD maps of Fig. 19.6 is not reflected in the sketches

It is worth noting here that for maps where the step size is small relative to the underlying structure, the number of misorientations with angle θ will in general overestimate the real length of the boundary of misorientation angle θ. This overestimation is due to the step-like nature of boundaries in EBSD maps (Cao et al. 2003a; Valke et al. 2006). For a fully equiaxed microstructure in an EBSD map made using a square grid, the value will be overestimated by a factor of $4/\pi$ (Cao et al. 2003b). The presence of orientation noise in the data requires that a minimum critical misorientation angle (θ^*) is chosen to determine the total boundary length. It is clear, therefore, that f_{HAB} will vary depending on the value chosen for θ^*. The variation of f_{HAB} with θ^* for both the untreated and the filtered data is shown in Fig. 19.8b. The dashed line gives the value for f_{HAB} obtained from TEM measurements (from a total of 224 boundaries, including measurements in two other regions not examined using EBSD). For the filtered data, a value close to the TEM data is obtained for $\theta^* = 0.5^\circ$. In contrast to the unfiltered data, the value of f_{HAB} increases by as much as 20% (absolute difference), as θ^* is varied from 1° to 2°. A more detailed analysis of this data, together with an additional comparison of the EBSD and TEM data with information obtained from conventional backscattered electron imaging and gallium-enhanced microscopy, is given elsewhere (Mishin et al. 2006).

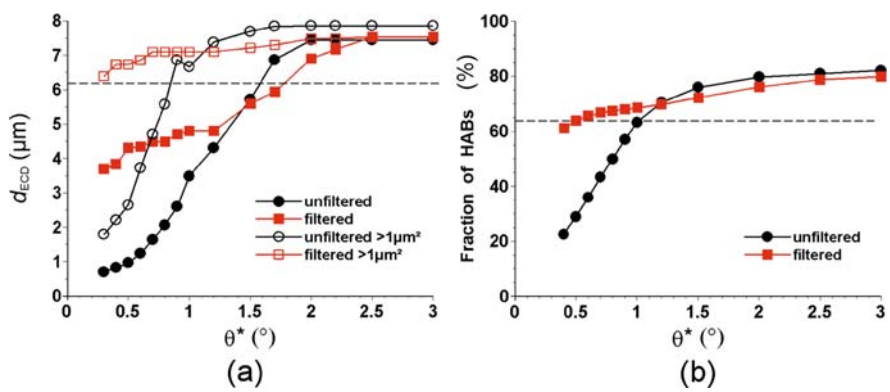


Fig. 19.8 Quantitative analysis of the data from the FSW sample: (**a**) graph showing d_{ECD} for the unfiltered and filtered data sets as a function of the minimum misorientation definition, θ^*. *Solid symbols* correspond to the data obtained directly from the maps. *Open symbols* represent the data after ignoring cells smaller than 1 μm^2 in area. (**b**) Fractions of high angle (>15°) boundaries from the unfiltered and filtered EBSD maps (relative to a minimum angle of θ^*). The *dashed lines* correspond to the values obtained from the multitilting TEM experiment

19.4 Heterogeneity in Microstructural Refinement

One advantage of the EBSD technique compared to TEM investigations is the fact that large areas can be mapped, allowing therefore an examination of heterogeneity in deformed microstructures. Heterogeneities are a general characteristic of deformed microstructures and may exist in many forms and over many length scales. At low strains, heterogeneity exists as a consequence of the grain orientation dependence of the deformed microstructure. With increasing strain, other forms of heterogeneity are observed, including bands of localized glide and shear bands. Another important heterogeneity in high strain deformed microstructures is the variation in the extent of microstructural refinement. This form of heterogeneity is particularly important in the context of research efforts to produce submicron grain size microstructures by deformation to large plastic strains, where a major objective is to develop a fine spacing between high angle boundaries. As discussed in the following, EBSD investigations are particularly well suited for such investigations, because useful information can be obtained from the detection of regions with different populations of low and high angle boundaries, even when the specific characteristics of the low angle boundaries in the microstructure cannot be completely identified.

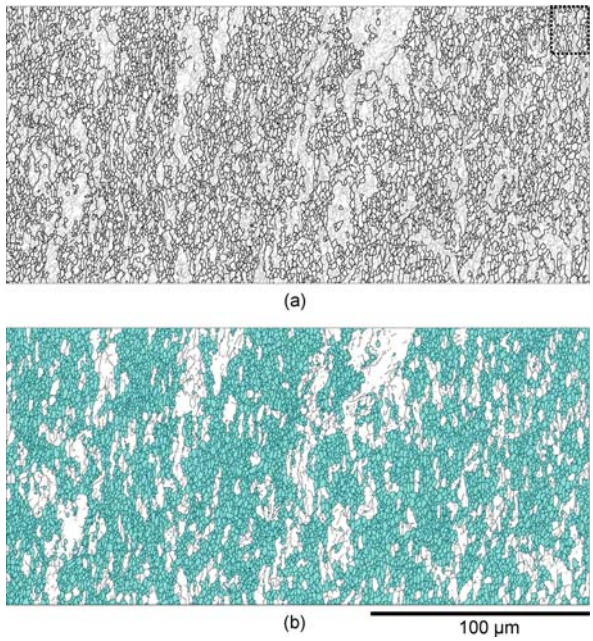


Fig. 19.9 EBSD maps from the ECAE-processed Al sample: (**a**) misorientation map. *Bold black lines* indicate high angle (>15°) boundaries, and *thin gray lines* correspond to low angle (2°–15°) misorientations. (**b**) LMR/HMR map. Low misorientation regions are *white.* High misorientation regions are colored *blue.* Misorientations >5° are shown as *thin lines* in this map. The *rectangle* in the upper right corner of (**a**) shows the area typically recorded on a TEM negative at a magnification of ×4000

19.4.1 Analysis of Local Heterogeneity

An example misorientation map, taken from a sample of Al (99.5% purity) deformed using equal channel angular extrusion extrusion (ECAE) to a strain of ∼10 via route Bc, is shown in Fig. 19.9a. The image shows that the refinement is not uniform throughout the microstructure. It is interesting to note that the box shown in the upper right corner of the image represents the area typically covered by a single TEM negative taken at a magnification of ×4000. It is clear that such a small area is unable to provide a proper description of the microstructure, and that therefore even qualitative TEM studies of such a material would require the use of foils with large thin areas combined with a suitable sampling strategy. In this respect the capability of the EBSD technique to map large areas provides useful complementary data to TEM investigations, even if all the very low angle boundaries cannot be detected in the EBSD data. Although such misorientation maps illustrate qualitatively the heterogeneity in the microstructural refinement, it is of interest also to obtain a more quantitative description of the heterogeneity. A simple and effective approach is to consider the microstructure as a two-phase mixture containing both high misorientation regions (HMRs) and low misorientation regions (LMRs), as explained in the following. First, a standard grain reconstruction process is carried out using some relatively low value (e.g., between 2° and 7°) for the misorientation angle definition, θ_{LM}. Each detected region of area greater than some chosen value (in this work, A_{LM}) is then defined as an LMR, with the remaining area defined as HMRs. Each LMR thus represents a large area in which the microstructure contains virtually only very low misorientations (Mishin and Godfrey 2008). Fig. 19.9b shows the map obtained by applying this procedure to the data

Table 19.1 Quantitative data for LMRs and HMRs in the maps shown in Figs. 19.9 and 19.10

EBSD data set	LMR area fraction (%)	Average LMR area (μm^2)	$\theta_{av}(>2^\circ)$	
			LMRs	HMRs
Fig. 19.9	34	26	6°	26°
Fig. 19.10	21	11	5°	27°

$\theta_{av}(>2^\circ)$: average value of all misorientations greater than 2° in each region

for the Al sample (using values of $\theta_{LM} = 5^\circ$ and $A_{LM} = 10\ \mu m^2$), where the LMRs are shown in white and the HMRs in blue.

Several quantitative parameters can now be extracted from the data. These include the area fraction of the LMRs and HMRs, and the average area of the LMRs. The latter parameter, together with the spatial arrangement of the LMRs, can be used to define a length scale for the heterogeneity in microstructural refinement. It is also possible to calculate the average misorientation for the boundaries within the LMRs and HMRs. It must be remembered, however, that such a parameter only includes misorientation angles above the EBSD detection limit (in the present case, chosen as 2°), i.e., $\theta_{av}(>2^\circ)$, and hence will overestimate the true average boundary misorientation, particularly for the LMRs. Some values taken from the EBSD data shown in Fig. 19.9 are given in Table 19.1. As expected for the LMRs, the $\theta_{av}(>2^\circ)$ value is much lower than that for the HMRs. Although this value is an overestimation of the true average misorientation, it does demonstrate that a significant volume of the material contains a microstructure typical of low strain deformation, even after deformation to very high strains.

In order to construct the LMR/HMR maps, a value of $\theta_{LM} = 5^\circ$ has been found to be suitable for several different high strain deformation microstructures. The value of A_{LM} must, however, be chosen for each material/deformation mode/strain individually. This is illustrated in Fig. 19.10 which shows data taken from a Cu sample deformed by equal channel angular extrusion (route A) to a strain of ~10. In this case a value of $A_{LM} = 2.5\ \mu m^2$ was used to separate the data into LMRs and HMRs. Quantitative data for this sample are given in Table 19.1. A comparison between Figs. 19.9 and 19.10 shows that the character of the heterogeneity in the Cu sample is somewhat different to that in the Al sample.

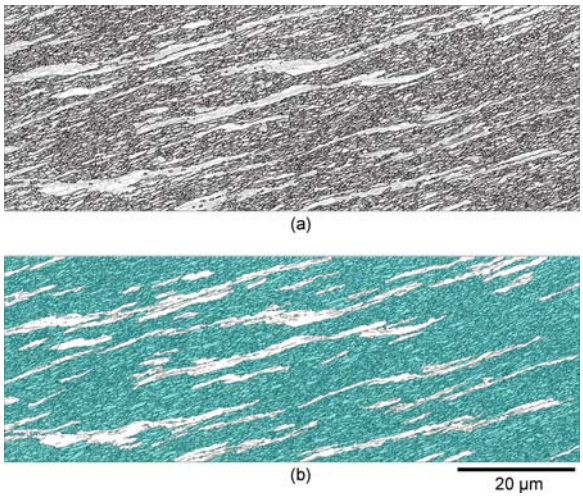


Fig. 19.10 EBSD maps from the ECAE-processed Cu sample: (**a**) misorientation map. *Bold black lines* indicate high angle (>15°) boundaries, and *thin gray lines* correspond to low angle (2°–15°) misorientations; (**b**) LMR/HMR map. Low misorientation regions are *white.* High misorientation regions are colored *blue.* Note that the definition of LMRs/HMRs is different from that used for constructing Fig. 19.9b; see text. Misorientations >5° are shown as *thin lines* in this map. The step size used for this map was 70 nm (to be compared with the maps shown in Fig. 19.11)

19.4.2 Potential for Analysis of Large-Scale Heterogeneities

The presence of heterogeneities in deformed microstructures illustrates the importance of investigating large areas in any given sample. One obvious approach to allow measurements to be taken over larger areas within a given amount of time is to use a larger EBSD step size. Problems will be encountered, however, with such an approach if the step size is too large compared to the underlying microstructure. Once the step size is comparable to the average boundary spacing, then the pixel-to-pixel misorientation information obtained from the EBSD data can no longer be assumed to represent the misorientations across dislocation boundaries in the microstructure. Some useful quantitative information can nevertheless be extracted from such large step size maps, particularly with regard to the investigation of heterogeneity in microstructural refinement. The reason for this is as follows. Consider a pixel in a large step size map where all misorientations to its neighboring pixels are less than some low value θ^*. This situation can

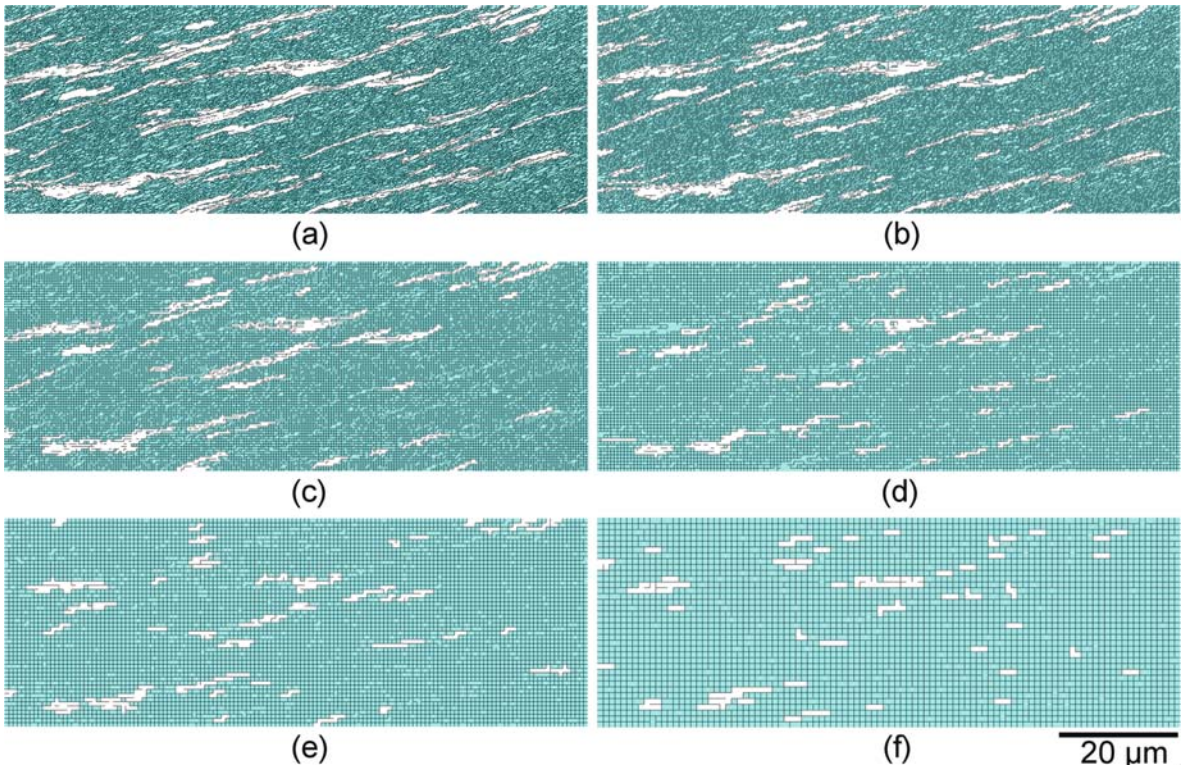


Fig. 19.11 Effect of the step size on the information about LMR/HMR heterogeneity present in the data from the ECAE-processed Cu sample. The maps were generated by removing pixels from the original EBSD data set (see Fig. 19.10) to simulate data at integer multiples of the original step size (70 nm): (**a**) ×2; (**b**) ×4; (**c**) ×6; (**d**) ×8; (**e**) ×10; (**f**) ×14

arise either because the pixel plus its neighbors cover a region that really does not contain any high angle boundaries, or because adjacent points in the measurement grid happen by chance to sample volumes with similar orientations, whilst volumes between the measurement points, containing different orientations, are missed. In certain cases this latter possibility may arise due to the frequent alternating nature of the crystal rotations across adjacent dislocation boundaries. However, in materials deformed to high strains such a situation is unlikely to occur for more than one or two adjacent pixel neighbors; and even in samples deformed to intermediate strains, it is not very likely, given the irregular spacing of dislocation boundaries, that the step size could be "in sync" with a series of regions of alternating orientation over a large number of pixels. The absence of misorientation angles greater than some low value θ^* within a given area can therefore be taken as a good indicator that the area does indeed contain at most only a small fraction of boundaries with misorientations greater than θ^*.

The availability of valuable information in large step size maps concerning heterogeneity in microstructural refinement is illustrated in Fig. 19.11.

The EBSD maps in Fig. 19.11 are derived from the data set shown in Fig. 19.10 (collected using a fine step size of 70 nm) and have been generated by removing pixels from the original EBSD data set to simulate data at integer multiples of the original step size. It can be seen from these maps that as long as the step size is smaller than the size of the LMRs, identification of regions where the microstructure contains only very low angle boundaries is still possible.

19.5 Summary and Conclusions

The presence of dislocation boundaries with very low misorientation angles causes a number of difficulties for EBSD investigations of deformed metals. As a consequence, in many cases it is easier to obtain

quantitative EBSD data concerning boundary misorientations and spacings from samples deformed to high strains than from low strain microstructures, because of the lower fraction of very low misorientation angle boundaries in heavily deformed materials. However, even highly deformed samples contain a fraction of very low angle boundaries, and the identification of these boundaries is important for a complete and accurate characterization of the deformed microstructure.

Postprocessing of EBSD data using the Kuwahara-based MSMV filter can help to reduce the level of orientation noise in the data and therefore to detect many of the very low angle boundaries. However, such filtering processes must be carried out carefully, because artifacts can be generated that may easily be mistaken for real features, either if unsuitable filter parameters are chosen, or if the boundary misorientation definition is taken too low. Investigations of the same region in both the TEM and using EBSD are very useful, therefore, in order to provide information on the ways in which orientation noise is generated in EBSD data from deformed metals. Recent attempts to significantly improve the angular resolution of EBSD using pattern correlation approaches (Wilkinson 2007; Bate et al. 2005; Wilkinson et al. 2006) are promising, though it is still not clear to what extent such procedures can be used for metals deformed over a wide range of plastic strains.

The fact that the EBSD technique allows orientation data to be collected from large areas of a sample is very useful in the analysis of the heterogeneity in microstructural refinement during deformation. For such investigations, the inability of the technique to identify very low angle misorientations is of less importance, because valuable information can be gained from the absence of misorientations above a certain angle. For samples deformed to high strains, the heterogeneity in refinement can be quantified by considering the deformed microstructure to comprise low misorientation and high misorientation regions. Similarly large step size maps can also provide useful information about the uniformity of refinement—even when the step size is taken so large that adjacent pixel misorientations can no longer be assumed to represent true boundary misorientations.

In conclusion, it can be noted that plastic deformation is inherently a multilength scale process. The capability of the EBSD technique to provide data over different length scales is therefore an important asset for investigation of deformed microstructures and this aspect of the technique should not be overlooked.

Acknowledgments Financial support from the Danish National Research Foundation through the Center for Fundamental Research: Metal Structures in Four Dimensions, and from the National Natural Science Foundation China (NSFC) under contract No: 50571049 is acknowledged. The authors are grateful to Dr. J.R. Bowen for providing the Cu sample.

References

Bate P, Knutsen RD, Brough I, Humphreys FJ (2005) The characterization of low-angle boundaries by EBSD. J Microsc 220:36–46

Bay B, Hansen N, Hughes DA, Kuhlmann-Wilsdorf D (1992) Deformation structures in lightly rolled pure aluminium. Acta Metall Mater 40:205–219

Demirel MC, El-Dasher BS, Adams BL, Rollett AD (2000) Studies on the accuracy of electron backscatter diffraction measurements. In: Schwartz AJ et al (eds) Electron backscatter diffraction in materials science. Kluwer Academic, New York

Cao WQ, Godfrey A, Liu Q (2003a) EBSP investigation of microstructure and texture evolution during equal channel angular pressing of aluminium. Mater Sci Eng A361: 9–14

Cao WQ, Godfrey A, Liu Q (2003b) Determining dislocation cell sizes for high-strain deformation microstructures using the EBSP technique. J Microsc 211:219–229

Godfrey A (2004) Edge preservation near triple junctions during orientation averaging of EBSP data. Scripta Mater 50: 1097–1101

Godfrey A, Mishin OV, Liu Q (2006) Processing and interpretation of EBSD data gathered from plastically deformed metals. Mater Sci Tech 22:1263–1270

Godfrey A, Wu GL, Liu Q (2002) Characterisation of orientation noise during EBSP investigation of deformed samples. Mater Sci Forum 408–412:221–226

Fundenberger JJ, Morawiec A, Bouzy E, Lecomte JS (2003) Polycrystal orientation maps from TEM. Ultramicroscopy 96:127–137

Hansen N (2001) New discoveries in deformed metals. Metall Mater Trans 32A:2917–2935

Hansen N, Juul Jensen D (1999) Development of microstructure in FCC metals during cold work. Philos T R Soc Lond 357A:1447–1469

Huang X, Juul Jensen D (2000) EBSD contra TEM characterization of a deformed aluminum single crystal. In: Schwartz AJ et al (eds) Electron backscatter diffraction in materials science. Kluwer Academic, New York

Hughes DA, Hansen N (2000) Microstructure and strength of nickel at large strains. Acta Mater 48:2985–3004

Humphreys FJ (2001) Grain and subgrain characterisation by electron backscatter diffraction. J Mater Sci 36: 3833–3854

Humphreys FJ, Bate P, Hurley PJ (2001) Orientation averaging of EBSD data. J Microsc 201:50–58

Humphreys FJ, Brough I (1999) High resolution electron backscatter diffraction with a field emission gun scanning electron microscope. J Microsc 195:6–9

Humphreys FJ, Huang Y, Brough I, Harris C (1999) Electron backscatter diffraction of grain and subgrain structures—resolution considerations. J Microsc 195:212–216

Li BL, Godfrey A, Meng QC, Liu Q, Hansen N (2004) Microstructural evolution of IF-steel during cold-rolling. Acta Mater 52:1069–1081

Liu Q (1995) A simple and rapid method for determining orientations and misorientations of crystalline specimens in TEM. Ultramicroscopy 60:81–89

Liu Q, Huang X, Lloyd DJ, Hansen N (2002) Microstructure and strength of commercial purity aluminum (AA 1200) cold-rolled to large strains. Acta Mater 50:3789–3802

Liu Q, Juul Jensen D, Hansen N (1998) Effect of grain orientation on deformation structure in cold-rolled polycrystalline aluminium. Acta Mater 20:1–19

Mishin OV, Godfrey A (2007) Characterization of boundary misorientations in a superplastic Al-alloy hot-deformed by ECAE. Mater Sci Forum 550:295–300

Mishin OV, Godfrey A (2008) Microstructure of ECAE-processed copper after long-term room-temperature Storage. Metall Mater Trans 39A:2923–2930

Mishin OV, Godfrey A, Östensson L (2006) Comparative microstructural characterization of a friction-stir-welded aluminum alloy using TEM and SEM-based techniques. Metall Mater Trans 37A:489–496

Pantleon W (1998) On the statistical origin of disorientations in dislocation structures. Acta Mater 46:451–456.

Prior DJ (1999) Problems in determining the misorientation axes for small angular misorientations, using electron backscatter diffraction in the SEM. J Microsc 195:217–225

Rauch EF, Veron M (2005) Coupled microstructural observations and local texture measurements with an automated crystallographic orientation mapping tool attached to a TEM. Materialwiss Werkst 36:552–556

Valke A, Pennock GM, Drury MR, De Bresser JHP (2006) Electron backscattered diffraction as a tool to quantify subgrains in deformed calcite. J Microsc 224:264–276

Wilkinson A.J (2001) A new method for determining small misorientations from EBSD patterns. Scripta Mater 44: 2379–2385

Wilkinson AJ, Meaden G, Dingley DJ (2006) High resolution mapping of strains and rotations using electron backscatter diffraction. Mater Sci Tech 22:1271–1278

Zaefferer S (2000) New developments of computer-aided crystallographic analysis in transmission electron microscopy. J Appl Crystallogr 33:10–25

Chapter 20

Application of EBSD Methods to Severe Plastic Deformation (SPD) and Related Processing Methods

Terry R. McNelley, Alexandre P. Zhilyaev, Srinivasan Swaminathan, Jianqing Su, and E. Sarath Menon

20.1 Introduction

Refinement and homogenization of microstructure are highly beneficial to the mechanical properties of engineering materials. Conventional thermomechanical treatments for this purpose typically include deformation processing to von Mises equivalent strains ≤ 5, while recently developed severe plastic deformation (SPD) processing methods have enabled systematic investigation of equivalent strains >10. Ultrafine grain sizes (even in the nanometer range) and strain hardening may contribute to dramatic improvements in ambient strength. Also, strength-toughness relationships as well as resistance to cyclic loading may be improved when grain refinement is combined with other strengthening mechanisms, although interactions among strengthening, toughening, crack initiation, and crack growth mechanisms are complex and often alloy-specific. Ultrafine grain size may also enhance forming behavior and enable superplasticity at lower temperatures and higher strain rates when comparison is made to conventional superplastic alloys.

Numerous SPD methods have emerged in recent years (Valiev et al. 1991; Lowe and Valiev 2000). Equal-channel angular pressing (ECAP) (Iwahashi et al. 1998; Langdon et al. 2000) and high-pressure torsion (HPT) (Ungár et al. 2000) usually involve deformation at low homologous temperatures. Accumulative roll bonding (ARB) is a modern adaptation of forge welding technology (Saito et al. 1999). Machining is usually viewed as a process for shaping by removal of chips of material using a cutting tool, but does entail SPD. Chip formation in plane strain machining involves intense, localized shear deformation that, in many ways, is similar to the deformation in ECAP (Brown et al. 2002; Swaminathan et al. 2005). Indeed, machining-derived processes, e.g., large-strain extrusion machining (LSEM), have been designed to enable the production of bulk SPD materials that are based on the pure metal as well as alloys of Al, Cu, Ni, Fe, and Ti. At low cutting speeds, LSEM may take place at ambient temperature while adiabatic heating at higher speeds may result in more complex thermomechanical histories. Such histories are inherent in friction stir processing (FSP) (Mishra 2003; Mishra and Ma 2005; Mishra and Mahoney 2007). Some have suggested that the term "SPD" should be restricted to approximately isothermal deformation at low homologous temperatures. Nevertheless, FSP involves extremely large local shear strains, and so is a closely related technology.

In the context of SPD processing, "refinement" usually refers to the production of equi-axed, ultrafine (≤ 1.0 μm) or nanoscale (≤ 100 nm) microstructure features throughout the bulk material. Elongated, ribbon-like dislocation cells or subgrain structures form at smaller equivalent strains during SPD at low homologous temperatures and then give way to highly refined, equi-axed structures at larger strains (e.g., Swaminathan et al. 2005). These structures apparently develop by recovery-dominated processes in the absence of high-angle boundary migration, and their evolution is also strain-path dependent. Interfaces in such structures are often high-angle in nature (disorientations $\geq 15^\circ$) but are not disordered high-angle

T.R. McNelley (✉)
Department of Mechanical and Astronautical Engineering, Naval Postgraduate School, Monterey, CA 93943–5146, USA
e-mail: tmcnelley@nps.edu

A.J. Schwartz et al. (eds.), *Bacterial Infections of Humans*,
DOI 10.1007/978-0-387-88136-2_20, © Springer Science+Business Media, LLC 2009

boundaries. Predictive models of the mechanisms by which SPD-induced microstructures evolve and transform into ultrafine grain structures with disordered high-angle boundaries have not been established. Indeed, the current understanding of microstructure control during conventional deformation processing and recrystallization treatments is largely empirical in nature, and so our ability to design processes to achieve particular microstructure outcomes is limited.

Microstructure evolution during thermomechanical processing generally is accompanied by the development of characteristic textures. Depending on material and processing conditions, the textures may reflect deformation or deformation and recovery effects alone, or may include the effects of recrystallization (Doherty et al. 1997). Advances in the characterization and understanding of such microstructures have involved grain-specific orientation determination utilizing convergent beam electron diffraction methods in transmission electron microscopy. These methods have high spatial and orientation resolution, but provide limited amounts of data. In contrast, electron backscatter diffraction analysis (EBSD) and orientation imaging microscopy (OIM) (Adams et al. 1993; Randle and Engler 2000) methods have enabled the acquisition of much greater amounts of grain-specific orientation data, although these methods are of lower spatial and orientation resolution.

Prior investigations in this laboratory have applied EBSD and OIM methods to the analysis of superplastic aluminum alloys (McNelley and McMahon 1996, 1997; McNelley et al. 1997, 1999, 2002; Pérez-Prado et al. 1998, 2001). Two distinct processing routes had evolved to enable superplasticity in aluminum; equivalent strains in the deformation stages of both processing routes are typically 2–3. One route involves the use of dispersed micron-sized constituent particles, or overaging treatments to produce precipitates $\sim$1.0 μm in diameter, and cold working. The particles serve as nucleation sites for discontinuous recrystallization by particle-stimulated nucleation (PSN) (Humphreys 1977), and grain sizes of 7–10 μm support moderate superplastic response in alloys processed in this manner (e.g., McNelley et al. 2008). The other route involves a continuous recrystallization reaction in materials having dispersions of fine (10–50 nm) particles intended to hinder the long-range migration of high-angle boundaries during deformation processing and superplastic forming (Bricknell and Edington 1979; Edington 1982; McNelley et al. 2002).

The EBSD and OIM analysis clarified the different mechanisms involved in these two different processing approaches. Random textures and disordered, high-angle boundaries due to PSN of recrystallization during heating to the superplastic forming temperature distinguished all alloys processed by severe cold working in the presence of micron-sized particle dispersions. In contrast, distinct brass- or copper-type deformation textures that had been formed during prior rolling were retained upon heating, and superplastic deformation of materials processed to contain fine, stable nanoscale particle dispersions. The continuous reaction in such materials involves the development of high-angle boundaries by dislocation reactions in highly misoriented cell walls in the absence of boundary migration. The formation of high-angle boundaries and persistence of the prior deformation texture well into the superplastic regime characterized all alloys that had been deformed in the presence of fine, stable, nanoscale dispersions.

Recent investigations have applied similar EBSD and OIM analysis approaches to the examination and characterization of materials processed by various SPD methods, including ECAP, HPT, machining, and FSP. Altogether, these studies suggest that highly refined grain structures may form by either discontinuous or continuous reactions during such processes. These investigations have also helped to understand microstructure evolution at various stages of SPD processing; and examples from ECAP of Al and Cu, machining of Cu, and FSP of a continuously cast AA5083 alloy are summarized in the following sections.

20.2 Microstructures During the Initial ECAP Pass

During ECAP, a billet is pressed through a die having two channels, of equal cross section, that intersect at an angle; this is illustrated in the schematic at the left in Fig. 20.1. The billet experiences simple shear without change in cross section and so the process is amenable to repetition. In idealized ECAP, the shear plane is the plane of the die channel intersection and the theoretical

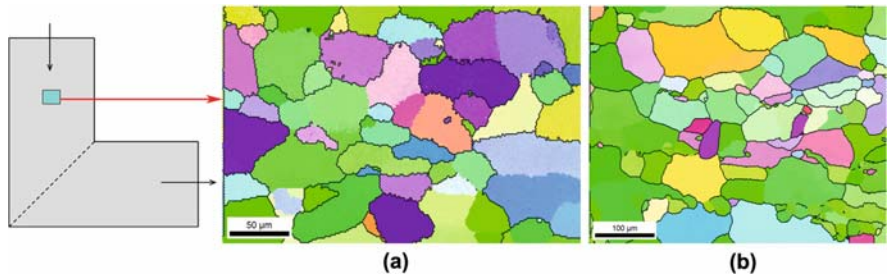


Fig. 20.1 A schematic of the ECAP process and orientation images for (**a**) Cu and (**b**) Al billets from locations in the die entrance channel for partially pressed billets

shear strain, $\gamma = 2.0$, corresponding to an equivalent strain, ϵ_{eq}=1.15 for a die having a 90° die channel angle and sharp inner and outer corners at the die channel intersection (Iwahashi et al. 1998). For repetitive ECAP the cumulative strain would be the strain per pass multiplied by the number of passes. Rotation of the billet about its longitudinal axis determines the nature of the strain path. If the billet is not rotated, or the rotation is + and –90° back and forth between successive passes, the straining is monotonic. Conversely, rotation by 90° or 180° in the same sense between successive passes results in redundant straining.

Die wall friction, material constitutive behavior, and relief at the inner and outer corners of the die channel intersection result in the spreading of deformation through a fan-shaped region around the plane of the die channel intersection and the formation of a dead zone at the outer corner of the intersection (see, e.g., Zhilyaev et al. 2006a, 2006b). Accordingly, the strain becomes nonuniform through the region of the intersection. These effects have been examined by OIM methods for commercially pure copper (99.95%) and Al (99.7%) billets that have been partially pressed to enable observation of the deformation field during the initial ECAP pass.

Billets 8 mm × 8 mm × 50 mm were machined from plates and fully annealed prior to ECAP. The billets were pressed at room temperature using a sharp-cornered 90° die until about half of the billet had passed through the die channel intersection. The die set was disassembled and the samples, in the shape of 90° elbows, were removed. The samples were sectioned in half along the flow plane (the plane defined by the die entrance and exit axes) and prepared by standard metallographic methods, concluding with electropolishing. Billet symmetry is monoclinic, and so the senses of the coordinate axes in the flow plane were carefully ascertained during OIM analysis. Typical methods of data acquisition and analysis were employed as have been described throughout this volume and elsewhere (e.g., Zhilyaev 2006a). During pressing, material in the die entrance channel is initially compressed to a small strain but experiences predominantly hydrostatic loading. OIM results from locations in the entrance channel are shown in Fig. 20.1a and b, and reveal grain sizes of ∼100 μm in the Cu and ∼200 μm in the Al, respectively. Texture data (not shown) indicate that the Cu exhibited both prior rolling as well as annealing components, while the Al retained mainly prior recrystallization components.

Microhardness measurements were made on the partially pressed samples as illustrated in Fig. 20.2. Five individual measurements were made at each location in the region of the die channel intersection as indicated by the inset in Fig. 20.2a. Overall, the Cu exhibits higher hardness and hardness increase due to ECAP when compared to the Al. Variations in the microhardness throughout the die entrance channel likely reflect variations in grain size and lattice orientation in the annealed and lightly deformed material in these regions. Strain hardening in response to shearing at the die channel intersection is more localized for the Cu and, in contrast, is spread out over a greater distance in the Al. Neither billet completely filled the outer corner of the die channel intersection, although the dead zone is most prominent for the Al. In both cases the lower billet regions exhibit higher hardness after passage through the die channel intersection. This implies that shearing is not uniform along the plane of the intersection.

Figure 20.3 shows orientation images from three locations in deformed material immediately adjacent to the shear plane for the partially pressed Cu billet. The orientation color key in the inset corresponds to the specimen normal for all of the orientation images in this chapter. In Fig. 20.3, the billet orientation in the microscope is also illustrated below the color key in the inset; from this, the shear direction is parallel to

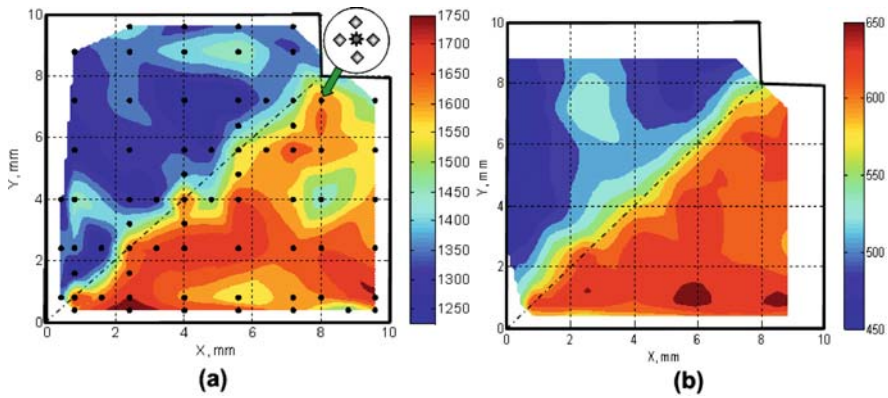


Fig. 20.2 Microhardness distributions from the region of the die channel intersection for partially pressed billets of (**a**) Cu and (**b**) Al

the vertical edge of these images. For idealized ECAP, the direction of maximum principal strain would be inclined at 22.5° in a clockwise sense from this edge. At the inner die corner (upper map), slip bands parallel to the shear plane and inclined at about 45° to the shear plane (i.e., parallel to the die exit channel) are apparent at the center-right; while a gradient in strain, reflected in long-range lattice rotation, is apparent in the grain at the left. High-angle boundaries have formed at many locations nearby prior boundaries in

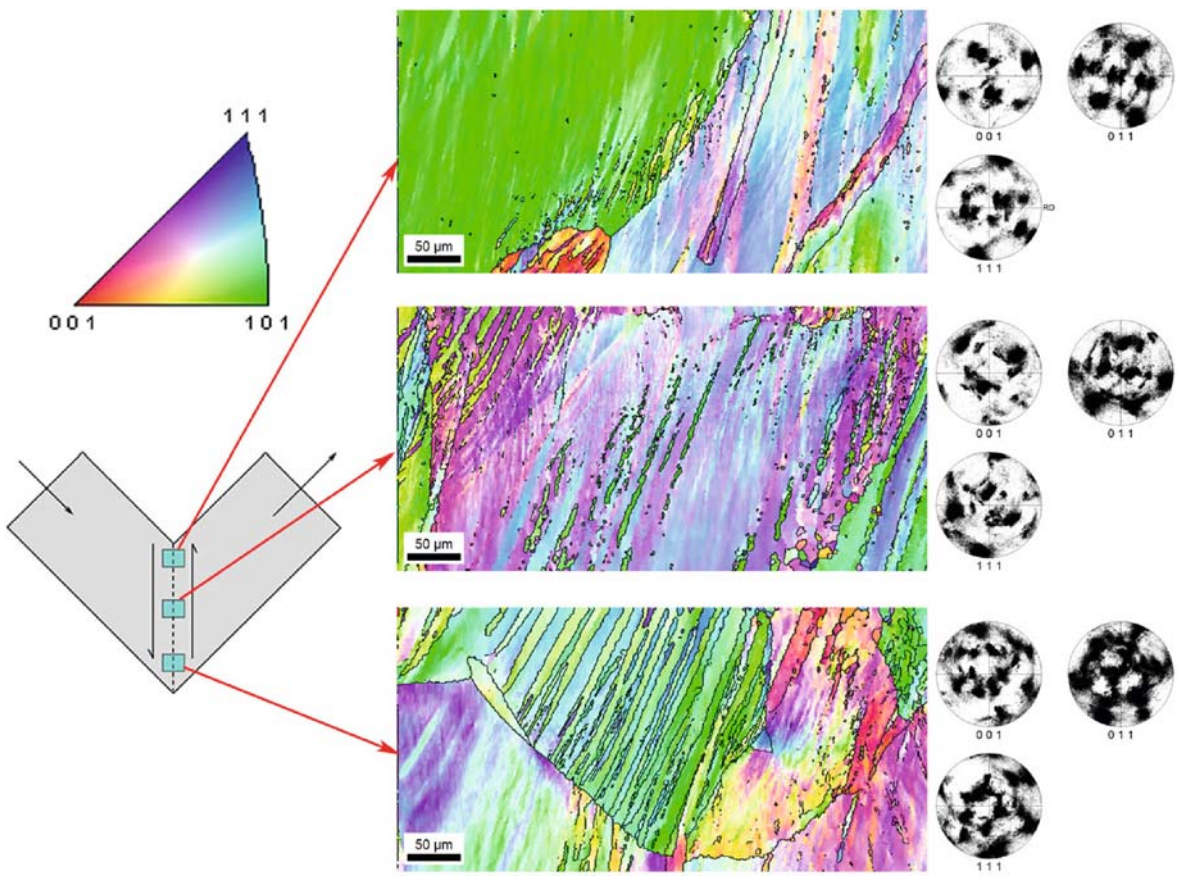


Fig. 20.3 Orientation images and discrete pole figures from the region of the die channel intersection for the partially pressed Cu billet. Boundaries of disorientation ≥15° are indicated by *dark lines* in the orientation images

the image from the region of the inner die corner. Slip bands are also apparent in the middle image but long-range lattice rotations were not seen in the images from the middle and outer corner (lower map). More deformation-induced structures surrounded by high-angle boundaries are apparent in the middle image, and these structures are elongated approximately along the direction of maximum principal strain.

The inset pole figures typically exhibit one or two individual orientations. At the inner die corner and mid region, these orientations may be near the C shear texture orientation $\{001\}<011>$, where the notation refers to {plane parallel to the shear plane}<direction parallel to the shear direction> (Kocks et al. 1998). At the outer die corner the texture component may be retained from the plate used to produce the billets; the location is in the dead zone. Factors contributing to the inhomogeneous hardness distribution include the coarse initial grain size, and inhomogeneous deformation across the plane of the die channel intersection that reflects, in turn, die wall friction and dead zone formation.

Corresponding data for Al is shown in Fig. 20.4, and comparison with the Cu data in Fig. 20.3 reveals greater inhomogeneity of deformation in the Al when compared to the Cu. The orientation image from the inner corner (upper image) suggests grain elongation along the direction of maximum principal strain, while grains are elongated more nearly along the axis of the die exit channel in the middle orientation image. Grain shape is nearly undistorted in the dead zone at the outer corner of the die channel intersection. More nearly equi-axed deformation structures have formed within grains, a reflection of the high stacking fault energy of Al and deformation at a higher homologous temperature. The inset pole figures reflect formation of A ($\{111\}<uvw>$) and B ($\{hkl\}<001>$) shear texture fibers, as well as the C orientation at the upper die

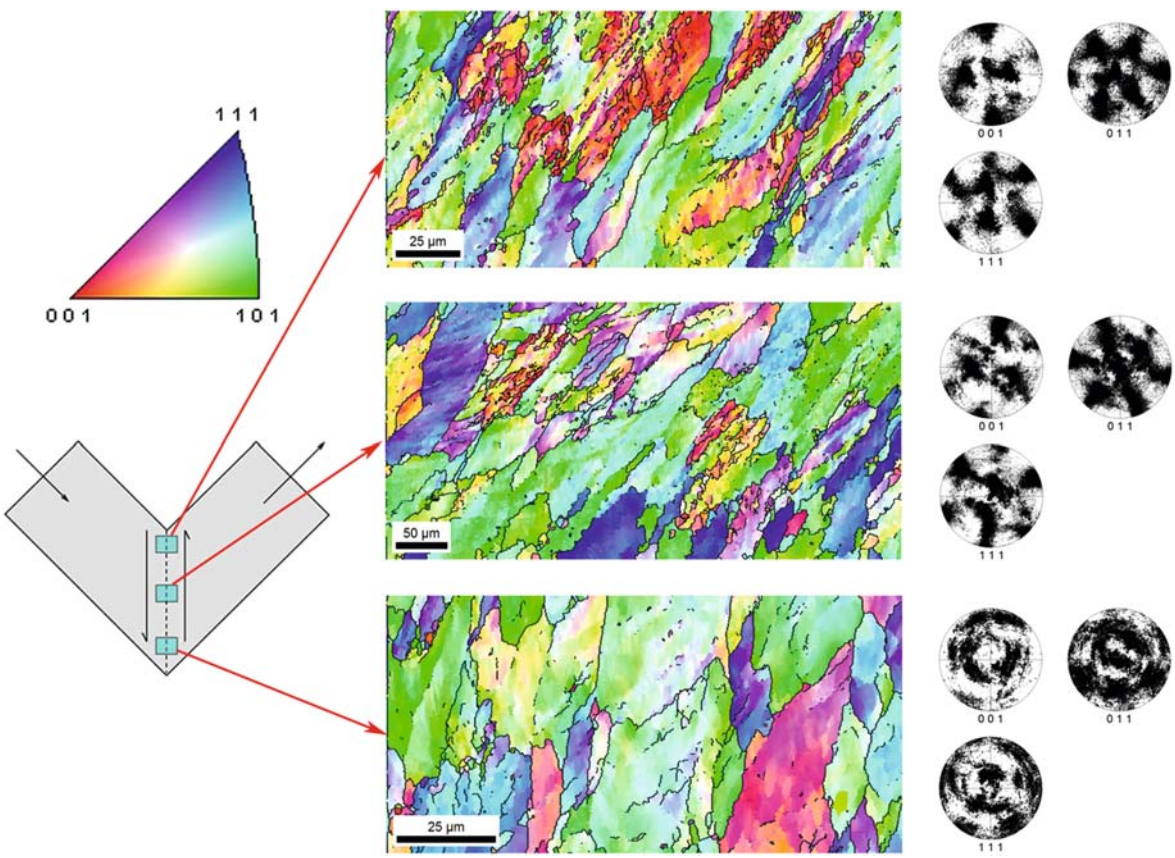


Fig. 20.4 Orientation images and discrete pole figures from the region of the die channel intersection for the partially pressed Al billet. Boundaries of disorientation $\geq 15^{\circ}$ are indicated by *dark lines* in the orientation images

corner and middle regions of the billet. These textures appear to be rotated away from the shear direction toward the die exit channel axis by 10°–20°. In contrast, the texture in the dead zone at the outer die corner appears to consist mainly of prior rolling texture orientations. Further details of microstructure and microtexture evolution during repetitive ECAP have been given elsewhere (Oh-ishi et al. 2005; Zhilyaev et al. 2006a, 2006b).

20.3 Microstructures Developed by Machining

A schematic of chip formation during plane strain machining is included as the inset to the left in Fig. 20.5. The chip material being removed experiences large strains as it passes through the shear plane. The principal machining parameters are the tool rake angle, α, the undeformed chip thickness, a_0, the deformed chip thickness, a_c, and the cutting speed, V_0. The bulk shear strain imposed in the chip depends on α and the shear plane angle, ϕ, according to: $\gamma = (\cos\alpha)/(\sin\varphi\cos(\varphi-\alpha))$, wherein ϕ depends in turn on α and the cutting ratio $r = a_0/a_c$ as $\tan\varphi = (r\cos\alpha)/(1 - r\sin\alpha)$ (Merchant 1945; Piispanen 1948). In a plane strain cutting experiment, the tool rake angle, α, is set and the cutting operation is then conducted. The shear strain, γ, in the chip may be calculated after measurement of the chip thickness, a_c, determination of the chip thickness ratio, r, and evaluation of tan ϕ. Plane strain conditions occur when the tool cutting edge is perpendicular to V_0, and a_0 is small compared to the chip width, a_w. The cutting speed, V_0, controls the strain rate and thus the temperature of the process. At low values of V_0, chip formation takes place at near ambient temperatures. In contrast, at very high values of V_0, temperatures on the order of the melting point of the material and strain rates as high as 1×10^5 s^{-1} may prevail in the deformation zone. In typical plane strain cutting experiments, plastic shear strain values that range between 1 and 15 may be readily obtained in a single stage of deformation simply by varying the tool rake angle. This is in contrast to repetitive ECAP wherein the plane of the shear changes from pass to pass and the straining may be either redundant or monotonic depending on the strain path.

Chips were produced by plane strain machining of commercial oxygen free high conductivity (OFHC) copper that had been annealed at 400°C for 4 hours in a controlled argon atmosphere (95 vol%Ar+5 cvol%H_2). The annealed copper's microstructure consisted of ~100 μm grains with annealing twins, and microtexture data revealed a weak cube component in the texture. Chips were produced with different levels of strain using high-speed steel tools of different rake angles; the machining parameters are summarized in Table 20.1. Further details of this experiment have been given previously (Brown et al. 2002; Swaminathan et al. 2005, 2007). The strain rates were 10–100 s^{-1} and deformation occurred under near-ambient temperature conditions. The deformed chip thickness, a_c, was measured and r, ϕ, and γ were estimated as described above; these parameter values are also included in Table 20.1.

The orientation images in Fig. 20.5 illustrate the effect of strain during SPD by machining. These maps were obtained in the plane defined by the chip flow direction (CFD) and rake face normal (RFN). Inspection of the inset reveals that this plane corresponds to the flow plane for ECAP. Typically, $r < 1$ for plane strain machining while $r = 1$ for ECAP, and this is a principal distinction between these two SPD processes. Elongated structures are apparent in the chip obtained by cutting with $\alpha = +40°$ and a corresponding shear strain $\gamma = 3$; this result is consistent with the elongated structures apparent after the initial ECAP pass (Fig. 20.3). At this strain, the pole figure data include a predominant B-fiber shear texture component. Larger shear strains are attained as the tool rake angle is decreased, and the elongation and subdivision of the equi-axed grains of the annealed material gives way to increasingly refined structures within elongating prior grains and, finally, to equi-axed structures at the largest strains examined in this study ($\gamma = 11$). The prior boundaries have become indistinguishable at the largest shear strain. Nevertheless, the pole figures include A- and B-fiber shear texture components at $\gamma = 7$, and B-fiber as well as the C orientation at $\gamma = 11$, indicating that these are deformation-induced and not recrystallization structures. The discrete pole figures show clearly that these shear textures are more diffuse at large strains. Corresponding disorientation distributions in Fig. 20.6 show that the relative fraction of high-angle boundaries increases as a function of increasing strain, although the persistence of low-angle

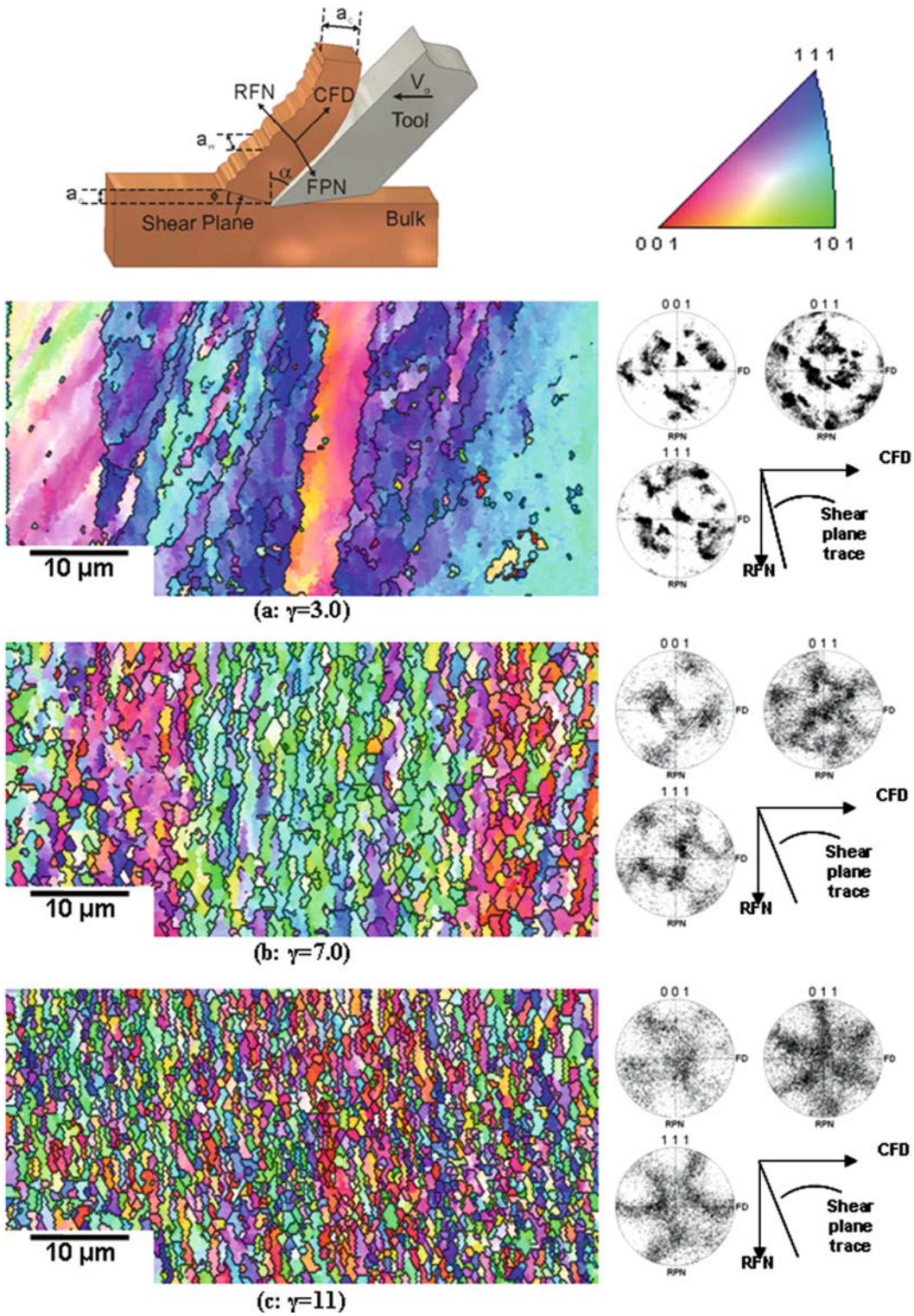


Fig. 20.5 A schematic of plane strain machining is included at the *upper left*. The orientation images and discrete pole figures illustrate the formation of elongated structures within prior grains and their complete transformation into ultrafine, equiaxed structures during SPD by machining. Shear textures are evident at all strains

Table 20.1 Deformation parameters for machining of Cu chips

V_o (mm/s)	a_o (mm)	a_w (mm)	α	r	φ	γ
18.3	0.11	3.81	+40°	0.31	16.5°	3
+20°	0.14	7.9°	7			
0°	0.09	5.2°	11			

boundaries in the disorientation distributions reflects, again, that these are deformation-induced microstructures.

Insight into the mechanisms of microstructure evolution and high-angle boundary formation has been gained from EBSD and OIM analysis of Cu subjected to SPD by plane-strain machining. An orientation image from a location on the FPN-CFD plane (i.e., the rake face) of a Cu chip subject to $\gamma = 3$ is shown in Fig. 20.7a. The spatial distributions of various texture components may be evaluated by highlighting these components in grain maps. Thus, an image quality (IQ) map, shown in Fig. 20.7b, and the pole figures, presented in Fig. 20.7c, for this region (i.e., Fig. 20.7a) have been highlighted with red and blue colors, each corresponding to one of the two crystallographically distinct variants of a prominent B-fiber component in the shear texture from this location in the microstructure. Note that the pole figure data have been rotated into the CFD-RFN plane (i.e., the flow plane) in Fig. 20.7c; this is the plane as employed in the pole figures of Fig. 20.5. The highlighting procedure shows that regions of lattice orientation corresponding to these variants have a band-like arrangement approximately parallel to the FPN in Fig. 20.7c, and that high-angle boundaries (≥40° disorientation and indicated by the irregular white lines in Fig. 20.7b) are interfaces between these bands. The point-to-origin profile plot in Fig. 20.7d corresponds to the linear traverse at the upper left in Fig. 20.7b, and demonstrates that the interfaces between the texture variants have disorientations of 50°–60°. The disorientation distribution for this location has a peak at 0°–5°, corresponding to the substructure evident in Fig. 20.7a, while the smaller peak at 55°–62.8° corresponds to the interfaces between the texture variant bands. This observation is consistent with deformation banding (Barrett 1939; Barrett and Levenson 1940; Lee et al. 1993; Lee and Duggan 1993; Kulkarni et al. 1998; McNelley et al. 2002) in microstructure evolution and the formation of high-angle boundaries during SPD.

20.4 Grain Refinement During FSP

Recent reviews of friction stir welding (FSW) and the allied process of FSP have given detailed descriptions of these technologies (Mishra 2003; Mishra and Ma 2005; Mishra and Mahoney 2007). Briefly, during FSP a cylindrical nonconsumable tool with a concentric projecting pin is rotated and forced into the surface of a metal. A combination of frictional and adiabatic heating in the metal leads to localized heating and soft-

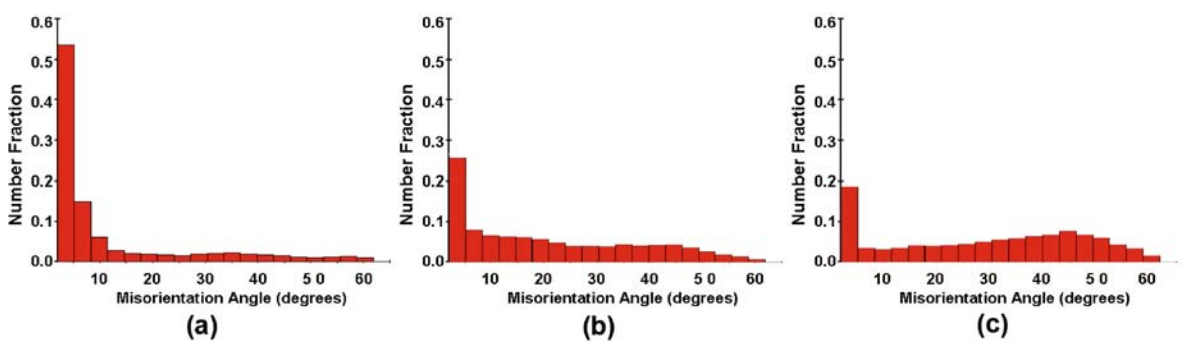


Fig. 20.6 Disorientation distributions for (**a**) $\gamma = 3.0$, (**b**) $\gamma = 7.0$, and (**c**) $\gamma = 11.0$, showing the buildup of the high-angle boundary populations in the deformation-induced structures of Fig. 20.5. The populations of high-angle (disorientation ≥15°) are: (**a**) 22.7%, (**b**) 53.4%, and (**c**) 72.0%

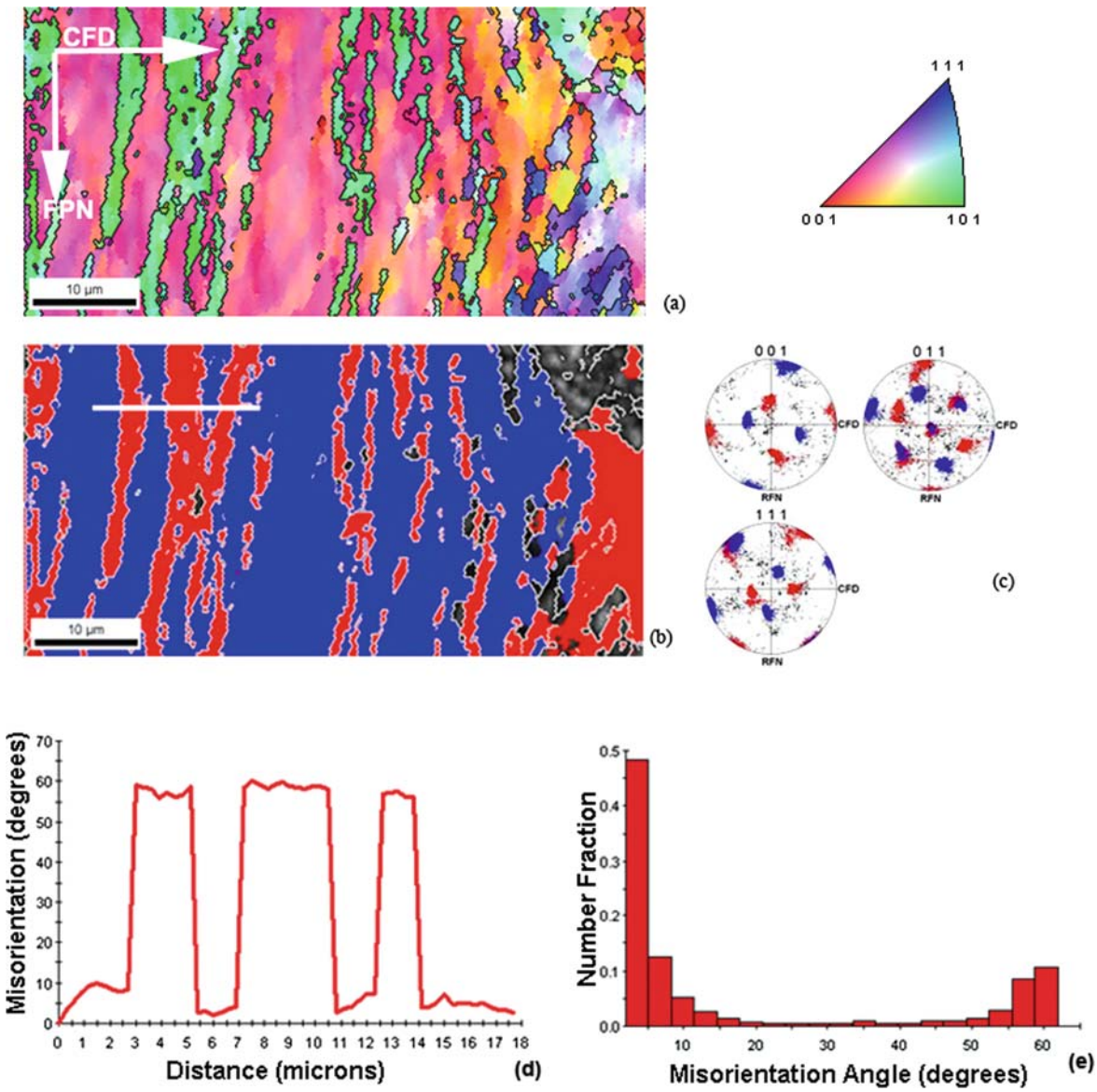


Fig. 20.7 An orientation image in (**a**) shows the microstructure on the rake face plane of Cu deformed to $\gamma = 3.0$ during plane strain machining. The highlighted IQ map, (**b**), and discrete pole figures, (**c**), show that high-angle boundaries are interfaces between variants of a B-fiber texture component at this stage of deformation. The point-to-origin traverse in (**d**) demonstrates that the variant interfaces have disorientations of 50°–60°; (**e**) the disorientation distribution is bimodal, with a large peak at 0°–5°, corresponding to a substructure and a smaller peak at 55°–62.8°, corresponding to variant interfaces

ening of the metal as the pin penetrates the surface. The tool may be traversed in a pattern on the work piece surface once the tool shoulder has come into contact with the surface. A volume of material surrounding the pin experiences SPD in a complex thermomechanical cycle; when applied to a cast metal this may result in the conversion of an as-cast microstructure to a wrought condition in locations subjected to the processing in the absence of macroscopic shape change.

An as-cast AA5083 material (Al-4.5wt.pct Mg-0.7wt.pct.Mn) plate produced by continuous casting to a thickness of 15 mm was sectioned to provide samples approximately 37 mm in width × 150 mm in length. The samples were subjected to FSP using an

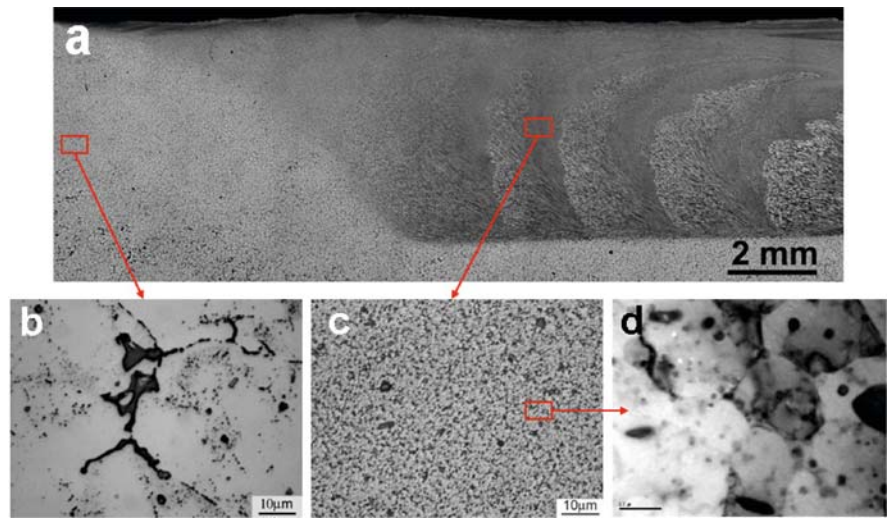


Fig. 20.8 Optical microscopy results after FSP of a continuously cast AA5083 material; the montage in (**a**) illustrates the SZ depth in the vicinity of the initial passes, while (**b**) shows the as-cast solidification and (**c**) the SZ microstructures at higher magnification. The TEM image in (**d**) shows the distribution of particles in the microstructure

H-13 steel tool with a threaded 5.2 mm pin. Processing was conducted at 350 rpm, a traversing speed of 102 mm min^{-1} and a step-over distance of 2 mm in a pattern of linear traverses on the as-cast material. A montage of optical micrographs in Fig. 20.8a shows a transverse section through the surrounding base metal (to the left) and processed region (the stir zone, or SZ) to the right. The SZ depth corresponds to the pin length. The as-cast base metal is shown at higher magnification in Fig. 20.8b and consists of coarse, irregularly shaped Al_6Mn constituent particles and finer but inhomogeneously distributed Al_8Mg_5 precipitates in a solidification microstructure. The FSP of this as-cast microstructure results in homogenization and refinement of both the coarse constituents and fine precipitates, as seen in Fig. 20.8c. The presence of constituents and precipitates of varying size resulted in difficulties in transmission electron microscopy interpretation of the SZ microstructure. Nevertheless, particles from 50 to 200 nm are distributed throughout the SZ, and many of the finer particles reside on boundaries in the microstructure, as seen in Fig. 20.8d.

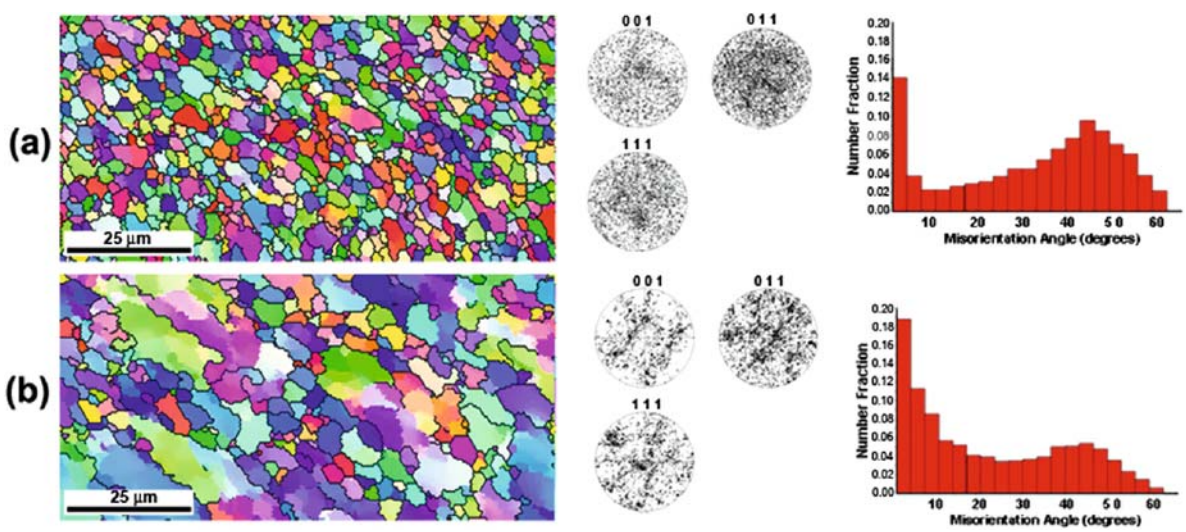


Fig. 20.9 OIM results from (**a**), the SZ, and (**b**), the TMAZ region of the FSP'ed AA5083 material that show refinement of the SZ microstructure to a grain size of ~1.0 μm as well as formation of a random texture and disorientation distribution in this region. The TMAZ exhibits a deformation-induced microstructure

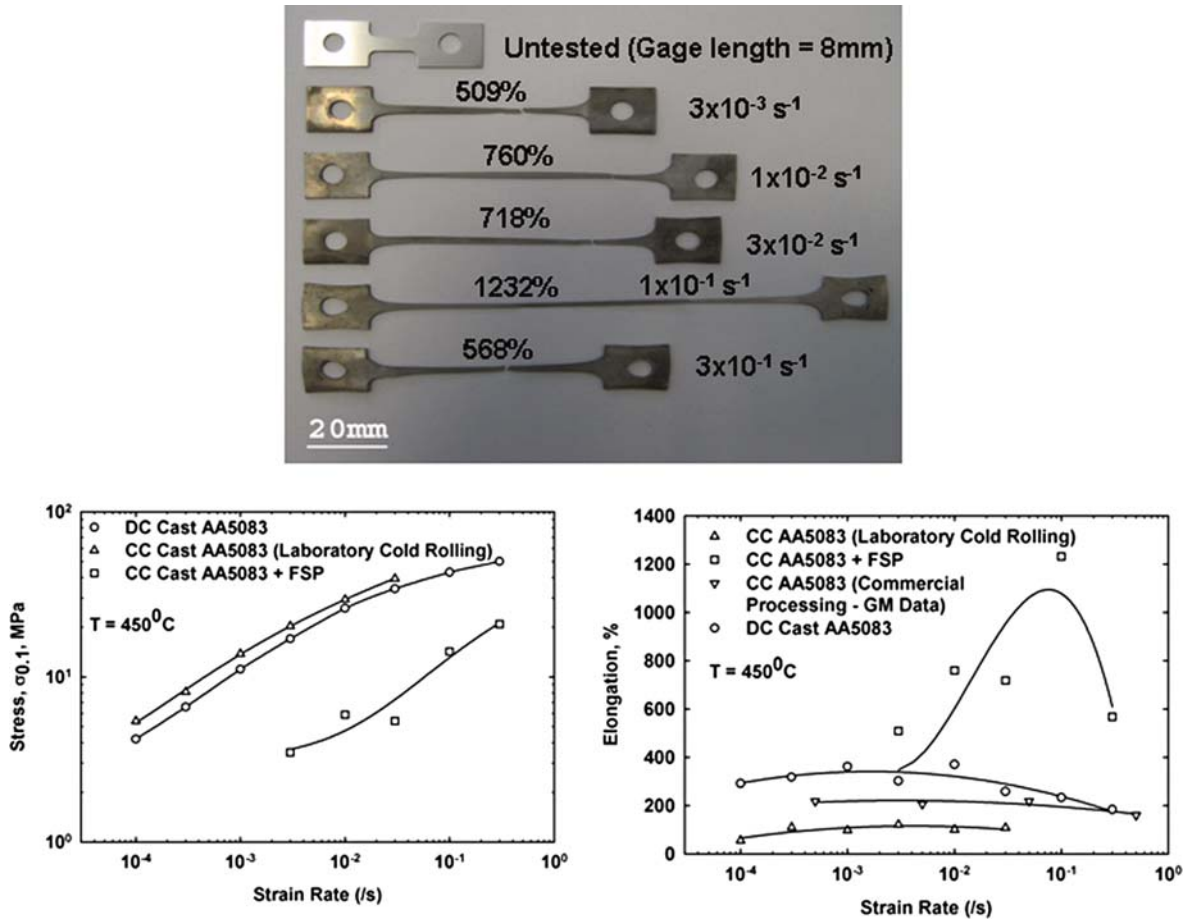


Fig. 20.10 Tension test coupons showing exceptional elongation (>1,200%) for SZ material; this reflects grain refinement and an increase in the strain rate sensitivity index, m, at strain rates $\dot{\varepsilon} \geq 10^{-2}s^{-1}$, as seen in the plots of stress as a function of strain rate and ductility as a function of strain rate during deformation at 450°C

A highly refined SZ grain structure was revealed by EBSD and OIM methods, as shown in Fig. 20.9a. The apparent SZ grain size is ~1.0 μm. A random texture and predominantly random disorientation distribution suggests PSN of recrystallization, although a population of low-angle boundaries is consistent with residual deformation effects after passage of the tool pin. A coarser grain size, shear texture components, and high population of low-angle boundaries are all apparent in the thermomechanically affected zone (TMAZ), as shown in Fig. 20.9b.

Miniature tensile samples were sectioned from the SZ region using wire electric discharge machining (EDM) followed by light grinding to remove surface damage. These samples were pulled to failure in tension using various nominal strain rates at 450°C. The untested and tested tensile samples are shown at the top in Fig. 20.10. The corresponding tensile properties are compared to data for conventionally processed AA5083 materials in plots of flow stress as a function of strain rate and ductility as a function of strain rate. The conventional processing relies on cold rolling of hot band material to a reduction of 75%, followed by heating to 450°C. Recrystallization provides a grain size of 7–8 μm. The finer grain size produced by FSP clearly reduces the flow stress and increases the strain rate sensitivity index, $m \equiv d \log \sigma \,/\, d \log \dot{\varepsilon}$. High values of m lead to necking resistance and improved ductility (Langdon 1982; Sherby and Wadsworth 1984). The enhanced ductility reflects not only the reduction

in grain size, but also a more homogeneous constituent particle distribution and a reduced tendency to cavitation.

20.5 Conclusions

The application of EBSD and OIM methods to the characterization of SPD-induced microstructures has provided invaluable insights into the evolution of microstructure during processing by the various SPD methods. The inhomogeneous distribution of deformation during initial ECAP passes on Cu and Al has been characterized by OIM and microtexture data. The development of elongated structures and the fragmentation of such structures to form highly refined, equi-axed structures at very large strains has been investigated by plane-strain machining. It must be recognized that EBSD and OIM methods in scanning electron microscopy are complementary to more highly resolving transmission electron microscopy techniques. The latter are necessary to investigate the detailed nature of the boundaries and interfaces produced by SPD. Finally, EBSD and OIM methods are invaluable in interpreting the mechanisms of formation of superplastic microstructures in Al alloys wherein deformation and recrystallization treatments are needed to refine microstructures in the absence of phase transformations.

Acknowledgements The authors acknowledge financial support from the Defense Advanced Research Projects Agency (DARPA; Dr. L. Christodoulou), the Office of Naval Research (ONR; Dr. J. Christodoulou), the Air Force Office of Scientific Research (AFOSR; Dr. V. Giurgiutiu), the University of Texas-Austin (Prof. E.M. Taleff), and General Motors, Inc. (Dr. P.E. Krajewski) during the course of these various investigations. APZ, SS, and JQS also acknowledge financial support from the U.S. National Research Council postdoctoral program.

References

Adams BL, Wright SI, Kunze K (1993) Orientation imaging: the emergence of a new microscopy. Metall Trans A 24A: 819–831

Barrett CS (1939) The structure of iron after compression. T Am I Min Met Eng 135:296–324

Barrett CS, Levenson LH (1940) The structure of aluminum after compression. T Am I Met Min Eng 137:112–126

Bricknell RH, Edington JW (1979) Textures in a superplastic Al-6Cu-0.3Zr alloy. Acta Metall 27:1303–1312

Brown TL, Swaminathan S, Chandrasekar S, Compton WD, King AH, Trumble KP (2002) Low-cost manufacturing process for nanostructured metals and alloys. J Mater Res 17(10):2484–2488

Doherty RD, Hughes DA, Humphreys FJ, Jonas JJ, Juul Jensen D, Kassner ME, King WE, McNelley TR, McQueen HJ, Rollet AD (1997) Current issues in recrystallization: a review. Mater Sci Eng A 238:219–274

Edington JW (1982) Microstructural aspects of superplasticity. Metall Trans A 13A:703–715

Humphreys FJ (1977) The nucleation of recrystallization at second phase particles in deformed aluminum. Acta Metall 25:1323–1344

Iwahashi Y, Horita Z, Nemoto M, Langdon TG (1998) The process of grain refinement in equal-channel angular pressing. Acta Mater 46:3317–1331

Kocks UF, Tomé CN, Wenk HR (1998) Texture and anisotropy. Cambridge University Press, Cambridge

Kulkarni SS, Starke EA, Kullmann-Wilsdorf D (1998) Some observations on deformation banding and correlated microstructures of two aluminum alloys compressed at different temperatures and strain rates. Acta Mater 46: 5283–5301

Langdon TG (1982) The mechanical properties of superplastic materials. Metall Trans A 13A:689–701

Langdon TG, Furukawa M, Nemoto M, Horita Z (2000) Using equal-channel angular pressing for refining grain size. JOM 52(4):30–33

Lee CS, Duggan BJ, Smallman RE (1993) A theory of deformation banding in cold rolling. Acta Mater 41:2265–2270

Lee CS, Duggan BJ (1993) Deformation banding and copper-type rolling textures. Acta Mater 41:2691–2699

Lowe TC, Valiev RZ (2000) Producing nanoscale microstructures through severe plastic deformation. JOM 52(4):27–29

McNelley TR, McMahon ME (1996) An investigation by interactive electron backscatter pattern analysis of processing and superplasticity in an aluminum-magnesium alloy. Metall Mater Trans A 27A:2252–2262

McNelley TR, McMahon ME (1997) Microtexture and grain boundary evolution during microstructural refinement processes in SUPRAL 2004. Metall Mater Trans A 28A: 1879–1887

McNelley TR, McMahon ME, Hales SJ (1997) An EBSP investigation of alternate microstructures for superplasticity in aluminum-magnesium alloys. Scripta Mater 36:369–375

McNelley TR, McMahon ME, Pérez-Prado MT (1999) Grain boundary evolution and continuous recrystallization of a superplastic Al-Cu-Zr alloy. Philos T R Soc A 357: 1683–1705

McNelley TR, Swisher DL, Pérez-Prado MT (2002) Deformation bands and the formation of grain boundaries in a superplastic aluminum alloy. Metall Mater Trans A 33A:279–290

McNelley TR, Oh-ishi K, Zhilyaev AP, Swaminathan S, Krajewski PE, Taleff EM (2008) Characteristics of the transition from grain-boundary sliding to solute drag creep in superplastic AA5083. Metall Mater Trans A 39A:50–64

Merchant ME (1945) Mechanics of the metal cutting process. I. Orthogonal cutting and a type 2 chip. J Appl Phys 16: 267–275

Mishra RS (2003) Friction stir processing technologies. Adv Mater Process 161(10):43–46

Mishra RS, Ma ZY (2005) Friction stir welding and processing. Mater Sci Eng R 50:1–78

Mishra RS, Mahoney MW (2007) Friction stir welding and processing. ASM International, Materials Park, OH

Oh-ishi K, Zhilyaev AP, McNelley TR (2005) Effect of strain path on evolution of deformation bands during ECAP of pure aluminum. Mater Sci Eng A 410–411:183–187

Pérez-Prado MT, McNelley TR, Ruano OA, González-Doncel G (1998) Microtexture evolution during annealing and superplastic deformation of Al-5%Ca-5%Zn. Metall Mater Trans A 29A:485–492

Pérez-Prado MT, González-Doncel G, Ruano OA, McNelley TR (2001) Texture analysis of the transition from slip to grain boundary sliding in a discontinuously recrystallized superplastic aluminum alloy. Acta Mater 49:2259–2268

Piispanen V (1948) Theory of formation of metal chips. J Appl Phys 19:876–881

Randle V, Engler O (2000) Texture analysis: macrotexture, microtexture & orientation mapping. Gordon and Breach, Amsterdam

Saito Y, Utsunomiya H, Tsuji N, Sakai T (1999) Novel ultra-high straining process for bulk materials—development of accumulative roll bonding (ARB) process. Acta Mater 47(2): 579–583

Sherby OD, Wadsworth J (1984) Development and characterization of fine-grain superplastic materials. In: Krauss G (ed) Deformation processing and microstructure. ASM International, Materials Park, OH

Swaminathan S, Shankar MR, Lee S, Hwang J, King AH, Kezar RF, Rao BC, Brown TL, Chandrasekar S, Compton WD, Trumble KP (2005) Large strain deformation and ultrafine grained materials by machining. Mater Sci Eng A 410–411:358–363

Swaminathan S, Brown TL, Chandrasekar S, McNelley TR, Compton WD (2007) Severe plastic deformation of copper by machining: microstructure refinement and nanostructure evolution with strain. Scripta Mater 56:1047–1050

Ungár T, Alexandrov I, Zehtebauer M (2000) Ultrafine-grained microstructures evolving during severe plastic deformation. JOM 52(4):34–36

Valiev RZ, Mulyukov RR, Ovchinnikov VV, Shabashov VA (1991) Mössbauer analysis of submicrometer grained iron. Scripta Metall 25:2717–2722

Zhilyaev AP, Oh-ishi K, Raab GI, McNelley TR (2006a) Influence of ECAP processing parameters on texture and microstructure of commercially pure aluminum. Mater Sci Eng A 441(1–2):245–252

Zhilyaev AP, Swisher DL, Oh-ishi K, Langdon TG, McNelley, TR (2006b) Microtexture and microstructure evolution during processing of pure aluminum by repetitive ECAP. Mater Sci Eng A 429(1–2):137–148

Chapter 21

Applications of EBSD to Microstructural Control in Friction Stir Welding/Processing

Sergey Mironov, Yutaka S. Sato, and Hiroyuki Kokawa

21.1 Introduction

Friction stir welding/processing (FSW/P) is an innovative solid-state joining/processing technique (Thomas et al. 1991; Mishra and Ma 2005). The basic concept of FSW/P is very simple, as shown in Fig. 21.1 (Park et al. 2003a). A specially designed tool rotating at high speed is plunged into work pieces to be joined/processed and then is traversed along the weld seam, or in a direction of interest in the case of friction stir processing (FSP). The rotating tool produces frictional heat which softens the material so that it is readily extruded around the tool. The simultaneous rotational and translation motion of the tool forces the material to flow around the tool, filling a cavity at the rear of the tool and thus creating a solid-state joint. During the flow, the material undergoes extreme levels of plastic deformation and thermal exposure, which drastically changes the microstructure in the center of the processed zone.

As a solid-state joining process, FSW avoids several problems associated with solidification in conventional fusion welding, and thereby provides defect-free welds characterized by good properties even in materials with poor fusion-weldability (e.g., Al and Mg alloys). Furthermore, fine-grained characteristics of FSP allow this technique to be considered a potential tool for microstructural refinement (Mishra et al. 2000). Due to the great practical importance of FSW/P, these technologies have attracted extensive research interest during the last two decades. The first works in this field were focused mainly on designing and optimizing of FSW/P technique. Presently, however, microstructural characterization is becoming one of the key issues.

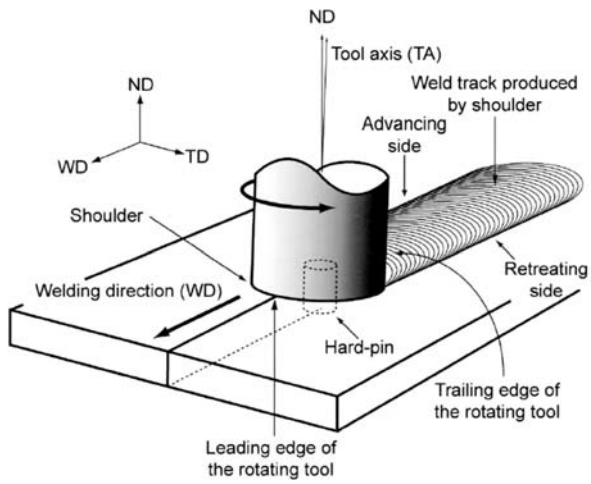


Fig. 21.1 Schematic illustration of the friction-stir-welding process

A unique characteristic of FSW/P is exceptionally high gradients of temperature, strain, and strain rate. As a result, the obtained microstructures typically show a drastic variation in microstructure morphology, grain size, misorientation distribution, and texture. Therefore, the electron backscatter diffraction (EBSD) technique, which enables the study of microstructures as well as microtextures of specific areas of interest at a high level of statistical detail, is very attractive for microstructural control in the FSW/P'ed materials.

S. Mironov (✉)
Department of Materials Processing, Graduate School of Engineering, Tohoku University, Sendai 980-8579, Japan
e-mail: smironov@material.tohoku.ac.jp

A.J. Schwartz et al. (eds.), *Electron Backscatter Diffraction in Materials Science*,
DOI 10.1007/978-0-387-88136-2_21, © Springer Science+Business Media, LLC 2009

Although EBSD is commonly considered to be a routine tool for microstructural observations, EBSD studies in the FSW/P field are just beginning. In this chapter, we give a brief overview of how EBSD is employed for microstructural control in FSW/P'ed materials and emphasize its great potential in this field.

21.2 Brief Explanations of FSW/P Terminology

FSW/P produces a fine equi-axed grain structure at the weld center in most metallic materials through dynamic recrystallization arising from frictional heating and significant plastic deformation. The recrystallized area, called the "stir zone," refers to the zone previously occupied by the tool pin. This microstructural region is sometimes also referred to as the "recrystallized zone" or "weld nugget." Material in the region adjacent to the stir zone is believed to undergo much lower levels of strain and temperature exposure, insufficient for recrystallization; this microstructural region is usually termed the "thermomechanically affected zone (TMAZ)." Outside the TMAZ, the material is affected only by the thermal cycle, and thus this microstructural region is usually defined as the "heat affected zone (HAZ)." The different microstructural zones existing in the transverse cross section after FSW are schematically shown in Fig. 21.2 (Mishra and Mahoney 2007).

The simultaneous rotational and translation motions of the welding tool during FSW/P create a characteristic asymmetry on the cross section. The side of the welding tool on which the motion of the surface of the welding tool is in the same direction as the traversing direction is referred to as the "advancing side (AS)." The opposite side, on which the motion of the surface of the welding tool is in the opposite direction from which the tool is moving, is referred to as the "retreating side (RS)."

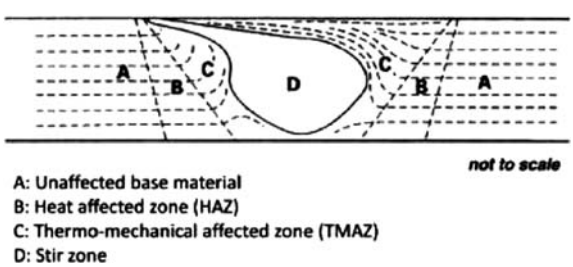


Fig. 21.2 Various microstructural regions in the transverse cross section of a friction stir welded material

21.3 Microstructural Evolution

One of the main aims of studying microstructure and texture is to predict the mechanical properties and post-FSW/P annealing behavior of a material. In order to improve our ability to control its properties, it is necessary to clearly understand how the final microstructure develops in the material.

Detailed EBSD studies of grain structure development during FSW of Al alloy 2195 have been performed by Prangnell and Heason (2005) and by Fonda et al. (2004, 2007). To study "actual" microstructural evolution by minimizing the microstructural changes during the cooling cycle of FSW, the authors applied the so-called stop-action technique, which consists of rapidly breaking the tool motion and immediately quenching the workpiece. Subsequent EBSD measurements have shown that microstructural development is a very complicated process. At the cold periphery of the deformation zone ahead of the tool, the original grains first split into coarse primary deformation bands (Fig. 21.3a) (Prangnell and Heason 2005). As the strain increases towards the tool, the distances between the original grain boundaries and the new deformation bands are reduced due to the geometric requirements of strain, resulting in the formation of elongated fibrous grains. Second-order deformation bands form within the primary ones, indicating that grain subdivision continues on a finer scale. In the region closer to the tool, high-angle grain boundaries (HABs) become wavy, showing local grain boundary migration. Development of this process breaks up the closely spaced HABs into strings of fine equi-axed grains (Fig. 21.3b) (Prangnell and Heason 2005). As a result, a mixed microstructure evolves, comprised of fine equi-axed grains with some retained high aspect ratio fibrous grains. In the vicinity of the tool, a reasonably uniform microstructure comprised of low-aspect ratio fine grains is formed (Fig. 21.3c) (Prangnell and Heason 2005). These grains are elongated in the shear direction with aspect ratios of ~1–3 and contain a significant (up to

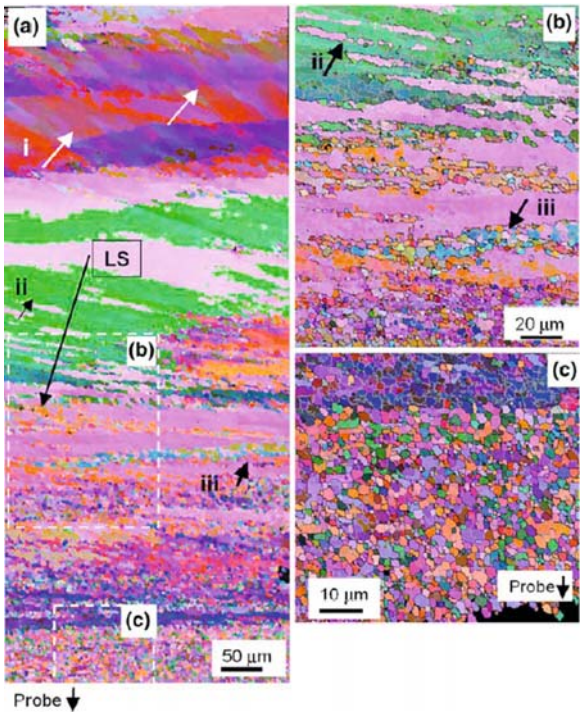


Fig. 21.3 Microstructural evolution during FSW of Al alloy 2195: EBSD map of the region directly ahead of the tool, showing the effect of the progressively increasing strain and temperature in the proximity of the tool (**a**), with selected regions shown at higher magnifications in (**b**) and (**c**)

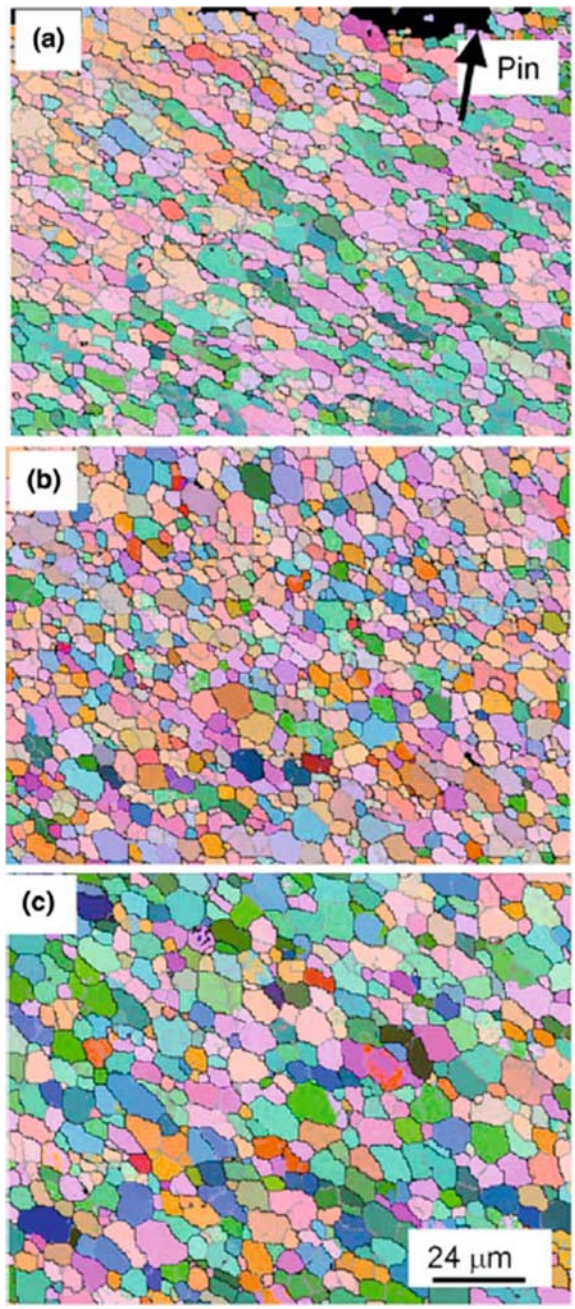


Fig. 21.4 EBSD maps showing microstructural development in thermal wake of welding tool: grain structure immediately behind the tool (**a**), grain structure 0.5 mm behind the tool (**b**), and grain structure 2 mm behind the tool (**c**)

~40%) fraction of low-angle boundaries (LABs). This microstructure becomes more equi-axed and slightly coarsened due to static annealing after passage of the tool (Fig. 21.4) (Prangnell and Heason 2005). This process is also accompanied by a reduction in the level of the retained LABs down to 25–30%.

EBSD study of microstructural evolution during FSP of pure iron (Mironov et al. 2008a) has shown that this process is broadly similar to that in Al alloy. Thorough EBSD analysis of microstructural morphology, grain size, misorientation distribution, and texture has shown that development of the grain structure during FSP of pure iron is a complex phenomenon involving geometrical effects of strain, grain subdivision, and thermally activated HAB migration. The original grains are first reoriented by strain in a flow pattern around the tool due to geometrical requirements of the strain, as shown in Fig. 21.5a (Mironov et al. 2008a). Simultaneously, the original grains are split by regular arrays of nearly parallel bands of LABs, thus

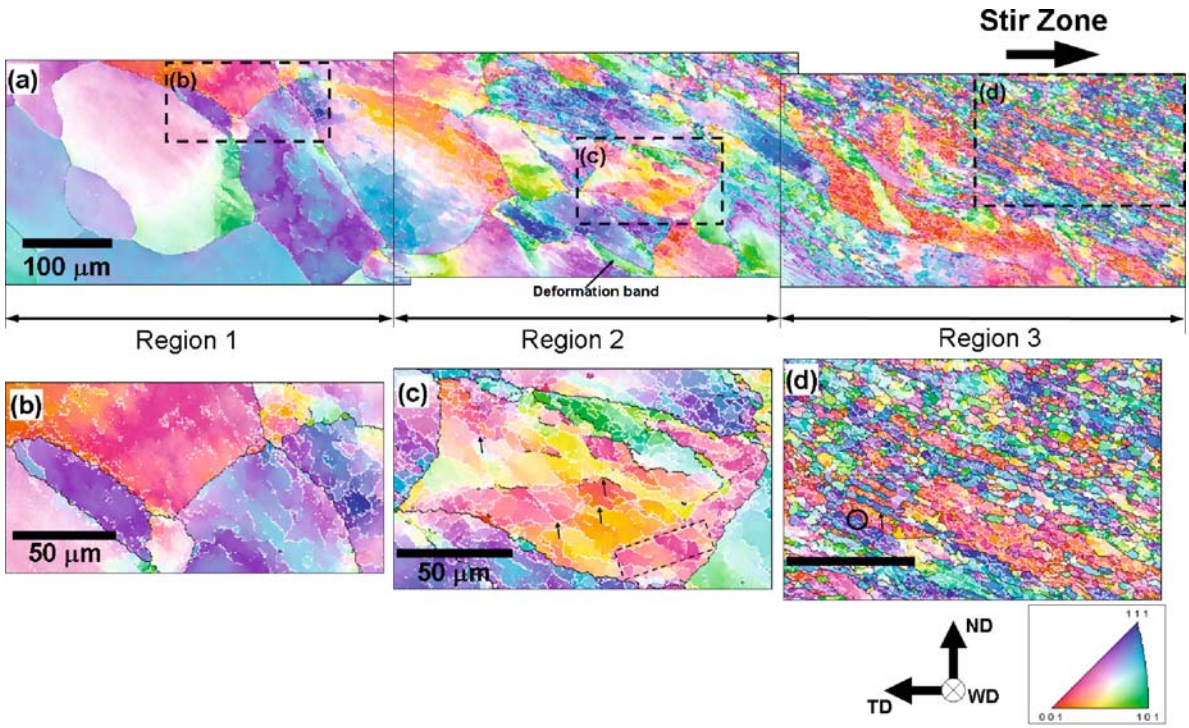


Fig. 21.5 Composite EBSD map illustrating microstructural evolution during FSP of pure iron (**a**), with selected areas shown at high magnification in (**b,,c, d**)

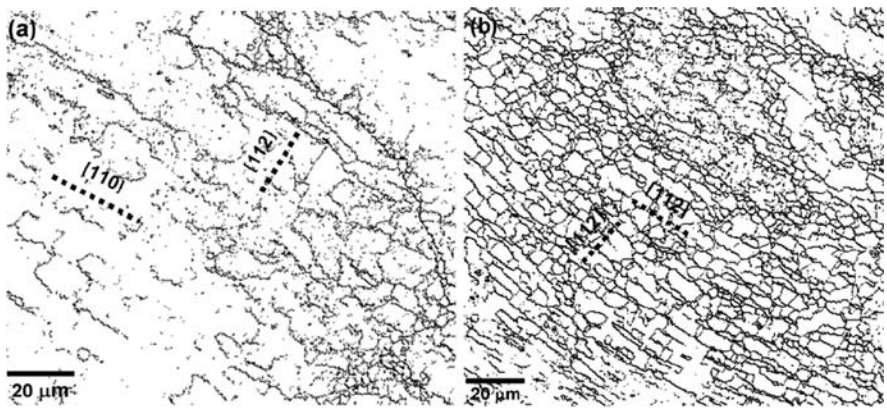


Fig. 21.6 Crystallographic alignment of grain boundary traces during FSP of pure iron: microstructure far from the stir zone (**a**), and microstructure proximal to the stir zone (**b**). Slip plane traces are shown by *dotted lines*

indicating the beginning stage of the grain subdivision process (Fig. 21.5c) (Mironov et al. 2008a). Boundary traces of the bands exhibit macroscopic as well as crystallographic directionality, tending to align with the flow patterns within the sample coordinate system, as well as with {110} and {112} slip plane traces within the grain reference frame (Fig. 21.6) (Mironov et al. 2008a). As the strain increases, misorientation of the

band boundaries increases and the distance between the bands decreases, eventually forming a lamellar-type microstructure consisting of HABs aligned in a common direction and cross-linked by LABs (Fig. 21.5d) (Mironov et al. 2008a). The HAB fraction as well as HAB spacing is found to be related to texture strength, thus evidencing that the grain subdivision process is governed by texture evolution. In the region close to the tool, the HABs become wavy due to local grain boundary migration (an example is encircled in Fig. 21.5d) (Mironov et al. 2008a). This process leads to limited discontinuous recrystallization.

In the study of microstructural evolution during FSW, a particular challenge is to understand the microstructural behavior of the materials, which experience allotropic phase transformation, e.g., Ti alloys. If the peak temperature during FSW exceeds the β-transus in Ti alloys, the material deforms in the high-temperature β-phase field. Upon cooling after FSW, the β-phase almost completely transforms into low-temperature α-phase, and thus the dynamic features of deformation cannot be directly observed in the postmortem microstructure. This significantly complicates interpretation of the microstructural evolution during FSW. The difficulty associated with the phase transformation in the high-temperature phase may be overcome (i) by adopting an indirect modeling technique involving reconstruction of the grain structure of the high-temperature phase, or (ii) by local orientation measurements in small quantities of the high-temperature phase retained at ambient temperature (if any). In this case, EBSD would be the most suitable method for microstructural analysis.

Recent studies of the microstructural evolution during FSW of Ti-6Al-4V alloy have confirmed the exceptional effectiveness of EBSD (Mironov et al. 2008b, 2008c). Local crystallographic measurements in the stir zone have shown that close-packed planes $\{0001\}_\alpha$ / $\{110\}_\beta$ and close-packed directions $<11\text{–}20>_\alpha$ / $<111>_\beta$ of the neighboring α and β phases are typically parallel (Mironov et al. 2008b). Moreover, extensive misorientation measurements have demonstrated that the misorientation distribution in the α phase is very close to that predicted for a variant inherited from the β phase, as shown in Fig. 21.7 (Mironov et al. 2008b). These results conclusively show that the crystallography of the α and β phases in Ti-6Al-4V FS weld is related via the Burgers orientation relationship (Mironov et al. 2008b, 2008c). This conclusion enables reconstruction of the grain structure of the high-temperature β phase by using the EBSD technique, as shown in Fig. 21.8 (Mironov et al. 2008c). Analysis of the reconstructed EBSD maps has shown that the β grains in the stir zone are severely sheared in a common direction and subsequently subdivided by transverse subboundaries, thus eventually forming strings of relatively low-aspect ratio grains (Mironov et al. 2008c). In the cited study, boundary traces of the reconstructed β grains were not straight over a

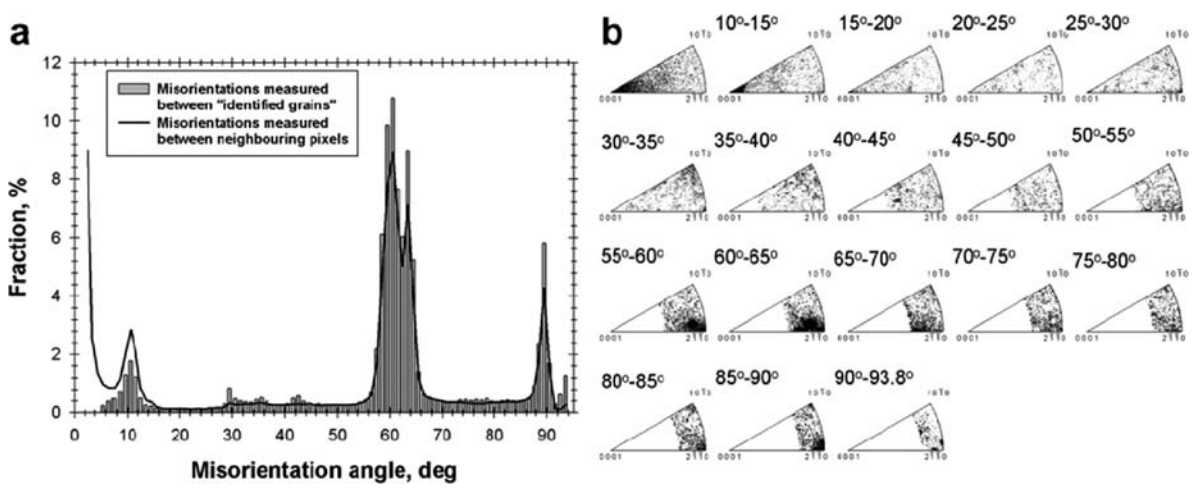


Fig. 21.7 Misorientation data for α phase obtained from FSW'ed Ti-6Al-4V alloy: misorientation-angle distribution (**a**) and misorientation-axis distribution (**b**)

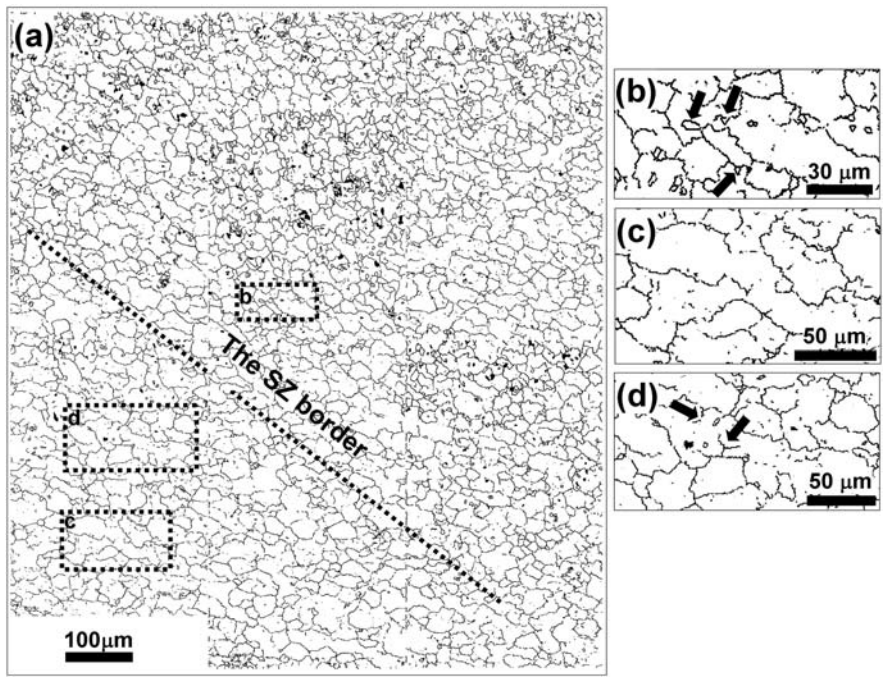


Fig. 21.8 EBSD grain boundary map of the reconstructed β grain structure in FSW'ed Ti-6Al-4V alloy (**a**), with selected regions shown at high magnification in (**b**, **c**, **d**)

long distance and exhibited bulges tending to form very small equi-axed grains (Fig. 21.8b, arrowed), this observation being interpreted as evidence of limited discontinuous recrystallization stimulated by local grain boundary migration (Mironov et al. 2008c). Therefore, the EBSD technique provides a unique opportunity to establish that microstructural evolution in the high-temperature β-phase field is also driven by a combination of geometrical effects of strain, grain subdivision, and local HABs migration.

21.4 Material Flow

The material flow during FSW is quite complex, and its understanding is important for optimal tool design and improvement of process reliability. Currently, this process is still not completely understood, one of the key difficulties being the impossibility of its direct observation during FSW.

As the material flow during FSW occurs in a solid state, this process may be interpreted in terms of intense plastic deformation at high temperatures. Hence, the material flow may lead to formation of a crystallographic texture in the stir zone. An example of the strong texture observed in the stir zone of an Al alloy is shown in Fig. 21.9 (Field et al. 2001). It is evident that the texture in the stir zone is different from that in the base metal (Fig. 21.9b), this observation being attributable to the material flow during FSW. Additionally, a strong cross-width texture gradient from the retreating side to the advancing side is seen in Fig. 21.9c. This interesting phenomenon may be associated with the heterogeneous nature of the material flow within the stir zone due to rotation of the welding tool. This figure conclusively demonstrates that analysis of the local texture and texture gradients by the EBSD method may provide fundamental knowledge on the material flow during FSW. Some previous studies have attempted to deduce the material flow during FSW using EBSD data obtained from the stir zone (Sato et al. 2001; Field et al. 2001; Park et al. 2003a).

Although the material flow during FSW is complicated, the predominant deformation mode is expected to be simple shear (Fonda et al. 2007). Indeed, several

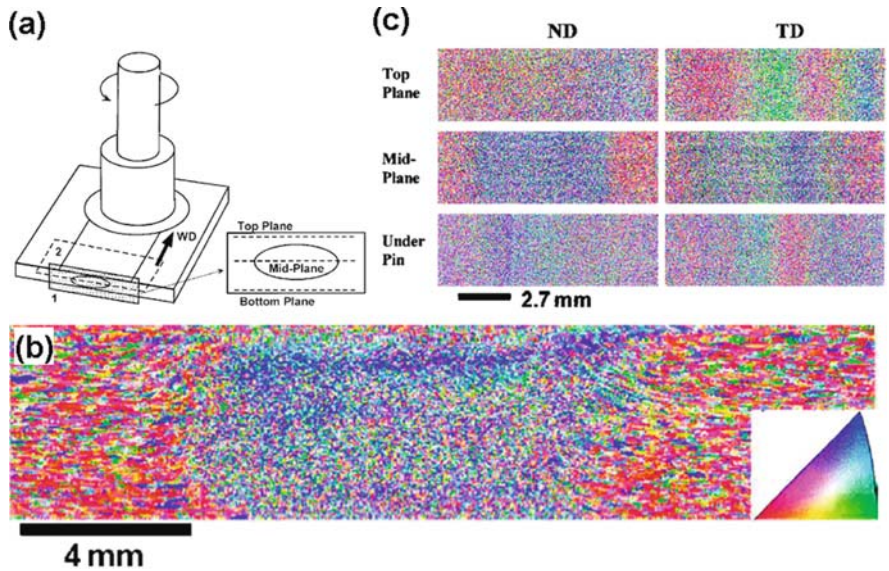


Fig. 21.9 (**a**) Schematic representation of the friction stir weld geometry and the associated analyzed planes. Plane 1 (the *shaded region*) shows the cross section analyzed, and plane 2 indicates the plane-view geometry, (**b**) orientation image from a complete cross section, and (**c**) plane view orientation images of an FSW joining 1100 Al plates at 700 rpm and 18 cm/min. ND and TD correspond to normal direction and transverse direction of the plate, respectively

studies performed on various materials have revealed formation of a simple shear texture within the stir zone (Sato et al. 2001; Field et al. 2001; Park et al. 2003a; Fonda et al. 2007). For example, {111} pole figures obtained from the base material and the center of the stir zone of FSW'ed Al alloy 6063 are shown in Fig. 21.10 (Sato et al. 2001), in which it can be seen that a typical recrystallization texture of the base material changes into a completely different texture during FSW. The newly developed texture consists of two texture components having a common pole near the welding direction (WD). A comparison of the experimental texture (Fig. 21.10) with ideal simple shear textures expected for fcc metals (Fig. 21.11) (Li et al. 2005) shows that the stir zone texture is very close to A/-A simple shear texture components. Texture analysis performed across the stir zone from the retreating side to the advancing side has demonstrated that tex-

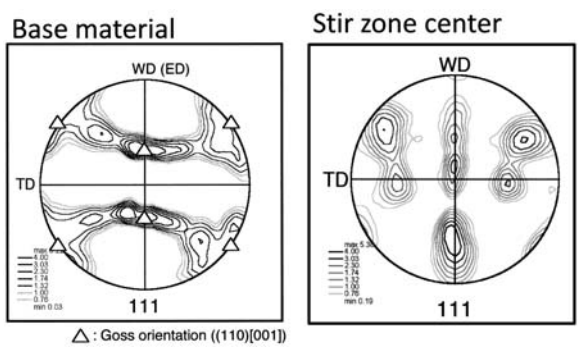


Fig. 21.10 {111} pole figures obtained from the base material and the stir zone center of FSW of extruded Al alloy 6063. ED: extruded direction, WD: welding direction, and TD: transverse direction

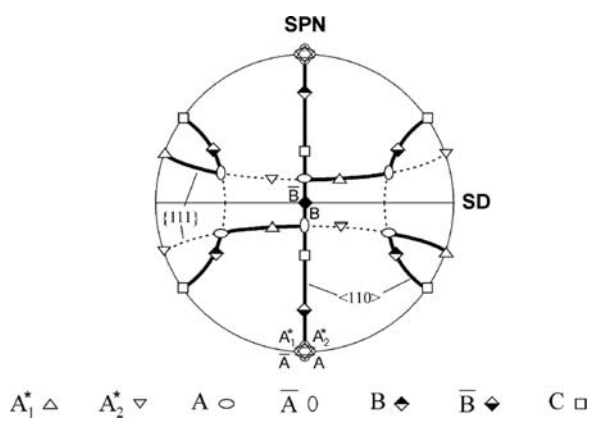


Fig. 21.11 {111} pole figures showing the main ideal orientations and fiber textures associated with simple shear deformation of fcc materials. SPN means shear plane normal and SD is shear direction in the pole figure

ture variation in the stir zone may simply be described in terms of the A/-A components which rotate around the plate normal direction (ND), which is close to the rotational axis of the welding tool. From these results, it is strongly suggested that the material flow during FSW mainly arises from simple shear deformation along the pin column surface in the rotational direction of the pin.

The local texture and texture gradient associated with the deformation history during FSW are much clearer in Mg alloys having an hcp crystal structure, because the material flow in these materials mainly arises from a basal slip. Representative (0002) pole figures taken from the base material and the stir zone center of FSW'ed AZ61 Mg alloy are presented in Fig. 21.12 (Park et al. 2003a). FSW produces a strong (0002) basal texture roughly perpendicular to the WD at the weld center. Texture analysis for the entire stir zone reveals that a trace of the (0002) is distributed so as to surround the pin column surface, as shown in Fig. 21.13. The local texture distribution in a Mg alloy also supports the conclusion that the material flow during FSW is characterized by simple shear deformation around the rotating tool.

It should be noted that the crystallographic texture observed in the stir zone is directly traceable to only the final deformation stage. This means that the behavior of the material flow in the early stage of FSW is hardly predictable by EBSD, because its remnant is usually erased by the final deformation stage. However, there is no doubt that texture analysis in the stir zone is a powerful tool to obtain additional information on the material flow unobtainable with other techniques.

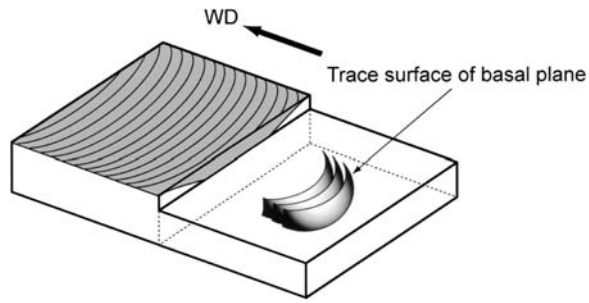


Fig. 21.13 Schematic of trace surface of basal plane produced in AZ61 Mg alloy

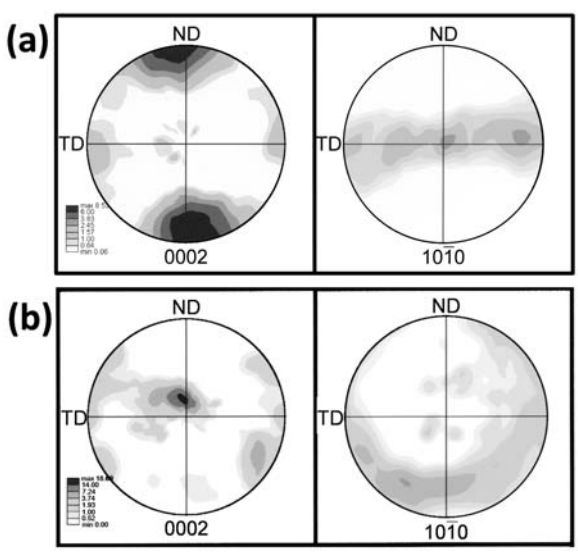


Fig. 21.12 (0002) and (10-10) pole figures of the base material (**a**) and stir zone center (**b**) in FSW'ed AZ61 Mg alloy. Since coordinate axes of the pole figures are the welding direction (WD), transverse direction (TD), and normal direction (ND) of the plate, the center of the pole figures corresponds to the WD

21.5 Structure-Properties Relationship

The various microstructural characteristics routinely provided by EBSD may also be employed for prediction (and even control) of the properties of FSW/P'ed materials. A few examples illustrating structure-properties relationships examined via EBSD are given below.

Mechanical behavior of Mg alloys is commonly accepted to be critically influenced by the crystallographic texture, because their material flow is mainly associated with a basal slip, as mentioned in the previous section. Detailed EBSD study of FSW'ed AZ61 Mg alloy has shown that the texture is essentially inhomogeneous within the stir zone and that (0002) basal slip planes are aligned roughly parallel to the pin column surface (Fig. 21.13) (Park et al. 2003a). Subsequent transverse tension tests of FSW joints have demonstrated that this creates a subsequent anisotropy of mechanical properties, and that the deformation is preferentially located within the regions with a high Schmidt factor (Park et al. 2003b), as shown in Fig. 21.14. Therefore, the unique capability of EBSD to measure the microtexture distribution enables the

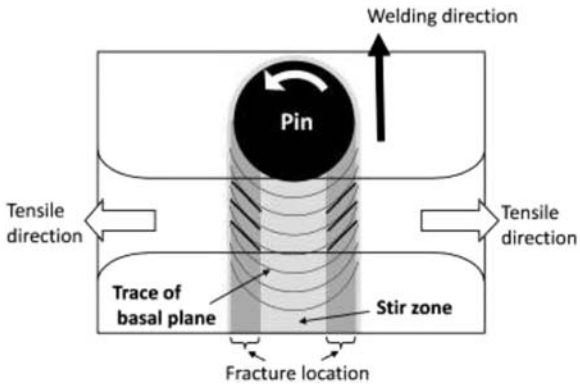


Fig. 21.14 Plane-view illustration of FSW'ed AZ61 Mg alloy showing relationship between trace of basal plane and fracture location during the transverse tensile test

prediction of the mechanical properties of FSW/P'ed Mg alloys.

It is generally believed that superplastic properties of materials significantly depend on the nature of grain boundaries. Generally, HABs are considered to be more advantageous for grain boundary sliding than LABs, this being one of the reasons for significant commercial interest in microstructural refinement. With EBSD, the HAB fraction in a material can be easily determined, and thus may be very useful for estimation of the superplastic behavior. For example, EBSD measurements in FSP'ed Al alloy 2024 have revealed an exceptionally high HAB fraction (∼95%, Fig. 21.15), and this observation has been

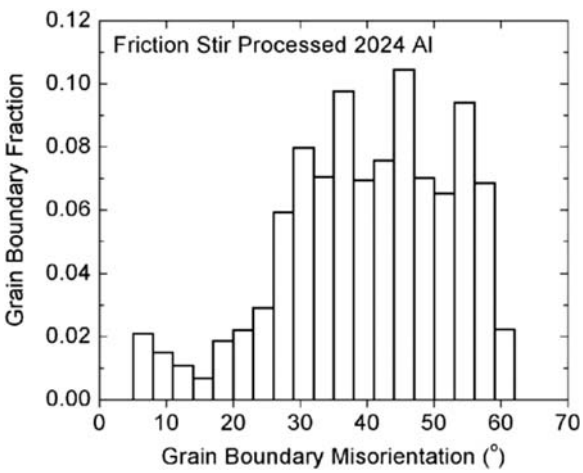


Fig. 21.15 Grain boundary misorientation distribution in FSP'ed Al alloy 2024

directly correlated with the high strain rate superplasticity found in this material (Charit and Mishra 2003).

21.6 Summary and Future Outlook

EBSD is an excellent tool for microstructural and texture control in FSW/P'ed materials. This technique can be successfully employed for fundamental insight into material flow and microstructural evolution as well as for quantification of the structure-properties relationship. Although this method has still not been widely applied in FSW/P, it is expected that its contribution will grow, especially in the field of phase transformations.

References

Charit I, Mishra RS (2003) High strain rate superplasticity in a commercial 2024 Al alloy via friction stir processing. Mater Sci Eng A 359:290–296

Field DP, Nelson TW, Hovanski Y, Jata KV (2001) Heterogeneity of crystallographic texture in friction stir welds of aluminum. Metall Mater Trans 32A:2869–2877

Fonda RW, Binget JF, Colligan KJ (2004) Development of grain structure during friction stir welding. Scripta Mater 51: 243–248

Fonda RW, Knipling KE, Bingert JF (2007) Microstructural evolution ahead of the tool in aluminum friction stir welds. Scripta Mater 58:343–348

Li S, Beyerlein IJ, Bourke, MAM (2005) Texture formation during equal channel angular extrusion of fcc and bcc materials: comparison with simple shear. Mater Sci Eng A 394:66–77

Mironov S, Sato YS, Kokawa H (2008a) Microstructural evolution during friction stir-processing of pure iron. Acta Mater 56:2602–2614

Mironov S, Zhang Y, Sato YS, Kokawa H (2008b) Crystallography of transformed β microstructure in friction stir welded Ti-6Al-4V alloy. Scripta Mater 59:511–514

Mironov S, Zhang Y, Sato YS, Kokawa H (2008c) Development of grain structure in β-phase field during friction stir welding of Ti-6Al-4V alloy. Scripta Mater 59:27–30

Mishra RS, Mahoney MW, McFaddens SX, Mar NA, Mukherjee AK (2000) High strain rate superplasticity in a friction stir processed 7075 Al alloy. Scripta Mater 42:163–168

Mishra RS, Ma ZY (2005) Friction stir welding and processing. Mater Sci Eng R 50:1–78

Mishra RS, Mahoney MW (eds) (2007) Friction stir welding and processing. ASM International, Materials Park, OH

Park SHC, Sato YS, Kokawa H (2003a) Basal plane texture and flow pattern in friction stir weld of a magnesium alloy. Metall Mater Trans 34A:987–994

Park SHC, Sato YS, Kokawa H (2003b) Effect of micro-texture on fracture location in friction stir weld of Mg alloy AZ61 during tensile test. Scripta Mater 49:161–166

Prangnell PB, Heason CP (2005) Grain structure formation during friction stir welding observed by the "stop action technique." Acta Mater 53:3179–3192

Sato YS, Kokawa H, Ikeda K, Enomoto M, Jogan S, Hashimoto T (2001) Microtexture in the friction-stir weld of an aluminum alloy. Metall Mater Trans 32A:941–948

Thomas WM, Nicholas ED, Needham JC, Murch MG, Templesmith P, Dawes CJ (1991) G.B. Patent Application No. 9125978.8

Chapter 22

Characterization of Shear Localization and Shock Damage with EBSD

John F. Bingert, Veronica Livescu, and Ellen K. Cerreta

22.1 Introduction

This chapter provides examples of the application of EBSD characterization to microstructures influenced by two conditions: (1) shear localization, and (2) dynamic deformation and damage from shock loading.

Regarding localization, the development of plastic instabilities and shear bands is significant to multiple applications ranging from rolling and metal cutting operations to dynamic loading environments such as auto impacts and ballistic events (Semiatin et al. 1984). In many loading scenarios failure is preceded by shear band or localization formation. Localization is typically enhanced at high strain rates because inadequate time for thermal diffusion promotes nonuniform strain (Clifton et al. 1984). Thermal softening leading to extreme plastic flow localization can result in adiabatic shear bands, in which large strains are localized within very narrow regions (Rittel et al. 2006). Plastic instability in general represents a potential failure mode that is difficult to predict by conventional continuum modeling approaches. Therefore, considerable research has been focused on its properties in order to avoid, or sometimes exploit, its occurrence.

The linkage between microstructure and instability has been examined most notably in the case of shear band development. In this case, the deformation state transitions from one of homogeneous strain to localized strain within a defined planar band of material. Shear bands are favored by the exhaustion of strain-hardening. Texture may also contribute to shear band formation through Taylor softening, in which the deformation texture evolves toward orientations that have lower resistance to subsequent deformation.

Dynamic deformation refers to the plastic deformation of materials under nonequilibrium conditions. In general, these conditions are encountered during the application of a rapid loading rate, leading to high strain rates. The response of a material to dynamic loading may be very different from quasi-static loading of an analogous stress state. This is due to the effects of increased rate on a material's constitutive properties and microstructural evolution, such as the suppression of dynamic recovery and decrease of thermal activation of dislocation mobility. At very high loading rates the effect of shock waves must also be considered. Deformation in the shock regime results in a discontinuous plastic wave front, and is characterized by the generation of a high density of defects. The evolution of damage is also generally different under dynamic conditions, and this is especially true in the case of shock loading.

Material response to dynamic loading has been observed for over 100 years, with systematic research on dynamic damage beginning with the work of Hopkinson (1914). However, detailed consideration of microstructural evolution and the effect of microstructure on dynamic material instability and damage is a more recent concern. The interested reader is referred to the review by Meyers and Aimone (1983) and the book by Meyers (1994) for an overview. Various models describing dynamic damage and fracture have been developed: for example, those of Johnson (1981) for ductile spall, and Grady (1982) for fracture and fragmentation. More recently, the use of crystal plasticity

J.F. Bingert (✉)
Materials Science and Technology Division, Los Alamos National Laboratory, Los Alamos, NM 87545, USA
e-mail: bingert@lanl.gov

A.J. Schwartz et al. (eds.), *Electron Backscatter Diffraction in Materials Science*,
DOI 10.1007/978-0-387-88136-2_22, © Springer Science+Business Media, LLC 2009

FEM has been applied to investigate the local initiation of dynamic localization from shock loading and shear testing (Radovitzky and Cuitino 2003; Becker 2004; Case and Horie 2007; Bronkhorst et al. 2006), building on quasi-static and dynamic theory developed by Asaro and Rice (1977) and Nemat-Nasser et al. (1994), among others.

The application of EBSD characterization to microstructures associated with shear localization, and dynamic deformation and damage, enables an enhanced understanding of microstructural evolution during these events. This chapter will draw on two examples to illustrate how EBSD data and its analysis have been applied to investigate the microstructural evolution of materials subjected to dynamic and shear loading conditions. The first of these involves the study of stress state and microstructural effects on strain localization and instability through constrained-shear mechanical tests. The second example considers the evolution of dynamic damage from shock loading, a process termed spallation. For each case the role of EBSD in providing insight into the mechanisms of damage evolution will be highlighted.

22.2 Shear Localization

Research on shear banding has typically focused on two areas; the development of predictive modeling for plastic flow instability, and the relationship of shear banding to initial microstructure. Microstructural alterations observed in shear-deformed metals include dynamic recovery, dynamic recrystallization, phase transformations, melting, and amorphization (e.g., Meyers et al. 2003; Xue et al. 2002). Recent studies have focused on correlating evolving microstructure and mechanical response during shear localization. Mechanisms that control substructures within shear bands appear to be strongly related to initial microstructure, its evolution, and therefore its work-hardening capability (Xue and Gray 2006a, 2006b; Dougherty et al. 2007). Certain polycrystalline textures, and grains favorably oriented for shear deformation, may also be more susceptible to the transmission of shear bands (e.g., Xue et al. 2008). An important consideration for material instability studies, especially those comparing different materials or establishing structure-property relations, is quantification of localization dimensions. The following investigations concern the role of EBSD in the characterization and quantification of shear localization structures.

22.2.1 Constrained Shear in Pure Fe—Shear Zone Geometry

The forced shear, or tophat, specimen is a sample geometry designed to probe the influence of microstructure, strain rate, temperature, and load on the evolution and growth of shear localization. The test was originally designed by Meyer and Manwaring (1986), but has been subsequently modified several times. This general specimen geometry defines and constrains the localization region and shear band formation, thus making it inappropriate for investigating shear band initiation. However, it is ideal for studying band evolution and growth because the initiation location within a specimen is predetermined (Bronkhorst et al. 2007).

In this investigation the influence of relative stress states on shear band characteristics within the deformation zone was explored. The stress states were affected by varying the tophat geometry. The four tophat dimensions used in this study are shown schematically in Fig. 22.1a. Figure 22.1b shows three views of a typical tophat sample, including a cross section of a post-tested specimen with the deformation region outlined. Over the range of four inner-hole diameters *ID*, the stress state in this shear zone (SZ) evolves from a combined loading state of shear and compression for Geometry A (the inner hole diameter is smaller than the outer hat diameter), to almost entirely simple shear loading in Geometry C (the inner hole diameter equals the outer hat diameter), to shear with some bending in Geometry D. To investigate the effect of different geometries on shear band structure, quasi-static compression tests were performed on samples machined into each of these configurations.

The material examined was electrical grade, hot finished, high-purity α-iron supplied as a 12 cm $\times$ 12 cm billet. The chemistry is provided in Table 22.1, while the average equiaxed grain size was 60 μm. The initial crystallographic texture was nearly random, as measured using X-ray diffraction (Gray et al. 2000). Specimens in each of the geometries shown in Fig. 22.1a

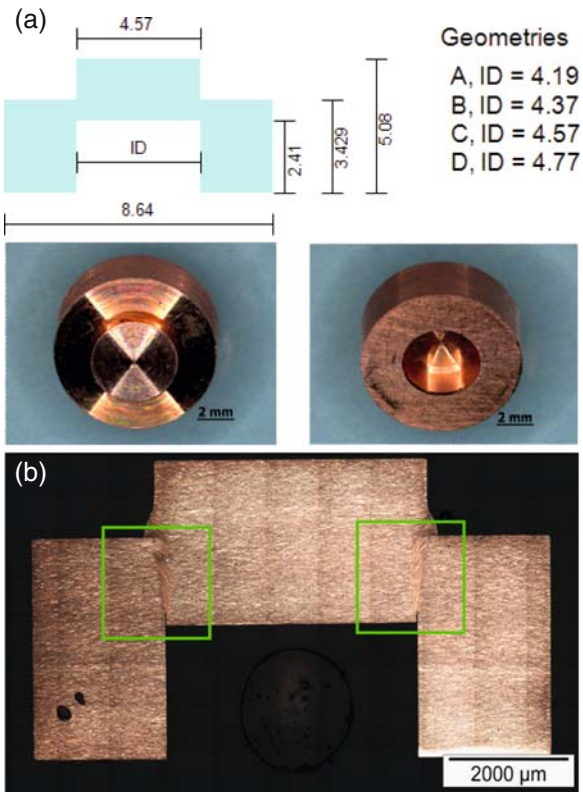


Fig. 22.1 The general tophat sample geometry; (**a**) schematic of cross-section with dimensions for A, B, C, and D samples, and (**b**) photos of a typical sample, including cross-section with SZ locations *highlighted*

Table 22.1 Chemical analysis of Fe (in ppm wt%)

C	Mn	Si	P	S	Cr	Ni	Fe
0.013	0.10	0.14	0.005	0.010	0.16	0.13	Bal.

were loaded in compression at a nominal rate of $10^{-3}s^{-1}$ and at 77 K to total displacements between 0.43 and 0.75 mm.

The mechanical test data for these tests is plotted in load vs. displacement in Fig. 22.2. The yield load and subsequent work-hardening rate decreased dramatically as the *ID* increased. For the largest diameters (C and D), the work-hardening rate is essentially flat and suggestive of shear localization with attendant thermally activated recovery processes. The relatively higher work-hardening rates in specimens A and B are indicative of the combined hoop and normal compressive loading state in the SZ gage section of these specimens.

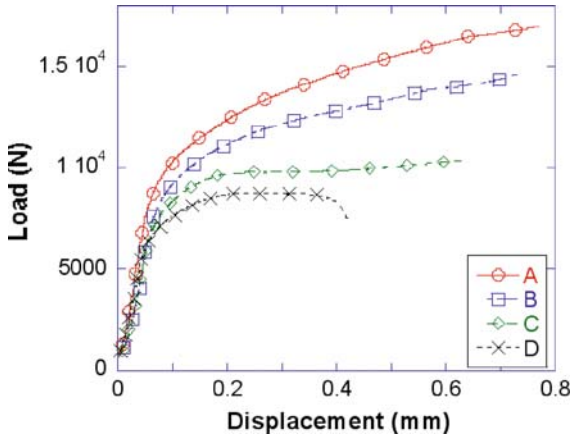


Fig. 22.2 Load vs. displacement compression data for each of the Fe tophat geometries

Postmortem specimens were cross-sectioned along the diameter and parallel to the loading axis, metallographically mounted, polished to 1 μm alumina, and etched with nital. EBSD was used to examine the SZ of each of these samples. Figure 22.3 shows crystal direction (CD) maps with respect to the section-normal (tangential) direction for the central region of the right side of the tophat SZ for each of the four geometries. These maps are rotated compared to the vertical SZ in Fig. 22.1 such that the shear direction is now horizontal. The SD as observed from the right-side SZ results in a negative simple shear strain. General high-angle boundaries (>15° misorientation) are delineated.

Qualitatively, deformation appears to become more intense in the SZ as the diameter of the inner hole approaches the diameter of the hat (closer to simple shear loading). However, estimation of the SZ widths is difficult from the CD maps. Therefore, two other mapping methods were applied to quantitatively estimate the width of the SZ: (1) kernel average misorientation (KAM), and (2) intragranular misorientation deviation (IMD). Both methods rely on deformation strain to develop intragranular misorientations through substructural evolution, such that the resultant misorientations provide a measurable signature of strain.

The KAM is a measure of the average misorientation of a point with respect to a selected number of its nearest neighbors. For the KAM maps shown

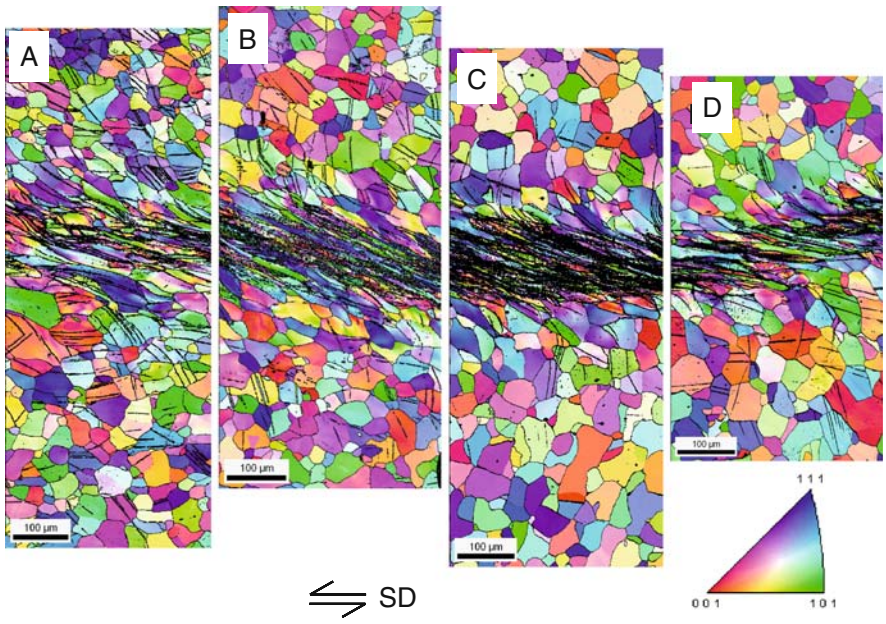


Fig. 22.3 EBSD crystal direction (CD) maps of the SZ for Fe tophat geometries A, B, C, and D. *Black lines* demarcate high-angle boundaries

in Fig. 22.4, five nearest neighbors were considered (∼ 2.5 μm radius around each point for the 0.5 μm step size scans), with a maximum misorientation of 6°. The KAM is more effective in resolving deformation regions than grain-based misorientation average calculations, especially for cases in which the gradient in deformation is fine compared to the grain size. The delineation of grain boundary regions at the edges of the SZs shows that strain was preferentially accommodated in proximity to the boundary network in the strain gradient region at the edges of the SZ. In contrast, the IMD measures the average of all deviations between each point in a grain and the grain's average orientation. IMD maps for the four samples are shown in Fig. 22.5. The selection of a lower misorientation threshold value of 2° resulted in a fairly contiguous SZ,

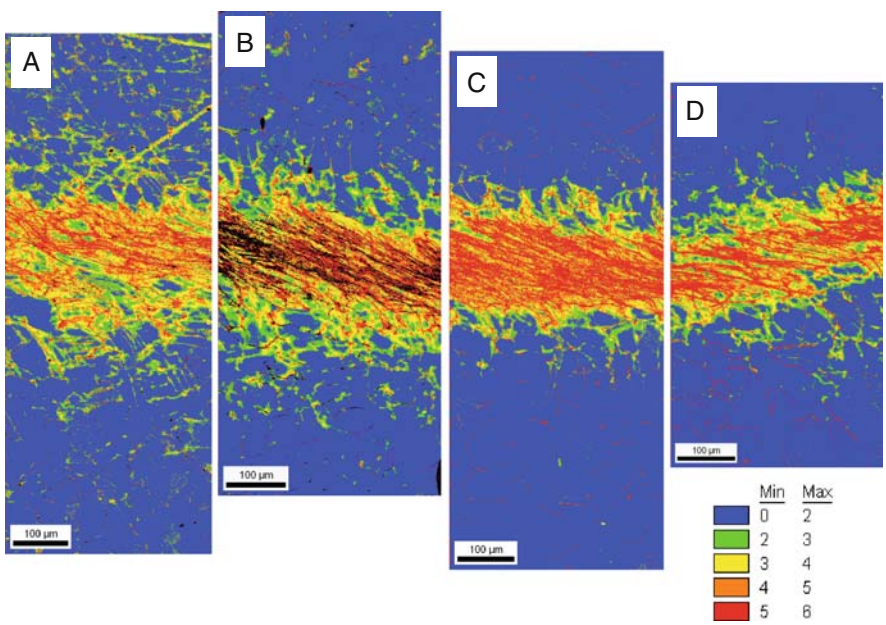


Fig. 22.4 EBSD kernel average misorientation (KAM) maps for Fe tophat geometries A, B, C, and D. 5-neighbor kernel with 6° maximum misorientation, scale in degrees of misorientation

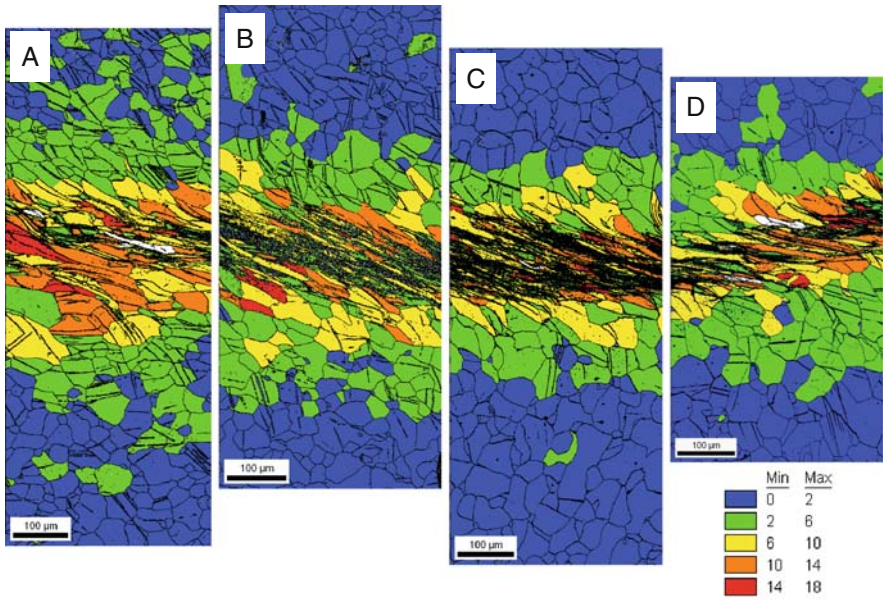


Fig. 22.5 EBSD intragranular misorientation deviation (IMD) maps for Fe tophat geometries A, B, C, and D. Scale in degrees of misorientation

with a well-defined matrix region consisting of grains below 2° IMD.

SZ width estimates were made from the KAM and IMD maps for all geometries. Initial observation suggested it would be more difficult to measure the KAM maps. Widths were determined for the maps by drawing parallel bounding lines on each side of the SZ. The location of the lines was fixed by the position in which the majority of the line was located in the matrix. Five width measurements perpendicular to the band length were averaged and rounded to the nearest 10 µm to provide the SZ width estimate. Figure 22.6 shows the SZ width results from both measurement techniques as a function of geometry. Although not as spatially resolved, the IMD map appears to provide greater utility for measuring the deformation zone than the KAM map. This is probably due to the greater uncertainty in determining the position of the bounding lines for the latter. The IMD calculation gives a more definitive location for the transition of the matrix to sheared material.

The IMD results show that SZ width is greatest in specimen A, reaches a minimum with specimen C, and increases slightly as the *ID* becomes wider than the hat diameter in sample D. This finding correlates well with the observed mechanical response (Fig. 22.2) of specimens A–C, where the strain-hardening rate decreases with increasing *ID*, indicating greater propensity for shear localization. Greater material instability and localization will result in narrower SZs. Note that estimation of SZ width from the CD maps (Fig. 22.3) might erroneously suggest that A was narrowest. Specimen D exhibited bulk instability and low strain-hardening, resulting in the smallest displacement of the four samples, and suggesting the SZ may be narrowest for this condition. However, the deviation from a simple shear geometry results in a slightly wider SZ than in C.

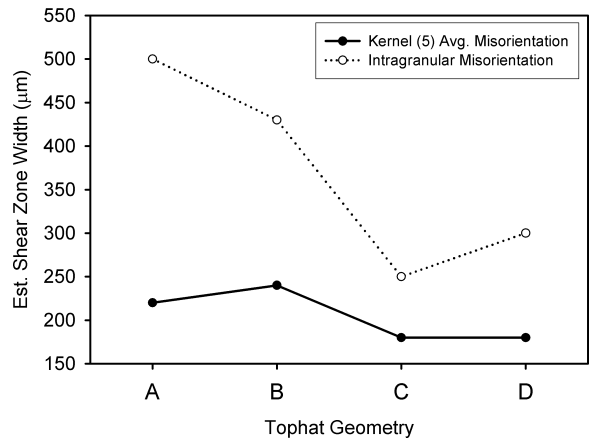


Fig. 22.6 Graph of SZ width as a function of tophat geometry for estimates from KAM and IMD mapping

Three conclusions can be drawn from these results: (1) shear localization is favored by the geometry that is closest to producing a solely simple shear loading state; (2) even slight variations away from this geometry result in measurable differences in both the bulk mechanical response (see Fig. 22.2) and SZ width; and (3) EBSD can provide a sensitive measure of the resulting SZ geometries.

22.2.2 Constrained Shear in Pure Fe—Texture Development

Deformation texture development was also examined in the Fe tophat samples as a function of specimen geometry and resultant localization behavior. For each EBSD data set, the central SZ was cropped based on KAM width measurements, so as to eliminate regions that may have experienced only modest shear strains. Within this heavily strained region, orientations with confidence indices (CIs) < 0.05 were not considered, although this led to a reduction of no more than 10% of orientations within the cropped region. No further cleanup procedures were applied. Orientation data were rotated so as to align the shear direction (SD) (estimated from the SZ alignment) with the horizontal axis.

Shear texture evolution in bcc metals has received significantly less attention than for fcc metals. Shear textures can be defined by {hkl}<uvw> associated with the {SP} <SD> sample reference frame. The primary bcc fibers are {110}//SP and <111>//SD. Since these fibers follow from the active slip plane and direction, this represents a transform of the fcc case. However, the conversion is not exact, since the {112}, and perhaps {123} and other planes, may be active in bcc's. The description of bcc shear texture components was originated by Montheillet et al. (1984), extended by Baczynski and Jonas (1996), and applied by Li et al. (2005, 2006). The four principal component types are defined as D $(11\bar{2})[111]$ and $(\bar{1}\bar{1}2)[111]$, E $(01\bar{1})[111]$ and $(0\bar{1}1)[111]$, F $(110)[001]$, and J $(0\bar{1}1)[\bar{2}11]$ and $(1\bar{1}0)[\bar{1}\bar{1}2]$. For simple shear, one orientation of each component may be dominant depending on the sign of the shear.

110 and 111 pole figures (PFs) recalculated from the orientation distribution function (ODF) are shown in Fig. 22.7. The conventional reference frame for shear deformation is to align the shear direction (SD) horizontally and the shear plane-normal (SPN) vertically. Since the tophat samples were prepared to provide a diametral metallographic section, the shear plane was assumed to be normal to the sectioned surface so that the SPN lies in the section plane. The PFs qualitatively appeared to contain features expected for bcc shear textures, but did not represent ideal shear textures.

The ODF was used to facilitate comparisons between textures for each geometry. To simplify the determination of predominant crystallographic orientations, the sample reference frame was rotated so that the SD was oriented parallel to the vertical axis and the SPN in the normal direction. The resultant $\phi_2 = 45^\circ$ sections (Bunge notation) of the ODF are shown in Fig. 22.8. No sample symmetry was assumed because of the simple shear deformation gradient, therefore ϕ_1

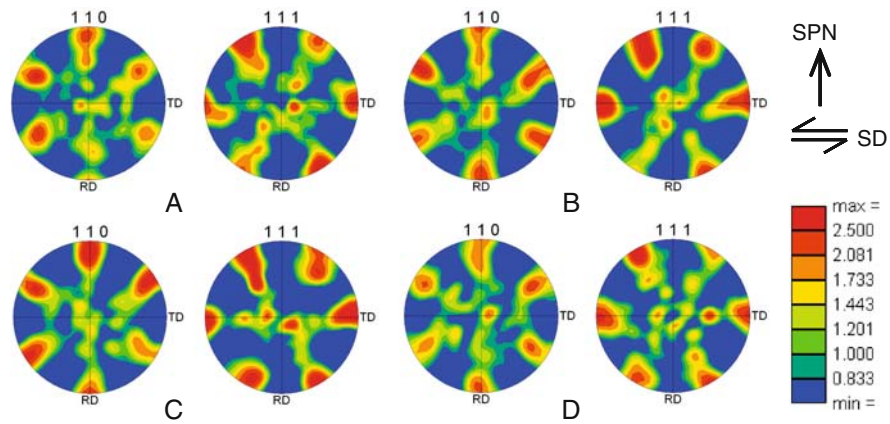


Fig. 22.7 Pole figures from the SZs in the Fe tophat specimens tested in the A, B, C, and D geometries. The sample reference frame in terms of the shear plane normal (SPN) and shear direction (SD) is oriented as shown

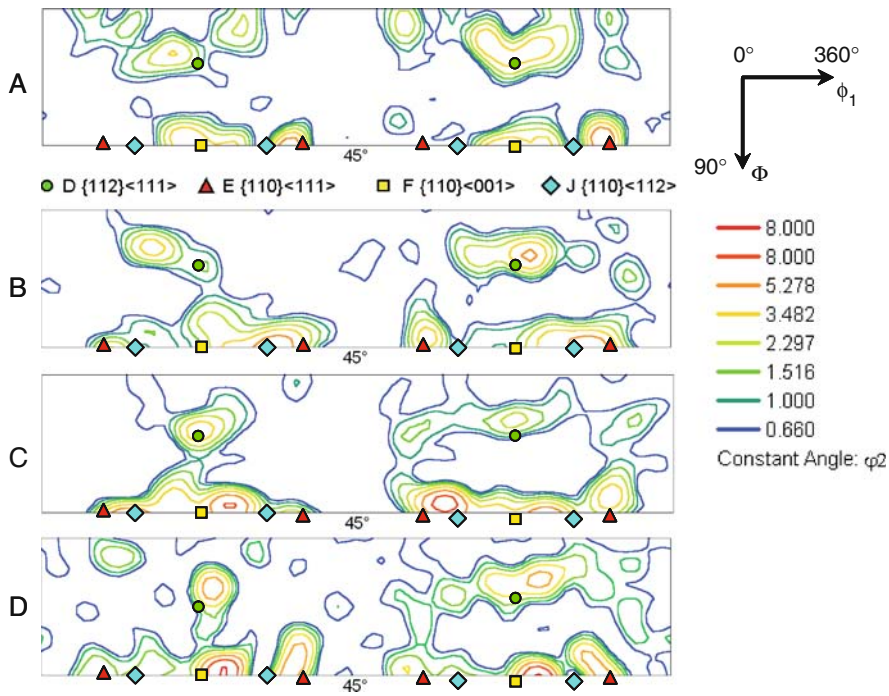


Fig. 22.8 $\phi 2 = 45^\circ$ ODF sections from the SZs in the Fe tophat specimens tested in geometries A, B, C, and D. The SPN and SD were reoriented to the ND and RD, respectively, to facilitate texture component identification

was extended to 360°. The $\phi_2 = 45^\circ$ section shows components of the $\{110\}$ fiber at $\Phi = 90^\circ$, along with the D components. Ideal component locations are shown for each section. Although local strains were very large, the texture strengths were moderate in all cases with a texture index of approximately 2.5. This is characteristic of shear textures, and is due to the continuous rigid rotation accompanying deformation, resulting in continuous lattice rotation with increasing strain.

Although none of the textures represent an ideal shear response, it is apparent that the evolved deformation texture was predominantly due to shear strain. The E, F, and J $\{110\}$ components also become more developed as the geometry approaches C. In addition, the D component is most closely aligned with the ideal location for the C geometry. Therefore, as the sample geometry approaches that of the ideal simple shear, the texture evolution reflects this trend in the strain path. Divergence from the ideal shear texture development is probably due to the nonuniformity of the shear strain field compared to homogeneous strain gradients developed in ideal torsion tests, along with deviations from simple shear strain conditions due to geometry effects, and the relatively small volume of material analyzed.

22.2.3 *Effect of Morphology on Grain Instability in Cu*

The effect of morphological texture on material instability was examined on high-purity copper using the tophat constrained shear experiment detailed in the previous section.

Prior to shear testing, an elongated grain structure was produced by upset-forging an OFE copper plate to a true strain of -1.8. The resulting texture was a strong <110> parallel to the compression axis. Tophat samples were sectioned in two orientations, such that the shear direction was normal to the grain long axis (TT) and parallel with the long axis (IP), as depicted schematically in Fig. 22.9. This corresponded to par-

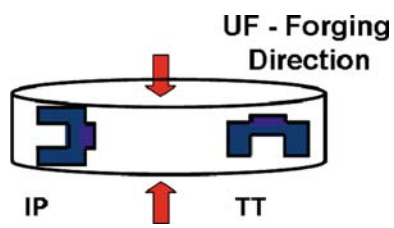


Fig. 22.9 Schematic of sample reference frame in upset-forged blank for TT and IP Cu tophat samples

allel with the upset-forge compression axis (CA) and normal to the CA, respectively. Figure 22.10 shows EBSD CD maps of the SZ that illustrate the difference in shear localization behavior between the two conditions under quasi-static bulk strain rates. The SZ appears to be much narrower in the IP sample, indicating a greater tendency for shear instability. For the TT case, the SZ is visually distinguishable from the matrix because of the perpendicular elongated grains serving as strain markers. However, the SZ is difficult to isolate in the CD map for the IP sample, since the shear direction is parallel to the long axis of the matrix grains.

Therefore, IMD maps were prepared similarly to the Fe tophat analysis, as shown in Fig. 22.11. However, the results are not as useful when applied to the Cu

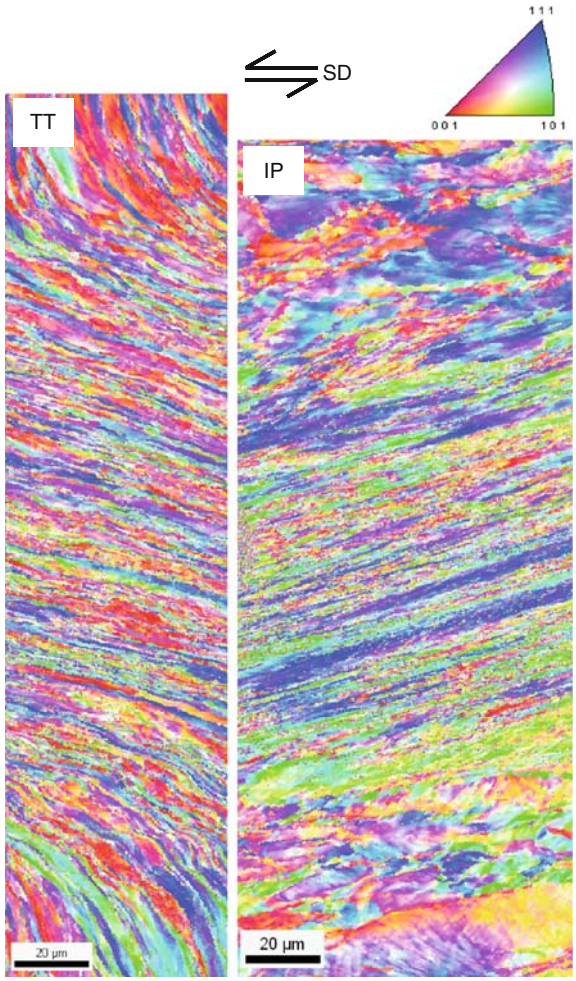


Fig. 22.10 EBSD CD maps of SZs from TT and IP Cu tophat samples

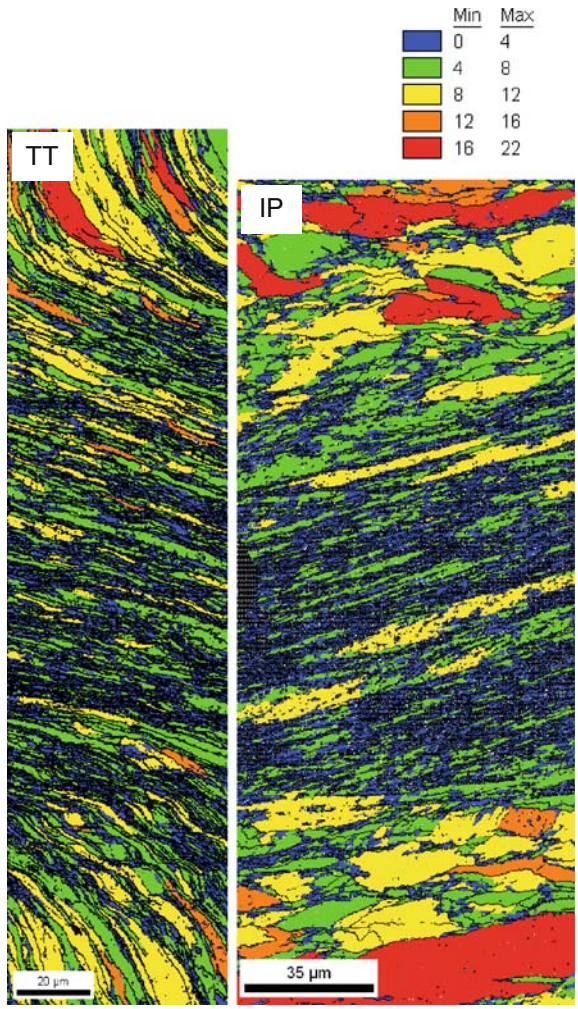


Fig. 22.11 EBSD IMD maps of SZs from TT and IP Cu tophat samples, from equivalent region as in Fig. 22.10. Scale in degrees of misorientation

tophats. In this case, the grains in the center of the SZ, those anticipated to be most heavily deformed, show the lowest IMD values. The inapplicability of this technique is due to the prestrained condition of the matrix. Being larger than the sheared grains, the greater IMD values in the matrix grains are a measure of the greater orientation spread, due solely to the size effect. Additional deformation of the matrix does not increase the spread, but merely refines the grain size so that the spread is measured over a smaller region.

KAM maps proved to be more insightful in delineating the SZ. Figure 22.12 shows KAM maps for the two regions considered previously, along with a second IP

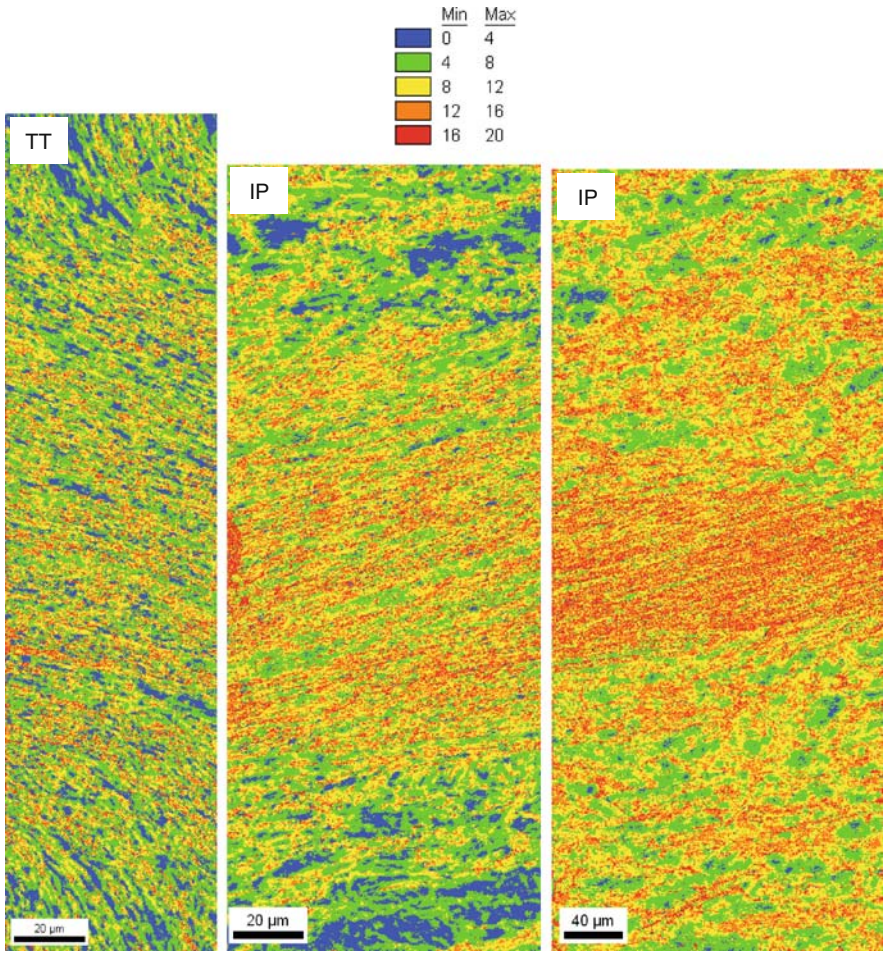


Fig. 22.12 EBSD KAM maps of SZs from TT and IP Cu tophat samples. IP region on right from different region than in Figs. 22.10 and 22.11. 3-neighbor kernel with 20° maximum misorientation, scale in degrees of misorientation

region on the right. For these maps, a 3-neighbor criterion was applied to the 250 nm step size scan data, with a maximum misorientation of 20°. The SZ width in the TT sample runs nearly the length of the IMD map, as indicated in the CD map in Fig. 22.10. For the IP sample, the SZ width is delineated by the increased kernel misorientation band. The second IP region is especially well defined. The resulting SZ width estimates are 210 μm for the TT sample and 120 μm for the IP orientation, a very significant difference in relative localization resistance.

Two candidates for the discrepancy in shear behavior as a function of shear orientation are initial texture and grain morphology. However, the initial texture would, if anything, favor enhanced localization in the TT sample, since the <110> slip direction is sharply aligned with the SD in this case. Therefore, it appears that the increased boundary area along the shear direction in the IP sample tends to enhance localization processes. This could be due to grain boundary sliding or other boundary-dominated strain accommodation mechanisms. In contrast, shearing across orthogonal boundaries in the TT condition results in a more diffuse shear region. The effect of grain morphology appears to be significant in the development of instabilities in copper.

22.3 Shock Loading Damage in Tantalum

Relationships between shock damage and microstructure have been experimentally examined by Meyers and Aimone (1983), Zurek et al. (1990), and Minich et al. (2004), among others. Precipitates, inclusions,

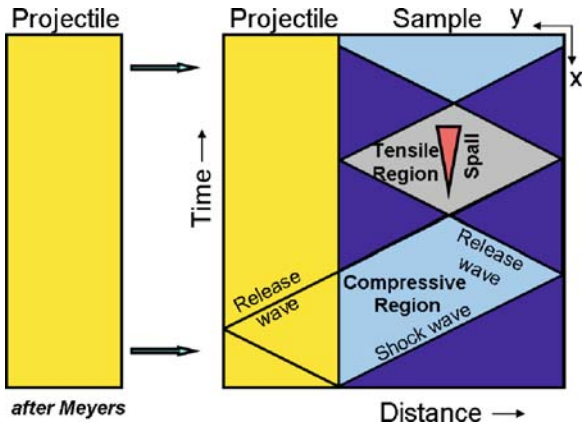


Fig. 22.13 Schematic of plate-on-plate shock loading in distance-time regime

and the grain boundary network represent regions of preferred damage initiation due to lower threshold energies for void nucleation. Larger grain sizes, culminating in single crystals, generally exhibit greater spall strengths. Postmortem characterization of incipiently spalled samples reveal intergranular void networks of different character, depending on the shock pressure; but the evolution of damage and details of the relationship between the microstructure and damage network remain unresolved.

In this study, samples sectioned from a tantalum plate were shock loaded using a plate-on-plate geometry, as shown schematically in Fig. 22.13. In this configuration, the intersection of the two tensile release, or rarefaction, waves results in a state of hydrostatic tensile stress. In ductile materials, this tensile state can result in damage development in the form of cavitation voids and subsequent plastic interaction between the voids. For the geometries used in these experiments, the impacting flyer plate was one-half the thickness of the target, resulting in a spall plane at the mid-thickness of the target. Following soft capture, in which the incipiently spalled sample is decelerated in a controlled manner so as to minimize any post-shock deformation, the recovered samples were sectioned normal to the shock direction in order to characterize the damage structure.

22.3.1 Effect of Shock Duration on Incipient Spall Structure

Spall parameters such as peak pressure and duration, along with microstructure, affect damage evolution in shocked materials. A comparison of two equivalently shocked samples, differing only by shock duration, was undertaken in order to study ductile damage evolution in shocked tantalum. These samples are referred to as short-duration (SD) and long-duration (LD). Table 22.2 provides the parameters for the two shock experiments.

Samples were serially sectioned along the thickness direction so as to reveal the incipient spall damage structure. Approximately 90 sections of 4 μm depth per section were captured via optical microscopy. In addition, for one of every five sections EBSD scans were performed over selected regions. Details of the void and damage distribution for the SD sample have been previously reported (Bingert et al. 2007). The following comparison between the LD and SD samples shows the significant effect of shock duration on damage.

Deformation regions were tracked by using IMD and KAM maps for each EBSD section, and the multiple sections were reconstructed to provide information on the damage structure in three dimensions. Figure 22.14 shows the connectivity of localized deformation between cavitation voids for the SD sample in a single two-dimensional section, using KAM (Fig. 22.14a) and IMD (Fig. 22.14b) maps. Both maps provide evidence of communication of local stresses between voids at short pulse duration. The deformation field does not appear uniformly around each void, but rather links specific voids in alignment. A three-dimensional view of the deformation field can be obtained through

Table 22.2 Experimental details for tantalum flyer plate

Sample ID	Flyer thk. (mm)	Target thk. (mm)	Impact velocity (m/s)	Peak pressure (GPa)	Pulse duration (ms)
Short Duration (SD)	2.08	4.06	199	5.6	1.1
Long Duration (LD)	4.04	8.00	200	5.6	2.2

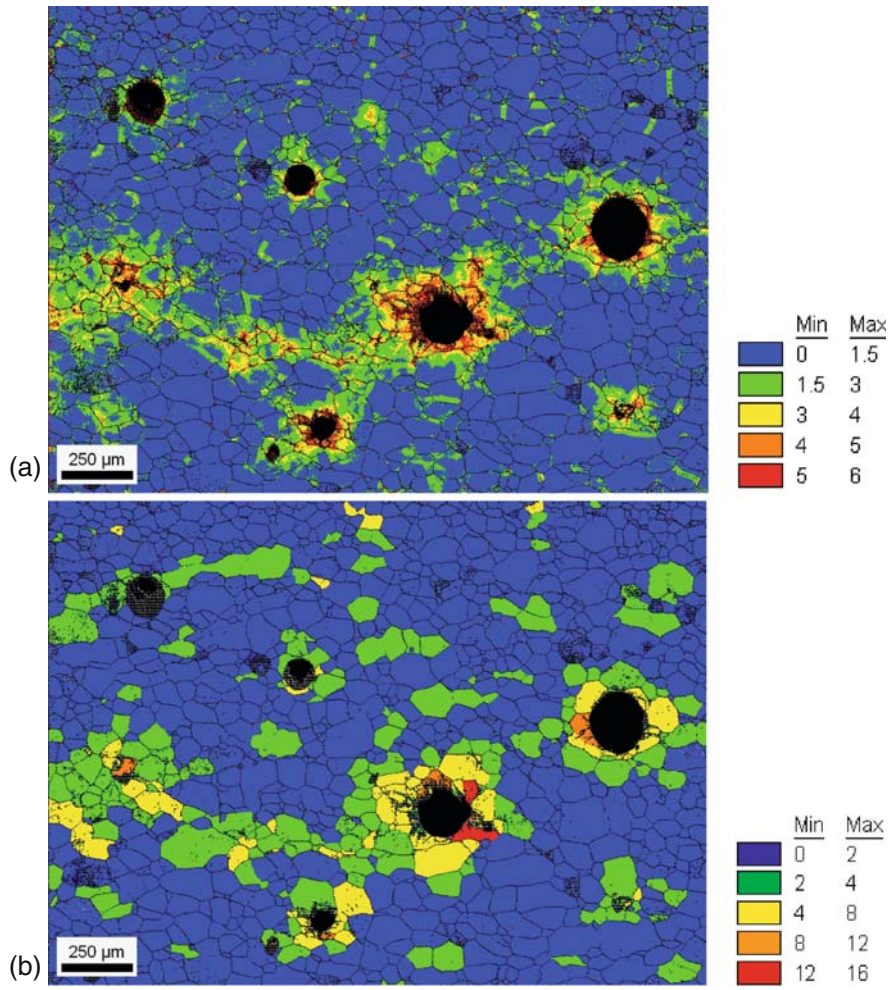


Fig. 22.14 EBSD maps illustrating strain localization in SD Ta incipiently spalled sample: (**a**) KAM map (5-neighbor with 6° maximum), and (**b**) IMD map. High-angle boundaries denoted

stacking of either of the misorientation maps. A reconstruction of the IMD maps for the SD sample is shown in Fig. 22.15, with a threshold value of 4° IMD, which is representative of significant deformation. Regions of similar color in this map represent contiguous grains. Comparing the 3D and 2D maps, the grains above the threshold are much more contiguous in 3D than is suggested in 2D. The formation of a continuous planar damage surface is revealed. The results show that although the damage appeared by optical microscopy to consist of isolated cavitation voids, EBSD analysis revealed precursor localization networks between cavitation voids.

The LD sample was characterized in a similar manner. Figure 22.16 displays the LD KAM and IMD maps that reveal increased degrees of intervoid linkage accompanying increased void density. Complex strain localization networks are visible through the sections, indicative of mixed-mode damage and the generation of a void sheeting mechanism. The resultant 3D stack of 4° threshold IMD maps is shown in Fig. 22.17. The deformation network for the LD samples is contiguous across the entire region, revealing the substantial effect of pulse duration on the development of incipient spall damage. Longer durations result in the nucleation of additional voids, the growth of existing voids, and the progression of strain localization between voids. The damage network at shorter durations appears to be a precursor state, with an already developing damage surface, that further evolves to a well-defined plane at longer durations. This would eventually evolve into a complete spall fracture at longer durations and/or greater pressure.

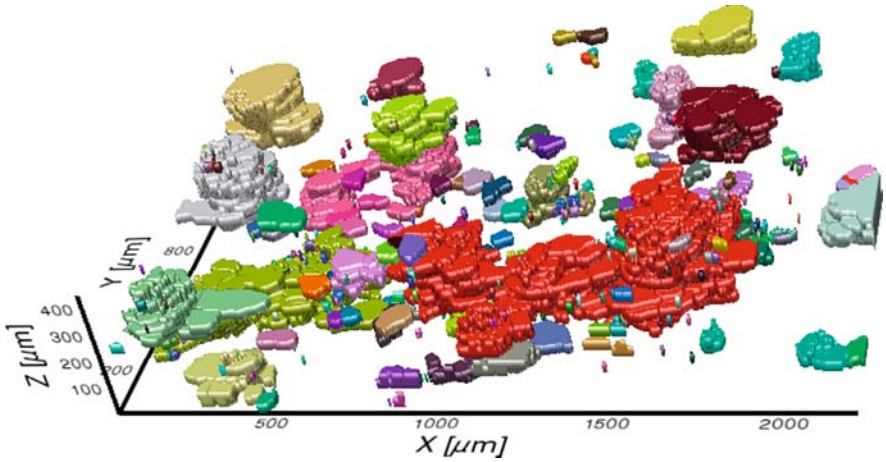


Fig. 22.15 Three-dimensional reconstruction of 4° threshold IMD for SD Ta incipiently spalled sample. Grains of like color are contiguous

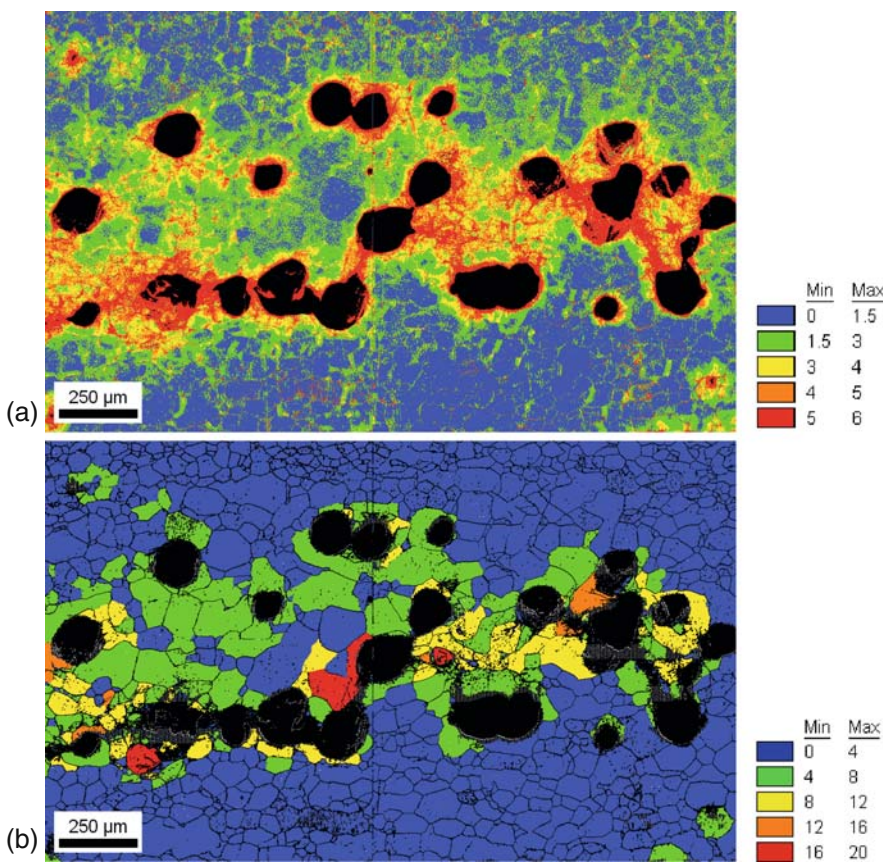


Fig. 22.16 EBSD maps illustrating strain localization in LD Ta incipiently spalled sample: (**a**) KAM map (5-neighbor with 6° maximum), and (**b**) IMD map. High-angle boundaries denoted in IMD map

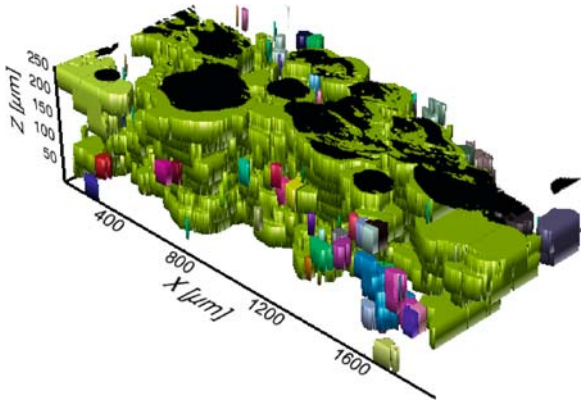


Fig. 22.17 Three-dimensional reconstruction of 4° threshold IMD for LD Ta incipiently spalled sample. Grains of like color are contiguous

22.3.2 Effect of Pressure on Incipient Spall Structure

A tantalum sample of the same pedigree as used in the flyer-plate experiment was shock loaded using a direct high-explosive drive. This resulted in a peak pressure of approximately 30.6 GPa, over five times the 5.6 GPa pressure experienced by the plate-on-plate samples. As opposed to the solely intergranular void initiation from the SD and LD samples, evidence of intragranular initiation can be observed in this sample. Figure 22.18 shows a CD map and accompanying KAM map of a grain containing several voids. In the CD map, several of the fine linear features were crystallographically identified as $\{112\} < 111 >$ bcc deformation twins. The arrows identify two intragranular voids that appear to have initiated at twin variant intersections. These intersections would be expected to be regions of high local stress intensity and to produce high compatibility stresses.

The KAM map also reveals an apparent linkage region between several voids, in this case an intragranular network. In addition, the map reflects the local strain network developed from the deformation twin field. Therefore, at higher pressures the damage threshold for intragranular void formation is surpassed. This is possibly achieved through the activation and interaction of deformation twins.

22.4 Conclusions

The foregoing descriptions provided examples of how EBSD was applied to investigations of shear localization and shock damage in materials. The conditions associated with these deformed structures represent heavily strained and/or high defect-density microstructures. Current EBSD systems allow the interrogation of statistically relevant regions of material that were formerly inaccessible to high-throughput analysis. EBSD was critical not only for its spatial specificity of orientation, but also to delineate specific regions within microstructures for analysis. To summarize these investigations:

- EBSD analysis resolved subtle differences in shear zone microstructure and texture in pure iron, resulting from the very sensitive relationship between tophat geometry and mechanical response.
- Grain morphology was shown to be an important variable in shear band development in copper. EBSD was used to identify and quantify the deformation regions.
- Three-dimensional reconstruction of incipiently spalled regions in a shocked tantalum plate revealed the effect of pulse duration on the damage evolution. EBSD was instrumental in mapping the precursor strain localization network between cavitation voids in the short duration sample.
- At very high shock pressures, intragranular damage was found in the tantalum associated with deformation twin variant intersections.

Acknowledgments Los Alamos National Laboratory (LANL) is operated by Los Alamos National Security, LLC, for the National Nuclear Security Administration of the U.S. Department of Energy under contract DE-AC52-06NA25396. The authors wish to thank Carl Trujillo, Anna Breiner, Mike Lopez, and Anna Zurek of LANL, Ben Henrie of Stanley Associates, and Daniel Worthington of the University of Texas at Austin for their contributions with experimental and characterization aspects of this work. Paulo Rigg, Cynthia Schwartz, Robert Hixson, Alexander Saunders, Frank Merrill, Chris Morris, Kris Kwiatkowski, and the LANSCE Proton Radiography team at LANL are acknowledged for providing the HE-drive tantalum sample. Partial support was provided by the Joint DoD/DOE Munitions Technology Development Program.

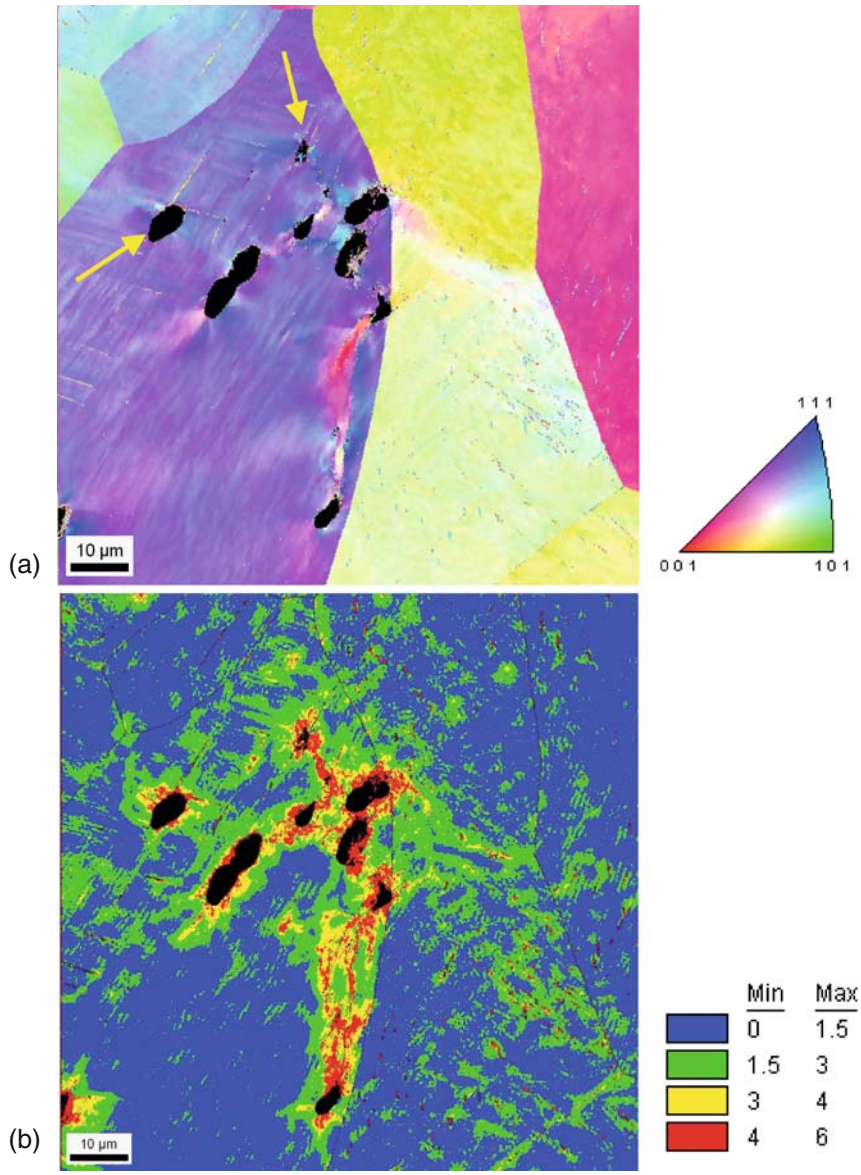


Fig. 22.18 EBSD maps from HE-driven Ta incipiently spalled sample: (**a**) CD map with arrows pointing to voids at twin intersections, and (**b**) KAM map (5-neighbor with 6° maximum), scale in degrees of misorientation

References

Asaro RJ, Rice JR (1977) Strain localization in ductile single crystals. J Mech Phys Solid 25:309–338

Baczynski J, Jonas JJ (1996) Texture development during the torsion testing of alpha-iron and two IF steels. Acta Mater 44:4273–4288

Becker R (2004) Effects of crystal plasticity on materials loaded at high pressures and strain rates. Int J Plasticity 20:1983–2006

Bingert JF, Henrie BL, Worthington DL (2007) Three-dimensional characterization of incipiently spalled tantalum. Metall Mater Trans A 38:1712–1721

Bronkhorst C, Cerreta E, Xue Q, Maudlin PJ, Mason TA, Gray III GT (2006) An experimental and numerical study of the localization behavior of tantalum and stainless steel. Int J Plasticity 22:1304–1335

Bronkhorst CA, Hansen BL, Cerreta EK, Bingert JF (2007) Modeling the microstructural evolution of metallic polycrystalline materials under localization conditions. J Mech Phys Solid 55:2351–2383

Case S, Horie Y (2007) Discrete element simulation of shock wave propagation in polycrystalline copper. J Mech Phys Solid 55:589–614

Clifton RJ, Duffy J, Hartley KA, Shawki TG (1984) On critical conditions for shear band formation at high-strain rates. Scripta Metall 18:443–448

Dougherty LM, Cerreta EK, Pfeif EA, Trujillo CP, Gray GT III (2007) The impact of peak shock stress on the microstructure and shear behavior of 1028 steel. Acta Mater 55:6356–6364

Grady DE (1982) Local inertial effects in dynamic fragmentation. J Appl Phys 53:322–325

Gray GT, Hayes DB, Hixson RS (2000) Influence of the shock-induced alpha-epsilon transition in Fe on its post-shock substructure evolution and mechanical behavior. J Phys-Paris 10:755–760

Hopkinson B (1914) Method for measuring the pressure produced in the detonation of high explosives or by the impact of bullets. T R Soc-Lond 213A:437–456

Johnson JN (1981) Dynamic fracture and spallation in ductile solids. J Appl Phys 52:2812–2825

Li S, Beyerline IJ, Bourke MAM (2005) Texture formation during equal channel angular extrusion of fcc and bcc materials: comparison with simple shear. Mater Sci Eng A 394:66–77

Li S, Gazder AA, Beyerlein IJ, Pereloma EV, Davies CHJ (2006) Effect of processing route on microstructure and texture development in equal channel angular extrusion of interstitial-free steel. Acta Mater 54:1087–1100

Meyer LW, Manwaring S (1986) Critical adiabatic shear strength of low alloyed steel under compressive loading In: Murr LE, Staudhammer KP, Meyers M (eds) Metallurgical applications of shock wave and high strain rate phenomena. Marcel Dekker, New York, p 657

Meyers MA, Aimone CT (1983) Dynamic fracture (spalling) of metals. Prog Mater Sci 28:1–96

Meyers MA (1994) Dynamic behavior of materials. Wiley Interscience, New York

Meyers MA, Xu YB, Xue Q, Perez-Prado MT, McNelley TR (2003) Microstructural evolution in adiabatic shear localization in stainless steel. Acta Mater 51:1307–1325

Minich RW, Cazamius JU, Kumar M, Schwartz AJ (2004) Effect of microstructural length scales on spall behavior of copper. Metall Mater Trans A 35:2663–2673

Montheillet F, Cohen M, Jonas JJ (1984) Axial stresses and texture development during the torsion testing of Al, Cu and α-Fe. Acta Metall 32:2077–2089

Nemat-Nasser S, Li Y-F, Isaacs JB (1994) Experimental/computational evaluation of flow stress at high strain rates with application to adiabatic shear banding. Mech Mater 17:111–134

Radovitzky R, Cuitino A (2003) Direct numerical simulation of polycrystals. In: Collection of technical papers—Structures, structural dynamics and materials conference, vol. 3, April 7–10, Norfolk, VA, pp 1920–1928

Rittel, D, Wang ZG, Merzer M (2006) Adiabatic shear failure and dynamic stored energy of cold work. Phys Rev Lett 96: 1–4

Semiatin SL, Staker MA, Jonas JJ (1984) Plastic instability and flow localization in shear at high rates of deformation. Acta Metall 32:1347–1354

Xue Q, Meyers M, Nesterenko VF (2002) Self-organization of shear bands in titanium and Ti-6Al-4 V alloy. Acta Mater 50:575–596

Xue Q, Gray GT (2006a) Development of adiabatic shear bands in annealed 316L stainless steel: Part I. Correlation between evolving microstructure and mechanical behavior. Metall Mater Trans A 37:2435–2446

Xue Q, Gray GT (2006b) Development of adiabatic shear bands in annealed 316L stainless steel: Part II. TEM studies of the evolution of microstructure during deformation localization. Metall Mater Trans A 37:2447–2458

Xue Q, Bingert JF, Henrie BL, Gray GT III (2008) EBSD characterization of dynamic shear band regions in pre-shocked and as-received 304 stainless steels. Mater Sci Eng A 473: 279–289

Zurek AK, Follansbee PS, Hack J (1990) High strain-rate-induced cleavage fracture in mild carbon steel. Metall Mater Trans A 21:431–439

Chapter 23

Texture Separation for α/β Titanium Alloys

Ayman A. Salem

23.1 Introduction

Over the past few decades, titanium and titanium alloys have been utilized in numerous applications due to their low density, high strength, and excellent corrosion resistance. With the highest strength to density ratio and a high melting temperature (1670°C), titanium alloys are always selected over other competing metallic materials, such as high strength aluminum alloys, for many high temperature aerospace applications (e.g., turbine engines).

Pure titanium has a body-centered cubic (bcc) crystal structure (β-phase) above 882°C (β- transus at which alpha + beta → alpha) and a hexagonal close-packed (hcp) crystal structure (α-phase) below the β-transus. The exact temperature for the allotropic transformation in titanium alloys is strongly dependent on the alloying elements. The α-phase has highly anisotropic properties due to its hcp crystal structure with a less-than-ideal c/a ratio (1.587). The anisotropy is mostly pronounced in the flow stress, strain hardening, and texture evolution during room temperature plastic deformation.

Titanium alloys are categorized in three major types based on the stable phase at room temperature, namely, α alloys, α/β alloys, and β alloys. The volume fraction of the stable phase at room temperature is controlled by alloying elements. While α-alloys are rich in α-stabilizers (e.g., Al, O, N, and C), β-alloys are rich in β-stabilizers (e.g., V, Mo, Nb, Cr, Fe, and Si). Adding α-stabilizers and β-stabilizers to titanium results in various α/β alloys with unique properties.

One of the most common α/β titanium alloys is Ti-6Al-4V, accounting for more than 80% of the total US market usage (Eylon and Seagle 2001). Compared to pure titanium, Ti-6Al-4V has higher strength, higher fatigue resistance, and higher corrosion resistance, which makes it the workhorse for many aerospace applications (airframes and turbine engines).

23.2 Microstructure of α/β Titanium Alloys

Microstructure and texture have significant effects on the mechanical behavior of α/β titanium alloys. Adjusting various thermomechanical processing (TMP) parameters can drastically alter the final microstructure and texture. Microstructures of α/β titanium alloys can be categorized into three major types: fully lamellar, fully equiaxed, and duplex (bimodal) (Fig. 23.1). The cooling rate during the allotropic transformation from the bcc β-phase to the hcp α-phase is the most important parameter controlling the final microstructure. Continuous slow cooling from the β field (above β transus) to the α/β phase field nucleates α-phase at β-grain boundaries, which eventually grow as parallel lamellae with the same crystal orientation. Each adjacent group of α-lamellae with the same orientation makes a colony. Each colony continues to grow within the same β grain until it meets other colonies nucleated at other grain boundaries. Within each colony, individual α lamellae are separated by retained β matrix, resulting

A.A. Salem (✉)
Wright Patterson Air Force Base, 2210 Tenth St. Building 655 Room 053, WPAFB, OH 45433, USA
e-mail: ayman.salem@wpafb.af.mil

A.J. Schwartz et al. (eds.), *Electron Backscatter Diffraction in Materials Science*,
DOI 10.1007/978-0-387-88136-2_23, © Springer Science+Business Media, LLC 2009

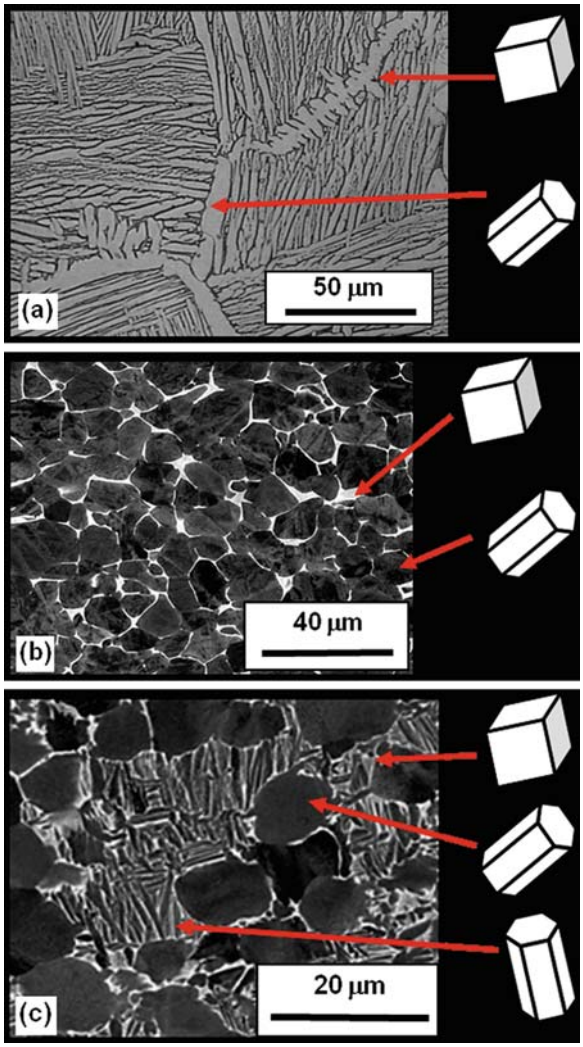


Fig. 23.1 (**a**) Optical micrograph of fully lamellar microstructure in Ti-6Al-4V: α-phase (*gray lamellae*), β-phase (*black lines*) (Semiatin and Bieler 2001); (**b**) backscatter electron image of fully equiaxed microstructure in Ti-6Al-4V: β-phase (*white areas*), α-phase (*gray particles*); (**c**) backscatter electron image of bimodal (duplex) microstructure in Ti-6Al-4V: primary α (*gray particles*), secondary α (*gray lamellae*) (Salem et al. 2008)

in a fully lamellar microstructure (Fig. 23.1a). Such a microstructure can also be obtained in a final step after various processing routes by heating the material to the β-phase field followed by slow cooling, in a process called β anneal. The main features that describe lamellar microstructure are the size of the α lamellae, the size of the α colonies, and the thickness of the α layers at the β grain boundaries. Those parameters are controlled by the cooling rate changing the microstructure from a colony type to a martensitic type: the former with thick α lamellae and large colonies resulting from a slow cooling rate such as furnace cooling; the latter with very fine α plates resulting from a fast cooling rate such as water quenching.

High-temperature large deformation of material with lamellar microstructure just below the β transus in the α/β phase field breaks down the α lamellae into small segments. Subsequent heat treatment in the α/β phase field (recrystalization below β transus) results in spherodization of the broken α lamellae into equiaxed α particles (so called primary alpha α_p). The volume fraction of α_p particles is controlled by the recrystalization temperature (Semiatin et al. 2003). At this stage, the material is to be cooled down by either slow cooling rates (such as furnace cooling), or by intermediate cooling rates (such as air cooling). In the first route, slow cooling promotes the growth of spherodized α_p particles into larger equiaxed α-particles, with a reduction in the β volume fraction until thin layers of β are retained at room temperature, separating α particles in a microstructure known as fully equiaxed (Fig. 23.1b). In the second route, an intermediate cooling rate minimizes the growth of α_p particles while enabling the transformation of the β phase into new short α lamellae in a matrix of retained β. The new α lamellae surrounded by retained β is identified as secondary alpha (α_s). The final microstructure at room temperature consists of equiaxed particles of primary alpha (α_p) and transformed lamellae of secondary alpha (α_s) in a matrix of beta (β) phase. Such a microstructure is called a bimodal or duplex microstructure (Fig. 23.1c). The volume fraction of α_s is a function of deformation temperature in the α/β phase field.

The unique features of the duplex microstructure in α/β titanium alloys result in higher yield strength, higher ductility, higher fatigue-crack-initiation resistance, and slower fatigue-crack-propagation rates than with a lamellar microstructure. As a result, duplex microstructure is the choice for many demanding applications such as fan blades, compressor blades, and disks in turbine engines (Lutjering and Williams 2003).

23.3 Texture of Ti-6Al-4V

In addition to microstructure, texture has a strong effect on the mechanical behavior of α/β titanium alloys. For example, high temperature simple

compression testing of Ti-6Al-4V reveals strong anisotropy in the peak flow stress, flow softening, and ovality of the originally right-circular-cylinder test samples (Semiatin and Bieler 2001). Such a pronounced anisotropy is related to the α-phase texture more than the β-phase texture. Individual crystals of the α-phase have an hcp crystal structure, which is known for a highly anisotropic mechanical behavior. Consequently, textured polycrystal titanium alloys inherit such an anisotropic behavior. Texture can be controlled by deformation temperature and processing routes. For example, unidirectional hot-rolling in the α/β phase field of Ti-6Al-4V with a duplex microstructure results in two major types of texture: the so-called basal/transverse (B/T), and the transverse (T). The former develops at *low* temperature deformation (e.g., 815°C) with high volume fraction of α phase accommodating plastic deformation. The latter develops during *high* temperature deformation (close to the β transus, e.g., 955°C) with high volume fraction of β phase accommodating plastic strain. Representing texture by $(0001)_\alpha$ pole figures, the B/T-type texture has the α phase basal poles located close to the plate-normal and transverse directions (ND and TD, respectively), while the T-type texture has the basal poles aligned with the transverse direction (TD) (Fig. 23.2). The strength of each texture component is controlled by the deformation temperature (Lutjering 1998).

A clear understanding of texture effects on the mechanical behavior of α/β titanium with duplex microstructure cannot be achieved by focusing only on the overall texture of the α phase. Separating the contributions from the α_p particles and the α_s lamella is crucial. As mentioned before, α_p texture evolves primarily during deformation in the two-phase (α/β) field, while that of the α_s results from the decomposition of the hot-worked β-matrix during cooling. Consequently, the textures of α_p and α_s are expected to evolve differently based on the TMP parameters used, and hence to affect the overall mechanical behavior of the material differently.

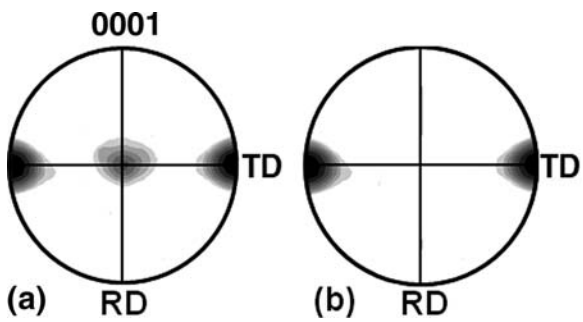


Fig. 23.2 Schematic of crystallographic texture formed during unidirectional hot-rolling of Ti-6Al-4V with duplex microstructure: (**a**) basal/transverse texture (B/T), (**b**) transverse texture (T)

23.3.1 Separation of Primary and Secondary Alpha Texture

The identical crystal structure and lattice parameters of α_p and α_s complicate the texture separation process. Consequently, conventional X-ray diffraction (XRD) or EBSD techniques cannot be applied directly to distinguish between them. Therefore, a number of techniques have been developed to determine the individual textures of α_p and α_s by correlating microstructure features to texture data of individual constituents. Generally, the following steps are followed in most separation techniques:

(i) Measure the overall alpha texture (α_p+ α_s) using XRD, neutron diffraction, or EBSD.
(ii) Capture the microstructure by optical microscopy or scanning electron microscopy.
(iii) Separate α_p and α_s in the micrographs.
(iv) Link specific regions for which microstructure and texture have been measured.
(v) Partition the texture data based on the difference in microstructure features of the α_p and α_s.

Brief summaries of the most recent approaches are presented in the next subsections.

23.3.2 EBSD + BSE Imaging Technique

Backscattered electron (BSE) images for α/β titanium alloys are often used to distinguish between areas occupied by α_s laminated with β-layers and areas occupied by α_p particles. At *low* magnifications, α_s lamellae appear lighter than α_p particles (Fig. 23.3). The lighter shade of gray of the α_s lamellae is due to the presence of β layers (enriched in vanadium) surrounding the α_s lamellae, resulting in an average Z number that is higher than that of the α_p

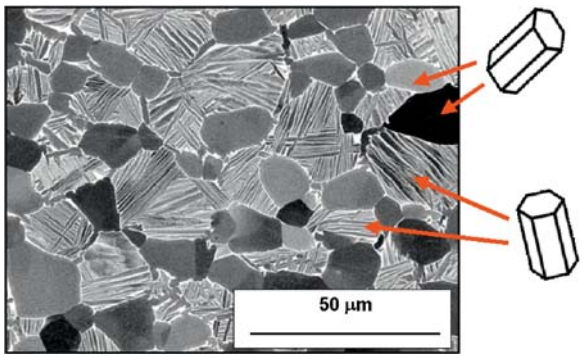


Fig. 23.3 Backscattered electron (BSE) image of Ti-6Al-4V revealing α_p particles as *dark areas* and α_s lamellae as *light gray areas* at low magnification. *White areas* surrounding α_s lamellae are β-phase: primary α (*dark particles*), secondary α (*light lamellae*)

particles. To separate the texture components based on BSE images, local orientations determined by the EBSD technique have to be linked to corresponding positions in the BSE images using special software that matches BSE images to EBSD inverse-pole-figure (IPF) maps by image rotation, resizing, translation, and shearing (Germain et al. 2005). Unfortunately, this technique is not suitable for α/β alloys with thick α_s lamellae (Fig. 23.1c), or for BSE images at *high* magnifications, because of the lower difference in the average Z number of the α_s+β areas and α_p areas.

23.3.3 EBSD or XRD + Heat Treatment Technique

Textures are presented mathematically by orientation distribution functions (ODFs). Consequently, mathematical subtraction and summation of various texture components is possible using ODFs. In the same vein, α_p texture (weighted by its volume fraction in the initial duplex microstructure) can be subtracted from the overall (α_p+α_s) texture to calculate α_s texture (Glavicic et al. 2006). In order to do this, the total alpha texture (α_p + α_s) in the duplex microstructure (Fig. 23.1c) is measured first using either EBSD or XRD techniques. Then, the separate α_p texture is measured after dissolving the α_s by a solution treatment followed by slow furnace cooling. Thus the duplex microstructure transforms into an equiaxed microstructure by enabling the growth of α_p particles, and eliminating the decomposition of the β matrix to α_s (Fig. 23.1b). Note that this technique is based on the assumption that there is no preferential growth of α_p particles and, hence, that the texture of α_p particles does not change during the heat treatment.

23.4 Texture Separation Using EBSD + EDS Technique

Synchronized in situ measurements of local orientations *and* compositions using EBSD and EDS within an SEM can be used to separate α_p and α_s texture. Using commercially-available EBSD data collection software (such as OIM® from EDAX) eliminates the need for additional heat treatments or special post-processing software for texture separation. The local composition variation enables the automated binning of texture readings from the two different microconstituents. Texture is then separated offline using the OIM® data analysis software. This technique is generally applicable to all α/β titanium alloys with duplex microstructure. It is demonstrated in the following subsections on a hot rolled sample of Ti-6Al-4V with a measured composition (in weight pct.) of 6.15 Al, 3.9V, 0.20 O, 0.21 Fe, 0.008 Ni, 0.01 C, 0.0031 H, and the balance Ti.

23.4.1 Procedures for the EBSD/ EDS

A hot rolled Ti-6Al-4V sample is first sectioned, then ground and lightly electropolished at –20 °C in a solution of 590 ml methanol and 60 ml perchloric acid. Following electropolishing, the sample is mounted on the tilting stage inside a field emission gun scanning electron microscope (FEG-SEM). The microscope is operated at 20 kV and 7 nA, with the stage tilted at an inclination of 70°. The EDS detector is fully retracted to avoid overexposure by the large current used to collect the EBSD data. Both EBSD and EDS detectors must be located on the same side of the microscope chamber (facing the surface of the sample), thus ensuring that both measurements are synchronized and collected from the same material point during the scanning

process. Local Kikuchi patterns and chemical composition are collected using EBSD and EDS systems from EDAX with a 0.3-μm step size and a 50 s/frame scan rate.

23.4.2 Microstructure Observations

A secondary electron (SE) image of the hot rolled Ti-6Al-4V sample reveals a duplex microstructure with 60% α_p particles within a matrix of α_s lamellae, wrapped in thin layers of the beta phase (Fig. 23.4a). The α_p particles are relatively equiaxed, while the α_s lamellae are stacked in bundles.

The complicated nature of the microstructure is often revealed by EBSD IPF maps (Fig. 23.4b) for the same area as the SE image. Particularly, each α_s lamella is recognized as a single grain by the OIM® software because of the small misorientations across the α_s lamellae within a given colony (less than 3°). As a result, a single color is assigned to all lamellae in the specific colony with no separating boundaries, which makes the α_s colonies indistinguishable from the neighbor α_p particles in the IPF maps.

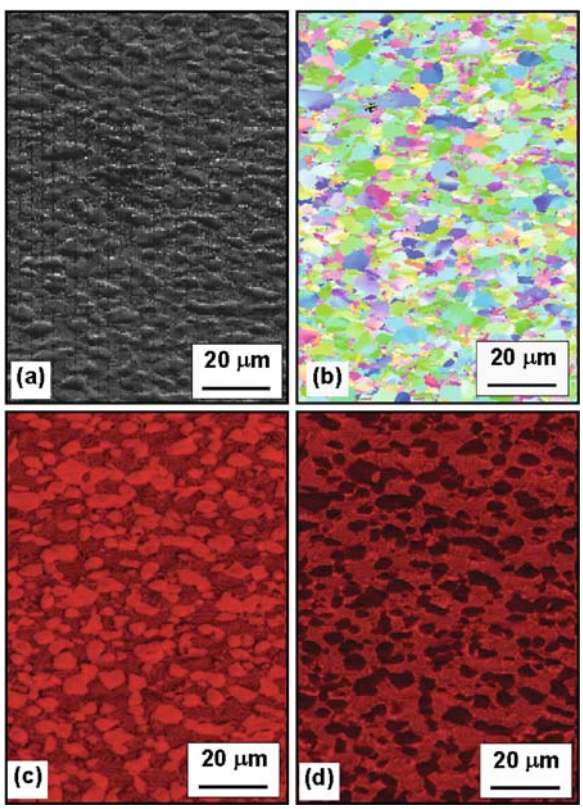


Fig. 23.4 SEM results for an electropolished sample of hot rolled Ti-6Al-4V: (**a**) secondary electron image, (**b**) normal-direction inverse-pole-figure map revealing α_p and α_s regions which are not distinguishable, (**c**) EDS map for Al, and (**d**) EDS map for V. In the EDS maps (**c**, **d**), *dark* or *light* shading is associated with a lower or a higher concentration, respectively, of the particular alloying element (Salem et al. 2008a)

23.4.3 Chemical Composition Maps (EDS)

The partitioning of alloying elements (Al, Fe, and V) makes it possible to use the EDS technique to quantify the Al and V concentration in the microstructure of Ti-6Al-4V samples. In general, a high concentration of an alloying element is assigned a light color, while a lower concentration is represented by a dark color. For example, the EDS map for Al (Fig. 23.4c) shows a measurable variation in concentration between α_p particles and α_s colonies.

A comparison between the aluminum EDS map and the SE image for the same areas confirms that the lighter areas (higher Al concentrations) are associated with the α_p particles, and the darker areas (lower Al concentrations) are associated with the α_s lamellae (Fig. 23.4d). However, better contrast between α_p particles and α_s lamellae is revealed in the EDS map for V (Fig. 23.4d). The darker areas (lower vanadium concentrations) are associated with α_p particles, and the lighter areas are associated with α_s lamellae. Vanadium partitions preferentially to the β phase between the alpha lamellae, while Al partitions preferentially to the α phase. The EDS measurements for the α_s regions are biased to the β layers, which are enriched in V and depleted in Al, thereby giving rise to the observed contrast.

The automatic separation of α_p and α_s is done by linking the concentration histograms to IPF maps (Fig. 23.5). Both the Al concentration and the V concentration histograms (Fig. 23.5a, b) reveal two overlapping Gaussian-like distributions. In the Al histogram, the lower Gaussian distribution is associated with α_s lamellae and the higher one with α_p particles. The opposite is true for the V histogram (the lower one corresponding to α_p particles and the higher one with α_s lamellae). Using the V histogram, the local minimum at which the two Gaussian-like histograms intersect is chosen as the point separating α_p and α_s

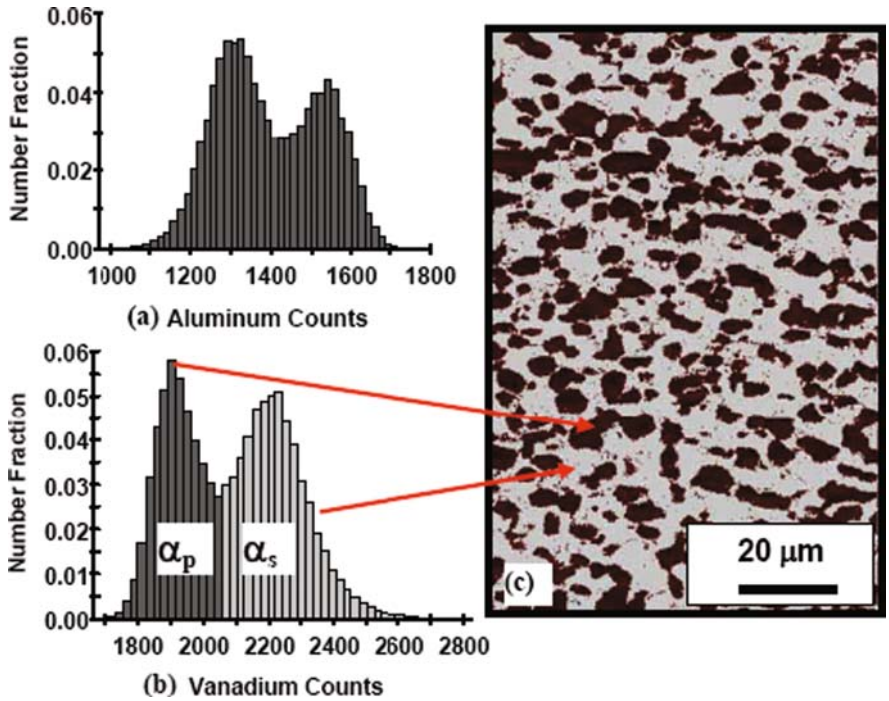


Fig. 23.5 EDS results for hot rolled Ti-6Al-4V: (**a**) Al histogram, (**b**) V histogram with α_s in *light gray*, and (**c**) the corresponding microstructure partitioned based on V content. In (**c**), α_s lamellae are *light gray*

for binning EDS, inverse-pole-figure, pole-figure, and image-quality data. Consequently, any datum with a V concentration lower than that corresponding to the point of intersection is considered to be α_p and the remainder are α_s (Fig. 23.5c).

To validate the technique, manual separation of the EBSD data based on the shape of the α_p particles can be compared to the results with the automatic separation. Such a manual method, although much more tedious, gives results similar to those obtained by partitioning the data automatically using the V concentration. The automatic separation of the EBSD data based on the Al concentration yields similar results to those obtained by partitioning the data using the V concentration. The practical applicability of the technique is illustrated in the following example.

23.5 Industrial Application: Controlling Texture During Hot-Rolling of Ti-6Al-4V

For mill suppliers, choosing the right conditions for hot-rolling of titanium alloys is an important task. The rolling temperature and the interpass reheating schedule play vital roles in controlling final texture, microstructure, properties, and cost. Clear understanding of the evolution of each individual texture component enhances the optimization of the TMP by avoiding unnecessary trial and error. The EBSD/ EDS technique captures the texture of α_p and α_s individually or as a whole. The recorded data can then be incorporated into sophisticated mathematical methods to calculate the texture of the high temperature β phase (Glavicic et al. 2003). Therefore, the EBSD/EDS technique can be a practical tool during the design of TMP processes.

The texture separation technique was applied to interpret texture development during hot-rolling of Ti-6Al-4V (Salem et al. 2008a). To establish the effect of rolling temperature, preforms of Ti-6Al-4V were hot rolled at either 815°C or 955°C to a 3:1 total reduction with a three-minute reheat between passes. The effect of the reheating schedule on texture and microstructure development was revealed by rolling an additional preform in a similar fashion at 955°C, but without interpass reheating. The rolling was performed parallel to the original rolling direction of the as-received plate for half of the samples, and perpendicular to the original rolling direction for the other half. Following industrial practice, all samples were air cooled after rolling.

The rolling temperature controls the variation of the evolved microstructure and texture by controlling the volume fractions of the α and the β phase. The amount of strain accommodated by the β phase varies with the deformation temperature (Semiatin et al. 2002), which results in variation in the transformation texture (α_s texture) decomposed from the hot-worked beta matrix. In the current case, the volume fraction of beta was ~0.2 at 815°C and ~0.7 at 955°C.

23.5.1 Microstructure Evolution

High temperature rolling (955°C with and without reheat) resulted in a duplex microstructure with a mixture of α_p and α_s lamellar colonies (Fig. 23.6). However, the absence of reheat resulted in shorter and highly deformed α_s platelets compared to those developed during rolling with reheat (Fig. 23.6c, d). On the other hand, low temperature rolling (815°C with reheat) yielded a microstructure free from α_s lamellae (Fig. 23.7a, b) with a 0.81 volume fraction of α_p.

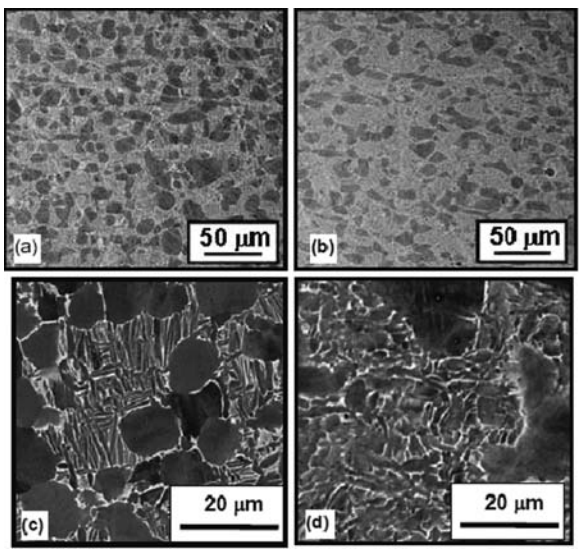


Fig. 23.6 BSE images of the microstructure after hot-rolling of Ti-6Al-4V material: (**a**, **c**) at 955°C + 3 min reheat, (**b**, **d**) at 955°C and no reheat (Salem et al. 2008b)

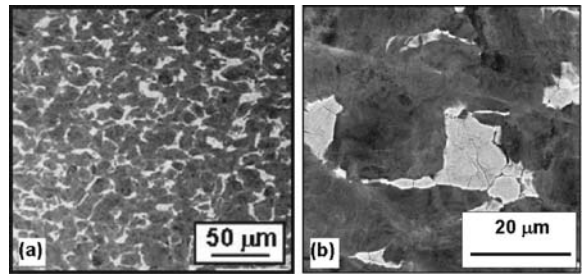


Fig. 23.7 BSE images of the microstructure after hot-rolling of Ti-6Al-4V material at 815°C + 3 min reheat at (**a**) low magnification and (**b**) high magnification (Salem et al. 2008b)

23.5.2 Overall Texture Evolution

Generally, the α phase (α_p+α_s, α_p, or α_s) texture is presented by $(0001)_\alpha$ pole figures while the β phase texture is presented by $(110)_\beta$ pole figures. The overall α phase texture (α_p+α_s) revealed that reducing the rolling temperature increased the intensity of basal poles along the transverse direction (TD), while reducing it along the rolling direction (RD) (Fig. 23.8). A new component with the basal poles tilted from the normal direction (ND) towards the RD (Fig. 23.8b) appeared when rolling at low temperatures (815°C). Rolling at high temperature (955°C) *without* reheating had a similar but weaker effect on the texture components compared to the observations for low temperature rolling (Fig. 23.8c).

The final texture reflects the combined effect of the starting texture and the evolved texture during deformation. Thus understanding the starting texture is crucial to understanding the final texture, and hence the deformation texture. For example, the texture component along the RD in Fig. 23.8 was inherited from the starting material with a strong texture component along the RD. If the starting texture were random, basal poles along the RD would not appear in the final pole figures (Peters and Luetjering 1980).

The combined effect of the strong textured starting material and the evolved texture during deformation was reflected during high temperature rolling (955°C *with* reheats), with a predominate texture component along the TD relative to the one along the RD (Fig. 23.8a). Rolling at 815°C weakened the intensity of the basal poles along the RD, strengthened the ones along the TD, and produced a component with basal poles titled ~20° from the ND (Fig. 23.8c).

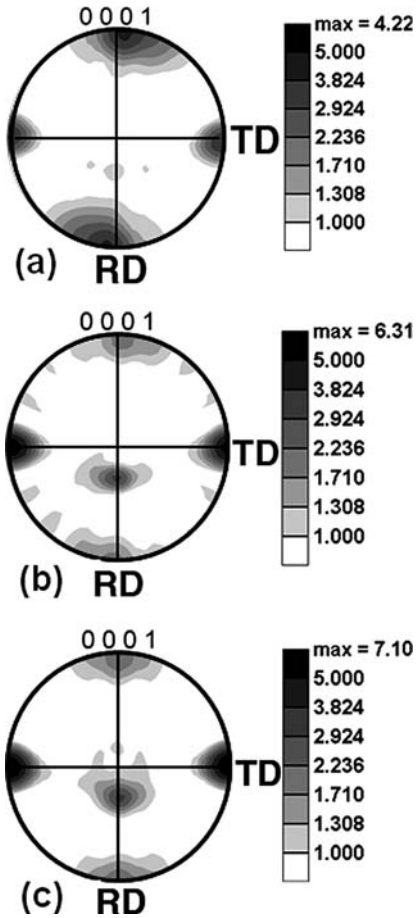


Fig. 23.8 Alpha phase (α_p+α_s) (0001) pole figures for Ti-6Al-4V after hot-rolling parallel to the rolling direction of the as-received plate at (**a**) 955°C + 3 min reheat, (**b**) 955°C + no reheat, and (**c**) 815°C + 3 min reheat (Salem et al. 2008b)

High temperature rolling (955°C) *without* reheating between passes combined features of high temperature rolling *with* reheating and low temperature rolling *with* reheating. The initial passes were conducted at high temperature and the T-type texture was dominant. In the last few rolling passes, the material cooled down to the low temperature regime, resulting in the B/T-type texture. Consequently, rolling without reheats resulted in high intensity of basal poles along the TD with a weaker intensity of the B-type texture, compared to rolling at 815°C with reheats (Fig. 23.8b,c). The fact that similar results were seen after rolling perpendicular to the reference/rolling direction in the starting material confirmed the effect of rolling temperature on final texture (Fig. 23.9a, b).

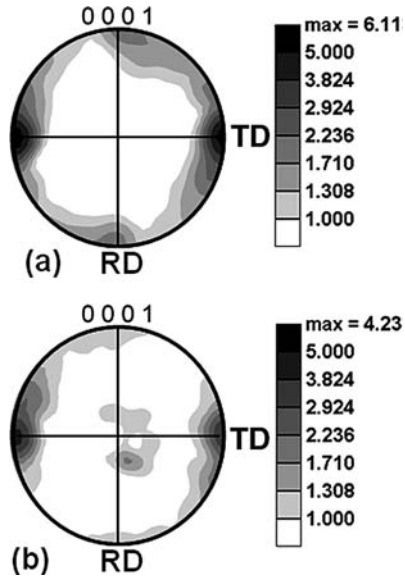


Fig. 23.9 Alpha-phase (α_p+α_s) (0001) pole figures for Ti–6Al–4V after cross rolling perpendicular to the rolling direction of the as-received plate at (**a**) 955°C + 3 min reheat and (**b**) 815°C + 3 min reheat (Salem et al. 2008b)

23.5.3 Primary-Alpha (α_p) Textures

The α_p texture that developed after high-temperature (955°C) rolling with reheat had a majority of the basal poles aligned with the RD (Fig. 23.10a), which would never be revealed just by considering the overall texture (Fig. 23.8a), with its predominance of the TD component. The masking effect of the α_p texture by the overall texture was due to the small volume fraction of α_p at 955°C. The strong α_p RD component following rolling at 955°C was inherited from the starting texture of the unrolled material. Such a strong RD component in the starting material did not change much during deformation, because most of the deformation was accommodated by the β phase with deformation of the α_p phase. The temperature drop during high-temperature rolling *without* reheating resulted in the decomposition of the beta matrix *during* deformation. This caused the α_p to become encapsulated in a stiff matrix of transformed beta. Plastic deformation of such a microstructure increased the amount of plastic strain accommodated by α_p relative to that during rolling with reheating. The result was the formation of an α_p deformation texture with a strong texture component along the TD and the appearance of basal poles close to the ND (Fig. 23.10b) (B/ T-type texture).

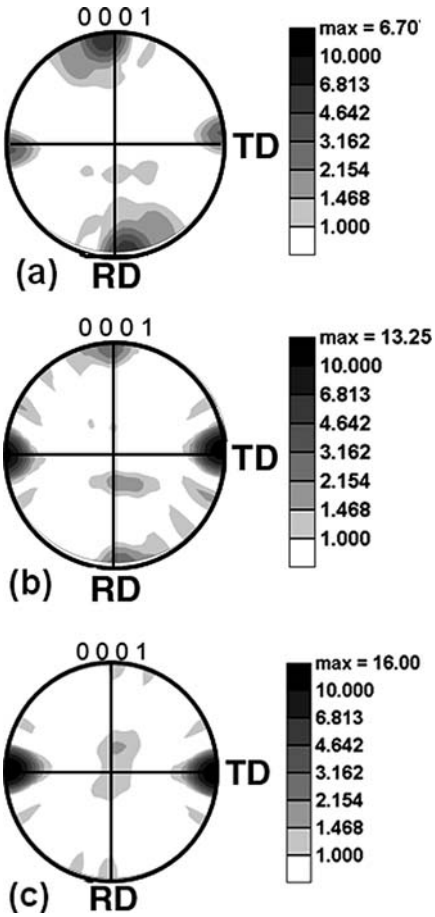


Fig. 23.10 Primary-alpha (α_p) (0001) pole figures determined by EBSD for Ti-6Al-4V rolled at (**a**) 955°C with 3-min interpass reheats, (**b**) 955°C with no reheating, and (**c**) 815°C with 3-min interpass reheats (Salem et al. 2008b)

In the same vein, the microstructure during low-temperature rolling (815°C) had a large amount of α_p and a small amount of β, which led to an increase in the intensity of the TD component, the disappearance of the RD component, and the appearance of the basal poles close to the ND for the α_p portion of the material (Fig. 23.10c). These results confirmed that the deformation of α_p contributes greatly to the formation of the B/T-type texture.

23.5.4 Secondary-Alpha (α_s) Texture

Separating the α_s textures using the EBSD/ EDS technique enabled the correlation of transformation texture to different stages of deformation during hot-rolling. High-temperature rolling (955°C) with reheating forced the soft β phase to accommodate most of the plastic strain. During cooling, the β phase may decompose into a new alpha phase on only *one* of the six possible {110} planes of the β phase, while maintaining the Burgers relationship $(0002)_\alpha \parallel (110)_\beta$ (Burgers 1934) in a process known as preferential variant selection. The strain accommodated by the β phase during the rolling process controls the variant selection process (Frederick 1973). As a result, the transformed texture had a strong component in the TD, with additional weaker components along the RD and at 45° to the RD and TD, which were also related to the parent β deformation texture (Fig. 23.11a).

The relationship between the α_s texture developed by high temperature hot-rolling with reheating and the corresponding β-deformation texture was established by comparing the $(0001)_\alpha$ pole figure for the α_s (Fig. 23.11a) and the $(110)_\beta$ pole figure for the beta (Fig. 23.12). Both pole figures had similar locations of intensity maxima, confirming the validity of the Burgers relationship during the decomposition of the β phase. However, there were clear quantitative differences in the intensities at specific locations. Particularly, the $(110)_\beta$ pole figure showed an essentially uniform intensity for all its texture components,

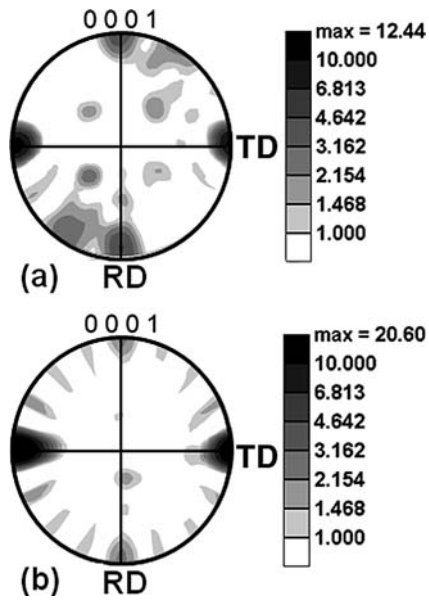


Fig. 23.11 Secondary-alpha (α_s) (0001) pole figures determined by EBSD/ EDS for Ti-6Al-4V rolled at (**a**) 955°C with 3-min interpass reheats, and (**b**) 955°C without interpass reheats

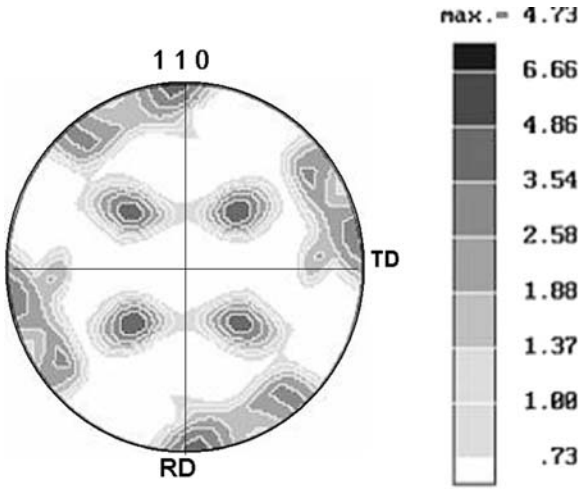


Fig. 23.12 Beta-phase (β) (110) pole figure of the starting Ti-6Al-4V material after heat treatment at 955°C for 4 hours and furnace cooling determined by the XRD technique

while the $(0001)_\alpha$ pole figure showed a stronger intensity along the TD and weaker intensities at the other locations. The difference in intensities was explained by the preferential variant selection during the β-to-α transformation. If preferential variant selection was absent, all twelve variants of the alpha phase would occur with equal probability, and the intensities of different locations in the $(101)_\beta$ pole figure would be similar to that in the $(0001)_\alpha$ pole figure (Gey et al. 1997).

During high-temperature rolling (955°C) *without* reheating, the β matrix decomposed to α_s lamellae continuously as the temperature dropped during deformation and between passes. Then the transformed alpha, α_s, accommodated some of the deformation. The result was a combination of deformation and transformation texture yielding very sharp α_s texture (Fig. 23.11b) because of the sharp texture of the β phase and a possible preferred variant selection during the transformation.

Low-temperature rolling at 815°C did not show any sign of α_s (Fig. 23.7).

23.6 Conclusions

EBSD/ EDS represent a practical tool to separate the textures of primary-alpha particles (α_p) and secondary-alpha lamellae (α_s) in α/β titanium alloys with a duplex microstructure. The vanadium partitioning in Ti-6Al-4V provides the most noticeable signature for automated discrimination of α_p particles and α_s lamellae that form by decomposition of beta phase during cooling. For hot-rolled plates, irrespective of the rolling temperature, the alpha phase texture includes a component with the basal poles along the TD. For high-temperature rolling with interpass reheating, this is the main component and results from the formation of α_s via preferential variant selection during the decomposition of the beta matrix. High-temperature rolling without reheating results in a basal/transverse-type deformation texture with a weak basal component. The strength of the basal component increases by decreasing the rolling temperature. Both α_p and α_s contribute to the basal/ transverse-type texture during low temperature rolling. The secondary-alpha (transformation) texture is correlated (through the Burgers relation between beta and alpha) to the deformation texture of the beta phase, with principal components along the TD and at ∼45° to the RD and TD. A quantitative difference in the intensity of specific components in the α_s and the parent β textures suggests preferential variant selection during the transformation.

Acknowledgments This work was conducted as part of the in-house research activities of the Metals Processing Group of the Air Force Research Laboratory's Materials and Manufacturing Directorate under Air Force Contracts F33615-03-D-5801. The support and encouragement of the laboratory management and the Air Force Office of Scientific Research (Dr. J. Fuller, program manager) are gratefully acknowledged. The guidance of the research group leader (Dr. S.L. Semiatin) is much appreciated.

References

Burgers WG (1934) On the process of transition of the cubic-body-centered modification into the hexagonal-close-packed modification of zirconium. Physica 1:561–586

Eylon D, Seagle SR (2001) Titanium technology in the USA—An overview. J Mater Sci Tech 17:439–443

Frederick SF (1973) Manufacturing methods for production process for titanium sheet with controlled texture. Report AFML-TR-73-265

Germain L, Gey N, Humbert M et al (2005) An automated method to analyze separately the microtextures of primary α_p grains and the secondary α_s inherited colonies in bimodal titanium alloys. Mater Charact 54:216–222

Gey N, Humbert M, Philippe MJ et al (1997) Modeling the transformation texture of Ti-64 sheets after rolling in the β-field. Mater Sci Eng A 230:68–74

Glavicic MG, Kobryn PA, Bieler TR et al (2003) An automated method to determine the orientation of the high-temperature beta phase from measured EBSD data for the low-temperature alpha-phase in Ti-6Al-4V. Mater Sci Eng A 346:50–59

Glavicic MG, Miller JD, Semiatin SL (2006) A method to measure the texture of secondary alpha in bimodal titanium-alloy microstructures. Scripta Mater 54:281–286

Lutjering G (1998) Influence of processing on microstructure and mechanical properties of (β α+β) titanium alloys. Mater Sci Eng A 243:32–45

Lutjering G, Williams JC (2003) Titanium. Springer-Verlag, Berlin, Germany

Peters M, Luetjering G (1980) Control of microstructure and texture in Ti-6Al-4V alloy. In: Kimura H, Izumi O (eds) Titanium'80, Science and Technology: Proceedings of the Fourth International Conference on Titanium. TMS, Warrendale, PA, pp 925–935

Salem AA, Glavicic MG, Semiatin SL (2008a) A coupled EBSD/ EDS method to determine the primary- and secondary-alpha textures in titanium alloys with duplex microstructures. Mater Sci Eng A 494:350–359

Salem AA, Glavicic MG, Semiatin SL (2008b) The effect of preheat temperature and interpass reheating on microstructure and texture evolution texture evolution during hot-rolling hot rolling of Ti-6Al-4V. Mater Sci Eng A 496:169–176

Semiatin SL, Bieler TR (2001) Effect of texture and slip mode on the anisotropy of plastic flow and flow softening during hot working of Ti-6Al-4V. Metall Mater Trans A 32A: 1787–1799

Semiatin SL, Montheillet F, Shen G et al (2002) Self-consistent modeling of the flow behavior of wrought alpha/beta titanium alloys under isothermal and nonisothermal hot-working conditions. Metall Mater Trans A 33A:2719–2727

Semiatin SL, Knisley SL, Fagin PN et al (2003) Microstructure evolution during alpha-beta heat treatment of Ti-6Al-4V. Metall Mater Trans A 34A:2377–2386

Chapter 24

A Review of In Situ EBSD Studies

Stuart I. Wright and Matthew M. Nowell

24.1 Introduction

In the first fully automated electron backscatter diffraction (EBSD) system (Wright and Adams 1992), later termed orientation imaging microscopy (OIM) (Adams et al. 1993), four seconds were required to index each EBSD pattern. A few in situ studies were performed using these early systems involving a tensile stage (Weiland et al. 1996) and a heating stage (Humphreys and Ferry 1996). While this was a big step forward, modern commercial systems are capable of speeds over three orders of magnitude faster. Fortunately, while automated EBSD technology was advancing, scanning electron microscope (SEM) technology was also advancing. Field emission gun based SEMs became widely available. The smaller, more intense beams in these microscopes enable the OIM technique to be applied at higher spatial resolutions and faster data collection speeds. These improvements have made OIM systems more capable of capturing the evolving microstructures during in situ experiments.

Some information can be gleaned from individual patterns obtained with a stationary beam during in situ heating or deforming of a sample. For example, observing the pattern before and after a phase change in a single crystal might be a useful experiment. However, much greater insight can generally be gained by collecting OIM scan data repeatedly during an in situ experiment. This chapter reviews four types of such experiments: first, experiments performed in the SEM preceded and/or followed by OIM analysis; second, deformation experiments in which a tensile stage is mounted in the microscope and OIM scans are collected with the sample held under tension at specified points along the stress-strain curve; third, heating experiments in which scans are collected with the sample held at temperature at specific points along a heating-cooling curve or time-temperature curve; and fourth, experiments performed using a stage capable of both deformation and heating. Another type of in situ work is the collection of three-dimensional data through serial sectioning. This is now possible with the advent of microscopes in which the SEM is combined with a focused ion beam (FIB). However, such work will not be covered in this chapter, because Chapters 8, 9, and 10 discuss such work in detail.

While many examples of in situ OIM work will be cited in this review, the references are not comprehensive. Nonetheless, an effort has been made to cite studies done by all of the research groups active in this arena, as well as across the spectrum of applications.

In order to perform OIM scans during in situ experiments in the SEM, the sample should be tilted to the standard 70° (or near 70°) during the experiment, the tilt angle well known for accurate orientation measurements. This requires good geometric compatibility between the SEM, the EBSD detector, and the deformation or heating stage. Another challenge is that samples can drift during in situ experiments. Thus it is generally necessary to perform some kind of drift correction during these experiments, either manually or under computer control.

It should be noted that there are examples of OIM studies being performed quasi in situ. In these cases a sample is polished and an area on the surface is marked in some manner (e.g., using microhardness indents).

S.I. Wright (✉)
EDAX-TSL, Draper, UT 84020, USA
e-mail: Stuart.Wright@ametek.com

A.J. Schwartz et al. (eds.), *Electron Backscatter Diffraction in Materials Science*,
DOI 10.1007/978-0-387-88136-2_24, © Springer Science+Business Media, LLC 2009

The sample is then placed in the microscope and the marked area scanned using OIM. Next, the sample is removed and some kind of experiment is performed ex situ. The sample is placed back in the microscope and scanned using OIM. This procedure is repeated. While such quasi in situ studies (Geiss et al. 2003; Huang et al. 2007; Panchanadeeswaran et al. 1996) can be helpful, this chapter focuses on experiments and scans performed completely within the SEM.

24.2 In Situ Postmortem Experiments

The first level of in situ analysis is using OIM to analyze microstructural changes occurring during experiments by pre- and/or postmortem analysis of the samples. Several examples of such analyses have been reported in the literature. A good example is the study of orientation effects on void formation and propagation during electromigration (Buerke et al. 1999; Choi et al. 2008; Meyer and Zschech 2007; Mirpuri and Szpunar 2005) The passivation layer of interconnect (IC) test structures is first thinned for SEM observation of the IC lines during the in situ experiments. The sample is placed in a holder equipped with both electrical feedthroughs and a heating stage. The sample is heated and current applied and the IC lines imaged. After the experiments, the overlayer is completely removed, so that OIM scans can be performed on the lines. While investigations using such an approach have been successfully performed, it should be noted that Geiss et al. (2003) have successfully performed in situ OIM scans during the in situ experiments.

Because OIM is a surface technique, in situ surface modification experiments lend themselves well to OIM analysis. Instruments combining an SEM with a focused ion beam (FIB) enable surfaces to be removed with the ion beam and then scanned using OIM without removing the samples from the vacuum chamber. In regards to OIM analysis, the combined SEM/FIB has been primarily used for preparing samples (Michael et al. 2006). For example, cross sections of fine features can be prepared and imaged by OIM; an example is shown in Fig. 24.1 of a gold wire mount cross-sectioned with the FIB and subsequently mapped using OIM. Two studies have extended the use of the combined SEM/FIB beyond sample preparation to analyze surfaces after ion milling to investigate the effects of various milling parameters on the resulting microstructure (Matteson et al. 2002; Michael 2006).

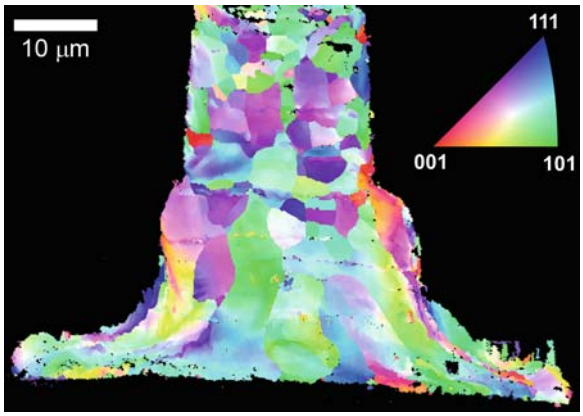


Fig. 24.1 A gold wire mount cross-sectioned and imaged using OIM in a combined SEM/FIB

Other types of postmortem OIM analyses of in situ surface modification include studies of oxidation. Pöter et al. (2005) investigated the growth of oxide layers on iron by placing samples on a heating stage in the SEM and then introducing various gas mixtures via capillary near the sample. The samples were characterized by EBSD prior to the in situ experiments. Geiss et al. (2003) used EBSD to study the development of strain during oxide formation on AlGaAs/GaAs multilayer samples after in situ oxygen plasma exposure. Phelan and Dippenaar (2004) have investigated Widmanstätten plate formation on samples of iron OIM directly after in situ surface heating via scanning laser confocal microscopy, as well as phase transformations in titanium using the same technique.

While in situ experiments followed by postmortem characterization by OIM provide insightful information on microstructural evolution, they represent only a preliminary level of in situ analysis. Coupling in situ OIM with in situ processing provides a more complete tracking of microstructural changes. The remainder of this chapter focuses on such experiments performed using tensile and heating stages designed for simultaneous observation by OIM. It should be noted that, in some instances, postmortem analyses of in situ heating (Cornen and Le Gall 2005) and deformation experiments (Takigawa et al. 2000) provide important information that might not be possible or practical to obtain by in situ OIM analysis in parallel with the in situ experiment. A good example is a study by De Hosson

and Ocelik (2003) on crack initiation at tungsten carbide particles in Ti-6Al-4V. In these studies, cracks were initiated during in situ tensile deformation. EBSD was used to identify the phases of particles formed around the tungsten carbide particles. Because phase ID is typically a slower process often requiring operator intervention, it does not lend itself to repeated examination at increasing deformation steps. Of course, the impracticality of repeated in situ OIM examinations does not diminish the value of such results.

24.3 Deformation Stage Experiments

The first example of in situ OIM during an in situ experiment was reported by Weiland et al. (1996). In these experiments, they tracked the lattice rotation of individual grains as well as grain fragmentation or subgrain formation during the deformation. The speed of OIM on these early systems was quite slow relative to modern systems. Several studies have been performed on more modern systems (Han et al. 2002; Tatschl and Kolednik 2003). As deformation progresses, the dislocation density increases, generally leading to more diffuse EBSD patterns as deformation proceeds. Thus, thermionic field emission gun SEMs are particularly helpful for OIM observation of in situ deformation studies, because they tend to produce beams with higher current density, enabling smaller beam sizes and interaction volumes.

As a specific example of in situ OIM and in situ deformation, a study of rolled and annealed 5754 aluminum has been performed. The material was fully recrystallized and had an average grain size of 30 microns. The samples were 32 mm in gauge length, 1.13 mm thick, and 7.41 mm wide in the gauge section. One side of the tensile sample was mechanically polished and lightly etched. OIM scans containing 18,200 points on a 250 × 250 micron grid with 2-micron steps between points were performed on the samples while they were held under tension at discrete strain steps. It should be noted that a slight drop in force and a slight increase in displacement was observed between the beginning of the scan and the end of the scan. The scans required approximately 6 min to complete. The sample was slightly notched to help insure that necking occurred in the area being characterized. Figure 24.2 shows a series of maps at several steps during an in situ tensile test for one of the samples. In addition, Fig. 24.2 shows the increase in orientation spread in an individual grain during the deformation. The black areas represent points for which the EBSD patterns could not be indexed. The increasing black area is due to the increasing surface roughness of the sample.

Several features of particular interest can be observed in the resulting maps. Two types of color changes can be observed. First, the variance in color within individual grains increases with increasing

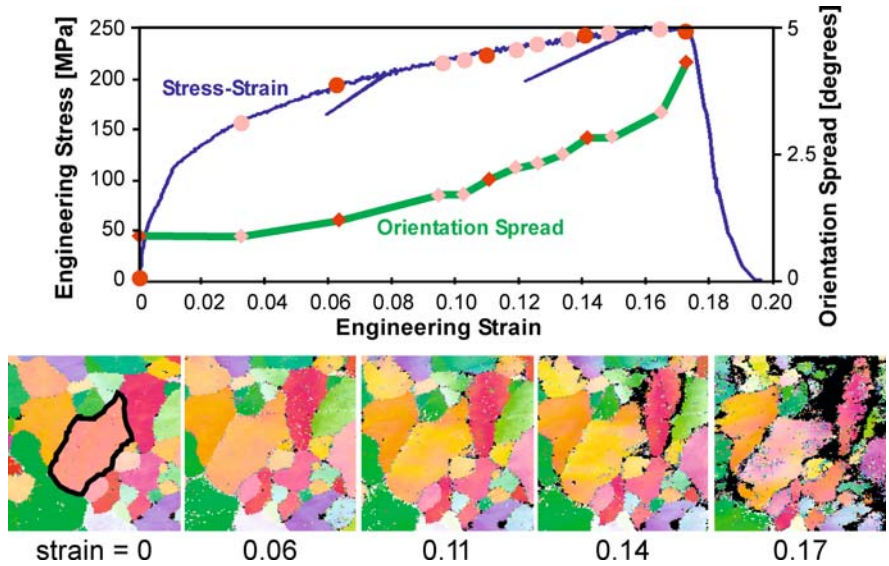


Fig. 24.2 Orientation maps generated from OIM scans at specific stress-strain steps and an accompanying plot showing the stress-strain curve and the orientation spread within the higlighted grain plotted as a function of strain

strain. This is a result of local misorientations arising from dislocations. Figure 24.2 highlights this effect for the outlined grain in the scan at zero strain. The orientation spread within the grain is tracked as a function of the bulk strain. Second, the overall color of certain grains changes with increasing strain. This is indicative of overall grain rotation leading to bulk texture changes. Bjerkaas et al. (2006) have monitored texture changes using in situ OIM as well as tracking the rotations of individual grains in an AlMgSi alloy.

Another feature in the maps is the increasing fraction of points shaded in black with increasing strain. The points shaded in black indicate points in the OIM scan that produced patterns which could not be indexed. This is indicative of increasing surface roughness (i.e., the "orange peel" effect). The surface topology negatively impacts EBSD pattern quality, because the beam/sample geometry requires a line of sight configuration that is progressively disrupted.

In situ OIM coupled with in situ deformation has also been used to study twinning in Mg-3Al-1Zn (Barnett et al. 2005). The technique has also been applied to study phase transformations in transformation-induced plasticity (TRIP) steels by Oh et al. (2002), and in supermartensitic stainless steel by Karlsen et al. (2008).

24.4 Heating Stage Experiments

In general, coupling OIM with in situ heating experiments requires a heating stage capable of measuring and controlling the temperature of the sample from outside the SEM specimen chamber, and designed to achieve the high tilts required for EBSD. An alternative to this approach is to heat the sample up outside the specimen chamber, and then place the hot sample in the chamber in the tilted position for EBSD analysis. OIM scans can then be repeatedly run over the surface of the sample, while the sample cools to ambient temperature (Lee et al. 2006; Mirpuri et al. 2006). Employing a heating stage provides much more control and flexibility, enabling in situ experiments to be performed on a wide range of materials (Piazolo et al. 2004; Seward et al. 2002; Wheeler et al. 2002). In situ OIM measurements make it possible to track changes in orientation with changes in time and/or temperature.

In general, two types of in situ temperature studies have been performed: the study of phase transformations and the study of recrystallization and grain growth. In the examples detailed here, the heating stage used is capable of temperatures up to 600–700°C. The samples were approximately 10 mm × 5 mm × 2 mm in size. One thermocouple was used to monitor and control the heating stage and a second to track the temperature at the specimen surface. The heating is very localized, and at these temperatures no deleterious effects on the OIM system nor on the SEM have been observed. It should be noted, however, that this can be dependent on the heater and heating configuration used.

24.4.1 Phase Transformation

The role of crystallographic orientation during phase transformations can be studied using OIM coupled with in situ heating. This has been done by Seward et al. (2004) for pure titanium and by Watanabe et al. (2004) for an iron alloy. Kirch et al. (2008) have used a laser-powered heating stage to study phase transitions in a low-carbon steel.

An in situ heating experiment has been performed using cobalt. Cobalt exhibits a martensitic transformation from a hexagonal phase (α) to a face-centered cubic phase (β) at 422°C. The transformation was captured by successive OIM scans as the sample was repeatedly heated and cooled. The complete reversibility in the phase transformation process is evident in the maps—no change in the selection of the variants was observed after several forward and reverse transformations.

In comparing orientations before and after the transformation, it was noted that the transformation follows the Nishiyama-Wasserman orientation relationship of (111) β || (0001) α. This is clear in Fig. 24.3, showing the EBSD patterns before and after the transformation. The (0001) and (111) poles are in exactly the same location in the patterns.

This is also evident in Fig. 24.4, which shows the (111) β and (0001) α pole figures from the individual orientation measurements within two grains which have not yet fully transformed. In both cases, one of the (111) poles in the cubic phase is perfectly aligned with the (0001) pole in the hexagonal phase. There are two

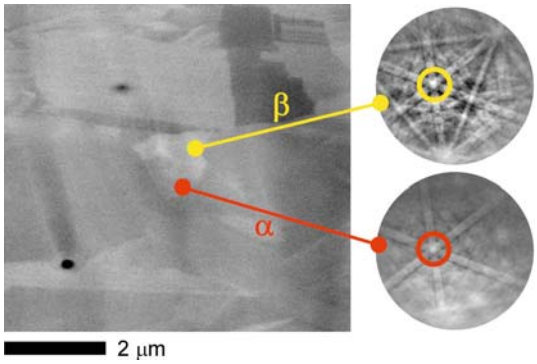


Fig. 24.3 EBSD patterns from a partially transformed grain with the (111) (*top*) and (0001) (*bottom*) poles *highlighted*

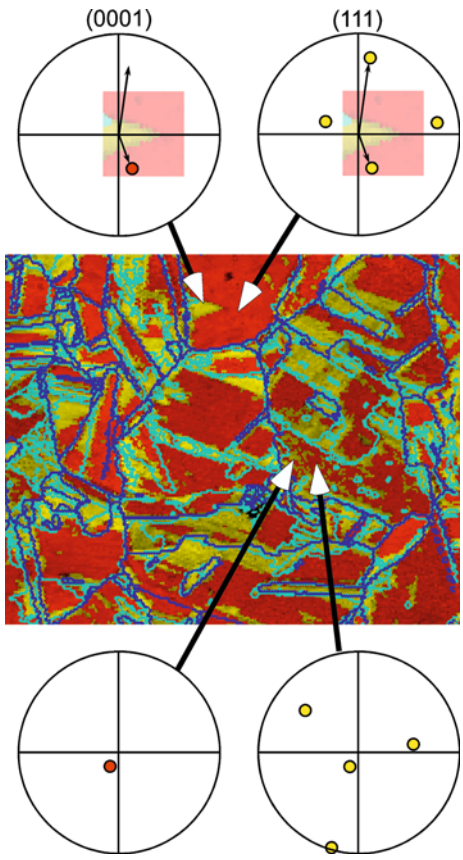


Fig. 24.4 OIM map of the phase transformation captured when the transformation was only partially completed; (0001) pole figures for the α phase and (111) pole figures for the β phase, at selected points in the OIM scan. The *blue lines* indicate the grain boundaries after the transformation to the β phase has completed, and the *cyan lines* are the final boundaries in the α phase

interesting features to note in this figure. In the grain at the top, a wedge of the β phase persists. The trace normal of one side of the wedge is aligned with both the (0001) and (111) poles. However, the trace normal of the top side of the wedge is only aligned with the (111) pole. From this observation, it is presumed that the bottom side of the wedge corresponds to a transforming interface, whereas the top side of the wedge corresponds to a stationary interface. In the second grain, the grain is very speckled, alternating apparently randomly between the α and β phases. Because the (0001) and corresponding (111) poles are very near the center of the pole figure, it is presumed that the interface plane is nearly parallel to the sample surface. Thus, it is very possible that the alternating nature of the grain may be an artifact of the EBSD measurement. The patterns from this grain are likely to be a convolution of one phase at the surface and the other phase just below the surface. Thus, the automated pattern indexing is likely to randomly extract one crystal system from the pattern over the other.

24.4.2 Recrystallization and Grain Growth

The majority of in situ heating experiments have been performed to study recrystallization, recovery, and subsequent grain growth. These studies have focused on many different aspects of these important phenomena, including grain boundary mobility, twin formation, nucleation, solute and precipitate effects, and selective growth. Aluminum and its alloys have received the most attention (Hurley and Humphreys 2004; Kajihara et al. 2006; Lens et al. 2005; Mattissen et al. 2004; Taheri et al. 2004; Takata et al. 2007; Van der Zwaag et al. 2006). Copper has also been investigated (Field et al. 2004; Mirpuri et al. 2004), as well as steel (Nakamichi et al. 2007; Seaton and Prior 2004; van Haaften et al. 2003) and rock salt (Piazolo et al. 2006).

An in situ experiment has been performed on samples of copper deformed via equal channel angle extrusion and heated to 160°C and held at temperature. OIM scans were repeatedly performed as soon as the sample reached 160°C at two-minute intervals. The scan area was 26 by 26 microns and a step size of 0.2 microns was used. The total number of orientation measure-

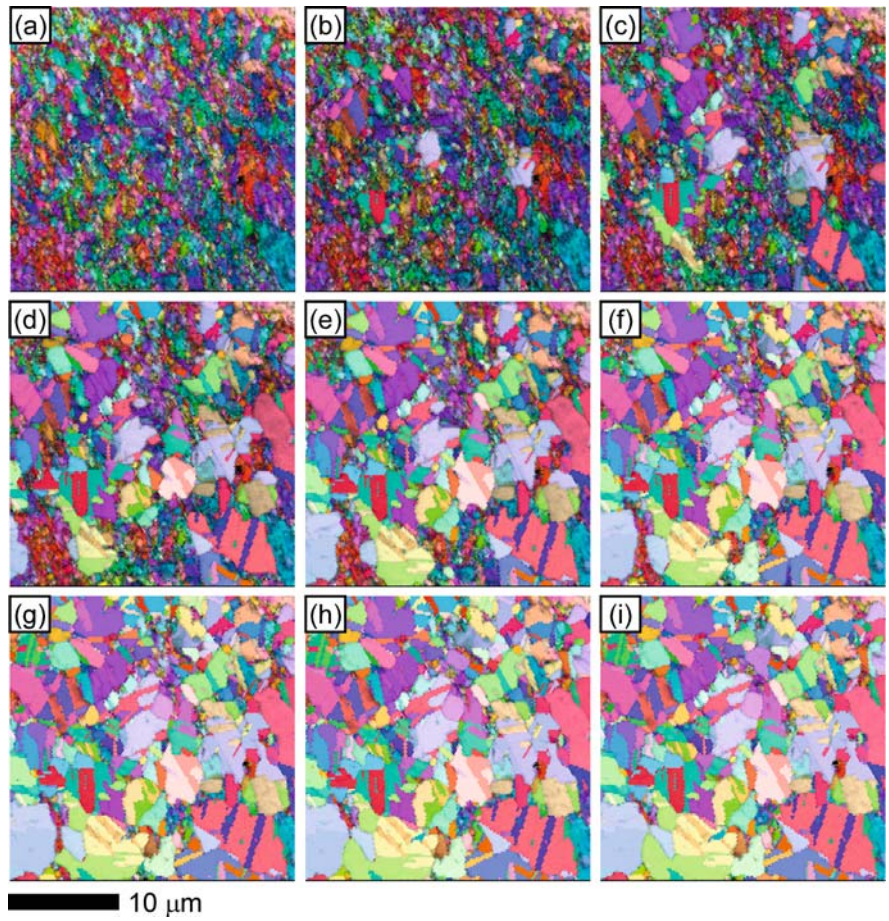


Fig. 24.5 Sequence of orientation maps overlaid on image quality maps from in situ heating of deformed copper at selected times. (**a**) The initial microstructure, and after (**b**) 12, (**c**) 20, (**d**) 30, (**e**) 46, (**f**) 66, (**g**) 86, (**h**) 108, and (**i**) 130 min

ments in each scan was 19,706. The scan was performed on a hexagonal scan grid. Selected OIM maps are shown in Fig. 24.5.

Note that in recrystallized grains, the color does not vary, whereas in the deformed grains the color varies slightly within the grains. The variation in color arises from local variations in orientation due to residual plastic strain. The local misorientation can be characterized by determining the spread in orientation within each "kernel" in the OIM scan. A "kernel" contains an orientation measurement and each of its six nearest neighbors. A neighbor is excluded from the kernel if it is oriented more than 5 degrees away from the measurement at the center of the kernel. Figure 24.6 shows the average kernel orientation spread for each scan plotted as a function of time at temperature. The plot also shows the average quality (IQ) of the diffraction patterns in each scan, and the average confidence index as well (the confidence

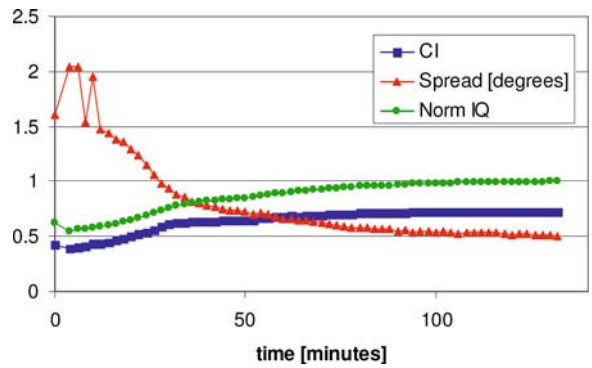


Fig. 24.6 Average kernal orientation spread from in situ heating of deformed copper at selected times

index, CI, is a measure of indexing reliability [Field 1997]). As would be expected, the orientation spread decreases as recovery and recrystallization proceed in the sample. The CI and IQ increase with time as the patterns become sharper in the recrystallized regions. These parameters all give an indication of how quickly the recrystallized grains are consuming the deformed regions in the microstructure.

It is impossible to tell from these maps whether, as new recrystallized grains appear, the grain was nucleated at the surface, or nucleated just below the surface and subsequently grown into the observed surface.

24.5 Combined Heating and Tensile Stage Experiments

If a heating stage and tensile stage are combined together, then deformation experiments can be done at temperature. Huang et al. (2003) have used such a stage to study dynamic recrystallization and superplasticity in an aluminum alloy.

Boehlert et al. (2008) have used this technique to study creep in udimet, a cobalt-nickel-chromium-tungsten alloy. In these experiments, in situ OIM maps were acquired over a 200 μm by 200 μm area, using a step size of 0.5 μm. Approximately 140,000 data points were collected in each scan. The duration of the scan was 20 min. Initially 95% of the patterns were indexed successfully; however, in each subsequent scan, the pattern quality decreased due to surface roughening, and consequently a smaller fraction of scan points were indexed successfully.

The results from this experiment show that grain boundary cracking occurs preferentially in random high angle boundaries (Fig. 24.7).



Fig. 24.7 A map of nickel superalloy having undergone in situ tensile creep at 760°C and 220 MPa (594 μm displacement). The *gray scale* used on the map is the average IQ in each grain. Boundaries shaded in *red* are random high angle boundaries (>10°) and those in *blue* are coincident site lattice boundaries. *Thick black lines* denote cracked boundaries

Most of the studies to date have been focused on relatively small scan areas. Thus, while these studies provide some insight, it should be noted that the number of grains and grain boundaries sampled are not statistically reliable. However, with the advent of higher speed systems, more statistically relevant studies are now tractable.

Another inherent limitation is that in situ observations of orientation changes during heating and deformation experiments are subject to free surface effects. Care must be taken to try to obtain complementary information from the bulk measurements to confirm any conclusions drawn from the surface measurements.

Because EBSD is a very surface-sensitive technique, the samples must be polished to produce good EBSD patterns. This can be difficult to do on some specimens intended for in situ work. In addition, any changes to the surface during the experiment can have deleterious effects on the patterns. For example, during deformation the surface can roughen (the so-called orange peel effect) making it difficult to get good EBSD patterns. During heating the surface may oxidize, which can reduce pattern quality.

24.6 Conclusions

When OIM is used in conjunction with in situ experiments in the SEM, it provides valuable insight into the role crystallographic orientation plays in dynamic phenomena such as recrystallization and deformation. OIM's utility for characterizing orientation changes during in situ experiments arises from the increased speeds available in modern systems.

The speed of the OIM system is more important for in situ experiments than for typical OIM measurements. If the scan is considerably slower than the dynamic event being characterized, then the microstructure at the end of the scan may differ from that at the beginning, giving the illusion of a spatially heterogeneous microstructure. For example, in some in situ recrystallization experiments, grains of a particular orientation have been observed at the top of a scan and grains of the same orientation have been observed farther down in the scan. In the next cycle, these two grains are joined together into a single grain. It is impossible to tell if the grain had a convex shape just below the surface resulting in two grains of similar orientation, or if one part of the grain appeared later in the same scan due to a sudden increase in the speed of grain growth between the first appearance of the grain and the second.

Despite these concerns, coupling OIM with in situ experiments provides insight into the role of crystallographic orientation in the dynamic evolution of microstructure.

Acknowledgements The authors acknowledge the contribution of Seiichi Suzuki of TSL Solutions for the engineering of the heating stage; Robert Kubic and Raja Mishra of General Motors for providing access to the in situ tensile stage; Tom Lillo of Idaho National Engineering and Environmental Laboratory for providing the copper ECAE sample; and Jeff Farrer of Brigham Young University for the gold wire mount results.

References

Adams BL, Wright SI, Kunze K (1993) Orientation imaging: The emergence of a new microscopy. Metall Trans A 24: 819–831

Barnett MR, Keshavarz Z, Nave MD (2005) Microstructural features of rolled Mg-3Al-1Zn. Metall Mater Trans A 36:1697–1704

Bjerkaas H, Fjeldbo SK, Roven HJ, Hjelen J, Chiron R, Furu T (2006) Study of microstructure and texture evolution using in situ EBSD investigations and SE imaging in SEM. Mater Sci Forum 519–521:809–814

Boehlert CJ, Longanbach SC, Nowell M, Wright S (2008) The evolution of grain-boundary cracking evaluated through in situ tensile-creep testing of Udimet alloy 188. J Mater Res 23:500–506

Buerke A, Wendrock H, Kötter T, Menzel S, Wetzig K, Glasow AV (1999) In situ electromigration damage of Al interconnect lines and the influence of grain orientation. Mater Res Soc Proc 563:109–114

Choi ZS, Monig R, Thompson CV (2008) Effects of microstructure on the formation, shape, and motion of voids during electromigration in passivated copper interconnects. J Mater Res 23:383–391

Cornen M, Le Gall R (2005) In situ recrystallization imaging of polycrystalline Ni-S alloy using SEM. Mater Res Soc Proc 907:63–67

De Hosson JTM, Ocelik V (2003) Functionally graded materials produced with high power lasers. Mater Sci Forum 426–432:123–130

Field DP (1997) Recent advances in the application of orientation imaging. Ultramicroscopy 67:1–9

Field DP, Nowell MM, Trivedi P, Wright SI, Lillo TM (2004) Local orientation gradient and recrystallization of deformed copper. Solid State Phenom 105:157–162

Geiss RH, Roshko A, Bertness KA, Keller RR (2003) Electron backscatter diffraction for studies of localized deformation. In: Weertman JR, Fine M, Faber K, King W, Liaw P (eds) Electron microscopy: Its role in materials science—Mike Meshii Symposium, TMS, Warrendale 329–336

Han JH, Baeck SM, Oh KH, Chung YH (2002) Orientation correction method of distorted samples during in situ deformations using a high resolution EBSD. Mater Sci Forum 408–412:203–208

Huang Y, Humphreys FJ, Ridley N (2003) In situ observations of microstructural evolution during deformation of Supral 100. Mater Sci Forum 447–448:381–386

Huang Y, Fu Q, Pan C (2007) 'In situ-tracking' observation of stainless steel microstructural development during elevated service using EBSD and SEM. Mater Sci Forum 561–565:2087–2090

Humphreys FJ, Ferry M (1996) Combined in situ annealing and EBSD of deformed aluminium alloys. Mater Sci Forum 217–222:529–534

Hurley PJ, Humphreys FJ (2004) A study of recrystallization in single-phase aluminium using in situ annealing in the scanning electron microscope. J Microsc 213:225–234

Kajihara K, Matsumoto K, Matsumoto K (2006) In situ SEM-EBSP observations of recrystallization texture formation in Al-3mass%Mg alloy. Mater Sci Forum 519–521:1579–1584

Karlsen M, Hjelen J, Grong Ø, Rorvik G, Chiron R, Schubert R, Nilsen E (2008) SEM/EBSD based in situ studies of deformation induced phase transformations in supermartensitic stainless steels. Mater Sci Technol 24:64–67

Kirch DM, Ziemons A, Lischewski I, Molodova X, Molodov DA, Gottstein G (2008) Laser powered heating stage in a scanning electron microscope for microstructural investigations at elevated temperatures. Rev Sci Instrum 79-043902:1–8

Lee H-J, Han HN, Kim DH, Lee U-h, Oh KH, Cha P-R (2006) In situ observation of the grain growth of the copper electrodeposits for ultralarge scale integration. Appl Phys Lett 89-161924:1–3

Lens A, Maurice C, Driver JH (2005) Grain boundary mobilities during recrystallization of Al-Mn alloys as measured by in situ annealing experiments. Mater Sci Eng A 403: 144–153

Matteson TL, Schwarz SW, Houge EC, Kempshall BW, Giannuzzi LA (2002) Electron backscattering diffraction investigation of focused ion beam surfaces. J Electron Mater 31: 33–39

Mattissen D, Wæro A, Molodov DA, Shvindlerman LS, Gottstein G (2004) In situ investigation of grain boundary and triple junction kinetics in aluminium—10 p.p.p. magnesium. J Microsc 213:257–261

Meyer MA, Zschech E (2007) New microstructure-related EM degradation and failure mechanisms in Cu interconnects with CoWP coating. AIP Conf Proc 945:107–114

Michael JR (2006) Gallium phase formation in Cu during 30 kV Ga+ FIB milling. Microsc Microanal 12:1248–1249 CD

Michael JR, Brewer LN, Miller DC, Zavadil KR, Prasad SV, Kotula PG (2006) Microscopy and microanalysis of nanoscale materials. Microsc Today 6–14

Mirpuri K-k, Szpunar J (2005) Orientation and microstructure dependence of electromigration damage in damascene Cu interconnect lines. Mater Sci Forum 495–497:1443–1448

Mirpuri K, Wendrock H, Menzel S, Wetzig K, Szpunar J (2004) High temperature behavior of Cu films studied in situ by electron backscatter diffraction. Microelectron Eng 76: 160–166

Mirpuri K, Wendrock H, Menzel S, Wetzig K, Szpunar J (2006) Texture evolution in copper film at high temperature studied in situ by electron backscatter diffraction. Thin Solid Films 496:703–717

Nakamichi H, Humphreys FJ, Bate PS, Brough I (2007) In situ EBSD observation of the recrystallization of an IF steel at high temperature. Mater Sci Forum 550:441–446

Oh ST, Park KK, Han HN, Park S-H, Oh KH (2002) Transformation behavior of retained austenite in hydroformed TRIP steel. Mater Sci Forum 408–412:1341–1346

Panchanadeeswaran S, Doherty RD, Becker R (1996) Direct observation of orientation change by channel die compression of polycrystalline aluminum—use of a split sample. Acta Mater 44:1233–1262

Phelan D, Dippenaar R (2004) Widmanstätten ferrite plate formation in low-carbon steels. Metall Mater Trans A 35A:3701–3706

Piazolo S, Sursaeva VG, Prior DJ (2004) Grain growth in Al: First results from a combined study of bulk and in situ experiments using a columnar structured Al foil. Mater Sci Forum 467–470:935–940

Piazolo S, Jessell MW, Prior DJ, Spiers C (2006) Temperature dependent grain boundary migration in deformed then annealed material: Observations from experimentally deformed synthetic rock salt. Tectonophysics 427:55–71

Pöter B, Parezanovic I, Spiegel M (2005) In situ scanning electron microscopy and electron backscatter diffraction investigation on the oxidation of pure iron. Mater High Temp 22:185–194

Seaton NCA, Prior DJ (2004) Nucleation during recrystallisation in Ti-SULC steel. Mater Sci Forum 467–470:93–98

Seward GGE, Prior DJ, Wheeler J, Celotto S, Halliday DJM, Paden RS, Tye MR (2002) High-temperature electron backscatter diffraction and scanning electron microscopy imaging techniques: In situ investigations of dynamic processes. Scanning 24:232–240

Seward GGE, Celotto S, Prior DJ, Wheeler J, Pond RC (2004) In situ SEM-EBSD observations of the HCP to BCC phase transformation in commercially pure titanium. Acta Mater 52:821–832

Taheri ML, Rollett AD, Weiland H (2004) In situ quantification of solute effects on grain boundary mobility and character in aluminum alloys during recrystallization. Mater Sci Forum 467–470:997–1002

Takata N, Ikeda K, Nakashima H, Tsuji N (2007) In situ EBSP analysis of grain boundary migration during recrystallization in pure aluminum foils. Mater Sci Forum 558–559: 351–356

Takigawa Y, Sakaida Y, Yasutomi Y, Ogawa S (2000) Simulation of microcrack propagation behavior in polycrystalline alumina having initial residual stress field. Ceram Eng Sci Proc 21:213–218

Tatschl A, Kolednik O (2003) On the experimental characterization of crystal plasticity in polycrystals. Mater Sci Eng A 342:152–168

Van der Zwaag S, Anselmino E, Miroux A, Prior D (2006) In situ SEM observations of moving interfaces during recrystallisation. Mater Sci Forum 519–521:1341–1348

van Haaften WM, Bi Y, van Leeuwen Y, Colijn J, Howe A (2003) Recrystallisation nucleation during annealing of Ti-SULC steel. Mater Sci Forum 426–432:1163–1168

Watanabe T, Obara K, Tsurekawa S (2004) In situ observations on interphase boundary migration and grain growth during α/γ phase transformation in iron alloys. Mater Sci Forum 467–470:819–824

Weiland H, Field DP, Adams BL (1996) Local texture evolution during deformation by in situ OIM analysis. In: Liang Z, Zuo L, Chu Y (eds) Proceedings of the eleventh international conference on textures of materials. International Academic Publishers, Xi'an, China 1414–1419

Wheeler J, Prior DJ, Seward GGE, Howe AA, Paden RS (2002) Hot pursuit: Capturing microstructure development in steel. Steel World 7:1–6

Wright SI, Adams BL (1992) Automatic-analysis of electron backscatter diffraction patterns. Metall Trans A 23:759–767

Chapter 25

Electron Backscatter Diffraction in Low Vacuum Conditions

Bassem S. El-Dasher and Sharon G. Torres

25.1 Introduction

Most current scanning electron microscopes (SEMs) have the ability to analyze samples in a low vacuum mode, whereby a partial pressure of water vapor is introduced into the SEM chamber, allowing the characterization of nonconductive samples without any special preparation. Although the presence of water vapor in the chamber degrades electron backscatter diffraction (EBSD) patterns, the potential of this setup for EBSD characterization of nonconductive samples is immense. In this chapter we discuss the requirements, advantages, and limitations of low vacuum EBSD (LV-EBSD), and explain how this technique can be applied to a two-phase ceramic composite, as well as hydrated biominerals, as specific examples of when LV-EBSD can be invaluable.

The ability to characterize specimens in an SEM at near atmospheric conditions has been around for some time (Robinson 1974), with the first commercial systems pioneered by Danilatos and ElectroScan Corporation being released some 20 years ago (Danilatos 1981, 1985, 1990; Danilatos and Postle 1983). Today, many commercial systems exist, and have become increasingly popular due to their ability to study insulating materials previously observed only in conventional SEMs after the application of a conductive coating.

B.S. El-Dasher (✉)
Lawrence Livermore National Laboratory, Livermore, CA 94550, USA
e-mail: eldasher2@llnl.gov

Operation of such low vacuum systems (also called environmental SEMs or ESEMs) rely on the use of multiple pressure limiting apertures within the column, allowing the electron gun to maintain a high vacuum (10^{-4} Pa), despite the chamber reaching pressures of up to 1 kPa. Chamber pressure control is by addition or removal of water vapor from a reservoir, and the presence of this vapor is what allows the direct imaging and analysis of insulators such as ceramics, polymers, and biological samples, without the concern of charging typically associated with conventional "high vacuum" SEMs (Merideth et al. 1996, Donald 2003).

Figure 25.1 illustrates schematically the charge balance process that occurs within the chamber. Some electrons leaving the sample surface collide with water vapor molecules and in the process ionize them. The combination of positively charged detector and negatively charged sample surface drives the ions to the sample and upon contact, the ions balance out the charge. During the ionization process, daughter electrons are also knocked out, and some of these go on to interact with other vapor molecules and in doing so produce a cascade of electrons. The specialized gaseous detector is designed to attract these cascade electrons, allowing imaging of the sample surface.

The collisions that produce the cascade electrons naturally are of concern when considering LV-EBSD analysis, as collisions of diffracted backscatter electrons with the water vapor degrade the diffraction pattern. Other tools that rely on characteristic radiation from the sample, such as energy dispersive spectroscopy (EDS), are also affected, with decreased effectiveness of quantitative analysis (Sigee 1998; Timofeeff et al. 2000; Mansfield 2000). Nevertheless, LV-EBSD is a valuable tool, as illustrated by work such

A.J. Schwartz et al. (eds.), *Electron Backscatter Diffraction in Materials Science*,
DOI 10.1007/978-0-387-88136-2_25, © Springer Science+Business Media, LLC 2009

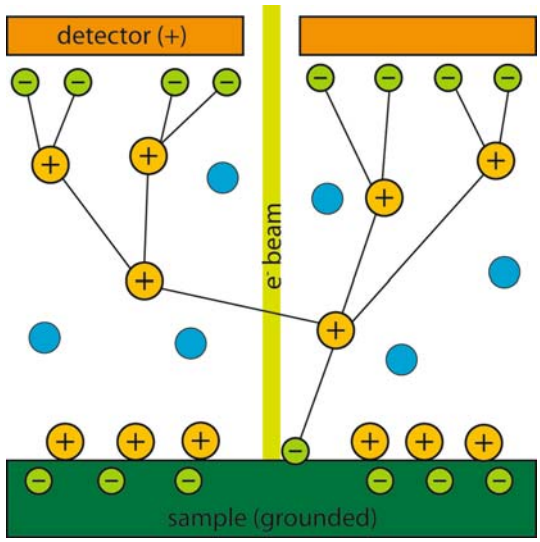


Fig. 25.1 Schematic of the charge balance and imaging process in an ESEM

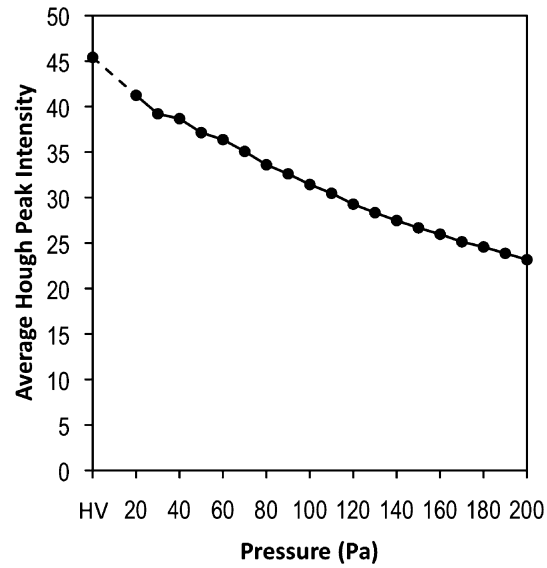


Fig. 25.2 Plot of average diffraction pattern peak intensity as a function of vapor pressure

as that on minerals (e.g., Habesch 2000) and ceramic composites (e.g., Sztwiertnia et al. 2006).

Through the use of LV-EBSD, studies on a variety of previously troublesome materials are now possible. In this chapter we identify the parameters important for successful LV-EBSD, and provide two distinct example applications to illustrate the approaches needed.

25.2 Considerations for Low Vacuum EBSD

While LV-EBSD is fundamentally similar to high vacuum (standard) EBSD, understanding how the chosen microscope parameters affect the quality of diffraction is important. In addition to the typical parameters of accelerating voltage and sample-to-detector distance, vapor pressure and dwell times also become critical factors. In general, all the parameters are chosen based on the sample material; and the more nonconductive a material is, the lower the voltage, and the shorter the dwell time or the higher the vapor pressure that is required. In practice, a combination of these parameters is what is employed, as too large a decrease in accelerating voltage or increase in vapor pressure would yield little to no diffraction.

As would be expected, the most significant effect on diffraction in LV-EBSD is caused by the presence of water molecules in the chamber. Although these molecules carry charge away from the sample surface and provide the ability to image nonconductive materials, they also absorb and/or deflect the backscattered electrons that make up the diffraction pattern. A demonstration of this effect is illustrated in Fig. 25.2, which plots the quality of diffraction patterns (measured as the average Hough peak intensity) collected from a silicon single crystal as a function of vapor pressure. A clear trend is observed, and the higher the vapor pressure, the lower the measured diffraction contrast. Figure 25.3 shows diffraction patterns collected with a 20 kV source at three different pressures. A comparison between the high vacuum (Fig. 25.3a) and the 50 Pa (Fig. 25.3b) patterns shows that although some contrast is lost at 50 Pa, the pattern is still quite clear and adequate for indexing. The 200 Pa pattern (Fig. 25.3c), while recognizable, is significantly weaker in both intensity and contrast, illustrating that the pressure needs to be limited in order to guarantee quality diffraction.

During the initial determination of parameters for a previously unexamined sample, it is suggested that

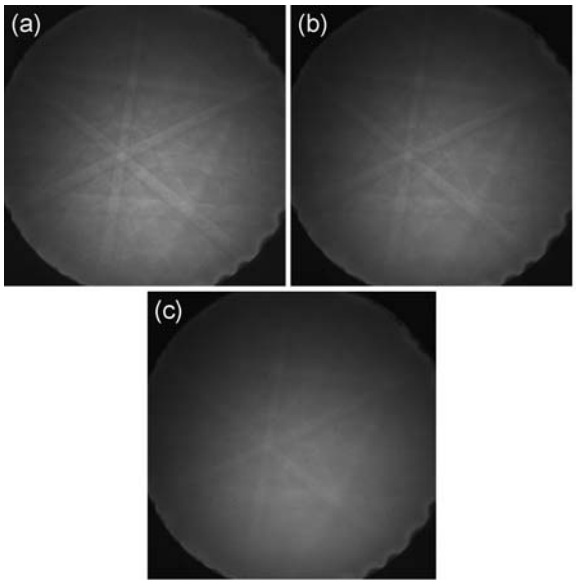


Fig. 25.3 Raw diffraction patterns from a silicon single crystal at (**a**) 10^{-4} Pa, (**b**) 50 Pa, and (**c**) 200 Pa

the highest possible accelerating voltage be used. This allows for the largest possible diffraction volume, which is important for maximizing the diffraction intensity of materials of interest such as oxides, nitrides, and biominerals, all of which contain a significant amount of low atomic number elements. The general rules for EBSD hold, however; and if the grain structure is too fine for the maximum accelerating voltage to be used due to overlapping diffraction patterns from neighboring grains, then a reduction in accelerating voltage is necessary.

Starting vapor pressure should be on the high end (e.g., 150 Pa), and then reduced in increments to as low a pressure as possible without allowing charging to take place. Charging should be evaluated with the beam collimated (i.e., in spot mode), and using the diffraction pattern. If the pressure required to eliminate charging is too high for quality patterns, then the accelerating voltage and/or beam spot size needs to be reduced. Although this has the undesirable side effect of decreasing diffraction contrast and hence requiring longer pattern collection times, it is necessary to iteratively adjust the parameters to achieve a balance between both beam and chamber parameters for a given sample material.

25.3 Example Applications

25.3.1 Microstructural Analysis of AlN-TiB_2 Ceramic Composite

This example is intended to illustrate how, despite the loss of signal cost associated with LV-EBSD, the technique can still be applied to one of the most challenging types of characterizations possible. We focus on AlN-TiB_2, a nonconductive ceramic composite (Sano et al. 2006a, 2006b), with the goal of collecting texture and grain distribution information without the use of a conductive carbon coating (since the samples were to undergo further surface characterization). Although this seems an ideal application of LV-EBSD, some difficulties arise due to the composition of the ceramic.

The first of these is the crystal structure of the constituents: they both are hexagonal. While possessing distinct structures, AlN is $P6_3mc$ and TiB_2 is P6/mmm (see Fig. 25.4); many low index interplanar angles are the same for both structures, making distinguishing them using EBSD patterns error prone and inconsistent at best. This then requires the use of simultaneous energy dispersive spectroscopy (EDS) to identify the phase. For a more detailed description of phase identification approaches, please see the chapters by El-Dasher and Deal, and Dingley and Wright.

As previously mentioned, the drawback to utilizing low vacuum mode is related to the water vapor, because it interferes with all characteristic radiation emitted from the sample, including X-rays. To gather sufficient signal to use EDS for phase discrimination,

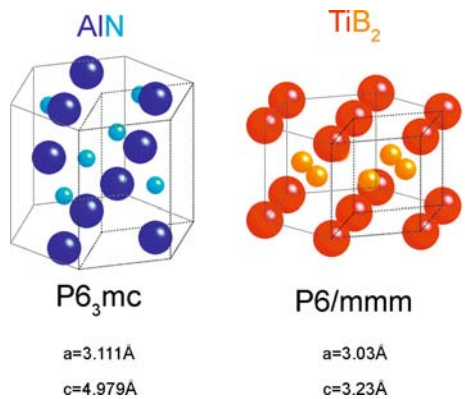


Fig. 25.4 Crystal structures of AlN and TiB_2

longer dwell times are needed (compared to diffraction collection), which causes local charging. In this specific example, as is likely for any example the reader may encounter, the correct settings were determined by trial and error. Microscope parameters (accelerating voltage and spot size) were chosen, as was the dwell time for the EDS collection, and a scan was performed over a small region. The EBSD patterns collected were examined manually during the scan to determine if charging was occurring due to the chosen dwell time. If it was, the spot size, dwell time, and/or vapor pressure were changed and the process was repeated until no charging was detected. The ultimate goal was achieving the maximum signal possible while eliminating charging.

Once the parameters were set, scans were performed in the traditional manner. Figure 25.5 shows EDS maps, illustrating the location of signals from both Al and Ti. This data, combined with the crystallographic information obtained from the EBSD patterns, can then yield a typical phase map as shown in Fig. 25.6.

This application then clearly illustrates that little needs to be given up when using LV-EBSD, because the capability of chemical discrimination using EDS can still be used if careful experimental parameter selection is performed.

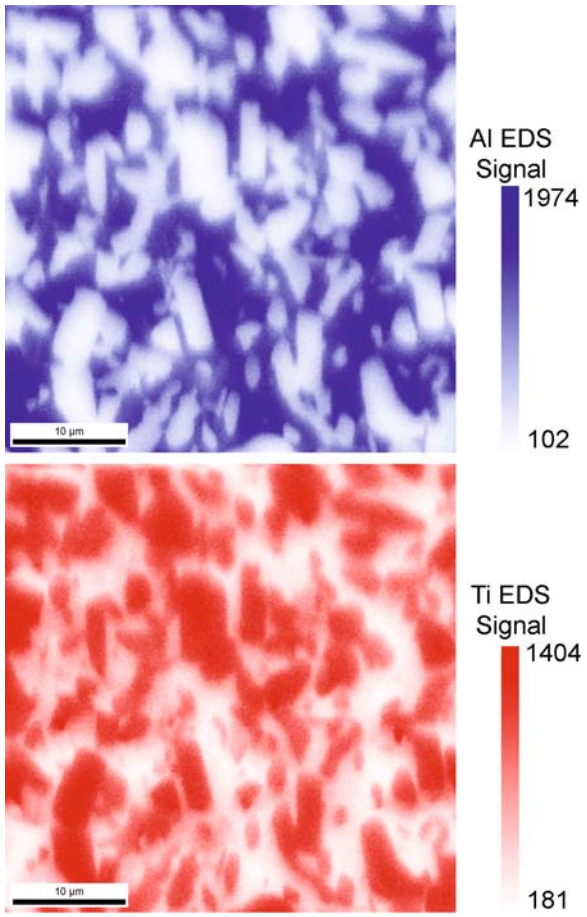


Fig. 25.5 Energy dispersive spectroscopy signals for both Al and Ti used to distinguish between the two crystal types

25.3.2 Characterization of $CaHPO_4 \cdot 2H_2O$ Single Crystals

In this example, we deal with a somewhat different problem than that discussed in the preceding section. Typical applications of LV-EBSD deal with nonconductive materials, but very rarely are these materials hydrated. Most, if not all, biomineral studies have been performed on dehydrated specimens, because of the severe charging that occurs when collimated electrons are incident on water-containing crystals.

The specific case discussed here considers a brushite ($CaHPO_4 \cdot 2H_2O$) single crystal being used for crystal growth/dissolution experiments (Giocondi and Orme 2006). Surface studies showed faceted etch pits (Fig. 25.7), and determination of the crystallography of these pits was needed in order to properly model the behavior. While X-ray diffraction is typically used for this type of characterization, the size of the crys-

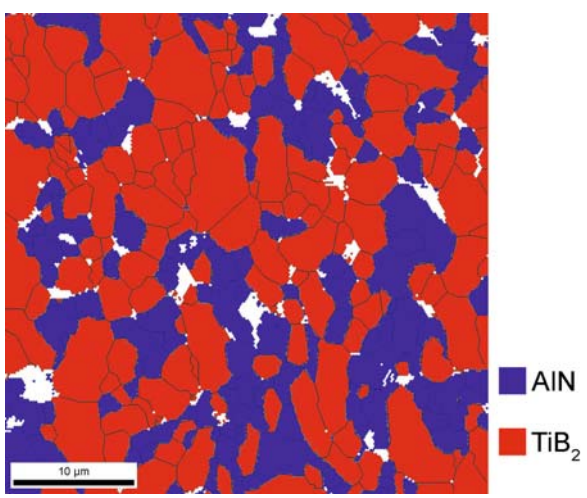


Fig. 25.6 Phase map identifying the phase of individual grains

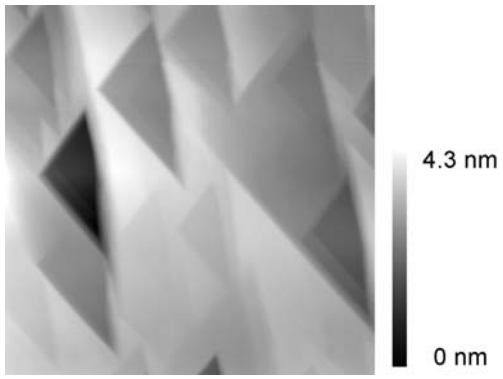


Fig. 25.7 Atomic force microscopy surface topography micrograph showing etch pits on a brushite single crystal

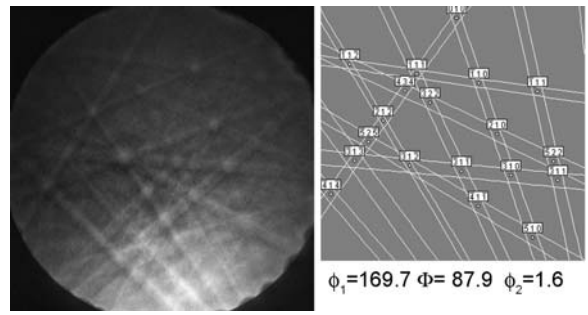


Fig. 25.9 Diffraction pattern from brushite single crystal. The orientation determined from indexing the diffraction pattern was used to simulate diffraction for verification

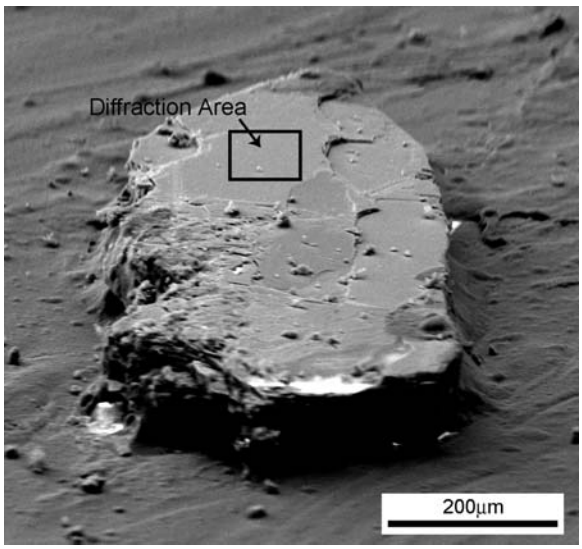


Fig. 25.8 SEM micrograph of the brushite single crystal examined

tals (see Fig. 25.8) made it difficult to yield a sufficient signal, leaving LV-EBSD potentially the sole alternative.

With the severe charging concern in mind, it is imperative that the beam not dwell on any area of the sample at any time. The first issue is the collection of the background signal. This was achieved by setting the microscope in scan mode and rastering the beam over an area that encompassed the whole sample at the fastest scan rate possible. While not ideal, this yielded a sufficiently accurate representation of the background. To collect the diffraction pattern, the beam was rastered at the highest scan rate again, although this time the area was limited to a small region on the crystal (shown in Fig. 25.8). This method was successful at yielding high-quality diffraction patterns, as shown in Fig. 25.9, and multiple patterns were collected from different areas of the crystal.

To index the diffraction patterns, two problems needed to be addressed first: how to accurately determine the pattern center, and which reflectors needed to be considered (no materials file for brushite exists). The pattern center was determined in a nontypical way: the exact working distance used in collecting the brushite diffraction patterns was noted, and the brushite crystal was removed and replaced with a silicon single crystal. The silicon crystal was then positioned at the exact same working distance, and reference patterns were collected. These patterns were then used to determine the pattern center.

To determine the appropriate reflectors, the powder diffraction file (PDF) for brushite was obtained from the International Centre of Diffraction Data (ICDD) database, and the most intense reflectors were used. Although this was a problem because its low symmetry (monoclinic) meant that there were a significant number of relatively strong reflecting planes, knowledge of the cleavage planes was used. Since brushite cleaves on either (010) or $(0\bar{1}0)$, and the sample being studied was prepared by cleavage of a larger crystal, the surface being examined could only be either of these planes. By rotating simulated patterns about both plane normals, it was determined that the surface being examined was indeed (010), and comparison of the simulated patterns with the acquired pattern was used to iteratively down-select the reflectors. The results

of this analysis are shown in the simulated pattern in Fig. 25.9.

Acknowledgments Part of this work was performed under the auspices of the U.S. Department of Energy by Lawrence Livermore National Laboratory, in part under Contract W-7405-Eng-48, and in part under Contract DE-AC52-07NA27344. We gratefully acknowledge Jennifer Giocondi and Christine Orme at LLNL for the brushite single crystals, as well as Tomoko Sano and James Campbell of the Army Research Laboratory for the ceramic composite.

References

Danilatos GD (1981) Design and construction of an atmospheric or environmental SEM (part 1). Scanning 4:9–20

Danilatos GD, Postle R (1983) Design and construction of an atmospheric or environmental SEM-2. Micron 14:41–52

Danilatos GD (1985) Design and construction of an atmospheric or environmental SEM (part 3). Scanning 7:26–42

Danilatos GD (1990) Design and construction of an environmental SEM (part 4). Scanning 12:23–27

Donald AM (2003) The use of environmental scanning electron microscopy for imaging wet and insulating materials. Nat Mater 2:511–516

Giocondi JL, Orme CA (2006) Unpublished data

Habesch SM (2000) Electron backscattered diffraction analyses combined with environmental scanning electron microscopy: potential applications for non-conducting, uncoated mineralogical samples. Mater Sci Tech 16:1393–1398

Mansfield JF (2000) X-ray analysis in the ESEM: a challenge or a contradiction. Mikrochim Acta 132:137–143

Meredith P, Donald AM, Thiel B (1996) Electron-gas interactions in the environmental SEM's gaseous detector. Scanning 18:467–473

Robinson VNE (1974) A Wet stage modification to a scanning electron microscope. 8th International congress for electron microscopy. Australian Academy of Science, Vol II, 50–51

Sano T, Glide G, Campbell J et al (2006a) Correlation between microstructure and mechanical properties for hot pressed TiB2-AlN composites. Presentation at the 30th international Cocoa Beach conference and exposition on advanced ceramics and composites, January 22–27, 2006. Cocoa Beach, FL

Sano T, Campbell J, Glide G et al (2006b) Investigation of the synergistic effect on the flexural strength of TiB2-AlN by microstructural characterization. Poster at the Gordon research conference for solid state studies in ceramics, August 13–17, 2006. Proctor Academy, Andover, NH

Sigee C (1998) Environmental SEM and X-ray microanalysis of biological materials. Mikrochim Acta 15:283–293

Sztwiertnia K, Faryna M, Sawina G (2006) Misorientation characteristics of interphase boundaries in particulate Al_2O_3-based composites. J Eur Cer Soc 26:2973–2978

Timofeeff MN, Lowenstein TK, Blackburn WH (2000) ESEM-EDS: an improved technique for major element chemical analysis of fluid inclusions. Chem Geol 164:171–182

Chapter 26

EBSD in the Earth Sciences: Applications, Common Practice, and Challenges

David J. Prior, Elisabetta Mariani, and John Wheeler

26.1 Development of EBSD in Earth Sciences

In the Earth's middle and lower crust and mantle, rocks deform by creep, and it has long been recognized that lattice preferred orientations[1] (LPO) of the mineral constituents in deformed rocks yield useful information on creep deformation mechanisms, conditions, and kinematics (Leiss et al. 2000; Turner and Weiss 1963; Wenk and Christie 1991). Bulk LPO data are traditionally measured by X-ray texture goniometry, and more recently using neutron and synchrotron sources (Leiss et al. 2000).

Although bulk LPOs are valuable, considerable extra information can be obtained with spatially resolved crystallographic measurements, most particularly the misorientations between grains—or more generally between measured data points (Randle 2004; Wheeler et al. 2001)—and/or the orientation relationships between phases. Many minerals have anisotropic optical properties, and it is possible to measure components of crystallographic orientations in thin sections of rock (30 μm-thick slices stuck to glass) by using a universal stage (goniometer stage) on a transmitted light microscope (Turner and Weiss 1963). Where the optical indicatrix has higher symmetry than the crystal, extra information from cleavage or twin plane measurements enables full orientation measurement. Such measurements can be made for individual grains or subgrains down to a few 10s of micrometres in size (the limit is the thickness of the thin section). The value of such data was first recognized in the early part of the 20th century by Sander (1930, 1970). The AVA (Achsenverteilungsanalyse) diagram Sander developed to represent such data is recognizable as the precursor of orientation maps generated from electron backscatter diffraction (EBSD) data. Manual collection of orientation data using a universal stage has provided the basis of some fundamental concepts: the subgrain rotation recrystallization mechanism (Poirier and Guillope 1979), for example. Such optical measurements are rather slow, and although they have been critical in developing large LPO databases, particularly for quartz (Law 1990; Schmid and Casey 1986), their use in collecting AVA-type data has been more limited. More automated optical methods have been explored over the years; the most successful and widely applied being the computer integrated polarization technique (CIP: Heilbronner and Pauli 1993) that provides AVA diagrams and LPO data related to quartz and calcite *c* axes (e.g., Oesterling et al. 2007; Pauli et al. 1996).

Electron diffraction provides spatially discriminated measurements of crystallographic orientation. Transmission electron microscopy (TEM) can be used, and some maps of crystal orientations and misorientations have been published (Fliervoet and White 1995; Shigematsu 1999; White 1977). However, the difficulty of using TEM to collect large data sets has limited more general application. Selected area electron channeling patterns (SAECP: Joy and Newbury 1972; Lloyd 1987) in the scanning electron microscope

[1] In geology the term texture is most commonly used to refer to the microstructure of a rock. Lattice preferredorientations (LPO) or crystallographic preferred orientations (CPO) are the terms most commonly applied by geologists to mean the same as the term texture used by metallurgists.

D.J. Prior (✉)
Department of Earth and Ocean Sciences, University of Liverpool, Liverpool, L69 3GP UK
e-mail: davep@liv.ac.uk

A.J. Schwartz et al. (eds.), *Electron Backscatter Diffraction in Materials Science*,
DOI 10.1007/978-0-387-88136-2_26, © Springer Science+Business Media, LLC 2009

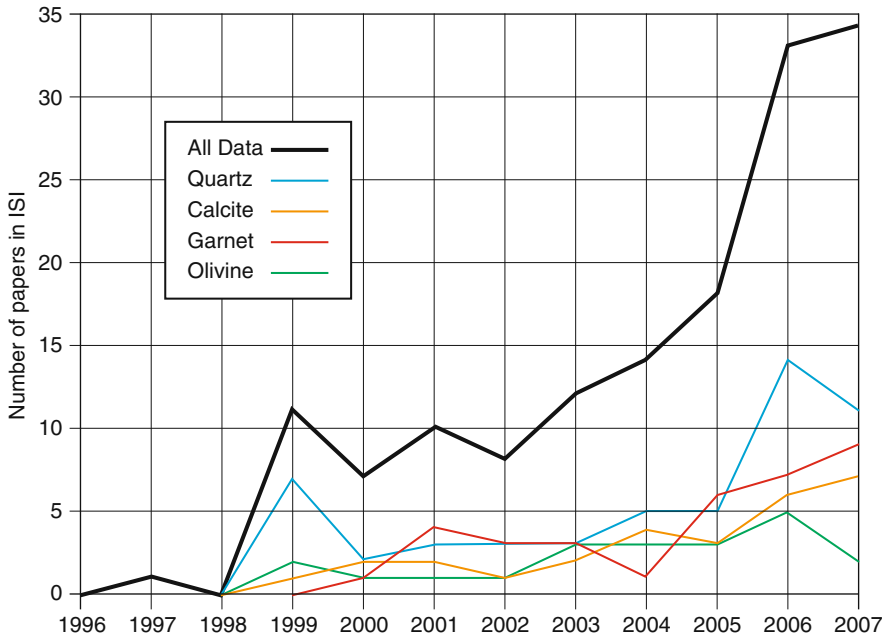


Fig. 26.1 Number of EBSD papers per year from the ISI web of science using title search terms "EBSD AND calcite," "EBSD AND garnet," "EBSD AND olivine," and "EBSD AND quartz" in the topic. "All data" is the sum of these 4 searches. These data underestimate the total number of geological EBSD publications and miss some key papers. Nevertheless, the data reflect well the growth in geological EBSD literature

(SEM) can be used to measure the full crystallographic orientation of any mineral. EBSD and SAECP give comparable information. Two forward-looking papers by Lloyd (Lloyd 1994; Lloyd et al. 1991) lay out a scientific agenda for application of SAECP, that is equally applicable to EBSD. EBSD (Venables and Harland 1973) was emerging as a practical technique (Adams et al. 1993; Dingley 1984) at about the same time as the geological applications of SAECP were under development; and although EBSD is simpler to apply, it was not considered seriously by geologists in the 1980s and early 1990s. The prime reason for this was that there was no perceived way of using imaging to locate EBSD data within the sample microstructure. The first published EBSD data from a rock (Kunze et al. 1994) used automated indexing and orientation mapping to get around this: the microstructure image was rebuilt from a grid of orientation measurements—as is familiar to all modern EBSD users. In the mid 1990s such methods were not generally applicable, because many minerals had severe misindexing problems. Thus the approach of using solid state detectors mounted below a tilted sample or attached to the EBSD camera (forescatter detectors: Day 1993; Day and Quested 1999) was adopted (Prior et al. 1996; Trimby and Prior 1999) to provide a qualitative orientation contrast image for the location of manually indexed EBSD data (Boyle et al. 1998; Faul and FitzGerald 1999; Fliervoet et al. 1999; Prior et al. 1999; Trimby et al. 1998). Automated EBSD and orientation mapping have become more prevalent as misindexing has become less problematic. Figure 26.1 shows that there has been a dramatic increase in EBSD-based publications in earth sciences in the last decade.

26.2 Current Practice, Capabilities, and Limitations

26.2.1 Range of Materials and Preparation

The full range of minerals to which EBSD has been applied is large and growing, although the literature is dominated by data from quartz, olivine, calcite, garnet, and pyroxenes (Figs. 26.1 and 26.2). EBSD data can be collected from natural or broken surfaces. However, most laboratories prepare polished sample surfaces for analysis. Polished thin sections are commonly used because they allow the samples to be analysed using transmitted light optics and because the polish quality is generally better than a sample block. For the vast majority of minerals (silicate, oxide, carbonate, and sulphide), preparation by mechanical

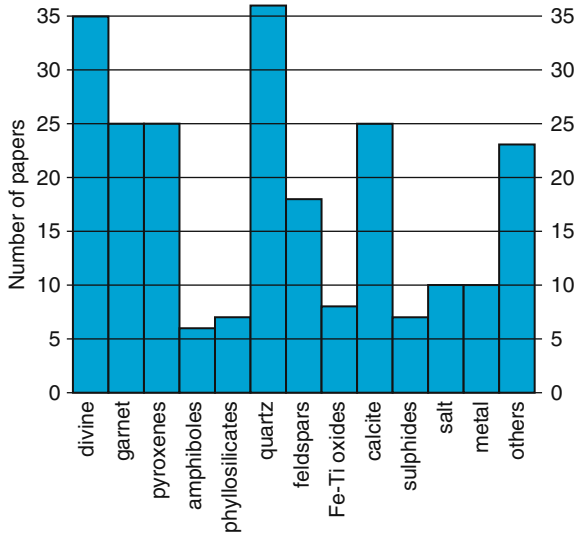


Fig. 26.2 Chart of the number of papers in the earth sciences that present EBSD data from specific minerals, mineral groups, and metals (in rocks and meteorites). These are compiled manually from a reference data file kept by the authors. Full references are not given for reasons of brevity

polishing followed by chemical mechanical polishing (Lloyd 1987; Prior et al. 1996) enables good quality EBSD patterns to be collected. Halite (Trimby et al. 2000) needs special treatment. Reduction/elimination of charge is commonly achieved by a few nm of carbon coat or by using a low vacuum in an environmental/variable pressure SEM (Habesch 2000). Both methods reduce slightly the intensity, contrast, and clarity of EBSD patterns. Highly porous samples can be dealt with by coating thickly with gold, repolishing, and then coating with carbon (Watt et al. 2006). The gold provides good conductivity across the pore spaces.

There are very few minerals that cannot be analyzed by EBSD. Some minerals create severe misindexing issues (see 26.2.4) that may limit the applicability of automated analysis; such minerals can always be examined manually. The most consistently problematic minerals are phyllosilicates, including micas and clay minerals. EBSD is used to distinguish clay polytypes (see, e.g., Kameda et al. 2005; Kogure 2002). This is done by looking at individual, separated clay grains lying on their basal plane. Attempts to analyse phyllosilicates in their microstructural context in a rock have been less successful. Valcke (Valcke 2003; Valcke et al. 2006) showed that clay minerals give poor indexing biased towards particular orientations, and can give unreliable LPO data. We have had similar experiences with micas. It is not yet clear whether this is an inherent feature of phyllosilicate structure or whether it is an artifact of preparation. New methods of sample preparation (based on ion milling) may provide solutions to phyllosilicate indexing problems.

26.2.2 Speed of Data Collection

The speed with which EBSD data can be collected depends on the mineral species. Simple structures such as NaCl, MgO, and perovskite can be indexed at 40–70 points per second; but most minerals are considerably slower, generally less than 20 points per second, and in some cases as slow as 1 or 2 points per second. Newer high-speed cameras do not yet impinge significantly on these figures. Unlike fcc metals, where the rate limiting step is the transfer speed of the EBSD patterns, the rate limit for mineral analysis is either the time required to gather enough signal (signal levels are lower than those for metals), or the computation time involved in indexing correctly the more complex structures. Although the signal level can be increased by increasing the beam current, most instruments have a limited beam current range for practical use, beyond which electron optics depreciate significantly.

26.2.3 Spatial Resolution

In principle, spatial resolutions should be no different to those achieved in metals or other industrial materials (Humphreys and Brough 1999). Few geological samples that have structures fine enough to test to the limits of EBSD resolution have been examined. We have worked in olivine (Watt et al. 2006), clinopyroxene, Fe-Ti oxides, and pyrite (Ohfuji et al. 2005) with step sizes as small as 50 nm, to collect data that have a 50 nm resolution (i.e., grain boundaries appear 1 pixel wide). Examples of high-resolution data in olivine are shown in Fig. 26.3. Attempts to achieve these resolutions in fine-grained quartz and feldspar samples have failed; this is because these materials suffer beam damage. Maximum resolutions achieved in quartz are about 250 nm, corresponding to the size

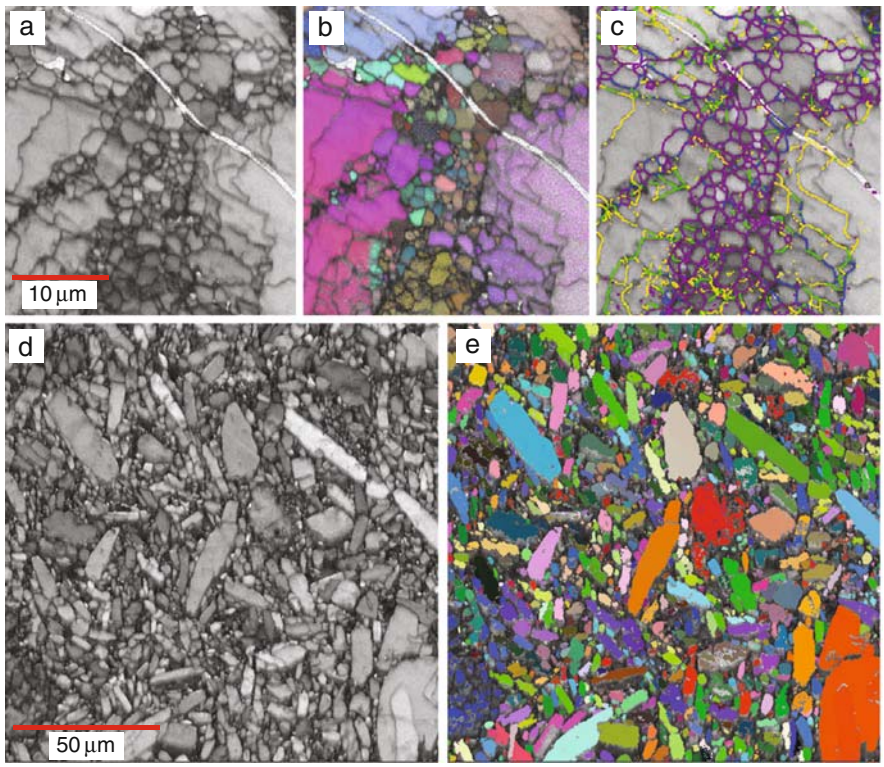


Fig. 26.3 High resolution EBSD data from olivine. (**a**) Pattern quality (band contrast) map of experimentally deformed and recrystallized olivine: 75 nm step size; sample courtesy of Z. Jiang at Yale. (**b**) All Euler colours superposed on pattern quality. (**c**) Grain boundaries superposed on pattern quality: *yellow* 2°–5°, *green* 5°–10°, *blue* 10°–20°, *purple* >20°. (**d**) Pattern quality (band contrast) map of the matrix of the Allende meteorite: 100 nm step size; sample courtesy of L. Howard at the Natural History Museum. This sample has a very high porosity. (**e**) All Euler colours superposed on pattern quality

of the damage halo associated with typical acquisition conditions and times. Resolution is best in the direction normal to the beam (the scanning direction), and this can be exploited to improve resolution on line scans (Haddad et al. 2006).

26.2.4 Misindexing

An ever present and evolving problem for geological users of EBSD is errors in the indexing process. We use the term misindexing to refer to points that are assigned an orientation that is different from the correct solution by an angle significantly greater than the angular error inherent in the EBSD indexing procedure (a degree at most). Nonindexing refers to points for which a solution cannot be found within predefined confidence limits (based on mean angular deviation or votes, depending upon the indexing algorithm) or within a predefined computation time or number of computational cycles. Geological users are used to much higher levels of misindexing/nonindexing than metallurgists. The principal reasons are the lower levels of signal in the EBSD patterns and the fact that lower symmetry materials have a more continuous spectrum of inter-band angles inherent in their structure; so that there is a greater likelihood of the set of angles measured from a pattern fitting more than one set of lattice planes, within prescribed angular tolerances. Often the misindexing will be systematic, and the misorientations across the boundaries between correctly indexed and misindexed points will be rational, high-angle rotations (Fig. 26.4b). This is because many low symmetry structures are a small distortion of (or deviations from) a higher symmetry structure. If the angular deviation from the higher symmetry structure is of the same order as, or smaller than, the angular tolerances used in EBSD indexing, then misindexing that has a rational axis and angle is likely. Such systematic misindexing corresponds to a symmetry operation in the higher symmetry structure, and can correspond to known twin operations; so that the presence of particular misorientations alone cannot then be used to filter out misindexed points. Correct indexing is often dependent on having different diffraction intensities for pseudosymmetrically equivalent diffraction bands. At present indexing algorithms

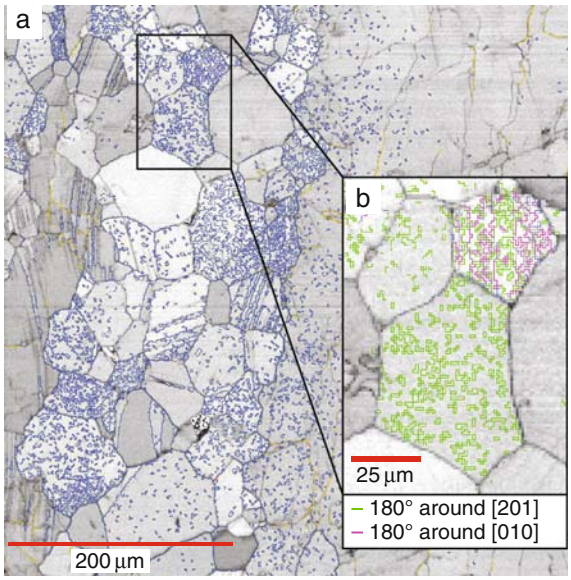


Fig. 26.4 Errors in automated EBSD mapping. Data are from plagioclase feldspar (Jotunheimen anorthosite from same location as Kruse et al. (2001). Step size 1 µm. (**a**) High angle boundaries (>10° in *blue*) superposed on a pattern quality (band contrast) map. The real grain boundaries and twin boundaries are mapped. In addition, many grains contain a checkerboard of misindexed points that give rise to a checkerboard of boundaries that are artifacts. Note the heterogeneity of error distribution. Some grains contain multiple errors; others have very few errors. (**b**) Inset shows that many of the error boundaries have rational misorientations indicating systematic misindexing

do not use intensities in a sophisticated way; using measured intensities may help reduce misindexing problems.

Having good quality patterns and having the camera as close as is physically possible to the sample are both crucial to minimizing errors. The common practice is then to set the indexing parameters in the data acquisition software (such as the number of Kikuchi bands used, or the resolution of patterns or of Hough space) to minimize the level of misindexing and nonindexing, whilst maintaining enough indexed points to reconstruct the sample microstructure with sufficient detail to achieve the scientific aims and without introducing artifacts that impinge on the data. Misindexing is more of a problem than nonindexing, so the parameters are usually set to effectively eliminate the former whilst minimizing the latter. If misindexing and nonindexing levels are too high, acquisition times and/or beam current can be increased to improve pattern quality. Our instruments can achieve indexing rates as high as 98–99% in fcc metals. In comparison, the highest indexing rates we have ever achieved in a rock are ~95% in a clean, single phase calcite sample. 70–80% indexing would be considered good. Real rocks tend to be polyphase and dirty, and indexing rates on the order of 50% are good for some samples.

Automated EBSD data need to be treated with caution in materials with high rates of misindexing and/or nonindexing. If map data are collected with sufficient resolution that the orientation map can be compared directly with a pattern quality map (i.e., each grain or subgrain contains many 10s of pixels), then misindexed points can be recognized as checkerboard patterns in the orientation data that are not visible in the pattern quality map (Fig. 26.4). As long as misindexed points are clearly subordinate to correctly indexed points in all grains (average <5% misindexing; with heterogeneity this may mean that some grains have 20–30% misindexed points) and overall indexing rates (within regions of the phases being indexed) are on the order of 50% or greater, map data can be reconstructed reliably using processing procedures as discussed below. Improvements in commercial indexing algorithms over the last few years are such that, with the camera positioned very close to the sample, all minerals that give good patterns can be mapped with sufficiently small error levels for the data to be useful.

Data processing is an essential tool for geological users, who need to eliminate errors and artifacts. Exact procedures depend upon the scientific requirements (see, for example, Bestmann and Prior 2003; Prior et al. 2002; Toy et al. 2008). Simple procedures, such as the replacement of single pixels that are different (by some misorientation) from all eight neighbours, are only appropriate in data with high indexing rates and very low misindexing rates. In most geological data sets indexing rates and misindexing rates are often heterogeneous: one grain may be fully indexed with no errors, another indexed correctly but with only a 10% indexing rate, and a third indexed with a 30% misindexing rate, as illustrated in Figs. 26.4 and 26.5. Such data need more sophisticated processing. "Growth" routines (we use the extrapolation routines in HKL software), in which nonindexed pixels with n neighbours that are the same orientation within a given tolerance take on the average orientation of those n neighbours, are a key tool. Growth to completion on the basis of 8, 7, or 6 neighbours does not create significant microstructural artifacts, nor does one step

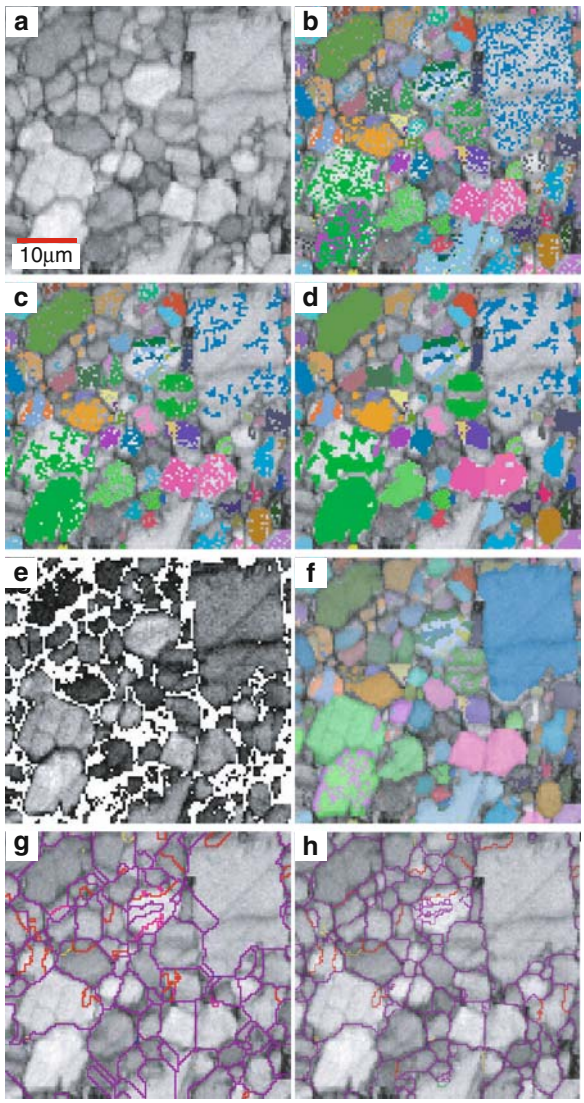


Fig. 26.5 Processing of EBSD data. Data are from an experimentally deformed anorthosite: sample courtesy of J. Tullis at Brown. Step size 200 nm (**a**) Pattern quality (band contrast) map. (**b**) Raw EBSD data. Note the heterogeneity in indexing level and misindexing. (**c**) Raw data with "small grains" removed. (**d**) Raw data with "small grains" removed and grains grown on the basis of 5 neighbours. (**e**) Pattern quality (band contrast) template used in data processing. (**f**) Data (all Euler colours) grown on the basis of 3 neighbours, with growth limited to the *grey* pixels in the template (**e**). (**g**, **h**) Grain boundary maps superposed on pattern quality: misorientations are: *yellow* 2°–5°, *green* 5°–10°, *blue* 10°–20°, *purple* >20°. Twin boundaries are *red*; (**g**) is the result of growing data on the basis of 3 neighbours without any restrictions, (**h**) is the result of growing data on the basis of 3 neighbours, limited by a set of templates (3 different thresholds), as shown in (**e**) and (**f**)

of growth on the basis of 5 neighbours (Fig. 26.5d). However, areas with low indexing rates will not be reconstructed. Growth on the basis of smaller numbers of neighbours can generate significant microstructural artifacts (Fig. 26.5 g). An approach that avoids this and works very well for samples with heterogeneous indexing rates is to use the pattern quality map as a template. In this approach, a threshold in pattern quality is picked (Fig. 26.5e) so that grain boundaries are not included, and growth, on the basis of <5 neighbours, is limited to pixels with pattern quality higher than this threshold (Fig. 26.5f). This can be repeated with several different thresholds to give an accurate final microstructure (Fig. 26.5 h). As long as misindexing is kept low (∼<20% in any given grain—the worst case grains) then misindexed points will not "grow" and can be eliminated by a size filter.

Mapping at a level of detail in which all errors can be identified is not always the most appropriate data collection strategy; the most efficient way of collecting LPO data uses step sizes of the same order as the grain size (in equigranular samples). However, there is no way to verify the data collected, and the present authors limit such analyses to minerals (such as calcite) in which we have a very high level of confidence that indexing is robust. Rapid collection of LPO data in minerals in which there is some scope for indexing error, but in which the problems are not very severe, such as quartz, olivine, pyroxenes, and garnet, can be achieved by setting a step size at ∼0.25 to 0.5 of the grain size. Processing of the data to define grains (Fig. 26.6) and elimination of grains below a certain size threshold (some small number of pixels) enable robust data to be collected. Data from minerals with more severe indexing problems (such as plagioclase feldspar) need to be collected with a step size small enough to compare the microstructure reconstructed from EBSD data with the image built from pixel-by-pixel measurements of pattern quality or band contrast, as outlined in the previous paragraph.

26.2.5 Polyphase Samples

Most rocks are polyphase and the ability of EBSD indexing to distinguish distinct phases becomes crucial. There is the potential for another kind of misindexing, in which a mineral is indexed as the wrong

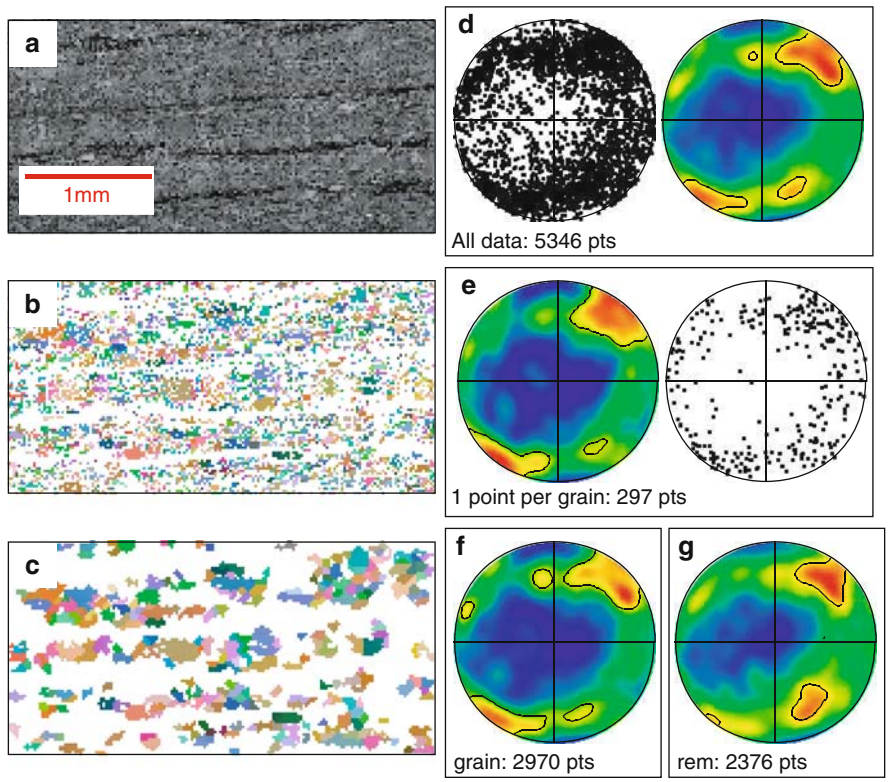


Fig. 26.6 Quartz data set collected for LPO analysis. Alpine fault mylonite sample (Toy et al. 2008). Step size 20 μm. (**a**) Pattern quality (band contrast) map. Quartz comprises ~ 60% of the sample; the layered structure relates to layers of mica (*dark*) and layers of quartz (with some feldspar). (**b**) Indexed points (all Euler colours). These are raw data; only quartz is indexed. (**c**) Processed data "grown" on the basis of 5 neighbours followed by removal of all grains <60 μm (3 pixels). (**d**) [0001] for all (raw) data. (**e**) [0001] with 1 point for every grain in (**c**). (**f**) [0001] for all raw data in the areas defined by the grains in (**c**). (**g**) Data excluded in (**f**) i.e., data in (**d**) minus data in (**f**)

phase. Distinction of minerals that are structurally distinct is not a problem. However, rocks can contain different minerals that remain indistinguishable by EBSD alone. Many minerals comprise solid solutions, and a rock may contain more than one distinct composition of those minerals. In practice, distinction of different compositions of clinopyroxene, amphibole, garnet, olivine, and plagioclase by EBSD alone is impossible using current, commercially available indexing routines. One can see why by examining the range of β angles in clinopyroxenes: diopside $\beta = 105.8^\circ$, jadeite $\beta = 107.6^\circ$, augite $\beta = \sim 105^\circ$, pigeonite $\beta = 108.5^\circ$ (Deer et al. 1992). The interplanar angular variations through the pyroxene series are below typical angular tolerances in indexing routines (on the order of a few degrees or more). Perhaps use of intensities or orders of diffraction in indexing may help. A simple experiment in which the patterns of two different compositions of plagioclase feldspar are compared (Fig. 26.7) suggests that the patterns are effectively identical. Thus distinction of some minerals, particularly different compositions in the same solid-solution, requires the interactive use of EDX data. Because this slows down data acquisition, new procedures, such as multivariate statistical approaches (Brewer et al. 2008), may be worth exploring.

26.3 Application of EBSD in Earth Sciences

A paper published in 1999 (Prior et al. 1999) outlines areas of the earth sciences in which EBSD might provide scientific insights. Although that paper failed to

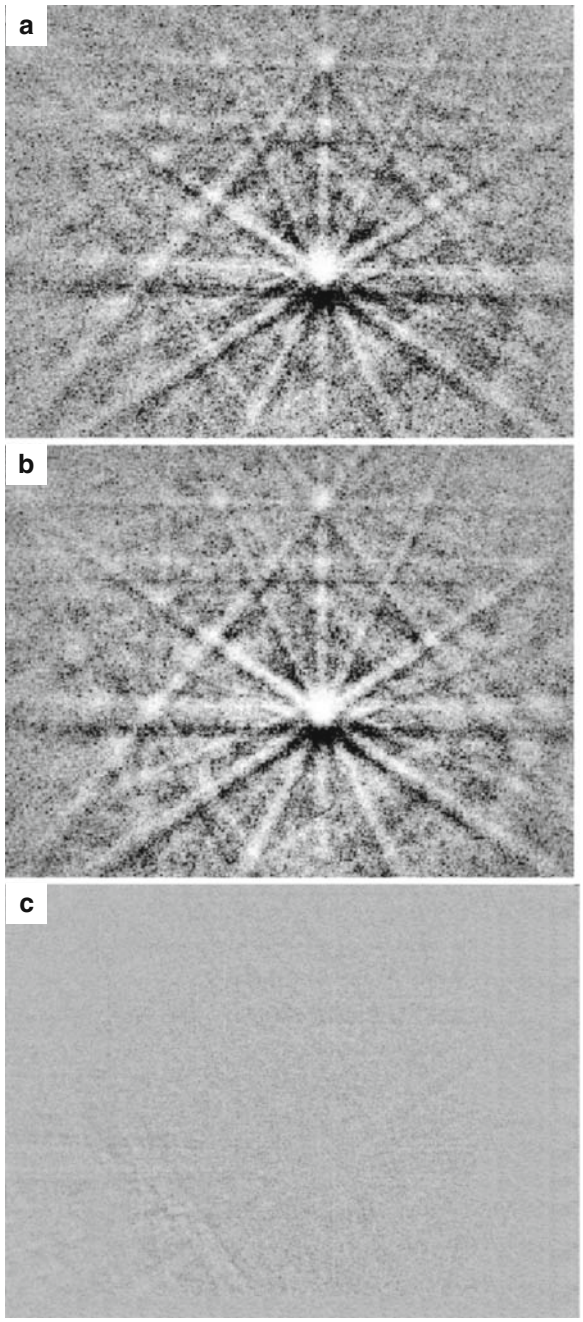


Fig. 26.7 EBSD data from a single, undeformed crystal of plagioclase feldspar zoned in composition from core to rim (see Fig. 4 in Trimby and Prior 1999). Patterns have been normalized (by subtraction of an inverted Gaussian blur followed by stretching) to remove any background or overall intensity differences. (**a**) Pattern from the rim (composition An_{35}). (**b**) Pattern from the core (composition An_{65}). (**c**) Digital subtraction of the core pattern from the rim pattern. The *weak lines* that can be seen can be removed, with creation of similar lines in another part of the image, by any 1-pixel movement of one pattern relative to the other

recognize the speed with which automated orientation mapping would come to dominate EBSD technology, the scientific applications highlighted remain the core of EBSD applications. Here we review the contribution that EBSD has made over the last decade.

26.3.1 Rock Deformation and Solid Earth Geophysics

The analysis of rocks deformed by creep mechanisms (hot worked), both in nature and in the laboratory, still represents the major area of research dependent upon EBSD in the earth sciences. The dominance of a few minerals in the EBSD literature is because these minerals—quartz (the most common mineral in the earth's upper crust), olivine (the most common mineral in the earth's upper mantle) and calcite (important in mountain belts such as the Alps)—have been of particular interest in rock deformation studies. EBSD provides the fastest way of generating LPO data (a few minutes to an hour for ~1000 grains, depending on the sample) and is applied to deformed rocks (e.g., Bestmann et al. 2000; Mainprice et al. 2004; Skemer et al. 2006; Toy et al. 2008) and deformation experiments (e.g., Heidelbach et al. 2003; Katayama et al. 2004; Pieri et al. 2001). The use of LPO data to model anisotropic physical properties, most particularly seismic velocity anisotropies (Mainprice 2003), has expanded with the development of EBSD methods (e.g., Tatham et al. 2008; Valcke et al. 2006; Vauchez et al. 2005; Vonlanthen et al. 2006). David Mainprice in Montpellier has developed a series of tools[2] that aid texture quantification and calculation of physical property anisotropies from these data.

LPO data are used to constrain dislocation creep slip systems (Wenk and Christie 1991), by comparison with numerical models of intracrystalline slip (e.g., Mainprice et al. 2004); and more commonly by suggesting that lattice planes aligned with foliation (~rolling plane) represent easy slip planes, and lattice directions aligned with lineation (~rolling direction) represent easy slip vectors (e.g., Katayama et al. 2004;

[2] ftp://www.gm.univ-montp2.fr/mainprice//CareWare_Unicef_Programs/

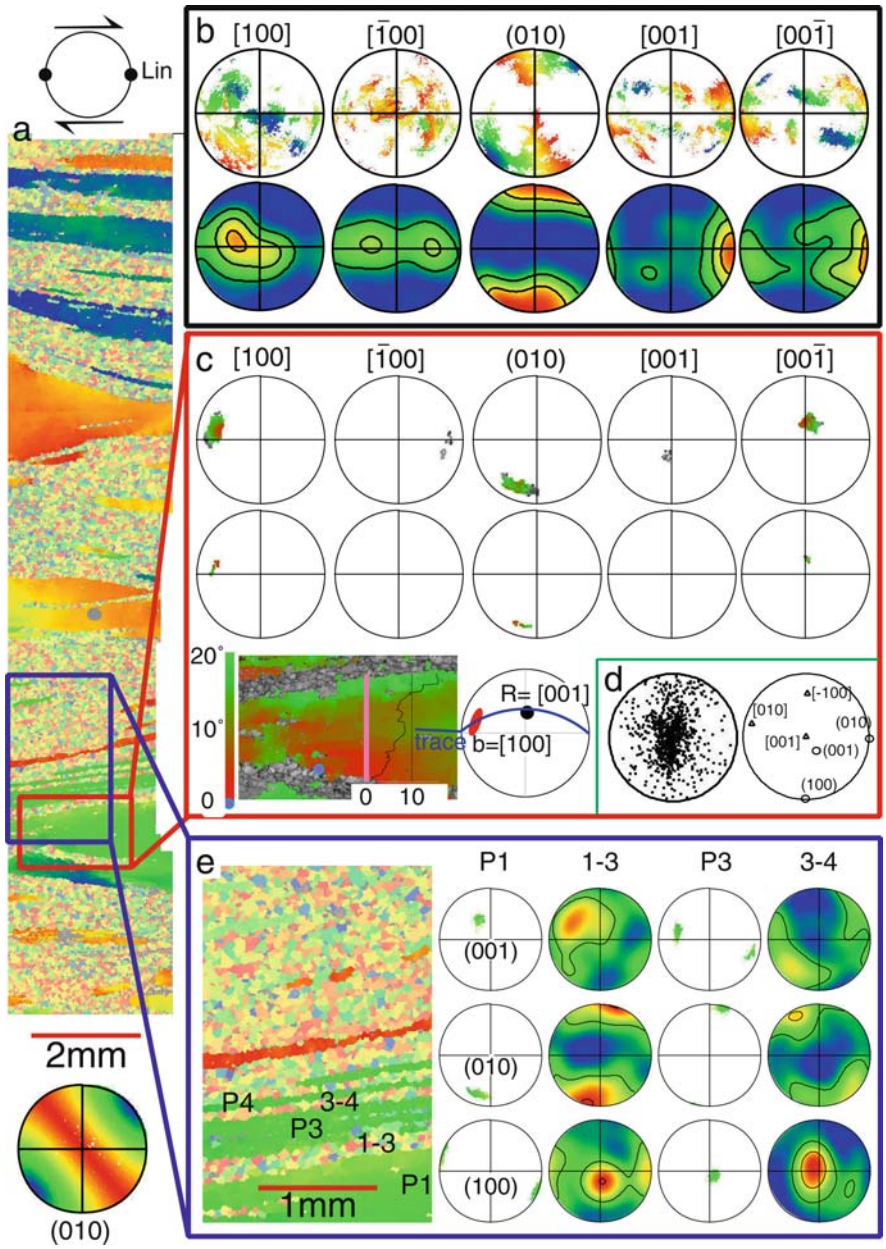


Fig. 26.8 EBSD data from a deformed plagioclase feldspar–rich rock (Jotunheimen anorthosite from same location as Kruse et al. (2001). (**a**) Map with step size 10 μm coloured according to the (010) orientation as shown in pole figure at the *bottom*. Reference frame shown above the map (Lin is lineation = rolling plane). (**b**) LPO data from the 68 porphyroclasts (large deformed grains) in (**a**). (010) Poles are clustered parallel to the pole to foliation and [001] parallel to lineation. (**c**) Data from one porphyroclast, shown in the inset map. Inset is coloured according to misorientation from the *blue dot*. *Top row* of stereonets are from whole of this porphyroclast. *Bottom row* are from the *pink line*, perpendicular to foliation. *Black irregular line* shows misorientation angle relative to *blue dot*, scale at bottom of the image. Stereonet next to image shows an interpretation of the geometric dislocations necessary to explain the distortions. R = rotation axis, b = burgers vector. Subgrain boundary plane, marked in *blue*, is measured using a universal stage and corresponds to the trace marked on the image. (**d**) Misorientation axis data from the porphyroclast shown in (**c**) plotted in inverse pole figure (IPF) together with IPF key of principle planes and directions. (**d**) Orientations of recrystallized grains (contoured plots with 15° counting cone) immediately adjacent to porphyroclasts (point data stereonets). Recrystallized grains inherit porphyroclast orientations, but have a much broader orientation spread

Mehl and Hirth 2008; Skemer et al. 2006). For example, the data shown in Fig. 26.8b is interpreted as deformation with (010)[001] as the easy slip system.

The microstructural information from orientation mapping EBSD data is becoming more important. The example used here to illustrate the importance of this type of analysis is a deformed rock (Figs. 26.8, 26.9, and 26.10) that is dominated by the triclinic mineral plagioclase feldspar. Triclinic materials have distinct advantages for misorientation analysis. There is only one way to describe the misorientation (disorientation = misorientation) and inverse pole figure (IPF) space is large so that, if axis errors are large (as will be the case for low angle boundaries), distinguishing different misorientation axes is potentially easier than in higher symmetry systems. Thirty percent of the earth's crust comprises plagioclase feldspar (solid solution from albite [$NaAlSi_3O_8$] to anorthite [$CaAl_2Si_2O_8$]); the behaviour of this mineral is of considerable importance to geologists.

Understanding of recovery and recrystallization is one area where EBSD mapping and misorientation analysis has been particularly important. The existing recrystallization models (Poirier and Guillope 1979; Urai et al. 1986; White 1977) applied in earth sciences, such as subgrain rotation recrystallization and grain boundary bulging (see Fig. 1 in Halfpenny et al. 2006), have geometric consequences that are testable with EBSD: particularly in cases where "parent" and "daughter" grains can be identified. Some new data from MgO (Mariani et al. 2009) are consistent with subgrain rotation models (that were based primarily on olivine and salt) and contrast to a growing body of data from other minerals, suggesting some material dependence of recrystallization behaviour and/or resultant microstructures. EBSD data from dynamically recrystallized calcite, quartz, orthopyroxene, plagioclase (Fig. 26.8e), and garnet show that the orientation spread of recrystallized grains is larger than that of the deformed parent (e.g., Bestmann and Prior 2003; Halfpenny et al. 2006; Mehl and Hirth 2008; Skemer and Karato 2008; Storey and Prior 2005). Typically, porphyroclasts (relict old grains) contain subgrain structures defined by low angle grain boundaries (usually $<5^\circ$) that have misorientation axes aligned with rational crystallographic directions (Bestmann and Prior 2003; Halfpenny et al. 2006; Storey and Prior 2005), supporting an origin from the recovery of dislocation creep deformation. An example of such data from plagioclase is shown in Fig. 26.8c. In contrast, boundaries between porphyroclasts and recrystallized grains are high angle (generally $> 30^\circ$: Fig. 26.9) and have random misorientation axes (Fig. 26.10). These data suggest that simple physical recrystallization models alone cannot always account for all observed microstructures. Grain boundary sliding of recrystallized grains, in addition to simple rotation and bulging mechanisms, provides a way to explain the observations.

Intragrain EBSD maps allow us to constrain slip systems from the internal distortions within grains (Lloyd et al. 1997; Prior et al. 1999, 2002). Some information comes from the low-angle misorientation axes alone (e.g., Bestmann and Prior 2003), but a fuller constraint requires analysis of the grain boundary plane or

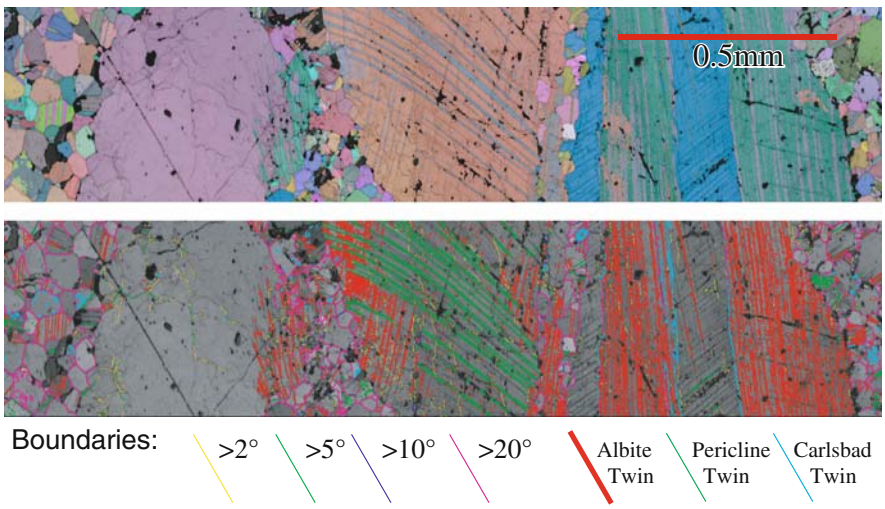


Fig. 26.9 Detailed data from the same sample as Fig. 26.8 (note: data are rotated 90°). Step size 1 μm. (**a**) All Euler map. (**b**) Grain boundary map superposed on pattern quality. Note that all boundaries between porphyroclasts (large, distorted grains) and recrystallized grains (small, equant, and undistorted) are high angle. Twin laws from Deer et al. (1992)

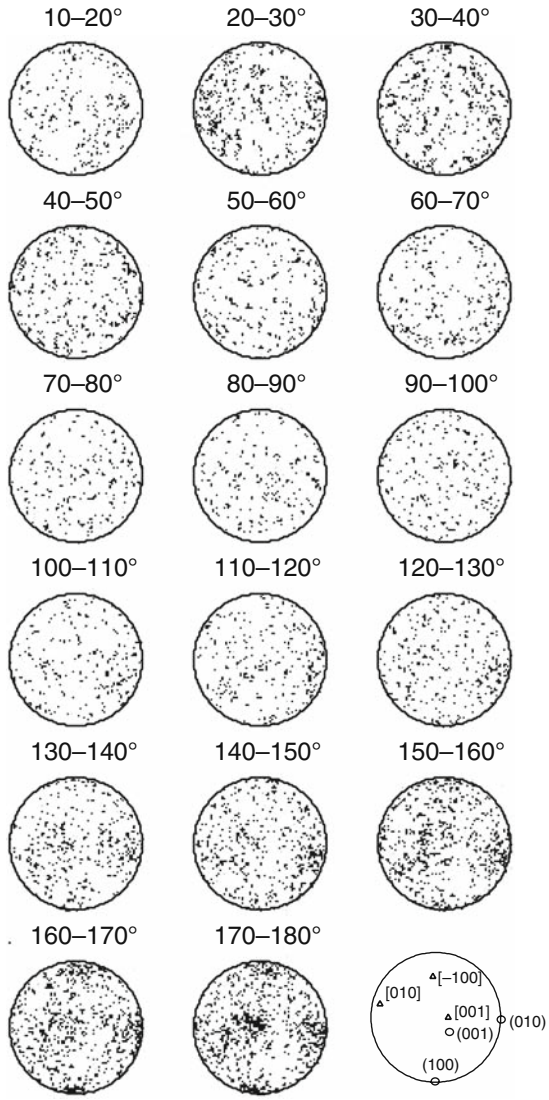


Fig. 26.10 Misorientation axes between porphyroclasts and neighbouring recrystallized grains extracted from the data set shown in Fig. 26.8. All are random, except the data $>160^{\circ}$, which show some inheritance of twin relationships with concentrations around known twin axes

grain boundary trace (Prior et al. 2002). We illustrate this with an example from plagioclase (Fig. 26.9c) in which we have misorientation data and measurements of subgrain boundary planes using a universal stage. The only known slip system that can explain the misorientation and boundary planes is (010)[100], with these dislocations arranged in a tilt wall. This result is consistent with TEM data (Kruse et al. 2001). In contrast, LPO data (Fig. 26.9b) suggest (010)[001] as the easy slip system. Analysis of a number of samples in a range of minerals yields different slip systems, from a misorientation analysis of distorted porphyroclasts to those interpreted from LPOs. This observation may be important in understanding dislocation-based deformation mechanisms in rocks.

26.3.2 Metamorphic Processes

Metamorphic rocks are those rocks whose mineralogy and/or microstructure change, driven by changes in rock temperature or pressure. Many metamorphic rocks are also deformed, and the high temperature deformation processes detailed in Section 26.3.1 can also be thought of as metamorphic processes. There is another important application of EBSD, however, namely, to the understanding of the mineral reaction processes and associated microstructural changes that occur during metamorphism. The potential for application to metamorphic problems was preceded by comparable work using SAECP (Lloyd et al. 1991). Interestingly, the majority of EBSD work on metamorphic problems relates to microstructures of the mineral garnet (e.g., Hawkins et al. 2007; Hirsch et al. 2003; Mainprice et al. 2004; Prior et al. 2002; Spiess et al. 2001; Storey and Prior 2005; Terry and Heidelbach 2004; Trepmann and Stockhert 2002; Whitney et al. 2008). Garnet is an important metamorphic mineral in the earth's crust and mantle, not because it is volumetrically significant, but rather because it is a mineral on which we often depend for estimates of rock pressure and temperature and for dating of metamorphic events, and because we interpret inclusion fabrics in terms of the rocks' thermomechanical history (see introduction in Whitney et al. 2008). The focus of EBSD studies on garnet may relate to the fact that garnet is optically isotropic, and until the mid 1990s we were blind to the full range and complexity of garnet internal microstructures. One extremely important outcome of these studies is the demonstration that we can develop large garnet grains by the coalescence of many smaller grains (Spiess et al. 2001; Whitney et al. 2008) grown from distinct nuclei; and that the misorientations between grains may be nonrandom, due to selection processes or rotations that modify the microstructure.

26.3.3 Meteorites

Although meteorites would seem an obvious target for EBSD studies, applications in meteoritics have come relatively slowly. Studies of stony meteorites have been focussed on the fabrics of the fine-grained olivine matrix (Sephton et al. 2006; Watt et al. 2006), and the implications these data have for the early history of the solar system and in using microstructures to help understand the thermal history of asteroidal bodies (Whattam et al. 2008). This area of study is clearly in its infancy. Detailed studies of metallic meteorites have been conducted by scientists in the physical metallurgy field (Goldstein and Michael 2006; He et al. 2005; Hutchinson and Hagstrom 2006; Nolze et al. 2006), and have focussed on understanding the α–γ orientation relationships in Fe-Ni metal.

26.3.4 Other Areas

EBSD is developing as a tool to constrain potential diffusion pathways and diffusion length scales in minerals. EBSD is used to examine the substructures of minerals used in radiometric dating, to characterise heterogeneities within minerals (Prior et al. 1999; Reddy et al. 2001), and to assess the potential for resetting of ages by deformation events (Reddy et al. 2007). Many minerals have anisotropic diffusivity and EBSD data provide an easy way to account for this in the analysis of composition gradients (Martin et al. 2008).

Although we know of ongoing work applying EBSD to igneous rocks (rocks crystallised from melt) and good work in PhD theses, there are as yet few published data sets related to igneous problems (Faul and FitzGerald 1999; Feinberg et al. 2004; Romeo et al. 2007).

EBSD-based studies of sediments and sedimentary rocks have started only in the last few years. Work thus far focuses on characterising intrinsic physical property anisotropies (Valcke et al. 2006) and on understanding processes involved in diagenesis. Diagenesis comprises the chemical and physical processes by which sediment becomes rock. EBSD studies have had a particular emphasis on how diagenesis will affect porosity and permeability (Haddad et al. 2006; Mork and Moen 2007), parameters of extreme importance to the hydrocarbon extraction industry.

Rock magnetism is an area where EBSD is likely to provide important information: rock magnetic properties relate, in part at least, to the submicrometre scale structure of magnetic carriers. Although some of these features may be below SEM resolution, SEM and EBSD together provide a powerful tool to develop the petrophysical understanding of rocks needed to accompany rock magnetic studies (Feinberg et al. 2004; Franke et al. 2007). The identification of fine Fe-oxides and Fe-Ti oxides is aided significantly by EBSD data (Franke et al. 2007). Furthermore, the microstructural relationships of coexisting oxides and their orientation relationships help interpret the history of phase development (phase transformation history) as a function of temperature and time, and puts significant constraints upon the interpretation of magnetic data (Davies, Hill, and Prior work in progress). Physical and crystallographic orientations of magnetic carriers, often most easily established by EBSD, can be influenced by magnetic field history and provide significant control on magnetic properties.

Crystalline structures, such as shells or pearls, created by organisms are often highly anisotropic and have distinct microstructures and LPOs that impart advantageous physical properties to the material. The study of such biomineralization (Cusack et al. 2007; Dalbeck and Cusack 2006; Dalbeck et al. 2006; Griesshaber et al. 2007; Saruwatari et al. 2006) is a new area of EBSD application that spans the boundaries of the geosciences and the life sciences and has potential in engineering.

EBSD is not widely used for mineral identification, primarily because geologists are accustomed to using an optical microscope for this purpose, and then using a microprobe to assist where grains are too small to resolve optically. There are some situations where chemical data alone do not suffice, and we have used EBSD; for example, to help distinguish fine-grained kyanite from sillimanite (both Al_2SiO_5), coesite from quartz (both SiO_2), and pyrite from marcasite (both FeS_2). Such applications are likely to become more important. EBSD has now played a crucial role in the discovery and characterization of new minerals, in situations where grains are too small/rare to be analysed by X-ray methods (Ma and Rossman 2008). With the development of a more fundamental understanding

of EBSD patterns (Michael and Goehner 2000; Winkelmann et al. 2007), such applications should become easier and more common.

26.4 Conclusions

1. EBSD data can be collected from most minerals. Phyllosilicates (including clays and micas) remain problematic.
2. Step sizes as small as 50 nm give 50 nm resolutions in minerals that are not damaged by the beam.
3. Orientation mapping using automated EBSD is possible on most minerals, so long as the step size is significantly smaller than the grain size so that errors can be assessed and removed. Some minerals (e.g., calcite) index with sufficient reliability to collect data with steps on the order of the grain size or larger.
4. Data processing routines are crucial to earth science EBSD users.
5. Some work on polyphase samples needs X-ray data to complement the EBSD, because EBSD alone cannot distinguish between different composition minerals within mineral families with a single structure (e.g., within the clinopyroxene family).
6. EBSD applications in earth sciences are dominated by studies of deformed rocks and of metamorphic rocks. Other applications are developing.

References

Adams BL, Wright SI, Kunze, K (1993) Orientation imaging—the emergence of a new microscopy. Metall Trans A 24(4):819–831

Bestmann M, Kunze K, Matthews A (2000) Evolution of a calcite marble shear zone complex on Thassos Island, Greece: microstructural and textural fabrics and their kinematic significance. J Struct Geol 22(11–12):1789–1807

Bestmann M, Prior DJ (2003) Intragranular dynamic recrystallization in naturally deformed calcite marble: diffusion accommodated grain boundary sliding as a result of subgrain rotation recrystallization. J Struct Geol 25(10): 1597–1613

Boyle AP, Prior DJ, Banham MH, Timms NE (1998) Plastic deformation of metamorphic pyrite: new evidence from electron backscatter diffraction and forescatter orientation—contrast imaging. Miner Deposita 34(1):71–81

Brewer LN, Kotula PG, Michael JR (2008) Multivariate statistical approach to electron backscattered diffraction. Ultramicroscopy 108(6):567–578

Cusack M, Perez-Huerta A, Dalbeck P (2007) Common crystallographic control in calcite biomineralization of bivalved shells. Crystengcomm 9(12):1215–1218

Dalbeck P, Cusack M (2006) Crystallography (electron backscatter diffraction) and chemistry (electron probe microanalysis) of the avian eggshell. Cryst Growth Des 6(11):2558–2562

Dalbeck P, England J, Cusack M, Lee MR, Fallick AE (2006) Crystallography and chemistry of the calcium carbonate polymorph switch in M. edulis shells. Eur J Mineral 18(5):601–609

Day A (1993) Developments in the EBSP technique and their application to grain imaging. PhD thesis, University of Bristol, Bristol, U.K.

Day AP, Quested TE (1999) A comparison of grain imaging and measurement using horizontal orientation and colour orientation contrast imaging, electron backscatter pattern and optical methods. J Microsc-Oxford 195:186–196

Deer WA, Howie RA, Zussmann J (1992) An Introduction to the rock forming minerals. Longman, Hong Kong

Dingley DJ (1984) Diffraction from submicron areas using electron backscattering in a scanning electron microscope. Scan Electron Microsc Part 2:569–575

Faul UH, FitzGerald JD (1999) Grain misorientations in partially molten olivine aggregates: an electron backscatter diffraction study. Phys Chem Miner 26(3):187–197

Feinberg JM, Wenk HR, Renne PR, Scott, GR (2004) Epitaxial relationships of clinopyroxene-hosted magnetite determined using electron backscatter diffraction (EBSD) technique. Am Mineral 89(2–3):462–466

Fliervoet TF, Drury MR, Chopra PN (1999) Crystallographic preferred orientations and misorientations in some olivine rocks deformed by diffusion or dislocation creep. Tectonophysics 303(1–4):1–27

Fliervoet TF, White SH (1995) Quartz deformation in a very fine-grained quartzo-feldspathic mylonite—a lack of evidence for dominant grain-boundary sliding deformation. J Struct Geol 17(8):1095–1109

Franke C, Pennock GM, Drury MR, Engelmann R, Lattard D, Garming JFL, von Dobeneck T, DekkerS MJ (2007) Identification of magnetic Fe-Ti oxides in marine sediments by electron backscatter diffraction in scanning electron microscopy. Geophys J Int 170(2):545–555

Goldstein JI, Michael JR (2006) The formation of plessite in meteoritic metal. Meteorit Planet Sci 41(4):553–570

Griesshaber E, Schmahl WW, Neuser R, Pettke T, Blum M, Mutterlose J, Brand U (2007) Crystallographic texture and microstructure of terebratulide brachiopod shell calcite: an optimized materials design with hierarchical architecture. Am Mineral 92(5–6):722–734

Habesch SM (2000) Electron backscattered diffraction analyses combined with environmental scanning electron microscopy: potential applications for non-conducting, uncoated mineralogical samples. Mater Sci Tech 16(11–12):1393–1398

Haddad SC, Worden RH, Prior DJ, Smalley PC (2006) Quartz cement in the Fontainebleau sandstone, Paris basin, France: crystallography and implications for mechanisms of cement growth. J Sediment Res 76(1–2):244–256

Halfpenny A, Prior DJ, Wheeler J (2006) Analysis of dynamic recrystallization and nucleation in a quartzite mylonite. Tectonophysics 427(1–4):3–14

Hawkins AT, Selverstone J, Brearley AJ, Beane RJ, Ketcham RA, Carlson WD (2007) Origin and mechanical significance of honeycomb garnet in high-pressure metasedimentary rocks from the Tauern Window, Eastern Alps. J Metamorph Geol 25(5):565–583

He YL, Godet S, Jonas JJ (2005) Representation of misorientations in Rodrigues-Frank space: application to the Bain, Kurjumov-Sachs, Nishiyama-Wassermann and Pitsch orientation relationships in the Gibeon meteorite. Acta Mater 53(4):1179–1190

Heidelbach F, Stretton I, Langenhorst F, Mackwell S (2003) Fabric evolution during high shear strain deformation of magnesiowustite (Mg0.8Fe0.2O). J Geophys Res-Sol Earth 108(B3):2154

Heilbronner RP, Pauli C (1993) Integrated spatial and orientation analysis of quartz c-axes by computer-aided microscopy. J Struct Geol 15(3–5):369–382

Hirsch DM, Prior DJ, Carlson WD (2003) An overgrowth model to explain multiple, dispersed high-Mn regions in the cores of garnet porphyroblasts. Am Mineral 88(1):131–141

Humphreys FJ, Brough I (1999) High resolution electron backscatter diffraction with a field emission gun scanning electron microscope. J Microsc-Oxford 195:6–9

Hutchinson B, Hagstrom J (2006) Austenite decomposition structures in the Gibeon meteorite. Metall Mater Trans A 37A(6):1811–1818

Joy DC, Newbury DE (1972) Scanning electron microscope selected area channeling patterns from 1 micron specimen areas. J Mater Sci 7(6):714

Kameda J, Yamagishi A, Kogure T (2005) Morphological characteristics of ordered kaolinite: investigation using electron back-scattered diffraction. Am Mineral 90(8–9): 1462–1465

Katayama I, Jung H, Karato SI (2004) New type of olivine fabric from deformation experiments at modest water content and low stress. Geology 32(12):1045–1048

Kogure T (2002) Identification of polytypic groups in hydrous phyllosilicates using electron backscattering patterns. Am Mineral 87(11–12):1678–1685

Kruse R, Stunitz H, Kunze K (2001) Dynamic recrystallization processes in plagioclase porphyroclasts. J Struct Geol 23(11):1781–1802

Kunze K, Adams BL, Heidelbach F, Wenk HR (1994) Orientation imaging microscopy of calcite rocks. In: Bunge HJ, Siegesmunde S, Skrotski W, Weber K (eds) Textures of geological materials. DMG Informationgesellschaft Verlag, Oberursel, Germany pp 127–146

Law RD (1990) Crystallographic fabrics: a selective review of their applications to research in structural geology. In: Knipe RJ, Rutter EH (eds) Deformation mechanisms, rheology and tectonics. Geological Society of London, London, pp 335–352

Leiss B, Ullemeyer K, Weber K, Brokmeier HG, Bunge HJ, Drury M, Faul U, Fueten F, Frischbutter A, Klein H, Kuhs W, Launeau P, Lloyd GE, Prior DJ, Scheffzuk C, Weiss T, Walther K, Wenk HR (2000) Recent developments and goals in texture research of geological materials—Preface. J Struct Geol 22(11–12):1531–1540

Lloyd GE (1987) Atomic-number and crystallographic contrast images with the SEM—a review of backscattered electron techniques. Mineral Mag 51(359):3–19

Lloyd GE (1994) An appreciation of the SEM electron channeling technique for microstructural analysis of geological materials. In: Bunge HJ, Siegesmunde S, Skrotski W, Weber K (eds) Textures of geological materials. DGM Informationgesellschaft Verlag, Oberursel, Germany, pp 109–126

Lloyd GE, Farmer AB, Mainprice D (1997) Misorientation analysis and the formation and orientation of subgrain and grain boundaries. Tectonophysics 279(1–4):55–78

Lloyd GE, Schmidt NH, Mainprice D, Prior DJ (1991) Crystallographic textures. Mineral Mag 55(380):331–345

Ma C, Rossman GR (2008) Barioperovskite, BaTiO3, a new mineral from the Benitoite mine, California. Am Mineral 93(1):154–157

Mainprice D (2003) Physical properties of rocks and other geomaterials: a special volume to honour professor H. Kern—Introduction. Tectonophysics 370(1–4):7–9

Mainprice D, Bascou J, Cordier P, Tommasi A (2004) Crystal preferred orientations of garnet: comparison between numerical simulations and electron backscattered diffraction (EBSD) measurements in naturally deformed eclogites. J Struct Geol 26(11):2089–2102

Mariani E, Mecklenburgh J, Wheeler J, Prior DJ, Heidelbach F (2009) Microstructure evolution and recrystallisation during creep of MgO single crystals. Acta Mater. DOI: 10.1016/j.actamat.2008.12.029

Martin VM, Morgan DJ, Jerram DM, Caddick MJ, Prior DJ, Davidson JP (2008) Bang! month-scale eruption triggering: Santorini volcano, Greece. Science 321:1178

Mehl L, Hirth G (2008) Plagioclase preferred orientation in layered mylonites: evaluation of flow laws for the lower crust. J Geophys Res-Solid Earth 113(B5)

Michael JR, Goehner RP (2000) Ab initio primitive cell calculations from EBSD patterns. Microbeam Analysis 2000 Proceedings. International Union of Microbeam Analysis Societies. Conference No 2. Kailua-Kona, Hawaii, USA. pp 203–204.

Mork MBE, Moen K (2007) Compaction microstructures in quartz grains and quartz cement in deeply buried reservoir sandstones using combined petrography and EBSD analysis. J Struct Geol 29(11):1843–1854

Nolze G, Wagner G, Neumann RS, Skala R, Geist V (2006) Orientation relationships of carlsbergite in schreibersite and kamacite in the north Chile iron meteorite. Mineral Mag 70(4):373–382

Oesterling N, Heilbronner R, Stunitz H, Barnhoorn A, Molli G (2007) Strain dependent variation of microstructure and texture in naturally deformed Carrara marble. J Struct Geol 29(4):681–696

Ohfuji H, Boyle AP, Prior DJ, Rickard D (2005) Structure of framboidal pyrite: an electron backscatter diffraction study. Am Mineral 90(11–12):1693–1704

Pauli C, Schmid SM, Heilbronner RP (1996) Fabric domains in quartz mylonites: localized three-dimensional analysis of microstructure and texture. J Struct Geol 18(10): 1183–1203

Pieri M, Kunze K, Burlini L, Stretton I, Olgaard DL, Burg JP, Wenk HR (2001) Texture development of calcite by deformation and dynamic recrystallization at 1000 K during

torsion experiments of marble to large strains. Tectonophysics 330(1–2):119–140
Poirier JP, Guillope M (1979) Deformation induced recrystallization of minerals. Bull Mineral 102(2–3):67–74
Prior DJ, Boyle AP, Brenker F, Cheadle MC, Day A, Lopez G, Peruzzo L, Potts GJ, Reddy S, Spiess R, Timms NE, Trimby P, Wheeler J, Zetterstrom L (1999) The application of electron backscatter diffraction and orientation contrast imaging in the SEM to textural problems in rocks. Am Mineral 84(11–12):1741–1759
Prior DJ, Trimby PW, Weber UD, Dingley DJ (1996) Orientation contrast imaging of microstructures in rocks using forescatter detectors in the scanning electron microscope. Mineral Mag 60(403):859–869
Prior DJ, Wheeler J, Peruzzo L, Spiess R, Storey C (2002) Some garnet micro structures: an illustration of the potential of orientation maps and misorientation analysis in microstructural studies. J Struct Geol 24(6–7):999–1011
Randle V (2004) Application of electron backscatter diffraction to grain boundary characterisation. Int Mater Rev 49(1): 1–11
Reddy SM, Potts GJ, Kelley SP (2001) Ar-40/Ar-39 ages in deformed potassium feldspar: evidence of microstructural control on Ar isotope systematics. Contrib Mineral Petrol 141(2):186–200
Reddy SM, Timms NE, Pantleon W, Trimby P (2007) Quantitative characterization of plastic deformation of zircon and geological implications. Contrib Mineral Petrol 153(6): 625–645
Romeo I, Capote R, Lunar R, Cayzer N (2007) Polymineralic orientation analysis of magmatic rocks using electron backscatter diffraction: implications for igneous fabric origin and evolution. Tectonophysics 444(1–4):45–62
Sander B (1930). Gefügehunde der Gesteine. Springer, Berlin
Sander B (1970). An Introduction to the study of fabrics of geological bodies (English translation). Pergamon Press, Oxford
Saruwatari K, Ozaki N, Nagasawa H, Kogure T (2006) Crystallographic alignments in a coccolith (Pleurochrysis carterae) revealed by electron backscattered diffraction (EBSD). Am Mineral 91(11–12):1937–1940
Schmid SM, Casey M (1986) Complete fabric analysis of some commonly observed quartz c-axis patterns. In: Hobbs BE, Heard HC (eds) Mineral and rock deformation: laboratory studies—the Paterson volume. American Geophysical Union, pp 246–261
Sephton MA, Howard LE, Bland PA, James RH, Russell SS, Prior DJ, Zolensky ME (2006) Delving into Allende's dark secrets. Astron Geophys 47(6):37–38
Shigematsu N (1999) Dynamic recrystallization in deformed plagioclase during progressive shear deformation. Tectonophysics 305, 437–452
Skemer P, Karato S (2008) Sheared lherzolite xenoliths revisited. J Geophys Res-Solid Earth 113, B07205
Skemer P, Katayama I, Karato SI (2006) Deformation fabrics of the Cima di Gagnone peridotite massif, Central Alps, Switzerland: evidence of deformation at low temperatures in the presence of water. Contrib Mineral Petrol 152(1):43–51
Spiess R, Peruzzo L, Prior DJ, Wheeler J (2001) Development of garnet porphyroblasts by multiple nucleation, coalescence and boundary misorientation-driven rotations. J Metamorph Geol 19(3):269–290
Storey CD, Prior DJ (2005) Plastic deformation and recrystallization of garnet: a mechanism to facilitate diffusion creep. J Petrol 46(12):2593–2613
Tatham DJ, Lloyd GE, Butler RWH, Casey M (2008) Amphibole and lower crustal seismic properties. Earth Planet Sci Lett 267(1–2):118–128
Terry MP, Heidelbach F (2004) Superplasticity in garnet from eclogite facies shear zones in the Haram Gebbro, Haramsøya, Norway. Geology 32(4):281–284
Toy VG, Prior DJ, Norris RJ (2008) Quartz fabrics in the Alpine Fault mylonites: influence of pre-existing preferred orientations on fabric development during progressive uplift. J Struct Geol 30(5):602–621
Trepmann CA, Stockhert B (2002) Cataclastic deformation of garnet: a record of synseismic loading and postseismic creep. J Struct Geol 24(11):1845–1856
Trimby PW, Drury MR, Spiers CJ (2000) Misorientations across etched boundaries in deformed rock salt: a study using electron backscatter diffraction. J Struct Geol 22(1):81–89
Trimby PW, Prior DJ (1999) Microstructural imaging techniques: a comparison between light and scanning electron microscopy. Tectonophysics 303(1–4):71–81
Trimby PW, Prior DJ, Wheeler J (1998) Grain boundary hierarchy development in a quartz mylonite. J Struct Geol 20(7):917–935
Turner FJ, Weiss LE (1963) Structural analysis of metamorphic tectonites. McGraw Hill, New York
Urai JL, Means WD, Lister GS (1986) Dynamic recrystallization of minerals. In: Hobbs BE, Heard HC (eds) Mineral and rock deformation (laboratory studies). American Geophysical Union, Washington DC pp 161–200
Valcke SLA (2003) Towards the prediction of seismic anisotropy in sedimentary rocks. MSc thesis, University of Leeds, Leeds, U.K.
Valcke SLA, Casey M, Lloyd GE, Kendall JM, Fisher QJ (2006) Lattice preferred orientation and seismic anisotropy in sedimentary rocks. Geophys J Int 166(2):652–666
Vauchez A, Dineur F, Rudnick R (2005) Microstructure, texture and seismic anisotropy of the lithospheric mantle above a mantle plume: insights from the Labait volcano xenoliths (Tanzania). Earth Planet Sci Lett 232(3–4): 295–314
Venables JA, Harland CJ (1973) Electron backscattering patterns—a new technique for obtaining crystallographic information in the SEM. Philos Mag 27: 1193–1200
Vonlanthen P, Kunze K, Burlini L, Grobety B (2006) Seismic properties of the upper mantle beneath Lanzarote (Canary Islands): model predictions based on texture measurements by EBSD. Tectonophysics 428(1–4):65–85
Watt LE, Bland PA, Prior DJ, Russell SS (2006) Fabric analysis of Allende matrix using EBSD. Meteorit Planet Sci 41(7):989–1001
Wenk HR, Christie JM (1991) Comments on the interpretation of deformation textures in rocks. J Struct Geol 13(10): 1091–1110
Whattam SA, Hewins RH, Cohen BA, Seaton NC, Prior DJ (2008) Granoblastic olivine aggregates in magnesian chondrules: planetesimal fragments or thermally annealed solar nebula condensates? Earth Planet Sci Lett 269: 200–211

Wheeler J, Prior DJ, Jiang Z, Spiess R, Trimby PW (2001) The petrological significance of misorientations between grains. Contrib Mineral Petrol 141(1):109–124

White S (1977) Geological significance of recovery and recrystallization processes in quartz. Tectonophysics 39(1–3): 143–170

Whitney DL, Goergen ET, Ketcham RA, Kunze K (2008) Formation of garnet polycrystals during metamorphic crystallization. J Metamorph Geol 26(3):365–383

Winkelmann A, Trager-Cowan C, Sweeney F, Day AP, Parbrook P (2007) Many-beam dynamical simulation of electron backscatter diffraction patterns. Ultramicroscopy 107 (4–5):414–421

Chapter 27

Orientation Imaging Microscopy in Research on High Temperature Oxidation

Bae-Kyun Kim and Jerzy A. Szpunar

27.1 Introduction

High temperature oxidation of steel has been studied for reducing steel losses and for understanding descaling of oxides (Kuiry et al. 1994; Tomellini and Mazzarano 1988; Sachs and Tuck 1968). Surface defects, such as scale pits and residues, are frequently observed on steel surfaces after hot rolling. The occurrence of surface defects is related to the formation of oxide scale. These defects are undesirable for the surface quality control of slab in the hot rolling process. The quality control of steel products is highly dependent on the removal of scale on slab during the hot rolling process. This is directly related to the scale structure formed in high temperature oxidation. When iron or steel is exposed to air at elevated temperatures, oxidation of iron forms scale that usually consists of various iron oxides developed at different temperatures. Indeed, magnetite (Fe_3O_4) and hematite (Fe_2O_3) are formed in the oxidation of iron below 570°C. Above 570°C, wüstite (FeO) grows quickly and becomes increasingly stable (Scully 1990; Béranger 1996). Therefore, it is necessary that the microstructural characteristics and behavior of the aforementioned three iron oxides are investigated for understanding the oxidation behavior taking place during the hot rolling process.

B.-K. Kim (✉)
Department of Mining and Materials Engineering, McGill University, Montreal, QC Canada; Corporate R&D Institute, Samsung Electro-Mechanics, Suwon, Kyungki-Do, Korea 443–743
e-mail: baekyun.kim@yahoo.ca; baekyun.kim@samsung.com

Prior to studies of the processing factors for scale removal, it is also crucial to characterize the microstructure of oxide scales. Since the oxide microstructure significantly affects the descaling process of hot-rolled slab and the pickling process (Chen and Yuen 2000; Tominaga et al. 1982), the characterization of iron oxide in high temperature oxidation is very important. At present, however, there are no studies identifying which microstructures are favorable for mechanical scale removal in the hot rolling process. There is no clear understanding of what kind of microstructures are developed in high temperature oxidation, how defects are formed in the oxidation process, and how stresses are distributed in the scale layer. Moreover, experimental methods capable of directly describing microstructural details at elevated temperatures are not well established.

The reason is that, because of the lack of experimental research tools for displaying them, the details of iron oxide microstructures are not investigated, and are also difficult to understand. Most conventional methods, such as backscatter electron images or fractography in SEM, can only provide the general characteristics of microstructures such as grain morphology and size. Also, since the microstructures of iron oxides are not chemically etched, they are known to be very difficult to observe.

The purpose of this research is to establish systematic tools for investigating and characterizing the oxide microstructure and for understanding oxide defects related to descaling. The purpose is also to understand how the oxide microstructure is formed during high temperature oxidation, and to extract useful information on microstructures that can be related to descaling in steel plants.

A.J. Schwartz et al. (eds.), *Electron Backscatter Diffraction in Materials Science*,
DOI 10.1007/978-0-387-88136-2_27, © Springer Science+Business Media, LLC 2009

In this chapter, new research tools and the results of high temperature oxidation of iron and low carbon steels are demonstrated. The oxide microstructures are systematically characterized by orientation imaging microscopy (OIM) observations of the cross-sectional area of the oxide layers. It is demonstrated that OIM using electron backscatter diffraction (EBSD) techniques, which can distinguish an individual grain orientation, can be an invaluable tool for visualizing the oxide microstructure and texture, and for studying oxide defects. The oxidation process and microstructure development are described using OIM maps, including image quality (IQ) and inverse pole figure (IPF) maps. The three different iron oxide phases can be distinguished, and the characteristics of oxides with different oxidation histories are compared. The characteristics of high temperature oxidation microstructure of iron are presented, with a description of iron oxide defects and cracking, as well as the interfacial microstructure between the layered iron oxides.

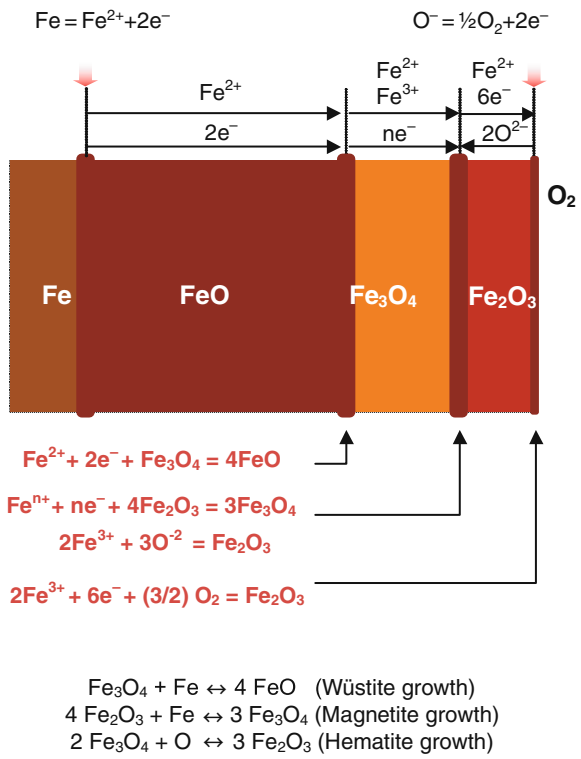


Fig. 27.1 Schematic diagram of oxidation mechanism for the diffusion-controlled growth of multilayered scale during isothermal heating above 570°C

27.2 High Temperature Oxidation

The process of iron oxidation can divided into two stages; (1) initial oxidation, proceeding at a linear rate, followed by a parabolic rate of oxidation; and (2) diffusion-controlled oxidation by ionic species through the newly formed oxide layer (Abuluwefa et al. 1996; Davies et al. 1951). The initial stage of iron oxidation can be divided into four reactions: (1) chemisorption of oxygen, (2) formation of a fine mosaic layer, (3) growth of the oxide crystal, and (4) the appearance of the second layer (Gulbransen and Ruka 1952).

In oxidation below 570°C, the overall oxidation rate is controlled by the growth rate of Fe_3O_4. At intermediate temperatures between 350 and 500°C, Fe_3O_4 nucleates and grows laterally over the surface. Once the thin layer is completely covered, the growth rate of Fe_3O_4 is parabolic. Due to the lower effective pO_2 at the Fe_3O_4 surface, the growth rate of Fe_3O_4 is slow, and nucleation and lateral growth by Fe_2O_3 occurs. Gulbransen and Ruka (1952) studied the structure of the oxide film after oxidation experiments around 570°C. They suggested that the oxide layer was formed under mechanical stresses, because of the larger lattice parameters of the growing oxide layer appearing in the first oxidation. Above 570°C, FeO is rapidly formed and exists as a type of complex cluster of vacancies.

A mechanism of high temperature oxidation of iron has been proposed, as shown in Fig. 27.1. During isothermal heating above 570°C, the three iron oxides grow in layered structures. More details for each ionic reaction at each phase interface are described elsewhere (Birks and Meier 1983; Pinder 1995; Scully 1990; Béranger 1996; Davies et al. 1951). Iron oxidizes with parabolic kinetics between 250° and 1000°C. At low temperature, iron oxidizes with a logarithmic kinetics. The growth of FeO and Fe_3O_4 is controlled by the outward diffusion of cations, whereas the growth of Fe_2O_3 at the Fe_3O_4/Fe_2O_3 interface is dominated by the inward diffusion of anions (Katrakova et al. 1998; Hauffe 1965). However, others have suggested that Fe_2O_3 growth occurs by outward cation migration (Bruckman and Simkovich 1972; Birks and Meier 1983). In oxidation, the outward diffusion indicates that the cation transport predominates

more than the anion transport, whereas the reverse is taken place for the inward diffusion.

The proposed model has two notable assumptions: (1) the reaction takes place under an isothermal heating process, and (2) the oxide growth is isotropic. The mechanism for high temperature oxidation by the diffusion of cations and electrons has been well established, but more details for oxidation under an anisothermal oxidation, such as a continuous oxidation, have not been addressed. For instance, if the sample is oxidized with temperatures varying from room temperature to high temperatures, the mechanisms for the initial formation of wüstite grains are unknown. The formation of initial wüstite grains is unlikely to require diffusion of cations and electrons. Therefore, the mechanism of high temperature oxidation of iron requires revision in the system of the continuous heating schedule and anisotropic oxide growth.

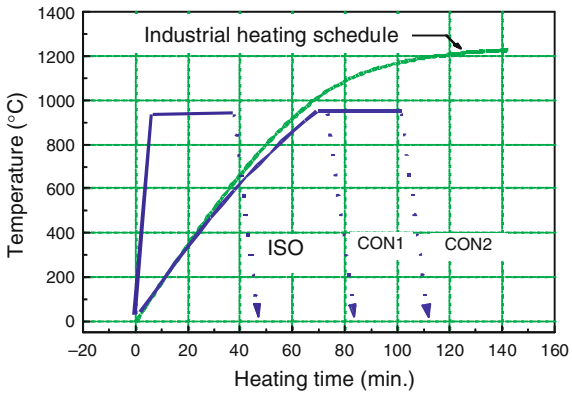


Fig. 27.2 Continuous heating schedules (CON1 & CON2) for simulating the industrial oxidation environment and the isothermal oxidation schedule (ISO)

27.3 Experimental Procedure

27.3.1 Oxidation of Samples and Oxide Formation

For microstructural investigation, various low carbon (LC) steel samples were oxidized up to 950°C under a continuous heating schedule simulating hot rolling conditions. In the hot rolling process of a steel plant, the temperatures for the "Roughing Mill Entry" and "Roughing Mill Exit" are around 1230° and 1115°C, respectively. The temperatures for the "Finishing Mill Entry" and "Finishing Mill Exit" are 1080° and 890°C, respectively. Consistent with a typical industrial schedule, the scales for microstructural investigation were formed during continuous heating up to 950°C as shown in Fig. 27.2. The average heating rate was approximately 14°C per minute. Oxidation in the continuous heating schedule was marked as "CON" and the isothermal oxidation, for comparison, as "ISO" in Fig. 27.2. In order to produce thicker oxide layers in the CON schedule, the specimen was held isothermally for 30 min. The heating was performed in air atmosphere.

Commercially pure Fe (>99.98%) samples were also oxidized with continuous heating in air up to 950°C, according to the CON1 schedule. The LC steel samples with carbon content of 0.069% were oxidized using the same heating condition, but held for 30 min, according to the CON2 schedule. The CON2 schedule was used to obtain thicker layers suitable for sample preparation for OIM examination.

The samples of the LC steels were isothermally oxidized for 30 min at 950°C in air according to the ISO schedule. In addition, another specimen was prepared by an isothermal oxidation for 100 h at 500°C and investigated to better understand the nucleation and grain growth of magnetite, and to illustrate the effect of thermal treatment on the microstructure. Long annealing was applied to ensure a thick magnetite layer, which could be easily analyzed by SEM.

Experiments for investigating the effect of the substrate and substrate texture on oxidation microstructure were conducted on pure Fe. The substrates were prepared by the following treatments: (a) as-received specimen, (b) cold-rolled with 70% reduction, and (c) annealed for 1 h at 800°C after 70% cold reduction. The experiments were designed to understand the role of the substrate in the oxidation behavior.

Before oxidation, all specimens were polished with 0.05-micron colloidal silica, cleaned with ethanol in an ultrasonic bath, and dried in the vacuum chamber. Oxidation experiments were conducted in an open tube furnace under an air atmosphere. After oxidation for each heating schedule, the oxidized samples were quickly transferred to a cold, steel block placed at the end of the tube furnace to enhance cooling. The furnace was sealed and Ar gas allowed to flow through

the tube. These techniques, designed for rapid cooling, were employed to prevent the transformation of wüstite into magnetite and iron at temperatures below 570°C. This transformation is well described elsewhere (Béranger 1996).

27.3.2 Sample Preparation and Geometry in OIM

The oxidized samples were hot-mounted in a PolyFast® phenolic resin with carbon filler manufactured by Struers. The mounting condition for a mounting press with a 30 mm cylinder was 20 kN and the heating temperature was 180°C for 6 min; the cooling time was 3 min. The cross-sectional area of the samples was observed for microstructural evaluation. This means that the surface observed is normal to the transverse direction (TD) of samples. The normal direction (ND) in the sample frame is parallel to the direction of oxide growth. Figure 27.3(a) shows the schematic structure of the mounted sample with respect to the sample reference system. The sample was mounted using metal support pieces to protect the edge of the oxide layer during grinding and polishing.

The mount assembly was ground down by 3 mm from the mount surface using SiC 120 grit on a grinding wheel speed of 150 rpm. Subsequent grinding steps involved SiC 240 grit, 320 grit, 400 grit, and 600 grit papers at 100∼150 rpm, followed by SiC 1200 grit and 2400 grit at 100 rpm. Finally, the

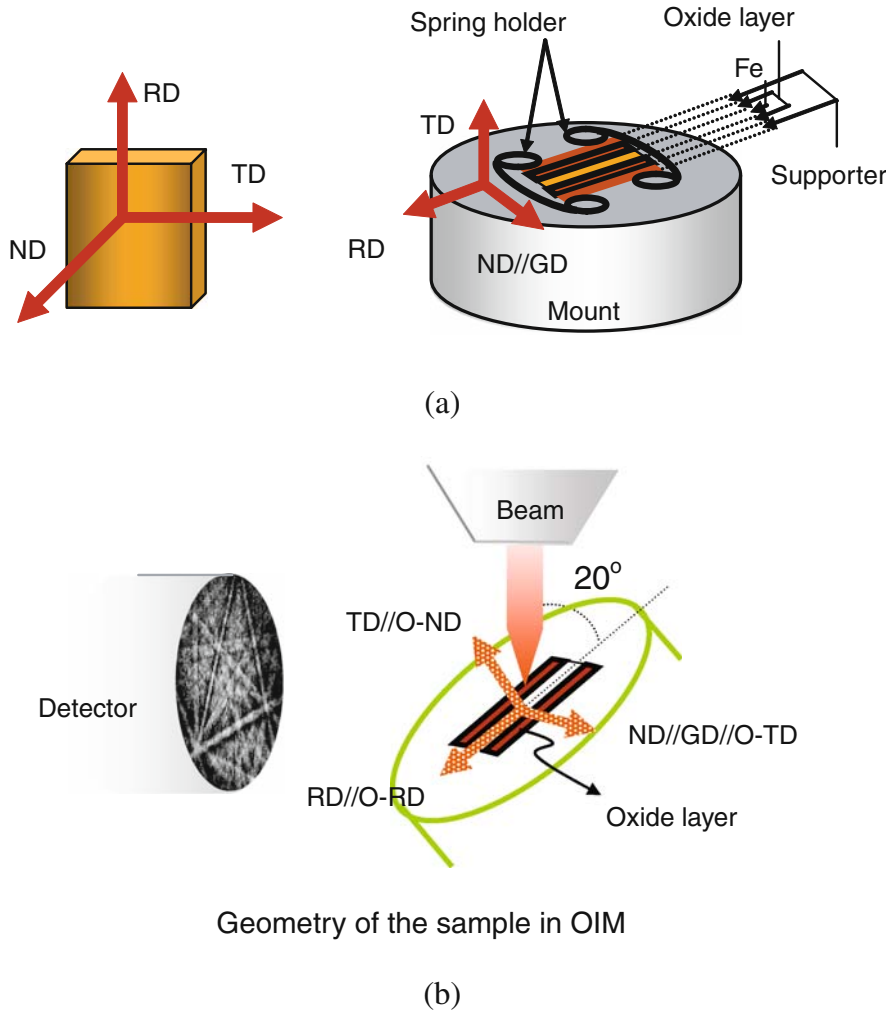


Fig. 27.3 Schematic diagram showing: (**a**) the sample reference frame and the mounting assembly, consisting of the oxide layer, the supporting metal pieces, and the pair of spring holders; and (**b**) a sample reference system in the OIM system. O-ND, O-RD, and O-TD are the normal, rolling, and transverse directions of the OIM reference system

samples were polished for at least three hours using a polishing cloth with 0.05 μm colloidal silica at 50∼100 rpm, or subjected to vibrational polishing with the 0.05 μm colloidal silica solution for 10∼24 h in the VIBROMET®2, from Buehler. The wheel speed of the polisher was kept slow, because the oxide is so fragile that surface artifacts and cracking can be induced during the grinding and polishing steps.

Vibratory polishing can produce a gentle polishing action due to its horizontal vibratory motion with a frequency of 7200 cycles per second, which yields an undamaged surface with exceptional flatness.

In OIM, the inverse pole figure (IPF) map is an orientational imaging map filled with pixels color-coded according to the orientation illustrated in the unit triangle of the inverse pole figure. An inverse pole figure of a certain direction describes the position of this sample direction with respect to the crystal reference frame. In order to construct the IPF map, it is important to align the sample properly with respect to the OIM stage.

Figure 27.3(b) shows a schematic diagram illustrating the sample reference system and the reference frame of the OIM system. Since the sample surface perpendicular to ND was oxidized, the direction of oxide growth, or the growth direction (GD), is parallel to ND. The normal direction in the OIM (O-ND) is defined as the direction normal to the surface of the sample mount, the rolling direction (O-RD) is parallel to the tilt direction of the sample stage, and the transverse direction (O-TD) corresponds to the direction of the tilt axis of the sample stage (TSL 2000). Therefore, GD or ND is aligned to O-TD and TD is aligned to O-ND in the OIM reference system.

27.3.3 Microstructure and Texture Measurement

Oxide microstructure was demonstrated using OIM. Orientation imaging micrographs or orientation maps are constructed from scans of crystal orientation data measured over a portion of the sample surfaces. These micrographs provide very useful information about oxide growth as well as a cross section of coating area. To get more reliable OIM results, a stable electron beam and small beam diameter are required. As the OIM scanning may take several hours or even days to acquire the orientational data, a durable SEM is highly recommended (Eades 2000). In this research, the Philips XL-30 FEG equipped with the TSL OIM system (Draper, Utah) is used. The XL-30 FEG SEM employs a Schottky thermally-activated field emission gun (for more details on OIM, please refer to Chapter 1).

In our measurements, the experimental parameters for SEM were: spot sizes of 3 and 5, accelerating voltages of 20 and 30 kV, and beam currents of 150 pA to 2.3 nA. For these experimental parameters, the beam diameter would be less than 10 nm. Theoretically, the minimum step size for the OIM is about 20 nm, but considering the interaction volume, about 50 nm can be considered as a practical minimum step size. The automatic scan was performed over the selected area with a hexagonal grid of 1 and 0.1 micron.

The substrate texture was measured using the Schulz reflection method in the Siemens D-500 X-ray texture goniometer with a Mo target (40 kV and 40 mA). The (011), (200), and (311) pole figures for the Fe phase were measured by step scanning with 5-degree intervals over the tilt angle range of 80°. Two seconds were required for each interval. For the calculation of the orientation distribution function (ODF), the collected data were analyzed using a texture software package, TexTool v.3.1 (Li 2001), based on the arbitrary defined cell (ADC) method (Pawlik et al. 1991). The substrate texture was illustrated using the inverse pole figures determined for ND.

The oxide texture was calculated from the data on individual grain orientations collected using OIM. In OIM, the grain orientation, which is expressed by the Euler angles, is determined using the direct space approach, as suggested by Matthies and Vinel (1993). The ODF is calculated by the discrete binning method with a bin size of 5 degrees.

27.3.4 Oxidation of Low Carbon Steel

Above 850°C, X-ray diffraction is not available for the investigation of oxidation behavior because the oxide is too thick to be penetrated by X-ray diffraction. OIM can be used to directly analyze the oxide microstructure and texture. Recently, several results on oxide characterization based on EBSD have been reported (Kim and Szpunar 2001a; Higginson et al. 2002; Birosca et al. 2004)

27.3.4.1 Microstructure Investigation by OIM

The quality of microstructural imaging obtained by OIM depends on how the sample surface is prepared in the polishing procedure. In particular, the polishing time and wheel speed have to be optimized. For OIM work, the sample preparation has been known to take more time for polishing ceramic materials than metals (Katrakova et al. 1998; Randle and Engler 2000). The best results were obtained when the wheel speed was less than 150 rpm and the polishing time was more than 3 h in the fine polishing stage after the conventional polishing. The polishing agent used was colloidal silica.

Figure 27.4 shows the difference in the quality of the micrographs obtained from OIM observation as a function of the polishing time. Each micrograph is represented by the gray IQ map. The IQ value represents the sharpness of Kikuchi patterns at the given scanning point. The IQ map therefore represents not only the real microstructure, but also the grain boundaries, voids, and even microcracks. In Fig. 27.4(a, b), artifacts from the polishing process, such as surface scratches and holes, are observed. After polishing for 3 h, the surface of the oxide layer is clean and the average IQ value is relatively high. The scratch lines on the oxide surface observed after a short polishing time were removed, although the scratch lines on the substrate still remain. Nonetheless, the oxide microstructure can be precisely illustrated when compared to the microstructure depicted by the conventional methods, such as etching and fracturing.

27.3.4.2 Phase Analysis

Phase analysis in OIM can be performed by the identification of Kikuchi patterns. Three phases of iron oxides and a ferrite steel phase were identified by different EBSD patterns (Kim and Szpunar 2001a). Figure 27.5(a, b, c, d) shows each set of the Kikuchi patterns obtained from Fe, FeO, Fe_3O_4, and Fe_2O_3, respectively. Since each phase found in the specimen has a different space group (steel: Im $\bar{3}$m, wüstite: Fm $\bar{3}$m, magnetite: Fd $\bar{3}$m, and hematite: R $\bar{3}$c), the phases can be distinguished by the pattern symmetry. Based on the characteristics of these patterns, such as the band widths and the reflectors for the candidate phases, the EBSD patterns can be indexed for each phase. The IQ map, color-coded for the different phases, can be constructed to demonstrate the results, as shown in Fig. 27.5(e). The blue region represents the iron phase, the red the wüstite phase, and the yellow the magnetite phase. Since the thickness of the hematite layer was so small that the OIM scanning with the 1 μm step size could not recognize it, this layer is not represented in Fig. 27.5(e). The irregular, inhomogeneous thin layer of hematite close to the surface, however, was found at high magnification when OIM measurements were made with a small step size. These results will be described at the end of this chapter. Under continuous oxidation up to 950°C, the three oxide layers form clearly and consecutively from the steel substrate. The phase ratio of the three phases can be approximated from the thickness of these layers. Since the thickness of wüstite, magnetite, and hematite

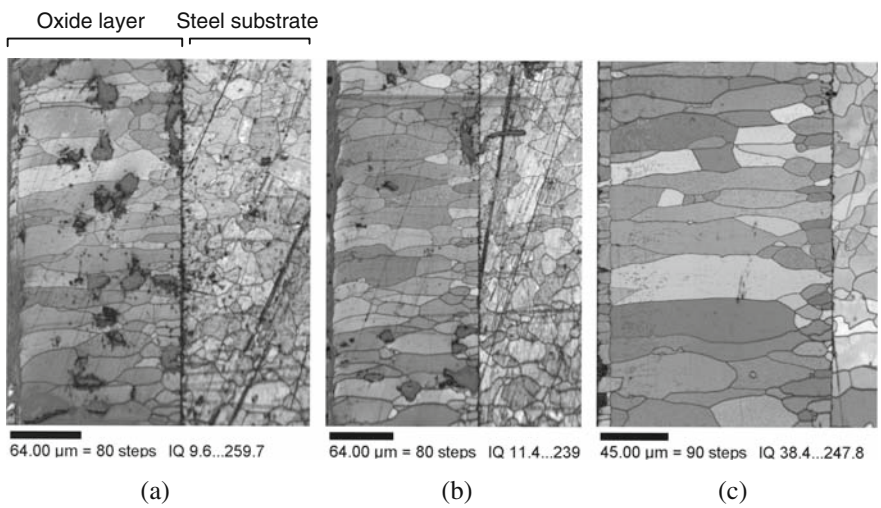


Fig. 27.4 The IQ map with varying polishing time in the fine polishing stage: (**a**) 1 h, (**b**) 2 h, and (**c**) 3 h

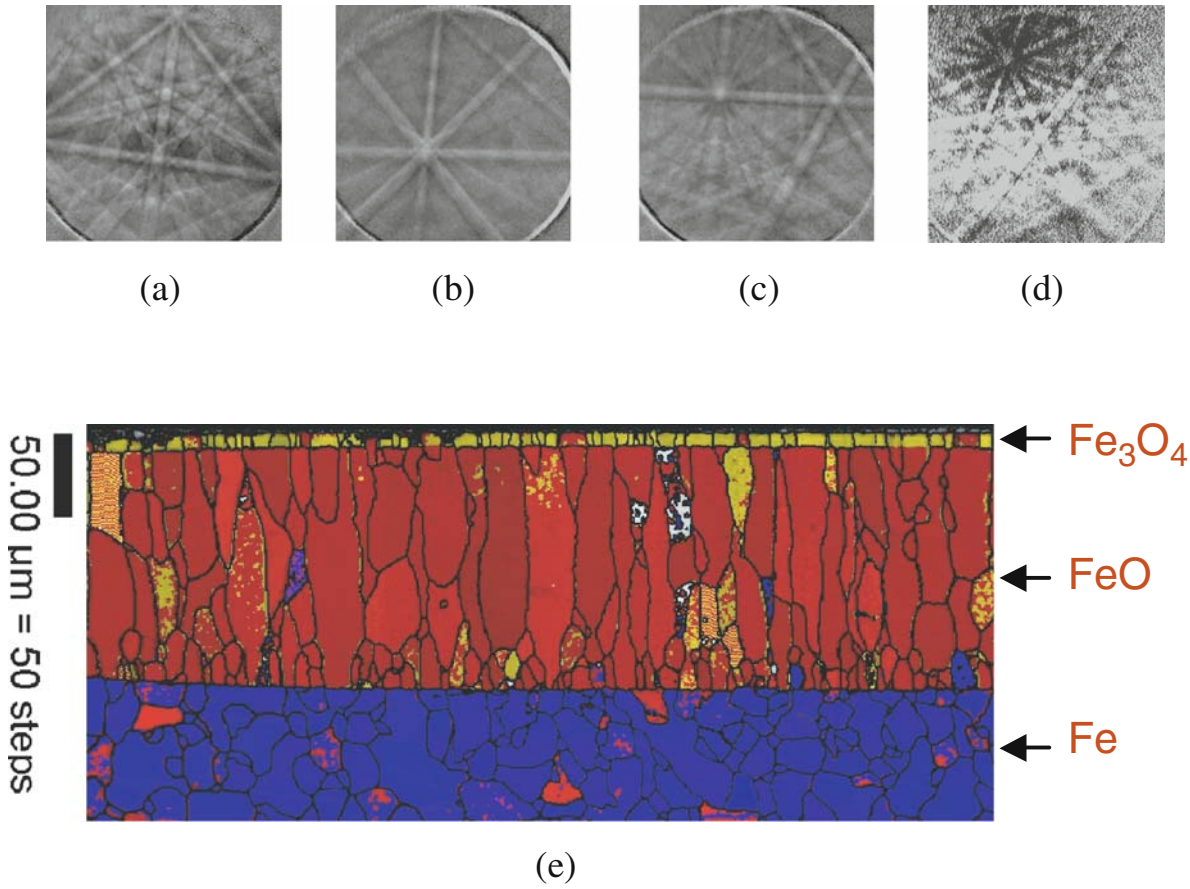


Fig. 27.5 EBSD patterns obtained from each phase: exemplary patterns of (**a**) Fe, (**b**) FeO, (**c**) Fe_3O_4, and (**d**) Fe_2O_3; (**e**) the IQ map color-coded with phases (the *blue* region: Fe, the *red*: FeO, and the *dark yellow*: Fe_3O_4)

is around 150, 8, and 0.8 microns, respectively, the ratio is FeO:Fe_3O_4:Fe_2O_3 = 94.4:5.0:0.6. The reason for the larger proportion of wüstite is that the mobility of defects in wüstite is greater than in magnetite or hematite (Birks and Meier 1983). Those defects that exist in wüstite may favor more rapid diffusion of iron ions and electrons.

Within each layer, there are several local regions having different colors than those of the surrounding area. These regions result from errors during the process of phase recognition. To explain the origin of the errors, the procedure of phase identification using EBSD will be addressed here first. Once EBSD patterns are obtained from a certain scanning point of an unknown phase, the point group and the space group are determined by examining prominent zone axes and the associated symmetries in the patterns. Based on the angles between the zone axes and the determined point group, indices of the Kikuchi lines are assigned on a trial basis. In the next step, the d spacings of the planes are measured from the angles, the widths of the bands, and the trial indices. Once this procedure is processed, the trial patterns can be simulated. When a good agreement between the simulated and experimental patterns is achieved, the unknown phase can be determined by the crystallographic data used for the simulated patterns (Michael and Goehner 1993; Goehner and Michael 1996; Baba-Kishi and Dingley 1989; Dingley and Randle 1992).

Unfortunately, as Fe, FeO, and Fe_3O_4 have different space groups but the same point group m $\bar{3}$m, it may be difficult to identify each phase in the Kikuchi patterns unless the pattern quality is so sharp that reflectors of each phase can be distinguished. Moreover, due to

the asymmetrical shape of Kikuchi lines in the Hough space, the width and position of each band are difficult to calculate. Therefore, the d spacing of each plane related to each reflector cannot be measured accurately. As a result, there is a possibility that the incorrect phase can be chosen when the patterns are blurred. That is the reason why different color areas in the region of the same phase are found. Recently, several new technologies for the phase identification and verification have been developed, such as the combination of EDS with the OIM system or the assessment of higher order Laue zone (HOLZ) rings for the reduced unit cell (Michael and Eades 2000; Wright and Nowell 2002; Baba-Kishi and Dingley 1989; TSL 2000). These methods may allow more reliable phase identification in the future and as discussed in chapters by Dingley and Wright, and by El-Dasher and Deal.

As mentioned earlier, phase identification requires high quality EBSD patterns, but there is a possibility that the pattern quality is not good enough. In order to reduce the experimental error for phase identification, the number of Kikuchi bands obtained must be increased and the contrast of the bands must be improved.

27.4 Results and Discussion

27.4.1 Grain Growth in Iron Oxide

27.4.1.1 Grain Growth of Wüstite

Wüstite is the oxide phase that, according to the iron-oxygen phase diagram, is formed above 570°C. According to experimental results obtained from in situ X-ray diffraction, the formation of wüstite in LC steels was recorded in the temperature region of 750° to 850°C. These oxidation experiments were conducted during continuous heating up to 950°C. The results obtained using OIM show that the overall shape of wüstite grains is columnar, as reported in Kim and Szpunar (2001a).

Analysis of the wüstite microstructure clearly shows that it can be divided into two distinct regions: the microstructure of the initial stage and the grain growth stage (Kim and Szpunar 2001a). The small grains of wüstite observed in the region close to the substrate have more equiaxial shape than the grains in the grain growth stage. The wüstite grains in the grain growth stage have a columnar cell structure. The grains in both stages of growth are textured with <001>//GD. The texture intensity of <001>//GD is strengthened as the oxides grow and the wüstite grains with <001>//GD have better defined columnar shape. These OIM texture results are in agreement with in situ X-ray experiments that show the increase of strength of the (002) wüstite peak with increasing temperature as described in Kim and Szpunar (2001b).

The results obtained using the OIM technique allow the description of a network of different wüstite grain boundaries. The different types of grain boundaries in this network may have different diffusion characteristics and may control transport of atoms through the network. A qualitative description of this network will help to understand the oxidation process of Fe. The study by Kim and Szpunar (2001a) shows the grain boundary character distribution (GBCD) in the initial and grain growth stage. This result demonstrates that the fraction of high angle boundaries with rotation angle $\theta > 25^{o}$ decreased and the fraction of low angle boundaries with rotation angle $\theta \leq 25^{o}$ increased during the continuous oxidation process.

These changes in the grain boundary characteristics are directly related to the diffusion of iron ions during high temperature oxidation (Kofstad 1988). In general, there are several diffusion paths for transport of atoms or reactants in the oxide layers: (1) through the oxide lattices, (2) along grain boundaries of oxides, and (3) along dislocations. With decreasing temperature, grain boundary diffusion plays a major role in oxide growth because the activation energy is lower than the lattice diffusion. At high temperature, lattice diffusion tends to predominate during oxidation. In the overall process of continuous oxidation, it is reasonable to assume that both diffusion mechanisms must be considered. As a general rule, since low angle grain boundaries have lower energy than high angle grain boundaries, diffusion of the reactants or atoms can be expected to be slow along low angle grain boundaries. Thus, because the frequency of low angle boundaries is higher in the growth stage, as shown in the study by Kim and Szpunar (2001a), the bulk diffusion mechanism of iron ions in wüstite grains plays a more important role than in the early stage of oxidation.

In order to form wüstite at the FeO/Fe_3O_4 interface, iron ions must be continually supplied through the columnar structure of the wüstite grains. The flux of iron ions is a function of diffusivity and concentration gradient of iron ions, and the distance between the substrate and the oxidation front. Additionally, the crystallographic orientation of these iron oxides may affect the diffusion flux. The oxide grains with low flux will have slow growth, whereas the grains with high flux will grow rapidly and dominate the layer. In low temperature oxidation, the large number of grain boundaries can help cation diffusion; but in high temperature oxidation, lattice diffusion is most likely to be the main mechanism for cation diffusion (Kofstad 1988). Lattice diffusion can be influenced by crystallographic geometry or texture developed during high temperature oxidation.

The columnar microstructure is closely related to the diffusion mechanism. Dubinin (2000) has reported that in solid solutions a diffusion layer typically has the columnar microstructure due to diffusion of various elements into a base metal after isothermal heat treatment at 900°, 1000°, and 1100°C. Prior to heat treatment, the surface of the base metals, such as Fe or Ni, was initially saturated with the various elements (Al, Mn, Cr, V, Mo, and W). The direction of columnar grains coincides with the vector of the maximum diffusion flux.

If a steady state diffusion process is assumed in high temperature oxidation, Fick's first law of diffusion can express the diffusion flux of iron ions:

$$J = -D_{ox}\frac{dC}{dx}, \tag{27.1}$$

where J is the flux of ions, D_{ox} is the diffusivity of iron in the oxide layer, C is the concentration of iron ions, and x is the diffusion distance along the diffusion path in the wüstite layer between the interfaces of Fe/FeO and FeO/Fe_3O_4. Figure 27.6 shows a schematic diagram of this diffusion. The difference in the concentration (ΔC) is constant because the iron ion concentration is a function of temperature. Thus, the only way to increase the diffusive flux is to choose the shortest diffusion path. In Fig. 27.6, the shortest path is the P1 direction normal to the interfaces. The iron ions, the main diffusion element in iron oxide, can be most rapidly transported through the shortest path in the wüstite layer. The rapid, massive transport of iron ions promotes the growth of wüstite at the wüstite/magnetite interface, according to the iron oxidation mechanism mentioned before. The transport rate increases with increasing temperature. Therefore, the diffusion-controlled growth of wüstite in high temperature oxidation will favor the formation of columnar morphology.

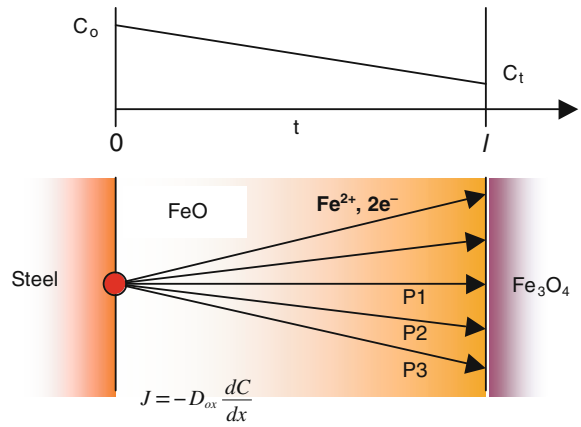


Fig. 27.6 Schematic diagram showing the iron ion content profile

27.4.1.2 Grain Growth of Magnetite

It is difficult to prepare the magnetite layer with a suitable thickness for microstructural observation after oxidation at low temperature. In order to describe the formation of the magnetite layer, an LC-steel sample was oxidized in air for 100 h at 600°C. As a result, a magnetite layer with the thickness of about 40 microns was formed.

Figure 27.7 shows the maps of oxide microstructure obtained using OIM. Figure 27.7(a, b) are the IQ and inverse pole figure (IPF) maps that show the morphology of magnetite grains after oxidation. Each color represents an orientation designated in the unit triangle of the inverse pole figure for a given sample direction. Figure 27.7(e) illustrates a color index notation for the growth direction (GD) of iron oxides. In Fig. 27.7(b), for instance, a red color grain has the <001> crystal direction oriented along the oxide growth direction (GD), which is perpendicular to the sample surface or the oxide/metal interfacial plane.

As shown in Fig. 27.7, the grains of magnetite do not form a layer structure. However, it is clear that the

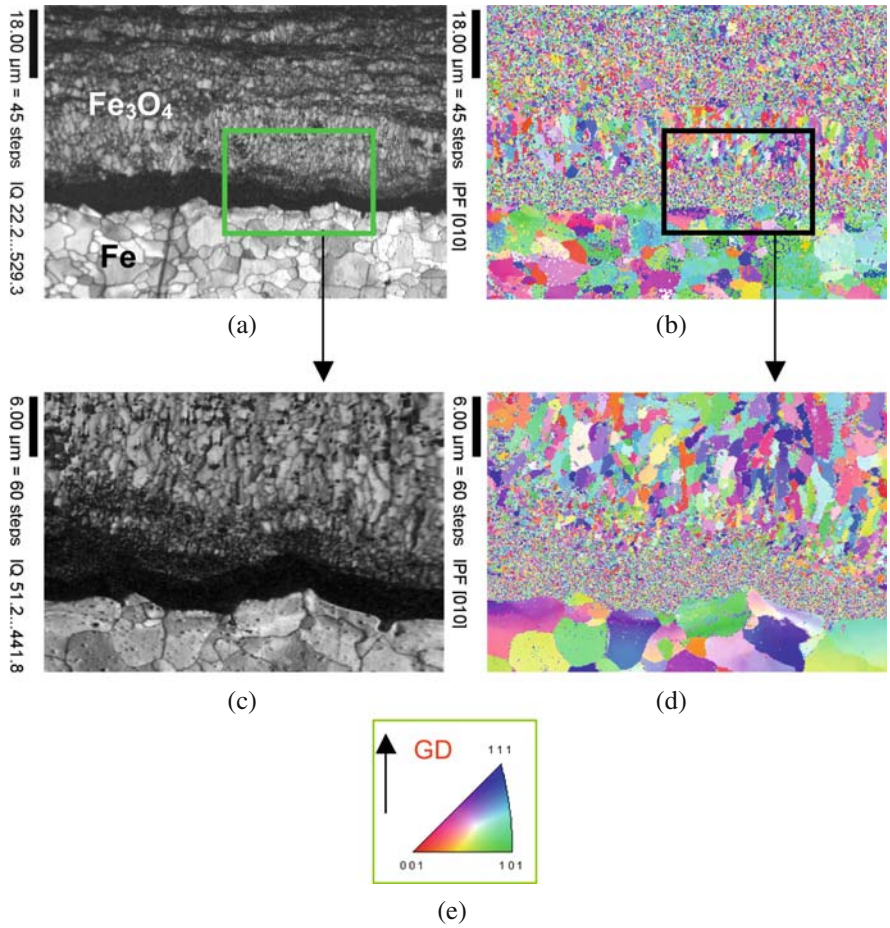


Fig. 27.7 The IQ and the IFP maps representing the magnetite layer: (**a**) the IQ and (**b**) the IPF maps obtained using the step size of 0.4 micron; (**c**) the IQ and (**d**) the IPF maps measured with the smaller step size of 0.1 micron within the indicated selected area; (**e**) the inverse pole figure unit triangle color-coded by crystal direction with respect to GD

grain size of the magnetite is smaller in the area close to the substrate. The bigger grains are further from the substrate and have a columnar shape as shown in Fig. 27.7(b, d).

Figure 27.8 shows the GD inverse pole figure of the magnetite grains. Figure 27.8(a) is the discrete inverse pole figure obtained from orientations of individual points, and Fig. 27.8(b) represents the calcu-

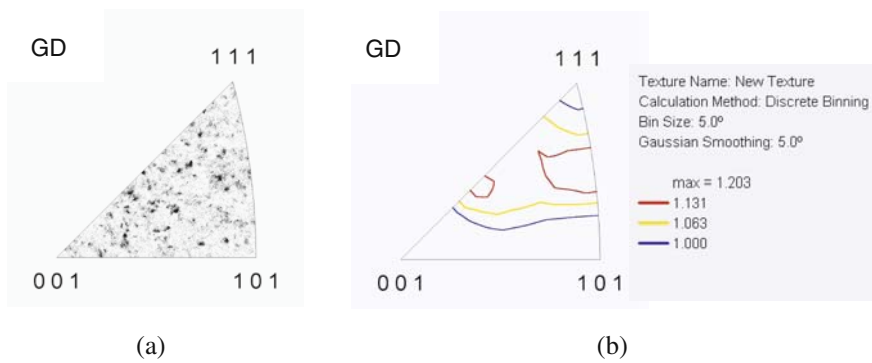


Fig. 27.8 Inverse pole figures of the magnetite layer presented in Fig. 27.7: (**a**) the raw data in the inverse pole figure, and (**b**) the calculated inverse pole figure, where the sample direction is parallel to GD

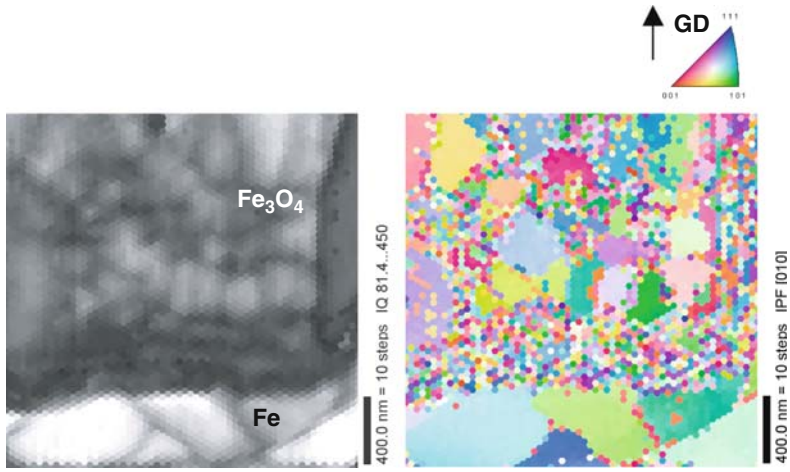


Fig. 27.9 Orientation micrographs showing details of the magnetite microstructure: (**a**) the IQ and (**b**) the IPF maps parallel to GD of magnetite layer with a step size of 0.04 μm

lated inverse pole figure of the magnetite grains presented in Fig. 27.7. The orientations of the magnetite grains are scattered within the whole orientation space, and the maximum texture intensity is around 1. This indicates that the magnetite grains are randomly oriented with respect to the direction of oxide growth.

Figure 27.9 shows the detailed micrographs of magnetite grains near the substrate. Apparently, the grains are a few hundred nanometers in size. This means that nucleation of magnetite starts at the surface of steel. Subsequently, some of these grains grow and form a columnar shape, having a length of several micrometers during continued oxidation.

During continuous high temperature oxidation up to 950°C, however, the microstructure of magnetite shows the unique <001> crystal direction along the GD. Figure 27.10 shows the microstructure and texture of magnetite grains formed during a continuous oxidation up to 950°C. The shape of the magnetite grains at the oxide surface is not columnar, but cubic. The grains mostly have the red color, indicating the preferred orientation with <001> parallel to the GD. The inverse pole figures of Fig. 27.10(c, d) also indicate the <001>//GD texture. It is evident that as a result of the continuous oxidation, the magnetite grains next to the wüstite layer have a cube-type cell structure with the <001>//GD texture. There is no clear reason for this texture to occur during high temperature oxidation, but minimized surface energy may explain this phenomenon. According to Davies and Parker (1989), the surface energies (SE) of the crystallographic planes of magnetite are: SE (100) = 1.5, SE (110) = 1.8, and SE (111) = 2.2 Jm^{-2}. The minimization of surface energies may favor the grain growth of magnetite with <001>//GD.

27.4.1.3 Grain Growth of Hematite

The hematite layer is rather irregular in thickness, and discontinuous thin layers are often observed. In Fig. 27.11, the hematite layers with thicknesses of a few hundred nanometers are displayed. After continuous oxidation of the LC steel up to 950°C, the hematite grains are on the surface of the magnetite layer, but are irregularly embedded within the magnetite. A wedge shape of Fe_2O_3 is frequently observed. More details will be given when the interfacial morphology of the oxidation of pure iron is analyzed. The hematite microstructure is difficult to analyze at temperatures below 850°C, because it forms very thin layers or whiskers.

27.4.2 Effect of the Oxidation Process on Microstructure

Despite different oxidation histories, oxide microstructures look rather similar; however, the grain size of the

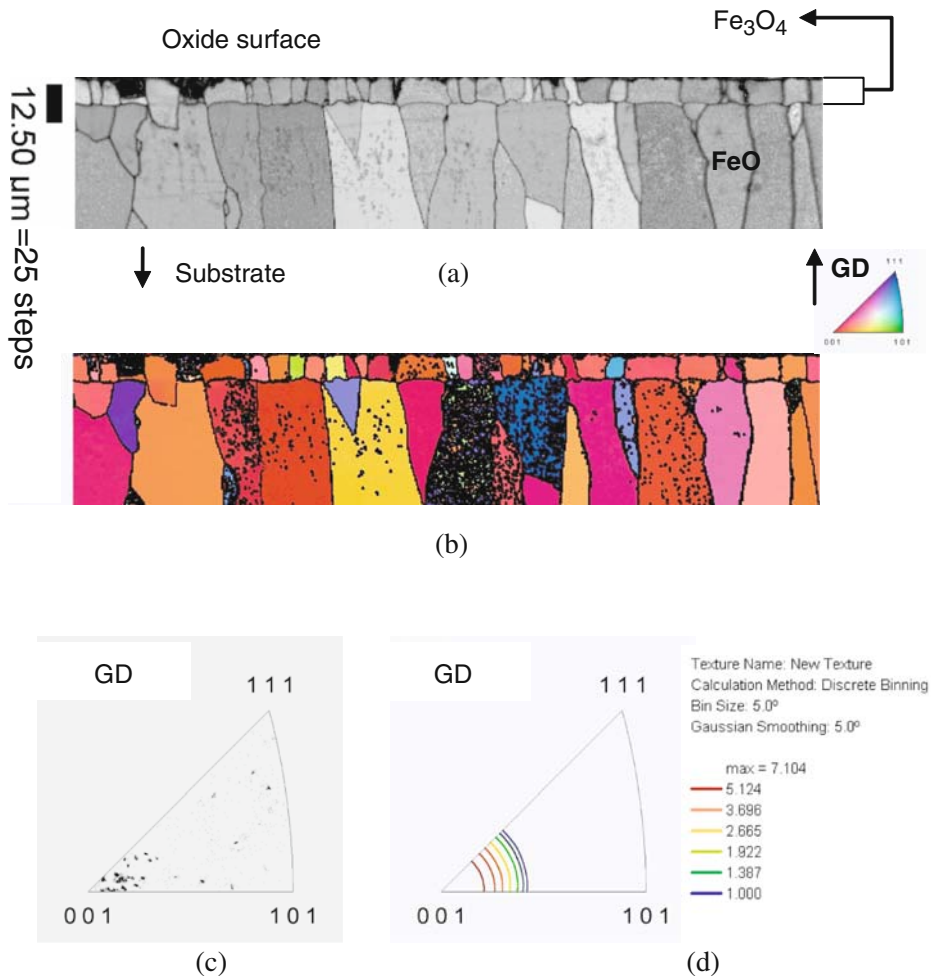


Fig. 27.10 Orientational micrographs and texture after continuous oxidation up to 950°C: (**a**) the IQ and (**b**) the IPF maps with 0.5 μm step size; (**c**) the discrete data of the magnetite grain orientation; and (**d**) the calculated inverse pole figure of the magnetite layer, parallel to GD

initial stage of the wüstite grains and the texture of the grains are different (Kim and Szpunar 2001b). The IQ and IPF maps can explain it. The entire microstructure of the oxide layer is depicted in Fig. 27.12(a, b). The orientation maps, the IPF maps parallel to the GD, are shown in Fig. 27.12(c, d).

Although the LC steel samples have different oxidation histories, the wüstite grains in both samples have a columnar shape. At the initial stage, however, the wüstite grains are larger in the specimen after isothermal oxidation for 30 min at 950°C (ISO) than in the specimen after continuous oxidation up to 950°C (CON2). Many grains with red color, indicating the <001>//GD texture, are found in the samples which underwent the continuous oxidation, but not in the samples that were oxidized isothermally. These results indicate that the oxidation history affects the texture and grain size of oxide.

These results may be explained by the following hypothesis. During continuous oxidation, fine magnetite grains are initially formed on the surface of the substrate at temperatures below 570°C. Above 570°C, the nucleation sites for the formation of wüstite are abundant because the fine magnetite grains already exist at the Fe_3O_4/Fe interface. The wüstite grains in the initial stage of formation can be smaller during continuous oxidation up to 950°C than during the isothermal oxidation at 950°C. In the specimen isothermally

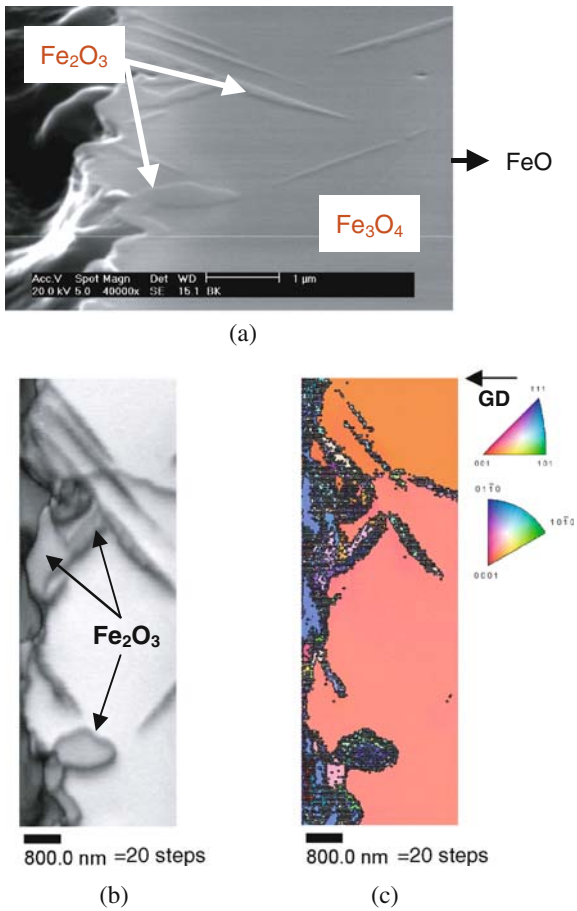


Fig. 27.11 Grain growth of hematite in high temperature oxidation: (**a**) a 70°-tilted SE image, (**b**) the IQ map, and (**c**) the IPF map to GD in OIM

oxidized at 950°C, however, there are no magnetite grains that can act as nucleation sites for wüstite grains at the specimen surface. Since the diffusion rate of iron ions is faster at higher temperature, the iron ions diffuse more quickly through the oxide and form new grains at the surface. Consequently, the grains in the initial stage of oxidation grow bigger and longer during isothermal oxidation than during continuous oxidation. Different microstructures result from the differences in the initial stage of wüstite growth. Based on this hypothetical explanation, the role of magnetite grains as nucleation sites may be important for wüstite morphology. Important factors to control the oxide microstructure are (1) fine magnetite grains, and (2) the growth competition between wüstite grains at the initial stage of oxidation.

It should be noted that even if the oxidation history is different, the magnetite texture is similar for both heating schedules. In the IPF maps presented in Fig. 27.12(c, d), the upper layers of oxide are magnetite and these layers mostly have the red color. These results illustrate that the texture of the magnetite layer after both heat treatments is <001>//GD. The texture and shape of magnetite grains obtained in high temperature oxidation of LC steels are not very dependent on the oxidation history.

27.4.3 Oxidation of Pure Iron

In pure iron, there are no alloying elements to complicate investigation of the oxidation process. In this section, the effect of substrate texture and surface deformation on oxidation and interface character will be investigated and compared to results obtained during oxidation of LC steels.

The samples produced by different metallurgical processes were oxidized under continuous oxidation up to 950°C according to the heating schedule CON1. This allows consideration of the development of the oxide microstructure following different metallurgical treatments of specimens with the same oxidation history. For this purpose, three samples were prepared using three different metallurgical treatments: (a) as-received (AR-PF), (b) cold-rolled with 70% reduction (CR-PF), and (c) annealed for 1 h at 800°C after 70% cold reduction (ANN-PF). The heat treatment of ANN-PF ensures that cold-rolled pure Fe is fully recrystallized. In studying the texture effect on oxidation, texture representation by ND inverse pole figures was used because the normal direction of the specimen is parallel to the direction that iron oxides grow (GD). Thereby, the inverse pole figures of GD (or ND) are used to explain the effect of substrate texture on oxidation behavior.

27.4.3.1 Effects of Substrate Deformation and Texture on Oxidation

Figure 27.13 depicts the IQ and IPF maps showing the microstructure of iron oxides after oxidation of pure iron processed according to AR-PF, CR-PF, and ANN-PF. The shape of the wüstite grains for all

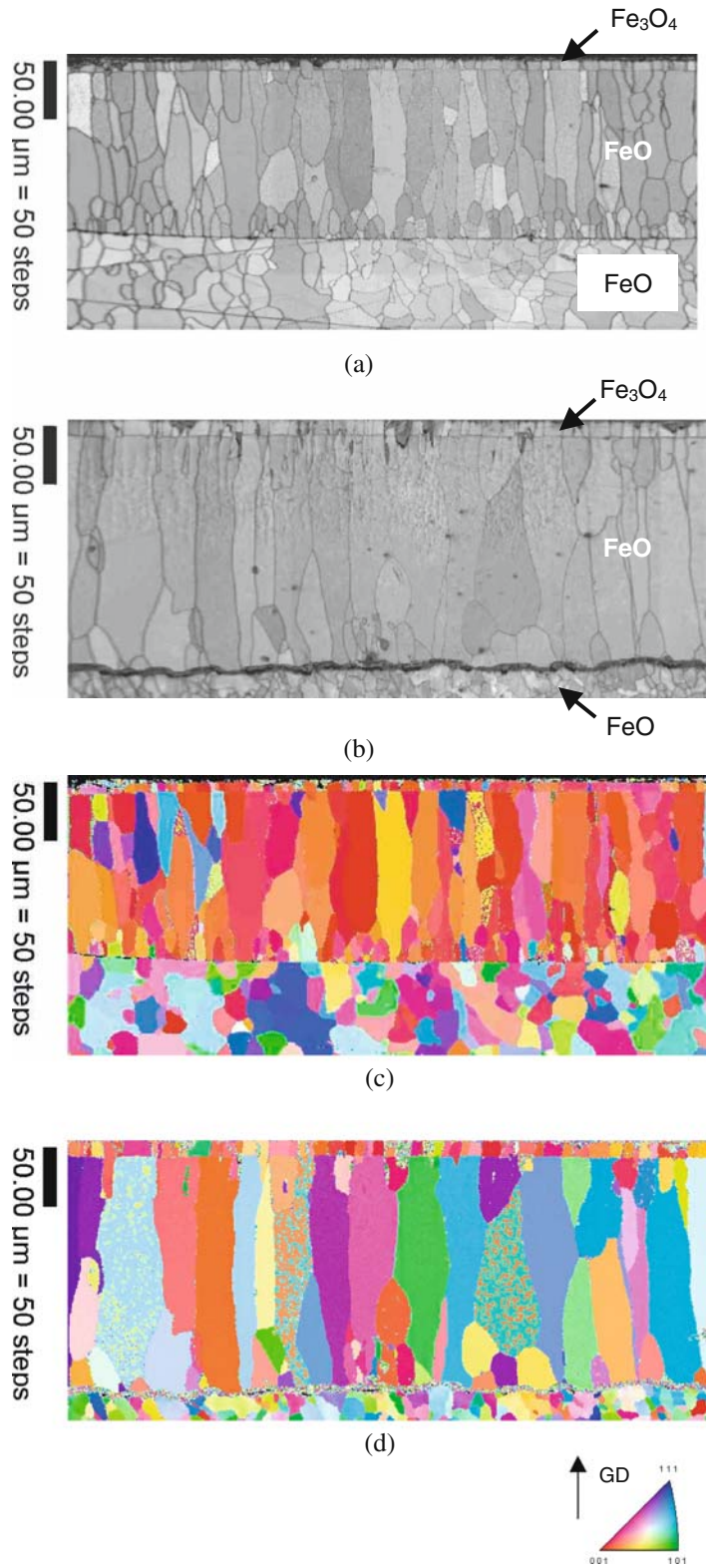


Fig. 27.12 Micrographs showing the microstructure of the oxide layer after oxidation with different oxidation schedules of CON2 and ISO: the IQ maps of the samples prepared by (**a**) CON2 and (**b**) ISO; the IPF maps to GD for oxides prepared by (**c**) CON2 and (**d**) ISO

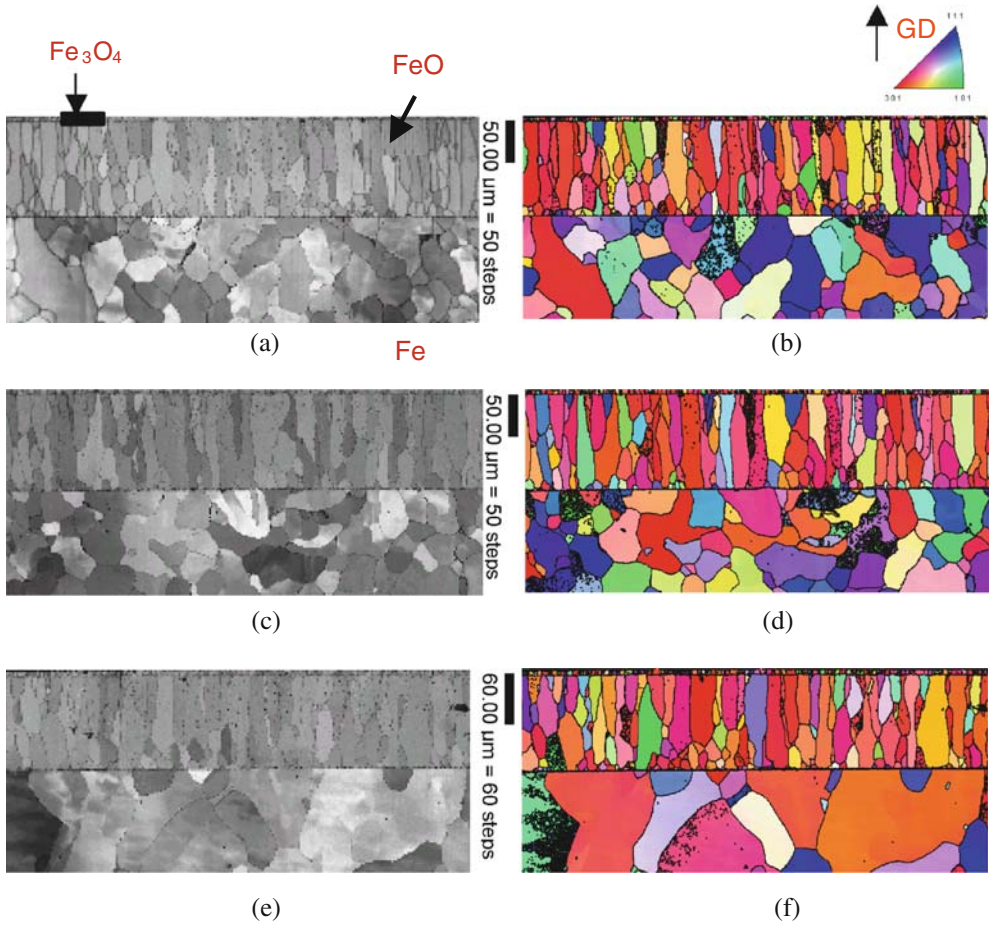


Fig. 27.13 Microstructure of scales on various pure Fe samples: (**a**) the IQ map and (**b**) the IPF map for the cross-sectional area of as-received pure Fe (AR-PF), (**c**) and (**d**) of a 70% cold-rolled pure Fe (CR-PF), and (**e**) and (**f**) of a pure Fe annealed for 1 h at 850°C after 70% deformation (ANN-PF)

specimens is similarly columnar. The oxide thickness ranges from 120 to 125 μm in AR-PF and CR-PF, whereas the thickness is around 120 μm in ANN-PF. The thickness difference between samples is not significant. As shown in the IPF maps for all specimens (Fig. 27.13(b, d, f)), wüstite grains marked with the red color are dominant, indicating that the grains with the <001>//GD are likely to develop during oxidation at high temperatures up to 950°C. Deformation of the substrate is unlikely to influence the oxide morphology.

Figure 27.14 shows the GD inverse pole figures of the substrate and wüstite. The substrate textures are obtained from X-ray diffraction and the wüstite textures are from OIM. Although the substrate textures are different, the wüstite layer has the <001>//GD texture for all substrates. No texture relationships between substrate and wüstite or between substrate and magnetite are found. The magnetite layer has the same texture as the wüstite layer. The reason for this has been already discussed in the previous sections.

As a result, during high temperature continuous oxidation up to 950°C, the microstructure of the oxide layers is likely to be independent of the processing history of the substrate, such as the amount of deformation in the substrate and the substrate texture. According to the results regarding isothermal and continuous oxidation, it is evident that the microstructure of iron oxides is more dependent on the heating profile during oxidation than on the substrate texture or deformation history.

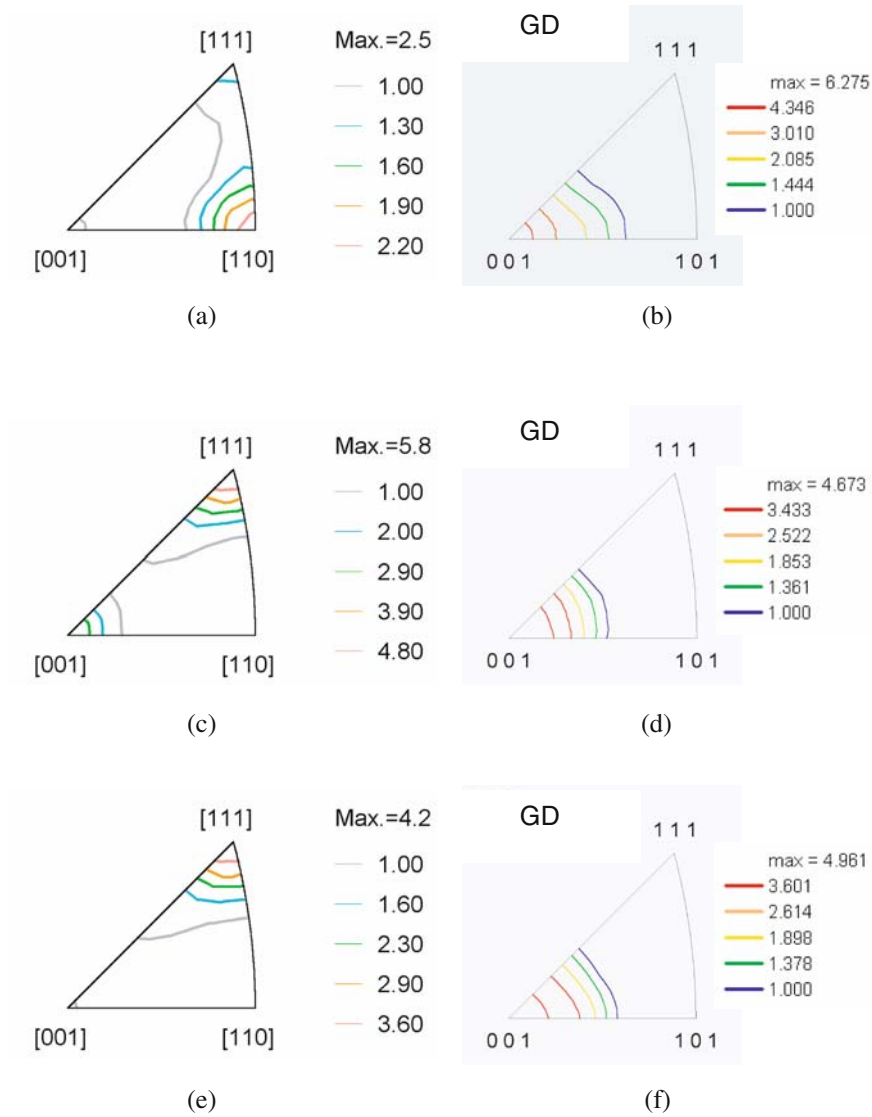


Fig. 27.14 GD inverse pole figures of (**a**) the substrate and (**b**) the wüstite layer for AR-PF, (**c**) and (**d**) for CR-PF, and (**e**) and (**f**) for ANN-PF

However, it has been reported that the oxidation rate in cold worked specimens is faster than in annealed specimens (Bredesen and Kofstad 1990; Caplan and Cohen 1966; Caplan et al. 1970a, 1970b; Carpenter and Ray 1973). These reports indicate that the concentration of vacancy sinks, such as grain boundaries or dislocations, in the substrate are responsible for the rate difference. Since the outward migration of cations during the oxidation process leaves vacancies at the oxide/substrate interface, pores formed by vacancy coalescence can hinder the iron ion transport. Conversely, the vacancy sinks in the substrate can attract the vacancies and cause vacancy removal by diffusion. If the concentration of the sinks increases because of cold working (i.e., an increase in dislocation density), the pore formation is suppressed and the diffusion rate of iron ions increases in the cold worked samples as compared to the annealed samples. Therefore, the increase in the sink concentration by cold working increases the oxidation rate in the cold worked specimen during oxidation, because of the effect of vacancy elimination. These effects are reduced with increased

purity of the substrate (Carpenter and Ray 1973); the oxidation rates of highly pure Fe are similar in both the cold worked and annealed samples. Moreover, Carpenter and Ray (1973) proposed that the differences in oxidation behavior are reduced with the increase of oxidation temperature.

As a result, for continuous high temperature oxidation of up to 950°C, cold deformation may not be important in determining the microstructure of iron oxides. Although the specimens are prepared by different metallurgical treatments and have different amounts of deformation, the probability that vacancies will be eliminated may not notably influence the high temperature microstructure of the iron oxides during continuous oxidation. Furthermore, even if there is an influence of the metallurgical treatment on oxidation at the lower temperatures, this influence will be diminished when heating is carried out up to 950°C. The sinks are likely to be eliminated by recrystallization at that high a temperature.

In the initial oxidation process, where the oxide thickness is a few nanometers, it is reported that epitaxial relationships between the substrate and the iron oxides can be observed (Kofstad 1988). Epitaxy can induce a preferred growth direction in a thin oxide film, which is dependent on orientation of the substrate (Kofstad 1988). In epitaxial growth, a crystallographic oxide plane with high atomic density appears to be parallel to a substrate plane with high atomic density. In oxidation of iron below 300°C, it has been reported that the Fe_3O_4 grains are oriented with (100), (111), (110) planes (Wagner et al. 1961; Béranger 1996), or with (100), (011), (111) planes (Swell and Cohen 1964), in that order. According to more recent results obtained using high-resolution transmission electron microscopy (HREM) for oxides formed at 300°C (Graat et al. 1997), the following orientation relationships between magnetite and ferrite were observed:

$$\begin{aligned} &(100)\ Fe_3O_4//(100)\ Fe \\ &[011]\ Fe_3O_4//[010]\ Fe. \end{aligned} \tag{27.2}$$

Also, other epitaxial relationships between planes in thermally grown oxide films were proposed by Cornell and Schwertmann (1996):

$$\begin{aligned} &(001)\ Fe//(001)\ FeO//(001)\ Fe_3O_4 \\ &(011)\ Fe//(111)\ Fe_3O_4//(001)\ Fe_2O_3. \end{aligned} \tag{27.3}$$

A tendency towards epitaxial growth of wüstite on iron was also observed at 700°C (Mehl et al. 1934; Béranger 1996; Gulbransen and Ruka 1952):

$$\begin{aligned} &(001)\ Fe//(001)\ FeO \\ &(011)\ Fe//(111)\ FeO \\ &(111)\ Fe//(021)\ FeO. \end{aligned} \tag{27.4}$$

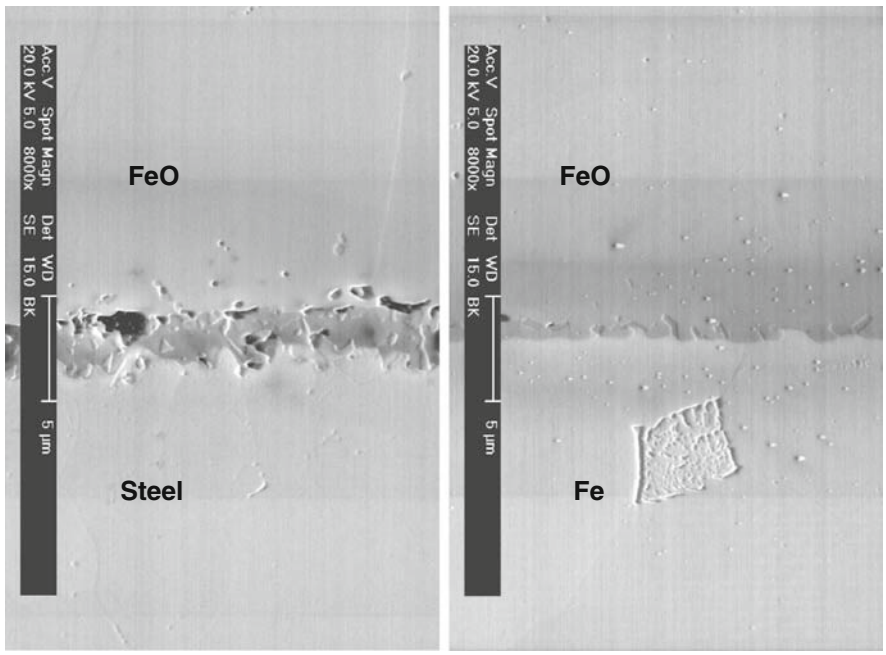
In this research, however, no such epitaxial growth is found. The substrate texture has no effect on oxidation under continuous heating up to 950°C. It is thought that epitaxy may disappear with increasing thickness of the oxide layer. There are several papers reporting the same results as those of this research in high temperature oxidation. During oxidation above 600°C and below 1200°C, the <001> fiber crystallographic texture in wüstite was observed, but no orientation relationship between the oxide layer and substrate was existed (Iordanova et al. 2000; Caudron et al. 1999; Buscail and Larpin 1996; Bredesen and Kofstad 1990). The magnetite phase shows the same type of <001> texture. In conclusion, both wüstite and magnetite develop the fiber texture with <001> // GD during high temperature oxidation.

27.4.3.2 Structure of Interfaces

Figure 27.15 shows typical secondary electron (SE) images of the interfacial microstructure after oxidation of LC steel and a cold-rolled pure Fe (CR-PF) under the same oxidation condition. Both interfacial microstructures show rather complicated interfaces; but in the LC steel sample, the thin complex layer between the steel and FeO is observed, unlike CR-PF. Since the plain, straight interface is likely to facilitate descaling, understanding the formation of the FeO/Fe interface of pure iron is important for descaling. Additionally, the structure of the interfaces between FeO/Fe_3O_4 and Fe_3O_4/Fe_2O_3 is important for understanding the oxidation mechanism.

Interface Between Fe and FeO

Figure 27.16 shows the wüstite/substrate interface after continuous oxidation of pure Fe under different metallurgical treatments. The interfaces are similar, but



(a) (b)

Fig. 27.15 SE images of the interfaces between wüstite and steel: (**a**) LC steel oxidized under the heating schedule CON2; (**b**) 70% cold-rolled pure Fe oxidized under the heating schedule CON1

the formation of fine wüstite grains at the interface is unique and was not reported earlier. The wüstite phase was identified by the Kikuchi patterns in OIM. At the FeO/Fe interface, there are fine wüstite grains having a granular shape elongated along the interface. The lengthwise size of the grains is between 600 and 2000 nm, and the average thickness of the oxide layer containing these fine grains is roughly 800 nm.

In LC steels, abnormal oxide structures were observed at the FeO/Fe interfaces. Details of interfacial characteristics for the LC steel are illustrated in Fig. 27.17. Instead of a thin oxide layer, a more complicated thick layer is found at the FeO/Fe interface. This layer consists of some unknown phase and wüstite grains identified by OIM. The alloying elements contained in LC steel might affect an intermediate layer structure. However, there have been no details of microstructure reported and no mechanism proposed, because of the difficulties of microstructural observation. From the IQ map, one can see that there are oxide grains on the order of microns in size, but structures of the intermediate layer cannot be identified because of a poor pattern quality. Alloying elements in LC steel may affect small granular grains of wüstite and may cause complicated oxide compounds to be formed. The mechanism for the formation of these wüstite granules has never been addressed.

The wüstite granules found at the FeO/Fe interface are likely to be formed at the initial stage of wüstite formation. According to the oxidation mechanism described in the beginning of this chapter, the wüstite phase can be formed by the reaction of Fe_3O_4 with iron ions at a temperature above 570°C (see Fig. 27.1). If the wüstite layer already exists, FeO can be formed at the Fe_3O_4/FeO interface without any additional supply of oxygen. This process is controlled only by the diffusion of iron ions and electrons through the entire wüstite layer. If the wüstite layer is not formed, the nucleation of wüstite at the Fe_3O_4/Fe interface has to be explained by another mechanism.

Figure 27.18 shows a schematic of the mechanism of formation of small wüstite grains under continuous oxidation from room temperature to 950°C. At the Fe_3O_4/Fe interface, magnetite grains with a grain size of a few hundreds of nanometers already exist. Also, iron ions and electrons are abundantly distributed along the interface (Fig. 27.18[a]). Wüstite can be

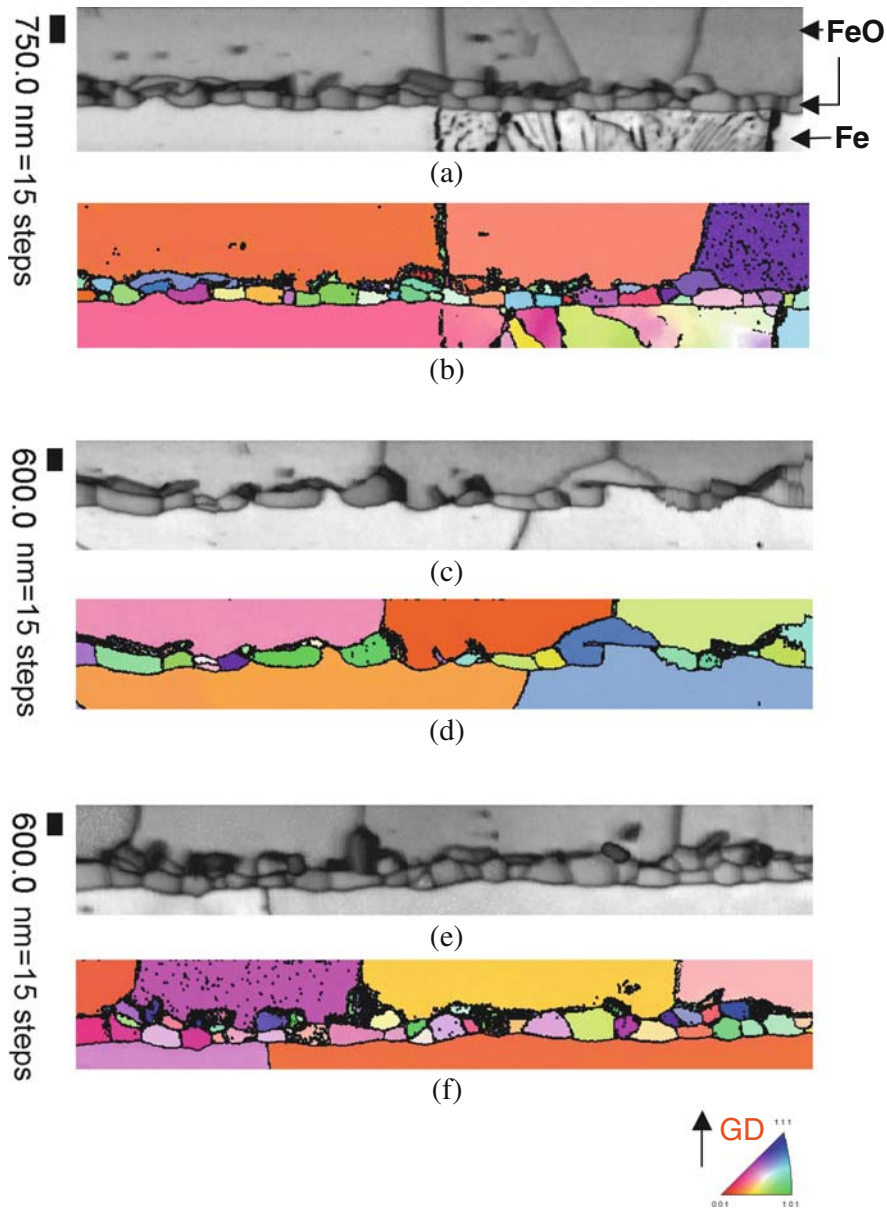


Fig. 27.16 Micrographs showing the microstructure at the interfaces of wüstite and pure Fe after different treatment: (**a**) the IQ map and (**b**) the IPF map for AR-PF, (**c**) and (**d**) for CR-PF, and (**e**) and (**f**) for ANN-PF. The IPF maps are constructed with respect to GD

formed by the direct reaction of Fe_3O_4 and Fe at the Fe_3O_4/Fe interface without any diffusion of reactants, such as iron ions and electrons, at temperatures over 570°C. As a result of the interfacial reaction, the wüstite grains begin to form along the interface (Fig. 27.18[b]). After wüstite layer forming, the new grains can hardly continue to grow, because wüstite can no longer be formed by the direct reaction of iron ions with magnetite at the Fe_3O_4/Fe interface. Moreover, the diffusivity of iron ions in wüstite is low because of the relatively low temperature. Once the initial wüstite layer is formed and the heating temperature increases for further oxidation, the reactants start to diffuse through the wüstite layer and a new wüstite

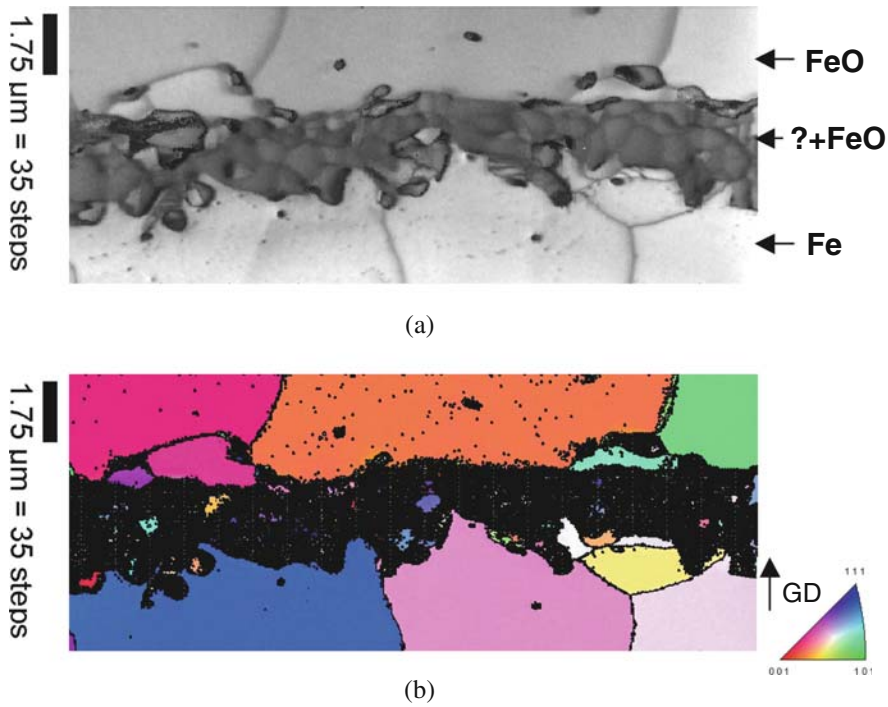


Fig. 27.17 Micrographs showing the microstructure at the interfaces of wüstite and LC steel: (**a**) the IQ map, and (**b**) the IPF map parallel to GD

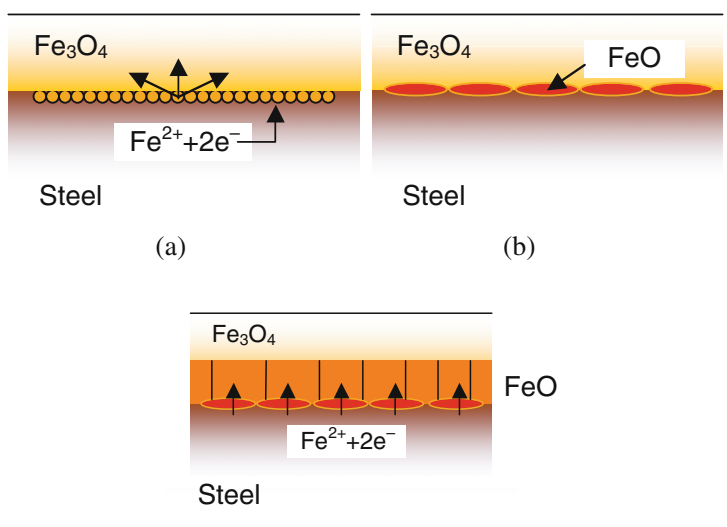


Fig. 27.18 Schematic diagrams showing the wüstite formation during high temperature oxidation: (**a**) just before the wüstite nucleation, (**b**) just after the formation of the wüstite granules, and (**c**) after high temperature oxidation

grain begins to form and grow at the Fe_3O_4/FeO interface (Fig. 27.18[c]). If one can assume that wüstite granules at the FeO/Fe interface are formed at the growth stage, the oxygen ions should be able to diffuse directly into the substrate through the oxide layers. This is unlikely to occur, because the oxidation is controlled by outward diffusion of Fe. Therefore, the proposed mechanism is very probable.

In the FeO/Fe interface, voids are frequently observed. Figure 27.19 shows the voids and their locations. The Fe^{2+} cations move outward to the free surface, and these migrations leave vacancies at the FeO/Fe interface. These vacancies make pores or voids as the oxidation process progresses. It is interesting to note the position of the voids because they are located above the granular layer of wüstite, and this indicates that they are likely to remain there after diffusion of cations and electrons through the granular wüstite. This result has never been reported before. These microstructures with voids or pores at the FeO/Fe interface may be favorable for mechanical descaling.

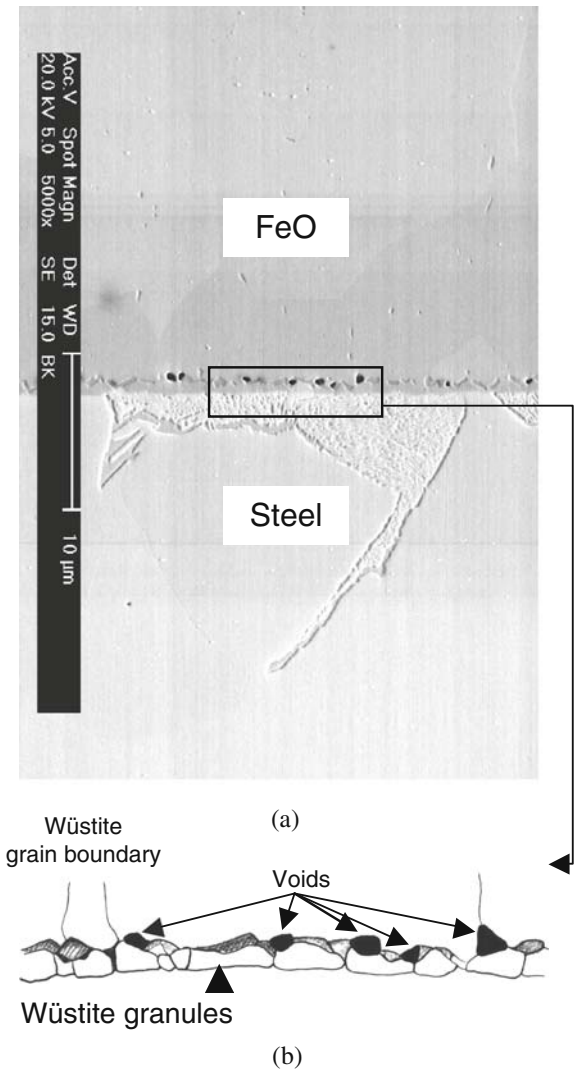


Fig. 27.19 Void formation at the interfaces of wüstite and pure Fe according to AR-PF. The specimens were oxidized using the heating schedule CON1: (**a**) the secondary electron (SE) image, and (**b**) the schematic diagram for the area selected in the image

Interface Between Fe_3O_4 and FeO

A typical interface between the Fe_3O_4/FeO layers is illustrated in Fig. 27.20 for the samples of AR-PF, CR-PF, ANN-PF, and LC steels. Although the pure Fe samples were prepared by different metallurgical treatments, the structural characteristics of the interfaces are similar in a manner related to the grain shape and the layer thickness of the magnetite (Fig. 27.20[a, b, c, d, e, f]). In the LC steel sample (Fig. 27.20[g, h]), the ratio of the number of magnetite grains to the number of wüstite grains at the interface is less than in the pure Fe samples, and the size of the magnetite grains is larger than in the pure Fe samples.

Interface Between Fe_2O_3 and Fe_3O_4

As in the LC steel sample (Fig. 27.11), the Fe_2O_3/Fe_3O_4 interface in pure iron shows complicated irregularities, and illustrates the hematite growth into magnetite grains (Fig. 27.21). The interfacial microstructures in the pure Fe samples were obtained using different metallurgical treatments. Under the CON1 heating schedule, the hematite layer is difficult to identify because the hematite grains are irregular and do not form a continuous layer structure. These grains have a wedge shape and are embedded within the magnetite grains. It should be noted that the growth direction of hematite grains usually has an angle of around 50–60 degrees with respect to the direction of oxide growth. Moreover, the hematite grains may span over two magnetite grains (Fig. 27.21[e, f, g]). The elongated grain morphology indicates a preferential growth direction for hematite.

The direction of hematite growth is likely related to the orientation relationship between magnetite and hematite as follows (Newcomb and Stobbs 1985; Condon et al. 1994; Watanabe and Ishii 1995; Lagoeiro 1998):

$$(111)\ Fe_3O_4//(0001)\ Fe_2O_3. \qquad (27.5)$$

The (111) Fe_3O_4 and (0001) Fe_2O_3 planes are crystallographic planes having close packed oxygen anions. Oxide growth occurs across close packed oxygen planes (Condon et al. 1994). In a cubic system, it is known that the interplanar angle between (111) and (001) planes is 60 degrees. Since the preferred orientation of the magnetite layer is <001>//GD, the hematite grains must grow at an angle of 60 degrees from the <001> crystal direction of magnetite. Therefore, the basal plan (0001) Fe_2O_3 is aligned parallel to the crystallographic plane in Fe_3O_4 where hematite is growing.

Such hematite growth may be facilitated by the inward diffusion of oxygen into magnetite, because

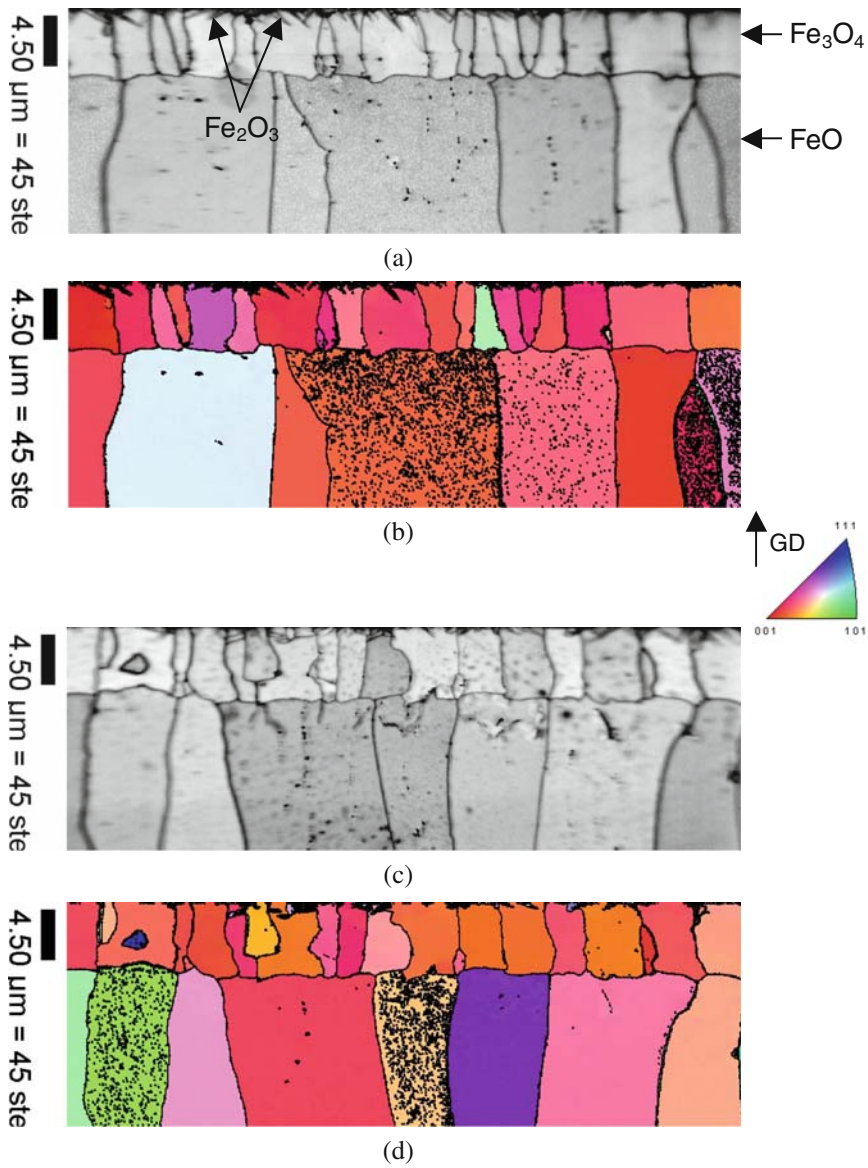


Fig. 27.20 Micrographs showing the microstructure at the interfaces of magnetite and wüstite: (**a**) the IQ map and (**b**) the IPF map for AR-PF, (**c**) and (**d**) for CR-PF, (**e**) and (**f**) for ANN-PF, and (**g**) and (**h**) for LC steel

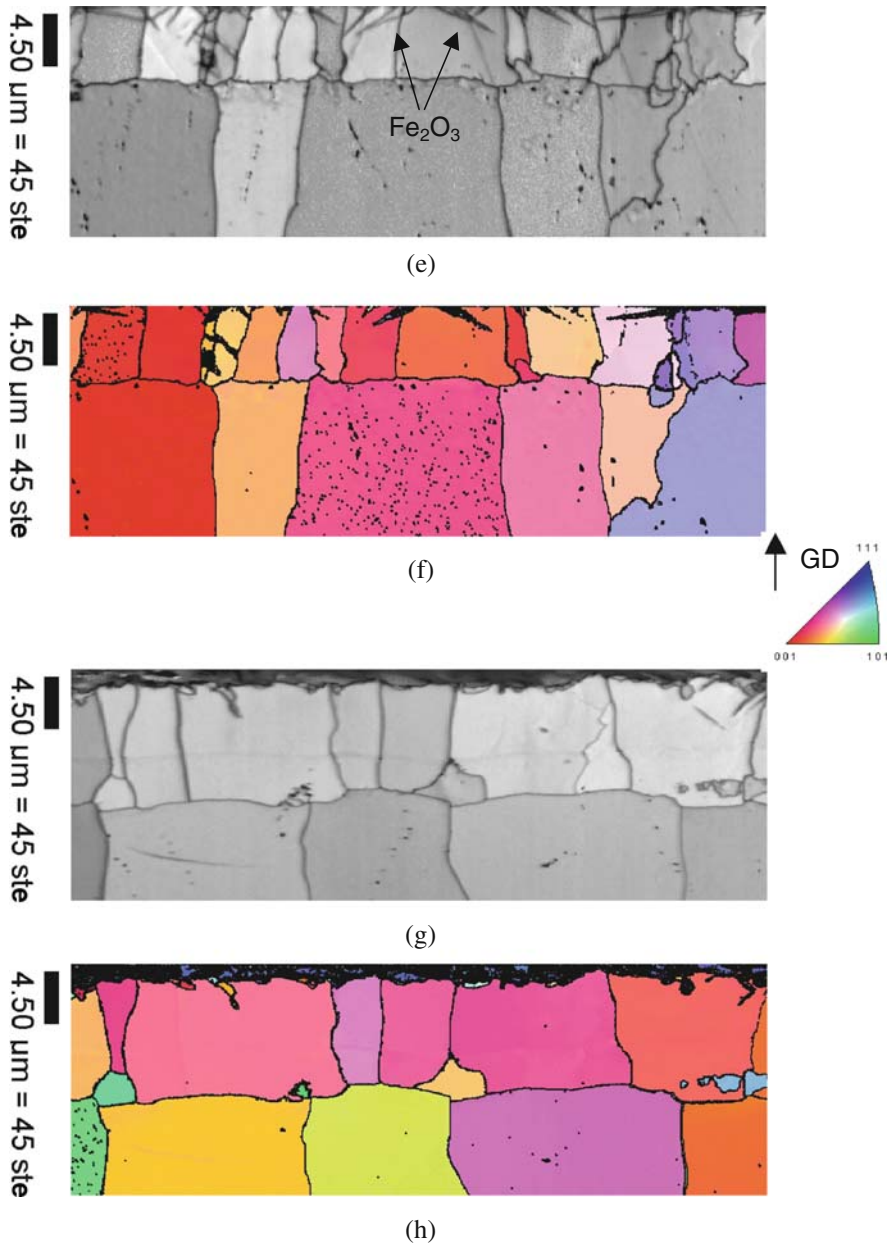


Fig. 27.20 (continued)

the hematite grains embed in the magnetite grains. As mentioned earlier, hematite forms at the hematite/air interface if the Fe cations are mobile, or at the Fe_3O_4/Fe_2O_3 interface if the oxygen anions are mobile. In order for hematite to form at the hematite/oxygen interface, iron ions should be able to diffuse through the magnetite layer and the hematite layer should be formed on the surface of the magnetite layer. However, the hematite grains were observed to be the wedge shape embedded in the magnetite grains, indicating that the outward diffusion of iron ions through the oxide layers is more difficult. Instead, the

diffusion of oxygen may occur preferentially within the magnetite grains, and the following reaction is likely taking place:

$$2Fe_3O_4 + O^{2-} = 3Fe_2O_3. \quad (27.6)$$

27.5 Cracks and Defects

In order to establish a model for the fracture of oxide scale in the hot rolling process, it is necessary to investigate the formation and propagation of cracks in iron oxides. Moreover, the formation of cracks within the scale in high temperature oxidation is likely to facilitate descaling. When no external stresses are applied to an oxidized specimen, cracks must originate from thermal stresses due to differences in thermal expansion between the substrate and the oxides. When the specimen is cooled down to room temperature, the magnitude of thermal stresses is roughly proportional to the difference between the oxidation temperature and room temperature.

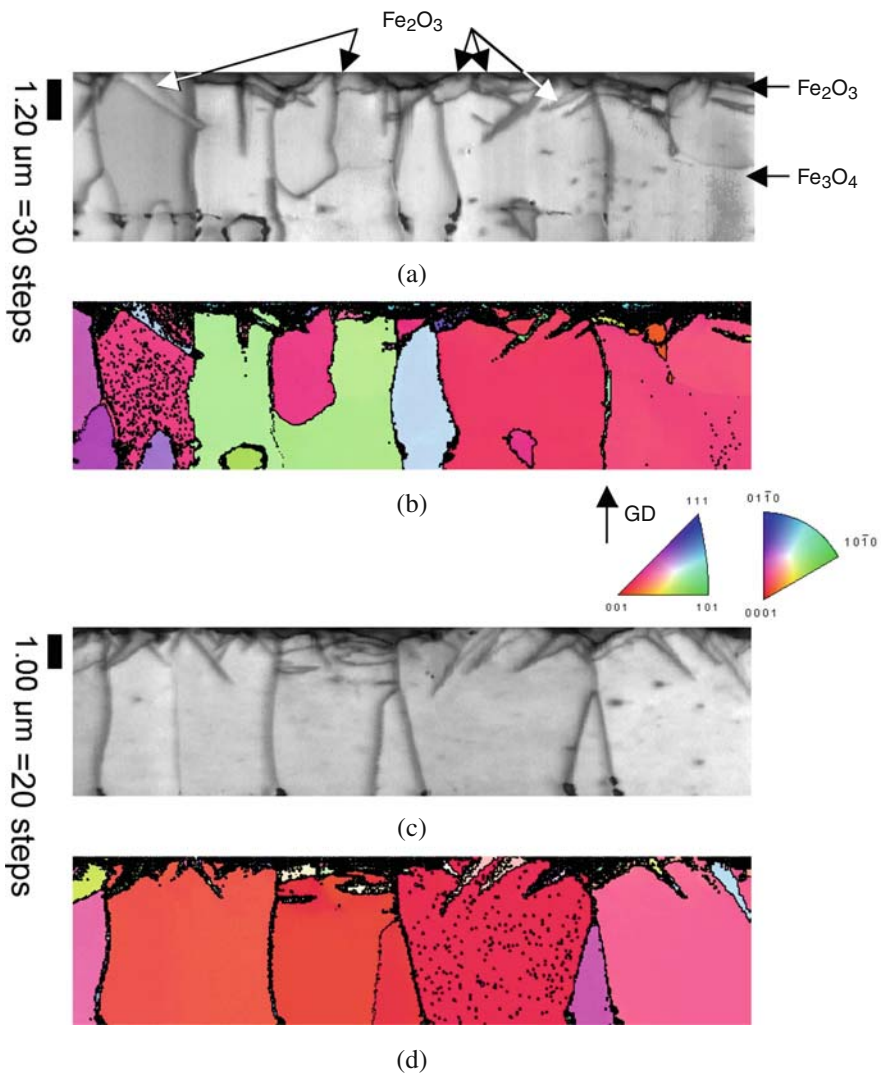


Fig. 27.21 Micrographs showing the microstructure at the interfaces of hematite and magnetite: (**a**) the IQ map and (**b**) the IPF map for AR-PF, (**c**) and (**d**) for CR-PF, and (**e**) and (**f**) for ANN-PF; (**g**) the SE image for ANN-PF

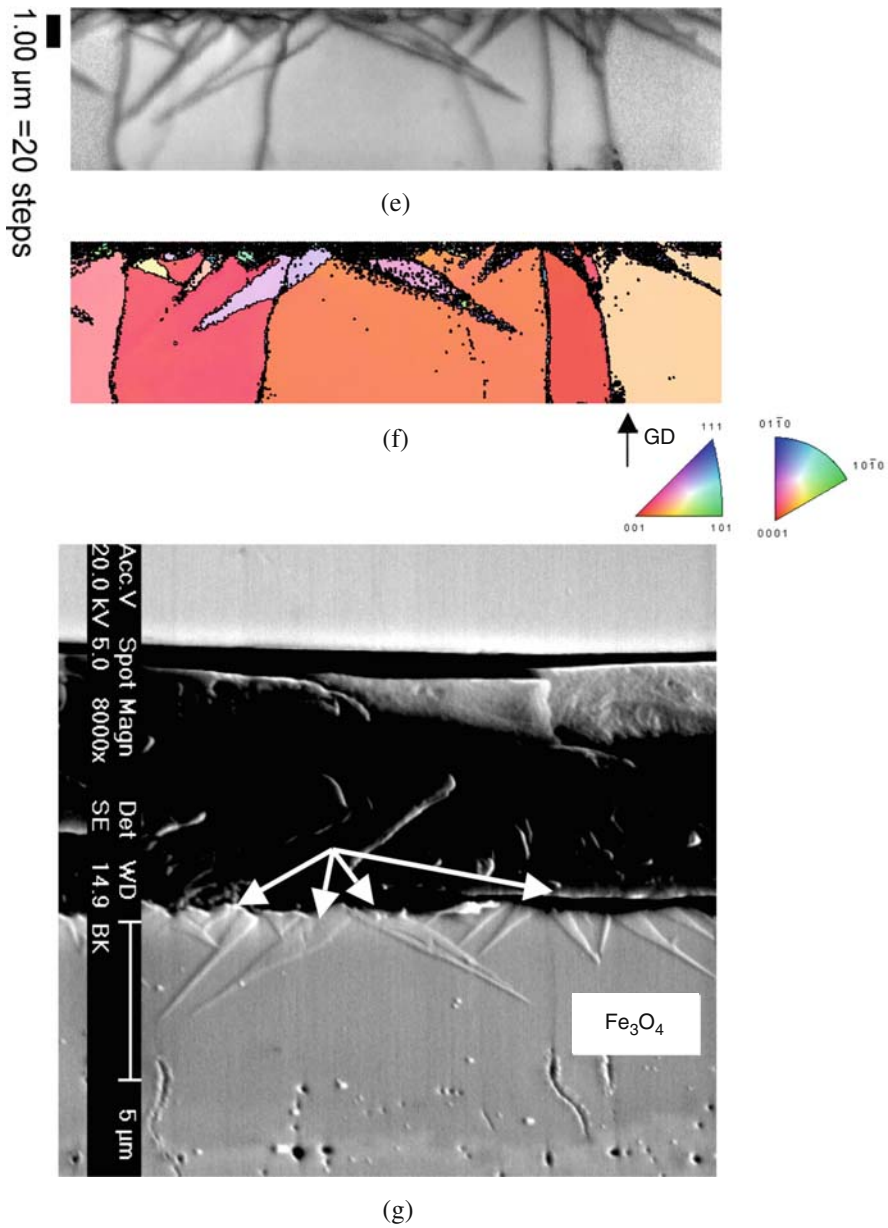


Fig. 27.21 (continued)

The specimens used for investigation of cracks and defects are obtained from continuous oxidation up to 950°C. Figure 27.22 shows micrographs related to fractured oxide layers. Typically, as seen in the secondary electron (SE) image in Fig. 27.22(a), the oxide layer is fractured through the entire layer. The OIM results reveal details of the microstructure. Figure 27.22(b) shows the IQ map, and Fig. 27.22(c, d) show the IPF maps for GD and RD, respectively. The direction RD is the direction normal to the cross-sectional area (see Fig. 27.3). As illustrated in Fig. 27.22(c, d), the colors of the magnetite grains around the fracture path are different, indicating that the grains have different crystal orientations. There-

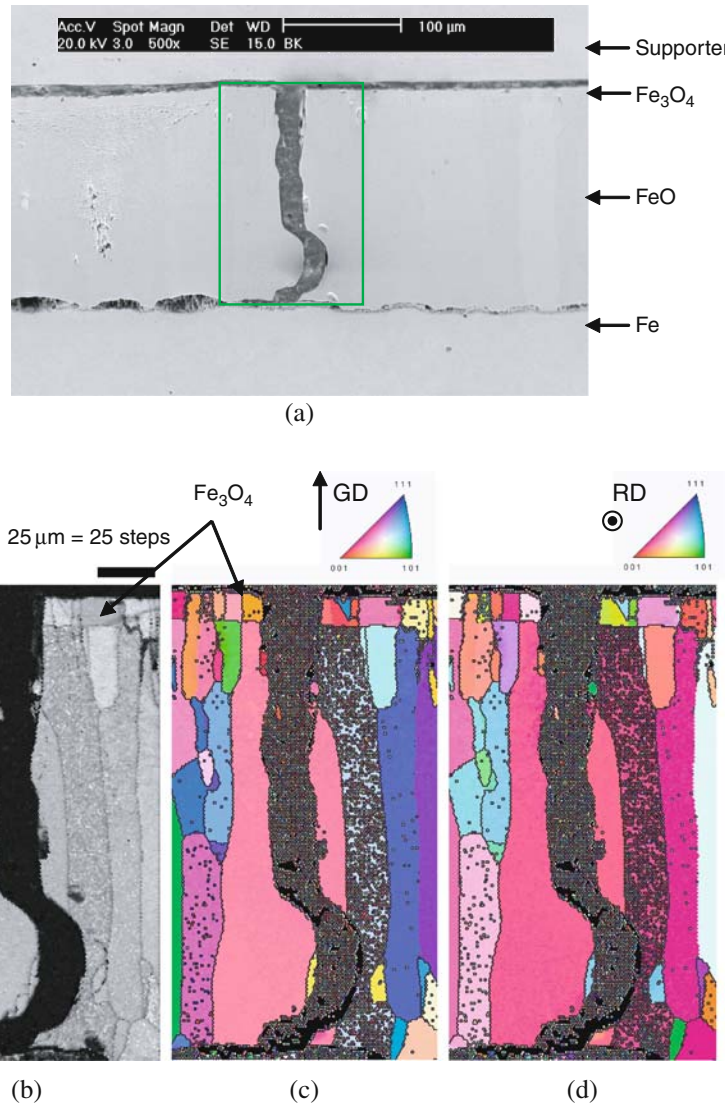


Fig. 27.22 Micrographs showing the macro crack of the oxide layer: (**a**) a tilted secondary electron image, (**b**) the IQ map, (**c**) the IPF map to GD, and (**d**) the IPF map to RD

fore, it is thought that a fractured path starts along the grain boundary of the magnetite grains and penetrates into the connected wüstite grains. The fracture line observed in the wüstite layer initially penetrates along the grain boundary of two wüstite grains and propagates into a wüstite grain.

Figure 27.23 provides more details illustrating crack propagation at the partially cracked area. One can see the crack line in the IQ map (Fig. 27.23[a]), but this line cannot be noticed in the IPF maps (Fig. 27.23[b, c]). The crack line starts from the grain boundary of two magnetite grains and propagates though the wüstite grain. The crack line observed in the IQ micrograph of Fig. 27.23(a) is confirmed by the SE image of Fig. 27.23(d).

It can be concluded from these observations that once the magnetite layer is under tensile stress and the interfacial boundary between magnetite and wüstite is strong, the crack is initiated at the weak grain boundaries of the magnetite grains and propagates through wüstite. When the bonding between the magnetite and wüstite grains is weak, the crack is likely to propagate

through phase boundaries between the magnetite and wüstite grains. More detailed micrographs of the interfacial area between magnetite and wüstite are necessary to precisely illustrate a cracking mode within the wüstite granules.

Voids are usually observed in the layers of Fe_3O_4 and in adjacent FeO. Figure 27.24 illustrates the microstructure showing voids and void coalescence. It is interesting to note that the tracers of voids and void coalescence in the wüstite layer extend beyond the interface into magnetite grains. Figure 27.25 shows the orientation imaging micrographs with another SE image. The IQ map of Fig. 27.25(a) displays the microstructure in which void tracers in wüstite are connected to the magnetite grain boundaries. Due to the small step size (100 nm) of the OIM scan, the small voids can be observed early in the OIM maps. Figure 27.25(c, d) also illustrate that void coalescence in the wüstite grains is connected to the magnetite grain boundaries and that the pores also exist in the magnetite grain boundaries. It is thought that these phenomena can provide favorable crack paths.

The micrographs in Fig. 27.26 represent OIM results for a larger area of the specimen. Many void

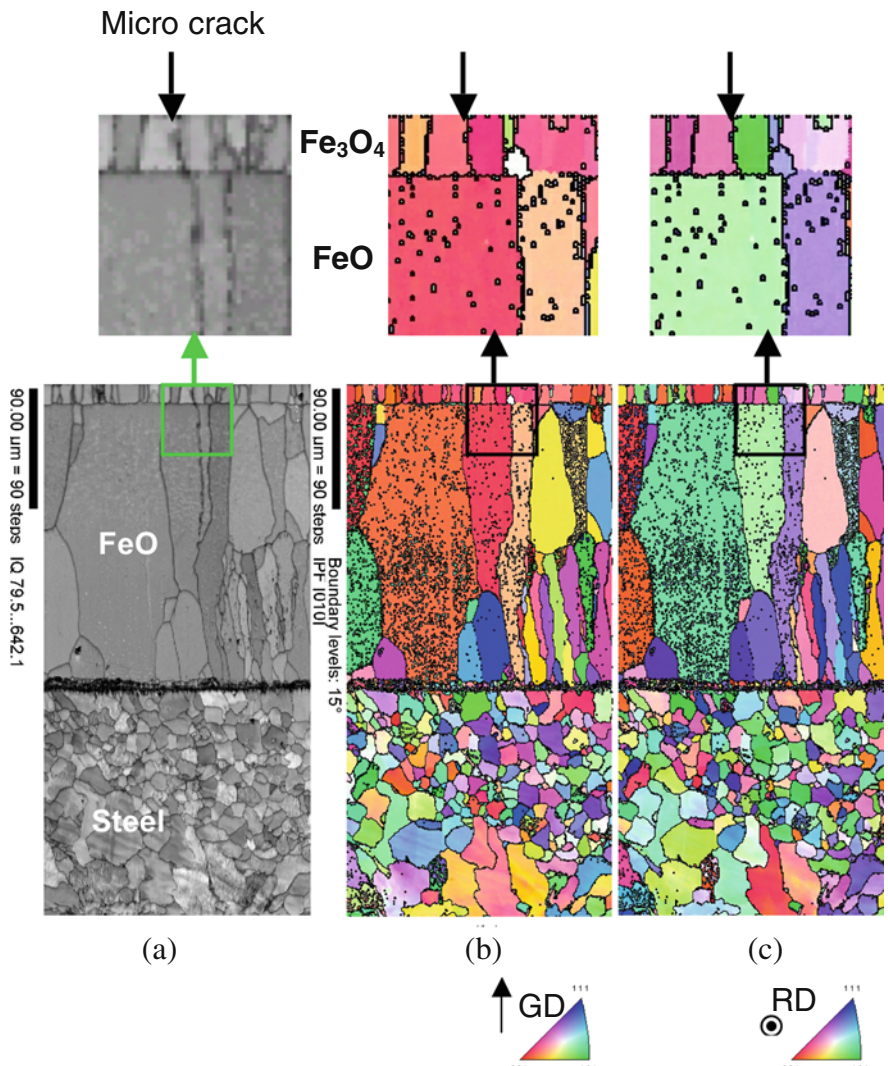
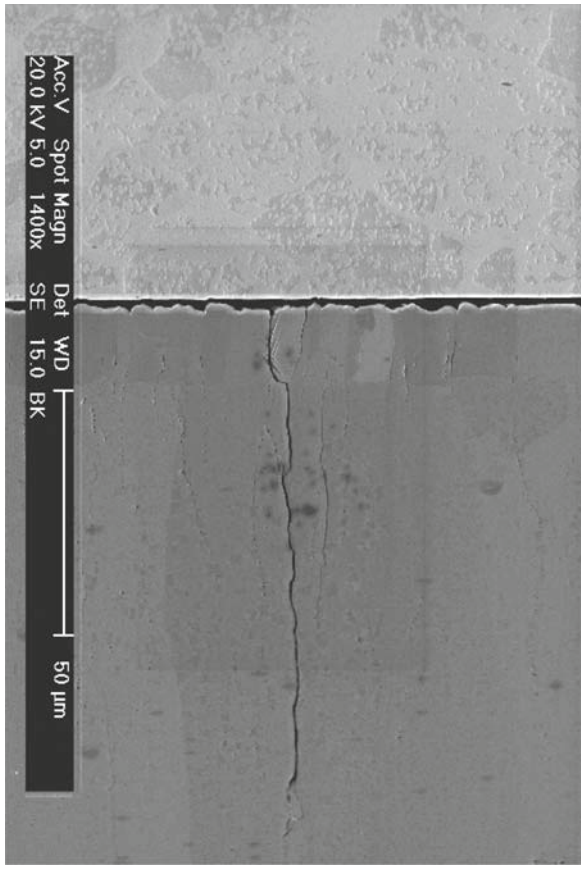


Fig. 27.23 Micrographs showing a microcrack in the magnetite and wüstite layer: (**a**) the IQ map, (**b**) the IPF map to GD, (**c**) the IPF map to RD, and (**d**) a tilt-corrected SE image for the area selected in the OIM map



(d)

Fig. 27.23 (continued)

lines within wüstite grains can be observed: these lines end at the Fe_3O_4/FeO interface or at the encounter with magnetite grains. Figure 27.26(b, c) illustrate that each line of void traces is well connected with the magnetite grain boundaries. Furthermore, the voids are also found at the magnetite grain boundaries. The voids in these figures are not as well represented as those in Fig. 27.25, because the scanning step size (400 nm) is bigger.

The defect structure discussed above cannot be found in the samples obtained under isothermal oxidation above 570°C. This means that the observed voids and defects are likely to be created by oxidation only under the continuous heating schedule. As mentioned earlier describing the mechanism of oxidation, wüstite grains are formed and grow at the Fe_3O_4/FeO interface. During this reaction, iron ion and electron surpluses proceed outward through iron ion vacancies (Birks and Meier 1983; Kofstad 1988). Since the grain boundaries of magnetite attract the vacancies or voids because of the higher energy of the grain boundaries, magnetite grain boundaries can act as sinks for point defects. Therefore, such vacancies or voids are concentrated around the sinks. As wüstite grows by the reaction of Fe_3O_4 with iron ions and electrons during continued oxidation, the concentrated defects coalesce and remain inside the wüstite. It is believed that coalescence of pores and voids can contribute to the crack propagations in iron oxides. Thus, under the tensile stress parallel to the oxide surface, the crack that initiated at the magnetite grain boundaries can easily propagate into the wüstite grains, where void coalescence has already occurred.

There is another factor contributing to crack initiation. The micrographs of Fig. 27.27 show the microstructures that are occasionally found near the

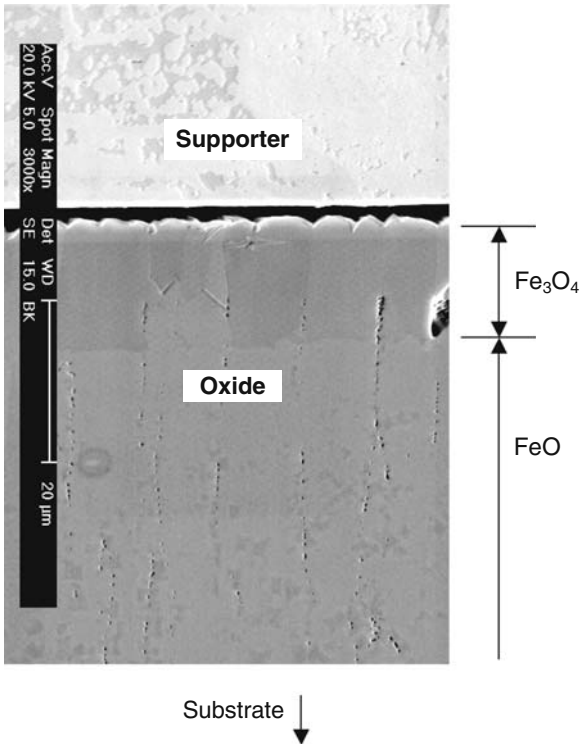


Fig. 27.24 Secondary electron image showing micro-void coalescence in the magnetite and wüstite layers

local cracks in the fractured magnetite layer. The preferential growth of hematite grains in certain areas of the magnetite layer is similar to the hematite growth observed in Fig. 27.21. The lath-type grains are tilted at an angle of 60–70 degrees to the <001> crystal direction of magnetite. In high temperature oxidation, growth stresses can be compensated within the magnetite layer to keep coherency with the wüstite layer. Hypothetically, in order to release the stress in the magnetite layer, the oxygen that diffused through the grain boundaries of magnetite can react with the magnetite grains and transform them into hematite. The difference in volume created by this transformation may initiate the cracks along the magnetite grain boundaries. In fact, it has been reported that the transformation of magnetite to hematite occurs along {111} planes, and that it results in the hematite domain along {111} in iron oxide minerals (Lagoeiro 1998). Also, it is proposed that the difference in volume created by this transformation and the shear stress acting on the interphase boundaries allows the oxidizing agent to penetrate along these planes, and as a result, an orientation relationship, {111} Fe_3O_4 // (0001) Fe_2O_3, between the magnetite and hematite grain is developed.

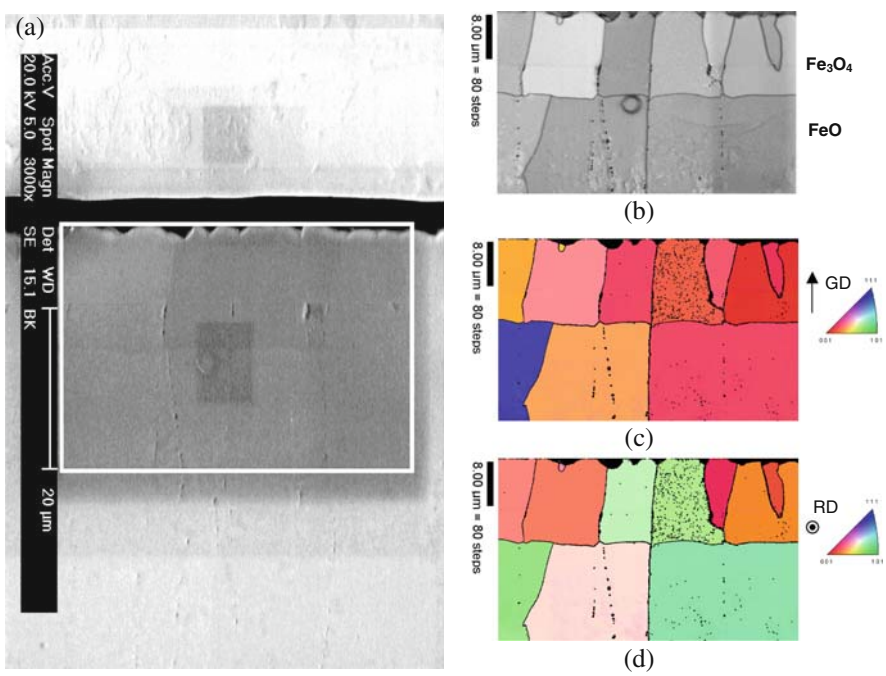


Fig. 27.25 Micrographs showing micro voids and their coalescence in the magnetite and wüstite layers: (**a**) a tilt-corrected SE image, (**b**) the IQ map, (**c**) the IPF map parallel to GD, and (**d**) the IPF map parallel to RD

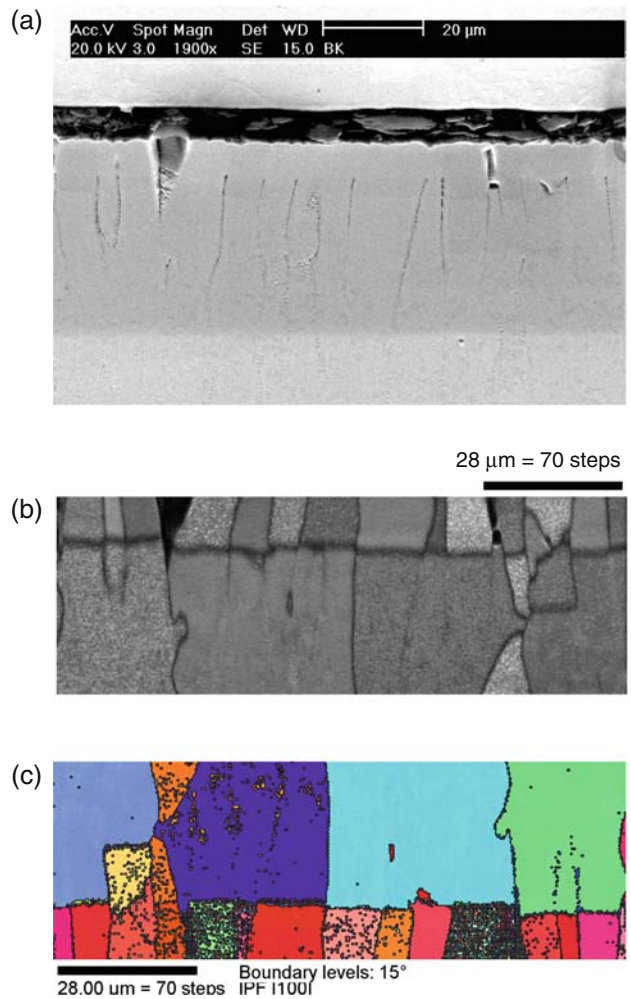


Fig. 27.26 Micrographs showing the micro-void coalescence in the wüstite layer connected into the magnetite grain boundaries: (**a**) a tilt-corrected secondary electron image, (**b**) the IQ map, and (**c**) the IPF map to GD

27.6 Conclusion

The microstructural investigations by OIM have been used for characterization of iron oxides formed during high temperature oxidation of low carbon (LC) steels and pure iron. Using OIM observations of the cross-sectional area of the oxide layers, the oxide microstructure is characterized. Interfaces between oxide phases are described and the structure of defects and pores is analyzed. It is demonstrated that orientational imaging mapping using EBSD techniques can help to understand the mechanism of high temperature oxidation and formation of iron oxide microstructures. The following conclusions can be drawn regarding oxidation of LC steels and pure iron.

(1) Under continuous heating up to 950°C, the oxide phases are composed of 94.4% FeO, 5% Fe_3O_4, and 0.6% Fe_2O_3.
(2) All iron oxides obtained during high temperature oxidation have anisotropic microstructures and are textured.
(3) Wüstite has a columnar cell structure and the length of the column is parallel to the diffusion path and normal to the surface of the substrate. The texture of wüstite grains is described as <001> fiber parallel to the growth direction (GD). The grain growth of wüstite can be divided into two stages: the initial nucleation stage and the grain growth stage. As the oxidation is followed from the initial stage to the growth stage, the texture intensity of <001>//GD component is

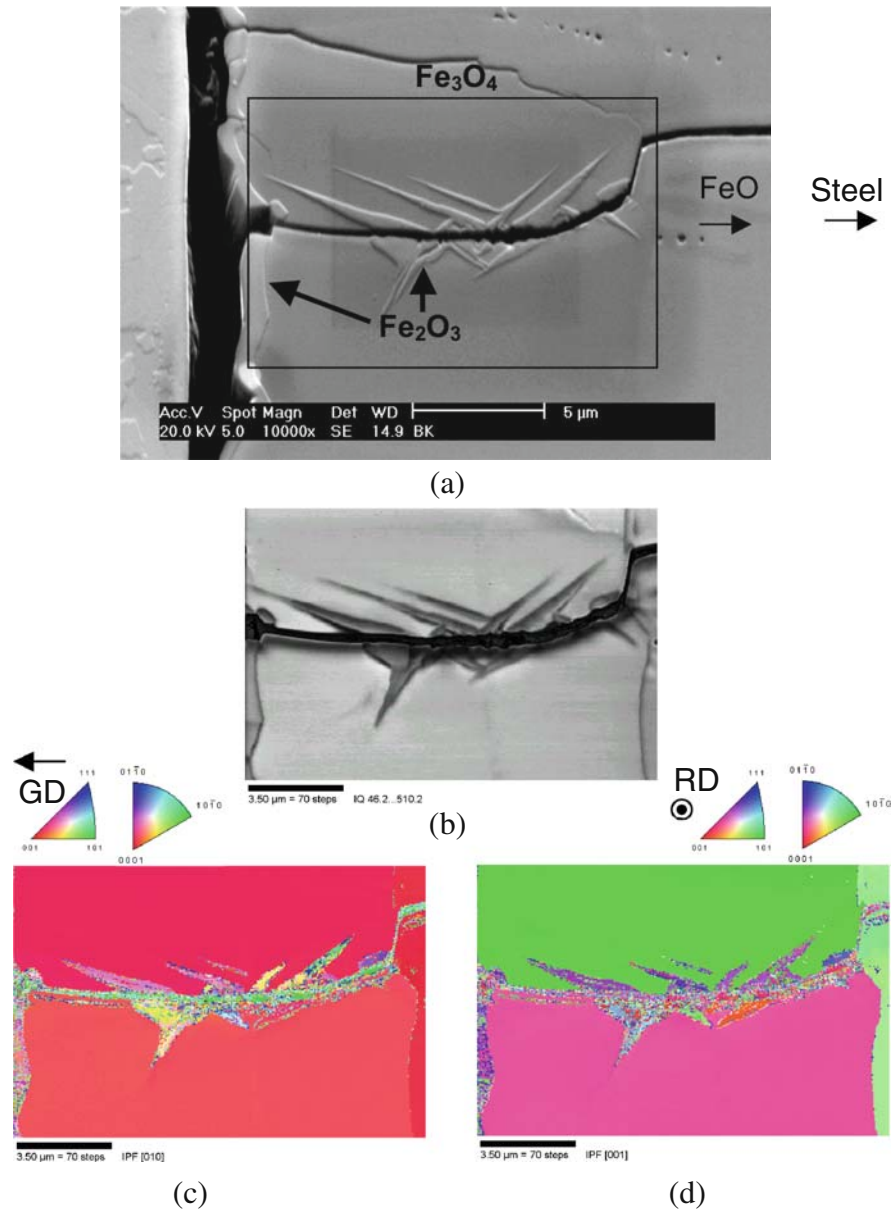


Fig. 27.27 Anisotropic grain growth of hematite and initiation of cracking: (**a**) a tilt-corrected SE image, (**b**) the IQ map, (**c**) the IPF map to GD, and (**d**) the IPF map to RD

strengthened and the fraction of low angle grain boundaries ($\theta \leq 25^\circ$) increases. Based on the characteristics of the grain boundary network, it can be concluded that the lattice diffusion of Fe ions is mainly responsible for oxide growth at high temperatures.

(4) At 600°C, magnetite randomly nucleates with grain sizes of hundreds of nanometers. At elevated temperature under continuous heating up to 950°C, magnetite has a cubic cell structure with <001>//GD. The minimization of surface energy may play a role in the development of this texture.

(5) Hematite grains have an irregular wedge shape embedded at the surface of the magnetite. Hematite does not form a layer structure.
(6) Oxidation during continuous heating and isothermal heating can influence wüstite texture, but does not affect the microstructure of wüstite. The influence of the thermal history on the magnetite structure is small.
(7) There are no effects of the substrate or its texture on oxide microstructure. Wüstite and magnetite have <001>//GD texture, regardless of which substrate was examined or which substrate texture was observed under continuous oxidation up to 950°C.
(8) The formation of wüstite granules at the FeO/Fe interface is likely to influence mechanical descaling in LC steels.
(9) The hematite grains grow at a constant angle of around 50–60 degrees with respect to GD. This growth can be related to the orientation relationship between magnetite and hematite: (111) Fe_3O_4 // (0001) Fe_2O_3. This grain growth direction is likely to result from the direction of the inward diffusion of oxygen.
(10) Microcracks initiate in magnetite grain boundaries and propagate into wüstite grains. Voids and void coalescence are observed in wüstite grains close to the Fe_3O_4/FeO interface and can contribute to the ease of crack propagation. The volume increase by the transformation of magnetite into hematite can also contribute to local concentrations of stress and crack initiation.

References

Abuluwefa H, Root JH, Guthrie RIL, Ajersch F (1996) Real-time observations of the oxidation of mild steel at high temperature by neutron diffraction. Metall Mater Trans B 27: 993–997

Baba-Kishi KZ, Dingley DJ (1989) Backscatter Kikuchi diffraction in the SEM for identification of crystallographic point groups. Scanning 11:305–312

Béranger G (1996) Oxidation. In: Béranger G, Henry G, Sanz G (eds) The book of steel (trans Davidson J.H). Intercept LTD, Andover, U.K.

Birks N, Meier GH (1983) Introduction to high temperature oxidation of metals. Edward Arnold, London

Birosca S, Dingley D, Higginson RL (2004) Microstructural and microtextural characterization of oxide scale on steel using electron backscatter diffraction. J Microsc 213:235–240

Bredesen R, Kofstad P (1990) On the oxidation of iron in CO_2 + CO gas mixtures: I. Scale morphology and reaction kinetics. Oxid Met 34:361–379

Bruckman K, Simkovich G (1972) Concerning the mechanism of scale growth due to cation diffusion in Fe_2O_3 and CuS. Corros Sci 12:595–601

Buscail H, Larpin JP (1996) The influence of cerium surface addition on low-pressure oxidation of pure iron at high temperatures. Solid State Ionics 92:243–251

Caplan D, Cohen M (1966) Effect of cold work on the oxidation of iron from 400 to 650°C. Corros Sci 6:321–335

Caplan D, Graham MJ, Cohen M (1970a) Effect of oxygen pressure and experimental method on the high temperature oxidation of pure Fe. Corros Sci 10:1–8

Caplan D, Sproule GI, Hussey RJ (1970b) Comparison of the kinetics of high-temperature oxidation of Fe as influenced by metal purity and cold work. Corros Sci 10:9–17

Carpenter DL, Ray AC (1973) The effect of metallurgical pretreatment on the kinetics of oxidation of iron at 700°C in pure gaseous oxygen. Corros Sci 13:493–502

Caudron E, Buscail H, Riffard F (1999) Initial oxidation stage of yttrium implanted pure iron at 700°C by in situ high temperature X-ray diffraction. Eur Phys J-Appl Phys 8:233–240

Chen RY, Yuen WYD (2000) A study of the scale structure of hot rolled steel strip by simulated coiling and cooling. Oxid Met 53(5/6):539–560

Condon NG, Murray PW, Leibsle FM, Thornton G, Lennie AR, Vaughan DJ (1994) Fe_3O_4 (111) termination of α- Fe_2O_3 (0001). Surf Sci 310:L609–L613

Cornell RM, Schwertmann U (1996) The iron oxides. VCH, Weinheim, Germany, 458

Davies MH, Simnad MT, Birchenall CE (1951) Mechanism and kinetics of the scaling of iron. J Met-T AIME 3:889–896

Davies MJ, Parker SC (1989) Unpublished works (Bath University) cited in: Robertson J, Manning, MI (1990) Mater Sci Techn 6:81–91

Dingley DJ, Randle V (1992) Microtexture determination by electron back-scatter diffraction. J Mater Sci 27:4545–4566

Dubinin GN (2000) On the columnar structure of a diffusion layer. Met Sci Heat Treat 42:89–93

Eades A (2000) EBSD: Buying a system. In: Schwartz AJ, Kumar M, Adams BL (eds) Electron backscatter diffraction in materials science. Kluwer Academic/Plenum, New York

Goehner RP, Michael JR (1996) Phase identification in a scanning electron microscope using backscattered electron Kikuchi patterns. J Res Natl Inst Stand Tech 101: 301–308

Graat PCJ, Brongers MPH, Zandbergen HW, Somers MAJ, Mittemeijer EJ (1997) HREM investigation of the constitution and the crystallography of thin thermal oxide layers on iron. In: Newcomb SB, Little JA (eds) Microscopy of oxidation, vol. 3. Institute of Materials, London, pp 503–514

Gulbransen EA, Ruka R (1952) Role of crystal orientation in the oxidation of iron. J Electrochem Soc 99:360–368

Hauffe (1965) Oxidation of metals. Plenum, New York

Higginson RL, Roebuckb B, Palmiere EJ (2002) Texture development in oxide scales on steel substrates. Scripta Mater 47:337–342

Iordanova I, Surtchev M, Forcey KS, Krastev V (2000) High-temperature surface oxidation of low-carbon rimming steel. Surf Interface Anal 30:158–160

Katrakova D, Maas C, Hohnerlein D, Mucklich F (1998) Experiences on contrasting microstructure using orientation imaging microscopy. Prakt Metall 35:4–20

Kim BK, Szpunar JA (2001a) Orientation imaging microscopy for the study of high temperature oxidation. Scripta Mater 44:2605–2610

Kim BK, Szpunar JA (2001b) Grain growth of iron oxides during high temperature oxidation. In: Gottstein G, Molodov DA (eds) Proceedings of the first joint international conference on recrystallization and grain growth, Aug. 27–31. Aachen, Germany

Kofstad P (1988) High temperature oxidation. Elsevier Applied Science, London

Kuiry SC, Roy SK, Bose SK (1994) A superficial coating to improve high-temperature-oxidation resistance of a plain-carbon steel under nonisothermal conditions. Oxid Met 41:65–79

Lagoeiro LE (1998) Transformation of magnetite to hematite and its influence on the dissolution of iron oxide minerals. J Metamorph Geol 16:415–423

Li H (2001) TexTools, ver. 3.1

Matthies S, Vinel GW (1993) On some methodical developments concerning calculations performed directly in the orientation space. Mater Sci Forum 157–162:1641–1646

Mehl RF, Candless EL, Rhines FN (1934) Orientation of oxide films on metals. Nature 134:1009

Michael JR, Eades JA (2000) Use of reciprocal lattice layer spacing in electron backscatter diffraction pattern analysis. Ultramicroscopy 81:67–81

Michael JR, Goehner RP (1993) Crystallographic phase identification in the scanning electron microscope: Backscattered electron Kikuchi patterns imaged with a CCD-based detector. MSA Bulletin 23:168–175

Newcomb SB, Stobbs WM (1985) Proceedings of Electron Microscopy and Analysis Group (EMAG) Conference. The Institute of Physics, Newcastle upon Tyne, 2–5 Sept., UK., 451

Pawlik K, Pospiech J, Lücke K (1991) The ODF approximation from pole figures with the aid of the ADC method. Texture Microstructure 14–18, 25–30

Pinder LW (1995) The oxidation resistance of low-alloy steels. In: Shreir LL, Jarman RA, Burstein GT (eds) Corrosion, vol. 1. Butterworth Heinemann, London

Randle V, Engler O (2000) Introduction to texture analysis: macrotexture, microtexture and orientation mapping. Gordon & Breach Science, Amsterdam, The Netherlands

Sachs K, Tuck CW (1968) Surface oxidation of steel in industrial furnaces. Proceedings of the conference reheating for hot working. Iron and Steel Institute, Publication No. 111, London, pp 1–17

Scully JC (1990) The Fundamentals of corrosion. Pergamon Press, Oxford

Swell PB, Cohen M (1964) The oxidation of iron single crystals around 200°C. J Electrochem Soc 111(5):501–508

Tomellini M, Mazzarano A (1988) High-temperature oxidation under time-dependent gas pressure: An application to steel oxidation. Oxid Met 29(3/4):179–191

Tominaga J, Wakimoto K, Mori T, Murakami M, Yoshimura T (1982) Manufacture of wire rods with good descaling property. Trans ISIJ 22:646–656

TSL (2000) OIM analysis user manual (ver. 3.07)

Wagner JB, Lawless KR Jr, Gwathmey AT (1961) T Metall Soc AIME 221:257–261

Watanabe Y, Ishii K (1995) Geometrical consideration of the crystallography of the transformation from α-Fe_2O_3 to Fe_3O_4. Phys Status Solidi A 150:673–686

Wright SI, Nowell MM (2002) Chemistry assisted phase differentiation in automated electron backscatter diffraction. Microsc Microanal 8(Suppl 2):682–683

Index

A
Aberrations, 3, 16, 54, 56, 60, 62
Accelerating voltage, 3, 7, 8, 9, 10, 76, 340, 341, 342, 365
Achsenverteilungsanalyse, 345
Acquisition speed, 14, 15, 124
Active rotation, 36, 37, 38
Adaptive mesh refinement, 158, 164
Adaptive orientation imaging, 13
Allotropic transformation, 317
Alpha-phase, 295, 317, 318, 319, 324
Aluminum, 3, 4, 19, 61, 62, 83, 142, 143, 207, 253, 264, 265, 268, 278, 317, 321, 331, 333, 335
Amphibole, 347, 351
Angle/axis system, 218
Angular resolution, 15, 27, 28, 30, 82, 119, 219, 233, 253, 260, 261, 263, 264, 265, 274
Anisotropy, 30, 155, 163, 169, 180, 298, 317, 319
Artifacts, 7, 9, 12, 15, 85, 93, 134, 195, 234, 237, 266, 267, 268, 269, 270, 274, 349, 350, 365, 366
Asymmetrical tilt grain boundaries, 225, 227
Auto correlation, 179, 237
Axis-angle parameter, 41–42

B
Background, 2, 4, 6, 7, 11, 15, 16, 17, 22, 30, 53–54, 57, 60, 62, 68, 72, 78, 82, 123, 139–140, 237, 343, 352
Backmapping, 12
Backscatter, 1–19, 21–32, 35, 53, 54, 59, 60, 62, 65, 75, 81–94, 97, 98, 110, 123, 139, 189, 194, 223, 231–247, 251, 263, 270, 278, 291, 318, 319, 320, 329, 339–344, 345, 361, 362
Backscattered electrons, 1, 8, 21, 23, 24, 25, 27, 28–30, 31, 53, 54, 59, 60, 62, 85, 86, 87, 88, 89, 90, 93, 110, 270, 319, 320, 340
Backscatter Kikuchi diffraction, 1, 10, 14, 17
Backscatter Kikuchi pattern, 1, 2, 4, 7, 8, 11, 12, 14, 15
Band contrast, 58, 88, 89, 348, 349, 350, 351
  thresholding, 89
Band-pass EBSD patterns, 61
Basal slip, 160, 161, 162, 298
Basal/transverse texture, 319
bcc shear texture, 306
Beam
  current, 8, 9, 10, 16, 113, 114, 120, 239, 347, 349, 365
  size, 8, 61, 260, 331
Bethe perturbation, 24, 25, 27
Bi-modal microstructure, 317, 318
Biomineral (hydrated), 339
Biomineralization, 356
BKD, 1, 10, 14, 17
BKP, 1, 2, 4, 7, 8, 11, 12, 14, 15
Bloch wave, 3, 22, 23, 24, 25, 26, 27
Blurriness, 58
Blurring, 59, 127, 233
Boundary
  length, 133, 218, 270
  plane, 109, 115, 118, 140, 203, 207, 212, 215, 216, 217, 218, 219, 220, 222, 223, 224, 225, 226, 227, 228, 353, 354, 355
Bragg angle, 3, 11, 17, 58, 75, 97, 232
Bragg diffraction, 58, 60
Bragg reflection, 3
Bragg's law, 3, 21
Brandon criterion, 203
Brass texture, 39, 40, 47
Brightness, 4, 8, 9, 16, 58, 68, 115
Bunge-Euler angles, 170, 171

Burgers relationship, 325
Butterfly peak, 12

C
Calcite, 345, 346, 347, 349, 350, 352, 354
Calibration, 5, 6, 7, 10, 12, 71, 82, 85, 87, 99, 106, 183–184, 185, 238, 258
Cameras, 5, 14, 82, 347
Capture angle, 55, 62, 68, 77, 233
Carbon coat, 341, 347
Cartesian vector, 114
C coefficients, 23
Ceramic composite, 339, 340, 341
Charge, 4, 5, 67, 255, 339, 340, 347
Charge coupled device, 5, 67
Chemical analysis, 35, 97, 303
Chemical composition, 321
  maps, 321–322
Chromatic aberration, 56, 60, 62
Circular harmonics, 46–47, 49, 50
Clay minerals, 347
Clinopyroxene, 347, 351
Clustering, 132, 148, 151, 177, 180, 205, 206
Clusters of grains, 201
  boundaries, 201, 205, 206
Coating, 4, 10, 339, 341, 347, 365
Cobalt, 332, 335
Coherent twinning, 118, 217, 221, 223
Coincident site lattice, 43, 203, 204, 216, 225, 335
Columnar microstructure of wüstite, 368, 380, 382
COM, 253–255, 345
Combinatorial materials science, 189–198
Combinatorial methods, 189–190
Computer integrated polarization (CIP), 345
Confidence index, 13, 334
Constrained shear, 302, 306, 307
Contamination, 4, 7, 8, 9, 10, 13, 19, 30, 65, 79, 88, 233, 237
Contrast, 1, 3, 4, 5, 13, 14, 16, 17, 25, 26, 27, 30, 53, 54, 57, 58, 60, 61, 62, 68, 72, 76, 77, 85, 87, 88, 89, 90, 92, 93, 94, 104, 110, 112, 126, 140, 141, 163, 183, 185, 209, 210, 211, 220, 228, 233, 235, 236, 268, 270, 278, 279, 282, 304, 309, 321, 340, 341, 346, 347, 348, 349, 350, 351, 354, 355, 368
Convergent beam electron diffraction, 3, 24, 232, 278
Cooling rate, 317, 318
Coordinate system, 13, 36, 37, 38, 41, 45, 46, 115, 134, 217, 294
Copper, 8, 17, 36, 39, 40, 42, 43, 44, 45, 47, 48, 49, 50, 82, 120, 174, 186, 187, 207, 216, 217, 226, 227, 228, 258, 278, 279, 282, 307, 309, 313, 333, 334
  texture, 36, 39, 40, 42, 43, 44, 45, 47, 48, 49, 50
Correlation(s), 1, 129, 132–133, 157, 177–187, 194, 195, 196, 201, 206, 211–212, 251, 258
  cross, 113, 181, 231, 233, 234–247
  function, 114, 157, 177, 178–179, 180, 181, 184, 185, 234, 236, 237
Creep mechanisms, 352
Critical scaling, 211
Crystal
  orientation map, 274
  plasticity, 158, 164, 165, 252, 301–302
  reference frame, 171, 219, 365
  structure, 3, 11, 12, 16, 83, 85, 86, 91, 97, 114, 118, 127, 189, 196, 225, 257, 298, 317, 319, 341
Crystallographic constraints, 205, 206–208, 212, 247
Crystallographic interface normal distribution, 134, 136
Crystallographic preferred orientations (CPO), 345
Crystallographic texture, 35, 36, 133, 169, 170, 201, 208, 296, 298, 302, 319, 377
C shear texture orientation, 281
Cube texture, 39, 40, 47
Cubic-orthorhombic, 170, 171
Cubic symmetry, 38, 71, 72, 85
Cumulative distribution function, 143
Cut-off energy, 55–56, 58, 60, 61, 62
Cutting scheme, 180, 181

D
Damage
  initiation, 162, 310
Data
  analysis, 113, 123, 190, 194, 197, 320
  collection and processing, 123–129
2D-3D relationships, 133, 139–140
3D depth resolution, 119
3-D EBSD, 2, 111, 119, 129, 133, 141
Debye-Waller factor, 13, 24–25, 27, 28, 31–32, 233
Deformation
  heterogeneity, 163, 165
  microstructures, 263, 264, 272
  stage experiments, 331–332
Depth of focus, 7, 10
Depth resolution, 3, 9, 19, 119, 260–261
Detectors, 9, 14, 65–68, 81, 320, 346

Diagenesis, 356
Diffraction
  pattern, 1, 2–3, 5, 6, 7, 8, 12, 13, 15, 16, 17, 21–32, 46, 53, 65, 66, 68, 69, 77, 81, 83, 84, 90, 91, 92, 93, 98, 104, 113, 115, 120, 189, 334, 339, 340, 341, 343
  vector, 59
Diffuse background, 53, 60, 62
Diffusion, 181, 190, 192, 193, 203, 209, 210, 211, 212, 301, 356, 362, 363, 367, 368, 369, 373, 376, 378, 379, 381, 382, 383, 390, 391, 392
Digitalbeam scan, 3, 5–7, 9, 10
Digital microstructures, 139, 140, 144, 149
Dimensionality, 139, 206
Discrete orientations, 35, 40–46, 49, 50
Dislocation
  boundaries, 263, 268, 272, 273
Disorientation, 123, 206, 222, 254, 277, 280, 281, 282, 284, 285, 286, 287, 354
Dispersion surface, 59
Distortion, 4, 5, 6, 7, 18, 55, 68, 70, 71, 72, 112, 113, 125, 134, 158, 164, 233, 267, 270, 348, 353, 354
3D orientation map, 114, 115, 116, 117, 118
3D orientation microscopy, 19, 110, 113, 115, 117, 119, 120
3D reconstruction, 2, 18, 82, 133, 134, 139–152, 194, 195
3D software, 114
Dual networks, 203, 204, 205, 207, 209
Duplex microstructure, 318, 319, 320, 321, 323, 326
Duration, 310–311, 313, 335
Dynamical diffraction, 22, 30, 31, 59, 68, 72, 98
Dynamical simulation, 21–32, 74
Dynamic deformation, 301, 302
Dynamic focusing, 6, 7, 10
Dynamic simulation, 21–32, 74
Dynamic theory, 302

E
EBSD step size, 221, 272
EBSP simulation, 68
ECP, 3, 53, 65, 66, 68, 232
Effective medium theory, 210, 211
Effective tensor, 35, 184–186
Eigen-microstructure, 178, 179
Eigenvalue, 24, 131
Eigenvector, 24, 131
Elasticity, 35, 140, 158, 165, 181, 182
Elastic scattering, 21, 22, 23
Elastic strain, 231, 232, 233, 242, 243
Electrodeposition, 115, 190
Electron
  channeling patterns, 3, 53, 65, 66, 68, 232, 345
  source, 55
Electron backscatter diffraction (EBSD), 1–19, 21–32, 35, 65, 81–94, 97, 98, 223, 231–247, 251, 263, 278, 291, 329, 339–344, 345, 362
Electrostatic lenses, 55
Ellipsoid, 130, 131, 133, 140, 141, 143, 144, 145, 146, 147, 148, 149, 150, 152
Energy dispersive spectroscopy (EDS), 1, 15, 81, 82, 83, 84, 85, 86, 87, 88, 89, 91, 97, 191, 320–321, 325, 339, 341, 342, 368
  thresholding, 86
Energy filter/filtering, 4, 30, 53–63, 68
  patterns, 53, 61
Environmental SEM (ESEM), 339, 340
Equal channel angular extrusion (ECAE), 271, 272, 273
Equal-channel angular pressing, 277, 278–282
Equiaxed microstructure, 270, 318, 320
Euler angles, 13, 45–46, 49, 50, 114, 126
Euler map, 354
Euler plot, 44, 45
Excitation volume, 7, 8, 16, 19
Extinction
  distance, 59
  rules, 3

F
Fast EBSD, 7, 13–15
Fast Fourier transform, 13, 157, 158, 162, 163, 165, 178, 179, 183, 184, 237, 251
Feldspar, 347, 349, 350, 351, 352, 353, 354
FE-SEM, 10
Fe-Ti oxide, 347, 356
FIB-EBSD, 110, 121
FIB-EBSD tomography, 110, 121
FIB-induced damage, 110, 124
FIB-OIM, 125
Field emission, 7, 8, 9, 56, 114, 264, 320, 329, 331, 365
Filtered orientation, 266
Filtered patterns, 53, 56, 57, 58, 61, 62
Filters, 54, 62, 129, 264, 267
Finite element simulation, 159, 162, 166, 194, 233
First-order bounds, 169, 171, 173

Five parameter analysis, 215, 224
Flat fielding, 7, 30, 82
Fluorescent screen, 53, 55, 56
Flyer plate, 310, 313
Focussed ion beam (FIB), 2, 16, 18, 56, 82, 109–121, 124, 125, 127, 128, 193, 195, 223, 232, 247, 261, 329, 330
  dual beam, 56, 223–224
Forescatter detectors, 346
Fourier coefficient, 24, 25, 27, 171, 172
Fourier series, 23, 46, 170, 171
Fourier transform, 13, 58, 125, 155, 157, 178, 183, 236, 237, 251
Friction stir welding/processing, 284, 291
Fundamental zone, 42, 43, 45, 129, 170, 218

G
Garnet, 68, 346, 347, 350, 351, 354, 355
Generalized spherical harmonics, *see* Harmonics
Geometrically necessary dislocation, 234, 247, 251, 252, 260
Geometrical set-up, 110–113
Gnomonic projection, 2, 68, 72, 97, 98
Gold, 10, 330, 347
Grain
  growth of iron oxide, 368–369
  instability, 307–309
  morphology, 141, 309, 313, 361, 381
  refinement, 277, 284–288
  size, 2, 3, 9, 10, 13, 36, 53, 61, 89, 121, 128, 129–130, 133, 139, 140, 143, 144, 147, 149, 151, 157, 165, 179, 180, 189, 190, 193, 194, 195, 196, 201, 206, 221, 222, 242, 271, 277, 278, 279, 281, 286, 287, 288, 291, 293, 302, 304, 308, 310, 331, 350, 370, 371–372, 378, 391
Grain boundary(ies)
  character, 139, 151, 152
  characterization, 7, 19, 219–221
  classification, 202, 212
  clusters, 205, 206
  connectivity, 205, 206
  correlations, 212
  crystallographic constraints, 206–208
  degrees of freedom, 152, 215
  high misorientation regions, 271, 272, 274
  inclination, 140
  low misorientation regions, 271, 272
  misorientation, 151, 299
  network, 201–212, 310, 391
  plane
    orientation, 218, 219, 222, 223
  properties, 151, 215, 219
  sliding, 299, 309, 354
  trace, 216, 217, 221, 223, 224, 294, 355
    reconstruction, 217, 218
  Σ-value, 216
Grain boundary character distribution (GBCD), 1, 135, 216, 218, 219, 221, 222, 223–224, 368
Green's function, 181, 182, 183, 184

H
Habit plane, 115, 227
Harmonics, 46–47, 48–49, 50, 170
Heating experiments, 329, 332, 333
Helium ion microscope, 18
Hematite, 361, 362, 366, 367, 371, 373, 381, 382, 383, 384, 389, 391, 392
Hexagonal-orthorhombic, 170, 172
Hexagonal symmetry, 100
Hexagonal-transversely isotropic, 170
High-angle boundary formation, 278, 284
High angle grain boundary fraction, 195, 254, 264, 269, 270, 282
Higher order Laue zones (HOLZ), 3, 24, 28, 76, 93, 368
  rings, 28, 76, 93, 107, 368
High-pass filter, 60, 61
High-pass patterns, 56, 60
High-pressure torsion, 277
High temperature
  deformation, 319, 355
  oxidation, 361–392
Homogenization
  and refinement, 286
  relation, 181
Hot rolling, 258, 319, 322–326, 361, 363, 384
Hough peak, 61, 340
Hough transform, 11–12, 61, 65, 74, 83, 107, 233, 234, 251
Hyperspherical harmonics, 48–49, 50

I
IBP, 8, 15–19
Image
  analysis, 93, 94
  quality, 5, 13, 92, 93, 115, 195, 251, 284, 322, 334, 362

Incipient spall, 310–312, 313
Incoherent twinning, 217
Indentation, 251
Indexing, 12–13
Inelastic scattering, 16, 21, 22, 23, 30, 32
Informatics, 194–196, 197
Information depth, 8, 9, 10, 119
In situ, 5, 13, 15, 18, 109, 166, 232, 320, 329–336, 368
In situ creep, 335
In situ deformation, 331, 332
In situ electromigration, 330
In situ focused ion beam (FIB), 2, 16, 18, 82, 110, 124, 193, 223, 232, 329, 330
In situ grain growth, 333
In situ heating, 329, 330, 332, 333, 334
In situ measurements, 320
In situ oxidation, 330
In situ phase transformation, 330
In situ recrystallization, 336
Intensity, 3, 4, 5, 6, 7, 8, 11, 12, 16, 17, 21, 22, 23, 24, 25, 26, 27, 30, 31, 32, 58, 60, 68, 72, 74, 82, 85, 91, 123, 134, 221, 224, 233, 236, 237, 238, 255, 313, 323, 324, 325, 326, 340, 341, 347, 352, 368, 371
Interaction volume, 3, 7, 8, 9, 331, 365
Interface normal distribution, 134, 136, 151
Interfaces, 14, 109, 114, 134, 192, 215, 216, 223, 277, 284, 285, 369, 377, 378, 379, 380, 381, 382, 384
Interfacial microstructures, 362, 377, 381
Intergranular misorientation deviation, 303, 305
Intergranular voids, 310, 313
Intermetallic, 90, 120
Inverse pole figure, 39, 40, 115, 116, 117, 118, 135, 208, 256, 259, 320, 321, 322, 353, 354, 362, 365, 369, 370, 371, 372, 373, 375, 376
Inversion, 74, 157, 179
Ion blocking patterns, 8, 15–19
Ion milling, 18, 110, 330, 347
Iron, 25, 57, 58, 60, 61, 65, 66, 193, 207, 216, 293, 294, 302, 313, 330, 332, 361, 362, 363, 364, 366, 367, 368, 369, 371, 373, 375, 376, 377, 378, 379, 381, 383, 388, 389
Iron oxide, 361, 362, 366, 368, 369, 373, 375, 377, 384, 388, 389
  cracks in, 384
  grain growth of, 368–369

K
Kernel average misorientation, 255, 303, 304, 305, 306, 308, 309, 310, 311, 312, 313, 314
Kikuchi bands, 2, 3, 12, 16, 17, 18, 21, 25, 26, 27, 28, 30, 54, 61, 68, 70, 72–74, 75, 77, 82, 85, 87, 89, 98, 99, 100, 102, 103, 104, 107, 232, 233, 349, 368
Kikuchi contrast, 53, 54, 58, 60
Kikuchi envelope, 3
Kikuchi line, 3, 11, 12, 25, 30, 31, 57, 58, 59, 60, 61, 62, 98, 104, 107, 367, 368
Kikuchi pattern, 2, 3, 4, 6, 7, 8, 10, 11, 12, 13, 14, 15, 25, 30, 58, 59, 60, 97, 321, 366, 367, 378
Kinematical, 3, 68, 72, 74, 88
Kossel cones, 97, 98

LaB_6, 9, 10
Lamellae, 114, 115, 116, 119, 317, 318, 319, 320, 321, 322, 323, 326
Lamellar microstructure, 155, 318
Large-strain extrusion machining, 277
Lateral resolution, 112, 119
Lattice
  symmetry, 100
  vibration, 13, 60
Lattice preferred orientations (LPO), 345, 347, 350, 351, 352, 353, 355, 356
Localization, 11–12, 15, 61–62, 158, 160, 165, 182, 183, 184, 301–314
  tensor, 182–184
Local strain, 183, 231, 232, 307, 313
Lognormal distribution, 144
Low angle boundary, 203, 293, 295, 299
Low energy electron diffraction (LEED), 55, 62
Low energy electrons, 4, 57
Low-loss electrons, 30
Low vacuum, 10, 339–343, 347

M
Machining, 210, 258, 277, 278, 282–284, 285, 287
Magnetite, 361, 362, 363, 364, 366, 367, 369–371, 372, 373, 375, 377, 378, 379, 381, 382, 383, 384, 385, 386, 387, 388, 389, 390, 391, 392
Matrix rotation, 13, 36, 40, 41
Mechanical polishing, 110, 121, 124, 128, 347
Mechanical stage, 5–7, 9
  scan, 6, 7
Mesa, 239, 240, 241, 242

Mesh refinement, 13, 156, 158, 160, 161, 162, 163, 164
Metamorphic rock, 355
Meteorites, 347, 356
MgO, 135, 217, 224, 225, 347, 354
Mica, 351
Micromechanical model, 158–159
Microstructural refinement, 264, 271–273, 274, 291, 299
Microstructure
  characterization, 166, 291
  evolution, 278, 284, 323
  function, 178, 183, 187
  generation, 140, 157–158
  gradients, 114, 193
  hull, 169, 187
  reconstruction, 110, 141, 156, 350
  sensitive design, 46, 169–175, 177–187
Mineral, 10, 65, 340, 345, 346, 347, 349, 350, 351, 352, 354, 355, 356, 389
Mis-indexing, 85, 346, 347, 348–350
Misorientation
  distribution function, 133, 151
Modified Kuwahara filters, 266
Monte Carlo, 22, 30, 54, 59, 142, 143–145, 149, 183, 186
Monte Carlo simulations, 22, 30, 54
Morphological descriptors, 129–133, 151
Morphological texture, 307
Moving screen method, 5
Multi-phase, 82, 163
  analysis of iron oxides, 366–368
Multiples of a random distribution (MRD), 136, 221, 222, 223, 224, 225, 227, 228

N

NaCl, 224–225, 228, 347
Nanocrystalline, 115–119
Nanomaterial, 7, 19
Neo-Eulerian mapping, 41, 42, 43, 44
Nickel superalloys, 335
Nonconductive, 339, 340, 341, 342
Non-indexing, 348, 349
Normal-incidence filter, 54, 55
n-point correlation, 177

O

Observation-based domain constraint, 142, 145–147
ODF, 9, 19, 133, 151, 169, 170–172, 306, 307, 365
Offline, 15, 320
Olivine, 346, 347, 348, 350, 351, 352, 354, 356
Orientation
  contrast, 1, 13, 16, 17, 19, 76, 346
  correlation, 1, 19
  discrete, 35, 40–41, 44, 45, 46, 49, 50, 145
  distribution function, 19, 45, 46–47, 49, 133, 151, 157, 165, 169, 170, 177, 306, 320, 365
  filtering, 266–268
  image, 113, 254, 259, 260, 279–285, 297
  map, 1, 4, 7, 9, 97, 109–121, 197, 217, 253–256, 261, 264, 267, 268, 269, 271–272, 311, 331, 334, 345, 346, 349, 352, 354, 357, 365, 372
  microscopy, 8, 9, 14, 15, 17, 18, 19, 109–121
  noise, 265–268, 270, 274
  probability distribution, 145
  relationship in high temperature oxidation, 361–390
  spread, 256, 257, 265, 266, 308, 331, 334, 353–354
  stereology, 1
Orientation imaging microscopy (OIM), 13, 179, 253, 278, 329, 361–390
Orthographic projection, 44
Overlayers, 62, 330
Oxidation of iron oxide, 361–363, 377
Oxide
  defects, 361–362
  microstructure, 361–362, 365, 366, 369, 371–373, 390, 392

P

Parameterization, 24, 40–46, 218–219, 266
Passive rotation, 37, 45
Pattern(s)
  center, 5, 6, 10, 91, 106, 343
  indexing, 8, 15, 333
  quality, 6, 9, 10, 13, 15, 115, 233, 332, 335, 348–351, 354, 367, 368, 378
  rotation, 251, 253–255
  sharpness, 58, 126
  shift, 231, 233, 234, 235–238
Pearlite, 114–116, 119
Percolation, 202, 204–212
Perovskite, 159, 347
Perturbation expansion, 181, 184
Phase
  discrimination, 13, 84, 85, 97, 98, 341
  identification, 1, 5, 28, 75, 81–94, 97–107, 189, 192, 196, 341, 367, 368, 392

instability, 301, 302, 305, 307–309
morphology, 85
β-phase, 295, 296, 317, 318, 319, 320, 326
Phosphor, 2–5, 8, 9, 10, 14, 17, 21, 23, 53, 57, 67–68, 70, 71, 72, 78, 237
Phyllosilicates, 347, 357
Pixel binning, 14, 82
Plagioclase, 75, 349, 350, 351, 352, 353, 354
Plane strain cutting, 282
Plasticity, 35, 158, 162, 164–165, 251–253, 258, 261, 301, 332
2-point correlation, 177, 178–179, 180, 181, 187
3-point correlation, 179
1-point statistics, 169, 170, 177
2-point statistics, 178, 179, 180, 181
Pole figures, 9, 19, 38–40, 47, 115, 280–285, 297, 298, 306, 319, 323, 324, 325, 332, 333, 365, 370, 371, 373, 375, 376
inversion, 157
Polishing, 18, 93, 110, 112, 117, 120, 121, 124, 127, 128, 261, 279, 320, 347, 364–366
Polyphase, 140, 349, 350–351
Porosity, 348, 356
Post-processing, 53
filtering, 267–268
Primary alpha, 318, 324–325, 326
Probability density, 23–25, 47–50, 161, 170
Probability distribution function, 143
Processing, 123–136
Projection, 36, 38, 44, 48, 73, 172, 222, 224, 225, 226, 227
Property
closure, 172–175, 184, 186, 187
contrast, 209, 210, 211
Pulse duration, 310, 311, 313
Pyrite, 347, 356
Pyroxenes, 346, 347, 350, 351

Q

Quadruple nodes, 201, 203, 204, 205
Quartz, 66, 75, 345, 346, 347, 351, 352, 354, 356
Quaternion, 42–45, 48, 49, 203, 266–267

R

Radon transform, 11–13, 15, 19
Random grain boundary, 208, 216
Reciprocity principle, 22–23
Reconstruction, 18, 36, 134–136, 139–152, 195, 217, 218, 312, 313
Recovery, 234, 277–278, 301, 302, 303, 333, 335, 354
Recrystallization, 7, 19, 121, 140, 151, 152, 278–279, 282, 287–288, 292, 295, 296, 297, 302, 332, 333–336, 345, 354
Reflection high energy electron diffraction (RHEED), 56, 65, 77–79
Registration, 124–126, 216
Residual strain, 234
Resolution, 7–9, 119–120, 265–266, 347–348
Retarding grid, 54, 55
RHEED, 56, 65, 77–79
Rigid-viscoplastic, 155, 158–159, 163
Rocking curve, 59
Rodrigues space, 42, 43, 44, 157
Rodrigues vector, 42, 43, 44
Rotation, 36–37, 44, 111, 116, 235, 239, 240, 244, 253–255
matrix, 13, 36, 40, 41

S

Sample
geometry, 39, 258, 302, 303, 307, 332
preparation, 1, 13, 15, 18, 81, 120, 193, 330, 347, 363, 364–365, 366
thickness, 59
Scaling laws, 206, 211
Scanning electron microscope, 1, 53–54, 55, 65, 81, 97, 124, 223, 264, 320, 329, 339, 345–346
Scanning ion microscope, 8, 16, 17, 18
Scanning transmission electron microscopy, 76–77
Scattering, 1, 6, 8, 10, 16, 17, 21–23, 24–25, 26–27, 30–32, 58–61, 120
Schottky field emission
gun, 57
Schrödinger equation, 23, 24
Secondary alpha, 318, 319, 325–326
colonies, 318, 321, 323
Secondary electrons, 16, 18, 53, 54
Secondary phases, 90, 91, 93
Segmentation, 126–127, 128, 131, 135, 136, 141, 218
Seismic velocity, 352
Selected area electron channeling patterns (SAECP), 345, 346, 355
Serial sectioning, 35, 109–121, 123–124, 130, 134, 135, 139, 194, 212, 215, 216–217, 223, 225, 329
Severe plastic deformation, 237, 277–288
Shape distribution, 19, 143, 144, 145, 146, 147, 149–150, 201

Sharpness, 13, 58, 74, 126, 136
Shear
  band, 271, 301–302, 313
  direction, 279, 281–282, 292, 297, 303, 306, 307, 308, 309
  localization, 301–314
  plane normal, 297, 306
  simple, 195, 196, 278, 296–299, 302, 303, 305–307
  texture, 281, 282, 283, 284, 287, 297, 306, 307
  zone, 302, 313
Shock
  damage, 301–314
  loaded, 310, 313
  loading, 301, 302, 309–310
Sigma grain boundaries, 217, 223–224, 226, 227–228
Simple shear, 195, 196, 278, 296–299, 302, 303, 305–307
Simulation, 21–32
  of EBSD data, 68, 155–166
Single crystal, 2, 6, 9, 10, 16, 35, 38, 40, 58, 60, 61, 68, 75, 171, 237, 238, 239, 242, 252, 253, 254, 255, 260, 261, 265, 310, 329, 340, 342–344
Size distribution, 121, 143, 146, 147, 148, 149, 151, 207
Slice alignment, 119
Slip systems, 158, 159, 160, 161, 162–163, 165, 173, 253, 352, 354–355
Spall, 301, 302, 310–314
Spallation, 302
Spatial resolution, 1, 3–4, 6, 7–9, 16, 18, 46, 62, 68, 81, 83, 109, 119, 166, 231, 232, 234, 247, 263, 329, 347–348
Special grain boundary, 206, 207, 210, 212, 228
Specimen tilt, 1, 3, 4, 6, 7, 9, 14, 17
Spectral representation, 170, 171
Speed, *see* Acquisition speed
Spherical angle, 41, 48, 218, 219
Spherical EBSD, 134
Spherical filter, 54, 55, 59
Spherical harmonics, 47–51, 170
Spherical kikuchi maps, 65–79
Spherodization, 318
Spot size, 3, 8, 10, 19, 91, 341, 342, 365
Stage, 5–7, 332–333, 335
Standard stereographic triangle, 38, 40
Statistical description, 141–142, 204
Statistically significant dislocations, 234, 247, 251–253, 259–261
Statistical parameter, 13, 38, 39, 61, 74, 81, 82, 133, 139–140, 141, 143, 148, 204–205
Stereographic projection, 36, 38–39, 44, 47, 116, 134, 224, 225, 226, 227
Stereological analysis, 218–219, 221–224
Stereology, 1, 7, 121, 219–221, 224, 227
Stopping power, 61–62
Strain
  mapping, 231–247
  measurement, 75, 231–233, 247
  path, 277–278, 279, 282, 307
Stress, 82, 156, 160, 162, 163, 182, 183, 195, 196, 212, 231, 232, 234, 235, 242, 287, 301, 302, 310, 313, 317, 319, 329, 331, 386, 388, 389, 392
Structure
  determination, 3, 12, 16, 24, 26, 30, 32, 91–92, 97–98, 109–110, 114
  of interfaces in iron oxide, 377–384
Structure-property relations, 172, 192, 197, 203, 206, 209, 210, 211, 302
Subgrain, 156, 202, 207, 208, 255, 274, 277, 331, 345, 349, 353, 354, 355
Superplastic, 277–278, 288, 299, 335
Symmetrical tilt grain boundary, 225, 227
Symmetrized harmonics, 49–50
Symmetry, 70, 71, 84, 97–107, 170, 189, 240–241, 366
Synchrotron X–ray diffraction, 81, 258, 260
Synthetic microstructures, 139, 143, 150, 152, 157

T

Tantalum, 309–310, 313
TEM–EBSD comparison, 268–270
TEM–orientation measurements, 7–9, 268–270
Tensile stage, 329, 335
Texture
  evolution, 175, 282, 295, 306, 307, 317, 323–324
  hull, 169, 171, 172, 174
  iron oxide, 377, 390
  separation, 317–326
Thermal diffuse scattering, 60–61
Thermionic gun, 9, 10
Thin sections, 90–91, 345, 346
Three-dimensional, 2, 23, 35, 36, 40, 43–44, 99, 109–121, 123–136, 155–158, 166, 172, 194, 202, 206, 212, 217, 233, 260, 310, 311–312, 313, 329
Ti-6Al-4V, 156, 165, 295, 296, 317–326, 331

Titanium alloys, 139, 155, 156, 158, 317–326
Tophat sample, 302, 303, 306, 307, 308
Topology, 201, 202, 203, 204, 209, 211, 332
Toroidal filter, 56
Trace analysis, 217–218
Transformation matrix, 101, 125, 171
Transmission electron microscopy (TEM), 1, 23, 26, 30, 53, 76–77, 278, 286, 288, 345, 377
Transmission Kikuchi diffraction, 6, 7, 8, 12
β-transus, 295, 317, 318, 319
Transverse texture, 319
Triclinic, 98–107, 354
Trigonal, 97, 100, 102, 104–106
Triple junction(s), 43, 125, 195, 201–207, 217, 218, 266, 274
  distribution, 206
  mathematical constraints, 204
T-type texture, 319, 324–325
Twin boundary, 118
Twinning, 156, 166, 206–208, 217, 228, 332
Twin related domains, 207, 212
Twist grain boundary, 217, 224, 225, 228

U
Udimet (cobalt-nickel-chromium-tungsten alloy), 335
Unfiltered patterns, 57, 58, 61
Unit cell, 2, 23, 24, 25, 91, 98–100, 101–102, 104, 107, 368
Universal stage, 345, 353, 355

V
Vacuum, 2, 5, 10, 13, 24, 65, 66–67, 330, 339, 340–341, 343, 347, 363
Vapor pressure, 340–341, 342
Variable pressure SEM, 10, 347
Viscoplasticity, 155, 159, 162, 163
Void sheeting, 311
Voids in magnetite, 388
Volume fraction, 8, 82, 89, 94, 116, 133, 140, 147, 151, 156–157, 158, 159, 169–175, 177, 180, 183, 184, 185, 186, 317, 318, 319, 320, 323, 324

W
Wave
  function, 22–24, 25
  vector, 23, 24, 25, 30–31
Wavelength, 1, 3, 7, 16, 57, 58, 81, 180, 234
Wavelength dispersive spectroscopy (WDS), 1, 81, 83
Welds, 258, 291
Wüstite, 361–382, 386–392

X
X-ray diffraction, 9, 81, 91, 97, 121, 157, 201, 212, 232, 258, 260, 302–303, 319, 342, 365, 368, 375
X-ray pole figure, 1, 9
X-ray spectroscopy, 811